3.4.5 Number of research papers per teacher in the Journals notified on UGC website during the year

Title of paper	Name of the author/s	Department of the teacher	Name of journal	Year of publication	ISSN number	Link to the recognition in UGC enlistment of the Journal
Reliable Load Balanced Routing Policy using Bayesian Optimization for SDN-IoT Applications	G.Seshadri Sekhar	CSE	Intelligent Systen and Applications in Engineering(ijisae) Vol:12,No:3(2024) DOI:24/03/2024	2024	2147-6799	https://ijisae.org/index.php/IJISAE/article/view/5269
Reliable Load Balanced Routing Policy using Bayesian Optimization for SDN-IoT Applications	P.Suresh	CSE	Intelligent Systen and Applications in Engineering(ijisae) Vol:12,No:3(2024) DOI:24/03/2025	2024	2147-6799	
Deep Learning based image caption genereation using VGG16 and LSTM	Dr.T.Sree Lakshmi	CSE	Tec Empresarial	2024	2481–2491,	https://revistas.tecac.cr/index.php/tec_empresarial/article/view-2024/2481
Enhancing brain tumor classification: Leveraging Pre-trained CNN models for efficient MRI Imge Analysis	Dr.N Sudhakar Reddy	CSE	International Neurourology Journal		P-ISSN 1659-2395 E-ISSN 1659-3359	

Modelling and Fabrication of Security Gadget for Tirumala	Dr.N Sudhakar Reddy	CSE	2nd World Conference on Information Systems for Business Management, NOVOTEL Bangkok on SIAM Square, Bangkok, Thailand	2023	Proceedings of ISBM 2023	https://link.springer.com/chapter/10.1007/978-981-99-8612-5_9
A miniaturized-slotted planar MIMO antenna with switchable configuration for dual-/triple-band notches	Dr.C.Chandrasekhar	ECE	AIP Advances	2024	2158-3226	https://www.scopus.com/sourceid/19900193962
Hierarchically porous polyaromatic carbon spheres decorated NiMn2O4 nanocomposite: efficient selective azo dye degradation from aqueous water and reduction of p-nitrophenol to p-aminophenol	Dr T Kaliraja	ECE	Carbon Letters	2024	1229–1237	https://www.scopus.com/sourceid/21100398885

CNN-based detection of cervical spinal cord injury	Dr G Chandraiah	ECE	International Journal of Medical Engineering and Informatics	2023	1755-0661	https://www.scopus.com/sourceid/19700175025
Image Segmentation based on Energy Fitting Models - A review	Dr C. Raju	ECE	International Journal on Recent and Innovation Trends in Computing and Communication	2023	2321-8169	https://www.scopus.com/sourceid/21101089961
Hybrid Cryptography and Steganography-Based Security System for IOT Networks	Dr C.Padma	ECE	International Journal On Recent and Innovation Trends In Computing and Communication	2023	2321-8169	https://www.scopus.com/sourceid/21101089961
Lifting Wavelets with OGS for Doppler Profile Estimation	P.Suresh Babu	ECE	International Journal of Electrical and Electronics Research	2023	2347-470X	https://www.scopus.com/sourceid/21101067520
Enhancing 5G Sub-3.5GHz Networks through optimization of microstrip Antenna Arrays with sequential rotation-based MIMO using Machine Learning Techniques	Dr K Raveendra	ECE	Journal of Electrical Systems	2024	1112-5209	https://www.scopus.com/sourceid/19700186890

Fault Prediction and Awareness for Power Distribution in Grid Connected RES using Hybrid Machine Learning	Dr K Raveendra	ECE	International Journal of Electric Power Components and Systems	2024	1532-5016	https://www.scopus.com/sourceid/16031#tabs=2
Streamlining Cancer Diagnosis & prognosis system using Hybrid CNN-NPR:Deep learning approaches	Dr.G.Sujatha	ECE	International Journal of intelligent systems and Applications in Engineering	2023	2147-6799	https://www.scopus.com/sourceid/21101021990
PAPR reduction using polynomial based compressing with Rapp model in GFDM	Dr.G.Sujatha	ECE	e-Prime - Advances in Electrical Engineering, Electronics and	2024	2772-6711	https://www.scopus.com/sourceid/21101132922
Clinical Healthcare Applications:Efficient Techniques for Heart Failure Prediction Using Novel Ensemble Model	Dr.G.Sujatha	ECE	Journal of Information Technology Management	2024	2980-7972	https://ugccare.unipune.ac.in/Apps1/User/WebA/Search

Lightweight APIT with Bat Optimization with Simulated Annealing Localization for Resource-Constrained Sensor Networks	T.Swarnalatha	ECE	Wireless Communications and Mobile Computing	2023	1530-8677	https://www.scopus.com/sourceid/17543#tabs=2
A Novel DV –HOP and APIT localization algorithm with BAT-SA algorithm	T.Swarnalatha	ECE	MDPI-Engineering Proceedings	2023	2673-4591	https://www.scopus.com/sourceid/21101128137
Functional analysis in the body environment for a circularly polarized hybrid reconfigurable textile antenna	Dr. S. Salma	ECE	Physica Scripta	2023	1402-4896	https://www.scopus.com/sourceid/29122
Design of Three-valued Logic Based Adder and Multiplier Circuits using Pseudo N-type CNTFETs	Dr.D.Srinivasulu Reddy	ECE	International Journal of Electrical and Electronics Research	2023	2347-470X	https://www.scopus.com/sourceid/21101067520
Unmanned Aerial Vehicle Design for Smart City Application	Dr.K.Lokesh Krishna	ECE	International Journal on Recent and Innovation Trends in Computing and Communication	2023	2321-8169	https://www.scopus.com/sourceid/21101089961

A Rail-To-Rail and Low Offset Novel Strongarm Comparator Circuit for Low Power Data Converter Architectures	Dr.K.Lokesh Krishna	ECE	International Research Journal of Multidisciplinary Scope	2024	2582-631X	https://www.scopus.com/sourceid/21101184716
Design and performance analysis of a novel vulture based FOPID controller for the nonlinear biological system	Dr.K.Lokesh Krishna	ECE	Scientific African	2023	2468-2276	https://www.scopus.com/sourceid/21100904987
Input Voltage-Level Driven Split-Input Inverter Level Shifter for Nanoscale Applications	Dr.V.Madhurima	ECE	MDPI-Electronics	2024	2079-9292	https://www.scopus.com/sourceid/21100829272#tabs=2
Face Recognition using computer vision and CNN algorithm	Dr T ChandraSekhar Rao	ECE	International Journal of intelligent systems and Applications in Engineering	2023	2147-6799	https://www.scopus.com/sourceid/21101021990
Optimal Deep Transfer Learning Enabled Object Detector for Anomaly Recognition in Pedestrian Ways	Allabaksh Shaik	ECE	Intelligent Decision Technologies	2024	1875-8843	https://www.scopus.com/sourceid/21100211724

Leveraging YOLOv5s with Optimization Based Effective Anomaly Detection in Pedestrian Walkways	Allabaksh Shaik	ECE	Expert Systems Wiley Publishers	2024	1468-0394	https://www.scopus.com/sourceid/24185#tabs=2
Efficient Extraction and Automated Thyroid Prediction with an Optimized Gated Recurrent Unit in Recurrent Neural Networks	Dr S Murali Krishna	**IT**	International Journal on Recent and Innovation Trends in Computing and Communication	Vol. 11, Sept. 2023	2321-8169	https://doi.org/10.21203/rs.3.rs-2319272/v1
BLDA-CSWDT Autoimmune Thyroid Disease Risks Predictive Model Using Machine Learning And Deep Feature Extraction Techniques	Dr S Murali Krishna	**IT**	International Journal of Biomedical Engineering and Technology	Vol.43, 2023	1752-6426	https://doi.org/10.1504/IJBET.2023.133791
End to End Image Privacy Method Using Customized Generative Adversarial Networks	Dr S Murali Krishna	IT	Journal of Data Acquisition and Processing	Vol. 39, 2024	1004-9037	https://sjcjycl.cn/ DOI:10.5281/zenodo.7546499
Sentimental Analysis of Movie Reviews Using NLP Techniques	K. Naresh	IT	IEEE Explorer	Aug 28 2023	979-8-3503-21	https://doi.org/10.1109/ICIRCA57980.2023.10220783

Experimental investigation and mechanical characterization of Al 5051with nickel/titanium powder metal matrix composites using stircasting	Dr. M.Chandra sekhara reddy	ME	Multiscale and Multidisciplinary Modeling, Experiments and Design, Springer Nature	Nov-24	Electronic ISSN 2520-8179 Print ISSN 2520-8160, 8, 77 (2025).	https://doi.org/10.1007/s41939-024-00680-4
Enhancing Mechanical Properties of Composites Through Hybridization with Bio-composites	Dr. Guru Mahesh	ME	Springer Proceedings in Materials, National Conference on Advancement in Materials Processing Technology	Oct-24	Online ISBN 978-981-97-6875-2, Volume 58	https://doi.org/10.1007/978-981-97-6875-2_9
Experimental and Numerical Analysis of Natural Fillers Loaded and E-Glass Reinforced Epoxy Sandwich Composites	Dr. Renugadevi K	ME	Journal of Materials Research and Technology, Elsevier Publication	Aug-24	Volume 32, September–October 2024, Pages 1235-1244, Online ISSN: 2214-0697 Print ISSN:	https://doi.org/10.1016/j.jmrt.2024.07.142
Investigation on Material Selection and Optimization for Enhanced Performance in Earth Tube Heat Exchangers	Dr. Vamsi Krishna Mamidi, Dr. Jagath Narayana Kamineni	ME	International Conference on Internet of Things and Connected Technologies, Artificial Intelligence in Internet of Things (IoT): Key Digital Trends, Springer Conference Series	Oct-24	pp 151–165,Online ISBN 978-981-97-5786-2	https://doi.org/10.1007/978-981-97-5786-2_12

Peel test and abrasive resistance experimentation on polycarbonate aluminium material	N. Balaji Ganesh, C. P. Balaji,	ME	Interactions Conference Proceeding, Springer Series	Aug-24	Electronic ISSN 3005-0731, Volume 245, article number 223	https://doi.org/10.1007/s10751-024-02029-2
Evaluation of material removal rate on tin composite using electro chemical and laser machining processes	Ravi Roopkumar, P. Karunya Moorthy	ME	Interactions Conference Proceeding, Springer Series	Aug-24	Electronic ISSN 3005-0731, Volume 245, article number 236, (2024)	https://doi.org/10.1007/s10751-024-02069-8
A Review of the Mechanical Properties of Biochar-Reinforced Aluminium 7075/SiC Composites	Dr. Gadham Setty Guru Mahesh	ME	IOP Conference Series, Journal of Physics, Volume 2837, 6th International Conference on Advancements in Materials and Manufacturing	Junly, 2024	ISSN: 1742-6596	10.1088/1742-6596/2837/1/012050
Modeling, fabrication, and burst testing of type-IV 3D printed plastic liner composite overwrapped pressure vessels	Dr. Jagath Narayana Kamineni	ME	International Journal on Interactive Design and Manufacturing (IJIDeM)	May-24	ISSN 1955-2513, May, 2024	https://doi.org/10.1007/s12008-024-01885-0

Enriching mechanical, wear, and corrosion behaviour of SiO/TiO reinforced Al 5754 alloy hybrid composites	Dr. Vamsi Krishna Mamidi	ME	Materials Letters/ Elsevier	February, 2024	Volume 361, p.136106/ ISSN: 1873-4979	https://doi.org/10.1016/j.matlet.2024.136106
Optimal Abrasive Jet Machining Parameters for Glass Fiber Reinforced Plastics	Dr. Rajesh N	ME	Journal of Polymer and Composites/ SDM Journals	Dec-23	Volume 11/ ISSN: 2321–2810,	https://doi.org/10.37591/JoPC
Experimental Analysis of the Mechanical and Machining Properties of an Aluminium Hybrid Metal Matrix Composite	Dr. Vamsi Krishna Mamidi	ME	Key Engineering Materials / Trans Tech Publications Ltd, Switzerland	Dec-23	Vol. 971, pp 3-12/ ISSN: 1662-9795	https://doi.org/10.4028/p-c3VwHP
Parameter Optimization for Electrical Discharge Machining of Stir Casted AA6063/Nano-SiC with Graphite Hybrid Composite Materials by Using Response Surface Methodology	Dr. M Vamsi Krishna	ME	Nano World Jounral	Sep-24	Volume 9 Supplement 3, 2023	https://doi.org/10.17756/nwj.2023-s3-012

Optimization of machining parameters & studies on characteristics of Monel k400 alloy using abrasive water jet Machining using ANFIS	Dr. Rajesh N	ME	Materials Today: Proceedings	Sep-23	Sep 2023, ISSN 2214-7853	https://doi.org/10.1016/j.matpr.2023.08.376
Investigation of the microstructure and mechanical properties of borosilicate reinforced magnesium nano composites	Dr. Jagath Narayana Kamineni	ME	Materials Today: Proceedings	Jul-23	July 2023, ISSN 2214-7853	https://doi.org/10.1016/j.matpr.2023.05.628
Chip morphology analysis in Al6061/CNT drilling with carbide and nano coated drills	Dr. Rajesh	ME	Materials Today: Proceedings	Jul-23	July 2023, ISSN 2214-7853	https://doi.org/10.1016/j.matpr.2023.05.389
Synthesis and characterization of silicon dioxide reinforced AZ91D magnesium composites	Dr. M.Chandra sekhara reddy	ME	Materials Today: Proceedings	Jun-23	June 2023, ISSN 2214-7856	https://doi.org/10.1016/j.matpr.2023.05.626

An equilibrium optimizer with deep recurrent neural networks enabled intrusion detection in secure cyber-physical systems	Dr Ch Santhaiah	**Cyber Secu**	AIMS Mathematics	26/03/2024	11718–11734.	https://www.aimspress.com/article/doi/10.3934/math.2024574
A Hybrid Approach using CNN and DQN Technique for Diagnosis Pneumonia in Chest X-Ray Images	Dr.Jasmine Sabeena	**Cyber Secu**	IJRITCC	13-08-2023	2321-8169	https://ijritcc.org/index.php/ijritcc/article/view/7631
Fault Detection and Diagnosis in Electric Vehicle Systems using IoT and Machine Learning: A Support Vector Machine Approach	Dr.Jasmine Sabeena	Cyber Secu	Journal of ElectricalSystems	13/03/2024	1112-5209	https://journal.esrgroups.org/jes/article/view/1414/1129
Fabrication of phase-pure and large-grained Cu3BiS3 films by a two-stage process for thin film solar cells	Dr.K.N.Chidamabara kumar	S & H	Solid State Sciences	26/03/2024	151 (2024) 107522	
Palladium-platinum nanostructures from fenugreek extract for Suzuki coupling reaction	Dr.K.N.Chidambara kumar	S & H	Inorganic Chemistry Communications	Feb-24	162 (2024) 112177	
Structural and Temperature Dependent-Magnetic and Dielectric Properties of CoNdxFe2−xO4 (0 ⩽ x ⩽ 0.1) Nanoparticles	Dr. K .Mohan babu	S & H	*ECS Journal of Solid State Science and Technology, 2024 13 023003*	Feb-24	Volume 13,number 2	

FTIR SPECTROSCOPY AND DIELECTRIC PROPERTIES OF RECONSTITUTED BUFFALO POWDERED MILK WITH WATER	Dr. N.Manohar reddy	S & H	Chelonian Conservation And Biology	Nov-23	| ISSN - 1071-8443 Vol. 18 No. 2 (2023	
Observations on the structural piezoelectric and impedance properties of cation-(La and Sn) modified lead zirconium titanate ceramics	Dr.P.Geetha	S&H	J Mater Sci:Mater Electron	Oct-2024	0957-4522	
Green synthesis of Mesona Blumes gum capped silver nanoparticles and their antioxidant, antibacterial and catalytic studies	Dr P. Babu	S&H	Materials Advances	Sep-23	2633-5409	
Two-stage-processed AgSbS2 films for thin-film solar cells	G. Manjula	S&H	Materials Science in Semiconductor Processing	August 2023	1369-8001 Volume 168 Page no.107821	

Spectroscopy and absolute photoluminescence quantum yield of Eu3 - doped zinc-tellurite glasses for solid state lightning applications	Dr.N.Manohar reddy	S&H	Physica B: Condensed Matter	July 2023	0921-4526 Volume 666	
PROPERTIES AND GENERALIZED SCHEME FOR PRODUCTION OF MILK POWDER	Dr.N.Manohar reddy	S&H	Journal of Advanced Zoology	June 2023	0253-7214 Volume 44 Issue 3 1373-1380	
DNA TRIKKY Based Security Mechanism for Radio Frequency Identification Protocol	Dr.K.Kumar	(Data Scier	IETE Journal of Research	2024	0974-780X	https://doi.org/10.1080/03772063.2024.2350933
Natural Language Processing: Bridging the Gap between Human Language and Machine Understanding	Dr.K.Kumar	(Data Scier	IEEE Explorer	2024	ISBN:979-8-3503-8428-4	https://doi.org/10.1109/TQCEBT59414.2024.10545250

An Empirical Review of HR Practices and Modernization in India's Retail Sector	Dr.Toopalli Sirisha	MBA	Journal of Management Research and Analysis, 2024;11(2):71–76,	2024	SSN: 2394-2770	https://doi.org/10.18231/j.jmra.2024.014
Fuel Cell Fed Electrical Vehicle Performance Analysis with Enriched Switched Parameter Cuk Converter	Dr. V Lakshmi Devi & Dr. Kumar K	EEE	RECENT ADVANCES IN ELECTRICAL & ELECTRONIC ENGINEERING	7/3/2023	10.2174/2352096516666230607125137	SCI
Design and implementation of hybrid MPPT controller for FC based EV system with boost DC-DC converter	Dr. SHAIK RAFI KIRAN	EEE	Journal of Intelligent & Fuzzy Systems	7/31/2023	https://content.iospress.com/search?q=author%3A%28%22Devadasu%2C+G.%22%29	SCI
Design and performance analysis of hybrid MPPT controllers for fuel cell fed DC-DC converter systems	Dr. SHAIK RAFI KIRAN	EEE	ELSEVIER : ENERGY REPORTS	Dec-23	https://doi.org/10.1016/j.egyr.2023.05.030	SCI

Economic Load Dispatch with Practical Constraints using Mountaineering Team-Based Optimization Technique	Dr. Y V Krishna Reddy	EEE	International Journal of Intelligent Systems and Applications in Engineering (IJISAE)	03-09 September 2023	2147-6799	SCOPUS
Power Quality conditioning using Two-level buck inverter based D-STATCOM	P Suneetha	EEE	INternational Journal of Applied Power Engineering (IJAPE)	-	Accepted for Publication	SCOPUS
Design and performance analysis of hybrid optimization MPPT controller for proton exchange membrane fuel cell system with DC-DC converter	Dr. SHAIK RAFI KIRAN	EEE	ELSEVIER Materials Today: Proceedings	7/26/2023	https://doi.org/10.1016/j.matpr.2023.07.077	WOS

AIMS Mathematics
2024, Volume 9, Issue 5: 11718-11734. doi: 10.3934/math.2024574
Research article | Special Issues

Previous Article Next Article

An equilibrium optimizer with deep recurrent neural networks enabled intrusion detection in secure cyber-physical systems

E Laxmi Lydia [1], Chukka Santhaiah [2], Mohammed Altaf Ahmed [3], K. Vijaya Kumar [4], Gyanendra Prasad Joshi [5,*], Woong Cho [6,*]

1. Department of Computer Science and Engineering, GMR Institute of Technology, Andhra Pradesh, Rajam 532127, India
2. Professor Department of CSE, SV College of Engineering, Karakambadi, Tirupati, India
3. Department of Computer Engineering, College of Computer Engineering & Sciences, Prince Sattam Bin Abdulaziz University, Al-Kharj 11942, Saudi Arabia
4. Department of Computer Science and Engineering, GITAM School of Technology, GITAM (Deemed to be University), Visakhapatnam, India
5. Department of Computer Science and Engineering, Sejong University, Seoul 05006, Republic of Korea
6. Department of Electronics, Information and Communication Engineering, Kangwon National University, Samcheok 25913, Gangwon State, Republic of Korea

Received: 23 January 2024 | Revised: 08 March 2024 | Accepted: 12 March 2024 | Published: 26 March 2024
MSC : 11T71, 68P25, 94A60
Special Issue: Advances of Artificial Intelligence-based mathematical modeling optimization in engineering applications

International Journal on Recent and Innovation Trends in Computing and Communication

A Hybrid Approach using CNN and DQN Technique for Diagnosis Pneumonia in Chest X-Ray Images

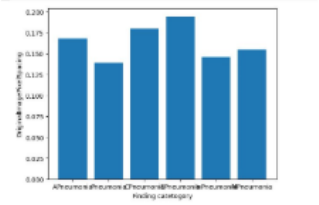

PDF

Jasmine Sabeena
Department of Computer Science and Engineering, Sri Venkateswara College of Engineering,Tirupati,India,

N. Chaitanya Kumar
Department of Computer Science and Engineering, Chadalawada Ramanamma Engineering College,Tirupati,India,

Abstract

J. Electrical Systems 20-3s (2024): 990-999

[1]Dr. Jasmine Sabeena

[2]Dr. Nitin Sudhakar Patil

[3]Priyanka Sharma

[4]Mr. T. Sathish Kumar

[6]Dr. Devang Kumar Umakant Shah

[7]Dr. Anurag Shrivastava

Fault Detection and Diagnosis in Electric Vehicle Systems using IoT and Machine Learning: A Support Vector Machine Approach

JES Journal of Electrical Systems

Abstract: - This research examines blame discovery and determination in electric vehicle (EV) frameworks utilizing Internet of Things (IoT) information and machine learning calculations, centring on a Support Vector Machine (SVM) approach. The study points to improving the unwavering quality and security of EV operations by precisely recognizing and diagnosing flaws in real time. The test comes about illustrates the adequacy of the SVM-based approach, with an exactness of 95%, accuracy of 94%, review of 96%, and F1-score of 95%. Comparative investigation with elective calculations such as k-Nearest Neighbors, Decision Tree, and Random Forest underscores the predominant execution of SVM in blame discovery and determination. The SVM calculation shows negligible misclassifications over distinctive blame

IETE Journal of Research

ISSN: (Print) (Online) Journal homepage: www.tandfonline.com/journals/tijr20

DNA TRIKKY Based Security Mechanism for Radio Frequency Identification Protocol

Vishu V, Keerthipati Kumar, Revathi A & Raja Kumar R

To cite this article: Vishu V, Keerthipati Kumar, Revathi A & Raja Kumar R (30 Jun 2024): DNA TRIKKY Based Security Mechanism for Radio Frequency Identification Protocol, IETE Journal of Research, DOI: 10.1080/03772063.2024.2350933

To link to this article: https://doi.org/10.1080/03772063.2024.2350933

Published online: 30 Jun 2024.

Submit your article to this journal

View related articles

View Crossmark data

Full Terms & Conditions of access and use can be found at
https://www.tandfonline.com/action/journalInformation?journalCode=tijr20

IETE JOURNAL OF RESEARCH
https://doi.org/10.1080/03772063.2024.2350933

Check for updates

DNA TRIKKY Based Security Mechanism for Radio Frequency Identification Protocol

Vishu V[1], Keerthipati Kumar[2], Revathi A[3] and Raja Kumar R[4]

[1]Department of Computer Applications, SRM Institute of Science and Technology, Ghaziabad, India; [2]Department of Computer Science and Engineering, SV College of Engineering, Tirupati, India; [3]Department of Computer Science and Engineering, Sri Venkateswara College of Engineering, Tirupati, India; [4]Mathematics Department, Sathyabama Institute of Science and Technology, Chennai, India

ABSTRACT

Radio frequency identification (RFID) technology has seen rapid expansion in recent years, used in a variety of applications like tracking, monitoring, ticketing, supply-chain management, contactless payments, etc. Several researchers have recommended elliptical curve cryptography (ECC) as a great cryptosystem to pair with RFID technology to increase security and privacy. However, RFID systems have major problems with insecure communication routes, which pose security concerns. In this research, a DNA TRIKKY based security mechanism has been proposed for RFID protocol to mutually authenticate the RFID tag and reader through insecure channels. The proposed solution uses a sponge structure and DNA-XOR to enhance the hash function generation process, preventing sensitive data from being leaked from the backend server. Informal security evaluations provide proof that the proposed method can withstand many attacks. According to performance evaluation, the proposed method performs better than the current protocols, making it ideal for use with RFID systems since it necessitates less processing time, communication costs, and storage costs particularly for the tag. According to the results, the proposed authentication paradigm works well with RFID tags that have limited resources. A comparison of the proposed protocol to other protocols shows that it performs more securely. Studies have found that this method outperforms other existing strategies.

KEYWORDS

RFID; security; privacy; DNA; authentication

1. INTRODUCTION

RFID is a wireless technology that reads tags attached to objects using radio frequency (RF) signals [1]. RFID is an important technology that has found its way into many applications like supply chain management, asset tracking, healthcare, and logistics [2]. There are three parts to an RFID system: a backend server, a reader, and a tag. Usually fixed, the reader connects to the server via a wired connection. An object has a tag affixed to it. The reader sends a radio signal to the tag to identify the object that has been marked, and the tag responds by sending back data that identifies the object (for example, its identifier). After that, the tag's response is sent by the reader to the server for additional processing. RFID technology has a wider range of applications because of the advancement of mobile technology, which allows readers to wirelessly connect to servers while they are portable [3].

Moreover, since no security standard has been developed for RFID technology, it cannot offer secure communication. As a result, new privacy and security issues exist for RFID-based healthcare systems, which is quite concerning. Confidentiality, integrity, authentication, and non-repudiation are the four fundamental security needs for any communication. Different security methods have been proposed for different applications to ensure secure communication in RFID-enabled application systems [4]. The RFID authentication protocol, which permits reciprocal authentication between a tag and the reader, is the most important of these protocols [5]. The wireless communication channels of the system are vulnerable to a range of attacks, including eavesdropping, tracing, impersonation, and other risks [6]. Therefore, the current research objective is to develop an RFID authentication technique that is lightweight, efficient and has a greater security level.

RFID system security has been addressed by several suggested authentication schemes. PKI, or public key infrastructure, is the foundation for several of these protocols. RFID protocols are unenviable because of their resource constraints [7]. Using lightweight cryptographic primitives, some systems have been presented. However, it turned out that a lot of these plans that relied only on lightweight primitives were vulnerable [8]. One of the most important security requirements of RFID authentication protocols is the provision of mutual validation between the server and the tag by all of these protocols.

© 2024 IETE

But against certain wireless assaults, the majority of these protocols are vulnerable. Numerous security vulnerabilities with radio frequency identification (RFID) technology are examined in detail [9,10].

Motivation: Over the past ten years, researchers have devised a variety of tactics to deal with the security and privacy concerns surrounding RFID authentication devices. Hash algorithms and symmetric key encryption are the foundation of several methods. However, to implement such systems, the backend server often needs to maintain track of all the details regarding items that have been tagged, including the secret session key and tag IDs. This suggests that in the case that the server is compromised or is maliciously attacked, the secret message and the associated secret data of the tags will be revealed. Consequently, the attacker can create a fake indistinguishable tag to pass the reader's authentication by using the sensitive data (secret key and unique ID, etc.) that has been acquired. Due to their lower processing capacity, security and privacy have been the main concerns for RFID devices. Furthermore, scalability is among the most crucial specifications for RFID technology. To overcome these challenges, a DNA TRIKKY based security mechanism has been proposed for RFID. The proposed method's primary contribution is listed as follows:

- This research's primary goal is to create a DNA TRIKKY-based RFID security mechanism that mutually authenticates RFID readers and tags via unsecure channels.
- The proposed approach enhances the hash function generation process by employing a sponge structure via DNA-XOR, preventing the leakage of private data from the backend server.
- This protocol has been designed and implemented in accordance with the security analysis.
- The effectiveness of the proposed techniques includes considerations for security needs, storage costs, communication costs, and computing expenses. Based on the comparison results, the proposed approach outperforms a state-of-the-protocols.

The remainder of this study is given as; Section 2 reviews related work. Section 3 explains the concepts used in the suggested technique. The security analysis of the suggested model is examined in Section 4. The proposed model's performance and comparative analysis will be discussed in Section 5. Section 6 finishes with a conclusion and suggestions for further research.

2. LITERATURE SURVEY

One of the most popular fields of research in a variety of applications is RFID-based authentication. Some of those techniques are illustrated briefly in this section.

In 2019, Dinarvand and Barati [11] developed an RFID authentication technique based on Elliptic Curve Cryptography (ECC). The presented technique outlines the necessary security conditions for RFID systems, including availability, scalability, forward security, data secrecy, tag anonymity, and mutual authentication. The protocol was shown to have a lower computational overhead and a greater security level when compared to related technologies.

In 2019, Huang et al [12] proposed an ultralightweight RFID authentication protocol based on permutation matrix encryption (UPBPM). Security study demonstrates that UPBPM can withstand all potential assaults. Performance analysis demonstrates that UPBPM utilizes lower computing resources on the tag without increasing communication costs.

An improved Hash-based efficient security authentication method was presented by Sun et al. [13] in 2019 to assess the security of RFID systems. It ensures two-way authentication, reduces tag costs, and boosts the efficacy of the secure authentication procedure by utilizing the reader's computational and storage power.

In 2019, Baashirah and Abuzneid [14] introduced a Serverless RFID Authentication Protocol based on ECC to protect the privacy and secrecy of the tag data, communications, and position. The effectiveness of the suggested protocol is contrasted with various prior frameworks based on computing cost and attack resistance.

In 2020, Xiao et al. [15] introduced the RFID authentication protocol SKINNY (short for LRSAS), which is based on a lightweight block cipher algorithm. The suggested technique guarantees reciprocal authentication and is immune to several attacks, according to security studies. Performance analyses demonstrate that the suggested method satisfies security requirements while being appropriate for low-cost tags. With this protocol, costs and security requirements are balanced.

In 2020, Tewari and Gupta [16] proposed a very lightweight mutual authentication method. Furthermore,

2024 International Conference on Trends in Quantum Computing and Emerging Business Technologies
CHRIST (Deemed to be University), Pune Lavasa Campus, India. Mar 22-23, 2024

2024 International Conference on Trends in Quantum Computing and Emerging Business Technologies (TQCEBT) | 979-8-3503-8427-7/24/$31.00 ©2024 IEEE | DOI: 10.1109/TQCEBT59414.2024.10545250

Natural Language Processing: Bridging the Gap between Human Language and Machine Understanding

Keerthipati Kumar[1]
[1]*Associate Professor, Computer Science and Engineering department*
S.V. College of Engineering,
Tirupati, Andhra Pradesh
Kumar.k@svce.edu.in

Mohammad Haider Syed[2]
[2]*Department of Computer Science,*
Saudi Electronic University
m.haider@seu.edu.sa

Saumya Bhargava[3]
[3]*Assistant Professor, Indira School Of Business Studies PGDM,*
Pune
Bhargava.smy@gmail.com

Lalit Lalitav Mohakud[4]
[4]*Ph.D,Assistant Professor, Department of Education, Jadavpur University*,
Kolkata 700032
lalitlalitav.mohakud@jadavpuruniversity.in

Mohammad Serajuddin[5]
[5]*Researcher, College of Dentistry*,
King Saud University
mserajuddin@ksu.edu.sa

Melanie Lourens[6]
[6]*Deputy Dean Faculty of Management Sciences, Durban University of Technology*
South Africa
melaniel@dut.ac.za
Orcid: 0000-0002-4288-8277

***Abstract- :*NLP in relation to deep learning models is focused on the review of NLP evolution from the middle of the 1950s up to present days. Today, NLP remains the pillar on which rests our digital age, connecting speech nuances of a human language and the computational power of machines. It is tracked along with the historical evolution from rule based systems to the paradigm shift to the machine learning decade since the nineties and constellations of the NLP components. The methodology involves using a conventional linguistic model alongside ultra-modern machine learning models to overcome ambiguity as well as contexts associated with other languages. The technical specifics and continuity loops under the Human-in-the-loop (HITL) framework are discussed. For example, they look at words like "uncommon" words, which have cultural implications in showing how involved human speech is. For instance, the strength of NPL can be depicted by being used in diverse sectors like health and social media. Finally, this article illustrates an advanced time when smart NPL units give topnotch solutions proving that interconnection between linguistics, computing and artificial intelligence is ongoing.**

Keywords: Machine Learning, Deep Neural Networks, Natural Language Processing (NLP), and Semantic Analysis as well as Human Interfaces with Machines (HMIM).

I. INTRODUCTION

Natural language processing stands as one of the most important technological advancement which has forged a profound connection between the complicated nuances of the human language and analytical power of machines. In an era where the digital interactions are penetrating every aspect of our lives natural language processing is serving as the linchpin and that is how it is enabling seamless communication between humans and machines. This journey of natural language processing and the evolution of it can be traced through several decades of research which spans over from rudimentary rule based systems to this current era of sophisticated deep learning models. As it will delve into the technical complications of natural language processing it is becoming apparent that this field is not only a tool but also a transformative force which is transcending the linguistic barriers and also reshaping the landscape of human machine interactions [1].The historical journey of natural language processing is a testament regarding the relentless pursuit of understanding and emulation of the complexity of the human language. From the starting days of machine translation experiments around 1950s to the adoption of statistical methods around 1970s and 1980s natural language processing has gathered some intellectual challenges and technological constraints. The development of machine learning around 1990s has sparked a paradigm shift and also created the groundwork for contemporary breakthrough regarding the leverage of deep neural networks and massive data sets bootstrap at the core level natural language processing consist of a constellation of components each of which are designed to unravel the layers of meaning encapsulated in human expression [2]. Starting from Tokenization, part of speech tagging and synthetic analysis to the complicated era of semantic analysis which is named entity recognition and sentiment analysis, these components work in a synergistic manner to decode the subtle identities of language. The challenge which is embedded regarding natural language processing for example ambiguity, contextual understanding and handling of rare words, the inherent complexities of human communication that machines strive to comprehend. Regarding the grand tapestry of technological advancement, natural language processing has come out not as a tool but also as a testament regarding humanities quest to bridge the gap between organic language and artificial intelligence [3]. It will embark on a journey regarding technical intricacies, the challenges regarding it and also the breakthroughs towards a landscape where the amalgamation of human ingenuity and computational power converges and that is how it ushers towards a new era of language which is not just processed but absolutely understood.

A. Research Questions

1. How NLP can address the gap between machine learning and human language?
2. What are the implications of NLP in various industries?

Authorized licensed use limited to: AMITY University. Downloaded on September 07,2024 at 08:54:09 UTC from IEEE Xplore. Restrictions apply.

DBLP BROWSE SEARCH ABOUT NFDI STOP THE WAR!

We've just launched a new service: our brand new **dblp SPARQL query service**. Read more about it in our latest blog post or try out some of the SPARQL queries linked on the dblp web pages below.

dblp computer science bibliography

search dblp

[+] [–] Ganesh A

[–] 2020 – today

2024

[j1] Ganesh A, K. Sree Divya, Chinthakunta Sasikala, Poornima E, Srinivasa Rao Nidamanuru, Sujith A. V. L. N, Gajula Ramesh: **Optimizing Task Scheduling: Exploring Advanced Machine Learning in Dew-Powered Cloud Environments.** Scalable Comput. Pract. Exp. 25(5): 3701-3714 (2024)

[+] SPARQL queries new

[–] Refine list

showing all 1 records

refine by search term

refine by type
Journal Articles (only)

refine by coauthor
K. Sree Divya (1)
Poornima E (1)
Gajula Ramesh (1)
Chinthakunta Sasikala (1)
Srinivasa Rao Nidamanuru (1)
Sujith A. V. L. N (1)

refine by orcid
no orcid (1)

refine by venue
Scalable Comput. Pract. Exp. (1)

refine by access
closed (1)

[+] Coauthor Index

Streamlining Cancer Diagnosis and Prognosis System using Hybrid CNN-NPR: Deep Learning Approaches

A. Ganesh
Dept.of. Computer Science and Engineering, Sri Venkateswara College of Engineering, Tirupathi, India

SivaKumar Depuru
School of Computing, Mohan Babu University, Tirupathi, India.

Basi Reddy A.
School of Computing, Mohan Babu University, Tirupathi, India

G. Sujatha
Dept.of. Electronics and Communications Engineering, Sri Venkateswara College of Engineering, Tirupathi, India

Keywords: CNN, Deep Learning, CNN-NPR, Cancer diagnosis, Prognosis system

ABSTRACT

In the context of medical science, advancements in technical infrastructure related to computer and life sciences have enabled the utilization of computational methods for medical diagnosis. As the number of cancer cases continues to rise rapidly, the existing diagnostic system is becoming out dated, necessitating the development of modern, productive, and optimized strategies. Accurately predicting the type of cancer is crucial for the diagnosis and treatment of the disease. Knowledge of cancer genes can significantly assist in comprehending, diagnosing, and identifying the different types of cancer. In this study paper, the identification and prediction of cancer type are achieved through the utilization of hybrid CNN-NPR several researchers have proposed different Convolutional Neural Network (CNN) models to date. Every model focused on a specific group of parameters that were utilized to imitate the gene pattern.

DOWNLOADS

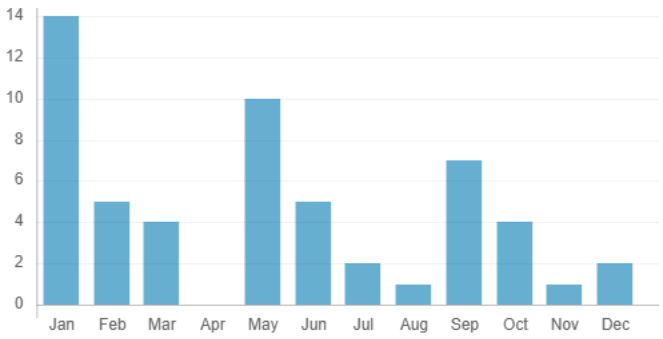

REFERENCES

Y. Wang, F. S. Makedon, J. C. Ford, and J. Pearlman, "HykGene: a hybrid approach for selecting marker genes for phenotype classification using microarray gene expression data," Bioinformatics, vol. 21, no. 8, pp. 1530–1537, 2005.

Published Paper : IJNRD2407109

Paper Title

Revolutionizing Diabetes Diagnosis:Harnessing Cutting-Edge Machine Learning Techniques for Early Detectionand Prediction

Authors

N.VaraLakshmi , Dr.P.Prathusha , Dr.K.Santhi , Dr.JasmineSabeena , Dr.R.Swathi

Keywords

Diabetes, Machine Learning, Early Detection, Health Complications, Timely Management

Abstract

In contemporary times, an unhealthy lifestyle, poor dietary habits, and the constant pres- sure of work contribute to the prevalence of diabetes, a condition that can give rise to various life-threatening health complications, including heart attacks, strokes, and kidney failure. Timely detection and accurate management of diabetes mellitus are crucial for mitigating its impact. Advanced machine learning methodologies prove to be highly effective in the early identification and prediction of diabetes. This system aims to provide a comprehensive analysis of diabetes diagnosis using machine learning algorithms. Cutting-edge approaches such as Support Vector Machine (SVM), Linear Discriminate Analysis (LDA),K-means, and decision tree-based algorithms like AdaBoost have demonstrated remarkable accuracy in predicting diabetes. Early intervention through the application of these machine learning techniques plays a pivotal role in effectively managing diabetes and minimizing its associated health risks.

Tec Empresarial
P-ISSN: 1659-2395; E-ISSN: 1659-3359

DEEP LEARNING-BASED IMAGE CAPTION GENERATION U
LSTM

T Sree Lakshmi[1] , Valaja Chaithanya[2], N Balavenkata

[1]Associate Professor in CSE, Sri Venkateswara college of Engine
[2]PG Scholar in CSE, Sri Venkateswara college of Engineerin
[3]Professor in EEE, Siddartha Institute of Science and Technol

ABSTRACT

Deep learning algorithms have transformed computer vision jobs i robots to analyze and grasp visual data with astounding accuracy. Image ca such task that has attracted a lot of attention; it entails automatically provi description of an image's content. This research investigates the use of Lon (LSTM) networks and Convolutional Neural Networks (CNNs) to cre generator.

The system learns to produce informative captions for photos by deep learning, notably the LSTM for sequence generation and the VG extraction. The work utilizes the Flickr8k dataset for training and evaluat effectiveness of the proposed approach through model training, caption ger using BLEU score. Through this work, a deeper understanding of the syne LSTMs in the context of image understanding and natural language p showcasing the potential for creating intelligent systems capable of unders visual content.

Keywords: LSTM, CNN, Deep Learning.

1. INTRODUCTION:

The rapid progress in Computer vision has undergone a paradigm learning. Empowering machines to comprehend and interpret vis

International Journal of
INTELLIGENT SYSTEMS AND APPLIC
ENGINEERING
ISSN:2147-6799 www.ijisae.org

Reliable Load Balanced Routing Policy using Bayesian
SDN-IOT Applications

[1]Dr. G. Srinivasan, [2]G. Seshadri Sekhar, [3]P. Suresh

Submitted: 25/01/2024 **Revised**: 03/03/2024 **Accepted**: 11/03/2024

Abstract: In this paper, we propose to design the reliable load balancing routing policy using Ba
Defined Network (SDN) and Internet of Things (IoT) heterogeneous applications. The main aim of this
path between the IoT gateway and the target IoT server while satisfying the servers' resource limits as
requirements of traffic like lower delay and higher throughput. For delay-aware traffic, the controller
lower delay and lower packet queue length. For bandwidth-aware traffic, the link quality, link ca
estimated and the forwarder nodes with high link capacity and quality with lower noise will be selected
will be selected. Then by applying Bayesian optimization, the optimum load balanced path is sele
simulation results, it has been shown that the proposed technique enhances the network throughput and

Keywords: *Software Defined Network (SDN), Internet of Things (IoT), Load balancing, Bayesian optim*

1. Introduction

Big data, cloud computing, and Internet of Things (IoT) have all aided to significantly boost traffic on conventional networks. The control and data planes of these networks are closely coupled, making them difficult to manage and expensive to operate and maintain. As a cutting-edge and creative networking paradigm, SDN offers programmability with simple network control and management that is required for the upcoming Internet. SDN provides access to the fundamental bearers and the network. In order to meet client needs at a reduced cost, numerous routes and superior approaches can share the carriers thanks to SDN's virtualization capability [1]. The IoT is a cutting-edge idea that enables varied networks to be used by flexible ecosystems. In particular, an IoT framework is constructed by connecting wireless networking devices,

the ability to create the be
flow forwarding policies,
traffic load balancing [3].
requests to resources throu
load balancing is used. A
load balancing was able to
performance. [4]. Load
network packets that ente
network packets across t
controllers in the older ne
balancer uses the least a
while optimising networl
resource utilisation, throug
dedicated server typically
traditional networks [6] [7]

However, one of the main
is how difficult it is to ma

Machine Learning Models for Classification of Sensitive Financial Documents

Kumar Akuthota
Dept. of CSE, School of Computing
Madanapalle Institute of Technology & Science, Madanapalle, Tirupati, A.P, India,
kumarcse5801@gmail.com

Dr.A.Ganesh
Dept. of CSE, Sri Venkateswara College of Engineering, Tirupati, A.P, India,
ganesh.a@svcolleges.edu.in

Basi Reddy A
Dept. of CSE in School of Computing Mohan Babu University, Tirupati, A.P, India,
basireddy.a@gmail.com

SivaKumar Depuru
Dept. of CSE in School of Computing Mohan Babu University, Tirupati, A.P, India,
sivakumar.d@vidyanikethan.edu

***Abstract*—This research proposes a machine learning-based approach for the automated classification of sensitive financial documents. The proposed method utilizes Support Vector Machines (SVM), Naive Bayes, and a rule-based classifier to classify categorized financial documents accurately. The system extracts relevant features from the documents and trains the models to classify them into predefined categories. The performance of each model is evaluated, and the results are compared to identify the best-performing model. The result shows that all methods achieved satisfactory results in terms of accuracy, F-Score, and execution time. The experimental results show that the Naïve Bayes classifier outperforms the other models, achieving an accuracy of 95% in classifying the financial documents. The total time consumption, which takes into account manual handling of missorts and classification of files that could not be sorted, was significantly lower for the Naive Bayes implementations. The proposed method can significantly reduce the time and effort required for manual classification and can improve the accuracy of the classification process. The version with a tolerance level performed best and showed higher precision, but lower accuracy. This research can have significant implications in the financial industry, where the automated classification of sensitive financial documents can improve operational efficiency and reduce the risk of errors.**

Keywords— Financial Documents, Classification, Machine Learning Models, Accuracy, Computing Time.

I. INTRODUCTION

The financial industry generates a vast amount of data in the form of various financial documents such as invoices, receipts, and contracts. These documents contain sensitive information related to financial transactions, making their classification and management a critical task. Manual classification of financial documents can be time-consuming, error-prone, and expensive. Moreover, the increasing amount of data and the complexity of financial documents make it challenging to classify them accurately using traditional methods.

By generalizing data, machine learning can be used to find patterns and solve important tasks. This is often more feasible and cost-effective than manual programming. With access to a lot of data, ambitious problems can be handled [3].

Machine learning is used for web searches, spam filters, recommendation systems, stock trading, and many other areas of use [4]. There are many types of machine learning, but classification is the most common. A classifier is a system that takes in data and returns a discrete value, a class[3]. There are a large number of algorithms that can be used for classification. Machine learning-based approaches have shown great potential in automating the classification of documents, including financial documents. In recent years, machine learning-based approaches such as Support Vector Machines (SVM) and Naive Bayes have been widely used in the classification of text documents. These approaches have proven to be effective in accurately classifying documents based on their content [5]. Rule-based classifiers have also been used in the classification of financial documents, where specific rules are defined to classify documents based on certain criteria [5].

Now a day, most of the financial data is acquired through e-mail contact with the banks and customers, where most of the data is compiled as PDF files. These documents need to be sorted into customer folders. Currently, this categorization is done manually, which costs the client a lot of resources in the form of staff time. By automating the classification and sorting of documents, the client wishes to streamline the process to time

The purpose of this work is to investigate whether a document classifier can streamline the work of handling documents containing classified financial data. More concretely, the main purpose is to examine whether it is possible to classify the client's documents by machine to the extent that an implementation can replace a human classifier. According to the client, it is important that the classifier has a high level of precision, and thus the study also aims to investigate how a high level of precision can be achieved. Furthermore, it is investigating which areas machine learning is suitable for and one aims to investigate whether a machine learning algorithm is suitable for an algorithm based on handwritten rules.

In this research, we used a machine learning model for the automated classification of sensitive financial documents. This study will evaluate two implementations of classifiers and their applicability in the field of text classification and more specifically document classification. Text classification is about assigning a label to a text or document. The three classifiers that will be compared are the Naive Bayes machine learning algorithm, Support Vector Machine (SVM), and a rule-based classifier. Furthermore, a version of Naive Bayes with an implementation of a confidence value was

XXX-X-XXXX-XXXX-X/XX/$XX.00 ©20XX IEEE

Published Paper : IJNRD2301262

Paper Title

Heuristic approach of Road-Traffic sign classification using AI

Authors

Kanna. Pravallika , Dr. R. Swathi , MD.Rafi

Keywords

Convolution Neural Network (CNN), German Traffic Sign Recognition (GTSR), Google Net, Text-to-speech translation, Traffic signs.

Abstract

Road Traffic signals are placed in particular positions to make sure the protection of vacationers. In this paper, we proposed a device for site visitors signal detection and recognition, in addition to a technique for extracting an avenue signal from an herbal complicated photo for processing and alerting the driving force via voice command. The reliability of the device is increased through different aspects such as noise, partial or absolute underexposure, partial or whole overexposure, considerable versions in shape saturation, extensive sort of viewing angles, view depth, and shape deformations of site visitors symptoms etc. The proposed structure is sectioned into three phases. The first of that is photo pre-processing, where the dataset`s enter files are quantified, which decides the enter length for getting to know purposes, and resizes the records for the getting to know step. A Convolutional Neural Network (CNN) is used to train within the segment side which further more offers the text-to-speech translation, with the

IJNRD.ORG ISSN : 2456-4184
INTERNATIONAL JOURNAL OF NOVEL RESEARCH AND DEVELOPMENT (IJNRD) | IJNRD.ORG
An International Open Access, Peer-reviewed, Refereed Journal

Blockchain Based Covid Vaccine Booking

Mr. G. Narahari Reddy[1], Dr. K. Sekhar[2], Dr. R. Suresh[3]
1 Dept. of CSE, SVCE, Tirupati, Email: narahari.1994@gmail.com
2 Professor, Dept. of CSE, SVCE, Tirupati, Email: sekhar.k@svcolleges.edu.in
3 Associate Professor, Dept. of CSE, SVCE, Tirupati, Email: Suresh.rm@svce.edu.in

Abstract – Immunization is all about using Block chain for managing and tracing the vaccine stocks, logistics and transparent distribution. Immunization gives you continuous visibility and enables actionable insights to track vaccine distribution and ensure a fair and equitable distribution. Immunization allows you to book your vaccination appointments and will also allow you to keep track of the vaccine being distributed. Block chain helps in maintaining the integrity and transparency of the whole process right from inception of the vaccine.

Index Terms – Vaccine report using Blockchain; COVID-19; Immunization programs; Transparent Vaccine status.

1. INTRODUCTION

The prevalence of corona virus which leads to respiratory infections with symptoms ranging from the common cold to more severe diseases such as Middle East Respiratory Syndrome (MERS) and Severe Acute Respiratory Syndrome (SARS). Since then, the eyes of the world have been on the pharmaceutical sector as industry leaders race to test, produce and distribute a vaccine to combat COVID-19.

On March 11, WHO concluded that COVID-19 could be a pandemic. Worldwide the partners are working together to reduce the spread of disease by developing multiple vaccines. Once a vaccine is approved by WHO for common people's disposal, attention will turn on to the orchestration and the planning done by the respective Governments for the vaccine status and the methods to be used by them such as patient health information and distribution, especially if special storage condition is required.

Name Of Vaccines Approved and Used in India are:

1. Covaxin
2. Covishield
3. Sputnik

2. RELATED WORK

For optimal distribution of vaccines, ICT solutions used to support immunization campaigns. A drive through vaccination stimulation tool was utilized to manage time efficiency, requirements of staff and intervals for immunization which was based on event processing and agent-based modelling. During the outbreak of influenza, distribution of vaccine for a heterogenous population has been done using mathematical modelling to ensure fairness and managing the number of doses.

IJNRD.ORG ISSN : 2456-4184
INTERNATIONAL JOURNAL OF NOVEL RESEARCH AND DEVELOPMENT (IJNRD) | IJNRD.ORG
An International Open Access, Peer-reviewed, Refereed Journal

Object Detection with Audio Feedback

Mr. S. Ranganath[1], Dr. K. Santhi[2], Dr. S. Jasmine Sabeena[3]
1 Dept. of CSE, SVCE, Tirupathi
2 Professor, Dept. of CSE, SVCE, Tirupathi
3 Associate Professor, Dept. of CSE, SVCE, Tirupathi

Abstract – Object recognition is one of the challenging applications of computer vision, which has been widely applied in many areas for e.g., autonomous cars, Robotics, Security tracking, Guiding Visually Impaired Peoples etc. With the rapid development of deep learning many algorithms were improving the relationship between video analysis and image understanding. All these algorithms work differently with their network architecture but with the same aim of detecting multiple objects within complex image. Absence of vision impairment restraint the movement of the person in an unfamiliar place and hence it is very essential to take help from our technologies and trained them to guide blind peoples whenever they need.

Index Terms: Tensor flow, Yolo_v3, Web Speech API, Deep Learning.

INTRODUCTION

Humans almost by birth are trained by their parents to categorize between various objects as children self is one object. Human Visual System is very accurate and precise that can handle multi-tasks even with less conscious mind. When there is large data then we need more accurate system to correctly recognize and localize multiple objects simultaneously. Here machines come into existence, we can train our computers with the help of better algorithms to detect multiple objects within the image with high accuracy and preciseness. Object Detection is the most challenging application of computer vision as it requires complete understanding of images. In other words, object tracker tries to find the presence of object within multiple frames and assigns labels to each object. There might be many problems faced by the tracker in terms of complex image, Loss of information and transformation of 3D world into 2 D image.

System Analysis & Feasibility Study

Existing Method:

In recent years many algorithms are developed by many researchers. Both machine learning and deep learning approaches work in this application of computer vision. This section outlines the journey of the different techniques used by the researchers in their study since 2012. Histograms of Gradient Descent (HOG) use SVM algorithm for detecting objects in real time. It is a feature detector used to

IJNRD.ORG ISSN : 2456-4184
INTERNATIONAL JOURNAL OF NOVEL RESEARCH AND DEVELOPMENT (IJNRD) | IJNRD.ORG
An International Open Access, Peer-reviewed, Refereed Journal

Loan Eligibility Prediction Using Machine Learning

Shaik.Bhanu[1], Dr. Y. A. Siva prasad [2]

[1]Research Scholar, Department of CSE, Sri Venkateswara College of Engineering, Tirupati
[2]Associate Professor, Department of CSE, Sri Venkateswara College of Engineering, Tirupati

Abstract:
With technological advancements and the expansion of businesses, the demand for loans has increased significantly, both for personal and business purposes. Due to limited assets, banks cannot grant loans to every applicant. Identifying the right candidates for loans is a complex and time-consuming process. Banks aim to deliver loans to individuals who can repay them on time and provide maximum profit. Thus, there is a need for a system that can analyse and streamline this process, saving time and resources. This paper aims to develop a more accurate loan prediction model using machine learning to reduce the risk involved in selecting appropriate loan applicants. By mining previous loan records and using bank loan rules, we will train a machine learning model to predict loan eligibility. We will use the sklearn library for our model and the train-test-split method to split the dataset. Various models, including Logistic Regression, Decision Tree (DT), Random Forest (RF), and Support Vector Machine (SVM), will be employed to achieve accurate results. Our experiments indicate that the Random Forest classifier provides the best accuracy.

Keywords: Logistic Regression, Decision Tree, Random Forest, Support Vector Machine.

I. Introduction

Granting loans is a critical revenue stream for banks, as it is a primary source of profit. Therefore, the precise allocation of loans is paramount. Incorrectly approving loans can lead to financial instability and diminished profits. Banks aim to invest their resources in reliable borrowers who will generate substantial interest returns. Before approving a loan, banks meticulously evaluate various factors such as the applicant's ability to repay, their financial stability, and the purpose of the loan. This manual evaluation process is time-consuming for both the bank and the customer [1].

A machine learning system can streamline this process by accurately predicting the suitability of a loan applicant. Automation ensures the integrity of the results, prevents tampering, and accelerates the approval process, significantly reducing the time required for decision-making and paperwork. This benefits both bank employees and customers by facilitating quicker loan processing [2].

The system's predictions are based on multiple factors, although in some cases, a single strong indicator might suffice for loan approval. Historical loan data will be mined to train the model. Data mining, which involves

Int. J. Nonlinear Anal. Appl. 13 (2022) 2, 1893–1905
ISSN: 2008-6822 (electronic)
http://dx.doi.org/10.22075/ijnaa.2022.27403.3588

On optimizing scalability and availability of cloud based software services using scale rate limiting algorithm

V. L. Padma Latha[a,*], N. Sudhakar Reddy[b], A. Suresh Babu[c]

[a]Department of Computer Science and Engineering, Sri Venkateswara College of Engineering, Tirupati, JNTUA University, Ananthapuramu, India

[b]Department of Computer Science and Engineerig, Sri Venkateswara College of Engineering, Tirupati, India

[c]Department of CSE, JNTUA College of Engineering , JNTUA University Anantapuramu, India

(Communicated by Javad Vahidi)

Abstract

In this paper, the scale rate-limiting algorithmic approach namely the Token bucket algorithm is utilized to optimize the performance of cloud based software services. In distributed applications, higher availability and scalability have long been a critical challenge. In cloud computing, offering highly accessible services is critical for retaining client satisfaction, confidence and avoiding revenue losses. The gateway Zuul is considered as the entryway to various services in the Spring Cloud based software service must perform the rate-limiting process and make sure the service's reliability in the event of excessive scalability. The token bucket rate-limiting technique cannot ensure core service availability. To address this issue, this study developed an overload protection technique depending on a URI configuration file in conjunction with the Zuul gateway that may filter requests before obtaining tokens. The token bucket rate-limiting algorithm is implemented the traffic limitation function and ensured the cloud platform service's reliability and availability. The estimation of scalability, as well as availability, demonstrates the level of service supplied to consumers in response to their requests. The elasticity measures are used to assess the cloud based software services performance in terms of scalability. In the future, cloud computing improvements and expansion might increase cloud-based software services.

Keywords: Performance optimization, scalability, availability, Cloud based software services, Rate-limiting, Token bucket algorithm
2020 MSC: 90C31

1 Introduction

Cloud computing produces convenient, ubiquitous, on-demand network access to a shared pool of configuration-based computing resources such as networks, applications, storage, servers, and services which are rapidly provisioned and published with limited communication or service provider communication [30]. Cloud computing is rapidly growing, but it is already having a big influence in a variety of fields. More businesses are moving to the cloud, and significant technological advancements are occurring. Organizations, companies and small companies alike can benefit

*Corresponding author
Email addresses: vlpadmalatha.svit@gmail.com (V. L. Padma Latha), principal@svce.edu.in (N. Sudhakar Reddy), asureshjntu@gmail.com (A. Suresh Babu)

Received: January 2022 *Accepted:* March 2022

International Journal of Recent Technology and Engineering (IJRTE)
ISSN: 2277-3878 (Online), Volume-12 Issue-1, May 2023

A Robust Method for Extracting Texture Features of Segmented Mammogram Images using M-ROI Technique

R Suresh, B. Vjaya

Abstract: ***Radiologists generally uses mammogram images for extracting masses or cancer effected breast issues using texture features of the images by segmenting techniques. The most commonly used technique in this process is region of interest (ROI). But this method fails for large collection of mammogram image database. To address this issue this present paper proposed multi-ROI (M-ROI) technique. This method not only reduces limitations of ROI but also finds the very suitable texture features. This paper also evaluated the efficiency of the proposed M-ROI method using first order and second order statistical techniques***

Index Terms: Benchmarked Images, Multi-ROI Segmentation, Region of Interest, Texture Features

I. INTRODUCTION

Texture features of the mammogram images are generally obtained by segmenting images into two regions i.e. cancer and non-cancer respectively. These two regions contain different patters or shapes. Segmentation is very powerful technique to detect such irregularities in the images. Using segmentation technique, we generally divide the image from extracting edges or boundaries. In mammogram images ill-defined [11] masses contain more intensity compare to other regions. And also, these regions contain circular based objects. Textures are very important in the analysis of the images. This task can be completed in two steps. In first step we segment the image and in second step we extract the texture features from the segmented parts in the first part[13]. Textures are very important in the analysis of the images.

ROI is one of most powerful and useful technique for segmenting and detecting various regions in the mammogram images. But there are some limitations using this technique. One of these limitations is not suitable for huge number of images [2]. To overcome this issue this paper proposed M-ROI based texture features. The efficiency of the proposed method is evaluated also, these regions contain circular based objects.

Manuscript received on 16 May 2019 | Revised Manuscript received on 12 April 2023 | Manuscript Accepted on 15 May 2023 | Manuscript published on 30 May 2023.
*Correspondence Author(s)
Dr. R. Suresh*, Professor, Department of Computer Science and Engineering, Sri Venkateswara College of Engineering, Tirupati (A.P), India. Email: suresh.rm@svce.edu.in, ORCID ID: https://orcid.org/0009-0004-4726-2398
B. Vijaya, Assistant Professor, Department of Computer Science and Engineering, Sri Venkateswara College of Engineering, Tirupati (A.P), India. Email: vijaya.bt@svce.edu.in, ORCID ID: https://orcid.org/0009-0009-7205-0860

The Authors. Published by Blue Eyes Intelligence Engineering and Sciences Publication (BEIESP). This is an open access article under the CC-BY-NC-ND license http://creativecommons.org/licenses/by-nc-nd/4.0/

Textures are very important in the analysis of the images. This task can be completed in two steps. In first step we segment the image and in second step we extract the texture features from the segmented using statistical techniques of the extracted features using Multi-ROI features.
The main features of the proposed method are:

1. Used ROI and proposed M-ROI for segmenting the mammogram images on large data sets.
2. Segmented images are used to extract texture features
3. In depth texture analysis for abnormal images
4. Extracted statistical features from ROI and proposed M-ROI segmentation are compared

This paper is organized as follows. Section 2 deals with the Background study of the present study. The proposed method details are given in section 3. The results and conclusions are given in Section 4 and 5 respectively.
The efficiency of the proposed segmentation mainly depends upon the illumination of the mammogram image. This problem mainly arises from the images having Low contrast. So we first need to enhance these images to improve the efficiency of the method. Contrast stretching [6] is one method for enhancing the image to improve the efficiency.

In Contrast stretching method image intensity can be improved by stretching range of values. The range upper and lower of intensity are needed before stretching. For example, in gray images 0 and 255 are lowest and highest values respectively. The eq1 can be used to enhance image in contrast stretching method.

$$p_{out} = (p_{in} - c)\left(\frac{b-a}{d-c}\right) + a \quad (1)$$

Where ‘a’ and ‘b’ represents lower and upper respectively and ‘Pin’ refers the pixel intensity.
Without effecting nature of the image we can alter the contract of the image using histogram equalization method [7]. In this method transformation procedure applied to transform gray pixels between input and output images and maximizes the contrast of the image. Eq 2 represents transformation from input to output images

$$D_B = f(D_A) \quad (2)$$

Another analyzing technique for representing the image is Wavelet transformation [3]. This method uses double filter bank i.e. Laplacian pyramid representation for coefficients in a smooth contour for the input mammogram images. These pyramids capture not only discontinuities but also provides record of discontinues. There are so many filters for reducing the blur of edges in the images.

© Copyright: All rights reserved.

AIP Advances

RESEARCH ARTICLE | FEBRUARY 21 2024

A miniaturized-slotted planar MIMO antenna with switchable configuration for dual-/triple-band notches

Saritha Vanka ; Chandrasekhar C

Check for updates

AIP Advances 14, 025039 (2024)
https://doi.org/10.1063/5.0190950

View Online Export Citation

Articles You May Be Interested In

Design and analysis of highly isolated hexa-band suppressed UWB MIMO antenna

AIP Conf. Proc. (February 2024)

Effects of metamaterials on MIMO antennas for X-band radar applications and parameter optimization with a machine learning model: A review

AIP Advances (April 2023)

Design and analysis of Minkowski fractal antenna for wideband THz frequency tuning/multiband operation in a MIMO antenna system

J. Appl. Phys. (May 2023)

15 December 2024 07:11:47

AIP Publishing

Special Topics Open for Submissions

Learn More

AIP Publishing

A miniaturized-slotted planar MIMO antenna with switchable configuration for dual-/triple-band notches

Cite as: AIP Advances 14, 025039 (2024); doi: 10.1063/5.0190950
Submitted: 10 December 2023 • Accepted: 24 January 2024 •
Published Online: 21 February 2024

View Online Export Citation CrossMark

Saritha Vanka[1,2,a] and Chandrasekhar C[3,a]

AFFILIATIONS

[1] Department of E.C.E, Jawaharlal Nehru Technological University, Anantapur, Ananthapuramu, Andhra Pradesh, India
[2] Department of E.C.E, Velagapudi Ramakrishna Siddhartha Engineering College, Vijayawada, Andhra Pradesh, India
[3] Department of E.C.E, Sri Venkateswara College of Engineering- Tirupati, Andhra Pradesh, India, Affiliated to Jawaharlal Nehru Technological University, Anantapur, Ananthapuramu, Andhra Pradesh, India

[a] **Authors to whom correspondence should be addressed:** vankasaritha2@gmail.com, vsaritha@vrsiddhartha.ac.in, and umashekar_2000@yahoo.com

ABSTRACT

This paper outlines the design and validation of a four-port compact Multi-Input Multi-Output (MIMO) antenna engineered to provide reconfigurable band notches within the ultra-wideband spectrum. The antenna features a circular monopole engraved with split ring slots along its radiating section, while a U-shaped slot is etched onto the feed line to facilitate band notches at specific frequencies—4.3 GHz (corresponding to INSAT), 6.8 GHz (aligned with Wi-Fi-6E), and 8.3 GHz (pertaining to X-band satellite). To ensure proper isolation, the MIMO elements are arranged orthogonally, and a decoupling periodic structure is strategically interposed between these elements to enhance isolation further. The incorporation of a PIN diode within the U-shaped slot introduces reconfigurability into the band notching mechanism. The MIMO antenna operates in two distinct modes depending upon the state of the PIN diode, either activated (ON) or deactivated (OFF). In the former mode, the antenna offers switchable band notches across three frequencies, while in the latter mode, it offers band notches at two specific frequencies. The validity of the antenna's performance is validated through real-time fabrication and measurement. Both simulated and measured results exhibit a notable correlation. The antenna stands as an appropriate candidate for future cognitive radio applications.

© 2024 Author(s). All article content, except where otherwise noted, is licensed under a Creative Commons Attribution (CC BY) license (http://creativecommons.org/licenses/by/4.0/). https://doi.org/10.1063/5.0190950

15 December 2024 07:11:47

I. INTRODUCTION

In recent times, there has been a significant surge in interest from researchers toward ultra-wideband (UWB) technology. This heightened attention follows the Federal Communications Commission's authorization of the unlicensed 3.1–10.6 GHz band for commercial applications in 2002. Nevertheless, practical applications of UWB antennas encounter challenges related to band overlapping. Certain narrow-band frequencies, such as WiMAX, WLAN, C-band satellites, and X-band ITU, coexist within the UWB spectrum, leading to electromagnetic interference. To mitigate the risk of interference, various methods have been introduced to incorporate band-notched characteristics. The penta-band rejections are realized using U slots and EBG structures for attenuating ISM, radar surveillance, WiMAX, C-band, and WLAN bands.[1] A UWB antenna realizing penta-band notches at LTE, C, WLAN, and X bands is proposed.[2] A loaded antenna is proposed for realizing quad-band notches at aviation service, Wi-MAX, and C-band satellite uplink and downlinks. The band notches are achieved using triple U-shaped slots etched on the radiator and a novel UBG structure beside the feedline.[3] The band notches are realized by using fork-shaped slots and EBG structures. Frequency reconfigurable antennas enable the efficient utilization of frequency resources, ensuring seamless provision of multiple services to end devices. When compared to conventional antennas, those with frequency reconfigurability present benefits, such as compact size, improved

© Author(s) 2024

gain, and optimized radiation patterns. The underlying principle of frequency reconfigurability involves altering the current distribution either electrically or mechanically.[4] Utilizing Multi-Input Multi-Output (MIMO) with switchable frequency bands represents an intelligent fusion for achieving frequency-agile multi-band communication[5] or notch frequency-switchable UWB applications in advanced high-speed communication devices. An article explores the efficacy of various methodologies in conferring band-notch characteristics and achieving reconfigurability for UWB applications.[6] An overview of reconfigurable MIMO antennas endowed with adaptable band-notch features is presented.[7] A rectangular patch antenna, featuring double slots in the ground plane, incorporates six Radio Frequency (RF) PIN diodes strategically positioned for frequency reconfigurability.[8] In addition, a pixel antenna that is frequency-reconfigurable is crafted using PIN diodes.[9] For beam switching, a novel proposal introduced an antenna using a reconfigurable metasurface.[10] This metasurface, comprising double-split square rings that are uniformly distributed and loaded with PIN diodes, serves dual functions as a wave reflector and a director. Furthermore, a frequency-and-pattern-reconfigurable planar antenna, leveraging a single PIN diode, is presented.[11] The article further presents a circularly polarized wave-fed circular-shaped antenna, printed on substrate silicon, offering dual-band-notch characteristics. The reconfigurability is achieved by employing RF MEMS switches inserted in U- and I-shaped slots.[12] Similarly, a circular fractal antenna by way of triple reconfigurable band notches is demonstrated, utilizing circular fractal iterations and ring resonators integrated with PIN diodes.[13] Moreover, a compact UWB antenna catering to underlay cognitive radio applications is conceived, featuring a switchable band notch at Wi-Max via a complementary split-ring resonator and a PIN diode.[14] A low-profile cognitive radio sensing/communicating antenna system is introduced, incorporating a slotted elliptical monopole antenna for the purpose of sensing and a triangular reconfigurable monopole antenna for communication, with reconfigurability facilitated by two PIN diodes.[15] The array of innovations continues with a rhombus-shaped fractal antenna resonating at ten distinct frequencies, contingent upon the corresponding capacitance value of a varactor diode.[16] A compact filtering antenna for UWB medical applications integrates a modified monopole antenna, defected microstrip structure, and double split ring resonators, with reconfiguration facilitated by PIN diode switches.[17]

In the realm of MIMO applications, a compact four-port multi-band diversity-based antenna is proposed, resonating at ISM, WiMAX, and Wi-Fi bands, leveraging stub-loaded meander line antennas with strategically placed Split-Ring Resonators (SRRs) to enhance isolation.[18] The advantages of employing reconfigurable filtennas and MIMO configurations are underscored as communication antennas for cognitive radio.[19] The UWB-MIMO property is exemplified through a design featuring two square monopoles detached by a T stub that is grounded, with reconfigurable operation implemented via PIN diodes incorporated in a parasitic resonant structure positioned in the ground.[20] A MIMO antenna introduces band notches that are reconfigurable at WLAN frequencies by incorporating switches into quarter-wave slots in the main radiator.[21] Another miniaturized UWB-MIMO antenna, offering both functionalities fixed in addition to reconfigurable band-stop, is obtainable. Here, PIN diodes are strategically placed in horizontal stubs in the ground surface to realize reconfigurable WLAN band notches, while a fixed band notch is attained at downlink X-band satellite frequencies.[22] Furthermore, a two-port MIMO antenna utilizing L-shaped slots and incorporating PIN diodes within these slots achieves frequency reconfigurability specifically at WLAN bands.[23] Another compact MIMO antenna with two ports, designed intended for cognitive radio applications, achieves reconfigurability through the insertion of a PIN diode in the decoupling network.[24] Finally, a low-profile WLAN band-notched two-port MIMO antenna with frequency reconfigurability is tailored for UWB applications.[25]

This paper introduces a UWB-MIMO antenna that incorporates frequency-reconfigurable band notches. The simulation performance is conducted using Ansys HFSS. Section II delves into the design and parametric analysis of the proposed MIMO antenna, specifically focusing on multiple band notches. Following that, Sec. III is dedicated to comparing the simulated results with the actual measurements. Section IV encapsulates the key findings and insights drawn from this study.

II. ANTENNA DESIGN

The antenna is manufactured on a Rogers substrate with a relative permittivity of 2.2 and a loss tangent of 0.02. The substrate has a thickness of 1.6 mm. The unit element's structure and dimensions are depicted in Fig. 1, and the specific values for these dimensions are outlined in Table I. This antenna comprises a circular monopole featuring split ring slots strategically designed to introduce band notches. It is fed through a strip line, incorporating a U-shaped slot to create an additional band notch. The ground plane is defective, incorporating a rectangular shape etched with three semi-circular slots. These slots are interconnected using a novel structure, ensuring a unified ground plane without compromising the antenna's performance. The band rejection characteristics are achieved through strategically placed Split-Ring Resonator (SRR) slots, etched on the circular monopole, and a U-shaped slot etched on the strip line feed, as illustrated in Fig. 1. Notably, a PIN diode is precisely inserted between the arms of the U-shaped slot, introducing the capability for switchable band notches. This innovative design enhances the antenna's versatility and adaptability for various operational scenarios.

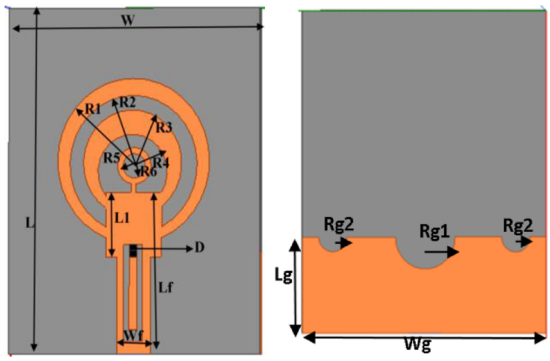

FIG. 1. Structure of the antenna.

15 December 2024 07:11:47

© Author(s) 2024

TABLE I. Antenna dimensions.

Parameter	Value (mm)	Parameter	Value (mm)	Parameter	Value (mm)
R1	6.7	R6	1.6	Lf	10
R2	5.1	Rg1	2	Wf	3
R3	4.2	Rg2	1	L1	5
R4	3.2	L	27	Lg	8
R5	1.8	W	20	Wg	20

A. Evolution stages and optimetrics

The progressive stages of the proposed antenna are shown in Fig. 2.

The initial design involves a circular patch with a complete ground plane, utilizing a microstrip line feed. The radius of the circular radiating element denoted as R1, undergoes variation within the range of 6–7 mm. After careful optimization, the specific value R1 = 6.7 mm is selected as the optimal parameter. The goal is to obtain an effective bandwidth covering from 3 to 20 GHz, covering the UWB to extended UWB frequencies. However, it is noted that the realized design operates effectively covering the range of 7–20 GHz, as depicted in Fig. 3.

The actual radius R1 of the circular radiator is given by the following equations:

$$R1 = \frac{F}{\left\{1 + \frac{2h}{\pi\varepsilon_r F}\ln\left(\frac{\pi F}{2h}\right) + 1.7726\right\}^{\frac{1}{2}}}, \tag{1}$$

$$F = \frac{8.791x10^9}{f_r\sqrt{\varepsilon_r}}, \tag{2}$$

$$f_r = \frac{1.8412v_0}{2\pi R1_{eff}\sqrt{\varepsilon_r}}. \tag{3}$$

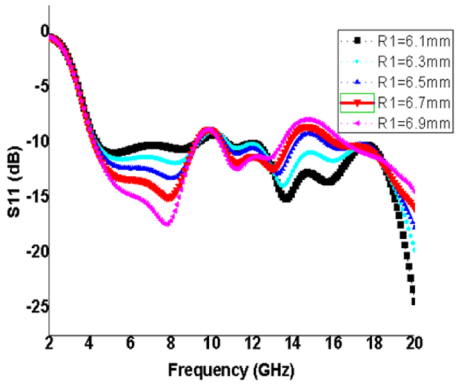

FIG. 3. Plot of S11 for parametric variation of R1.

The effective radius of the circular radiator is calculated by using the following equation:

$$R1_{eff} = R1\left\{1 + \frac{2h}{\pi\varepsilon_r R1}\ln\left(\frac{\pi R1}{2h}\right) + 1.7726\right\}^{\frac{1}{2}}. \tag{4}$$

The microstrip line feed dimensions are obtained by using the following equations:

When (Wf/h) > 1,

$$\varepsilon_{eff} = \frac{\varepsilon_R + 1}{2} + \left[\frac{\varepsilon_R - 1}{2\sqrt{1 + 12\left(\frac{h}{Wf}\right)}}\right], \tag{5}$$

$$Z_o = \frac{120\pi}{\sqrt{\varepsilon_{eff}\left[\frac{Wf}{h} + 1.393 + \frac{2}{3}\ln\left(\frac{Wf}{h} + 1.444\right)\right]}}. \tag{6}$$

Stage 2 comprises a circular patch accompanied by a ground structure featuring a defected rectangle shape. The length of the rectangle

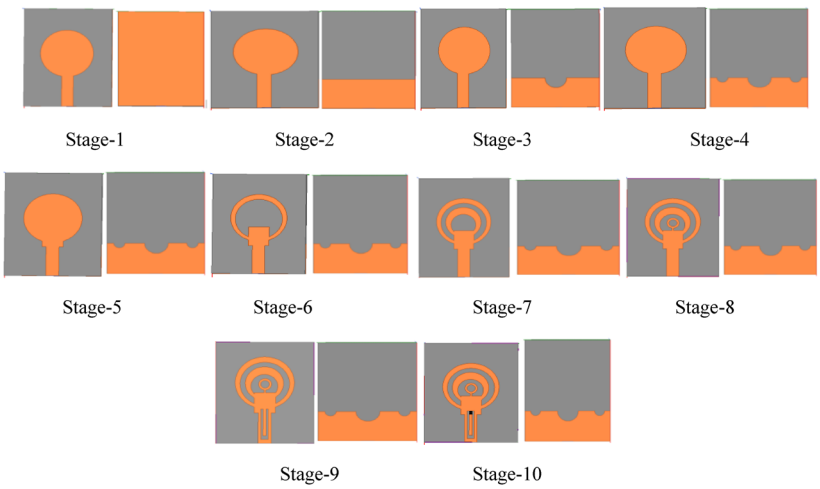

FIG. 2. Evolution stages of the proposed antenna.

15 December 2024 07:11:47

© Author(s) 2024

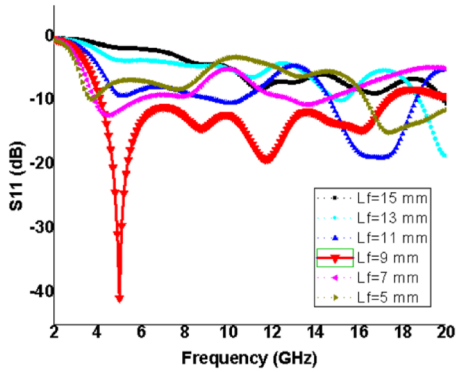

FIG. 4. Plot of S11 for parametric variation of Lf.

is systematically adjusted within a range spanning from 15 to 5 mm. The objective behind this variation is to enhance the impedance bandwidth, particularly aiming for improved performance at lower frequencies. After optimization, a specific length value of Lf = 9 mm is identified as the optimal parameter. This structured configuration demonstrates effective operation across the spectrum starting from 4 to 20 GHz, as illustrated in Fig. 4. This adjustment made enhanced performance at lower frequencies.

The dimensions of defected ground are found using the following equations:

$$L_g = 6h + W_g, \tag{7}$$

$$W_g = 6h + L_g. \tag{8}$$

In Stage 3, modifications are made to the defected ground plane. A semi-circular slot is precisely engraved at the center of the rectangle with the intention of enhancing the impedance bandwidth. The radius of this semi-circular slot, denoted as Rg1, is systematically adjusted within the range of 2–3 mm. Following optimization, a specific value of Rg1 = 2 mm is identified as the optimal parameter. This modified structure exhibits active operation across a wide range of 3.5–20 GHz, as visually depicted in Fig. 5. The introduction of

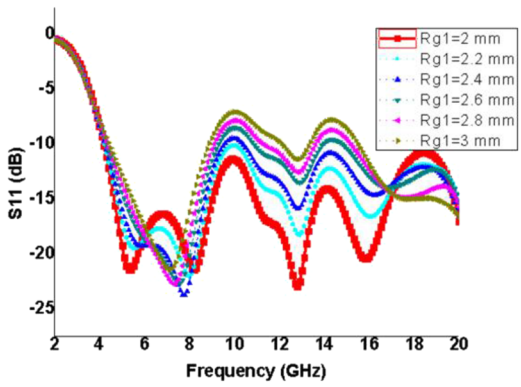

FIG. 5. Plot of S11 for parametric variation of Rg1.

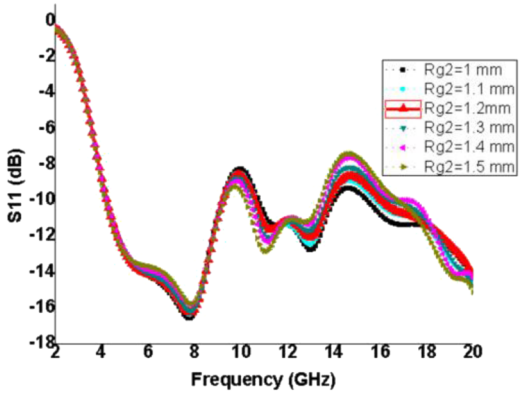

FIG. 6. Plot of S11 for parametric variation of Rg2.

the semi-circular slot at the middle of the ground plane contributes to the desired improvement in impedance bandwidth, aligning with the overall design objectives. In Stage 4, two more semi-circular slots are etched at the extremes of the rectangle to improve the impedance bandwidth. The value of the radius of slots Rg2 = 1–1.5 mm is varied for optimization. Rg2 = 1.2 mm is chosen as the optimetric value. This structure operated from 3 to 20 GHz, which is presented in Fig. 6. Stage 5 incorporates a quarter-wave transformer into the feed line to achieve a further reduction in return loss. Moving on to Stage 6, alterations are made to the circular patch, transforming it into a circular ring to facilitate the creation of a band notch. The inner radii of the ring, denoted as R2 and R4, undergo systematic variation. After optimization, specific values of R2 = 5.1 mm and R4 = 3 mm are identified as optimal. This adjustment is implemented with the specific goal of creating a band notch in the INSAT band, as prominently illustrated in Figs. 7 and 8. These modifications contribute to enhancing the antenna's overall performance and its ability to operate within specific frequency bands. In Stage 7, another circular ring is inserted. This forms a split ring slot between the two rings whose dimensions are designed by using the following equation:

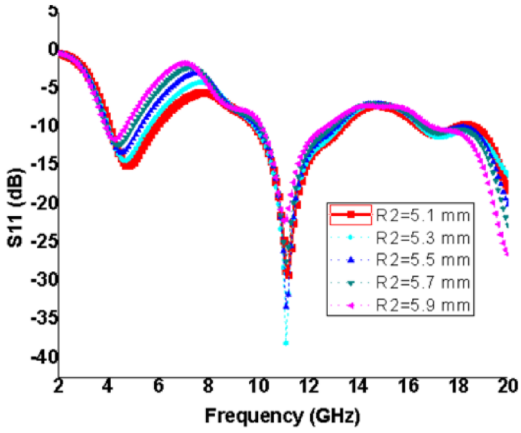

FIG. 7. Plot of S11 for parametric variation of R2.

15 December 2024 07:11:47

© Author(s) 2024

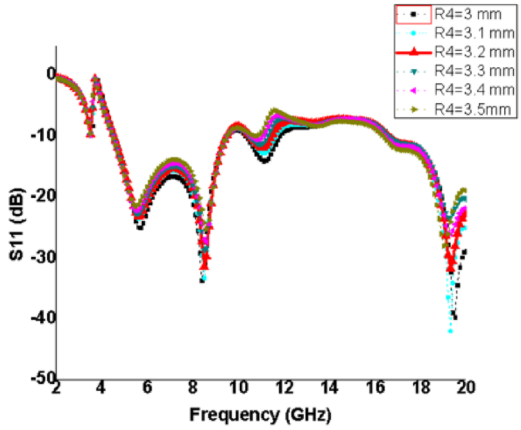

FIG. 8. Plot of S11 for parametric Variation of R4.

The length of split ring slot 1 is given by

$$L_{s1} = \frac{c}{2f_{center}\sqrt{\varepsilon_{eff}}}, \tag{9}$$

where

$$L_{s1} = 2\pi(R_2 - R_3) \text{ for INSAT band notch.} \tag{10}$$

This structure provided a band notch for the INSAT band.

In Stage 8, another ring is inserted to form another split ring slot 2 to provide a band notch in X-band, and its length is given by

$$L_{s2} = \frac{c}{2f_{center}\sqrt{\varepsilon_{eff}}}, \tag{11}$$

where

$$L_{s2} = 2\pi(R_3 - R_4) \text{ for X band notch.} \tag{12}$$

The radii R5 and R6 are varied for optimization and their optimum values are found to be 1.5 and 1 mm. This is shown in Figs. 9 and 10.

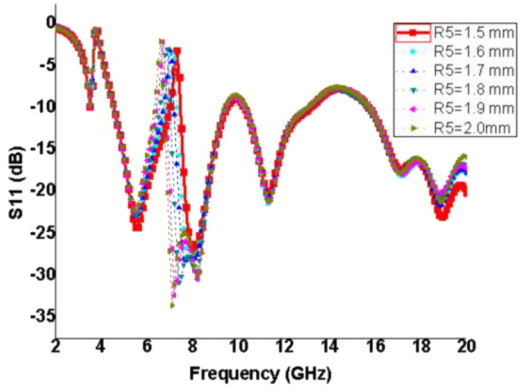

FIG. 9. Plot of S11 for parametric variation of R5.

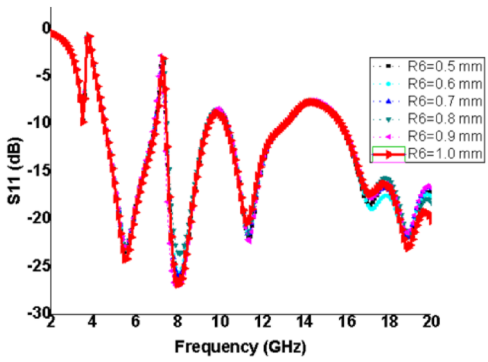

FIG. 10. Plot of S11 for parametric variation of R6.

In Stage 9, an additional enhancement is made by incorporating a U-shaped slot aimed at providing a band notch specifically in the Wi-Fi band. The dimensions of this U-shaped slot are chosen according to a specified equation to ensure optimal performance and targeted notch characteristics. The precise dimensions determined by the specified equation contribute to the effective implementation of the U-shaped slot and its intended impact on band rejection in the Wi-Fi frequency range.

The length of the U-shaped slot is given by

$$L_{s3} = \frac{c}{2f_{center}\sqrt{\varepsilon_{eff}}}, \tag{13}$$

$$L_{s3} = 2 * (length\ of\ vertical\ slots\ in\ U\ shape\ slot) + length\ of\ horizontal\ slot\ in\ U\ shape\ slot \tag{14}$$

for the Wi-Fi band notch.

In Stage 10, the integration of a PIN diode (BAR 6403) into the U-shaped slot introduces reconfigurability to the band notching mechanism. By toggling the diode between the ON and OFF states, the antenna is capable of operating in two distinct modes. In mode 1, with the diode switched ON, the antenna delivers triple notches at 4.3 GHz (4.1–5 GHz), 6.8 GHz (6.3–7.4 GHz), and

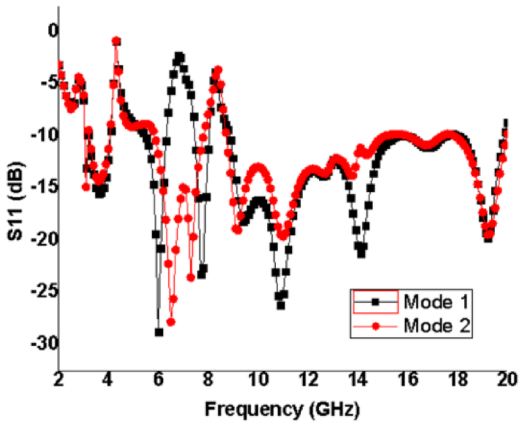

FIG. 11. Plot of S11 for mode 1 and mode 2.

15 December 2024 07:11:47

© Author(s) 2024

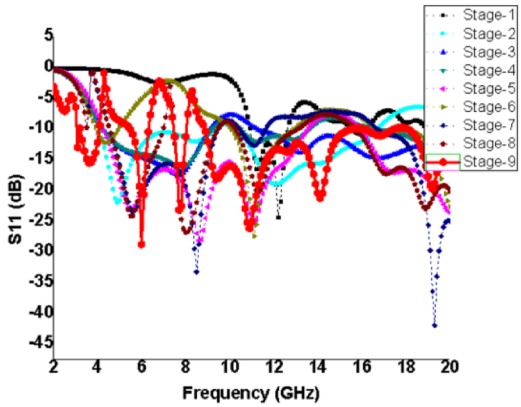

FIG. 12. Plot of S11 for all stages.

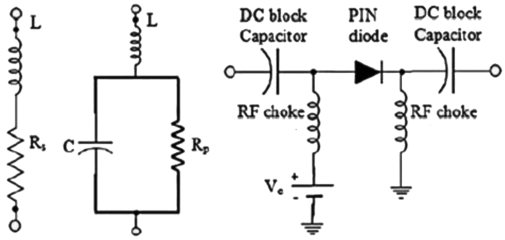

FIG. 13. Equivalent circuit of the PIN diode with the biasing circuit. (a) ON. (b) OFF. (c) Biasing circuit.

8.3 GHz (8.1–8.8 GHz). Conversely, in mode 2, with the diode switched OFF, the antenna provides double notches specifically at 4.3 GHz and also 8.3 GHz. These operational modes are visually represented in Fig. 11, showing the adaptability and versatility brought about by the reconfigurable PIN diode in achieving different notching configurations based on the operational requirements.

The plot of reflection coefficients for all the stages is displayed in Fig. 12. All optimetric values are represented in red color curves in all the figures.

The corresponding equivalent and biasing circuits of the PIN diode in both ON and OFF cases are shown in Fig. 13. In the ON case, L = 0.6 μH and Rs = 2.1 Ω, and in the OFF case, L = 0.6 μH, Rp = 3 KΩ, and C = 0.17 pF.

B. Surface current distribution

The surface current circulations at the corresponding triple notches are visualized in Fig. 14. Notably, it is discerned that split ring slot 1 plays a pivotal role in generating the 4.3 GHz band notch, evident from the concentration of surface current predominantly around the ring when the diode is in the ON state. This specific configuration is depicted in Fig. 14(a). Similarly, the U-shaped slot is identified as the key contributor to the 6.8 GHz notch band. In the ON state of the diode, the surface current is prominently intense all over the U-shaped slot, as illustrated in Fig. 14(b). These observations underscore the significance of specific components in the antenna design, reaffirming their roles in achieving targeted band-notching characteristics.

In the OFF state, a distinct surface current distribution pattern is evident throughout the antenna, rather than being concentrated around the U-shaped slot. This observation signifies that the 6.8 GHz band is not notched under these conditions, as illustrated in Fig. 14(c). Conversely, the 8.3 GHz band notch is attributed to the influence of split ring slot 2. In the OFF state, the surface current is notably concentrated all over this specific slot, as depicted in Fig. 14(d). These insights further corroborate the dynamic nature of the antenna's operational modes, highlighting the distinct contributions of various components to the achievement of specific band-notching characteristics.

C. Design of MIMO antenna for realizing reconfigurable multiple band notches

In the pursuit of achieving a MIMO configuration, the unit elements are strategically arranged in an orthogonal orientation to each other. To maintain a common reference plane, ground planes

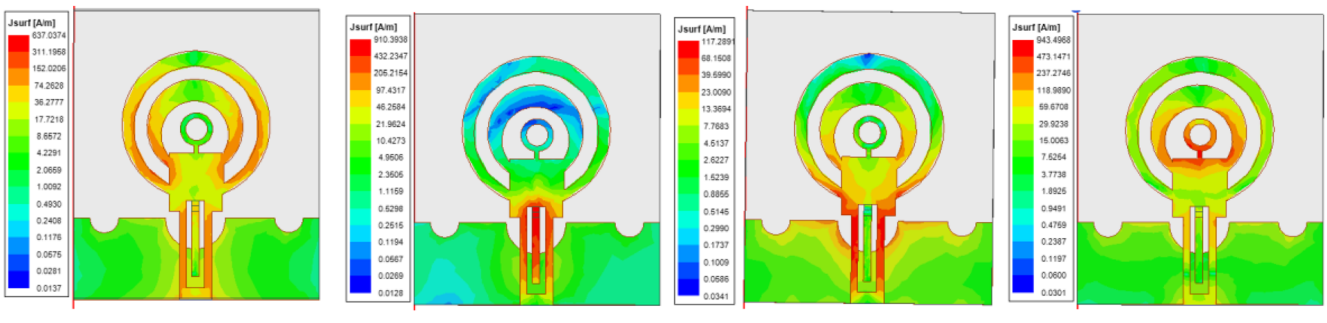

FIG. 14. Surface current circulation. (a) 4.3 GHz (diode—ON). (b) 6.8 GHz (diode—ON). (c) 6.8 GHz (diode—OFF). (d) 8.3 GHz (diode—ON).

15 December 2024 07:11:47

© Author(s) 2024

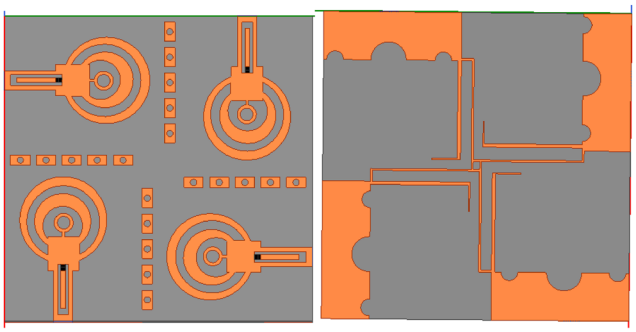

FIG. 15. Structure of MIMO antenna.

of these unit elements are interconnected through a structure comprising narrow metallic lines. In addition, periodic structures, characterized by rectangles with circular slots, are introduced between the elements. The purpose of these structures is to bolster isolation between the elements.

This arrangement and integration of periodic structures are vividly illustrated in Fig. 15. The implementation of this design has proven to be effective, providing substantial isolation levels exceeding 20 dB. This emphasizes the success of the employed strategies in minimizing interference and optimizing the performance of the MIMO configuration.

The printed prototype of the designed MIMO antenna is displayed in Fig. 16.

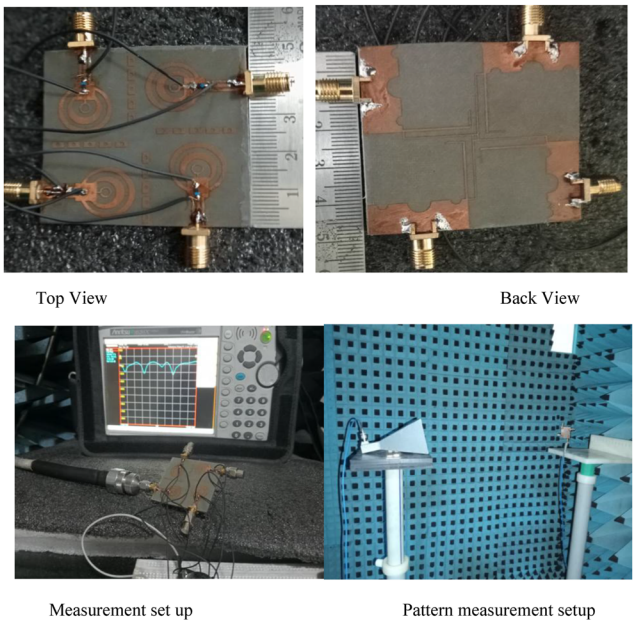

FIG. 16. Prototype—measurement setup.

III. EXPERIMENTAL RESULTS

A. Scattering parameters

The measurement of S parameters for the printed MIMO antenna is conducted using an Agilent vector network analyzer with model number N5242A. The plots of simulated and measured reflection coefficients are visually represented in Fig. 17. In addition, the plots of transmission coefficients are shown in Fig. 17. The operational range of the antenna spans from 2 to 20 GHz, featuring triple notches of 4.1–5.1, 6.4–7.4, and 8.1–8.8 GHz, with center frequencies at 4.3, 6.8, and 8.3 GHz, respectively. The transmission coefficient plot affirms that the elements in the MIMO configuration are adequately isolated, consistently maintaining levels well below −20 dB throughout the whole operational band.

A noteworthy feature of the antenna is the incorporation of PIN diodes, with four diodes inserted in the four elements. The PIN diodes, positioned at the U-shaped slot, introduce reconfigurable characteristics. The antenna works in two distinct modes based on the state of the diodes. In mode 1, where all diodes are in the ON state, the antenna provides triple-band notches. In mode 2, where all diodes are OFF, the antenna provides dual-band notches.

The simulated as well as measured reflection coefficients in both modes are visually depicted in the respective figures, and a comparison plot between the two modes is presented in Fig. 17. These results demonstrate the antenna's adaptability and functionality in different operational configurations, showcasing the successful integration of reconfigurable characteristics. The plots of simulated and also measured transmission coefficients are displayed in Fig. 18 for both modes, and the comparison plot for transmission coefficients in the presence and nonexistence of decoupling structure is displayed in Fig. 19. It concludes that the insertion of periodic structures in between all the elements improved the isolation.

The surface current circulation is visually depicted in Fig. 20. In this configuration, all ports, except the excited one, are appropriately terminated with 50 Ω broadband-matched loads. The notched frequencies are strategically set at 4.3, 6.8, and 8.3 GHz.

As illustrated in Fig. 20, the currents are primarily confined within the region of the active element and the protruded ground. In the vicinity of the neighboring ports, the currents are observed to be very low. This visual representation underscores the excellent isolation achieved by the antenna, as the surface current circulation is effectively localized, minimizing interference and promoting efficient operation across the specified frequency bands.

B. Radiation patterns

The patterns of radiation at its operating frequencies are portrayed in Fig. 21. An observation reveals that the antenna exhibits closely omnidirectional radiation pattern characteristics, allowing it to efficiently transceive signals in all directions. The simulated patterns are denoted by red and blue solid curves, while the measured patterns are denoted by red and blue dotted curves in the elevation and azimuthal planes, respectively.

The red solid curve signifies the simulated pattern in the elevation plane, and the corresponding red dotted curve represents the measured pattern. Similarly, the blue solid curve indicates the sim-

15 December 2024 07:11:47

© Author(s) 2024

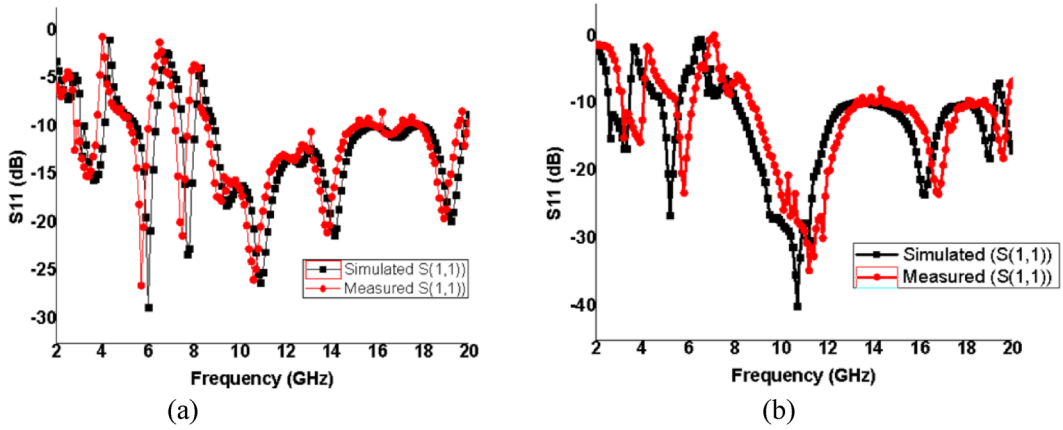

FIG. 17. Simulated and measured S11 plots. (a) Mode 1. (b) Mode 2.

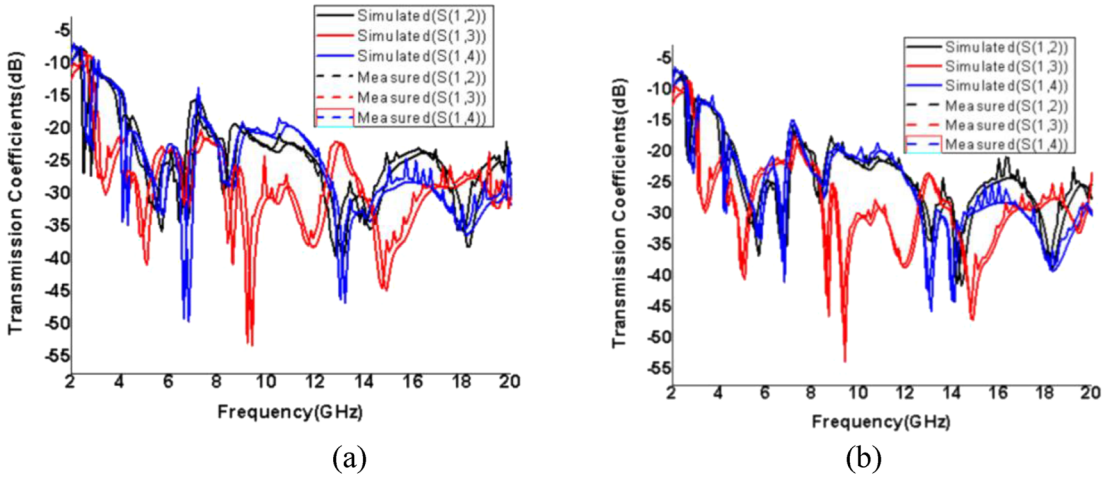

FIG. 18. Simulated and measured transmission coefficient plots. (a) Mode 1. (b) Mode 2.

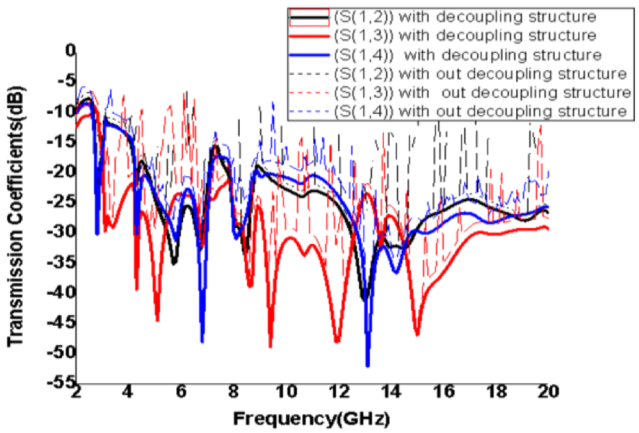

FIG. 19. Comparison plot of transmission coefficients with and without decoupling structure.

ulated pattern in the azimuthal plane, and the corresponding blue dotted curve illustrates the measured pattern.

Figure 21 provides a visual representation of the two-dimensional patterns of radiation in both the elevation and azimuthal planes at the specified operating frequencies within the UWB spectrum. These patterns highlight the antenna's ability to radiate and receive signals effectively in a broad range of directions, aligning with the desired omnidirectional radiation characteristics.

The three-dimensional radiation patterns are displayed in Fig. 22. The gain at the operating frequencies 3.5, 5.5, and 10 GHz is 3.8, 6.6, and 5.4 dBi, respectively.

C. MIMO performance parameters

The trivial metrics of performance of any MIMO antenna, which are given by ECC, CCL, and DG, have been analyzed for verification to make certain that its multi-channel performance is very high. The discussion of these metrics is detailed below.

15 December 2024 07:11:47

© Author(s) 2024

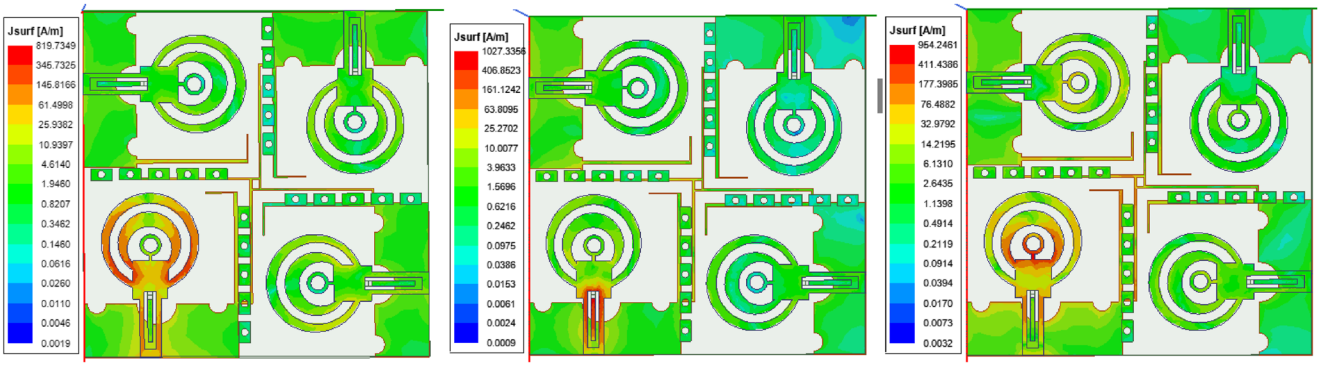

(a) 4.3 GHz (b) 6.8 GHz (c) 8.3 GHz

FIG. 20. Distribution of surface current in the MIMO configuration. (a) 4.3 GHz. (b) 6.8 GHz. (c) 8.3 GHz.

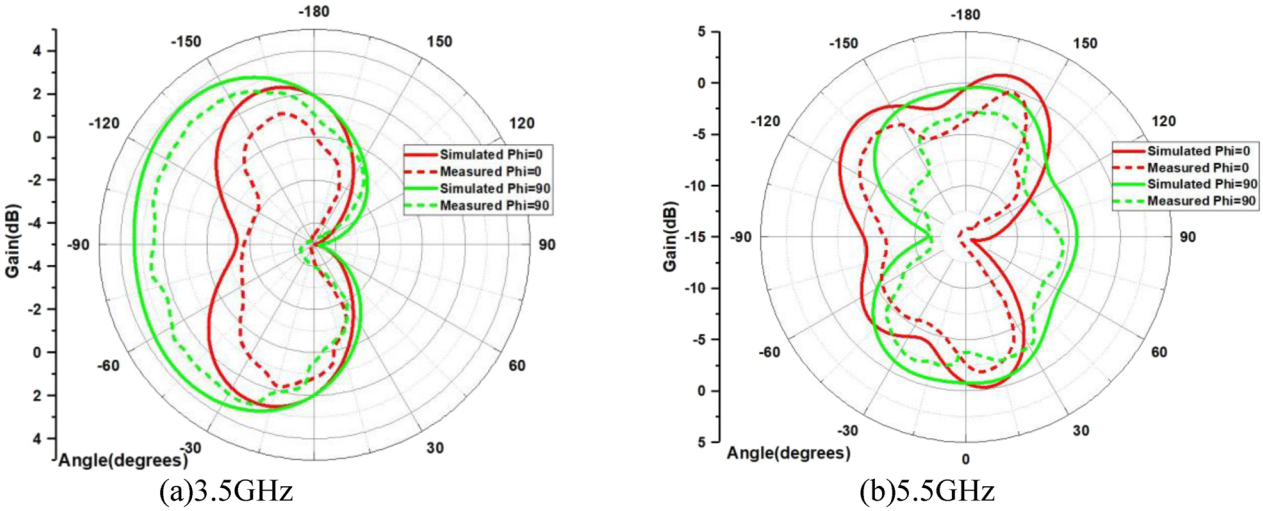

(a)3.5GHz (b)5.5GHz

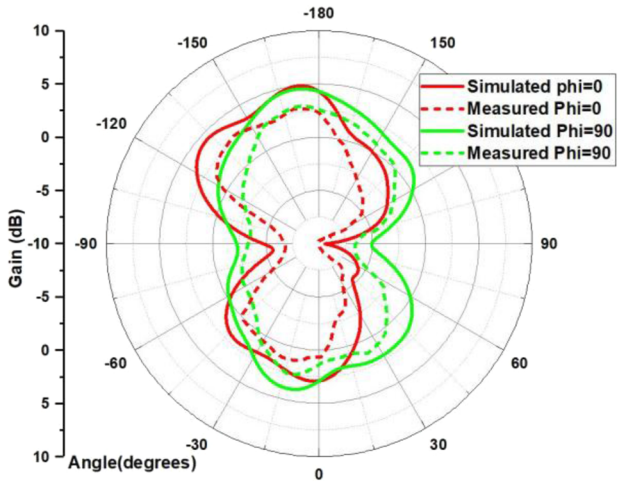

(c) 10 GHz

FIG. 21. Radiation patterns at far field. (a) 3.5 GHz. (b) 5.5 GHz. (c) 10 GHz.

15 December 2024 07:11:47

© Author(s) 2024

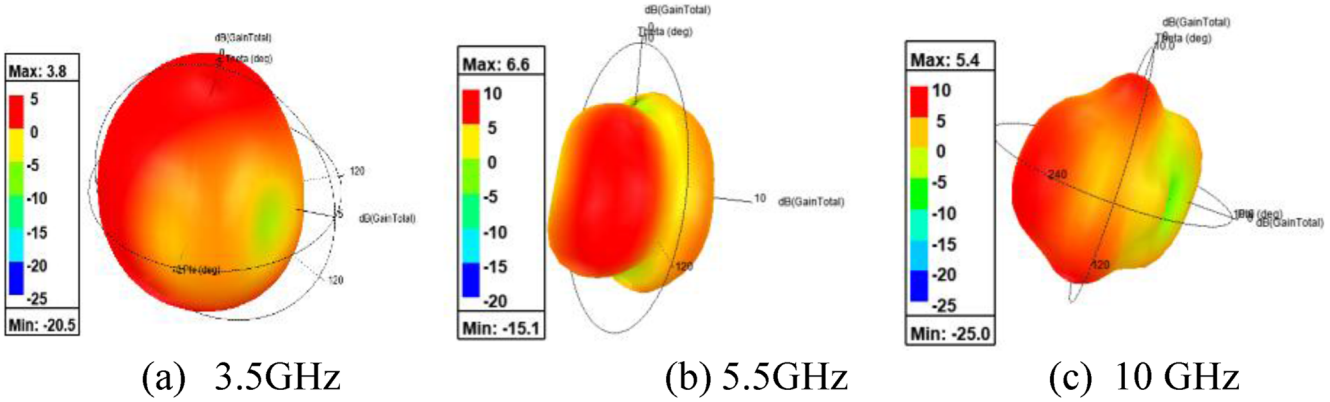

FIG. 22. 3D radiation patterns at operating frequencies. (a) 3.5 GHz. (b) 5.5 GHz. (c) 10 GHz.

1. Envelope correlation coefficient (ECC)

Certainly, the envelope correlation coefficient is a crucial metric that provides insights into the diversity performance of each MIMO radiator. ECC values below 0.1 generally indicate excellent diversity performance in practical scenarios. ECC is typically evaluated using far-field parameters and can be detailed by the following equation:[18]

$$\rho_e = \frac{\left|\int_0^{2\pi}\int_0^{\pi}(XPR\cdot E_{\theta 1}.E_{\theta 2}^{*}.P_{\theta}+E_{\varphi 1}.E_{\varphi 2}^{*}.P_{\varphi})d\Omega\right|^2}{\int_0^{2\pi}\int_0^{\pi}(XPR.E_{\theta 1}.E_{\theta 2}^{*}.P_{\theta}+E_{\varphi 1}.E_{\varphi 2}^{*}.P_{\varphi})d\Omega X\int_0^{2\pi}\int_0^{\pi}(XPR.E_{\theta 1}.E_{\theta 2}^{*}.P_{\theta}+E_{\varphi 1}.E_{\varphi 2}^{*}.P_{\varphi})d\Omega}. \quad (15)$$

Figure 23 shows the simulated as well as measured ECC plots. It is apparent that values of ECC are thoroughly not as much of greater than 0.05 throughout the operative band apart from notched bands.

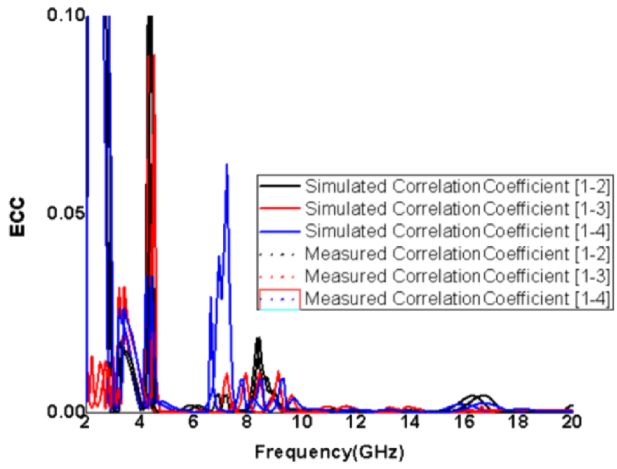

FIG. 23. ECC plot.

2. Diversity gain

Equation (16) calculates diversity gain (DG), which is a key metric in assessing the effectiveness of diversity schemes in a MIMO configuration. The DG provides insights into the transmitted power loss when diversity techniques are implemented. The equation and its outcome in Fig. 24 indicate that the DG is consistently close to 10 dB across the entire operating band,

$$\mathrm{DG} = 10\sqrt{1-\mathrm{ECC}^2}. \quad (16)$$

3. Channel capacity loss (CCL)

The CCL is an essential metric for evaluating the impact of correlation in a MIMO system. It is often assessed using Eqs. (17)–(19), and Fig. 25 presents the obtained CCL values. CCL is typically expressed in bits per second per Hertz (bits/s/Hz), and a lower CCL value is desirable as it indicates less loss in the capacity of the MIMO channel. In your context, achieving a CCL well below the typical required value of 0.4 bits/s/Hz throughout the operational band is a positive outcome. This suggests that the correlation influence in the proposed MIMO configuration is effectively managed, and the chan-

15 December 2024 07:11:47

© Author(s) 2024

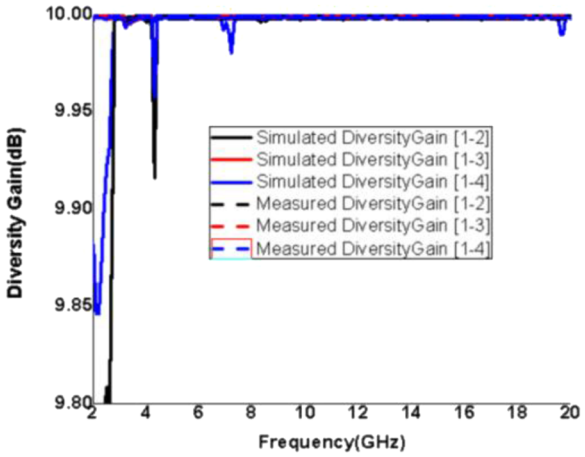

FIG. 24. DG plot.

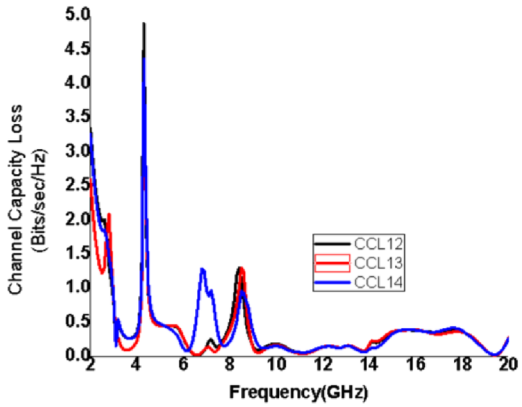

FIG. 25. Plot of CCL.

nel capacity loss is minimized, contributing to the overall efficiency and reliability of the communication system,

$$CCL = [-\log_2 \det(R)], \tag{17}$$

where R represents the correlation matrix that is defined as $R = \begin{bmatrix} \sigma_{11} & \sigma_{12} \\ \sigma_{21} & \sigma_{22} \end{bmatrix}$.

The elements in the above matrix are expressed as

$$\sigma_{ll} = 1 - (|S_{ll}|^2 - |S_{lm}|^2), \tag{18}$$

$$\sigma_{lm} = -(S_{ll}^{*} S_{lm} + S_{ml} S_{mm}^{*}). \tag{19}$$

4. Group delay

The plot of frequency vs group delay between various ports is displayed in Fig. 26. It is between 0.80 and 2ns excluding the notched bands.

5. Radiation efficiency

The consistent high-radiation efficiency exceeding 80% throughout the operational band is a notable achievement. Figure 27, where the radiation efficiency for both mode I and mode II is plotted, shows a remarkable balance between 90% and 98% in both modes across the entire operating band. It is particularly interesting to observe that the radiation efficiency remains high in both operational modes, even though there are slight dips at specific frequencies. In mode I, there are drops at 4.3, 6.8, and 6.3 GHz, while in mode II, drops are observed at 4.3 and 8.3 GHz.

The mention of achieving high radiation efficiency through the use of Rogers RT5880 dielectric substrate is significant.

The selection of the substrate material plays a crucial role in defining the overall performance, and in this case, it contributes to the consistently high radiation efficiency observed across the operating frequencies.

The results obtained by simulation and measurement maintain a good correlation between them but a slight trivial difference is found. This is due to cable losses as coaxial cables are used during the measurement process.

Table II illustrates the comparison of reconfigurable MIMO antennas in terms of dimensions, number of ports, and number of reconfigurable band notches in cited references. To determine how much more compact the proposed antenna is with respect to cited reference designs, the following formula is used:

$$Percentage\ of\ reduction = \frac{(Reference\ antenna\ size - Proposed\ antenna size)}{Reference\ antenna\ size} \times 100. \tag{20}$$

The antennas cited in the above table provide either single or dual reconfigurable band notches, but the proposed design provides triple-/dual-band notches and all the cited designs have only two ports in MIMO configuration. In conclusion, the proposed antenna presents a compact design featuring four ports and stands out by offering multiple reconfigurable band notches that are not addressed in the literature. As per the author's knowledge, this unique combination of features sets the antenna apart from existing literature. The reconfigurability aspect, coupled with the ability to notch multiple bands, enhances the antenna's versatility and adaptability, making it

15 December 2024 07:11:47

© Author(s) 2024

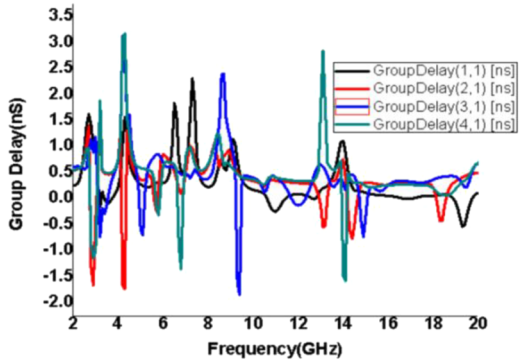

FIG. 26. Plot of group delay.

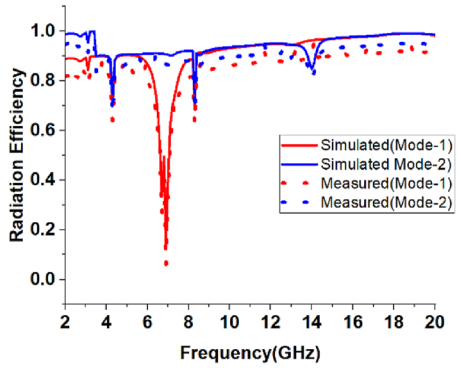

FIG. 27. Radiation efficiency plot.

a novel contribution to the field. The proposed antenna is 7% smaller than the existing designs. Hence, its compact size further adds to its practicality, potentially making it a valuable solution for various communication applications.

IV. CONCLUSION

This paper introduced a miniaturized four-port diversity antenna with the unique capability of multiple reconfigurable band notches, designed specifically for 5 G cognitive radio applications. The integration of periodic rectangles with circular slots between the antenna elements serves as a decoupling structure, contributing to enhanced isolation despite the compact nature of the proposed antenna. The reconfigurable feature enables the antenna to operate in two distinct modes, providing adaptability to different operational scenarios. Notably, the antenna demonstrates effectiveness in overcoming interferences from INSAT, Wi-Fi-6E, and X-band satellite bands. The good correlation observed between simulated and measured results further supports the suitability of the designed antenna for MIMO-UWB applications.

ACKNOWLEDGMENTS

The authors thanked the Principal and Management of the Jawaharlal Nehru Technological University Anantapur, Ananthapuramu, Sri Venkateswara College of Engineering, Tirupati, and the Velagapudi Ramakrishna Siddhartha Engineering College for providing facilities to pursue the required research for publishing this paper.

AUTHOR DECLARATIONS

Conflict of Interest

The authors have no conflicts to disclose.

Author Contributions

Saritha Vanka: Conceptualization (equal); Investigation (equal); Methodology (equal); Validation (equal); Writing – original draft (equal); Writing – review & editing (equal). **Chandrasekhar C**: Supervision (equal); Writing – review & editing (equal).

TABLE II. Comparison of parameters.

References	Size of antenna (mm^3)/No. of ports	No. of band notches	Isolation (dB)	% Of compactness comparison for single element/remarks
19	80 × 70 × 1.6/2	WiMAX, WLAN	=15	17.7/Limited to two band notches, limited to two ports
20	20 × 40 × 1.6/2	WiMAX, WLAN	>15	Limited to two band notches, limited to two ports
21	40 × 23 × 1.5/2	WLAN	>15	Limited to single band notch, limited to two ports
22	22 × 36 × 1.6/2	WLAN	>20	Limited to single band notch, limited to two ports
23	40 × 23 × 1.6/2	WLAN	>20	Limited to single band notch, limited to two ports
24	48 × 24 × 1.6/2	WLAN	>20	1.7/Limited to single band notch, limited to two ports
25	45 × 26 × 1.6/2	WLAN	>20	1.5/Limited to single band notch Limited to two ports
Prop	48 × 48 × 1.6/4	INSAT, Wi-Fi (6E), X-band	>20	Provides dual/triple band notches, features four ports, average compactness—6.96

15 December 2024 07:11:47

© Author(s) 2024

DATA AVAILABILITY

Data sharing is not applicable to this article as no new data were created or analyzed in this study.

REFERENCES

[1] S. Modak, T. Khan, and R. H. Laskar, "Penta-band notched ultra-wideband monopole antenna loaded with electromagnetic bandgap-structures and modified U-shaped slots," Int. J. RF Microwave Comput.-Aided Eng. **29**, e21963 (2019).

[2] S. Modak, T. Khan, and R. H. Laskar, "Penta-notched UWB monopole antenna using EBG structures and fork-shaped slots," Radio Sci. **55**(9), e2019RS006983, https://doi.org/10.1029/2019rs006983 (2020).

[3] S. Modak, T. Khan, and R. H. Laskar, "Loaded UWB monopole antenna for quad band-notched characteristics," IETE Tech. Rev. **39**, 568 (2021).

[4] T. Ali, M. M. Khaleeq, and R. C. Biradar, "A multiband reconfigurable slot antenna for wireless applications," Int. J. Electron. Commun. **84**, 273 (2019).

[5] H. Islam *et al.*, "Bandstop filter decoupling technique for miniaturized reconfigurable MIMO antenna," IEEE Access **10**, 19060–19071 (2022).

[6] P. P. Shome, T. Khan, and R. H. Laskar, "A state-of-art review on band-notch characteristics in UWB antennas," Int. J. RF Microwave Comput.-Aided Eng. **29**, e21518 (2018).

[7] V. Saritha and C. Chandrasekhar, "A study and review on frequency band notch characteristics in reconfigurable MIMO-UWB antennas," Wireless Pers. Commun. **118**(4), 2631–2661 (2021).

[8] R. JothiChitra and V. Nagarajan, "Frequency reconfigurable antenna using PIN diodes," in *Twentieth National Conference on Communications (NCC)* (IEEE, 2014), pp. 1–4.

[9] R. George, S. Kumar, S. A. Gangal, and M. Joshi, "Frequency reconfigurable pixel antenna with PIN diodes," Prog. Electromagn. Res. Lett. **86**, 59–65 (2019).

[10] S. Chaimool, T. Hongnara, C. Rakluea, P. Akkaraekthalin, and Y. Zhao, "Design of a PIN diode-based reconfigurable metasurface antenna for beam switching applications," Int. J. Antennas Propag. **2019**, 7216324 (n.d.).

[11] K. Sharma, A. Karmakar *et al.*, "Reconfigurable dual notch band antenna on Si-substrate integrated with RF MEMS SP4T switch for GPS, 3G, 4G, bluetooth, UWB and close range radar applications," Int. J. Electron. Commun. **110**, 152873 (2019).

[12] A. A. Palsokar and S. Lahudkar, "Frequency and pattern reconfigurable rectangular patch antenna using single PIN diode," Int. J. Electron. Commun. **125**, 153370 (2020).

[13] A. H. Nazeri, A. Falahati, and R. M. Edwards, "A novel compact fractal UWB antenna with triple reconfigurable notch reject bands applications," Int. J. Electron. Commun. **101**, 1–8 (2019).

[14] A. A. Mohammed, F. M. Alnahwi, S. A. Abdulkareem *et al.*, "A compact monopole antenna with reconfigurable band notch for underlay cognitive radio applications," in *International Conference on Advances in Sustainable Engineering and Applications (ICASEA)* (IEEE, 2018), pp. 25–30.

[15] A. A. Abdulhameed, F. M. Alnahwi *et al.*, "A compact cognitive radio UWB/reconfigurable antenna system with controllable communicating antenna bandwidth," Aust. J. Electr. Electron. Eng. **16**(1), 1–11 (2019).

[16] K. Madhusudhana and S. P. Hegde, "Reconfigurable fractal microstrip antenna with varactor diode," Global Transitions Proc. **3**(1), 183–189 (2022).

[17] A. Alhegazi, Z. Zakaria, N. A. Shairi *et al.*, "Reconfigurable filtering-antenna with triple band notches for UWB applications," Int. J. Eng. Res. Technol. **12**, 3076–3081 (2019).

[18] A. Ramachandran, S. Mathew, V. Rajan *et al.*, "A compact triband quad-element MIMO antenna using SRR ring for high isolation," IEEE Antennas Wireless Propag. Lett. **16**, 1409–1412 (2016).

[19] Y. Tawk, J. Costantine, and C. G. Christodoulou, "Reconfigurable filtennas and MIMO in cognitive radio applications," IEEE Trans. Antennas Propag. **62**(3), 1074 (2013).

[20] R. Mathur and S. Dwari, "Compact planar reconfigurable UWB-MIMO antenna with on-demand worldwide interoperability for microwave access/wireless local area network rejection," IET Microwaves, Antennas Propag. **13**(10), 1684–1689 (2019).

[21] A. Quddus, R. Saleem, and M. Bilal, "Reconfigurable band-notched UWB-MIMO antenna," in *16th Mediterranean Microwave Symposium (MMS)* (IEEE, 2016), pp. 1–4.

[22] R. Saleem, A. Quddus, M. Bilal *et al.*, "A wideband MIMO antenna with fixed and reconfigurable band notch characteristics for UWB systems," in *2020 IEEE International Symposium on Antennas and Propagation and North American Radio Science Meeting* (IEEE, 2020), pp. 471–472.

[23] A. Quddus, R. Saleem, S. Arain *et al.*, "Electronically reconfigurable WLAN band-notched MIMO antenna for ultra-wideband applications," Appl. Comput. Electromagn. Soc. **36**(8), 1108–1111 (2021).

[24] H. Islam, S. Das, T. Ali *et al.*, "A frequency reconfigurable MIMO antenna with bandstop filter decoupling network for cognitive communication," Sensors **22**(18), 6937 (2022).

[25] H. Medkour, S. Lakrit, S. Das *et al.*, "A compact printed UWB MIMO antenna with electronically reconfigurable WLAN band-notched characteristics," J. Circuits, Syst., Comput. **31**(03), 2250045 (2022).

15 December 2024 07:11:47

© Author(s) 2024

ScienceDirect

e-Prime - Advances in Electrical Engineering, Electronics and Energy

Volume 8, June 2024, 100502

PAPR reduction using polynomial based compressing with Rapp model in GFDM

P.V. Naganjaneyulu [a], U. Sreenivasulu [b], M. Nageswara Rao [c], G. Sujatha [d]

Show more

Outline | Share Cite

https://doi.org/10.1016/j.prime.2024.100502

Get rights and content

Under a Creative Commons license

open access

Highlights

- To attack PAPR problem, in this paper, we propose a polynomial based companding method with iterative expansion that is called polynomial-based companding technique (PCT). Based on our simulation results, a great amount of PAPR reduction can be achieved through utilization of our proposed technique.
- Through simulations, we have also investigated the bit error rate (BER) performance of the system while adopting our PCT method. Our simulations reveal that there is a tradeoff between PAPR reduction and BER performance.
- The simulation results show that the PAPR of the proposed GFDM is reduced by 4 dB and 5 dB as compared to conventional GFDM signal and conventional OFDM, respectively at CCDF of 10^{-2}.

Abstract

Generalized Frequency Division Multiplexing (GFDM) has been considered as an attractive candidate to replace Orthogonal Frequency Division Multiplexing (OFDM) for the fifth generation (5 G) mobile networks. GFDM system has better spectral characteristics compared to the OFDM system due to the usage of properly selected pulse shaping filters. Non-causal ideal filters, such as the raised cosine (RC), are commonly used in the GFDM systems. Here, Generalized frequency division multiplexing is a promising candidate to deploy. However, as an intrinsic property of multi-carrier modulation, the high signal amplitude fluctuation can cause several degradation effects when the signal is affected by nonlinearities. The pulse shaping filters are designed using the computationally efficient quadratic programming (QP) approach. Therefore, the aim of this paper is to evaluate the performance of Generalized frequency division multiplexing systems undergoing nonlinear amplification. We evaluate the bit error ratio using high power amplifier, namely the Rapp model. The results show that the fault rate is apparently affected according to the particular high power amplifier model and its transmission parameters.

Previous Next

Keywords

Generalized frequency division multiplexing; Polynomial-based companding technique; PAPR; BER

Introduction

Future wireless communication systems must meet the fundamental needs of faster speed and greater coverage. High data speeds, high efficiency, and low latency are promised by the fifth generation (5 G) standard, but putting 5 G systems based on MTM (machine-to-machine) communications and the Internet of Things (IoT) into practice still presents significant challenges. Low out-of-band emission and synchronous relaxation [1].

Tight synchronization between users is necessary to avoid this since OFDM signals are particularly sensitive to time and frequency offsets [2]. Several novel techniques, including FBMC, UFMC, GFDM, and RB-OFDM, were put forth in [3] to address this weakness of OFDM. We examine the effectiveness of GFDM among different techniques and take into account its applicability for 5 G networks. Data is transmitted in time-frequency blocks in GFDM, which eliminates the need for several subcarriers. As a result, the PAPR of the GFDM system may be lower than that of the OFDM system given the identical spectral efficiency circumstances. However, it also creates self-induced interference, which can be reduced at the receiver side using interference cancellation techniques [4]. In this system, GFDM becomes spectrally efficient in comparison to OFDM systems by adding a cyclic prefix between blocks [4], [5]. GFDM systems are a desirable alternative for 5 G communication networks because of this feature. However, when the subcarriers mimic OFDM subcarriers, the PAPR issue in GFDM is accentuated and made worse by the presence of high-power amplifiers [6]. The literature discusses a

variety of PAPR reduction methods for OFDM systems, including coding, partial transmission sequences, clipping and filtering, tone preservation, tone injection, companding, and precoding. The PAPR of OFDM signals can be decreased via precoding.

New applications are emerging, such as machine-to-machine (M2M) communication, which refers to extensive wireless connections between machines without human involvement, and fifth-generation wireless communication [7] communication systems, such as the Internet of Things (IoT) (5 G) We The network must meet certain conditions. For instance, numerous CFOs will cause a significant degree of MAI (numerous Access Interference) on a network uplink of multiple embedded devices or machines using OFDMA (Frequency Division Multiple Access). Strict synchronization is necessary to avoid this interference, but it places a significant burden on the network [8].

Literature survey

Due to its desirable qualities, GFDM has recently attracted a lot of interest and has been chosen as a candidate waveform for 5 G [9]. One subset of "filtered multicarrier techniques" is the flexible multicarrier modulation scheme known as GFDM [10]. From the viewpoint of the filter bank, GFDM is an FBMC system where circular filtering at the subcarrier level takes the role of linear filtering. The system employs tail biting, also known as cyclic pulse shaping, to transmit two-dimensional blocks made up of data symbols spread over time-frequency resources. To avoid speed loss brought on by lengthy cyclic prefix (CP) requirements, tail biting preserves cyclic characteristics in both the time and frequency domains [11]. The ramp-up and ramp-down of multi-carrier signals that were transiently filtered by the prototype filter by circular pulse shaping are thus eliminated by GFDM.

The high PAPR (Peak-to-Average Power Ratio) of multicarrier systems is one of their key drawbacks. To overcome this problem, [12] takes into account key GFDM characteristics such as the ability to reduce the amount of subcarriers and to alter the parameters of the pulse-shaping filter. The issue is not resolved by fewer subcarriers because this invariably leads to poorer PAPR in multi-carrier systems. As a result, it is still necessary to have many subcarriers while lowering peaks as much as feasible [13].

This study extends the "polynomial-based companding technique" (PCT) previously suggested for OFDM in [14] to GFDM to address the PAPR issue. The goal of this research is to adapt PCT to work with GFDM. In this method, the transmitter employs a polynomial-based compression function, and the receiver employs an iterative approach as a repetition of the transmitter's transformation. Compared to other companding techniques, this significantly raises the signal-to-noise ratio (SNR) necessary to obtain a certain bit error rate (BER) in the expansion operation. The expansion is included in the demodulation procedure in [15] because it is coupled with an FFT (Fast Fourier Transform) block. Consequently, it cannot be used directly with multi-carrier systems like GFDM. We generalize the receiver spreading method in this work such that it can be used with any multicarrier modulation system. One of the main contributions of this paper is this. GFDM PAPR can be successfully reduced with PCT while still achieving high BER performance, according to simulation studies. A trade-off exists between computational complexity, PAPR reduction capabilities, and BER performance, according to our numerical investigations [16].

Problem definition

Large peaks in the transmitted signal are frequently caused by the structural overlap of subcarriers in multicarrier modulation schemes. The PAPR stands for the peak-to-average power ratio of the multicarrier signal. The dynamic range or change in transmitted signal power is defined by the PAPR metric. The power amplifier (PA) will become saturated by a big PAPR, which will result in nonlinearity, significant distortion, and a decline in BER performance, or interference between neighboring channels. This is brought on by the regeneration of out-of-band radiation brought on by intermodulation products. The transmitted signal's PAPR is described in the manner as follows.

$$PAPR\ (x(n)) = \frac{max[x(n)]^2}{e\left[|x(n)|^2\right.} \quad (1)$$

Two major categories can be used to categorize the PAPR reduction techniques for multicarrier signals. Before multicarrier modulation, the first group of techniques used distortion-free methods. These methods do have significant drawbacks, though, including high computational complexity, extra information overhead, a limited number of system parameters, and slow speed. After multicarrier modulation, approaches for signal distortion fall under the second category. The fundamental drawback of these methods is BER degradation. Companding is an effective signal distortion technique that requires little complexity and no bandwidth extension. This work focuses on PCT, a companding technique that is intended to lessen the BER performance cost as well as computational complexity.

System model

In Fig. 1, the system model is displayed. The process of data transfer can be explained as follows. A convolutional encoder first encrypts the binary data that needs to be transmitted before interleaving it. Baseband modulation (QPSK, 16-QAM, etc.) is the following step. The blocks with K_M elements are then created from the complicated modulation symbols, where M is the total number of slots and K is the number of subcarriers. The GFDM modulation is then used. In other words, the individual subcarrier data streams are upconverted to pulse form and then oversampled. To enhance the signal before transmission, use a specialized HPA model. Each action is offered inversely on the receiver side depending on the transmitter's stage of signal processing.

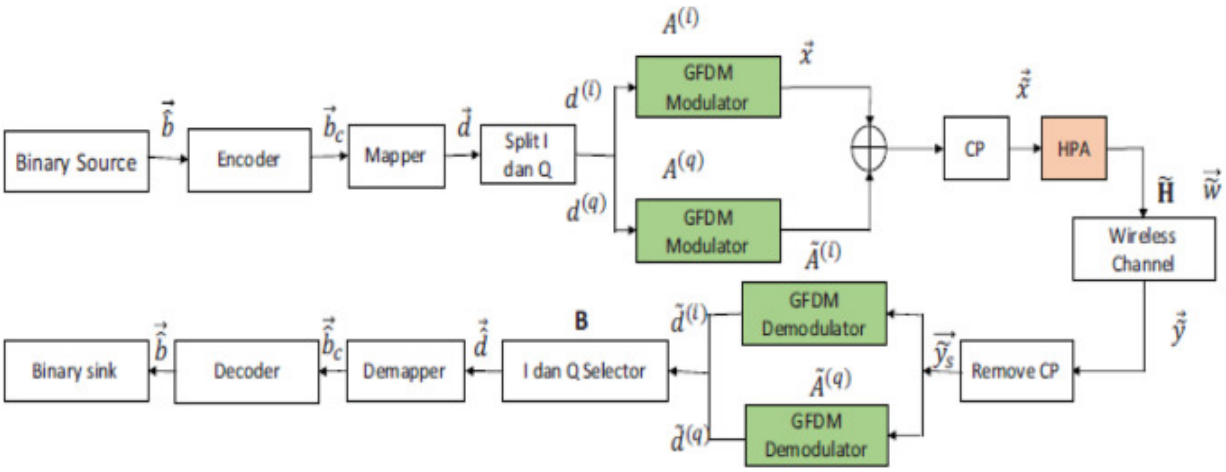

Download: Download high-res image (266KB)

Download: Download full-size image

Fig. 1. System model block diagram.

Several unique compression polynomials are used in the approach used on the transmitter. By effectively lowering PAPR, this method demonstrates that polynomial function order can be determined by striking a balance between complexity and performance. At the transmitter, the normalized signal is condensed using a nonlinear polynomial function. As a result, PAPR is decreased while keeping steady peaks and increasing average signal energy. Careful function selection is necessary for the effective implementation of iterative algorithms at the receiver. There are several restrictions on the selection of polynomial coefficients depending on the expected characteristics of the curve. These circumstances are:

1. The function must be invertible between [−1,1] to apply a one-to-one mapping to a signal. Within the aforementioned range, this enables the receiver to function in reverse. It follows that this function must increase and that its extreme point, where the differential change's sign is located, must lie outside of this range.

2. The function has to be unusual. As a result, even-order terms' coefficients must be zero.

3. The function must pass through the origin in the aforementioned range, taking its minimum at (−1,−1) and its maximum at (1,1) along the way.

4. To lower PAPR as effectively as feasible, the steepest slope at the origin and the lowest slope at the pole (ideally zero) should be chosen. The slope is steeper at (0,0) for higher order polynomials, as shown in Fig. 2.

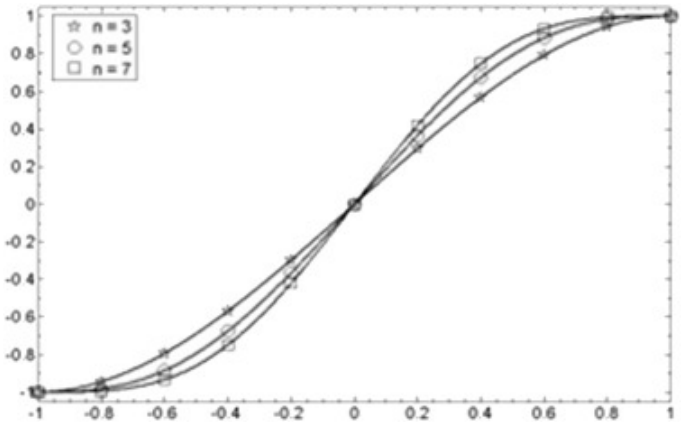

Download: Download high-res image (94KB)

Download: Download full-size image

Fig. 2. Calculated polynomials of order 3, 5, 7.

5. The simulation results show that a key limiting element is the existence of switching points (points at which the inclination changes) within the function range. For a specific BER performance, the transition point raises the SNR requirement. As a result, switch points other than the origin are prohibited for functions in the range [−1,1]. Any polynomial function of odd degree can satisfy the aforementioned conditions. Now let's define:

$$f(x) = a_p x^p + a_p x^{p^2} + \ldots + a_5 x^5 + a_3 x^3 + a_1 x \tag{2}$$

p being an odd number. The following is how coefficients for polynomials of orders 3, 5, and 7 are derived.

$$p = 3 : a_3 = -\tfrac{1}{2}, a_1 = \tfrac{3}{2} \tag{3}$$

$$p = 5 : a_5 = \tfrac{3}{8}, a_3 = -\tfrac{5}{4}, a_1 = \tfrac{15}{8} \tag{4}$$

$$p = 7 : a_7 = -\tfrac{5}{16}, a_5 = \tfrac{21}{16}, a_3 = -\tfrac{35}{16}, a_1 = \tfrac{35}{16} \tag{5}$$

Fig. 2 illustrates these operations. Because there are fewer known parameters than unknown parameters for higher order polynomials, the coefficients cannot be readily derived in the same way.

The polynomial-based compressor should be added to the IFFT after computing the real and imaginary components of x[n]. So:

$$Re\{x[n]\} = \tfrac{1}{N} \textstyle\sum_{k=0}^{N-1} (A_r[n,k]) \tag{6}$$

$$Im\{x[n]\} = \tfrac{1}{N} \textstyle\sum_{k=0}^{N-1} (A_i[n,k]) \tag{7}$$

Where

$$A_r[n,k] = Re\{X[k]\} Cos\left(\tfrac{2\pi kn}{N}\right) - Im\{X[k]\} Sin\left(\tfrac{2\pi kn}{N}\right) \tag{8}$$

$$A_i\,[n,k] = Im\,\{X\,[k]\}\,Cos\left(\tfrac{2\pi kn}{N}\right) + Re\,\{X\,[k]\}\,Sin\left(\tfrac{2\pi kn}{N}\right) \tag{9}$$

The results of applying the pth order compressing function to *Re*[n] and Im[n] can be displayed as follows, respectively:

$$\mathrm{Re}\,\{y\,[n]\} = a_p\left(\tfrac{1}{N}\textstyle\sum_{k=0}^{N-1} A_r\,[n,k]\right) \wedge p + \ldots + a_1\left(\tfrac{1}{N}\textstyle\sum_{k=0}^{N-1} A_r\,[n,k]\right) \tag{10}$$

$$\mathrm{Im}\,\{y\,[n]\} = a_p\left(\tfrac{1}{N}\textstyle\sum_{k=0}^{N-1} A_i\,[n,k]\right) \wedge p + \ldots + a_1\left(\tfrac{1}{N}\textstyle\sum_{k=0}^{N-1} A_i\,[n,k]\right) \tag{11}$$

where the compressed signal is represented by y[n]. The constellation shapes of the original and compressed signals are depicted in Fig. 3.

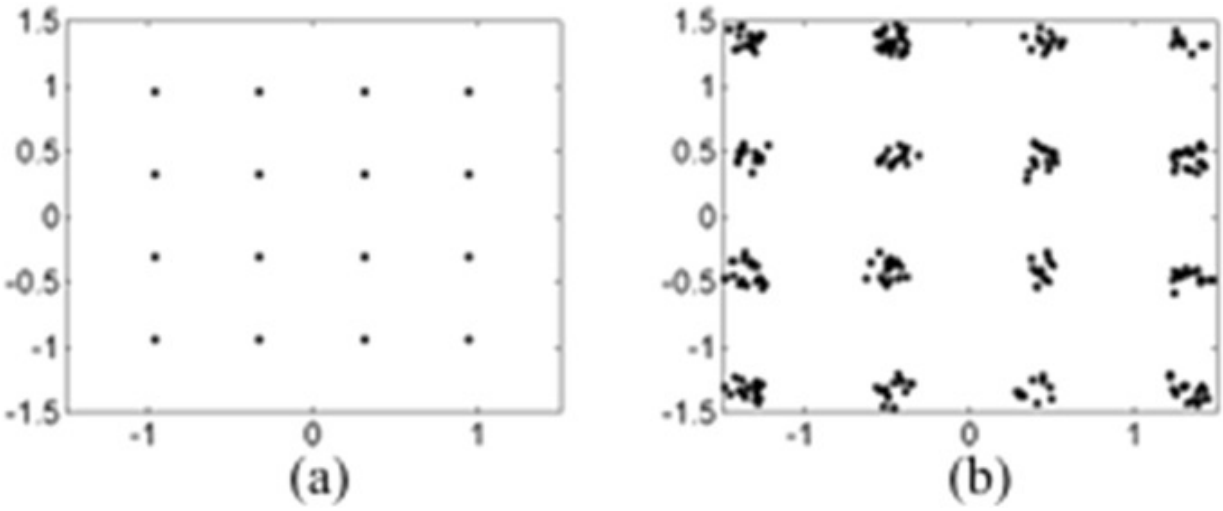

Download: Download high-res image (132KB)

Download: Download full-size image

Fig. 3. The signal constellation for (a) the original signal and (b) its compressed version in the frequency domain.

Receiver

Three common GFDM receiver types ZF (zero forcing), MF (matching filter), and MMSE (minimum mean square error) receivers can be derived from matrix representation. Now imagine that the signal is transmitted via an AWGN channel and that the receiver time samples, r[n], are represented by a vector, r.

$$\boldsymbol{r} = \boldsymbol{x} + \boldsymbol{w} \tag{12}$$

where x is the transmitted vector from (12) and w is the AWGN noise with zero mean and variance.

Results and discussion

In this work, simulation experiment carried out by MATLAB 2021a and to assess the PAPR and BER performance of the GFDM system. The Rapp HPA SSPA model is used in the simulation. To compare the effectiveness of PAPR and BER, simulations of existing OFDM systems and systems using the proposed technique are also performed. The binary source data is encoded using a four-state convolutional encoder with polynomial (6,7)8 in octal notation and code rate 1 = 2 to boost resilience to nonlinear noise distortions. The bits are according to the mapper using Gray-mapped QPSK or 16-QAM constellations after interleaving with the random permutation vector. 5 sub-symbols and 512 subcarriers are used in each block. A root-raised cosine filter with a 0.2 roll-off factor serves as the pulse-shaping filter. The simulation configuration ignores the cyclic prefix since we use an AWGN channel model. Osat is set to 1, and Rapp HPA model parameter s is set to 3.

Bit error rate (BER)

For reference, the figure below displays the BER performance of GFDM and OFDM without the use of HPA. Additionally, the ZF GFDM receiver selection and the pulse-shaping filter features result in a minimal performance difference between OFDM and GFDM. In the Rapp model, Fig. 4 compares the BER performance of OFDM and GFDM utilizing QPSK as the baseband modulation. We can see that using HPA causes the error rate to significantly worsen. However, applying the Saleh model results in a lower BER.

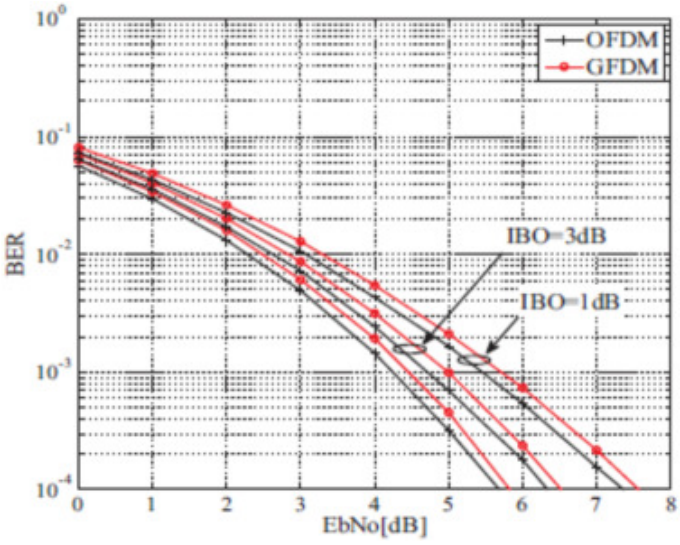

Download: Download high-res image (388KB)

Download: Download full-size image

Fig. 4. BER performance of GFDM and OFDM.

Fig. 5 illustrates the extremely high mistake rate, particularly for smaller IBO levels. Fig. 7 displays the 16-QAM's BER performance. The error rate is larger than QPSK, as can be shown. As demonstrated in Fig. 8, the BER of the Saleh model is also worse.

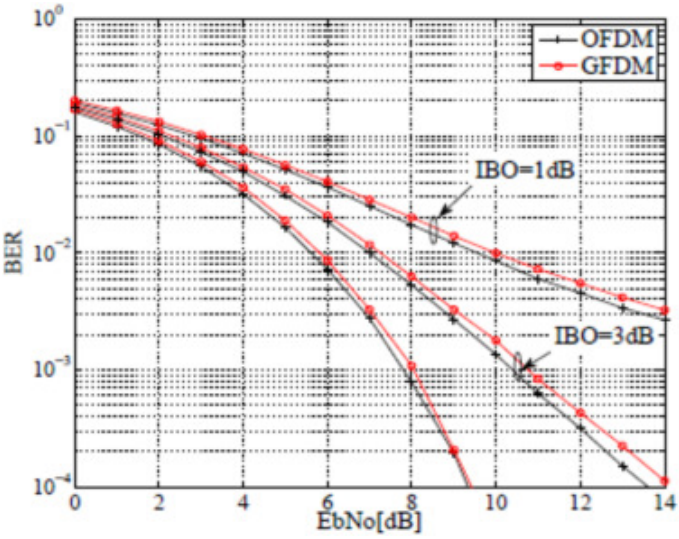

Download: Download high-res image (388KB)

Download: Download full-size image

Fig. 5. BER performance of GFDM and OFDM, respectively, using 16-QAM and Rapp HPA model with different IBO values.

In the BER performance of the GFDM system when different IBO values and roll-off factors of the RRC pulse shaping filter, respectively, will be revealed. Here, we set the EbN0 values to 4 dB and alternate the IBO and roll-off values. In Fig. 7 the BER performance of GFDM using QPSK as baseband modulation under Rapp model is shown when different IBO values are used and the roll-off factor of the RRC filter is changed. It can be seen that the error rate is strongly dependent on the IBO value as well as the roll-off factor. Especially for low IBO values and high roll-off factors the error rate is very high.

The impact of polynomials of various degrees is depicted in Fig. 9, where the lowest amount of iterations needed for optimum performance is at the receiver. The polynomials of degree 3, 5, and 7 were used to generate the curves in this figure over 3, 7, and 9 iterations, respectively (Fig. 6).

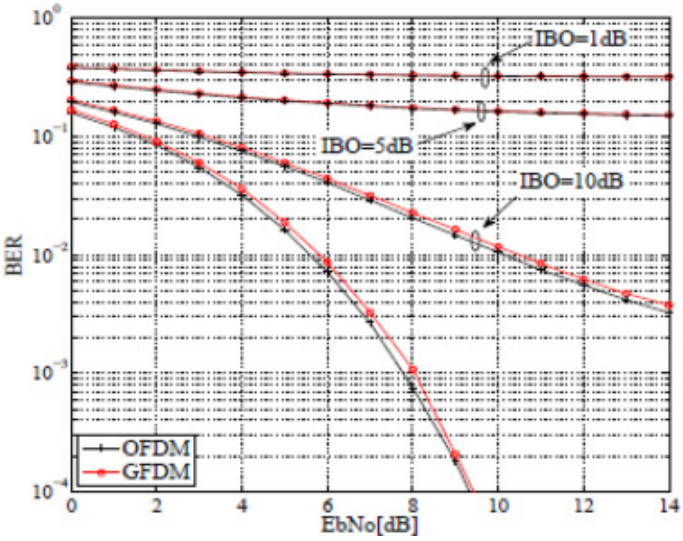

Download: Download high-res image (532KB)

Download: Download full-size image

Fig. 6. BER performance of GFDM and OFDM, respectively, using 16-QAM and Saleh HPA model with different IBO values.

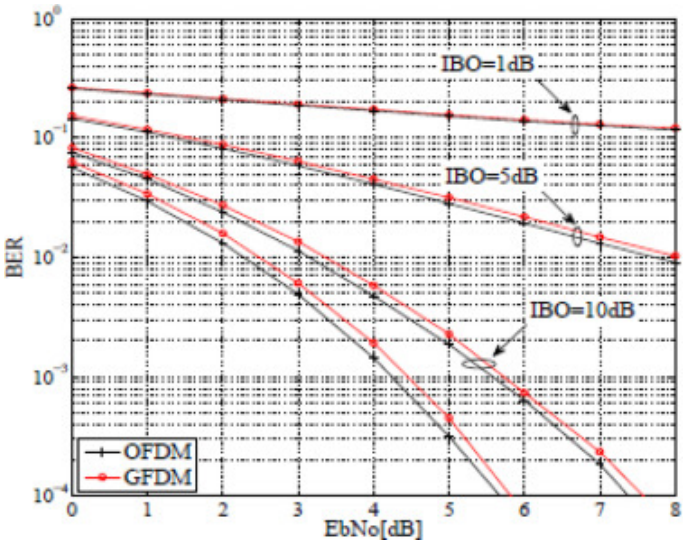

Download: Download high-res image (540KB)

Download: Download full-size image

Fig. 7. BER performance of GFDM and OFDM, respectively, using QPSK and Saleh HPA model with different IBO values.

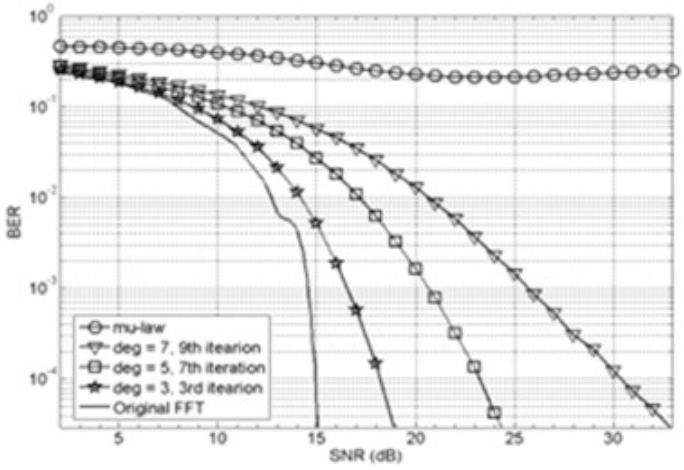

Download: Download high-res image (222KB)

Download: Download full-size image

Fig. 8. Effect of polynomial order on system performance.

Conclusion

This study examines the impact of nonlinear amplification on GFDM system BER performance. According to the simulation results, nonlinear amplification severely reduces the GFDM system's overall BER performance. Additionally, we discovered a large discrepancy in error rates between the

IBO values and the HPA model. Furthermore, it is obvious that the filter is an essential component of GFDM design because it affects the system's performance. These findings highlight the significance of researching PAPR reduction methods. We do GFDM active constellation expansion, optional mapping, tone reserve, etc. to handle nonlinearity-related difficulties.

Research involving human participants and/or animals

This article does not contain any studies involving Human Participants and/or Animals performed by any of the authors.

Informed consent

Not applicable.

Availability of data and materials

Data sharing not applicable to this article as no datasets were generated or analyzed during the current study.

Funding

No funding received by any government or private concern.

CRediT authorship contribution statement

P.V. Naganjaneyulu: Formal analysis, Resources. **U. Sreenivasulu:** Supervision, Validation. **M. Nageswara Rao:** Writing – original draft. **G. Sujatha:** Writing – original draft, Writing – review & editing.

Declaration of competing interest

The authors declare that they have no known competing financial interests or personal relationships that could have appeared to influence the work reported in this paper.

Recommended articles

Data availability

No data was used for the research described in the article.

References

[1] R.A. Kumar, K.S. Prasad

Performance analysis of GFDM modulation in heterogeneous network for 5G NR
Wirel. Pers. Commun., 116 (3) (2021), pp. 2299-2319
Feb.

Crossref ↗ View in Scopus ↗ Google Scholar ↗

[2] P. Banelli, S. Buzzi, G. Colavolpe
Modulation formats and waveforms for 5G networks: who will be the heir of OFDM?: an overview of alternative modulation schemes for improved spectral efficiency
IEEE Signal Process. Mag., 31 (6) (2014), pp. 80-93
Oct.

View in Scopus ↗ Google Scholar ↗

[3] G. Wunder, P. Jung, M. Kasparick, T. Wild, F. Schaich, Y. Chen, S.T. Brink, I. Gaspar, N. Michailow, A. Festag, L. Mendes
'5G NOW: non-orthogonal, asynchronous waveforms for future mobile applications
IEEE Commun. Mag., 52 (2) (2014), pp. 97-105
Feb.

View in Scopus ↗ Google Scholar ↗

[4] M. Matthe, N. Michailow, I. Gaspar, G. Fettweis
Influence of pulse shaping on bit error rate performance and out of band radiation of generalized frequency division multiplexing
Proceedings of the IEEE International Conference on Communications Workshops (ICC) (2014), pp. 43-48
Jun.

Crossref ↗ View in Scopus ↗ Google Scholar ↗

[5] H. Lin, P. Siohan
An advanced multi-carrier modulation for future radio systems
Proceedings of the IEEE International Conference on Acoustics, Speech, and Signal Processing (ICASSP) (2014), pp. 8097-8101
May

Crossref ↗ View in Scopus ↗ Google Scholar ↗

[6] Y. Ma, N. Wu, J.A. Zhang, B. Li, L. Hanzo
Generalized approximate message passing equalization for multi-carrier faster-than-Nyquist signaling
IEEE Trans. Veh. Technol., 71 (3) (2022), pp. 3309-3314
Mar.

Crossref ↗ View in Scopus ↗ Google Scholar ↗

[7] H.F. Wang, F.B. Ueng, Y.S. Shen, K.X. Lin
Low-complexity receivers for massive MIMO-GFDM communications
Trans. Emerg. Telecommun. Technol., 32 (4) (2021)
Art. no. e4219

Google Scholar ↗

[8] S.M.J.A. Tabatabaee, M. Rajabzadeh, M. Towliat
A novel lowcomplexity GFDM relay communication system: relay selection and filter-and-forward
IEEE Trans. Signal Process., 69 (2021), pp. 5147-5158
Crossref ↗ View in Scopus ↗ Google Scholar ↗

[9] E. Catak, A. Moldsvor, M. Derawi
Transceiver design for GFDM with hexagonal time–frequency allocation using the polyphase decomposition
Electronics, 9 (11) (2020), p. 1862
Nov.
Crossref ↗ Google Scholar ↗

[10] M.Q. Khan, M.D. Nisar
'Spatial transmit diversity for GFDM via low complexity transceiver design
Proceedings of the IEEE 93rd Vehicular Technology Conference (VTC-Spring) (2021), pp. 1-5
Apr.
Google Scholar ↗

[11] S.M.J.A. Tabatabaee, M. Towliat, M. Rajabzadeh
'Novel transceiver beamforming schemes for a MIMO-GFDM system
Phys. Commun., 47 (2021)
Aug.Art. no. 101376
Google Scholar ↗

[12] W.D. Dias, L.L. Mendes, J.J.P.C. Rodrigues
Low complexity GFDM receiver for frequency-selective channels
IEEE Commun. Lett., 23 (7) (2019), pp. 1166-1169
Jul.
Crossref ↗ View in Scopus ↗ Google Scholar ↗

[13] F.T. Miandoab, B.M. Tazehkand
NOMA performance enhancement based imperfect SIC minimization using a novel user pairing scenario involving three users in each pair
Wirel. Netw., 26 (5) (2020), pp. 3735-3748
Jul.
Google Scholar ↗

[14] T.A. Almohamad, M.F.M. Salleh, M.N. Mahmud, I.R. Karas, N.S.M. Shah, S.A. Al-Gailani
Dual-determination of modulation types and signal-to-noise ratios using 2D-ASIQH features for next generation of wireless communication systems
IEEE Access, 9 (2021), pp. 25843-25857

Crossref ↗ View in Scopus ↗ Google Scholar ↗

[15] T.A. Almohamad, M. Salleh, M.N. Mahmud, A.H.Y. Saaed, S.A. Al-Gailani
Automatic modulation recognition in wireless communication systems using feature-based approach
Proceedings of the 10th International Conference on Robotics, Vision, Signal Processing & Power Applications (2019), pp. 403-409
Crossref ↗ View in Scopus ↗ Google Scholar ↗

[16] B. Avanzi, G.B. Beaulieu, P.L. de Micheaux, F. Ouimet, B. Wong
A counterexample to the existence of a general central limit theorem for pairwise independent identically distributed random variables
J. Math. Anal. Appl., 499 (1) (2021)
Jul.Art. no. 124982
Google Scholar ↗

Cited by (0)

Dr. P V Naganjeneyulu awarded Ph.D. from Jawaharlal Nehru Technological University Kakinada Andhra Pradesh, India. Currently he is working as Professor in Mizoram University, Mizoram, India. His research interests are in the areas of OFDM, 5 G Communications, Artificial Intelligence, Machine Learning, Deep Learning. Wireless Sensor Networks and Digital Image Processing

Dr P. V. Naganjaneyulu, rofessor. Department Of ECE, School of Engg, Mizoram university (A Central university), Tanhril, Aizwal-Mizoram, 796,004, Pvn1978@mzu.edu.in

Pvnaganjaneyulu@gmail.com

9,490,650,030

Dr.U.Sreenivasulu, is presently working as Assistant Professor, ECE,SRKR Engineering college., Bhimavaram. He done Ph.D. in Wireless Communication & Networks from JNTU, Hyderabad.. He has authored more than 16 Research papers in National and International conferences and Journals. He published 1 Indian patent . And interested research areas are Wireless Communication, VLSI Design and Embedded Systems. :Dr.U.Sreenivasulu, : Assistant. Professor, SRKR ENGINEERING COLLEGE BHIMAVARAM(B9), Department:ECE Mail id: sreenu.u@gmail.com, Mobile no:9,885,138,058

Dr M. Nageswara Rao B.Tech., M.Tech.,PhD

Dr M. Nageswara Rao obtained his B.Tech degree from VITAM, Vishakapatnam, India during 2006. He obtained his M. Tech. from Narasaraopet Engineering College, Narasaraopet, and PhD from KL Deamed to be University, Guntur. He possesses 15 years of teaching experience. Presently he is working as Associate Professor in the department of ECE, Sri Mittapalli College of Engineering, Guntur Dt, A. P., India. His research interest includes signal, image processing.

Dr M.Nageswara Rao, Associate professor, Sri Mittapalli college of Engineering, mail Id: nagmedikonda@gmail.com, Mobile No:9,491,186,158.

Dr.G.Sujatha, is presently working as professor, ECE,S.V.C.E., Tirupati. She did her Ph.D. in VLSI Design from JNTU, Hyderabad. She is Life Member of I.M.E.S. of A professional society for researchers. She has authored more than 18 Research papers in National and International conferences and Journals. She published 1 Indian patent . Her interested research areas are VLSI Design and Embedded Systems.

Dr. G.Sujatha, M.Tech,ph.D, M.I.M.E.S, Designation: Professor, Department:ECE, SVCE, Karakambadi road, Tirupati, Pincode:517,507, Mail id: sujatha.g@svcolleges.edu.in, Cell no:9,959,505,760

© 2024 Published by Elsevier Ltd.

ELSEVIER

All content on this site: Copyright © 2024 Elsevier B.V., its licensors, and contributors. All rights are reserved, including those for text and data mining, AI training, and similar technologies. For all open access content, the Creative Commons licensing terms apply.

RELX™

Journal of Information Technology Management

Print ISSN: 2008-5893

Online ISSN: 2423-5059

Clinical Healthcare Applications: Efficient Techniques for Heart Failure Prediction Using Novel Ensemble Model

Ashwitha Anni Poojari *

*Corresponding author, Department of Information Technology, Manipal Institute of Technology Bengaluru, Manipal Academy of Higher Education, Manipal, Karnataka, India. E-mail: ashwitha.a@manipal.edu

Uppala Sivaji

Department of IT, Institute of Aeronautical Engineering, Dundigal, Hyderabad. E-mail: sivaji.u117@gmail.com

Bhavani Rupa Devi

Department of CSE, Annamacharya Institute of Technology and Sciences, Tirupati. E-mail: rupadevi.aitt@annamacharyagroup.org

Gandela Sujatha

Department of Electronics and Communication, Sri Venkateswara College of Engineering Karakambadi road, Tirupati, Andrapradesh, India. E-mail: sujatha.g@svcolleges.edu.in

Konduru Reddy Madhavi

School of Computing, Mohan Babu University, Tirupati, A.P., India. E-mail: kreddymadhavi@gmail.com

Tammineni Ravi Kumar

Department of CSE, Aditya Institute of Technology and Management, Tekkali, A.P. E-mail: ravi.4u.kumar@gmail.com

Abstract

Heart failure is a severe medical ailment that significantly impacts patients' well-being and the healthcare system. For improved results, early detection and immediate treatment are essential. This work aims to develop and evaluate predictive models by applying sophisticated ensemble learning techniques. In order to forecast heart failure, we used a clinical dataset from Kaggle. We used the well-known ensemble techniques of bagging and random forest

(RF) to create our models. With a predicted accuracy of 82.74%, the RF technique, renowned for its versatility and capacity to handle complex data linkages, fared well. The bagging technique, which employs several models and bootstrapped samples, also demonstrated a noteworthy accuracy of 83.98%. The proposed model achieved an accuracy of 90.54%. These results emphasize the value of group learning in predicting cardiac failure. The area under the ROC curve (AUC) was another metric to assess the model's discriminative ability, and our model achieved 94% AUC. This study dramatically improves the prognostic modeling for heart failure. The findings have extensive implications for clinical practice and healthcare systems and offer a valuable tool for early detection and intervention in cases of heart failure.

Keywords: Machine Learning, Heart Failure, Cardiovascular diseases, Ensemble learning, Healthcare

Journal of Information Technology Management, 2024, Vol. 16, Issue 1, pp. 149-166
Published by University of Tehran, Faculty of Management
doi: https://doi.org/10.22059/jitm.2024.96380
Article Type: Research Paper
© Authors
Received: December 17, 2023
Received in revised form: January 06, 2024
Accepted: February 02, 2024
Published online: February 29, 2024

Introduction

Cardiovascular disease is an ailment that occurs in the heart or blood vessels. It is one of the primary causes of death, which includes other heart-related issues. According to World Health Organization (WHO) data, cardiovascular diseases, such as heart attacks and strokes, affect approximately 17 million people, leading to fatalities (Ashraf, 2021). According to the Centers for Disease Control (CDC), around 610,000 individuals die annually due to heart illness (Dangare, 2012). Modern cardiovascular diseases such as coronary artery disease, heart failure, arrhythmias, and stroke pose significant global health challenges (Austin, 2013). Several risk factors, such as hypertension, high cholesterol, diabetes, obesity, and lifestyle choices, influence these diseases. It is crucial to manage the time after getting a heart attack because the patient's chances of survival decrease if they don't receive proper attention promptly. Therefore, CVD prevention and management are essential. It is better to be proactive than reactive. These are critical findings for health professionals and researchers. Numerous research studies have been carried out to forecast the likelihood of cardiovascular disease, with the primary objective being to prevent these diseases, which contribute significantly to global mortality (Zhang, 2020). Cardiology has transformed, focusing more on prevention, early intervention, and lifestyle adjustments. Cardiology now incorporates sophisticated diagnostic tools, minimally invasive procedures, and innovative surgical techniques. Digital technologies have become essential in preventing CVD, offering several benefits. These technologies encourage the adoption of healthier lifestyles, help individuals maintain these changes, identify CVD risk factors early, and provide personalized care and

management. Additionally, healthcare professionals receive valuable clinical decision support from these technologies (Islam, 2021).

We represented the cardiovascular disease prediction and the death event, a probability measurement of whether the death risk is affirmative or negative. The UCI dataset is the most common dataset utilized in different research. Ensemble Model, the proposed model of this research, we compared the precision, recall, and F1 score evaluation with the Random Forest (RF), Bagging model. We choose the ensemble model regarding the machine learning model because the expected performance may not be reflected with the traditional machine learning methods. The data preprocessing technique has been applied to improve the data quality for data training. Our proposed model achieved the highest precision, explained in the Result section.

Research Objectives and Motivation

1. This objective involves utilizing sophisticated statistical and machine learning techniques to build a robust predictive model for heart failure. The model will be trained on a comprehensive dataset that includes relevant clinical parameters, biomarkers, and patient information.
2. Exploring correlations between variables, identifying potential outliers, and understanding distributions will inform feature selection and model development.
3. One of the primary goals is to provide a tool with direct clinical relevance, especially in the early detection of heart failure. By leveraging the predictive model, healthcare professionals can identify individuals at risk, enabling them to intervene promptly and potentially prevent or mitigate the severity of heart failure.

The motivation behind this study lies in the compelling need to address the global health burden caused by lung cancer. Early detection of lung cancer can guide to more satisfactory treatment and ultimately reduce survival.

Contribution

This research study creates several notable contributions:

- Applying the Random Forest ensemble model demonstrates a thorough understanding of advanced machine learning techniques. This contribution showcases the effectiveness of RF in predicting heart failure, highlighting its potential as a powerful tool in clinical decision support systems.
- The utilization of Bagging, a technique that leverages multiple models trained on bootstrapped data samples, represents a significant contribution. This approach not only diversifies the models but also enhances predictive accuracy. Our research thus introduces an additional dimension to ensemble learning methods, comprehensively evaluating their effectiveness in heart failure prediction.

- Developing a novel ensemble model represents a pioneering contribution to the field. This innovation signifies our commitment to pushing the boundaries of predictive modeling. Introducing a new ensemble technique has demonstrated a keen ability to think critically and creatively, potentially offering a unique solution to heart failure prediction.

Literature Review

A comprehensive analysis of different machine learning and deep learning techniques was conducted to formulate predictive models for heart disease are reviewed in this section.

A proposed ”UCI Heart Disease” application utilized ensemble machine learning to assess 14 characteristics from 76 attributes. The author claims that the proposed model, XGBoost, achieved an accuracy of 81%. However, it should be noted that no comparison was made with traditional classifiers (Sai Shekhar, 2020). Another study from various experiments in this area compared Logistic regression, Naive Bayes, Decision Tree, Random Forest, Artificial Neural Networks, Multi-Layer Perception, and Deep Neural Networks. Though Ml is convenient in Heart disease prediction, the significance is the comparison between different machine learning classifiers. But Logistic regression achieved 93%, which is comparatively the highest accuracy (Katarya, 2021). Researchers conducted a study to develop a method for detecting heart disease early. They analyzed various risk factors associated with cardiac patients and used multiple learning classifiers to process the dataset. Among the different classifiers, the SVM had an impressive accuracy rate of 84.33% (Babu, 2017).

Another research introduces an innovative healthcare system designed to predict heart disease. This system employs ensemble deep learning techniques and feature fusion, effectively combining sensor data with electronic medical records to create comprehensive healthcare; the Cleveland dataset was previously employed individually, utilizing a limited set of only 16 features. Using an information gain technique, it identifies and selects crucial elements and refines the model by calculating specific feature weights for each class through a conditional probability approach. Notably, the results demonstrate that this novel system outperforms existing methods, achieving higher accuracy in heart disease prediction through a hybrid deep learning method (Ali, 2020). Based on a well-structured dataset containing information on 304 patients with a history of heart problems and other medical conditions. The dataset includes age, resting blood pressure, and fasting sugar levels. The study highlights the effectiveness of machine learning algorithms, especially K-nearest neighbors (KNN) and logistic regression. These algorithms have shown superior results in predicting and classifying patients with heart disease compared to other algorithms used in previous research. The study achieved an impressive maximum accuracy of 88.5% by applying KNN and logistic regression (LK, 2021). A separate study utilized a supervised learning approach, achieving an impressive 99% accuracy rate using the Random Forest (RF) algorithm. This was accomplished through a rigorous 10-fold cross-validation process. This study used a heart

disease dataset from Kaggle. However, the dataset may not represent all heart disease cases in the population. (Ali M. M., 2021).

A new model called MARKER-HF has been developed. It utilizes a boosted decision tree algorithm to distinguish between high and low-risk patients. The model has been assessed for its ability to predict the risk of death in different patient groups, including the UCSD, UCSF, and BIOSTAT-CHF populations. The results indicate that the proposed model has a high potential for accurate risk prediction, scoring 88% validity for mortality risk (Ahmed, 2017). Maruf et al proposed the bagging model in research work (Al Maruf, 2023). The dataset used in their research is imbalanced. Louridi et al. (2019) and Dwivedi et Al. (2023) both utilized the K-Nearest Neighbors method on the AFIC dataset. The results were, respectively, 90.16% and 80%. 46% of the 450 statistics from Kita Hospital Jakarta Enriko were accurate. Using AdaBoost, the Cleveland dataset improved the outcome by 56.13%. Shetty (Chicco, 2020) obtained 89% accuracy using the Starlog 270 data, and Chaurasia produced 75.9% accuracy using the same technique and a hybrid approach. The accuracy of an artificial neural network model was 82.5%, and the accuracy of a hybrid norm was 78.88%, according to Cheng and Chaurasia an ATTICA dataset was chosen as the subject of this inquiry. Depending on the type of classifier and training dataset, the Hellenic Score showed 20% specificity, 58% NPV, 85% accuracy, 87% PPV, and 97% sensitivity. Although the ML algorithms' specificity, accuracy, sensitivity, PPV, and NPV, respectively, ranged from 65% to 84%, 46% to 56%, 67% to 89%, and 24% to 45%.

The Hoeffding classifier used ensemble models to predict the risk of heart disease and had a CVD prediction accuracy of 88.56%. The Framingham and Cleveland tests showed 91% and 93% classification accuracies, respectively (Kavitha, 2021). The accuracy, sensitivity, and specificity of the three different ensemble approaches were 93.44%, 89.28%, and 96.96%, respectively (Al Maruf, 2023) . A novel hybrid classifier selection technique dubbed HRFLC that combines random forest, AdaBoost, and linear correlation was first demonstrated using 280 instances of the UCI dataset (Dinesh, 2018). Several researchers used an ensemble model in their investigation (Raza, 2019; Kumar, 2022; Shorewala, 2021). From the above information in this section, we have reviewed the most recent research work that has been conducted on the relevant topic (Nagarajan, 2021; Rajendran, 2021; Subasi, 2021). From these research findings, we proposed our system and showed the evaluation in the next section.

Methodology

Throughout our research, we followed a structured approach consisting of several steps, including data collection, preprocessing, model building, and analysis of the model outcomes. We proposed a new model based on our findings, which we evaluated using various metrics. To visualize our research flow, shown in Figure 1.

Dataset description

The Kaggle cardiovascular disease dataset has been used in our proposed system. The dataset includes the patient's age, anemia, creatinine phosphokinase, diabetes, ejection fraction, high pressure, platelets, serum creatinine, Serum Sodium, Sex, Smoker, and Time. The dataset has several columns, and the target class death event is binary classification 0 and 1. The dataset encompasses 299 entries, each representing an individual's pertinent medical information about heart health. Key features include age, presence of anemia, creatinine phosphokinase levels, diabetes status, ejection fraction percentage, high blood pressure indication, platelet count, serum creatinine levels, serum sodium levels, gender.

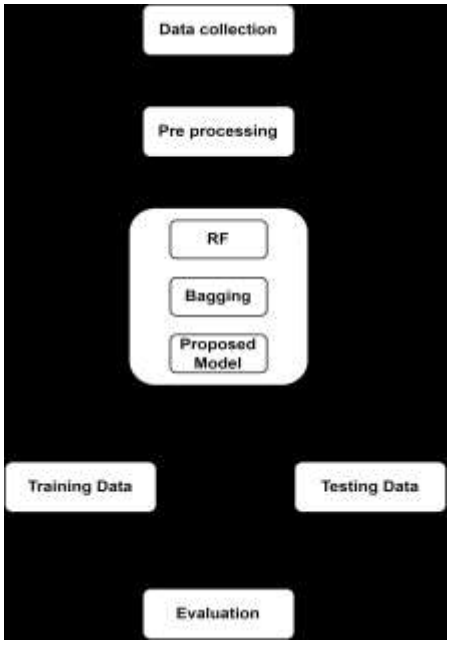

Figure 1. Flow of our research smoking habits, and the duration of observation.

Conducting a thorough statistical analysis reveals noteworthy insights. The age range spans 40 to 95 years, with a mean of approximately 60.83 years. About 43.14% of individual's exhibit anemia, while roughly 41.81% have diabetes. Creatinine phosphokinase levels range widely, from 23 to 7861, with a mean of approximately 581.84. Ejection fraction percentages range from 14 to 80%, with a mean of 38.08%. Notably, around 35.12% of individuals have high blood pressure, and approximately 32.11% are smokers. Platelet counts vary significantly, ranging from 25100 to 850000. Serum creatinine levels range from 0.5 to 9.4, with a mean of approximately 1.39. Serum sodium levels range from 113 to 148, with a mean of 136.63. The dataset's gender distribution is slightly skewed towards males, constituting about 64.88%, while females account for 35.12%. Approximately 32.11% of individuals experienced heart-related events leading to death. The observation period ranges from 4 to 285 units, with a mean duration of approximately 130.26. This comprehensive statistical analysis provides valuable insights into the distribution and characteristics of the

dataset's features, offering a deeper understanding of cardiovascular health factors and their potential associations with heart-related events.

The dataset attributes are:

- **Anaemia:** Anemia is a medical condition that arises due to a drop in healthy red blood cells or a drop in haemoglobin situations, leading to an impairment in the blood's capability to carry oxygen. Polychrome causes of anemia include iron or vitamin scarcities, habitual conditions, or inheritable factors. Symptoms of anemia include fatigue, weakness, and conciseness of breath, and treating anemia depends on relating and addressing the bearing cause. Proper opinion and operation of anemia are essential to ensure that the body's tissues and organs admit optimal oxygen delivery, promoting overall health and well-being.
- **Creatine phosphokinase:** It is a pivotal enzyme in varied tissues, including muscles and the brain. CPK has different isoenzymes in specific tissues, similar to CK- MM in cadaverous strength, CK- MB in the heart muscle, and CK- BB in the brain and nervous system. Measuring CPK situations in the blood is essential for diagnosing and covering muscle or heart damage conditions, including heart attacks and muscular diseases.
- **Ejection Fraction:** EF is a crucial cardiac parameter that measures the percentage of blood pumped out by the left ventricle during each contraction. EF is an essential diagnostic tool for heart conditions. A reduced EF can lead to heart dysfunction, especially heart failure, while a high EF may indicate specific cardiac issues.
- **Platelets:** Platelets are thrombocytes, which are tiny blood cells essential for blood clotting. Produced in the bone marrow, they play a vital role in stopping bleeding by forming clots at the site of blood vessel injuries.
- **Serum Creatinine:** This blood test measures the amount of creatinine present in the blood. Creatinine is a waste product produced by the muscles and removed by the kidneys. Monitoring the level of serum creatinine is essential for evaluating kidney function since higher levels can indicate kidney issues.
- **Serum Sodium:** A blood test that checks the serum sodium levels. Sodium is an essential electrolyte that is crucial in maintaining fluid balance and nerve function. Any abnormality in the serum sodium levels can indicate various medical conditions such as dehydration, kidney issues, or other health problems.

Classification

Before applying the proposed ensemble model, we applied two baseline ensemble models. We used Random Forest and Bagging Ensemble.

Random Forest (RF): Random Forest is a powerful ensemble learning technique frequently employed in binary classification tasks, such as predicting heart failure. It operates

by constructing numerous decision trees, each trained on a bootstrapped dataset sample, thereby introducing diversity. At each split in the trees, only a random subset of features is considered, enhancing robustness [23]. In the case of binary classification, the final prediction is determined by a majority vote among the individual trees. Mathematically, let T represent the number of trees, and pt (1|xi) be the predicted probability of the positive class by tree t. The final prediction for a given sample xi is calculated as:

$$\hat{y}_i = \begin{cases} 1, & if\ \frac{1}{T}\sum_t^T p_t(1|x_i) > 0.5, \\ 0, & otherwise \end{cases}$$

In the context of heart failure prediction, for a new patient's features, the Random Forest model will consider the opinions of all its constituent trees and predict whether the patient is at risk of heart failure based on the majority decision. This technique is known for its accuracy and robustness, making it a popular choice in medical prediction tasks.

Bagging: Bagging, or Bootstrap Aggregating, is an ensemble learning method often employed for predicting heart failure. It entails building multiple base models, typically decision trees, on different subsets of the training data.

In the context of heart failure prediction, let T represent the number of base models. For classification, the final class prediction $\hat{y}_i$ for a given patient's features xi is calculated as:

$$\hat{y}_i = arg\max_c \frac{1}{T}\sum_{t=1}^T \mathcal{P}_t(c|x_i)$$

Where pt (c|xi) is the predicted probability of class c by base model t. This equation signifies that the class determines the final prediction with the highest average predicted probability across all base models.

In the case of regression, the final prediction $\hat{y}_i$ is computed as:

$$\hat{y}_i = \frac{1}{T}\sum_{t=1}^T y_t(x_i)$$

Where yt (xi) represents the predicted value by base model t. This formula indicates that the final regression prediction is the average of the predicted values from all base models.

By applying bagging, especially in heart failure prediction, one can leverage the combined knowledge of multiple models to make more accurate and robust predictions, which is crucial in critical healthcare applications.

Proposed model

In this section, we have presented our proposed model. We denote the dataset as D, where D = {(xk,yk), k ∈ N}. The free inconstant is xk = [xk1,xk2,xk3,...,xkp] (Equation 1),

D = {(xk,yk)},k = 1,2,...,N (1)

While yk signifies the dependent variable, where yk takes values in {0,1}. Each instance or row's independent variable is expressed as xj = [x1j,x2j,x3j,...,xNj] .

xk = [xk1,xk2,xk3,...,xkp] (2)

The weighted mean of the variable xj is computed as

$$x_j = \frac{1}{N}\sum_{k=1}^{N} \mathcal{W}'_k x_{kj,} \quad (3)$$

Where wk′ ≥ 0 and [redacted]= 1. Notably, higher weighted data elements exert more influence on the weighted mean compared to lower weights. Additionally, it is worth noting that the weights are non-negative. We have applied randomization for the proposed data split algorithm. This means that in every divided step, it arbitrarily selects from the set {N}[Here,N =Natural number]. This variation makes generating a variable number of trees possible, reducing variation and improving efficiency.

We begin with the original dataset D, representing the entire trial. It is divided between distinct homogeneous sets. At each step, single data is randomly chosen from {N} and labeled as j. The chosen data is then taken out of the set to make room for more choices. D is then split into two partitions, as shown in Equation (4).

$$D = \begin{cases} D_{11,} \; if \; x_{ij} < x_j, \\ D_{12,} \; if \; x_{ij} \geq x_j, \end{cases} \quad (4)$$

Considering each child node independently, namely viewing D11 and D12 as root nodes and applying Equation (4) recursively, we obtain D21, D22 from D11 and D23, D24 from D12. Until a halting rule is satisfied, this partitioning process continues. To prevent over-partitioning of the dataset, we used two stopping rules. Maximum tree height is used as first, denoted as Hmax. This stops the method from running endlessly or from excessively splitting the input dataset. Thus, first stops growing when H = Hmax. Tree height is defined as H = 0 for main node, and H = 1 for D11 and D12, and so on.

Second, the tree stops expanding if the partition shrinks sufficiently regarding the number of instances it contains. As N (Dkl) is how many instances there are in a node Dkl, the tree-building process stops when N (Dkl) ≤ Nmin, where Nmin is the anticipated bare minimum of examples in the split shown in equation 5.

H = Hmax or N (Dkl) ≤ Nmin (5)

Once the dataset is partitioned, we apply the Classification task (CART) method to model each split. It calculates the likelihood of incorrectly classifying a given variable when a random selection uses Gini Impurity.

$$Gini = 1 - \sum_{i=1}^{J} \mathcal{P}_i^2 \quad (6)$$

We now possess a forest of Tmax trees, all fitted with the CART algorithm. We employ the AB-WAE to calculate an ensemble from these CART models. This ensemble technique modifies the weighted ageing classifier ensemble [?]. Given Pa (Ψk) as the correct prediction

frequency of classifier Ψk and itter(ψk)total iterations Ψk has spent in the ensemble, the classifier's weight ω(Ψk) is determined as shown in Equation (7).

$$w(\Psi_i) = \begin{cases} \frac{P_a(\Psi_i)}{P_\Pi} & if\ P_a(\Psi_i) > P_{\Pi a} \\ \frac{P_a(\Psi_i)}{\overline{itter(\psi_i)}} & else \end{cases} \quad (7)$$

The final predictions of the model Ψ is obtained using Equation (8),

$$\Psi(x) = if\ \sum_{t=1}^{T_{max}} w\,(\Psi_t) F(i)_t(x) = \max_{j\in\{1,2,\ldots,j\}} \sum_{t=1}^{T_{max}} w(\Psi_t) F\,(j)_t\,(x) \quad (8)$$

Where F (k)t(x) and F(j)t(x) represent the predictions of the t-th tree for class k and j respectively. According to their accuracy and the amount of time they have been in the ensemble, the different classifiers are given weights in this ensemble technique. Classifiers whose weights fall below a specified threshold are removed from the ensemble [?]. The ensemble is guaranteed to produce the best outcomes when accuracy is used as the optimization criterion. The proposed method is depicted in Figure 2.

Results and Discussion

In this research, we harnessed the power of ensemble learning techniques in machine learning, amplifying predictive performance by combining multiple models. Leveraging Google Colab and Python as the programming language, we employed various ensemble methods in the Scikit-learn library. This included Random Forests, a robust decision tree-based ensemble, and Bagging, a technique that creates multiple subsets of the dataset for training. We experimented with the powerful and flexible library to further enhance predictive accuracy, known for its speed and performance. By utilizing ensemble learning, we aimed to create robust models capable of handling complex datasets and delivering superior predictive outcomes. We used Python programming language for this.

In this section, we commence with an in-depth analysis of the heart failure dataset, focusing on discerning influential factors contributing to heart failure. Subsequently, we will expound upon the outcomes of employing our predictive model for heart failure prognosis. In a dedicated subsection, we will provide a concise overview of the classifier's performance, evaluating its effectiveness using various assessment metrics alongside the proposed model.

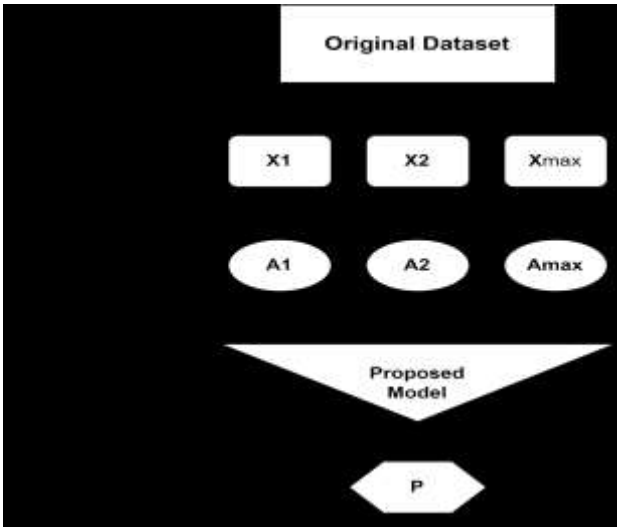

Figure 2. Architecture of the proposed model

Exploratory data analysis

Firstly, we will draw the histogram for all columns. Creating histograms for each column is a crucial step as it enables us to represent the distribution patterns within the data visually. This visualization aids in promptly detecting any potential outliers or irregularities. Furthermore, it grants us a comprehensive understanding of the general structure of the data distribution. Moreover, histograms furnish valuable insights into the dataset's range, dispersion, and central tendencies - pivotal metrics for various analytical endeavors. Hence, generating histograms for all columns is an indispensable component of exploratory data analysis, empowering us to make well-informed decisions rooted in the data's characteristics.

A deficiency in the quantity or quality of red blood cells characterizes anemia. Creatine phosphokinase (CPK), an essential enzyme, is crucial in various bodily functions. When CPK levels are significantly elevated, it often indicates injury or stress to muscle tissue, the heart, or the brain. From Figure 3, the typical range for CPK levels varies, with males falling between 39 to 308 U/L and females between 26 to 192 U/L. However, CPK levels can surge as high as 5,000 U/L in certain circumstances. Ejection fraction, another vital metric, gauges the percentage of blood expelled from the heart during each contraction. An average ejection fraction typically falls between 50% and 75%, while a borderline ejection fraction can range between 41% and 50%. Platelets, also known as thrombocytes, are blood cells crucial for clotting. A standard platelet count ranges from 150,000 to 450,000 platelets per microliter of blood. Serum creatinine level, determined through a blood test, assesses kidney function.

The typical range for serum creatinine is 0.74 to 1.35 mg/dL for adult men and 0.59 to 1.04 mg/dL (52.2 to 91.9 micromoles/L) for adult women. Elevated levels exceeding 1.2 for women and 1.4 for men may signify early kidney dysfunction. Serum sodium, a critical electrolyte, usually falls between 135 and 145 milliequivalents per liter (mEq/L) in a healthy individual. Deviations from this range, either too high or too low, may indicate underlying

kidney issues, dehydration, or other medical conditions. Understanding these parameters is pivotal in assessing and monitoring overall health. As evident from the visual representation in Figure 4, it is apparent that there is a striking similarity in the distribution between the two entities. This observation strongly suggests a high degree of mutual information associated with this feature. The resemblance in distribution patterns indicates a significant level of.

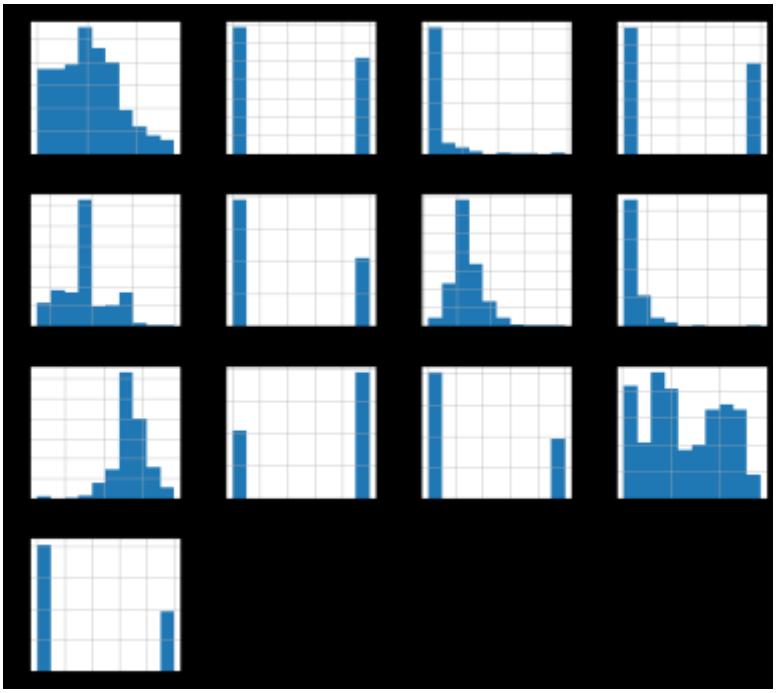

Figure 3. Histogram of all columns

Figure 4. Distribution of creatinine phosphokinase vs death interdependence or shared information between the two variables.

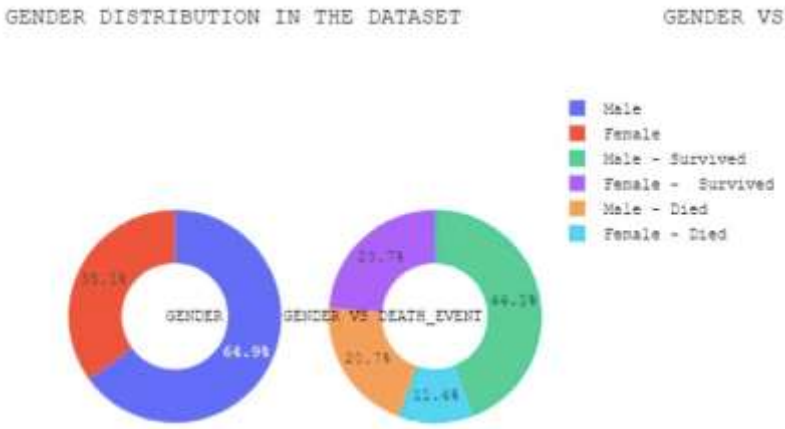

Figure 5. Distribution of gender in the dataset

The presented plot provides a comprehensive view of the dataset's gender distribution and its relationship with the occurrence of death events. The first pie chart in Figure 5 illustrates the proportion of males to females in the dataset, indicating a balanced representation of both genders. Moving to the second pie chart, it delves deeper into the data by categorizing each gender based on their survival status. Specifically, it distinguishes between males and females who have survived and those who have unfortunately experienced a death event. This visualization aids in understanding the gender-specific trends in survival outcomes within the dataset. The doughnut-like structure of the pie charts adds a layer of visual clarity, allowing for easy comparison of proportions. Furthermore, the annotations strategically placed at the center of each chart provide clear labels, enhancing interpretability. Overall, this plot offers valuable insights into the interplay between gender distribution and survival outcomes, which is critical in understanding potential patterns and making informed decisions in medical analyses. From the figure, females are 35.1%, and males are 65.9%. The male survival rate is 44.1%, and the female survival rate is 23.7%. From the analysis, males died at 20.7%, and females died at 11.4%.

Result of the proposed model

After exploratory data analysis, we will present our classifier's performance. Firstly, we have calculated all the classifier's precision, recall and f-score. In Table 1, we have presented the result of our proposed ensemble model and another two models. In this comprehensive model evaluation shown in Table 1.

Table 1. Performance of the proposed model

Model	Precision	Recall	F1-Score
RF Model	83.24%	82.54%	82.89%
Bagging Model	84.54%	86.27%	85.39%
Proposed Model	88.71%	88.34%	88.53%

Table 1, we scrutinized three distinct models - the RF, Bagging, and Proposed Ensemble. The RF model demonstrated a precision of 83.24%, indicating its proficiency in correctly identifying positive instances. Furthermore, with a recall of 82.54%, it displayed a commendable ability to capture a substantial proportion of positive cases. The resultant F1-Score of 82.89% exemplified a harmonious balance of precision and recall. The Bagging Model showcased a slightly improved precision at 84.54%. This precision indicated a heightened accuracy in the identification of actual positive instances. The model's recall, however, was particularly noteworthy at 86.27%. The F1-Score of 85.39% emphasized the model's effectiveness, showcasing its proficiency in balancing positive and negative.

Enter the Proposed Model, which outshone both counterparts with an outstanding precision of 88.71%. This signifies an exceptional ability to pinpoint positive cases accurately. The recall of 88.34% further underlined its prowess in identifying positive instances. This culminated in an exemplary F1-Score of 88.53%, affirming a robust equilibrium between precision and recall.

This comprehensive analysis elucidates that the Proposed Model emerges as the frontrunner in this evaluation. Its superior performance is evident in its ability to identify positive instances while minimizing false positives and negatives. This positions the Proposed Model as the most promising candidate among the models examined, demonstrating its potential as an effective tool in this problem domain. Three different models were evaluated based on their accuracy scores in the context of heart failure.

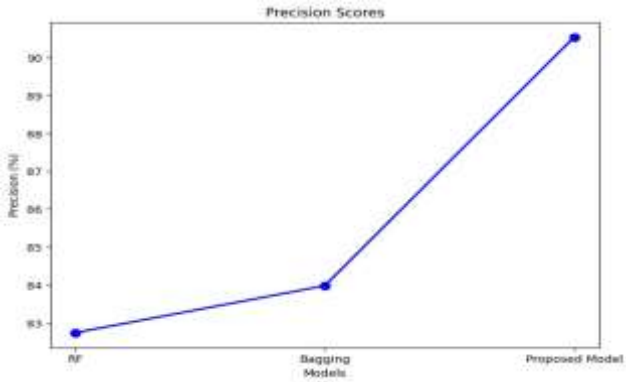

Figure 6. Accuracy of the proposed model

Prediction. From Figure 6, The RF model achieved an accuracy of 82.74%, indicating that it correctly classified approximately 82.74% of all cases. The Bagging model performed better, with an accuracy of 83.98%, suggesting that it could accurately classify about 83.98% of the cases. However, the Proposed Model stood out with an impressive accuracy of 90.54%. This indicates that the Proposed Model excelled in accurately identifying cases of heart failure, surpassing the other models' overall accuracy. It demonstrates the potential effectiveness of this model in heart failure prediction based on the available data.

In heart failure prediction, the Receiver Operating Characteristic (ROC) curve is a critical tool for assessing the performance of classifiers. It visually represents the trade-off between positive and false favorable rates, offering insights into a model's ability to distinguish between positive and negative cases. We have shown graphically the best ROC value in Figure 8. The Random Forest model exhibits a respectable ROC value of 91%, demonstrating a solid discriminatory capacity. The Bagging model elevates this performance further, achieving a notable ROC value of 92%. However, the Proposed Model truly shines, boasting the highest ROC value at 94%. This exceptional result signifies its ability to differentiate between positive and negative cases of heart failure accurately. These promising ROC values underscore the potential clinical utility of our models in predicting heart failure with a high degree of accuracy.

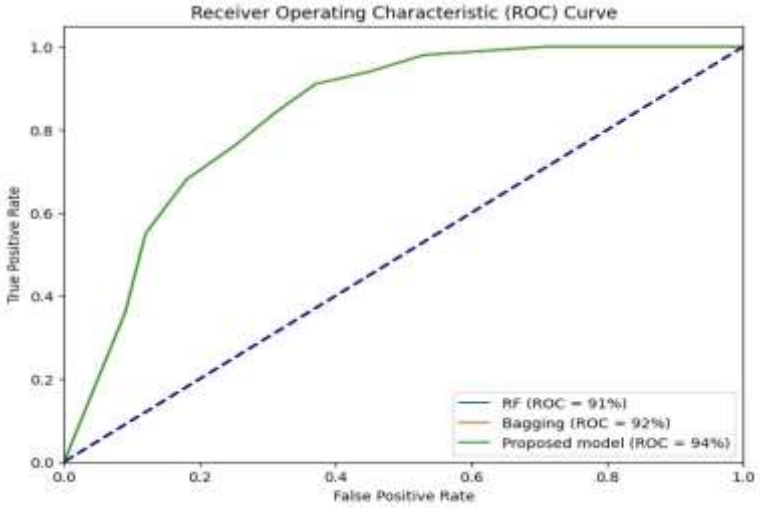

Figure 7. ROC value of the proposed model

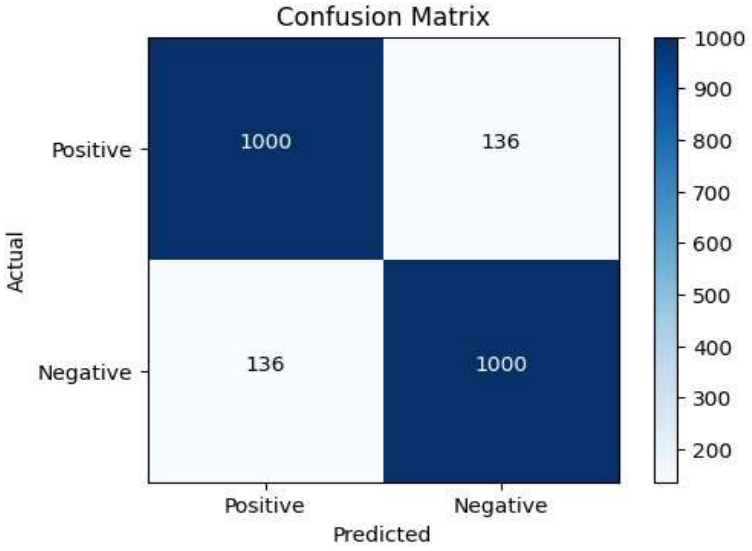

Figure 8. Confusion matrix of the proposed model

Conclusion

Detecting and managing cardiovascular complaints is a significant health challenge worldwide. This exploration proposes an innovative approach to enhance heart complaint prediction. The technique involves an ensemble model with a delicacy-grounded weighted aging classifier ensemble, outperforming conventional models like RF and Bagging. The proposed model achieved an average of 88 across three essential evaluation criteria: perfection, recall, and F1- score. This system can efficiently prognosticate heart complaint threats and give precious clinical advice. Combining machine learning technology and clinical perceptivity can enhance patient issues and address this significant global health concern. The study involved a comprehensive analysis of ROC angles, which validated the model's superior performance in identifying heart disease. Detecting and managing cardiovascular complaints is a significant health challenge worldwide. This exploration proposes an innovative approach to support heart complications. The technique involves an ensemble model with a delicacy-grounded weighted aging classifier ensemble, outperforming conventional models like RF and Bagging. The proposed model achieved a normal of 88 across three essential evaluation criteria: precision, recall, and F1- score. This system can efficiently prognosticate heart complaint threats and give precious clinical advice. Combining machine learning technology and clinical insights can enhance patient issues and address this significant global health concern. The study involved a comprehensive analysis of ROC curves, which validated the model's superior performance in identifying heart disease.

Conflict of interest

The authors declare no potential conflict of interest regarding the publication of this work. In addition, the ethical issues including plagiarism, informed consent, misconduct, data fabrication and, or falsification, double publication and, or submission, and redundancy have been completely witnessed by the authors.

Funding

The author(s) received no financial support for the research, authorship, and/or publication of this article.

References

Ahmed, S. T. (2017). A study on multi objective optimal clustering techniques for medical datasets. In *2017 international conference on intelligent computing and control systems (ICICCS)* (pp. 174-177).

Ahmed, S. T. (2023). AITel: eHealth Augmented Intelligence based Telemedicine Resource Recommendation Framework for IoT devices in Smart cities. *IEEE Internet of Things Journal*.

Al Maruf, A. a. (2023). Prediction of Heart Disease and Heart Failure Using Ensemble Machine Learning Models. In *International Conference on Machine Learning, IoT and Big Data* (pp. 481-492).

Ali, F. a.-S.-S. (2020). A smart healthcare monitoring system for heart disease prediction based on ensemble deep learning and feature fusion. *Information Fusion*, 208-222.

Ali, M. M. (2021). Heart disease prediction using supervised machine learning algorithms: Performance analysis and comparison. *Computers in Biology and Medicine*, 104672.

Ashraf, M. a. (2021). *Prediction of cardiovascular disease through cutting-edge deep learning technologies: an empirical study based on TENSORFLOW, PYTORCH and KERAS.* Springer.

Austin, P. C. (2013). Using methods from the data-mining and machine-learning literature for disease classification and prediction: a case study examining classification of heart failure subtypes. *Journal of clinical epidemiology*, 398-407.

Babu, S. a. (2017). Heart disease diagnosis using data mining technique. In *2017 international conference of electronics, communication and aerospace technology (ICECA)* (pp. 750-753).

Chicco, D. a. (2020). Machine learning can predict survival of patients with heart failure from serum creatinine and ejection fraction alone. *BMC medical informatics and decision making*, 1--16.

Dangare, C. S. (2012). Improved study of heart disease prediction system using data mining classification techniques. *International Journal of Computer Applications*, 44-48.

Dinesh, K. G. (2018). Prediction of cardiovascular disease using machine learning algorithms. In *2018 International Conference on Current Trends towards Converging Technologies (ICCTCT)* (pp. 1-7).

Islam, S. M. (2021). Digital health approaches for cardiovascular diseases prevention and management: lessons from preliminary studies. *Mhealth*.

Katarya, R. a. (2021). Machine learning techniques for heart disease prediction: a comparative study and analysis. *Health and Technology*, 87--97.

Kavitha, M. a. (2021). Heart disease prediction using hybrid machine learning model. In *2021 6th international conference on inventive computation technologies (ICICT)* (pp. 1329-1333).

Kumar, S. S. (2022). Unstructured Oncological Image Cluster Identification Using Improved Unsupervised Clustering Techniques. *Computers, Materials \& Continua*.

LK, S. S. (2021). COVID-19 outbreak based coronary heart diseases (CHD) prediction using SVM and risk factor validation. In *2021 Innovations in Power and Advanced Computing Technologies (i-PACT)* (pp. 1-5).

Louridi, N. a. (2019). Identification of cardiovascular diseases using machine learning. In *2019 7th mediterranean congress of telecommunications (CMT)* (pp. 1-6).

Nagarajan, S. M. (2021). Feature selection model for healthcare analysis and classification using classifier ensemble technique. *International Journal of System Assurance Engineering and Management*, 1-12.

Rajendran, N. A. (2021). Heart disease prediction system using ensemble of machine learning algorithms. *Recent Patents on Engineering*, 130-139.

Raza, K. (2019). Improving the prediction accuracy of heart disease with ensemble learning and majority voting rule. In *U-Healthcare Monitoring Systems* (pp. 179-196).

Sai Shekhar, M. a. (2020). Heart Disease Prediction Using Machine Learning. In *International Conference on Emerging Trends and Advances in Electrical Engineering and Renewable Energy* (pp. 603-609).

Shorewala, V. (2021). Early detection of coronary heart disease using ensemble techniques. *Informatics in Medicine Unlocked*, 100655.

Subasi, A. a. (2021). Intrusion detection in smart healthcare using bagging ensemble classifier. In *International Conference on Medical and Biological Engineering* (pp. 164-171).

Zhang, Z. a. (2020). Enhanced character-level deep convolutional neural networks for cardiovascular disease prediction. *BMC medical informatics and decision making*, 1-10

Bibliographic information of this paper for citing:

Poojari, Ashwitha Anni; Sivaji, Uppala; Devi, Bhavani Rupa; Sujatha, Gandela; Madhavi, Konduru Reddy & Kumar, Tammineni Ravi (2024). Clinical Healthcare Applications: Efficient Techniques for Heart Failure Prediction Using Novel Ensemble Model. *Journal of Information Technology Management,* 16 (1), 149-166. https://doi.org/10.22059/jitm.2024.96380

Copyright © 2024, Ashwitha Anni Poojari, Uppala Sivaji, Bhavani Rupa Devi, Gandela Sujatha, Konduru Reddy Madhavi and Tammineni Ravi Kumar

Advertisement

Wireless Communications and Mobile Computing / Volume 2023, Issue 1 / 7982038

Research Article | Open Access

Lightweight APIT with Bat Optimization with Simulated Annealing Localization for Resource-Constrained Sensor Networks

T. Swarna Latha, K. Bhanu Rekha, Alachewn Wubie Ferede

First published: 27 May 2023
https://doi.org/10.1155/2023/7982038
Citations: 3

Academic Editor: Kalidoss Rajakani

This article is part of Special Issue: Explorations in Pattern Recognition and Computer Vision for Industry 4.0

Abstract

In a wireless sensor network, information processing, and information acquisition, localization technology is the key to making it practically possible application. Approximate Point-in-Triangulation (APIT) is the most widely used localization estimation which has high accuracy in localizing the nodes and ease of deployment of nodes in the real-time environment. Though it has numerous key advantages, some of the drawbacks which make it a little setback in preference are the unevenness in the distribution of nodes. Tracking is more appropriate for mobile sensor nodes than tracking is for static sensor nodes. The two main types of localization algorithms are range-based and range-free techniques. In an indoor setting, the projected range (distance) between an anchor and an unknown node is very inaccurate. By utilizing a large number of already existing access points (APs) in the range-free localization approach, this issue can be overcome to a great extent. The utilization of multisensor data, such as magnetic, inertial, compass, gyroscope, ultrasonic, infrared, visual, and/or odometer, is stressed in recent research to further increase localization accuracy. The tracking system also makes location predictions for the future based on historical location data. To overcome this issue, the proposed localization algorithm of APIT with Bat-SA proves its efficiency. Due to its low localization error, the traditional Bat method is more accurate than APIT. The proposed Bat using the SA algorithm is found to perform better than the traditional APIT algorithm in terms of convergence of computing rate and success rate. In order to mimic the suggested APIT method, it is paired with the Bat-SA localization technique. Simulation evaluation proves the performance efficiency of the proposed algorithm. The performance metrics parameters are latency, node distribution map, positioning error map, and neighbor relationship diagram which are used to evaluate the proposed method.

1. Introduction

A difficult problem in a sizable mobile sensor network is the localization and tracking of wireless sensor nodes. Numerous applications, such as location-based services, network optimization, and environment characterization. The node's position in a 2D/3D space is calculated using localization techniques. Sensing, monitoring, surveillance, and tracking are some of the main uses for the localization techniques, for instance, space applications on the earth and the moon, military surveillance, intruder detection, environment monitoring (such as soil health and temperature), agriculture monitoring, health monitoring (such as smart homes), habitat monitoring, and pollution control. It can be used in locations that are on land, beneath water, or underground. Connectivity and coverage, localization and tracking, data aggregation and latency minimization, privacy and security, time synchronization, MAC protocol and sleep scheduling, cross layer optimization, routing and topology control, and congestion control are some of the various research areas in wireless sensor networks. To provide accurate information on the position of sensor nodes, self-localization has to be implemented in sensor nodes for estimating the position information. In general, global positioning system (GPS) is commonly used in various applications. Because of its high cost, it is not best suited for many high-cost applications. Some of its other drawbacks are difficulty in installation and maintenance costs in some of the peculiar applications. Hence, only a very few sensor nodes in a WSN are equipped with GPS for positioning information, whereas the other nodes in the network need a better self-localization algorithm for the estimation of position information. Many localization algorithms have been proposed by researchers in the recent decade. Based on the mechanisms adopted for estimating the location, the localization techniques are broadly classified into two categories based on the range of node placement range free and range based. In a range-based mechanism, absolute distances along with angle measures are used while calculating the distances such as TDOA, TDA, RSSI, and AOA. The localization based on the range is found to be precise but cost-ineffective, and also, it is mostly applicable for large-scale implementation. Range-free localization is based on network connectivity. Range-free localization depends on the hardware limitation of the implanted sensor nodes. It is found to be cost-effective when compared with range-based applications.

Some of the most commonly used range-free algorithms are DV-hop, Centroid, APIT, and Amorphous. In recent years, several improved APIT algorithms are proposed as an effective localization techniques. A novel PIT algorithm is proposed based on the position of anchor nodes. An algorithm is drawn between the three anchor nodes targeting the target node inside the triangle by judging the COG of the intersection of the selected anchor nodes' coverage area formed within the triangle. An improved APIT algorithm on localization is proposed which determines the proposition of determining the target node if the sum of the areas of the three triangles formed by selecting the target node is found to be greater than the area of the triangle formed by selecting the anchor nodes. If the area of the target node triangle is found to be less than the area of the anchor node triangle, then the target node is said to be outside the triangle. In another modified APIT algorithm, the application area is partitioned into four overlapping and nonoverlapping areas. This is done by deploying four new anchor nodes in the corner of the application area. To reduce the computational complexity, care is taken more in selecting the anchor nodes. By comparing the strength of the received signal strength, each target node can select its own subregion. Then, APIT algorithm is implemented in these selected subregions. Then, the small area and narrow triangle are eliminated. The target node is incorrectly identified as being outside the triangle, per the APIT algorithm's theory. The APIT localization algorithm refers to this issue as an in-to-out error. The anchor

nodes' transmitted beacon signal cannot be received due to the unique distribution of the neighboring nodes. As the target node travels towards the neighboring nodes, this occurs at their location, which is simultaneously reduced. In this instance, it is assumed incorrectly that the target node is located inside the triangle. An out-to-in error is the technical term for this error. Node position, data collection, power consumption of the node in real time, node distance and its mobility in the real-time network, accuracy vs. complexity with the increase in network scalability, and propagation error with increased node density are some of the complexities identified in optimizing a WSN. Applications for wireless sensor networks can be found in many different industries. The foundational technology of the WSN is node localization. The distance vector hop (DV-Hop) algorithm is the most often used localization algorithm among the several available localization techniques [1–37].

1.1. APIT Localization Algorithm: An Introduction

APIT is a conventional range-free localization scheme with its own limitations. The basic idea of the APIT algorithm is that position of the anchor nodes is first identified by the target nodes. This is done by the target nodes by the beacon signals that it receives from the anchor nodes. The anchor nodes broadcast these beacon signals. These beacon signals carry various information like the ID of the anchor nodes, their positions, and the power required and consumed for its transmission. The target nodes are those nodes, which try to find their own location, whereas the anchor nodes are those nodes that are equipped with high-power transmitters and localization devices. Among the n anchor nodes, the target nodes choose any three anchor nodes. In the APIT mechanism, the target nodes try to find out their location based on the anchor nodes; it has chosen to form the triangulation area. The target node tries to find out whether it lies within the formed triangulation or not. By trying out all the combinations, the target nodes would form C3 n triangles. COG of the intersection of all the possible triangles formed is found by the target node to find out its estimated position. Figure 1 represents the overview of the triangular area formation of the APIT algorithm.

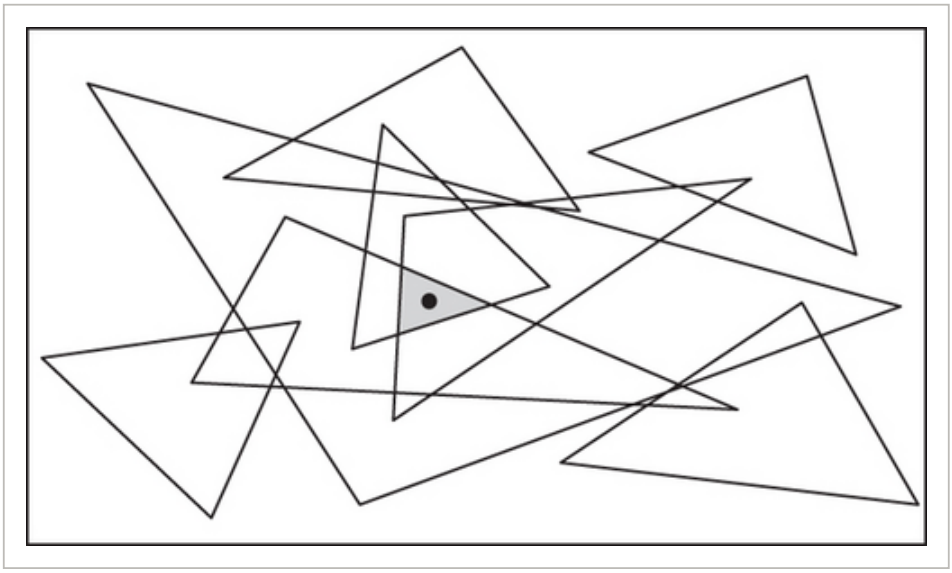

Figure 1

Open in figure viewer | PowerPoint

Overview of APIT algorithm.

The theoretical concept used to determine whether the target node lies inside or outside the triangular area is called Point-in-Triangulation (PIT). The working principle of PIT defined as a target node *T* is considered, and a given TABC is formed which is comprised of three anchor nodes and one target node. There exists a direction along which *T* moves such that it always stays away from the position of the vertices of the triangle or else close to the vertices. Then, the target node *T* is said to lie outside the triangle formed; else, it lies inside the triangular area [13].

1.2. Principle of APIT Algorithm

Practically, in a wireless sensor network, sensor nodes are fixed so that there is no random movement, so PIT tests are found to be infeasible in many practical applications. To overcome this issue in the PIT test without the mobility of sensor nodes in the network, APIT is proposed. The basic idea of APIT is that every target node rivals the movement of nodes by comparing the beacon RSSI received from the anchor nodes with respect to its neighbor sensor nodes. These nodes are the adjacent nodes that are also found within the communication range of the target node. Figure 2 shows the identification of the target node within the triangular area as inside the triangle or outside the triangular area as outside the triangle. Figure 2(a) shows the scenario where none of the target node's neighbors are further close or farther from the three anchor nodes of the triangle. When the neighbor nodes move away or closer to all three anchor nodes simultaneously, then the target node is said to lie within the triangle. The neighbor nodes include target nodes as well as the anchor nodes. The next scenario is shown in Figure 2(b) where the target node moves to the position of its neighbor node say node 4, where it is close to the anchor nodes simultaneously; in such cases, the target node assumes that it lies outside the triangulation area.

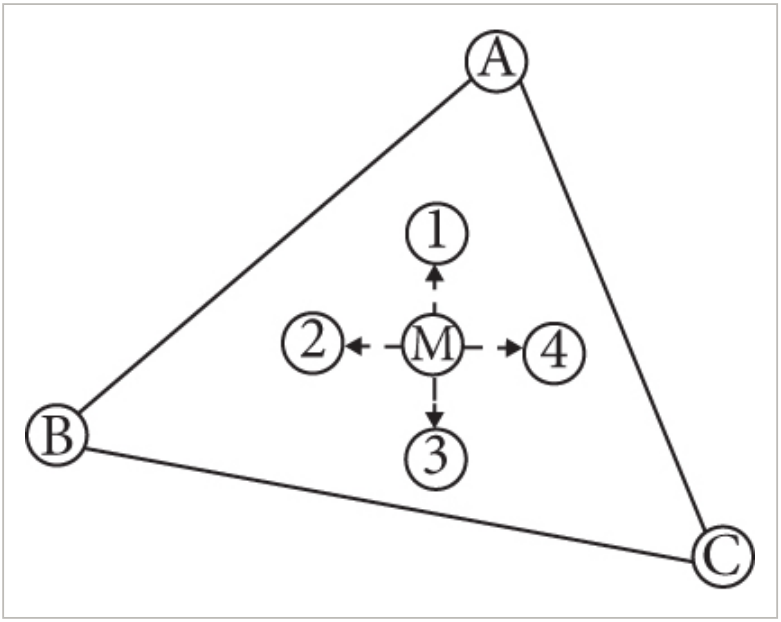

Figure 2 (a)

Open in figure viewer | PowerPoint

(a) APIT: inside case. (b) APIT: outside case.

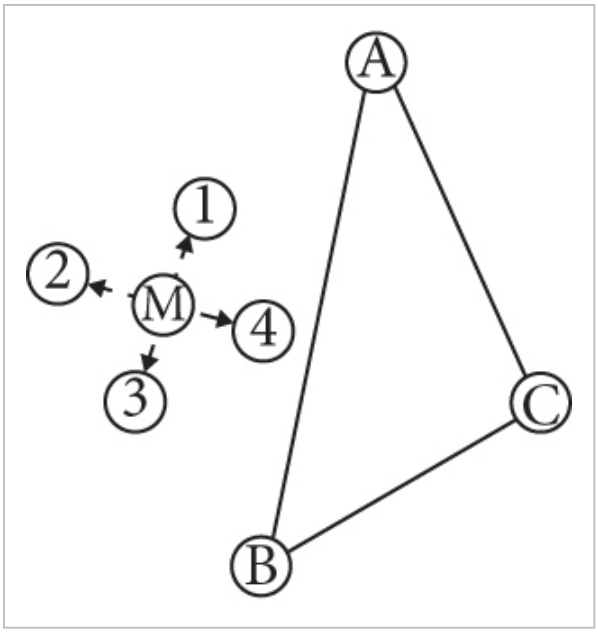

Figure 2 (b)

Open in figure viewer | PowerPoint

(a) APIT: inside case. (b) APIT: outside case.

1.3. Work Motivation of APIT Algorithm

An APIT localization algorithm has the following key advantages:

(i) Less communication overhead

(ii) High localization accuracy

Some of its limitations are as follows:

(i) Dependency on its neighbor nodes

(ii) Impact of the increased network density

(iii) Distribution of nodes in the network

1.4. Miscalculation of APIT Test

In the APIT test of localization basically, there are possibilities of two errors to occur as follows:

(i) In-to-out error

(ii) Out-to-in error

Figure 3(a) shows that the target node *M* actually lies within the triangular area of MABC, but as one of its neighbor nodes lies outside the triangular area and farther from the side AB of the triangle, the target node moves towards the neighbor node as it receives the RSSI of the beacon signals it receives from the

anchor nodes gets faded and decreases simultaneously. According to the idea of the APIT algorithm, the target node is wrongly determined as its location lying outside the triangle. This miscalculation is termed an in-to-out error in the APIT localization algorithm.

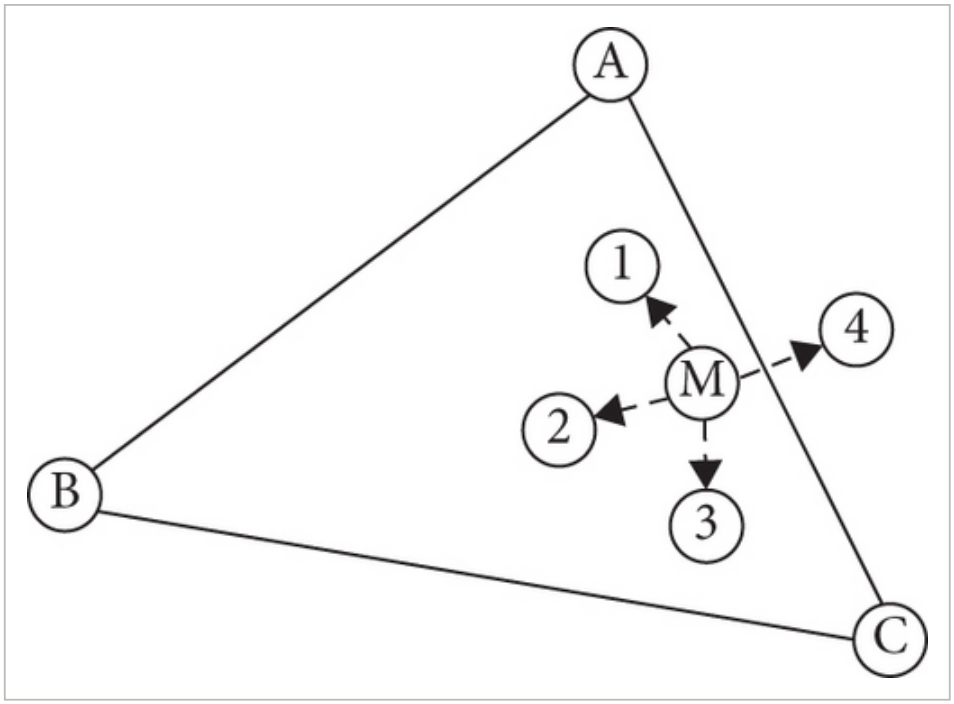

Figure 3 (a)

Open in figure viewer | PowerPoint

(a) APIT: in-to-out error. (b) APIT: out-to-in error.

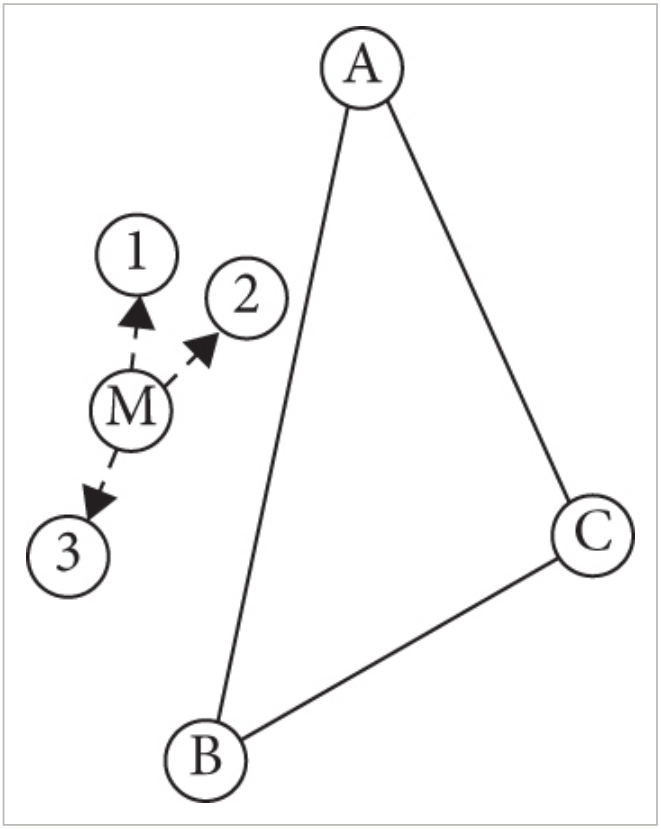

Figure 3 (b)

Open in figure viewer | PowerPoint

(a) APIT: in-to-out error. (b) APIT: out-to-in error.

The other error scenario is shown in Figure 3(b). Actually, the target node *M* lies outside the triangular area. The special distribution of the neighbor nodes leads to the nonreception beacon signal sent by the anchor nodes. This happens at the position of the neighbor nodes which is reduced simultaneously when the target node moves towards them. In this case, it is falsely understood that the target node lies within the triangle. This miscalculation is called an out-to-in error.

Hence from the above study, it is understood that APIT as a standalone algorithm suffers from the effect of increased node density and the distribution of nodes in the network. Hence to improve the efficiency of the APIT algorithm and to overcome the deficiency, this work combines the APIT algorithm with the Bat-SA algorithm which is found to be suitable for all kinds of wireless sensor network topology and varying scales.

1.5. Bat Algorithm

Bat algorithm is a type of metaheuristic searching algorithm. The following rules are the framework of the Bat algorithm:

(i) Echolocation is used to sense the distance of the target

(ii) Signals are transmitted randomly with varying frequency, and it is adjusted automatically to proximity. The pseudocode for the conventional Bat algorithm is given below

Pseudocode 1: Bat algorithm.

1. Objective function $f(x)$ is $(x1, x2, \cdots\cdots\cdots x4)^T$

2. Initialize Bat where (x = 1, 2, 3, $\cdots.n$) and Vi

3. Define the pulse frequency f_i at various Bat population values

4. Initialize rate r_i and loudness A_i

5. While t < maximum number of iterations

6. Adjust frequency and generate new set of solutions

7. Update new velocity and location

8. If rand > r_i

9. Select the best solution among the available solution set

10. Generate the local solution around the best solution set

11. End if

12. Generate a new solution by a random fly

13. If rand < A_i and $f(x_i < f(x^{'}))$

14. Accept the new solution

15. Increase the value of r_i and reduce the value of A_i

16. End if

17. Rank the Bat solution and find out the current best solution

18. End while

19. Post process results and its visualization

1.6. Simulated Annealing Algorithm

The goal of SA algorithm is to start with intense and then reduce the intensity of search. The pseudocode for a basic SA algorithm is given below.

Pseudocode 2: Simulated annealing algorithm.

S1 = an initial solution is set

T = an initial temperature is set

REPEAT

REPEAT

S2 = neighbour of the node S1 is identified

UNTIL a criteria is established by the node S2

ΔE = obj(S2) – obj(S1)

IF (ΔE>0) THEN // Noe S2 is chosen as better than node S1

S1 = S2

ELSE with probability EXP(ΔE/ T)

S1 = S2

END IF

Decrease T

UNTIL the stop criteria

End

Instead of the best movement, a random movement is chosen in the SA algorithm. If this chosen movement is found to improve the search, then it is accepted; else, the probability of movement is taken as 1. This probability is found to reduce with a decrease in temperature. Inappropriate search movements occur with an increase in temperature, and it gets reduced with a reduction in temperature. The value of temperature is multiplied by a coefficient value ranging between 0 and 1. Local optimality problem is encountered with a decrease in temperature. So a value near 1 is chosen say 0.998.

The steps involved in getting the start of a SA algorithm and its preparation are discussed below.

1.7. Getting Started and Preparation

The problem information is first identified, and the various adjusting parameters are obtained.

(1) An answer near the current answer is identified that satisfies the set criteria

(2) Answer obtained is evaluated

(a) If the newly identified neighbor is better than the existing one, go to NA (new answer)

(b) The probability > random number, go to NA else step 1

(3) Update the problem parameters and algorithm. Go to step 1

In the first step, the number of sensors needs to be identified for the user. As a request is raised by a user, a binary path solution is randomly generated. In the SA algorithm, an optimized path solution is created from the primary path. Two indexes are randomly chosen for a neighbor node. The indexes represent sensor nodes that are prone to change. Dijkstra's algorithm is used for identifying the relay nodes in identifying the path between the BS and the destination node. The overall energy optimization of the nodes of the path established is reduced, thereby adding a value of 1 to the network lifetime. The loop is continued until the desired value of optimization is reached. Table 1 shows the values used for the simulation of the network. Figure 4 shows the flowchart of simulate annealing algorithm.

Table 1. Simulation values.

Parameters	Value
Network size	500∗500 m
SNode's location	Uniform distribution
Node's location	Uniform distribution
Node's initial energy	0.1 J
Super node initial energy	0.5 J
Communication range	90 m

Parameters	Value
Sensing range	60 m
Number of nodes	300
Number of SNodes	25
Number of target	20
Elect	50 nJ/bit

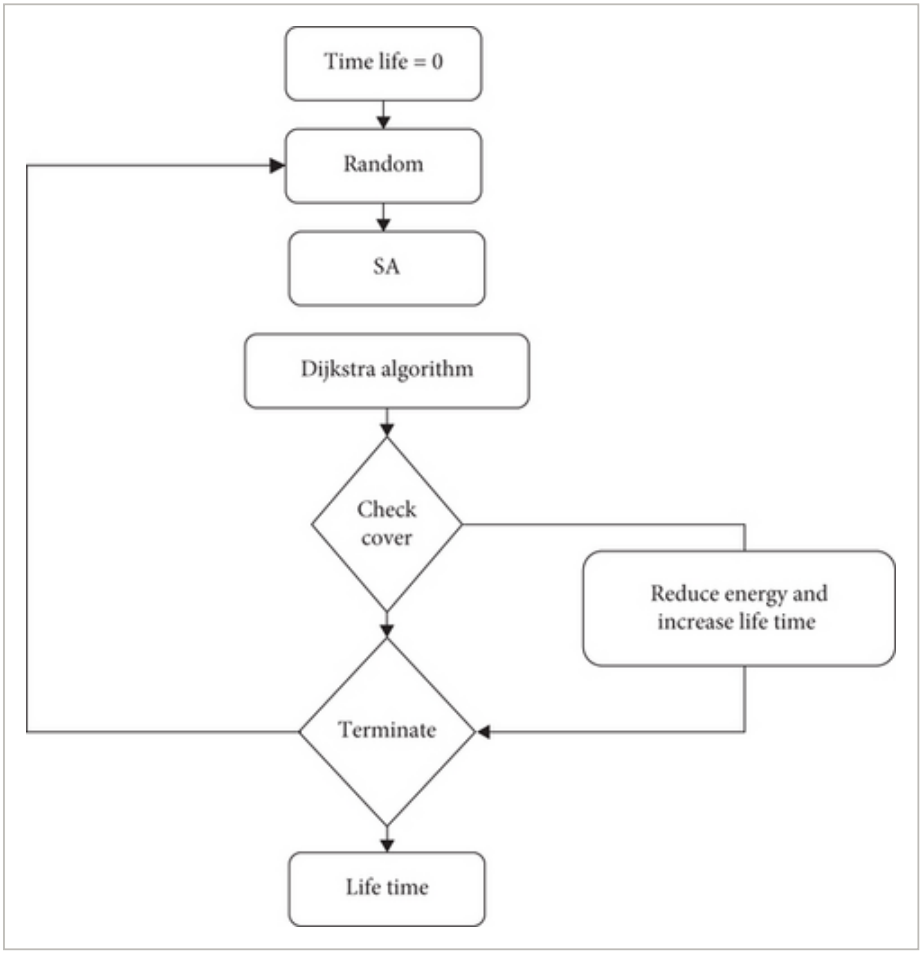

Figure 4

Open in figure viewer | PowerPoint

Flowchart for SA algorithm.

1.8. Proposed Bat with Simulated Annealing Algorithm

Some of the complexities identified in optimizing WSN are as follows:

(i) Node position

(ii) Data collection

(iii) Power consumption of node, i.e., real time

(iv) Node distance and its mobility in real-time network

(v) Accuracy vs. complexity with the increase in network scalability

(vi) Propagation error with increased node density

1.9. Overall Working Principle of APIT with Bat-SA Algorithm

PIT tests are discovered to be impractical in many practical applications because sensor nodes in a wireless sensor network are fixed to prevent random movement. APIT is suggested as a solution to this problem in the PIT test without the network's sensor nodes being mobile. The fundamental tenet of APIT is that each target node compares its movement to neighboring sensor nodes by comparing the beacon RSSI it receives from the anchor nodes. These nodes are the neighboring nodes that are also present within the target node's communication range. A particular kind of metaheuristic search method is the Bat algorithm. The Bat algorithm's foundation is comprised of the following rules: target distance is detected via echolocation, and signals are randomly delivered at varied frequencies, and they are automatically adjusted for closeness. The SA algorithm seeks to increase search intensity initially before reducing it.

1.10. Simulation of the Proposed APIT with Bat-SA Algorithm

MATLAB simulation tool is used for the proposed work. The network area considered is a 1000 m radius. In a conventional APIT algorithm, the error in obtaining the position of the neighbor nodes and latency is increased.

The performance metrics parameters are considered, and the results are obtained by using APIT and the proposed Bat with SA algorithms. Figure 5 shows the node distribution map of APIT without the Bat-SA algorithm.

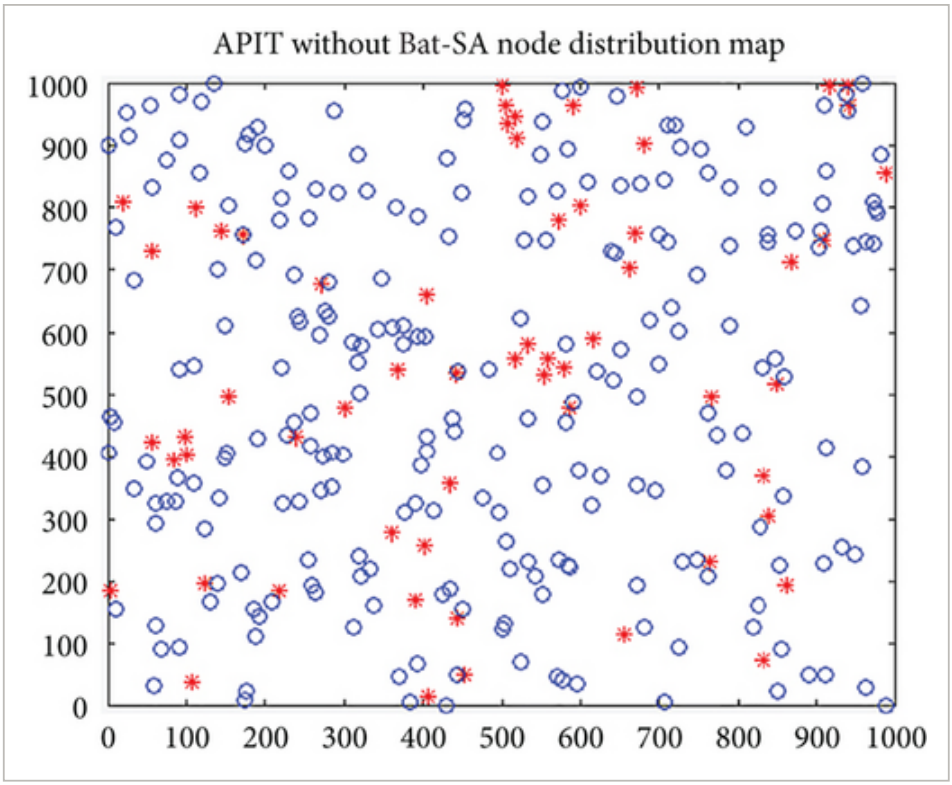

Figure 5

Open in figure viewer | PowerPoint

Node distribution map of APIT.

Figure 6 shows the positioning error map of the APIT algorithm without the Bat-SA algorithm.

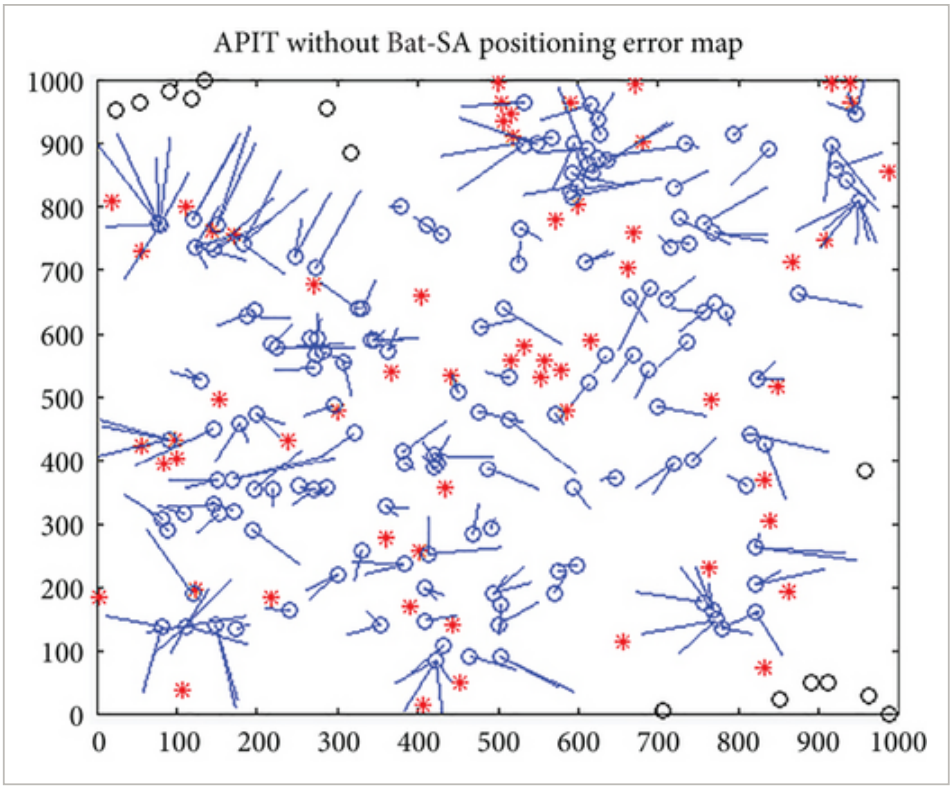

Figure 6

Open in figure viewer | PowerPoint

Positioning error map of APIT.

Figure 7 shows the neighbor relationship diagram obtained for the APIT localization algorithm.

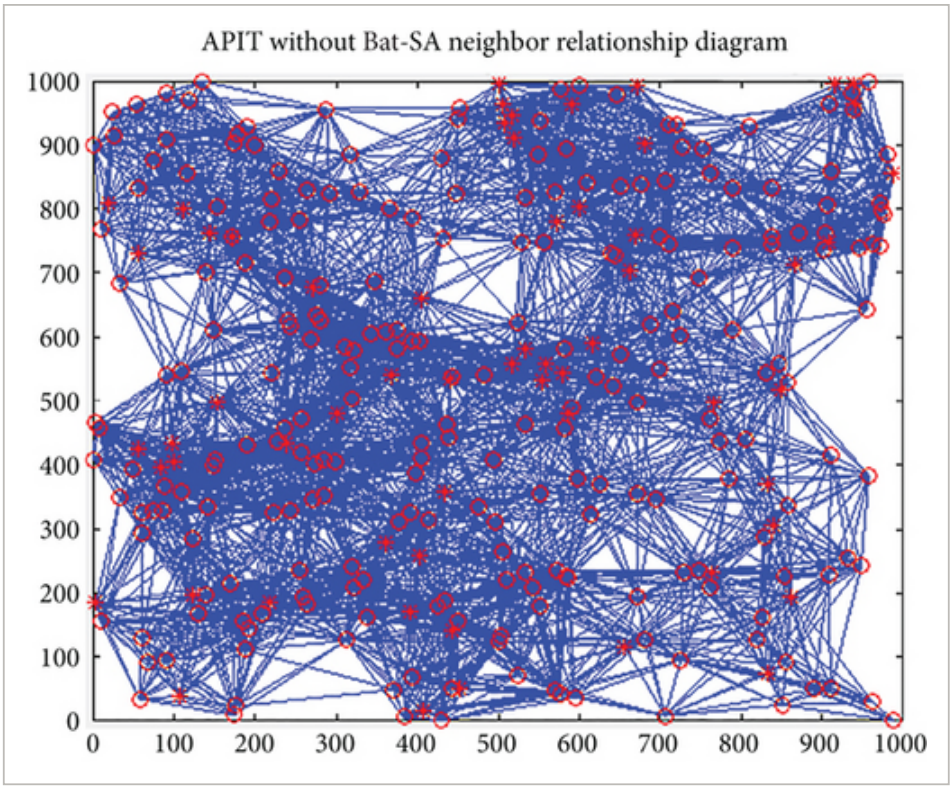

Figure 7

Open in figure viewer | PowerPoint

Neighbor relationship diagram of APIT.

Figure 8 shows the node distribution map for the proposed APIT with the BSA-SA algorithm. The nodes in the network are more evenly distributed than the node distribution done by the APIT algorithm.

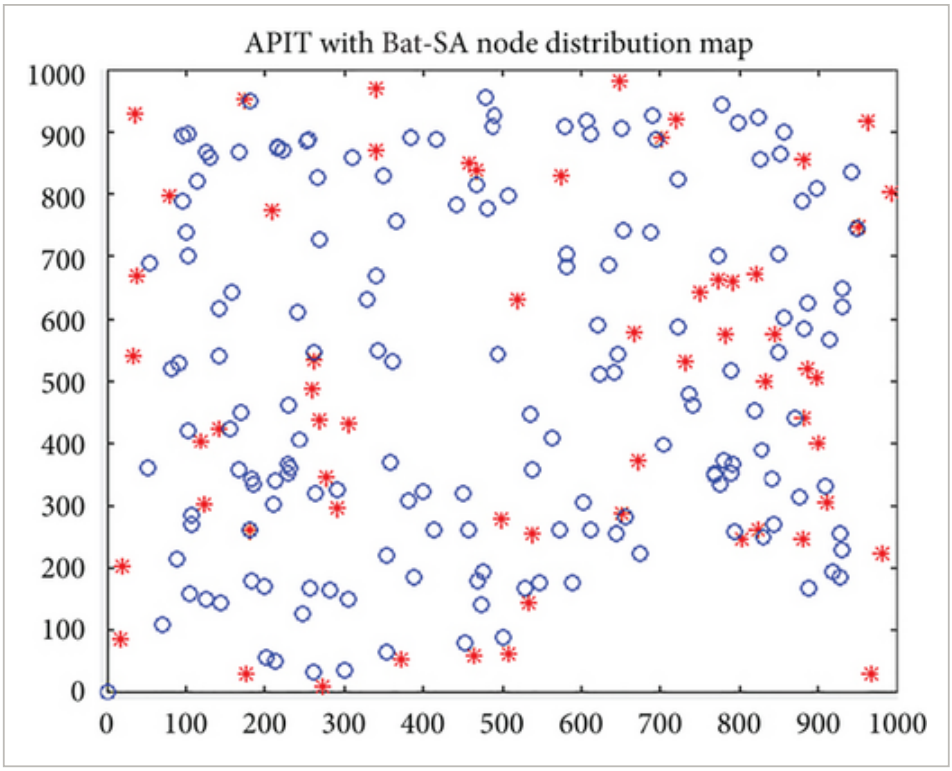

Figure 8

Open in figure viewer | PowerPoint

Node distribution map of APIT with Bat-SA.

Figure 9 shows the positioning error map obtained by using the proposed APIT with the Bat-SA localization algorithm. Less positioning error occurred when the proposed APIT with Bat-SA localization algorithm is used. The proposed algorithm achieves less node positioning error when compared with the conventional APIT localization algorithm.

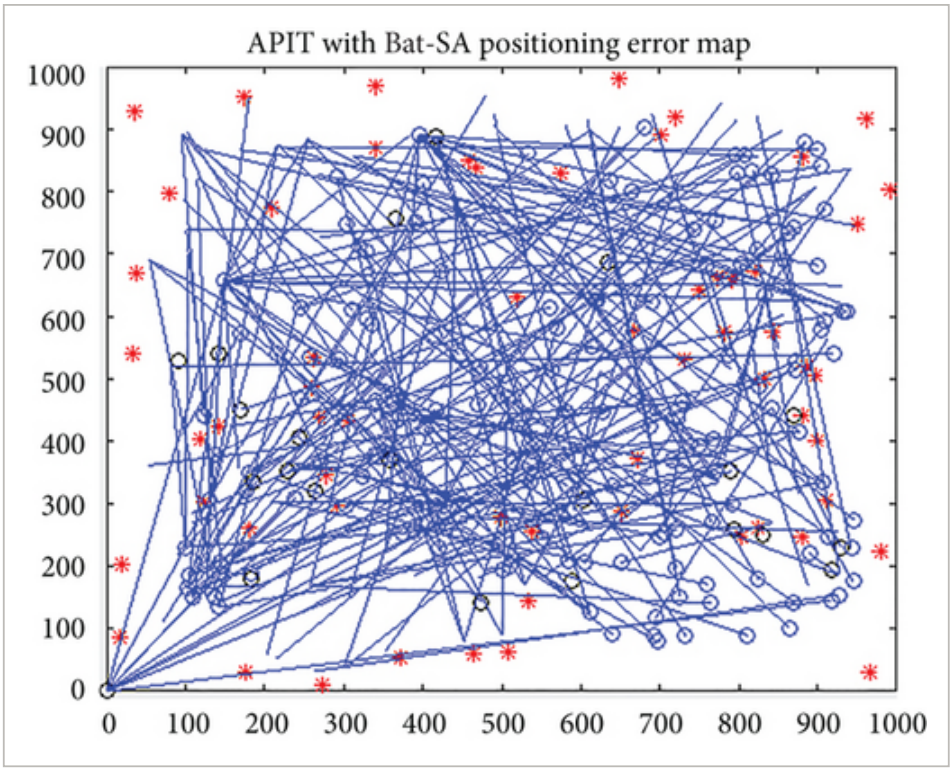

Figure 9

Open in figure viewer | PowerPoint

Positioning error map of APIT with Bat-SA.

Figure 10 shows the neighbor relation diagram obtained for APIT with the Bat-SA algorithm. From the diagram obtained through simulation of the proposed algorithm, it is proved that the relationship among the neighbor nodes is well established than the neighbor relationship attained through the APIT localization algorithm.

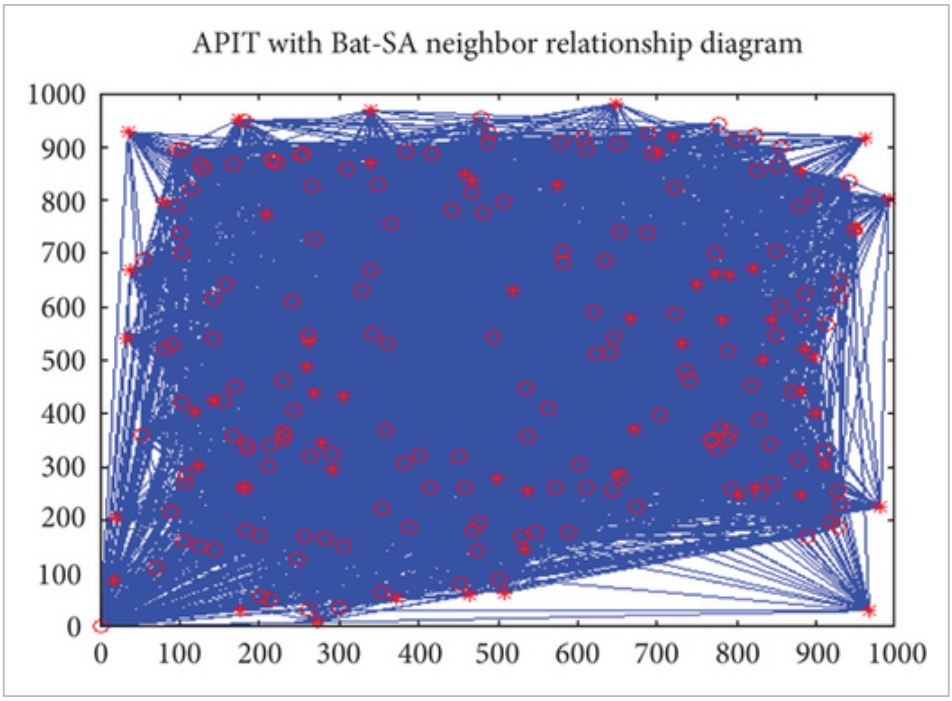

Figure 10

Open in figure viewer | PowerPoint

Neighbor relationship diagram of APIT with Bat-SA.

Figure 11 shows the shift vs. position error of APIT with and without the Bat-SA algorithm.

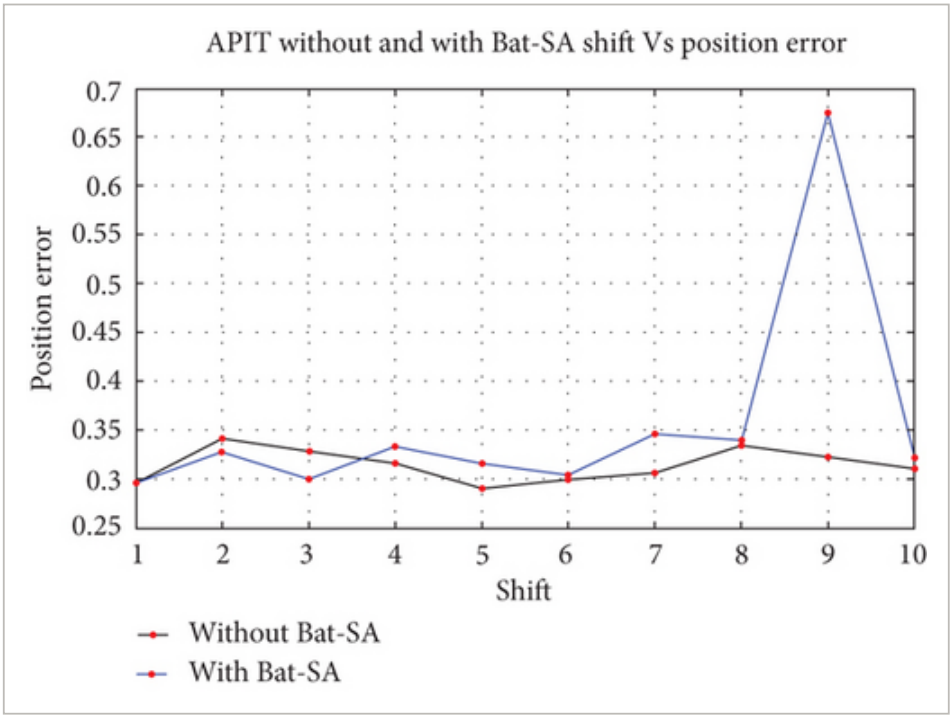

Figure 11

Open in figure viewer | PowerPoint

Anchor shift vs. position error of APIT with and without Bat-SA.

Figure 12 shows the comparative result of anchor shift vs. latency of APIT with and without the Bat-SA algorithm. Latency is found to be comparatively less in APIT with Bat-SA than in APIT without the Bat-SA algorithm.

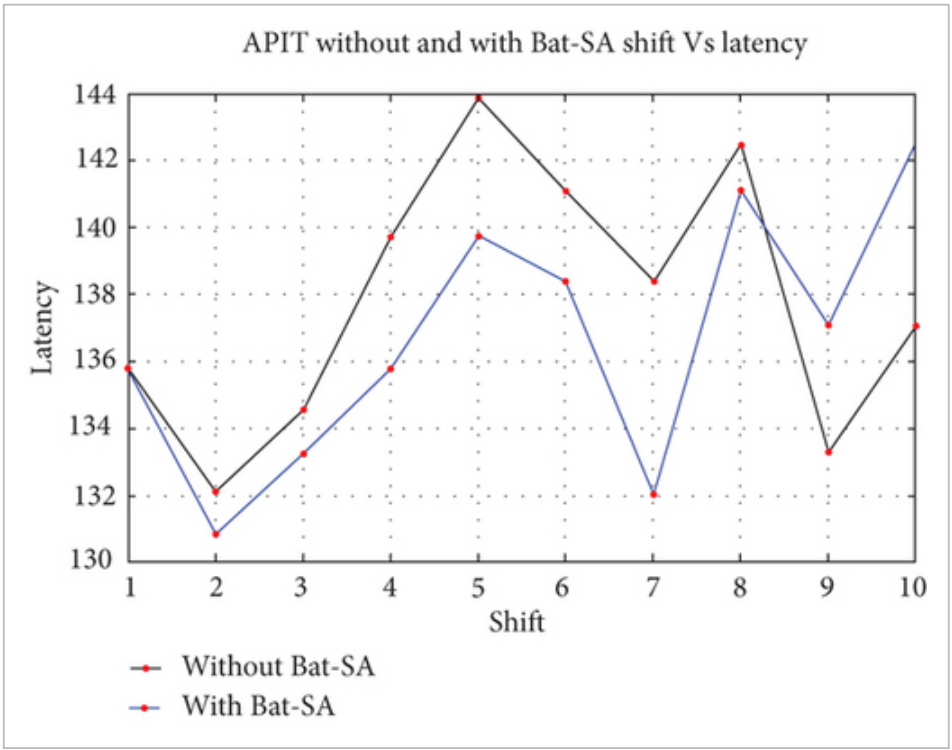

Figure 12

Open in figure viewer | PowerPoint

Anchor shift vs. latency of APIT with and without Bat-SA.

Simulation result of the APIT with Bat-SA algorithm for positioning error of nodes is performed for various iterations, and the result obtained is shown in Figure 13. It is found that the positioning error gets reduced as the number of iterations gets increased. Latency is also decreased for APIT with the Bat-SA algorithm with increased iterations, and the result obtained is shown in Figure 14.

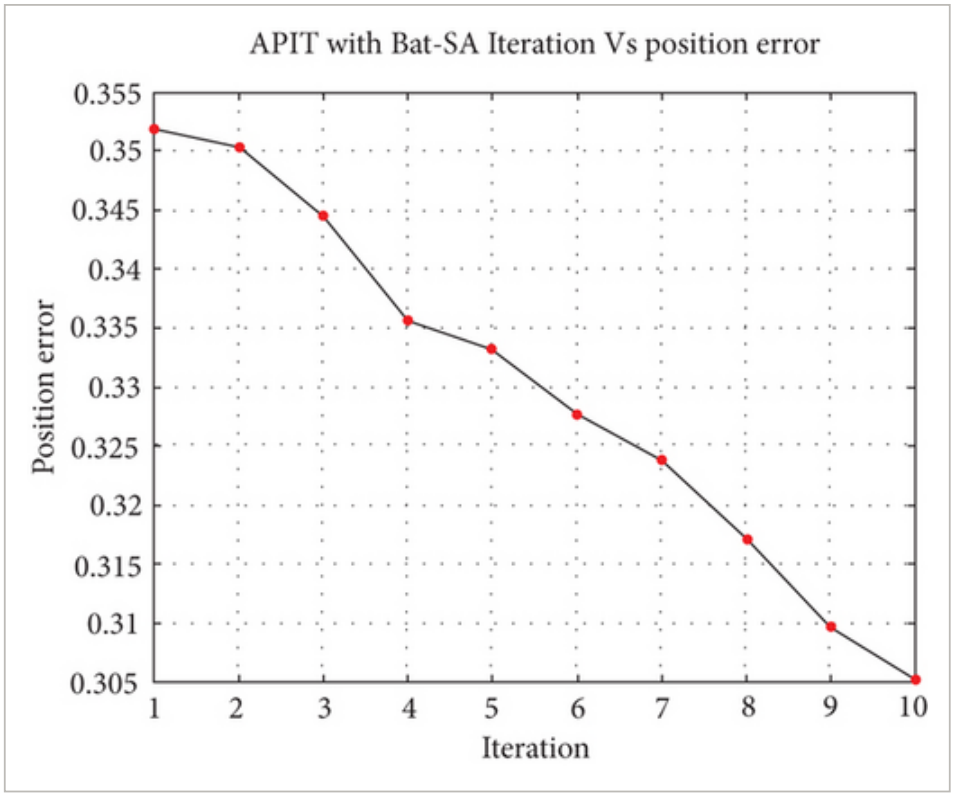

Figure 13

Open in figure viewer | PowerPoint

Iteration vs. position error of APIT with Bat-SA.

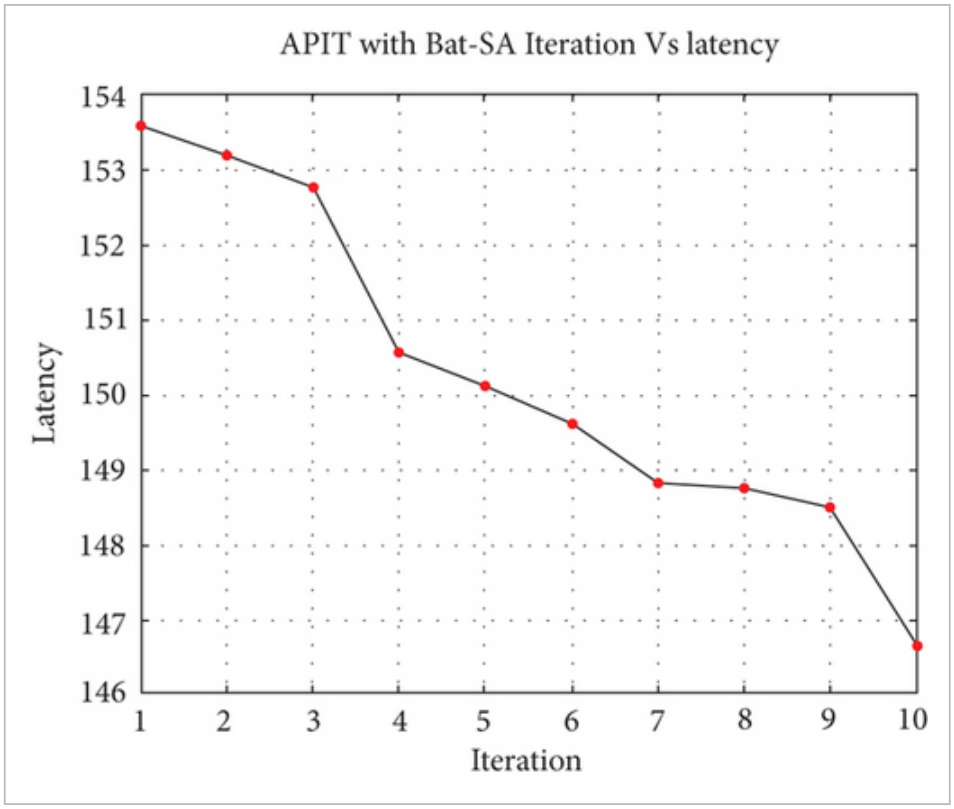

Figure 14

Open in figure viewer | PowerPoint

Iteration vs. latency of APIT with Bat-SA.

Simulation is performed for communication radius against position error for APIT without and with the Bat-SA algorithm. Figure 15 shows that the positioning error is found to be less in the case of APIT with the Bat-SA algorithm.

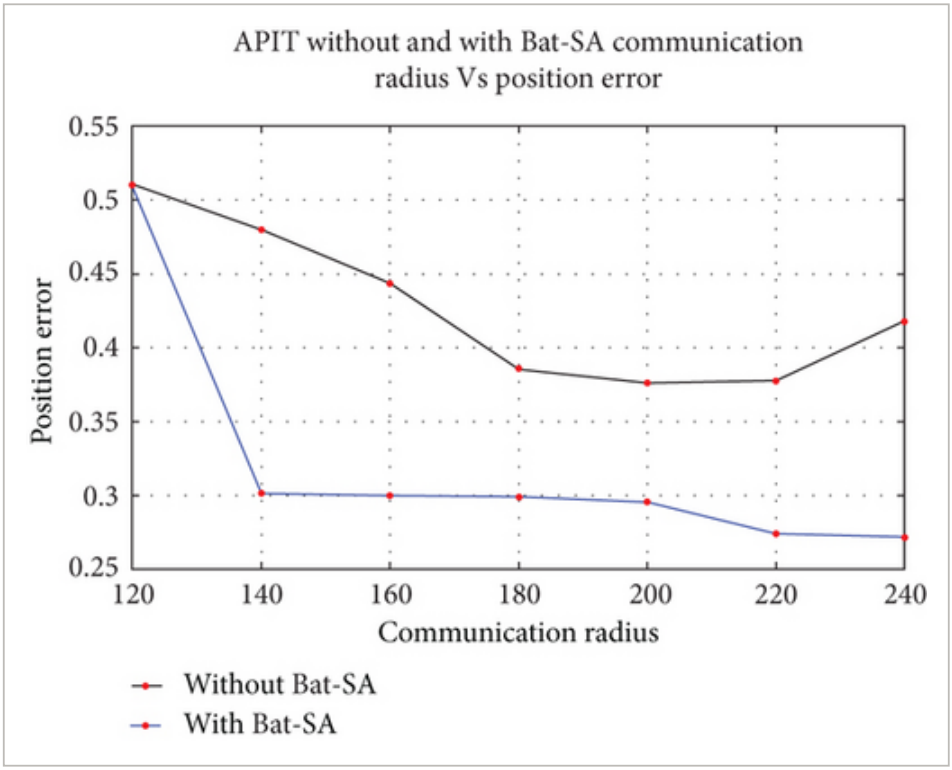

Figure 15

Open in figure viewer | PowerPoint

Communication radius vs. position error of APIT without and with Bat-SA.

Figure 16 shows the comparison of communication radius against latency for APIT without and with the Bat-SA algorithm. The results show that APIT with Bat-SA algorithm proves to be efficient for its significantly reduced latency against the increase in communication radius.

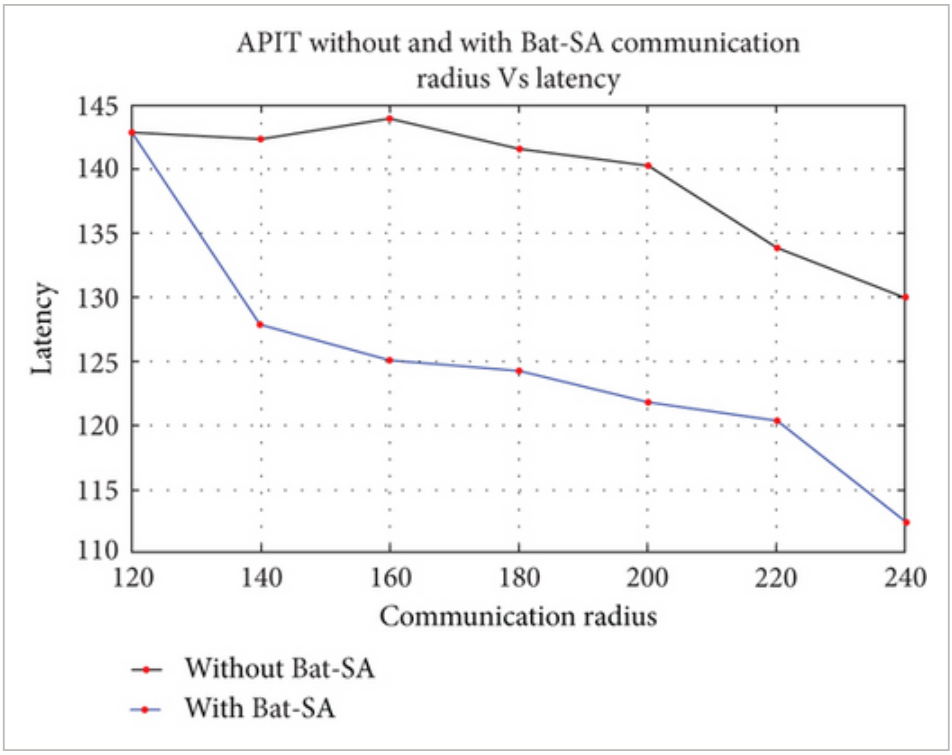

Figure 16

Open in figure viewer | PowerPoint

Communication radius vs. latency of APIT without and with Bat-SA.

Figure 17 shows the simulation results for area vs. position error of APIT without and with the Bat-SA algorithm.

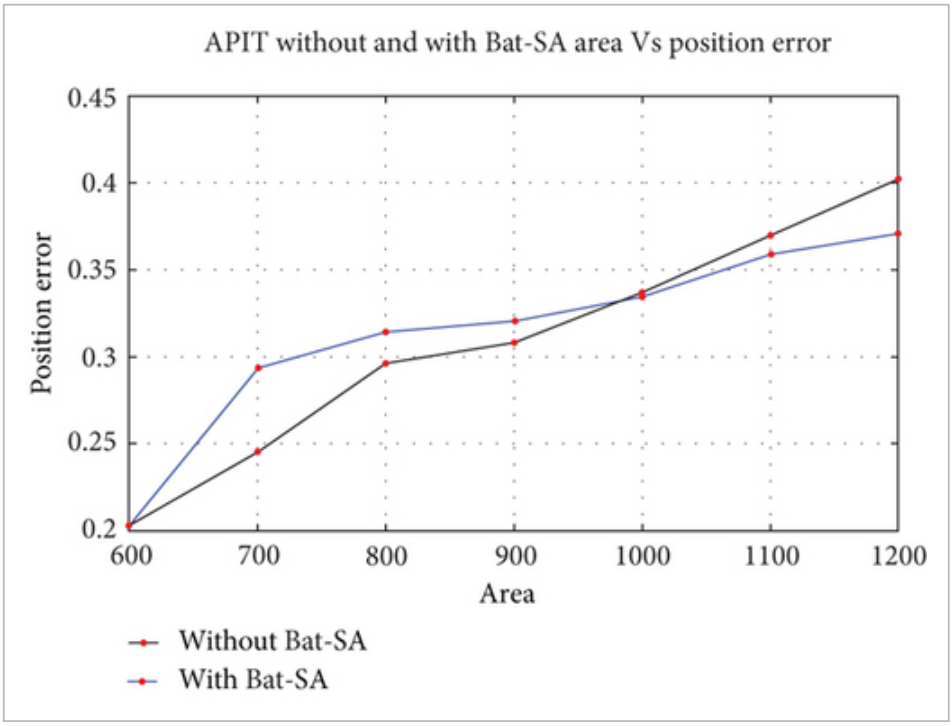

Figure 17

Open in figure viewer | PowerPoint

Comparison of area vs. position error of APIT without and with Bat-SA.

Figure 18 shows the simulation results for area vs. latency of APIT without and with the Bat-SA algorithm. From the result, it is proved that APIT outperforms the function of APIT without the Bat-SA algorithm in the case of area vs. latency parameter check.

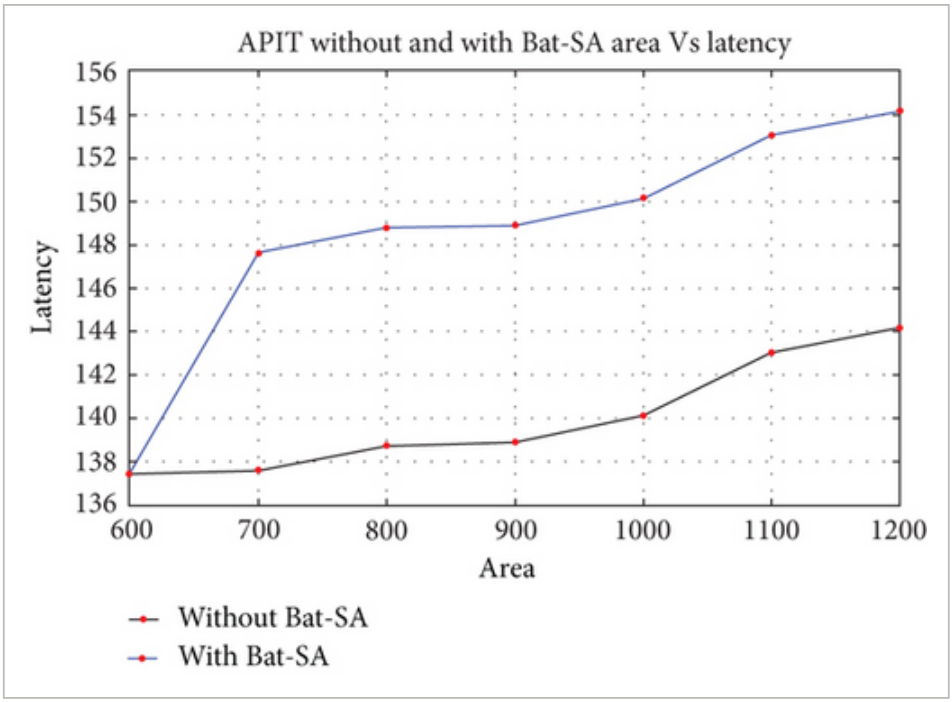

Figure 18

Open in figure viewer | PowerPoint

Comparison of area vs. latency of APIT without and with Bat-SA.

2. Conclusion and Future Work

The conventional Bat algorithm than APIT has good accuracy since it provides minimal localization error. The convergence of the computing rate and the success rate of the proposed Bat with the SA algorithm is found to have better performance than the conventional APIT algorithm. Hence, the proposed algorithm of APIT is combined with the Bat-SA localization algorithm and is simulated. From the simulated results obtained, it is proved that the computing time is also reduced with an increase in the scalability of the network area. The position error and latency are also decreased than the conventional APIT localization algorithm. The relationship among the nodes is also more well established than in the APIT algorithm. The simulation also shows the consistency of the proposed algorithm. Thus, the overall system performance is increased, and the localization of WSN is significantly optimized by using the proposed APIT with Bat-SA algorithm.

Conflicts of Interest

The authors declare that they have no conflicts of interest.

Open Research

Data Availability

The datasets used and/or analyzed during the current study are available from the corresponding author on reasonable request.

References

1 Hofmann-Wellenhof B., Lichtenegger H., and Collins J., *Global Positioning System: Theory and Practice*, 2001, Springer, VerlagWien, https://doi.org/10.1007/978-3-7091-6199-9.

Google Scholar

2 Pal A., Localization algorithms in wireless sensor networks: current approaches and future challenges, *Network Protocolsand Algorithms*. (2010) **2**, no. 1, 45–73, https://doi.org/10.5296/npa.v2i1.279.

Google Scholar

3 Shu Y., Cheng P., Gu Y., Chen J., and He T., Toc: localizing wireless rechargeable sensors with time of charge, *InProceedings IEEE (INFOCOM'2014)*, 2014, Toronto, Canada, 388–396.

Google Scholar

4 Wang J., Gao Q., Cheng P., Yu Y., Xin K., and Wang H., Lightweight robust device-free localization in Wireless Networks, *IEEE Transactions on Industrial Electronics*. (2014) **61**, no. 10, 5681–5689, https://doi.org/10.1109/TIE.2014.2301714, 2-s2.0-84900537930.

Web of Science® Google Scholar

5 Wang J., Gao Q., Wang H., Cheng P., and Xin K., Device-free localization with multidimensional wireless link information, *IEEE Transactions on Vehicular Technology*. (2015) **64**, no. 1, 356–366, https://doi.org/10.1109/TVT.2014.2318084, 2-s2.0-84921361647.

Web of Science® Google Scholar

6 Bahl P. and Padmanabhan V. N., RADAR: An in-buildingRF-based user location and tracking system, *Nineteenth Annualjoint Conference of the IEEE Computer and Communications Societies (INFOCOM'2010)*, 2000, Tel Aviv, Israel, 775–784.

Google Scholar

7 Zhang W., Yin Q., Feng X., and Wang W., DistributedTDOA estimation for wireless sensor networks based on frequency-hopping in multipath environment, *In vehicular technology conference (VTC'2010-spring)*, 2010, Taipei.

Google Scholar

8 Niculescu D. and Nath B., Ad hoc positioning system (APS) using AOA, *In twenty-second annual joint conference ofthe IEEE computer and communications (INFOCOM'2003)*, 2003, NJ, USA, 1734–1743.

Google Scholar

9 Kumar P., Reddy L., and Varma S., Distance measurementand error estimation scheme for RSSI based localization inwireless sensor networks, *In 2009 Fifth IEEE Conference Onwireless Communication and Sensor Networks (WCSN'2009)*, 2009, Allahabad, India.

Google Scholar

10 Bulusu N., Heidemann J., and Estrin D., Gps-less low-cost outdoor localization for very small devices, *Personal Communications IEEE*. (2000) **7**, no. 5, 28–34, https://doi.org/10.1109/98.878533, 2-s2.0-0034291601.

Web of Science® Google Scholar

11 Niculescu D. and Nath B., Dv based positioning in ad hocnetworks, *Telecommunication Systems*. (2003) **22**, no. 1/4, 267–280, https://doi.org/10.1023/A:1023403323460, 2-s2.0-0038703640.

Web of Science® Google Scholar

12 Nagpal R., *Organizing a global coordinate system fromlocal information on an amorphous computer*, 1999, AI Memo 1666,MIT.

Google Scholar

13 He T., Huang C., Blum B. M., Stankovic J. A., and Abdelzaher T., Range-free localization schemes for large scale sensor networks, *In Proceedings of the 9th Annual International Conference on Mobile Computing and Networking*, 2003, New York, USA.

Google Scholar

14 Deng B., Huang G., Zhang L., and Liu H., Improvedcentroid localization algorithm in WSNs, *In 3rd Internationalconference on Intelligent System and Knowledge Engineering (ISKE'2008)*, 2008, Xiamen, China, 1260–1264.

Google Scholar

15 Tian S., Zhang X., Liu P., Sun P., and Wang X., ARSSIbaseddv-hop algorithmfor wireless sensor networks, *In Internationalconference on Wireless Communications, Networking and Mobilecomputing (WiCom'2007)*, 2007, Shanghai, China, 2555–2558.

Google Scholar

16 Qian Q., Shen X., and Chen H., An improved node localization algorithm based on dv-hop for wireless sensor networks, *Computer Science and Information Systems*. (2011) **8**, no. 4, 953–972, https://doi.org/10.2298/CSIS110222051Q.

Web of Science® Google Scholar

17 Cheng W., Li J., and Li H., An improved APIT locationalgorithm for wireless sensor networks, *Advances in electricalengineering and automation*, 2012, springer, Netherlands, 113–119.

Google Scholar

18 Han G., Xu H., Duong T. Q., Jiang J., and Hara T., Localization algorithms of wireless sensor networks: a survey, *Telecommunication Systems*. (2013) **52**, no. 4, 2419–2436, https://doi.org/10.1007/s11235-011-9564-7, 2-s2.0-84879915071.

Web of Science® Google Scholar

19 Xiangqun L., Heng G., and Linlin L., An improved APIT algorithm based on direction searching, *In 5th Internationalconference on Wireless Communications, Networking and Mobilecomputing (WiCom'09)*, 2009, Beijing, China.

Google Scholar

20 Xu D., Zhang B., and Hou Z., Novel PIT localization algorithm based on coverage of anchors in WSN, *Journal of Networks*. (2012) **7**, no. 9, 1349–1354, https://doi.org/10.4304/jnw.7.9.1349-1354, 2-s2.0-84866759121.

Google Scholar

21 Zeng Wang J. and Jin H., Improvement on APIT localizationalgorithms for wireless sensor networks, *In Internationalconference on Networks Security, Wireless Communications and Trusted Computing (NSWCTC'09)*, 2009, Wuhan, China, 719–723.

Google Scholar

22 Hosseinirad S. M., Niazi M., Pourdeilami J., Basu S. K., and Pouyan A. A., On improving APIT algorithm for betterlocalization in WSN, *Journal of AI and Data Mining*. (2014) **2**, no. 2, 97–104.

Google Scholar

23 Rappaport T. S., *Wireless Communications: Principlesand Practice*, 2002, PTR, New Jersey.

Google Scholar

24 Rathish C. R. and Rajaram A., Efficient path reassessment based on node probability in wireless sensor network, *International Journal of Control Theory and Applications*. (2016) **34**, 817–832.

Google Scholar

25 Basha S. R., Sharma C., Sayeed F., Arularasan A. N., Pramila P. V., Shinde S. K., Pant B., Rajaram A., and Yeshitla A., Implementation of reliability antecedent forwarding technique using straddling path recovery in Manet, *Wireless Communications & Mobile Computing*. (2022) **2022, article 6489185**, 9, https://doi.org/10.1155/2022/6489185.

Web of Science® Google Scholar

26 Rathish C. R. and Rajaram A., Hierarchical load balanced routing protocol for wireless sensor networks, *International Journal of Applied Engineering Research*. (2015) **10**, no. 7, 16521–16534.

Google Scholar

27 Indira D. N. V. S. L. S., Ganiya R. K., Babu P. A., Xavier A. J., Kavisankar L., Hemalatha S., Senthilkumar V., Kavitha T., Rajaram A., Annam K., and Yeshitla A., Improved artificial neural network with state order dataset estimation for brain cancer cell diagnosis, *BioMed Research International*. (2022) **2022**, 10, https://doi.org/10.1155/2022/7799812, 7799812.

CAS PubMed Web of Science® Google Scholar

28 Ganesh P., Naidu G. B. S. R., Swaroopa K., Rahul R., Almadhor A., Senthilkumar C., Gangodkar D., Rajaram A., and Yeshitla A., Implementation of hidden node detection scheme for self-organization of data packet, *Wireless Communications and Mobile Computing*. (2022) **2022**, 9, https://doi.org/10.1155/2022/1332373, 1332373.

Web of Science® Google Scholar

29 Dinesh M., Arvind C., Mole S. S. S., Kumar C. S. S., Sekar P. C., Somasundaram K., Srihari K., Chandragandhi S., and Sundramurthy V. P., An energy efficient architecture for furnace monitor and control in foundry based on Industry 4.0 using IoT, *Scientific Programming*. (2022) **2022**, 8, 1128717, https://doi.org/10.1155/2022/1128717.

Web of Science® Google Scholar

30 Kannan S. and Rajaram A., Enhanced stable path routing approach for improving packet delivery in MANET, *Journal of Computational and Theoretical Nanoscience*. (2017) **4**, no. 9, 4545–4552.

Google Scholar

31 Anand R. P. P. and Rajaram A., Effective timer count scheduling with spectator routing using stifle restriction algorithm in manet, *IOP Conference Series: Materials Science and Engineering*. (2022) **994**, no. 1, article 012031.

Google Scholar

32 Kumar K. V. and Rajaram A., Energy efficient and node mobility based data replication algorithm for MANET, 2019, Rathish and Rajaram.

Google Scholar

33 Rathish C. R. and Rajaram A., Sweeping inclusive connectivity based routing in wireless sensor networks, *ARPN Journal of Engineering and Applied Sciences*. (2018) **3**, no. 5, 1752–1760.

Google Scholar

34 Mahalakshmi K., Kousalya K., Shekhar H., Thomas A. K., Bhagyalakshmi L., Suman S. K., Chandragandhi S., Bachanna P., Srihari K., and Sundramurthy V. P., Public auditing scheme for integrity verification in distributed cloud storage system, *Scientific Programming*. (2021) **2021**, 5, 8533995, https://doi.org/10.1155/2021/8533995.

Web of Science® Google Scholar

35 Divakaran J., Malipatil S., Zaid T., Pushpalatha M., Patil V., Arvind C., Titus T. J., Srihari K., Vignesh M. R., Gadgay B., and Sundramurthy V. P., Technical study on 5G using soft computing methods, *Scientific Programming*. (2022) **2022**, 7, 1570604, https://doi.org/10.1155/2022/1570604.

Web of Science® Google Scholar

36 Shitharth S., Meshram P., Kshirsagar P. R., Manoharan H., Tirth V., and Sundramurthy V. P., Impact of big data analysis on nanosensors for applied sciences using neural networks, *Journal of Nanomaterials*. (2021) **2021**, 9, 4927607, https://doi.org/10.1155/2021/4927607.

Web of Science® Google Scholar

37 Swarna Latha T. and Bhanu Rekha K., A hybrid metaheuristic bat algorithm with simulated annealing for node localization in wireless sensor network, *Mathematical Statistician and Engineering Applications*. (2022) **71**, no. 3.

Google Scholar

Citing Literature

Download PDF

ABOUT WILEY ONLINE LIBRARY

Privacy Policy
Terms of Use
About Cookies
Manage Cookies
Accessibility
Wiley Research DE&I Statement and Publishing Policies
Developing World Access

HELP & SUPPORT

Contact Us
Training and Support
DMCA & Reporting Piracy

OPPORTUNITIES

Subscription Agents
Advertisers & Corporate Partners

CONNECT WITH WILEY

The Wiley Network
Wiley Press Room

Copyright © 1999-2024 John Wiley & Sons, Inc or related companies. All rights reserved, including rights for text and data mining and training of artificial intelligence technologies or similar technologies.

engineering proceedings

MDPI

Proceeding Paper

A Novel DV-HOP and APIT Localization Algorithm with BAT-SA Algorithm

Thangimi Swarna Latha [1,2,*], K. Bhanu Rekha [1] and S. Safinaz [1]

[1] Department of Electronics and Communications Engineering, School of Electronics Engineering, Presidency University, Bangalore 560064, Karnataka, India; bhanurekha@presidencyuniversity.in (K.B.R.); safinazs@presidencyuniversity.in (S.S.)
[2] Department of Electronics and Communications Engineering, SV College of Engineering, Tirupati 517507, Andhra Pradesh, India
* Correspondence: swarnalatha.tg@svce.edu.in

Abstract: Localization technology is essential for making wireless sensor networks(WSN)'s information processing and information collecting applications actually feasible. The beacon information is made available to the unknown nodes using the route exchange protocol. These data are more useful for determining the coordinates of neighboring nodes. Consequently, it was discovered that the algorithm for localizing nodes always has a flaw. Consequently, a brand-new metaheuristic termed Bat with simulated annealing is proposed to fix the flaw in the WSN standard node localization technique. The overall effectiveness of identifying the nodes is enhanced as a result of the large reduction in localization errors. The most popular localization estimation methods are the distance vector hop (DV-Hop) technique and approximate point-in-triangulation (APIT), which have high node localization accuracy and simple deployment in real-time environments. The primary benefits and their disadvantages, which give it a slight disadvantage in preference, are presented in this work. Both strategies are compared for their conventional performance and efficiency when combined with the Bat-SA algorithm.

Keywords: meta heuristic; Bat; location algorithm; DV-Hop; simulated annealing

check for updates

Citation: Latha, T.S.; Rekha, K.B.; Safinaz, S. A Novel DV-HOP and APIT Localization Algorithm with BAT-SA Algorithm. *Eng. Proc.* **2023**, *59*, 91. https://doi.org/10.3390/engproc2023059091

Academic Editors: Nithesh Naik, Rajiv Selvam, Pavan Hiremath, Suhas Kowshik CS and Ritesh Ramakrishna Bhat

Published: 20 December 2023

Copyright: © 2023 by the authors. Licensee MDPI, Basel, Switzerland. This article is an open access article distributed under the terms and conditions of the Creative Commons Attribution (CC BY) license (https://creativecommons.org/licenses/by/4.0/).

1. Introduction

WSN has many uses because it is one of the most efficient and dependable techniques for gathering and processing data. In order to study and monitor environmental changes in locations where people are unable to travel, aircraft are used to deploy the wireless sensor nodes. The WSN nodes collect environmental data and are typically randomly dispersed around the monitoring region. It is found that in these circumstances, the nodes' deployment position is significant. Due to limitations on cost, power, and stability, it would be very difficult to manually install a GPS receiving device for every sensor node [1].

The effectiveness of the WSN as a whole is significantly impacted by the absence of location data in such environments. A WSN is thus strongly dependent on localization technologies. The nodes convey the data they have collected to the destination node or monitor node across a number of hops. Since the WSN is self-organizing, each node may recognize or learn details about its surrounding nodes independently. It is found that the nodes of the wireless network have greater power than conventional nodes in a communication link. Data derived from nodes are transmitted to the base station using a multi-hop method [2–5]. Unknown nodes and beacon nodes are the two main categories of nodes in a WSN. In general, the unknown nodes are unaware of their location, as opposed to beacon nodes, which are aware of their whereabouts thanks to the GPS device that is deployed with them. The two types of localization algorithms are as follows:

- Distance-free;

- Distance-based.

Received signal strength indicator (RSSI), the angle of arrivals, time difference of arrivals, and the time of arrival are a few of the distance-based algorithms. Algorithms for localization without regard to distance or range include MAP, approximate triangle point test, amorphous algorithms, and DV-HOP. The perfect distance between the deployed node is identified by the distance-based localization algorithm in order to locate the closest nodes in the network. Therefore, location awareness is essential in highly sensitive applications like military and underwater communication, among others [6].

The availability of the geographic locations of the sensor nodes is thus discovered to be complicated by localization. Triangulation, multilateration, or trilateration are the geometric methodologies used for position determination depending on the characteristic of the communication signals. Although distance-based localization approaches have a high degree of precision, they are not economical [7] and shown in Figure 1.

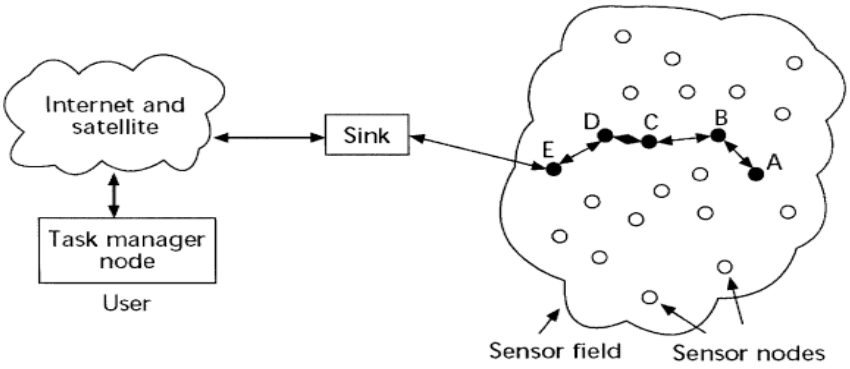

Figure 1. WSN network.

2. DV-HOP-Based Methodology

The main notion underlying the DV-HOP method is that unknown nodes must first ascertain the beacon node's maximum hop count. After multiplying the ratio of the average hop to the necessary minimum hops, the hop average distance has been determined. As the last step, when computingthe distance between the unknown node and beacon node, the existing DV-HOP algorithms have a number of problems, some of which are listed below. Beacon localization is less accurate. Lower coverage rate in sparse environments. Figure 2 describes the design of nodes in a WSN with the conventional DV-Hop approach [8–10]. At the start, every anchor node broadcasts a signal to the entire WSN. The anchor node is identified by initializing one as count value for the HOP. The minimum count value isconsidered by the beacon. Astale node is detected as a beacon with a higher hop count value than a specific anchor node, and it is disregarded as a result [11–13].

The network floods the new nodes that it does not identify as stale nodes. At each intermediate hop, these nodes increase their value for the hop count. Every node in the network finds a path to its anchor node using this technique that requires the fewest hops. Figure 3 depicts DV-HOP implementation.

The widely used APIT range-free localization technique has certain shortcomings. In the main structure of the APIT method, the target nodes detect the place of the anchor nodes first. This is performedusing the beacon signals that the target nodes receive from anchor nodes. These beacon signals are generated by anchor nodes.

Beacon signals carry a variety of data, including the IDs of anchor nodes andthe power used for transmission and for the position in the transmission. Generally, anchor nodes consume more power and are equipped for the localization of the devices. The target nodes select from the list three of the 'n' anchor nodes. During APIT process, target nodes attempt to identifytheir own locations by using the anchor. The target node searches for a position within the designated triangulation area. The target nodes would generate C3 triangles by testing each combination. The target node finds its COG inorder to determine

its estimated position by locating the intersection of all probable triangles. Figure 4 shows the generic triangle area generation using the APIT method. The theoretical idea of point-in-triangulation (PIT) demonstrates whether the localization triangle zone is present on the exterior or interior of the zone. A TABC with threeanchor nodes andonetarget node is constructed while keepingin mind the target node T. T can travel in a way that either keeps it a long way from the triangle's vertices or brings it fairlyclose to them. The 'T'target node is present at the exterior of the triangle, and if this is the case, theninside the triangle if the opposite is true [14].

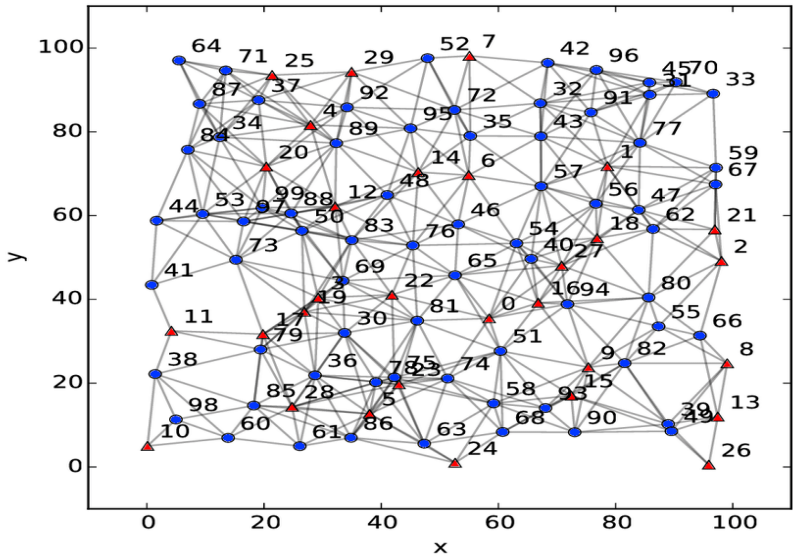

Figure 2. WSN configuration using DV-HOP algorithm.

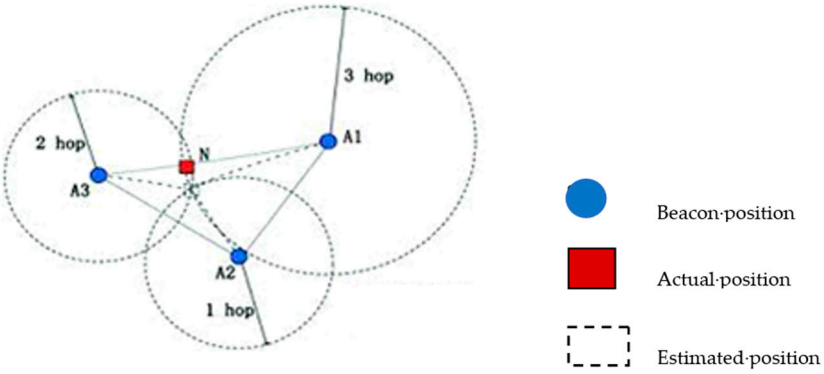

Figure 3. DV-HOP methodology.

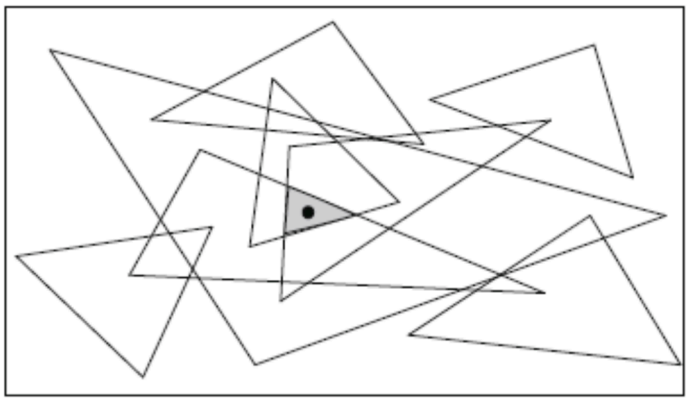

Figure 4. Overview of APIT algorithm.

3. Principle of APIT Algorithm

Due to the fixed nature of sensor nodes in WSN, which prevents random mobility, PIT studies have been demonstrated to be inapplicable in a variety of practical applications. As a result, the problems in PIT are generally overcome by the APIT algorithm, in which there is no change in the network sensor point. It can be observed that anchor nodes are received from the RSST, and every final node action is described with a link tothe sensor nodes and is compared with the standard initial algorithm of the APIT. All the nodes are present together in the interior of the design, which is compared with the target node to obtain the range of communication. Figure 2 demonstrates the position of the target node andwhether the node is present on the interior or exterior of the triangle zone. No neighbor of the target node is located nearer or further away from any of the triangle's three anchor nodes. The target nodes are always present in the interior of the triangle, and the rest of the nodes, like the anchor, are locatedcloseto the nodes. Target nodes and anchor nodes are also included in the neighbor nodes. The target node moves to the location of a nearby node, let us say node 4, and we can assume that since it is equallyclose to the anchor nodes, it is outside the triangulation area [15–17].

4. Simulation Results

The network region is bounded by a 1000 m radius. The position of nearby nodes can be determined viaa normal DVHOP algorithm; however, it does so with increased latency and inaccuracy. The proposed Bat with SA methods DVHOP and APIT canbe used to acquire the performance metrics parameters and outcomes. In terms of latency, the anchor shift illustrates randomization [18]. The performance of the DV-HOP and APIT algorithms with and without the Bat-SA localization approach is compared based on the results of the simulation. When assessing performance, the following variables are considered:

Changing Communication Radius

- Step size 100 and changing the area from 600 to 1200;
- Node shifting.

Changing radius from 120 to 240 with step size 20. Figures 5 and 6 show the comparison of the simulation results of APIT and DV-hop without Bat-SA methodology.

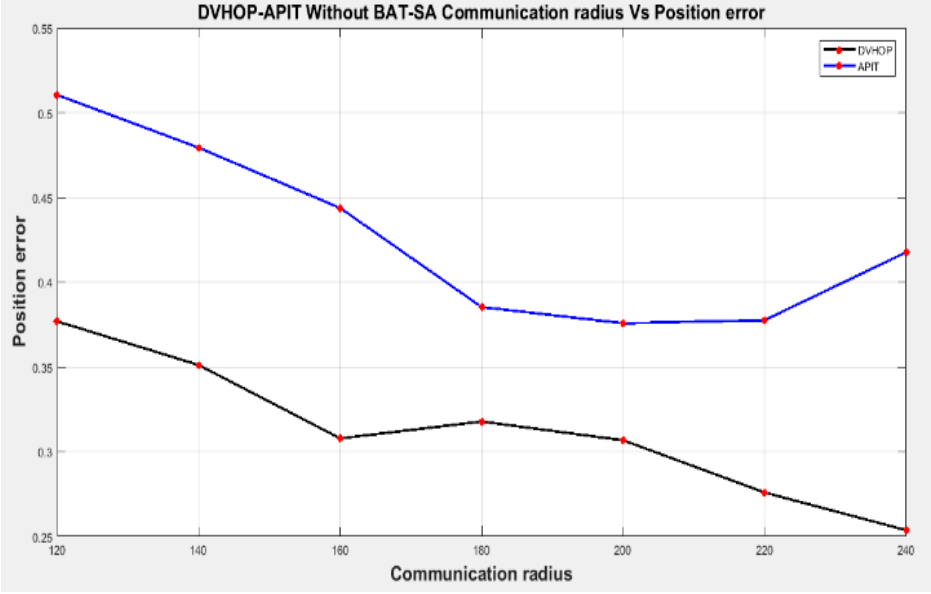

Figure 5. Position error vs.communication radius between DV-Hop and APIT.

Simulation results comparison between DV-Hop and APIT using the Bat-SA method areshown Figures 7 and 8.

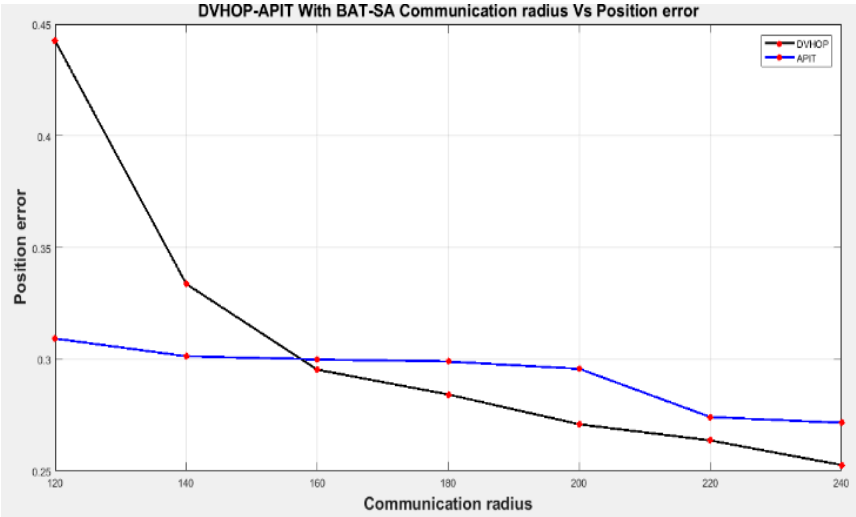

Figure 6. Position error vs.communication radius between DV-Hop and Bat-SA.

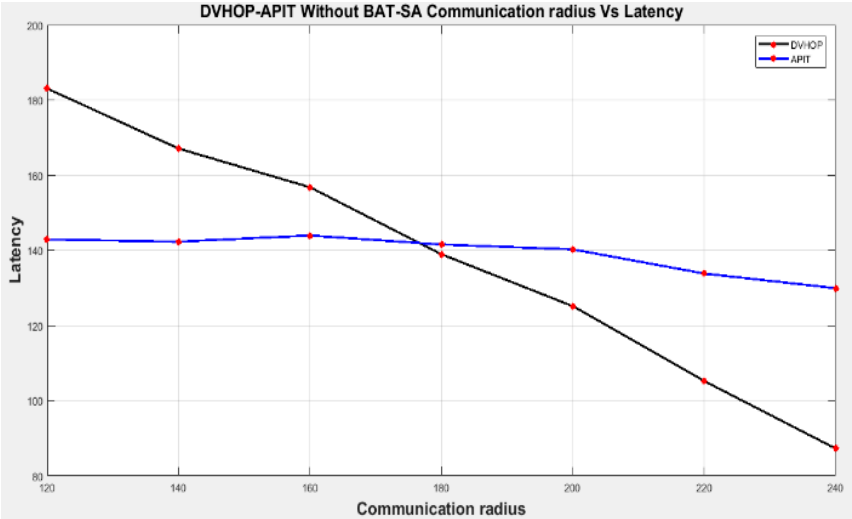

Figure 7. Latency vs.communication radius between DV-Hop and APIT.

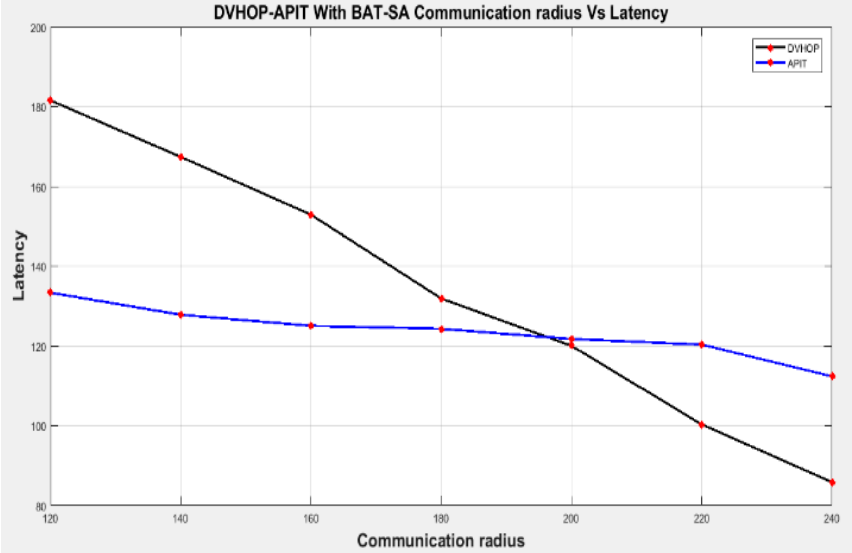

Figure 8. Latency vs. communication radius between DV-Hop and APIT with Bat-SA.

Figures 9 and 10 compare APIT with DV-Hop without the Bat-SA method for the parameter areasregardingposition errors and latency [19]. The comparisons of APIT with DV-Hop without the Bat-SA method between the parameter areas with position errors and latency areshown in Figures 11 and 12.

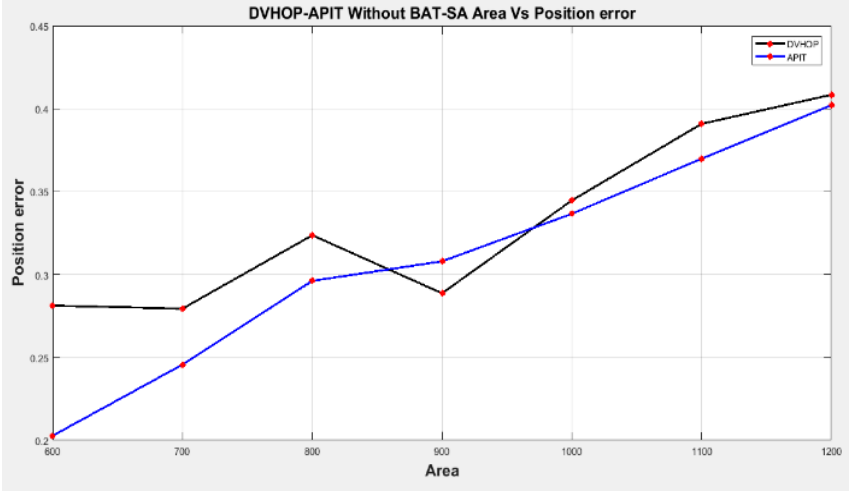

Figure 9. Position error vs. area between DV-Hop and APIT without Bat-SA.

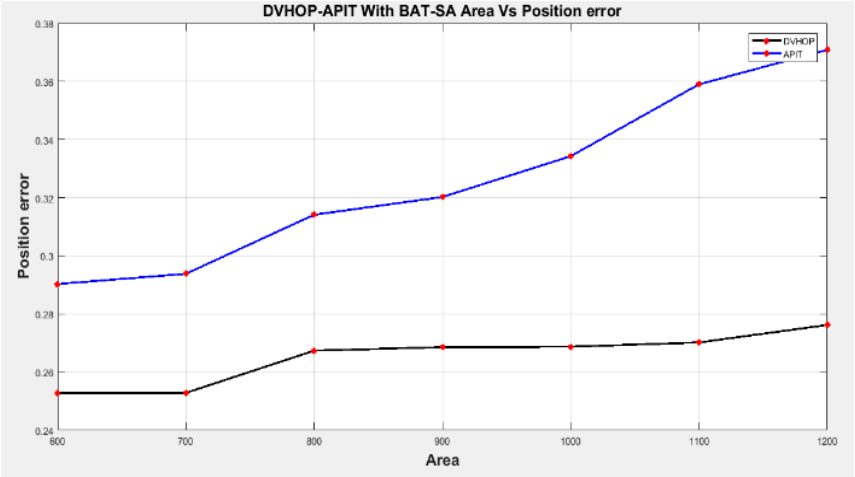

Figure 10. Position error vs. area between DV-Hop and APIT with Bat-SA.

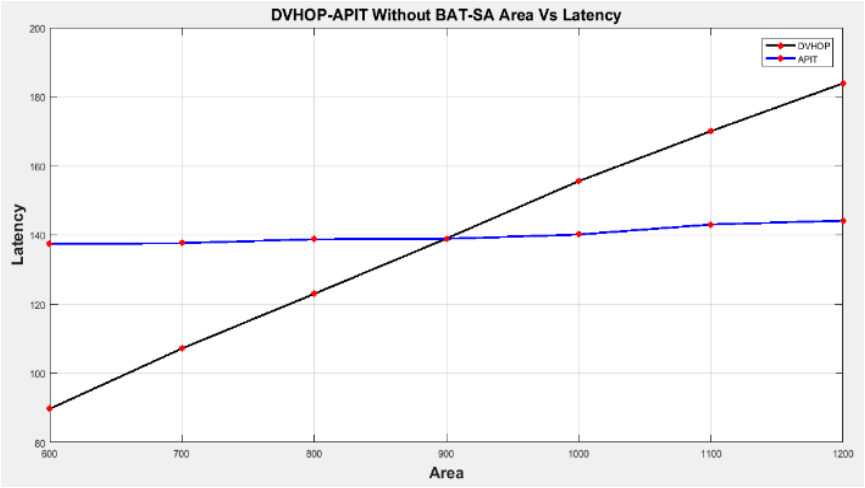

Figure 11. Area vs. latency between DV-Hop and APIT without Bat-SA.

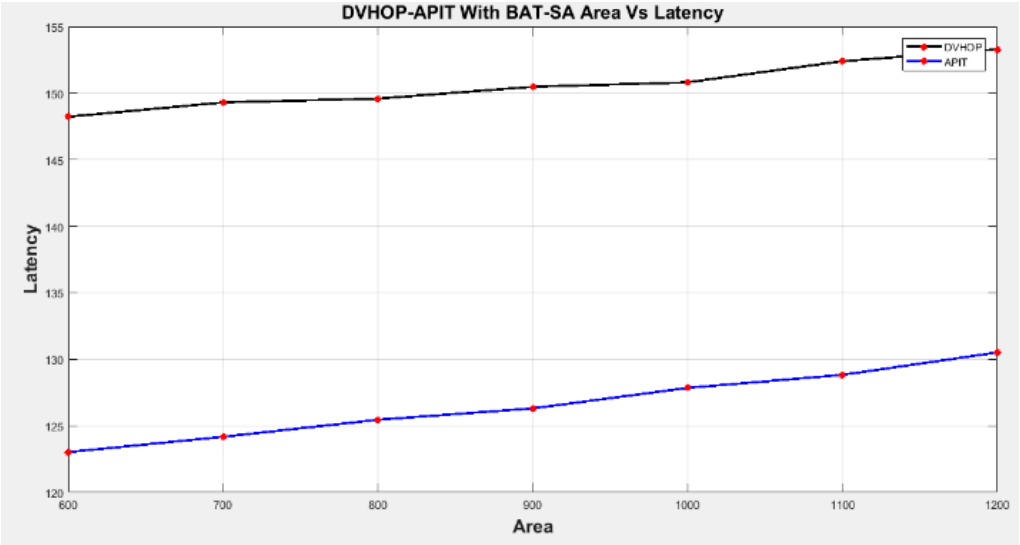

Figure 12. Area vs. latency between DV-Hop and APIT with Bat-SA.

Table 1 illustratesthe error tolerance of the proposed and existing methods. The error tolerance is low in the proposed method.

Table 1. Error tolerance of proposed and existing methods.

Algorithm	Max. Error	Min. Error	Average Error
Standard DV-Hop	0.374R	0.0382R	0.3011R
DV-HOP Anchor	0.877R	0.0222R	0.2414R
DV HOP (PSO)	0.789R	0.0200R	0.2311R
Proposed DV HOP	0.647R	0.0055R	0.1101R

Nodes are horizontally moved by one position: The comparison of the APIT and DV-Hop algorithms without the Bat-SA method is shown in Figure 13. Nodes move horizontally by one position. The nodes move to one position ten times [20]. The comparison of the APIT and DV-Hop algorithms with the Bat-SA method is shown in Figures 14 and 15. It is evident from the aforementioned simulation findings that the DV-Hop and APIT algorithms surpass the Bat-SA method in terms of efficiency.

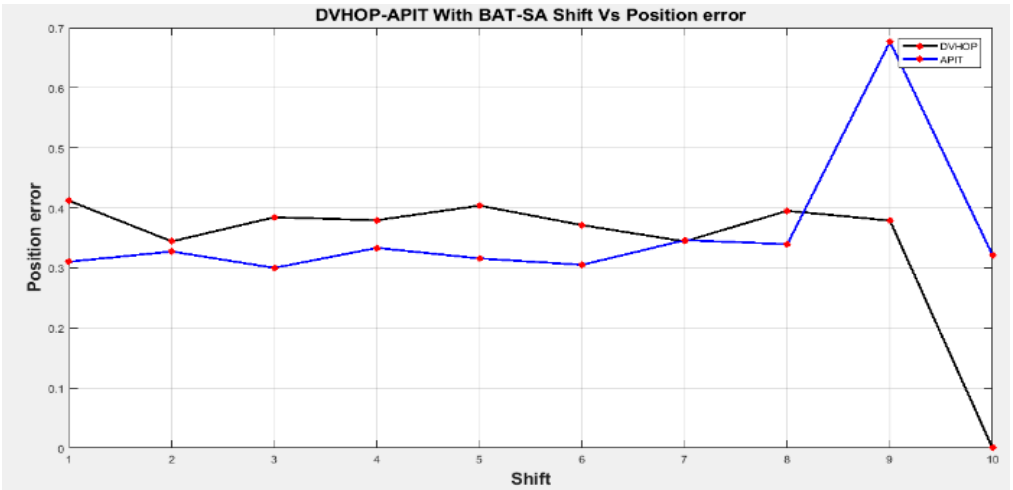

Figure 13. Position error vs.shift between DV-Hop and APIT with Bat-SA shifting the nodes.

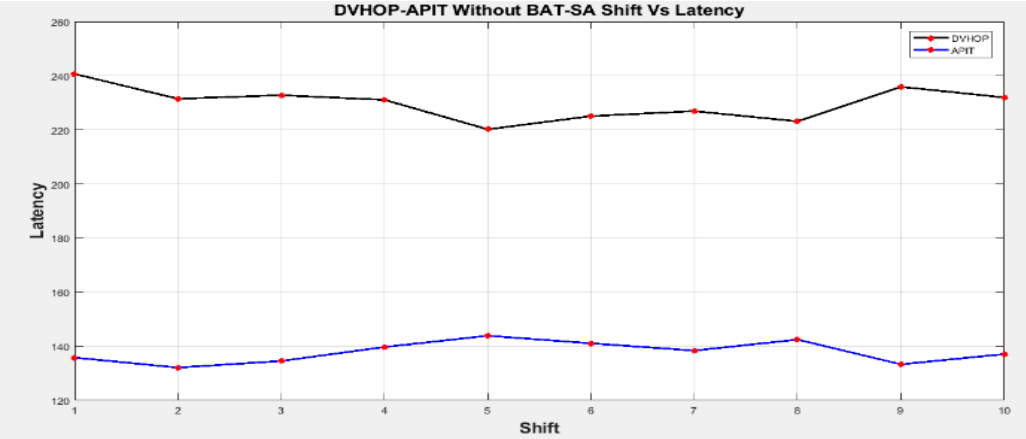

Figure 14. Shift vs. latency between existing and proposed method.

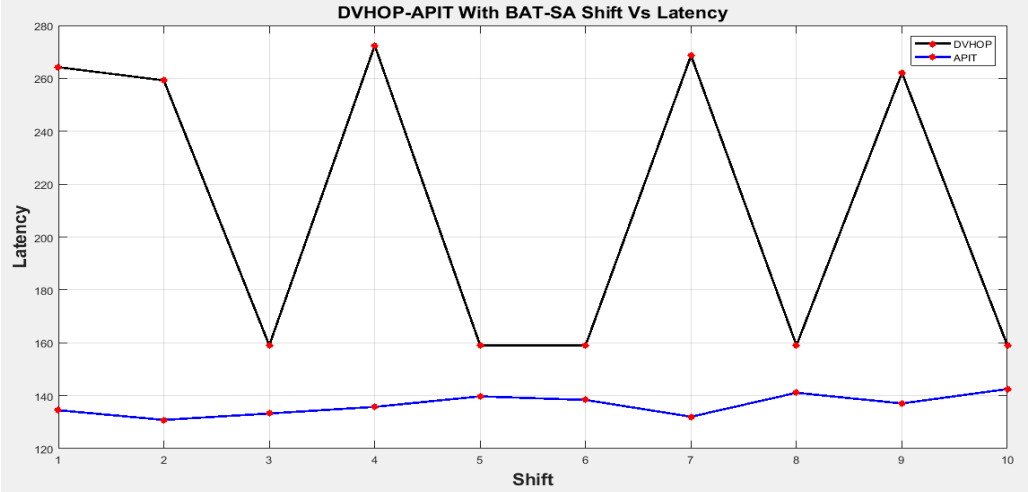

Figure 15. Shift vs. latency betweenproposed and existing DV-HOPs.

5. Conclusions

Compared to APIT, the conventional Bat method is more accurate. The suggested Bat with SA approach achieves better results than the traditional APIT and DV-HOP methods in terms of convergence, calculation rate, and success rate. The simulations' findings show that when network area scalability rises, computation time falls. Additionally, compared to the conventional localization process, position accuracy and latency are enhanced. The association between the nodes is more firmly located than in the APIT algorithm. The simulation also shows the consistency of the proposed approach. Thus, the results of the entire system are enhanced, and the WSN is considerably optimizedwiththe help of DV-HOP and APIT with Bat-SA method. The APIT with Bat-SA localization approach outperforms the DV-HOP algorithms in a comparison of their efficacy. Future work on this subject may concentrate on multi-objective programming and the creation of novel optimization methods for localization challenges.

Author Contributions: Conceptualization, T.S.L., K.B.R. and S.S.; methodology, T.S.L., K.B.R. and S.S.; software, T.S.L., K.B.R. and S.S.; validation, T.S.L., K.B.R. and S.S.; formal analysis, T.S.L., K.B.R. and S.S.; investigation, T.S.L., K.B.R. and S.S.; resources, T.S.L., K.B.R. and S.S.; data curation, T.S.L., K.B.R. and S.S.; writing—original draft preparation, T.S.L., K.B.R. and S.S.; writing—review and editing, T.S.L., K.B.R. and S.S.; visualization, T.S.L., K.B.R. and S.S.; supervision, T.S.L., K.B.R. and S.S.; project administration, T.S.L., K.B.R. and S.S. All authors have read and agreed to the published version of the manuscript.

Funding: This research received no external funding.

Institutional Review Board Statement: Not applicable.

Informed Consent Statement: Not applicable.

Data Availability Statement: Data is present within the article.

Conflicts of Interest: The authors declare no conflicts of interest.

References

1. Niculescu, D.; Nath, B. Ad hoc positioning system (APS) using AOA. In Proceedings of the IEEE INFOCOM 2003, Twenty-Second Annual Joint Conference of the IEEE Computer and Communications Societies (IEEE Cat. No. 03CH37428), San Francisco, CA, USA, 30 March–3 April 2023.
2. Shu, Y.; Cheng, P.; Gu, Y.; Chen, J.; He, T. TOC: Localizing wireless rechargeable sensors with time of charge. *ACM Trans. Sens. Netw. (TOSN)* **2015**, *11*, 1–22. [CrossRef]
3. Hofmann-Wellenhof, B.; Lichtenegger, H.; Collins, J. *Global Positioning System: Theory and Practice*; Springer Science & Business Media: Berlin, Germany, 2012.
4. Harter, A.; Hopper, A. A distributed location system for the active office. *IEEE Netw.* **1994**, *8*, 62–70. [CrossRef]
5. Pal, A. Localization algorithms in wireless sensor networks: Current approaches and future challenges. *Netw. Protoc. Algorithms* **2010**, *2*, 45–73. [CrossRef]
6. Sarada, C.; Lakshmi, K.V.; Padmavathamma, M. Spatial Intuitionistic Fuzzy C-means with Calcifications enhancement based on Nonsubsampled Shearlet Transform to detect Masses and Microcalcifications from MLO Mammograms. In Proceedings of the 2023 Advanced Computing and Communication Technologies for High Performance Applications (ACCTHPA), Ernakulam, India, 20–21 January 2023; pp. 1–10.
7. Wang, J.; Gao, Q.; Cheng, P.; Yu, Y.; Xin, K.; Wang, H. Lightweight robust device-free localization in wireless networks. *IEEE Trans. Ind. Electron.* **2014**, *61*, 5681–5689. [CrossRef]
8. Sarada, C.C.; Lakshmi, K.V.; Padmavathamma, M. MLO Mammogram Pectoral Masking with Ensemble of MSER and Slope Edge Detection and Extensive Pre-Processing. *IJRITCC* **2023**, *11*, 135–144. [CrossRef]
9. Avanija, J.; Kumar, K.E.; Kumari, C.U.; Jyothi, G.N.; Raju, K.S.; Madhavi, K.R. Enhancing Network Forensic and Deep Learning Mechanism for Internet of Things Networks. *J. Sci. Ind. Res.* **2023**, *82*, 522–528.
10. Tian, S.; Zhang, X.; Liu, P.; Sun, P.; Wang, X. A RSSI based dv-hop algorithm for wireless sensor networks. In Proceedings of the International Conference on Wireless Communications, Networking and Mobile Computing (WiCom'2007), Shanghai, China, 21–25 September 2007; pp. 2555–2558.
11. Latha, T.; Swarna, K.; Rekha, B.; Ferede, A.W. Lightweight APIT with Bat Optimization with Simulated Annealing Localization for Resource-Constrained Sensor Networks. *Wirel. Commun. Mob. Comput.* **2023**, *2*, 7982038. [CrossRef]
12. Han, G.; Xu, H.; Duong, T.Q.; Jiang, J.; Hara, T. Localization algorithms of wireless sensor networks: A survey. *Telecommun. Syst.* **2013**, *52*, 2419–2436. [CrossRef]
13. Miriam, H.; Doreen, D.; Dahiya, D.; Rene Robin, C.R. Secured Cyber Security Algorithm for Healthcare System Using Blockchain Technology. *Intell. Autom. Soft Comput.* **2023**, *35*, 1889–1906. [CrossRef]
14. Aziz, O.; Farooq, M.S.; Khelifi, A. Domain and challenges of big data and archaeological photogrammetry with blockchain. *IEEE Access* **2022**, *10*, 101495–101514. [CrossRef]
15. Ali, A.; Pasha, M.F.; Fang, O.H.; Khan, R.; Almaiah, M.A.; Al Hwaitat, A.K. Big data based smart blockchain for information retrieval in privacy-preserving healthcare system. In *Big Data Intelligence for Smart Applications*, 1st ed.; Baddi, Y., Gahi, Y., Maleh, Y., Alazab, M., Tawalbeh, L., Eds.; Springer International Publishing: Berlin, Germany, 2022; Volume 994, pp. 279–296.
16. Muheidat, F.; Patel, D.; Tammisetty, S.; Lo'ai, A.T.; Tawalbeh, M. Emerging concepts using blockchain and big data. *Procedia Comput. Sci.* **2022**, *198*, 15–22. [CrossRef]
17. Singh, S.; Rathore, S.; Alfarraj, O.; Tolba, A.; Yoon, B. A framework for privacy-preservation of IoT healthcare data using Federated Learning and blockchain technology. *Future Gener. Comput. Syst.* **2022**, *129*, 380–388. [CrossRef]
18. Aliahmadi, A.; Nozari, H.; Ghahremani-Nahr, J. A framework for IoT and Blockchain Based on Marketing Systems with an Emphasis on Big Data Analysis. *Int. J. Innov. Mark. Elem.* **2022**, *2*, 25–34. [CrossRef]
19. Alshehri, M. Blockchain-assisted cyber security in medical things using artificial intelligence. *Electron. Res. Arch.* **2023**, *31*, 708–728. [CrossRef]
20. Deepa, N.; Pham, Q.V.; Nguyen, D.C.; Bhattacharya, S.; Prabadevi, B.; Gadekallu, T.R.; Pathirana, P.N. A survey on blockchain for big data: Approaches, opportunities, and future directions. *Future Gener. Comput. Syst.* **2022**, *131*, 209–226. [CrossRef]

Disclaimer/Publisher's Note: The statements, opinions and data contained in all publications are solely those of the individual author(s) and contributor(s) and not of MDPI and/or the editor(s). MDPI and/or the editor(s) disclaim responsibility for any injury to people or property resulting from any ideas, methods, instructions or products referred to in the content.

IOPscience

IOPscience Journals Books Publishing Support Login

PAPER

Functional analysis in the body environment for a circularly polarized hybrid reconfigurable textile antenna

D Ram Sandeep, B T P Madhav[8], S Salma, K Srinivasa Rao, L Govinda, Yepuri Aarthi Hasitha and M C Rao

Published 20 September 2023 • © 2023 IOP Publishing Ltd

Physica Scripta, Volume 98, Number 10

Citation D Ram Sandeep *et al* 2023 *Phys. Scr.* **98** 105522

DOI 10.1088/1402-4896/acf807

1. Received 18 May 2023
2. Revised 12 August 2023
3. Accepted 8 September 2023
4. Published 20 September 2023

Check for updates

Buy this article in print

Journal RSS

Sign up for new issue notifications

Abstract

This paper presents the functional analysis of a hybrid reconfigurable circularly polarized (CP) textile antenna in different on-body environments. The Tai-Chi sign inspires the current textile antenna design, where the primary radiator and ground elements are sickle-shaped structures. Hybrid reconfigurability was achieved by successfully operating two RF PIN-Diodes in the basal ground plane's elliptical and rectangular structures. Thus, four switching states are attained by operating the textenna at 3.5, 4.5 and 5.4 GHz in the S1. 4.39 and 5.8 GHz in S2, 5 and 5.9 GHz in S3 and 2.4, 4.3, 5.8, and 9.4 GHz in S4 state. The reconfigurable textenna was devised to function on the human body. Its functional behavior in proximity to the human body was

rigorously validated through testing involving bending at various vertical and horizontal angles. Additionally, a Specific Absorption Rate (SAR) analysis was conducted using a three-layered human phantom. The results revealed that the maximum SAR value is below 1.6 W Kg^{-1} for 1 gram of tissue and 2 W kg^{-1} for 10 grams of tissue. These findings establish the safe operational parameters for the proposed model. The developed antenna functionalities were also tested in other circumstances like body sweating environment and interaction with body fluids (Blood, Plasma, SBF and DMEM). In these body fluid conditions, a peak gain of 4.88 dBi at S1, 6.97 dBi at S2, 7.99 dBi at S3, and 4.13 dBi at S4, was observed while interacting with Plasma, and the measured efficiency in the above configuration is between 77%–79%. The textenna durability analysis was measured using an electrochemical workstation while interacting with different body fluids. All these results confessed the applicability of the developed antennas for on-body wireless communication applications in different on-body conditions.

Export citation and abstract BibTeX RIS

← **Previous** article in issue

Next article in issue →

Access this article

The computer you are using is not registered by an institution with a subscription to this article. Please choose one of the options below.

Login

Access through your institution

IOPscience login

Find out more about journal subscriptions at your site.

Purchase from

Article Galaxy
CCC RightFind

Purchase this article from our trusted document delivery partners.

Rent from

Read this now at deepdyve

This article is available from DeepDyve.

Make a recommendation

To gain access to this content, please complete the Recommendation Form and we will follow up with your librarian or Institution on your behalf.

For corporate researchers we can also follow up directly with your R&D manager, or the information management contact at your company. Institutional subscribers have access to the current volume, plus a 10-year back file (where available).

You may also like

JOURNAL ARTICLES

Review of graphene for the generation, manipulation, and detection of electromagnetic fields from microwave to terahertz

Design and characterization of a circular ring monopole antenna and its MIMO configuration for sub-6 GHz, sub-7 GHz and mm-wave 5G applications

A compact circularly polarized dual port MIMO antenna with DGS and parasitic patch for modern wireless communication and IOT applications

Low-profile robust circularly polarized textile patch antenna for WBAN and ISM applications

Enhancing connectivity/mobility in WBAN applications through detachable wearable multi-band MIMO antenna

A 1-bit electronically reconfigurable beam steerable metasurface reflectarray with multiple polarization manipulations

IOPSCIENCE

Journals

Books

IOP Conference Series

About IOPscience

Contact Us

Developing countries access

IOP Publishing open access policy

Accessibility

IOP PUBLISHING

Copyright 2024 IOP Publishing

Terms and Conditions

Disclaimer

Privacy and Cookie Policy

Text and Data mining policy

PUBLISHING SUPPORT

Authors

Reviewers

Conference Organisers

This site uses cookies. By continuing to use this site you agree to our use of cookies.

FOREX Publication
Open Access | Rapid and quality publishing

International Journal of
Electrical and Electronics Research (IJEER)
Research Article | Volume 11, Issue 2 | Pages 518-522 | e-ISSN: 2347-470X

Design of Three-valued Logic Based Adder and Multiplier Circuits using Pseudo N-type CNTFETs

K. Maheswari[1], M. L. Ravi Chandra[2], D. Srinivasulu Reddy[3] and V. Vijaya Kishore[4*]
[1]*G. Pullaiah College of Engineering and Technology, Kurnool, India*
[2]*Srinivasa Ramanujan Institute of Technology, Ananthapuramu, India*
[3]*S V College of Engineering, Tirupati, India*
[4]*Mohan Babu University (erstwhile Sree Vidyanikethan Engineering College), Tirupati, India*

***Correspondence:** V. Vijaya Kishore; kishiee@rediffmail.com

ABSTRACT- This work presents a novel technique to develop the three-valued logic (TVL) circuit schematics for very large-scale integration (VLSI) applications. The TVL is better alternative technology over the two-valued logic because it provides decreased interconnect connections, fast computation speed and decreases the chip complexity. The TVL based complicated designs such as half-adder and multiplier circuits are designed utilizing the Pseudo N-type carbon nanotube field effect transistors (CNTFETs). The proposed TVL half adder multiplier schematics are developed in HSPICE tool. Additionally, the delay and circuit area for the half- adder and multiplier circuits are investigated and compared to the complementary circuits. The memory usage and CPU time for the proposed circuits are also analyzed. It is observed that the proposed circuit designs show the improved performance up to 43.03% on an average over the complementary designs.

Keywords: VLSI, Ternary logic, CNTFET, Pseudo N-type CNTFET, and HSPICE.

ARTICLE INFORMATION

Author(s): K. Maheswari, M. L. Ravi Chandra, D. Srinivasulu Reddy and V. Vijaya Kishore;

Received: 22/02/2023; **Accepted**: 17/05/2023; **Published**: 30/06/2023;
e-ISSN: 2347-470X;
Paper Id: IJEER 2202-10;
Citation: 10.37391/IJEER.110238
Webpage-link:
https://ijeer.forexjournal.co.in/archive/volume-11/ijeer-110238.html

Publisher's Note: FOREX Publication stays neutral with regard to Jurisdictional claims in Published maps and institutional affiliations.

1. INTRODUCTION

Conventionally, the VLSI digital systems are performed with the conventional logic in Boolean space [1]. Recently, the TVL is used to design the digital circuits because it offers reduced chip-area, low interconnect complexity, reduced digits needed to represent a number, low power dissipation, *etc.* over the conventional logic. The TVL designs using the traditional complementary metal oxide semiconductor (CMOS) technology requires multi-threshold transistors [2]. However, the multi-threshold voltage CMOS transistors are acquired by biasing the bulk terminal. Using the bulk biasing technique to design the TVL circuits is time consuming and complex task. Hence, the researchers looked for alternative technologies such as quantum-dot FETs, reversible logics, single-electron transistors and CNTFETs [3-8]. Out of them, using CNTFET technology is optimistic way to develop the TVL digital logic circuits because the multi-threshold CNTFETs can be obtained by changing the diameter of CNT [2]. Moreover, the CNTFET technology offers 10 times more energy efficiency compared to CMOS technology while designing the circuits.

Using CNTFETs, various TVL digital logic circuits such as basic gates, universal gates, adders, multipliers are presented in existing literatures [7-18]. All these existing designs are developed using complementary CNTFETs. The complementary designs utilize additional transistors that increase the chip complexity [7]. Hence, in this work, the Pseudo N-type CNTFETs are utilized to design TVL circuit schematics. Using Pseudo N-CNTFETs, various TVL circuits are developed in [19]. In [19], only the basic gates and MIN circuit designs are presented. From the analysis, it is noticed that the Pseudo N-type CNTFET TVL circuits shows up to 40% improvement in area with a similar delay on average over the complementary designs. It is worth noting that there are no complicated designs presented. Thus, in this work, the complicated designs such as TVL half-adder and multiplier are presented utilizing Pseudo NCNTFETs. The HSPICE tool is used for verifying functionality and analyzing the performance. Additionally, our proposed TVL adder and multiplier circuit performance are examined with complementary designs.

The major efforts of this work are four namely:

- A technique is presented to design TVL circuit schematic using Pseudo NCNTFETs.
- The numerical equations are stated to calculate CNTFET chirality vectors, diameter, band gap, and threshold value.
- The complex circuits such TVL adder and multiplier circuits are designed.
- Finally, the half-adder and multiplier designs are compared with complementary CNTFET designs.

Rest of the study is arranged as follow: the background of TVL logic and CNTFETs are presented in *Section 2. Section 3* presents the TVL half-adder and multiplier architectures, design, and functionality. *Section 4* describes the performances

FOREX Publication
Open Access | Rapid and quality publishing
International Journal of Electrical and Electronics Research (IJEER)
Research Article | Volume 11, Issue 2 | Pages 518-522 | e-ISSN: 2347-470X

of proposed circuits and its comparison with complementary circuits and the *Section 5* discuss the conclusions of the study.

2. SYSTEM MODEL

2.1 CNTFET based TVL Logic

TVL logic consists of three logic states represented by *logic 0*, *logic 1* and *logic 2* that corresponds to voltage values 0, $0.5V_{DD}$ and V_{DD}, respectively. A TVL function is F(y) mapped from {logic 0, logic 1, logic 2}^{n} to {1ogic 0, logic 1, logic 2}, where y is given as $\{y_1, y_2, y_3, \ldots\ldots\ldots\ldots, y_n\}$. The two-input basic and universal gate functions in TVL y_i and y_j are expressed in *equation (1)*. The detailed discussion on ternary inverter circuits, basic gates and universal gates are discussed in the specialized writings of [7-9].

$$\begin{aligned}
&\overline{y_i} = -y_i + 2 \rightarrow \text{Inverter}\\
&y_i . y_j = min\{y_i, y_j\} \rightarrow \text{AND}\\
&y_i + y_j = max\{y_i, y_j\} \rightarrow \text{OR}\\
&\overline{y_i . y_j} = \overline{min\{y_i, y_j\}} \rightarrow \text{NAND}\\
&\overline{y_i + y_j} = \overline{max\{y_i, y_j\}} \rightarrow \text{NOR}
\end{aligned} \quad (1)$$

Table 1: Calculated CNT diameters and threshold voltages for various chirality vectors

Chirality Vector (p, q)	CNT Diameter (nm)	Threshold Voltage (V)	
		N-CNTFET	P-CNTFET
(8, 0)	0.63	0.69	-0.69
(10, 0)	0.78	0.55	-0.55
(16, 0)	1.25	0.34	-0.34
(19, 0)	1.48	0.29	-0.29

In recent days, the CNTFET technology is widely used to design the TVL circuit because the threshold value of transistor is altered by varying CNT diameter. This excellent property makes the CNTFET compatible for implementing TVL circuits. The CNTFET is different from the CMOSFET in a way the drain region and source region in the FETs are connected. In CMOSFETs, the silicon substrate is connecting the channel, whereas in CNTFETs, the CNT creates the channel. A CNT is rolled graphene layer with a vector $Ch = pi+qj$ where, i and j are the unit lattices. Where p and q define the chirality values of CNT. The CNT acts as a metal when $p = q$ or $p - q = 3i_g$, where i_g is integer, else the CNT is semiconductor. The chiral vectors which are utilized for developing the TVL circuits are placed in *table 1*. This table also provides the relation among the vectors, CNT diameter, threshold values for *p*- and *n*- CNTFETs. The structure of CNTFET and its I-V characteristics for different chiralities are shown in *figure 1* and *figure 2*, respectively.

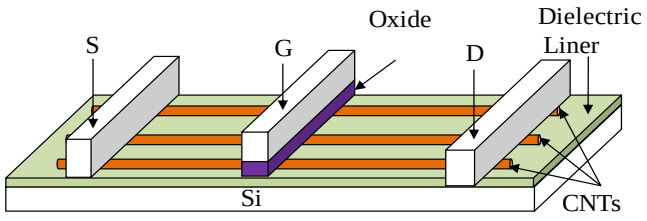

Figure 1. Physical structure of CNTFET

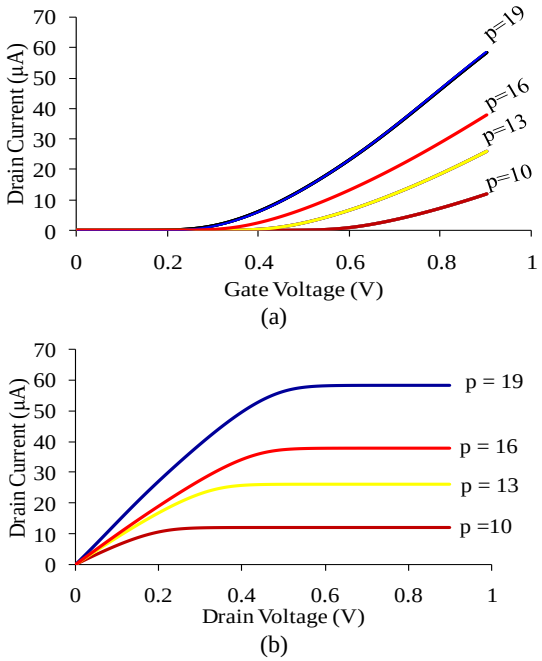

Figure 2. I-V curves (a) IDS vs VGS and (b) IDS vs VDS

2.2 Survey on Existing CNTFET TVL Circuits

Using CNTFETs, the various TVL circuits are developed and presented in [7-19]. In [7], the TVL gates, half adder and multiplier designs are presented. From the performance investigations, it is noticed that the presented designs provide reduced power and delay compared to resistive-load CNTFET designs. The TVL memory cell using CNTFETs are discussed in [8]. The presented TVL memory shows a significant improvement in area up to 41.6% over the CMOS memory cell. In [9], a technique provided to develop the TVL half adder and multiplier circuits. From the results, it is investigated that the half adder improvement of 19.2% and 74.07%, and multiplier shows 24.67% and 81.12% in terms of transistor count and PDP over the existing circuits. The TVL full adder circuit is presented in [10]. The TVL full adder improved the PDP compared to the previous circuits. In [11], the CNTFET based TVL flip-flop is designed using Schmitt trigger. It is noticed that the flip-flop functions correctly and provides high performance over those existing flip-flops. The TVL inverter using CNTFET is designed in [12] and compared its PDP with the resistive load CNTFET inverter. The presented inverter improved the PDP up to 300% over the resistive load CNTFET inverter. The pair of TVL half adder circuits is presented in [13]. One half adder circuit is designed with the conventional technique (*i.e.*, Design 1) and other is developed using the ternary to binary decoder *(i.e.*, Design 2), respectively. It is noticed that the design 2 shows the PDP, power, and delay up to 66%, 63% and 09%, respectively over conventional design techniques. In [14], the 3trit and 9trit adders are designed and compared their performance with the direct realization techniques. Form the results, it is investigated that the 3trit adder shows 79% improvement and 9trit adder shows 88% improvement in PDP compared to the direct realization techniques. In [15], the various TVL logic circuits such as inverter, NAND gate, decoder, adder and multiplier circuits

FOREX Publication
Open Access | Rapid and quality publishing
International Journal of Electrical and Electronics Research (IJEER)
Research Article | Volume 11, Issue 2 | Pages 518-522 | e-ISSN: 2347-470X

developed and compared with existing 15 design techniques. Furthermore, 180 simulations are performed to improve the performance. It is noticed that the proposed designs reduced the PDP and transistor count compared to existing designs. The TVL prefix adders using CNTFET are designed in [16]. Five CNFET TVL adders that utilize different prefix circuits in carry are developed. The result shows that the prefix-adders improved up to 58% of power, 50% of delay and 80% of PDP compared to existing TVL adder circuits. In [17], the complex designs such as half-adder, full-adder, half-subtractor and full-subtractor are developed using CNTFETs. The proposed designs show high-performance over the existing designs. The TVL full adder design is implemented and presented in [18]. The proposed full-adder has improved the power and PDP up to 86.92% and 97% in comparison with two recent existing designs. It is noticed that all these designed using the complementary CNTFETs and only few works are presented on Pseudo N-CNTFETs. In [19], the TVL circuits are presented using Pseudo N-CNTFETs are presented. In this paper, only the basic gates are presented and no complex circuits are designed. Hence, in this paper, we developed the complex designs such as half-adder and multiplier using Pseudo N-CNTFETs.

3. PSEUDO N-CNTFET BASED TVL ADDER AND MULTIPLIER CIRCUITS

The TVL gates presented in literature paper [19] is used to develop the various complex circuits such as adders, multipliers, subtractors and so on. In this work, we developed the TVL half-adder and multiplier as complex circuits. To design theses complex circuits, a TVL decoder shown in *figure 3* is utilized. The output of TVL decoder is stated by

$$y_r = \begin{cases} 0, \text{if } y = r \\ 2, \text{if } y \neq r \end{cases} \quad (2)$$

Where r is TVL states. This decoder is designed using the one positive TVL NOT gate, two negative TVL gates NOT and a universal NOR gate.

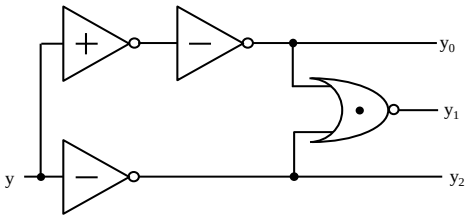

Figure 3. Circuit schematic of TVL decoder

Table 2: Truth table of half-adder and multiplier

Input x	Input y	Half-Adder		Multiplier	
		Sum	Carry	Product	Carry
0	0	0	0	0	0
0	1	1	0	0	0
0	2	2	0	0	0
1	0	1	0	0	0
1	1	2	0	1	0
1	2	0	1	2	0
2	0	2	0	0	0
2	1	0	1	2	0
2	2	1	1	1	1

The major advantage of TVL is to speed up the computations. Since the TVL consists of three logic states, the number of digits needed for TVL family is $\log_3 2$ which less than the binary logic. Thus, N bit is considered for binary logic, whereas the $\log_3 2$ is considered for TVL logic.

3.1. Pseudo N-CNTFET based TVL Half Adder Design

A TVL half adder is developed to validate the correctness of the Pseudo N-CNTFET design. *Table 2* shows the TVL half adder truth table. The transient response equation for TVL adder is expressed as

$$\text{Sum} = 2 \cdot (x_2 y_0 + x_0 y_2 + x_1 y_1) + 1 \cdot (x_2 y_2 + x_1 y_0 + x_0 y_1) \quad (3)$$

$$\text{Carry} = 1 \cdot (x_1 y_2 + x_2 y_2 + x_1 y_2) \quad (4)$$

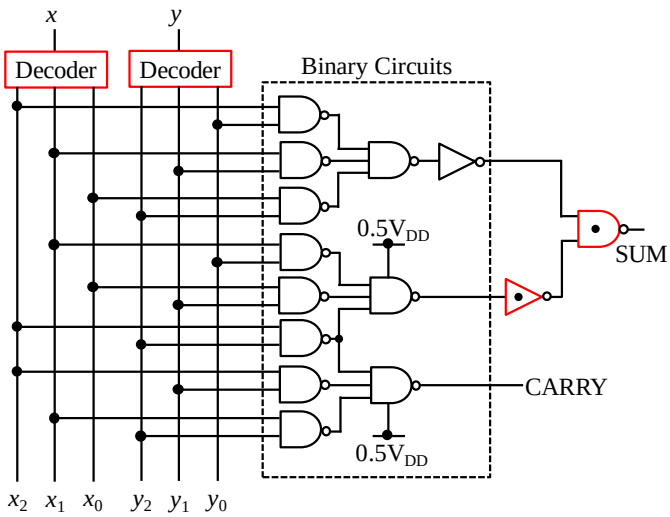

Figure 4. Proposed TVL half adder

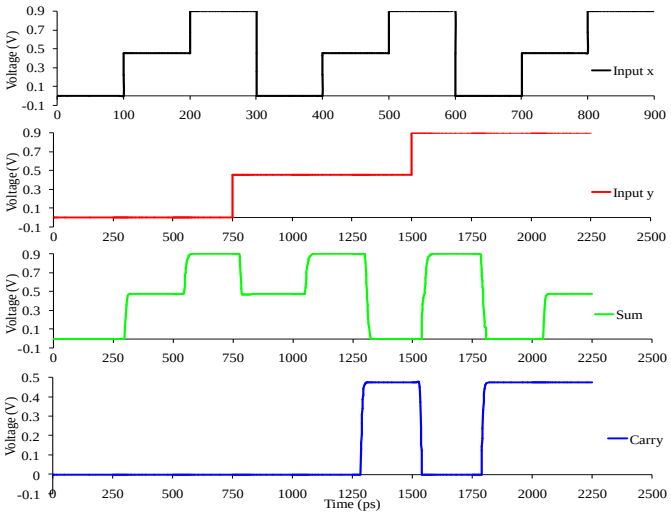

Figure 5. Transient response of TVL half adder

The circuit schematic of TVL half adder using Pseudo N-CNTFETs is shown in *figure 4*. In *figure 4*, the decoder provides the unary outputs for the inputs and the logic gates computes

FOREX Publication
Open Access | Rapid and quality publishing
International Journal of Electrical and Electronics Research (IJEER)
Research Article | Volume 11, Issue 2 | Pages 518-522 | e-ISSN: 2347-470X

the functions of *equations (3) and (4)*, respectively. The industry standard HSPICE simulator is used to develop the proposed Pseudo N-CNTFET based circuits using CNTFET SPICE model presented in [20-21]. This model conceives a real and circuit-compatible CNTFET for SPICE simulations and considers realistic device non-idealities. *Figure 5* shows the response of TVL half-adder. It is noticed that the TVL adder operates correctly according to *table 2*. Furthermore, the performance of TVL adder is also noticed in terms of propagation delay and circuit area. The obtained delay and circuit area for the proposed Pseudo N-CNTFET based half adder are 102.2ps and 4.1fm^2, respectively.

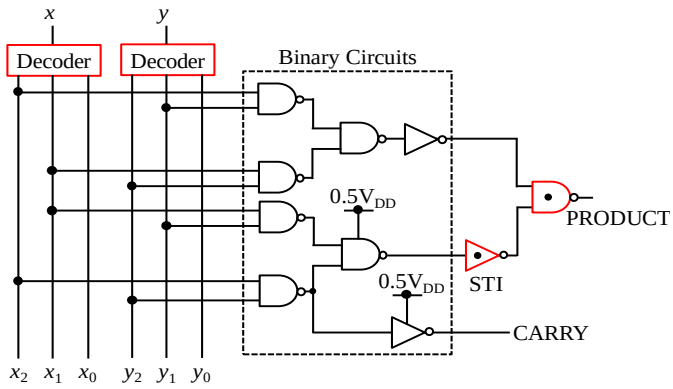

Figure 6. Propose TVL Pseudo NCNTFET based Multiplier

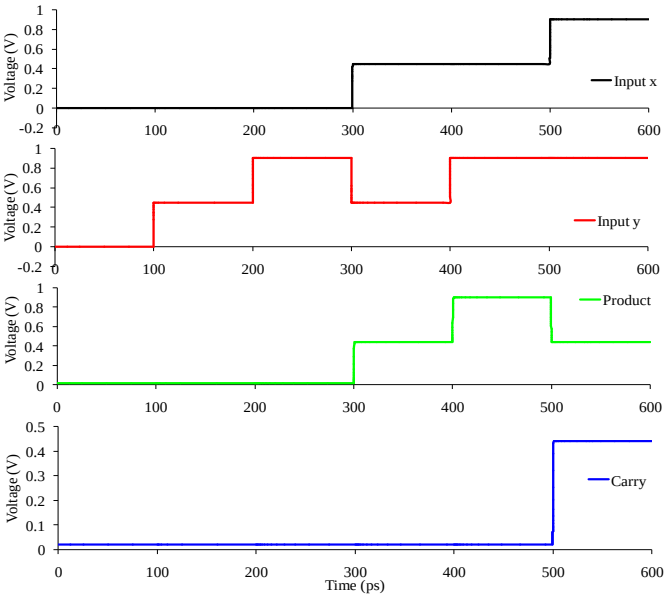

Figure 7. Output response of proposed TVL based multiplier

3.2 Pseudo N-CNTFET based TVL Multiplier Design

A TVL multiplier circuit is also developed and validated the correctness with its truth table presented in *table 2*. The transient response equation for TVL multiplier is stated as

$$\text{Product} = 2 \cdot (x_1 y_2 + x_2 y_1) + 1 \cdot (x_1 y_1 + x_2 y_2) \quad (5)$$

$$Carry = 1 \cdot x_2 y_2 \quad (6)$$

The circuit schematic of TVL multiplier using Pseudo N-CNTFETs is shown in *figure 6*. The output of multiplier is shown in *figure 7*. It is noticed that the proposed multiplier operates correctly according to truth table given in *table 2*. Furthermore, the performance of multiplier is also evaluated in terms of propagation delay and circuit area. The obtained delay and circuit area for the proposed Pseudo N-CNTFET based multiplier are 95.2ps and 3.4fm^2, respectively.

4. PERFORMANCE STUDY OF PROPOSED CIRBUITS WITH COMPLEMENTARY CIRCUITS

The performance such as delay and circuit area of Pseudo N-CNTFET designs are examined with complementary designs to show the efficaciousness of proposed method. For complementary, the CNTFET diameters 1.48nm, 1.01nm and 0.78nm are used and their threshold voltages are 0.28V, 0.42V and 0.55V, respectively. The TVL half-adder and multiplier are developed by CNTFETs. *Figure 8* shows comparisons of proposed and complementary designs. The proposed designs improved the delay, and circuit area up to 34.73% and 25.04%, respectively for half adder 30.30% and 20.18% for multiplier over the complementary designs. Moreover, the memory usage and CPU time for the proposed circuits are investigated. Using the I7–2600 processor with 3.4 GHz frequency and 8 GB RAM, the CPU time and memory usage are investigated and shown in *figure 9*. The Pseudo NCNTFETs based TVL circuits shows reduced memory and CPU time compared to the complementary based CNTFET designs. Hence, the utilizing Pseudo CNTFET designs for TVL applications provide high performance compared to complementary designs.

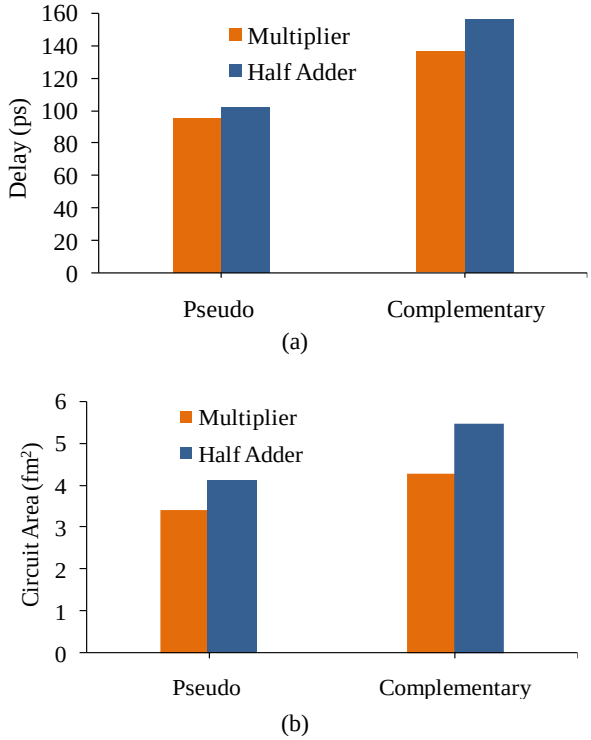

Figure 8. Performance comparison of multiplier and half adder (a) Delay and (b) Circuit area

FOREX Publication
Open Access | Rapid and quality publishing
International Journal of Electrical and Electronics Research (IJEER)
Research Article | Volume 11, Issue 2 | Pages 518-522 | e-ISSN: 2347-470X

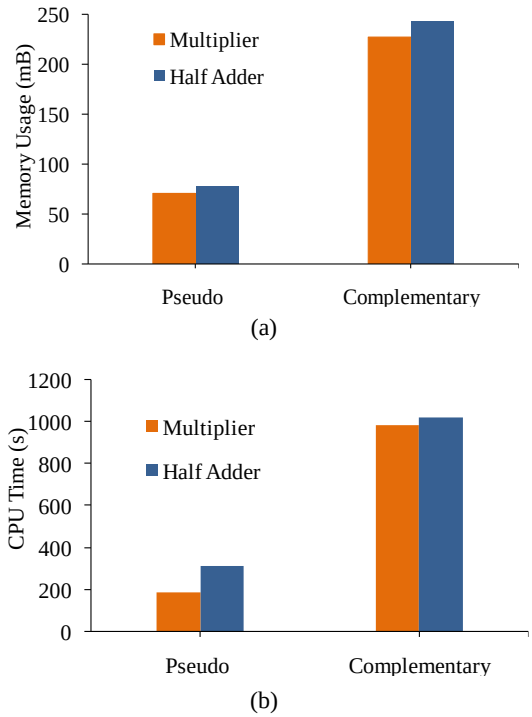

Figure 9. Pseudo N-CNTFET based TVL multiplier and half adder (a) Memory and (b) CPU Time

5. CONCLUSION

A novel TVL circuit schematics are presented in this work. The TVL based half adder and multiplier circuits are developed utilizing Pseudo N-CNTFETs because the CNTFET threshold voltage values are altered by the CNT chirality vector. All the proposed circuit designs are developed and simulated in HSPICE. The performance parameters such as circuit area and delay of the proposed designs are also analyzed and improved up to 32.5% and 22.6%, respectively compared to the complementary CNTFET circuit schematics. Furthermore, the memory usage and CPU time consumed for the proposed designs are investigated and improved up to 68.4% and 75.13%, respectively over the complementary designs. Thus, using the proposed technique is a best solution for designing TVL logic applications.

Conflicts of Interest: No conflict of interest

REFERENCES

[1] Madhuri, B. D.; Sunithamani, S. Design of Ternary Logic Gates and Circuits using GNRFETs. IET Circuits, Devices & Systems 2020, 14, 972-979.

[2] Gadgil, S.; Vudadha, C. Design of CNTFET-Based Ternary ALU Using 2:1 Multiplexer Based Approach. IEEE Transactions on Nanotechnology 2020, 19, 661-671.

[3] Karmakar, S.; Chandy, J. A.; Jain, F. C. Design of Ternary Logic Combinational Circuits Based on Quantum Dot Gate FETs. IEEE Transactions on Very Large Scale Integration (VLSI) Systems 2013, 21, 793-806.

[4] Begum, A. Y.; Balaji, M.; Satyanarayana, V. Quantum Dot Cellular Automata using a One-bit Comparator for QCA Gates. Materials Today: Proceeding 2022, 66, 3539-3549.

[5] Nesa, R. P. M.; Thangkhiew, P. L. A Review on Fundamentals of Ternary Reversible Logic Circuits. 2020 International Conference on Computational Performance Evaluation (ComPE), 2020, 738-743.

[6] Wu, G.; Cai, L. Ternary Multiplier of Multigate Single Electron Transistor: Design using 3-T Gate. IEEE ICCA 2010, 1567-1571.

[7] Lin, S.; Kim, Y. -B.; Lombardi, F. CNTFET-Based Design of Ternary Logic Gates and Arithmetic Circuits. IEEE Transactions on Nanotechnology 2011, 10, 217-225.

[8] Lin, S.; Kim, Y. -B.; Lombardi, F. Design of a Ternary Memory Cell Using CNTFETs. IEEE Transactions on Nanotechnology 2012, 11, 1019-1025.

[9] Zarandi, A. D.; Reshadinezhad, M. R.; Rubio, A. A Systematic Method to Design Efficient Ternary High Performance CNTFET-Based Logic Cells. IEEE Access 2020, 8, 58585-58593.

[10] Kim, S.; Lee, S. -Y.; Park, S.; Kim, K. R.; Kang, S. A Logic Synthesis Methodology for Low-Power Ternary Logic Circuits. IEEE Transactions on Circuits and Systems I: Regular Papers 2020, 67, 3138-3151.

[11] Madhuri, B. D.; Sunithamani, S.; Basha, S. J.; Kumar, V. R. Design of Hardened Flip-flop using Schmitt Trigger based SEM Latch in CNTFET Technology. Circuit World 2020, 47.

[12] Lin, S.; Kim, Y.; Lombardi, F. A Novel CNTFET based Ternary Logic Gate Design. 2009 52nd IEEE International Midwest Symposium on Circuits and Systems, Cancun, Mexico, 2009.

[13] Sahoo, S. K.; Akhilesh, G.; Sahoo, R.; Muglikar, M. High-Performance Ternary Adder Using CNTFET. IEEE Transactions on Nanotechnology 2017, 16, 368-374.

[14] Sridharan, K.; Gurindagunta, S.; Pudi, V. Efficient Multiternary Digit Adder Design in CNTFET Technology. IEEE Transactions on Nanotechnology 2013, 12, 283-287.

[15] Jaber, R. A.; Kassem, A.; El-Hajj, A. M.; El-Nimri, L. A.; Haidar, A. M. High-Performance and Energy-Efficient CNFET-Based Designs for Ternary Logic Circuits. IEEE Access 2019, 7, 93871-93886.

[16] Vudadha, C.; Srinivas, M. B. Design of High-Speed and Power-Efficient Ternary Prefix Adders Using CNFETs. IEEE Transactions on Nanotechnology 2018, 17, 772-782.

[17] Sridevi, V.; Jayanthy, T. Minimization of CNTFET Ternary Combinational Circuits using Negation of Literals Technique. Arabian Journal of Science and Engineering 2014, 39, 4875-4890.

[18] Fereshteh, J.; Paiman, K. Low-power Consumption Ternary Full Adder based on CNTFET. IET Circuits, Devices & Systems 2016, 10, 365-374.

[19] Liang, J.; Chen, L.; Han, J.; Lombardi, F. Design and Evaluation of Multiple Valued Logic Gates Using Pseudo N-Type Carbon Nanotube FETs. IEEE Transactions on Nanotechnology 2014, 13, 695-708.

[20] Deng, J.; Wong, H.-S. P. A Compact SPICE Model for Carbon-Nanotube Field-Effect Transistors Including Nonidealities and its Application—Part I: Model of the Intrinsic Channel Region. IEEE Trans. Electron Device 2007, 54, 3186–3194.

[21] Deng, J.; Wong, H.-S. P. A Compact SPICE Model for Carbon-Nanotube Field-Effect Transistors Including Nonidealities and its Application—Part II: Full Device Model and Circuit Performance Benchmarking. IEEE Trans. Electron Device 2007, 54, 3195–3205.

© 2023 by the K. Maheswari, M. L. Ravi Chandra, D. Srinivasulu Reddy and V. Vijaya Kishore. Submitted for possible open access publication under the terms and conditions of the Creative Commons Attribution (CC BY) license (http://creativecommons.org/licenses/by/4.0/).

International Journal on Recent and Innovation Trends in Computing and Communication
ISSN: 2321-8169 Volume: 11 Issue: 11s
DOI: https://doi.org/10.17762/ijritcc.v11i11s.8294
***Article Received:** 03 July 2023 **Revised:** 28 August 2023 **Accepted:** 18 September 2023*

Unmanned Aerial Vehicle Design for Smart City Application

Birasalapati Doraswamy[1*], M. N. Giriprasad[1], K. Lokesh Krishna[2]
[1]Department of Electronics and Communications Engineering,
Jawaharlal Nehru Technological University Anantapur (JNTUA),
Ananthapuramu, Andhra Pradesh-515002, India
[*1]Email: dsbira@gmail.com, {[1]e-mail: giriprasadmn.ece@jntua.ac.in}
[2]Department of Electronics and Communications Engineering,
SV College of Engineering, Tirupati, Andhra Pradesh-517502, India
[2]e-mail: kayamlokesh78@gmail.com

Abstract- Nowadays, Unmanned Aerial Vehicles (UAVs) or drones are also one of the applications to provide the required services and to gather information from the target location. Because smart city applications effectively deal the drone interaction and enhance the human lifestyle with drones. Moreover, UAVs are generally utilized due to their privacy threats, lower cost, pose security, and versatility, which request dependable detection at lower altitudes. However, the less sensing module in the drone has earned the low sensing accuracy of location tracking. So, this paper aims to develop a novel Firefly-based Recurrent Neural Mechanism (FRNM) to enrich the sensing capacity of the drone vehicle. In addition, the sound of the research is medicine delivery through UAVs in emergencies. This UAV system is one of the most crucial features to delivering essential medical items aids by reaching properly correspondent patients. Moreover, the client's needs are stored in the FRNM cloud then that stored data is trained to the UAV machine. Hereafter, based on the trained details, the drone can reach the destination and has delivered the requested medicine to the specific clients. The planned design is drawn in Network Simulator (NS2) environment, and the robustness of the projected replica is valued by calculating the chief parameters. Hereafter, the improvement score was valued by the comparison assessment. Hence, the FRNM has reported the finest performance by earning less location finding duration, running period, and error rate.

Keywords*:* Medicine delivery; Sensing module; Client requests; Optimization; Recurrent neural deep learning.

I. INTRODUCTION

Nowadays, intelligent facilities are much-needed to get the daily need for survival [1]. Everyone can realize the need and advances of the smart city during this COVID pandemic [2]. So in these cases, several people are affected by living conditions, the economy and health [3]. In that situation, UAVs [4] have been used to supply food and medicine [5]. Hence, this technology was welcomed by many people to protect their lives from the COVID pandemic and to get the needed things at the required time [6]. On the other hand, to manage the public in an emergency or other pandemic situation [7], the governing and urban environment could be more suitable for rapid services [8]. So, the smart application is the needed framework for economic and lifestyle development [9].

In the COVID situation, the UAV application can be utilized a lot to reduce the COVID risk by avoiding crowds in public places [10]. So, the crowd was formed to get the needed thing for people's survival. The needed items are shared with specific users using drones, like door delivery [11]. For this drone application, the Internet of Things (IoT) [12] is the most required parameter to sense the public situation and to start the service policies [13]. Hence, many research works have proved that, without IoT, the smart city becomes a dream [14]. So, the IoT plays an essential role in all smart city applications, especially drone appliances, to collect data in the particular target cities and to send the data to the management [15]. Moreover, the drone's sensing function is based only on the updated deep or machine learning model. So to sense the needed data, the intelligent model should be designed with the required parameters [16, 17].

Here, the UAEs system constantly connects to the base station and receives updates on atmospheric conditions and weather data. This makes it sensible, and it decides to optimize the path dynamically [18, 19]. This is necessary to avoid aberrant atmospheric behavior and destructive potential by considering the real-time problem and needs, such as geographically challenging regions to trace and provide critical little things, medical kits, and so on [20, 21]. Although roads serve and justify the link to residential areas, severe weather conditions and some transportation challenges prevent medical products from being delivered on time. Many organizations have adopted drone technology to tackle such issues, which has developed as an innovation [22, 23].

International Journal on Recent and Innovation Trends in Computing and Communication
ISSN: 2321-8169 Volume: 11 Issue: 11s
DOI: https://doi.org/10.17762/ijritcc.v11i11s.8294
***Article Received:** 03 July 2023 **Revised:** 28 August 2023 **Accepted:** 18 September 2023*

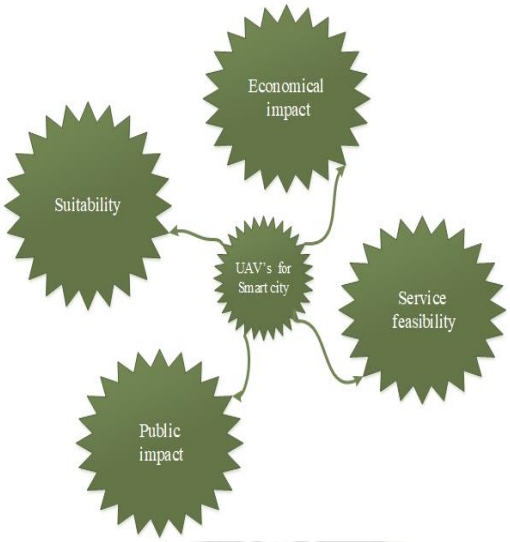

Figure 1. UAV for smart city

Several architectures, like automated decision [24], light polarization [25], etc., have been implemented in the past to train the UAVs with people addresses, but they gave inferior results because of the effective algorithm. Therefore, the present research has aimed to develop a novel optimized deep learning mechanism in the UAV application to improve the sensing function. The process of the current research article is described as follows,

- Initially, the user needs are trained to the system and stored in one specific folder
- Then the required number of UAV's was designed, then the address of each user is upgraded to the UAV memory
- Then a novel FRNM was designed to find that exact user location with the use of training data of UAV's
- Hereafter, the performance metrics are calculated based on location identification, energy usage, delay, Run time, mean square error

The sections of the discussed research work is described as follows, associated works related to drone appliance is exposed in section 2, System model with issues are explained in section 3, section 4 has detailed the planned novel concepts, the outcomes of the discussed procedures are drawn in section 5, then the research discussion is end in section 6.

II. RELATED WORKS

This section provides a general examination of the proposed DL and UAV models and frameworks for medical networks and technology. This has been claimed in data collection jobs and secure remote access to social media platforms, among other things. The cumulative popularity of UAVs in mobile networks is the connectedness of various social networks, increasing data exchange across networks, and the empowerment of social robotics research. Recent Associated literatures are discussed below,

IoT has played an important role to enhance the smart city facilities by collecting the patient data through the specific sensors. Gera *et al*. [24] have designed an automated decision making scheme to diagnosis the disease from the gathered data. Hence, this system has attracted by many users. But in some time the data transmission delay has occurred.

Beg *et al*. [25] have presented the light polarization strategy in UAV system to identify the emergency cases and to consider it as the first priority of medical services. Hence, this model is useful to predict the emergency cases by traffic. Some of the emergency cases can easily be identified are violation, accident, etc. But this model has consumed more energy services.

Richards [26] has designed the fly high approach to afford the medicine door to door delivery by knowing the needs of people needs. Here, the importance of civil structure was highlighted, because based on the civil structures the user location was found. Moreover, the shareholder activities also combined in UAV's to offer the better delivery rate. But the trained structure details in UAV's might cause transmission delay.

The drone application was well utilized in COVID situation to reduce the disease spreading issues by delivering the people needs to door-to-door delivery system. So, Cheema *et al*. [27] have designed the drone system with the use of artificial intelligence strategies. Here, the drone application is framed with artificial intelligence strategy for making the appropriate decision to find the people needs. But, framing the design has taken more time.

To enable the security to the public and to know the user needs, Ullah *et al*. [27] have designed deep learning based UAV sensing module with 5G services. Moreover, the proposed system is checked with different intelligent models, still the finest results are only got for the security monitoring and capturing module. However, it has failed to predict the user needs in an accurate way. The process of the current research article is described as follows,

- Initially, the user needs are trained to the system and stored in one specific folder.
- Then the required number of UAV's was designed, then the address of each user is upgraded to the UAV memory.
- Then a novel FRNM was designed to find that exact user location with the use of training data of UAV's.
- Hereafter, the performance metrics are calculated based on location identification, energy usage, delay, Run time, mean square error.

International Journal on Recent and Innovation Trends in Computing and Communication
ISSN: 2321-8169 Volume: 11 Issue: 11s
DOI: https://doi.org/10.17762/ijritcc.v11i11s.8294
Article Received: *03 July 2023* ***Revised:*** *28 August 2023* ***Accepted:*** *18 September 2023*

III. SYSTEM AND PROBLEM STATEMENT

Nowadays, the application drone became the most needed sector in this society to improve the people's life style and to reduce the human risk and effort. Also it is very useful in natural disaster situation. Nevertheless, the majority of current commercial UAV applications require an operator to pilot the vehicle using distant controller expedients [28]. Instead, the introduction of self-sufficient UAVs for the manipulation of processes that found dramatic variation in the dual comportments of cargo logistics and deliveries in smart cities has captivated the shipping logistics and delivery businesses [29]. As a result, it is critical to address the responsiveness on certain technological characteristics of UAVs, whose appreciation facilitates the appraisal of the actual potential of such vehicles [30].

However, designing the decision model in the drone is the most complicated task because of vast data. In many scenarios, it is utilized to deliver the things to the people but identifying the people location using the trained data is some more complex. Advances in technology cause an increase in the competences and effectiveness of UAVs, resulting in their rapid evolution or application in various areas such as medical, engineering, profitable, and entertainment applications, that is, the ability to gather real-time data at on-time delivery, cost-effectiveness and on-time payloads deliveries [31]. This issues have been motivated this present research work towards this drone application in smart city area. The system description with issues is explained in Figure 2.

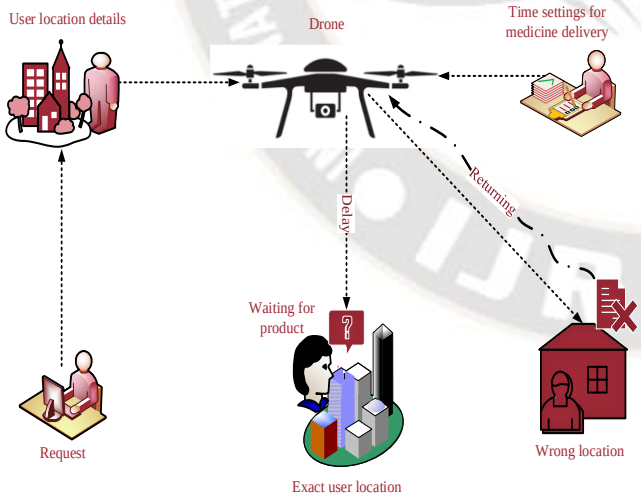

Figure 2. System model with identified issues

IV. PROPOSED METHODOLOGY

The present research work has focused to invent innovate drone application system for door-to-door medical supply system. Moreover, a novel Firefly based Recurrent Neural Mechanism (FRNM) was designed to sense the requested user location.

Initially, the needs of user related to medicine is stored in the cloud storage, by analysing the cloud data the location of users was identified. Then that address of the user is updated in drone memory then with the help of FRNM the location of user was found and medicine was supplied. Then, the optimization fitness function is updated to the classification layer or identification layer of the neural network. Based on this updated fitness module the correspondent user agents are sensed and medicines are supplied to the requested users with the help of UAVs. Hence, the planned model is described in Figure 3.

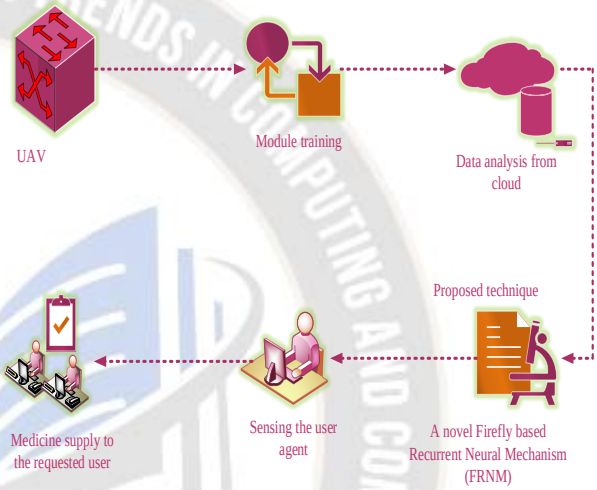

Figure 3. Proposed methodology

4.1 Process of FRNM methodology

The planned model is the combination of meta-heuristic and DL approaches. Here, the meta-heuristics as firefly algorithm [29] was utilized and the recurrent neural layer is used as DL model. Combination of these two strategies can provides finest results in terms of performance metrics. Several optimizations are utilized in different numerical solution; however, the reason of selecting this particular firefly algorithm is to find the target location with accurate measure. Usually, the fitness of the firefly is based on distance prediction between the partner fireflies. This reason has turned the interest to make use of firefly in this UAV application.

- FRNM Cloud constructer

The need of this frame is to receive the user needs and stored in the recurrent neural system memory. Several blocks are designed to save the user needs in day order, numerous things users can requests different items. But, the current research article has primarily focused the medicine supply in the emergency situation. So, from the set of requested data, medical data request are identified in the initial stage. The gathering process of the user's requests is exposed in eqn. (1).

International Journal on Recent and Innovation Trends in Computing and Communication
ISSN: 2321-8169 Volume: 11 Issue: 11s
DOI: https://doi.org/10.17762/ijritcc.v11i11s.8294
***Article Received:** 03 July 2023 **Revised:** 28 August 2023 **Accepted:** 18 September 2023*

$$C_r = gather(n^*) \quad (1)$$

The FRNM cloud design is visualized in Figure 4, it contains totally four blocks like user needs, medicine requests, other requests and location saving blocks.

Here, the cloud side receiver is defined as C_r and the user requests or needs are defined as n^*. When, the user's needs are received then it has been stored in the memory layer, the detailed stored in the memory layer was users' needs and location address.

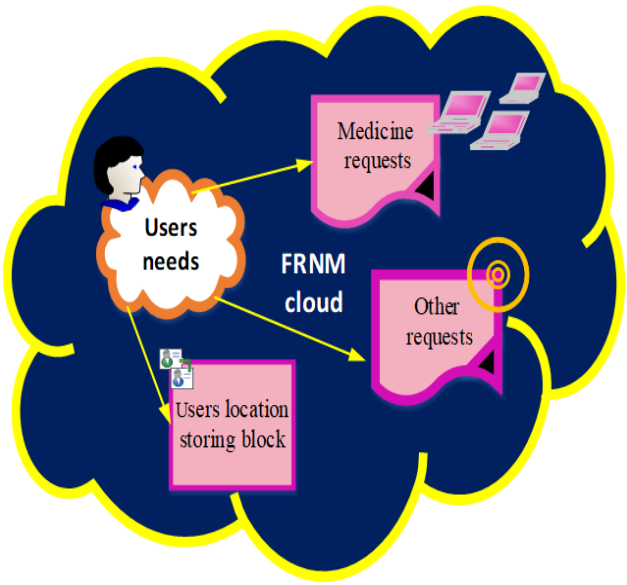

Figure 4. FRNM cloud design

4.2 UAV training phase

Users requests and location details are stored in the recurrent hidden frame, hence the activation of the hidden frame is described using eqn. (2),

$$f(h) = H_a(V_m p(h)) + V_n f(h-1) \quad (2)$$

where, the activation parameter of the hidden layer is denoted as $f(h)$, H_a is the hidden function variable and the hidden output metrics are denoted as H_o. Also, $p(h)$ and $q(h)$ are the input & output vector variables. Moreover, the 3 correlation matrices have been determined as V_m, V_n and V_o. The output vector variable is defined using eqn. (3),

$$q(h) = H_o(V_o f(h)) \quad (3)$$

Here, ua is the user address and uaN means n number of user address, these details were trained to the UAV's, which are ready to travel. Hence, FRNM layers are drawn in Figure 5.

After, the training phase, the time was set that has included start time P_Y and end time P_Z, also the error parameter is exposed as $pr_s(t)$.

$$\beta^s{}_{total}(P_Y, P_Z) = \sum_{t=P_Y}^{P_Z} pr_s(t) \quad (4)$$

Fe has denoted the firefly fitness, if the drone takes extra duration than the fixed end duration then the error value was reported. Here, $D_{Y,Z}$ is the distance amid starting and target.

$$P_{Y(t+1)} = P_Y + \beta^s(P_Y - P_Z) + R_d \quad (5)$$

The firefly best solution is upgraded to the classification layer of recurrent model to trance the requester destination. Hence, the parameter utilized to trace the right location is detailed as β^s, also, the reaching duration is represented as R_d. The designed FRNM procedure is exposed in Algorithm 1.

After specifying the time parameter, the path planning was designed in the sensing module that is explained using eqn. (6),

$$\beta^p = ap(P_Y - P_Z) \quad (6)$$

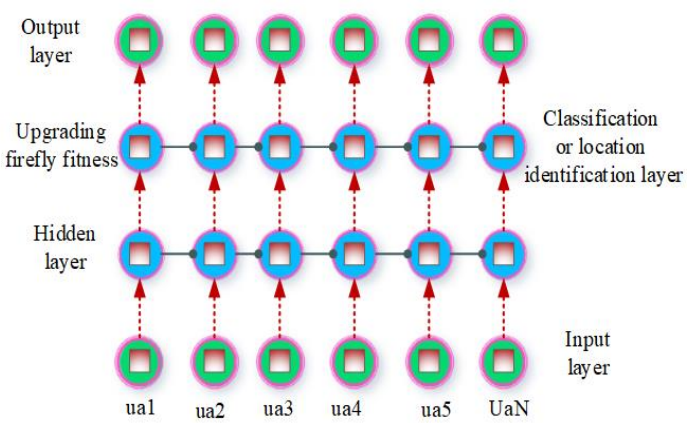

Figure 5. Proposed FRNM layers

Algorithm 1. FRNM

Start
{
***Initialize** UAV's (g1,g2,g3)*
// Here, g1,g2,g3 are the utilized drones
User request storing ()
{

$$user \leftrightarrow needs + l^* \rightarrow m^*$$

// here, m^* *represents the memory layer and users location is denoted as* l^*

$$analyze = needs(subject)$$

// analysing the requested things

$$if(subject = medicine)$$

{
Medicine requested user
}else (different things)
UAV training phase ()
{

$$Train(n^* \,\&\, l^*) \rightarrow UAV$$

International Journal on Recent and Innovation Trends in Computing and Communication
ISSN: 2321-8169 Volume: 11 Issue: 11s
DOI: https://doi.org/10.17762/ijritcc.v11i11s.8294
Article Received: *03 July 2023* ***Revised:*** *28 August 2023* ***Accepted:*** *18 September 2023*

// Here, n^* *is the user needs, the prepared UAV has been trained with users location and needs.*

}

UAV machine setting frame

{

$\text{int}\, Y, Z;$

//Here, Y is the travel initiating region of drone and Z is the target location

$start(Y) \rightarrow end(Z)$

$endZ = user(l^*)$

$start(Y) \cap end(Z) \rightarrow np$

// Here, np *is the nearest path, the UAV was moved by finding the nearest path*

$UAV \leftrightarrow user = inital \leftrightarrow arival\ time$

// By defining the users location to the drone, starting and ending time was fixed

Return $\rightarrow starting\ \ place$

}

Parameter estimation

}

stop

The available path identification between the source and target is values using eqn. (6), here, available path is depicted as ap and the path searching is determined by β^p Once, the available ways are found then the minimum way distance were found using the travelling time parameter.

$$\beta^p = time_estimation(ap) = \min_dis\tan ce \quad (7)$$

Hence, the travelling time of the available distance was measured by eqn. (7), finally, the minimum travelling time path was identified.

Moreover, the acceleration of the drone is depending on the weather condition, if the atmosphere has contained high rage of moisture and humidity then the acceleration of drone became slow. Also, it has required more duration to reach the end point. The UAV's functions and regulation process are detailed in Figure 6.

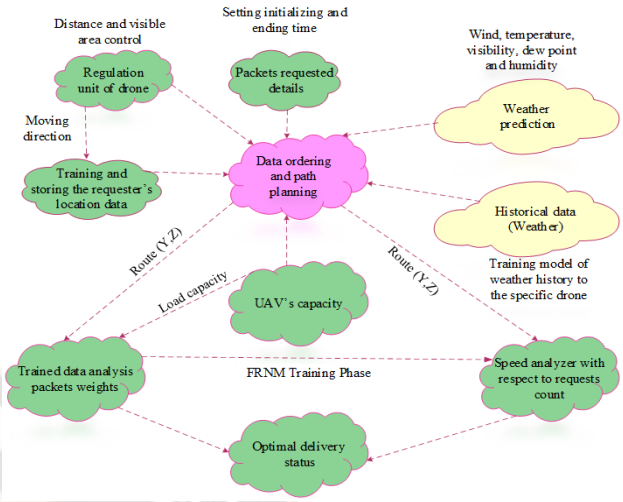

Figure 6. Internal process of UAV

V. RESULTS AND DISCUSSION

The discussed research work is executed in NS2 platform, and also running in UBUNTU platform. Initially, the require mount of nodes are designed with the appropriate lables, in those nodes some are medicine requested nodes (clients), UAV's, drone management and normal nodes (casual users). In the initial phase, the requester can send the needed medicine report to the FRNM cloud memory. In the NS2 platform, the FRNM cloud memory is named as drone management. Moreover, the clouds has included the descriptions abut users need and location. Hereafter, those stored data is trained to the UAV machine, the sensing module of the UAV was updated by the FRNM model.

Several optimizations are utilized in different numerical solution; however, the reason of selecting this particular firefly algorithm is to find the target location with accurate measure. Usually, the fitness of the firefly is based on distance prediction between the partner fireflies. This reason has turned the interest to make use of firefly in this UAV application.

5.1. Case study

To value the robustness rate of the constructed paradigm, initially 120 nodes are designed in the NS2 environment. According to this current research, the 120 nodes are considered as users or clients. The client's needs are saved in the cloud memory that hub is coloured as blue. Drones location sensing module is upgraded with the FRNM module.

International Journal on Recent and Innovation Trends in Computing and Communication
ISSN: 2321-8169 Volume: 11 Issue: 11s
DOI: https://doi.org/10.17762/ijritcc.v11i11s.8294
***Article Received:** 03 July 2023 **Revised:** 28 August 2023 **Accepted:** 18 September 2023*

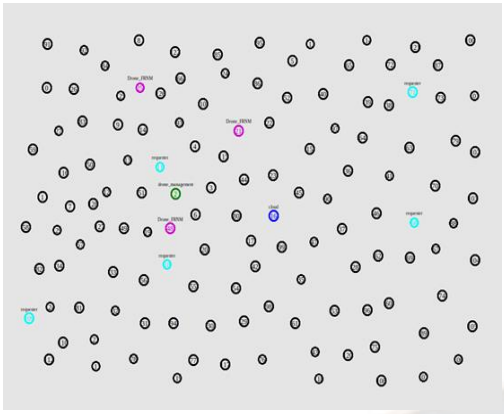

Figure 7. Node designed frame

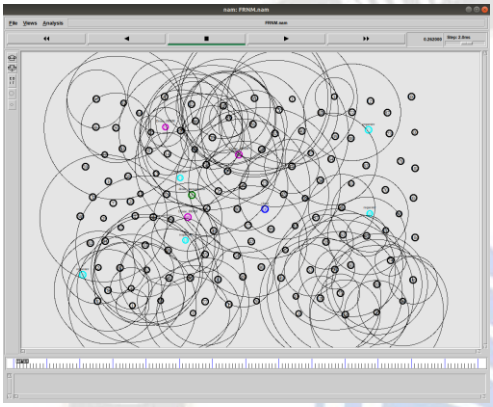

Figure 8. Data broadcasting and location searching frame

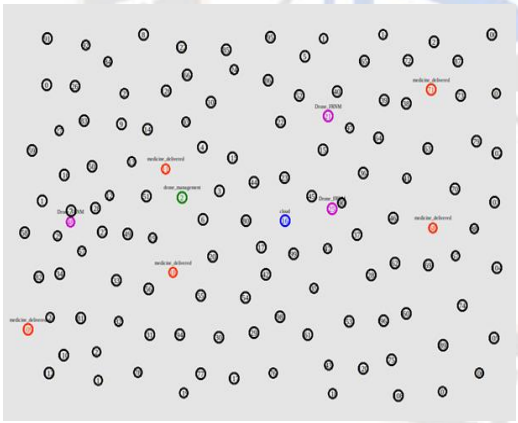

Figure 9. Request delivered

Here, totally 3 drones were utilized that is mentioned in the rose colour. To train the user requested details to the specific drone, drone management is needed that is denoted in the green colour. Also, the medicine requesters are represented in sky blue colour, the node designed frame in NS2 is explicated in Figure 7.

After training the user requests and their location to the drone, then it has initiated the location finding process that is depicted in Figure 8. For the drone application, the location was identified by the help of GPS. After the identification of all available paths, medicine is transferred to the requester.

Finally, the initiated drones have reached to the destination and the medicine was delivered that is viewed in Figure 9. When, the things were delivered then the drone return to the drone management location, in where it has been initiated. The red colour node has denoted the medicine delivered to the particular client.

5.2 Performance assessment

In any system validating the function is the crucial task to value the proficient score of the specific paradigm. Considering that, this performance assessment section is discussed broadly to justify the successive measure of the planned design. Hence, to estimate the planned design**,** 120 nodes are designed in the NS2 platform in that 3 Drones are set.

5.2.1 Travelling distance and duration

The travelling distance and travelling duration of the UAVs are important parameters to prove the proposed model efficiency. Here, three UAVs are taken as travelling distance and travelling duration with number instances, which are estimated that is drawn in fig.10.

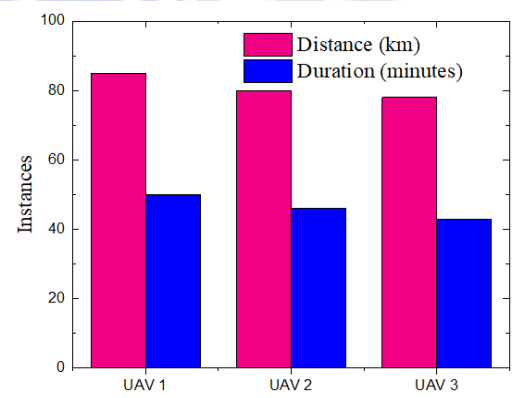

Figure 10. UAV's travelling distance and time

5.2.2 Error rate

After initiating the drone, based on the travelling and sensing process the error was measured. The measure of flaw was calculated in three phases that are duration error, distance error, and data training flaw in drone applications. The three states error estimation is tabulated in table.1 and fig.11.

International Journal on Recent and Innovation Trends in Computing and Communication
ISSN: 2321-8169 Volume: 11 Issue: 11s
DOI: https://doi.org/10.17762/ijritcc.v11i11s.8294
Article Received: *03 July 2023* ***Revised:*** *28 August 2023* ***Accepted:*** *18 September 2023*

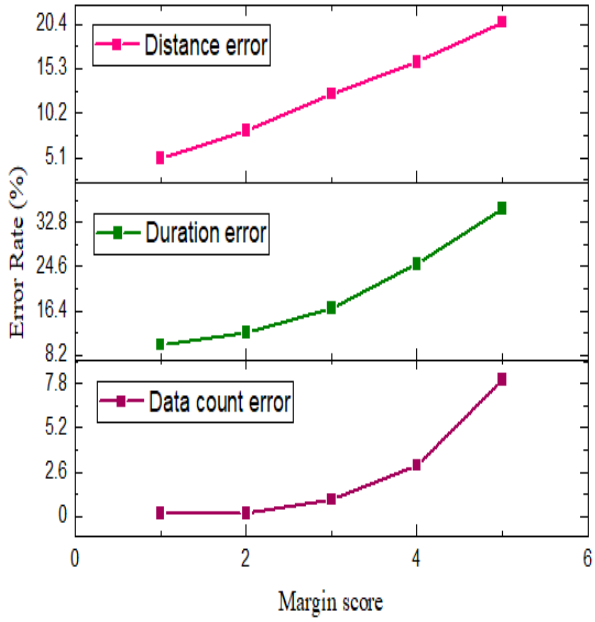

Figure 11. Error assessment

Moreover, error rate validation of the proposed module is calculated based on three error factors such as data count error, duration error and distance error.

TABLE 1 ERROR ANALYSIS

Margin score	Error validation		
	Data count error	Duration error	Distance error
1	0.2	10	5
2	0.2	12.3	8.2
3	1	16.8	12.4
4	3	25.1	16.1
5	8	35.3	20.6
6	16.2	30.5	2
7	14	39	27
8	20	44.9	24

As discussed in the proposed section, the rapidity of the vehicle is based on weather conditions. If, the weather atmosphere is clear then the UAV has the finest rapidity score.

5.2.3 Speed analysis

The speed of the drone is the crucial factor to maximize the robustness score because the drone system is enabled for emergency cases. So, the rapidity measure of the UAV application is the significant metric to maximize the drone system. Here, the acceleration of the drone is valued on the basis of the amount of packet delivery requests. The measured acceleration of the UAV is exposed in fig.12.

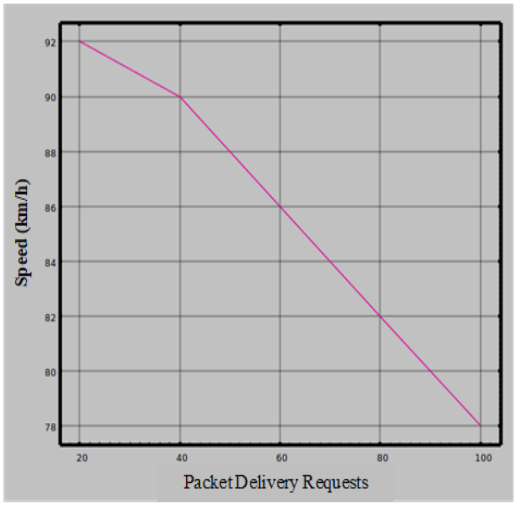

Figure 12. Assessment of speed

TABLE 2 TIME MEASUREMENT

Data counts	Running time	Location searching time
20	0.052	0.048
40	0.064	0.056
60	0.069	0.06
80	0.075	0.064
100	0.08	0.069

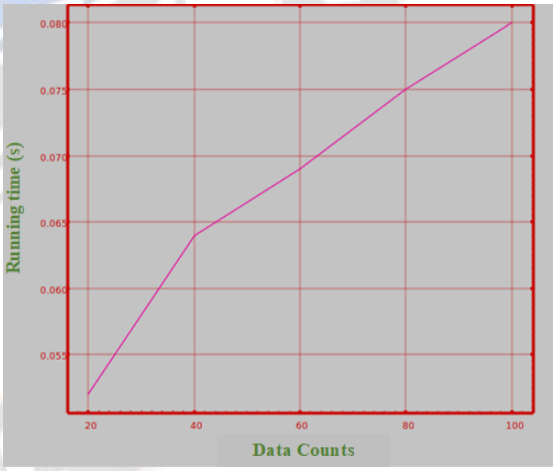

(a)

International Journal on Recent and Innovation Trends in Computing and Communication
ISSN: 2321-8169 Volume: 11 Issue: 11s
DOI: https://doi.org/10.17762/ijritcc.v11i11s.8294
***Article Received:** 03 July 2023 **Revised:** 28 August 2023 **Accepted:** 18 September 2023*

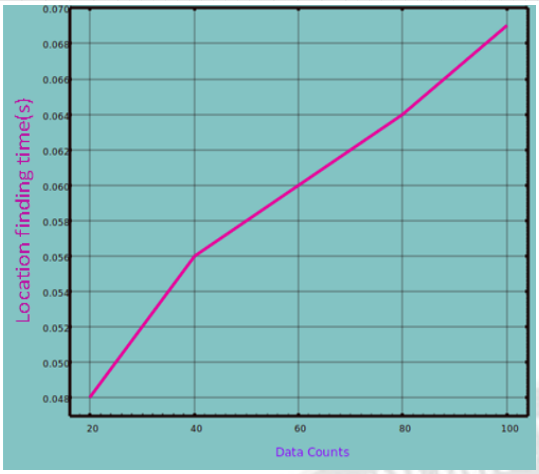

(b)

Figure 13. Time estimation: a) running time, b) location finding time

The requester addresses are stored in the server cloud, while initiating the drone system; the saved info is forwarded to the drone management. Then, the UAV's are trained with the gathered requester details. Based on that, the drone has travelled to reach the specific spot to deliver the requested items.

The time measurement was taken in dual phases that are location finding and execution duration, which is sketched in Table 2.

5.3 Comparative analysis

In this UAV application, the metrics error was calculated by analysing the duration and distance error. Here, the error that raised by the drones travelling long distance is compared with other schemes like Drone services (DS) [28], Self Adaptive Model (SAM) [20] and Optimized Drone [22].

This kind of error is often raised by selecting farthest path instead of shortest path. Hence, the error in path selection has tended to achieve the wide range of distance error. The earned error measure by DS is 41%, SAM 50%, but the designed FRNM has yield the less error measure as 27%. These exact statistics are exposed in Figure 14.

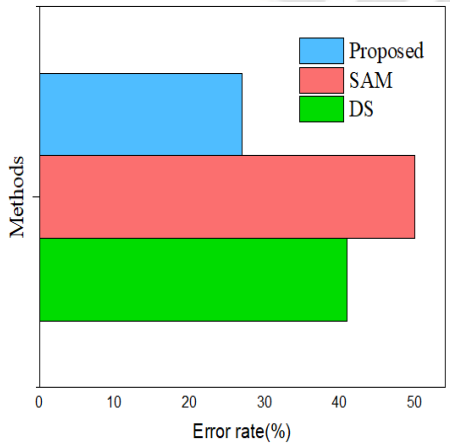

Figure 14. Measure of error

The execution duration of the simulation environment is based on the location identification time. If the drone has taken more duration to find the location then it has needed more period to complete the execution. Hence, the execution duration of the DS is 0.1s, OD 0.07s, also the designed FRNM has required less execution period as 0.05s. These detailed validations are exposed in Figure 15.

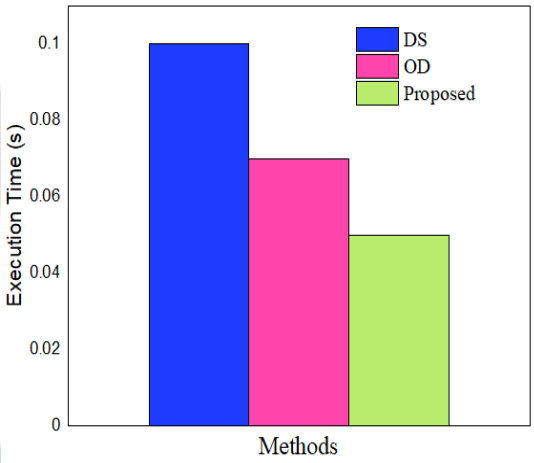

Figure 15. Execution time assessment

5.4 Discussion

The outcome of the discussed model has gained the fair results in all key metrics; this shows the flexibility of the created module in the drone cells.

Also, the plan of this present research method will help to maximize the advances in the smart city application. To prove the achieved outcomes three schemes are obtained and compared with one another, those details are shown in Table 3.

TABLE 3 ROBUSTNESS ASSESSMENT

Robustness Evaluation			
Methods	DS[28]	SAM[27]	proposed
Error (%)	41	50	27
Methods	DS	OD[26]	proposed
Execution time (s)	0.1	0.07	0.05

VI. CONCLUSION

The present research has implemented for medicine transferring system using the drone application. For that, a novel FRNM was designed with suitable parameters to train the UAV's sensing module. Initially, a set of user nodes are created in the NS2 environment then the requester nodes are set. Hereafter, the requester has asked the needed resources then it is stored to the cloud. Moreover, the UAV's are trained with the medicine details and their location address. Once, the training

International Journal on Recent and Innovation Trends in Computing and Communication
ISSN: 2321-8169 Volume: 11 Issue: 11s
DOI: https://doi.org/10.17762/ijritcc.v11i11s.8294
***Article Received:** 03 July 2023 **Revised:** 28 August 2023 **Accepted:** 18 September 2023*

is completed then it has started travelling to reach the destination, based on the minimum distance, it will choose the shortest path. After delivering the medicine, it has returned to the initialize position. Hereafter, the robustness score of the designed FRNM was estimated with some metrics like error, running and location searching time. The designed approach has earned the finest outcome by earning the reduce error values as 27% and less running duration in 0.05s, hence the gained scores are much better than the compared techniques. Also comparing the earliest scheme, the presented novel FRNM has minimized error measure up to 20% and the execution duration up to 2%. Hence, the presented FRNM scheme is suitable for drone application to upgrade the sensing module by offering better location tracing report. In future, designing the security based system in the cloud architecture will gain the best confidential report.

ACKNOWLEDGEMENTS

None.

REFERENCES

[1] M. Ouiss, A. Ettaoufik, A. Marzak, and A. Tragha, "A Parallel Genetic Algorithm for Solving the Vehicle Routing Problem with Drone Medication Delivery," In: F. Saeed, T. Al-Hadhrami, E. Mohammed, and M. Al-Sarem, eds, Advances on Smart and Soft Computing, Singapore: Springer, 2022, pp. 225-233. https://doi.org/10.1007/978-981-16-5559-3_19

[2] A. C. de Araujo and A. Etemad, "End-to-End Prediction of Parcel Delivery Time with Deep Learning for Smart-City Applications," IEEE Internet Things J. Vol. 8(23), 2021, pp. 17043-17056. DOI: 10.1109/JIOT.2021.3077007

[3] S. M. S. M. Daud, M. Y. P. M. Yusof, C. C. Heo, L. S. Khoo, M. K. C. Singh, M. S. Mahmood, and H. Nawawi, "Applications of drone in disaster management: A scoping review," Sci Justice, Vol. 62(1), 2022, pp. 30-42. https://doi.org/10.1016/j.scijus.2021.11.002

[4] N. Thakur, P. Nagrath, R. Jain, D. Saini, N. Sharma, D. J, "Hemanth. Artificial Intelligence Techniques in Smart Cities Surveillance Using UAVs: A Survey," In: U. Ghosh, Y. Maleh, M. Alazab, A. S. K. Pathan eds," Machine Intelligence and Data Analytics for Sustainable Future Smart Cities, Cham: Springer, 2021, pp. 329-353. https://doi.org/10.1007/978-3-030-72065-0_18

[5] R. Gupta, A. Kumari, and S. Tanwar, "Fusion of blockchain and artificial intelligence for secure drone networking underlying 5G communications," Trans Emerg Telecommun Technol, Vol. 32(1), 2021, pp. e4176. https://doi.org/10.1002/ett.4176

[6] M. P.Nisingizwe, P. Ndishimye, K. Swaibu, L. Nshimiyimana, P. Karame, V. Dushimiyimana, J. P. Musabyimana, C. Musanabaganwa, and S. Nsanzimana, "Effect of unmanned aerial vehicle (drone) delivery on blood product delivery time and wastage in Rwanda: a retrospective, cross-sectional study and time series analysis," Lancet Glob Health, Vol. 10(4), 2022, pp. e564-e569. https://doi.org/10.1016/S2214-109X(22)00048-1

[7] M. Patchou, B. Sliwa, and C. Wietfeld, "Flying Robots for Safe and Efficient Parcel Delivery Within the COVID-19 Pandemic," 2021 IEEE International Systems Conference (SysCon), IEEE, 2021. DOI: 10.1109/SysCon48628.2021.9447142

[8] M. Kalinin, M. Krundyshev and D. Zegzhda, "AI Methods for Neutralizing Cyber Threats at Unmanned Vehicular Ecosystem of Smart City, In: T. Devezas, J. Leitão, A. Sarygulov, eds, The Economics of Digital Transformation: Approaching Non-stable and Uncertain Digitalized Production Systems, Cham: Springer, 2021, pp. 157-171. https://doi.org/10.1007/978-3-030-59959-1_10.

[9] P. L. Mehta, R. Kalra, and R. Prasad, "A Backdrop Case Study of AI-Drones in Indian Demographic Characteristics Emphasizing the Role of AI in Global Cities Digitalization," Wirel Pers Commun, Vol. 118(1), 2021, pp. 301-321. https://doi.org/10.1007/s11277-020-08014-6

[10] R. Anand, M. S. Muneshwara, T. Shivakumara, M. S. Swetha, and G. N. Anil, "Emergency Medical Services Using Drone Operations in Natural Disaster and Pandemics," In: G. Ranganathan, X. Fernando, F. Shi, eds, Inventive Communication and Computational Technologies, Singapore: Springer, 2022, pp. 227-239. https://doi.org/10.1007/978-981-16-5529-6_19

[11] M. A. Rahman, M. S. Hossain, A. J. Showail, N. A. Alrajeh, and M. F. Alhamid, "A Secure, Private, and Explainable IoHT Framework to Support Sustainable Health Monitoring in a Smart City," Sustain Cities Soc, Vol. 72, 2021, pp. 103-083. https://doi.org/10.1016/j.scs.2021.103083

[12] M. Ouiss, A. Ettaoufik, A. Marzak and A. Tragha, "A Parallel Genetic Algorithm for Solving the Vehicle Routing Problem with Drone Medication Delivery," In: F. Saeed, T. Al-Hadhrami, E. Mohammed and M. Al-Sarem, eds. Advances on Smart and Soft Computing, Singapore: Springer, 2022, pp. 225-233. https://doi.org/10.1007/978-981-16-5559-3_19

[13] H. Khan, K. K. Kushwah, S. Singh, H. Urkude, M. R. Maurya, and K. K. Sadasivuni, "Smart technologies driven approaches to tackle COVID-19 pandemic: a review," 3 Biotech, Vol. 11(2), 2021, pp. 1-22. https://doi.org/10.1007/s13205-020-02581-y

[14] T. Subha, R. Ranjana, D. Kailash and S. Abisha, "Drone Usage in Delivery of Vaccines in Indian Scenario," In: J. C. Bansal, A. Engelbrecht, P. K. Shukla, eds, Computer Vision and Robotics, Singapore: Springer, 2022, pp. 141-153. https://doi.org/10.1007/978-981-16-8225-4_11

[15] S. H. Alsamhi, F. Afghah, R. Sahal, A. Hawbani, M. A. A. Al-qaness, B. Lee and M. Guizani, "Green internet of things using UAVs in B5G networks: A review of applications and strategies," Ad Hoc Netw, Vol. 117, 2021, pp. 102-505. https://doi.org/10.1016/j.adhoc.2021.102505

[16] U. Ukaegbu, L. Tartibu and M. Okwu, "Unmanned Aerial Vehicles for the Future: Classification, Challenges, and Opportunities," 2021 International Conference on Artificial Intelligence, Big Data, Computing and Data Communication Systems (icABCD), IEEE, 2021. DOI: 10.1109/icABCD51485.2021.9519367

[17] Z. Ullah, F. Al-Turjman, L. Mostarda, and R. Gagliardi, "Applications of artificial intelligence and machine learning in smart cities," Comput Commun, Vol. 154, 2020, pp. 313-323. https://doi.org/10.1016/j.comcom.2020.02.069

International Journal on Recent and Innovation Trends in Computing and Communication
ISSN: 2321-8169 Volume: 11 Issue: 11s
DOI: https://doi.org/10.17762/ijritcc.v11i11s.8294
***Article Received:** 03 July 2023 **Revised:** 28 August 2023 **Accepted:** 18 September 2023*

[18] S. A. Mohsan, N. Q. Othman, Y. Li, M. H. Alsharif, and M. A. Khan, "Unmanned aerial vehicles (UAVs): practical aspects, applications, open challenges, security issues, and future trends," Intelligent Service Robotics, 2023, pp. 1-29.

[19] S. I. Khan, Z. Qadir, H. S. Munawar, S. R. Nayak, A. K. Budati, K. D. Verma, and D. Prakash, "UAVs path planning architecture for effective medical emergency response in future networks," Phys Commun, Vol. 47, 2021, pp. 101-337. https://doi.org/10.1016/j.phycom.2021.101337

[20] N. B. Roberts, E. Ager, T. Leith, I. Lott, M. Mason-Maready, T. Nix, A. Gottula, N. Hunt, and C. Brent, "Current summary of the evidence in drone-based emergency medical services care," Resuscitation Plus, Vol. 13, 2023, pp. 100-347.

[21] A. Hamdi, F. D. Salim, D. Y. Kim, A. G. Neiat, and A. Bouguettaya, "Drone-as-a-service composition under uncertainty," IEEE Trans Serv Comput. 2021. DOI: 10.1109/TSC.2021.3066006

[22] T. Swain, M. Rath, J. Mishra, S. Banerjee, and T. Samant, "Deep Reinforcement Learning based Target Detection for Unmanned Aerial Vehicle," In2022 IEEE India Council International Subsections Conference (INDISCON) 2022 (pp. 1-5). IEEE.

[23] R. Yesodha, and T. Amudha, "A bio-inspired approach: Firefly algorithm for Multi-Depot Vehicle Routing Problem with Time Windows," Comput Commun, Vol. 190, 2022, pp. 48-56. https://doi.org/10.1016/j.comcom.2022.04.005

[24] S. Gera, M. Mridul, and S. Sharma, "IoT based Automated Health Care Monitoring System for Smart City," 2021 5th International Conference on Computing Methodologies and Communication (ICCMC), IEEE, 2021. DOI: 10.1109/ICCMC51019.2021.9418487

[25] A. Beg, A. R. Qureshi, T. Sheltami, and A. Yasar, "UAV-enabled intelligent traffic policing and emergency response handling system for the smart city," Pers Ubiquitous Comput, Vol. 25(1), 2021, pp. 33-50. https://doi.org/10.1007/s00779-019-01297-y

[26] D. Richards, "Flying high: a human perspective of unmanned aerial systems in future cities," Theor Issues Ergon Sci. 2021, pp. 1-16. https://doi.org/10.1080/1463922X.2021.1957517

[27] M. A. Cheema, R. I. Ansari, N. Ashraf, S. A. Hassan, H. K. Qureshi, A. K. Bashir, and C Politis, "Blockchain-based secure delivery of medical supplies using drones," Comput Netw, Vol. 204, 2022, pp. 108-706. https://doi.org/10.1016/j.comnet.2021.108706

[28] E. H. Abualsauod, "A hybrid blockchain method in internet of things for privacy and security in unmanned aerial vehicles network," Computers and Electrical Engineering. Vol. 99, 2022, pp. 107-847.

[29] B. Jacob, A. Kaushik, P. Velavan, and M. Sharma, "Autonomous drones for medical assistance using reinforcement learning," Advances in Augmented Reality and Virtual Reality, 2022, pp. 133-56.

[30] C. Zhang, Y. Qiu, J. Chen, Y. Li, Z. Liu, Y. Liu, J. Zhang, C. S. Hwa, "A comprehensive review of electrochemical hybrid power supply systems and intelligent energy managements for unmanned aerial vehicles in public services," Energy and AI, 2022, pp. 100-175.

[31] N. Nasser, Z. M. Fadlullah, M. M. Fouda, A. Ali, M. Imran, "A lightweight federated learning based privacy preserving B5G pandemic response network using unmanned aerial vehicles: A proof-of-concept," Computer Networks, Vol. 205, 2022, pp. 108-672.

International Research Journal of Multidisciplinary Scope (IRJMS), 2024; 5(1):42-49 IRJMS

Original Article | ISSN (O): 2582-631X DOI: 10.47857/irjms.2024.v05i01.0133

A Rail-To-Rail and Low Offset Novel Strongarm Comparator Circuit for Low Power Data Converter Architectures

Lokesh Krishna K*, Srinivasulu Reddy D, Chandrasekhar Rao T

Department of ECE, Sri Venkateswara College of Engineering, Tirupati, Andhra Pradesh, India. *Corresponding Author's Email: kayamlokesh78@gmail.com

Abstract

With the rapid improvements in the design of advanced high performance communication receivers, hand-held electronic devices are in widespread usage for some time. These devices facilitate high speed and secured access to internet data. The demand for realizing a smart and better usage experience puts forth strict requirements on the design aspects of next-generation high speed low power complementary metal oxide semiconductor (CMOS) receiver design. One of the major modules in the implementation of high speed low power CMOS receiver device is the analog to digital converter (ADC) architecture. In the process of conversion from analog to digital signals, Quantization and sampling operations are vital and are realized using comparator circuits. The comparator design has a significant role in the design of data converter architecture. Several comparator architectures exist, but StrongARM topology is discussed and implemented in this work due to its negligible static power dissipation and rail to rail output voltages. The proposed novel comparator architecture is designed and simulated in 90nm CMOS process using Cadence Virtuoso tool and operated at supply voltage of VDD=1.5V, a clock frequency of 250MHz. Compared to the previous designs, the energy delay product was reduced by 8% which is an important observation to be observed for use in wireless sensor node applications.

Keywords: Comparator, Double-tail, Kick back noise, Low power, Single-tail, StrongARM.

Introduction

Technological innovations in the current century period have motivated professionals to make electronic gadgets smarter. These advancements are progressing at a brisk pace, facilitating faster changes and increase in computing power. Various technologies such as virtual reality, augmented reality, mobile internet, artificial intelligence, cloud computing, biometric devices, 3D printing machines, genomics, quantum computing, block-chain, industrial automation and robotics. In all these technologies, communications with nearby devices play a major role in its effective functioning. The fourth generation and fifth generation communications evolved to offer reliable and steadfast data transfer globally. At present the usage of high performance electronic gadgets enables high speed and safe access to the internet. The ever increasing demand of lower latency values, better connectivity, stable and high speed data transmission poses stringent requirements for next level high speed communication designs. The above high performance requirements are met by the inclusion of an efficient Analog to Digital Converter (ADC) architecture in the communication transceiver hardware. ADC architectures are essential and omnipresent in all receiver architectures.

ADC transforms a continuing time continuing amplitude voltages to distinct time distinct amplitude voltages and is random. It is a vital integrated circuit in a high performance analog radio frequency integrated circuit system and acts as interface in converting real-time signals to digital signals. It is vitally important that high speed ADC is very much essential for high speed transceiver architectures. The concerned parameter is sampling rate i.e. it specifies how fast the converter architecture is capable of sampling the continuous signal and converting it into discrete signal voltages. The influential modules in the accurate design and analysis of any ADC architectures are High-gain amplifier blocks and comparator circuits.

This is an Open Access article distributed under the terms of the Creative Commons Attribution CC BY license (http://creativecommons.org/licenses/by/4.0/), which permits unrestricted reuse, distribution, and reproduction in any medium, provided the original work is properly cited.

(Received 15th October 2023; Accepted 01st January 2024; Published 30th January 2024)

Comparator circuit is otherwise called as Single-bit digital circuit. The selection and use of CMOS comparator circuit in the design of ADC architecture is crucial as it is mainly responsible in achieving the target specifications such as accuracy, speed, reduction of kickback noise and low power dissipation. Other specification include such as input referred noise, offset and hysteresis voltages. Several comparator architectures are available in the previous works such as Two-stage, Open-loop, Push-pull, comparator driving large capacitive loads, Singe-tail, Double-tail, Triple-tail latch, Switched capacitor comparator, StrongARM comparator, Regenerative comparators, Fully-differential two and three stage latch comparators, and high speed comparator circuits comprising of cascaded preamplifiers, latches and output driver circuits. Circuit designers often trade-off with different specifications and prefer double-tail comparators for use in high speed data converter circuits. In general a comparator circuit is implemented by a differential pair consisting of P-channel and N-channel metal oxide semiconductor transistors (MOS) followed by an active load stage, decision stage and an amplifying stage. For high speed circuits additional amplification stage may be added to the circuit. Figure 1, shows the different stages in a typical comparator circuit.

A comparator circuit compares two signal voltages (given input voltage with a standard reference voltage) and outputs a discrete value i.e. logic high or logic low. It can also be used to compare a signal whether it is above zero or below zero voltage. The input pre-amplifier circuit stage consists of a differential pair with active loads. This stage provides sufficient amplification before it is fed at the output stage.

Another important function of this stage is to reduce the inherent kick-back voltage generated by the decision stage. The decision module or latch module is the core section of the comparator circuit. Some amount of hysteresis is included in the circuit to reduce the small levels of noise occurring at the input side of the circuit. This stage determines which of the input signal voltage is larger and amplifies the difference of both the input voltages. The circuit should also be capable of distinguishing input signal voltages lying in the range between microvolts to millivolts. The gain of the circuit should be higher so as to provide positive feedback in the circuit. The final stage also known as post-amplification stage is necessary to avoid the loading effect of the next following stages. It generally includes an inverter circuit preceded by a self-biased input differential stage and the output voltage should not suffer from slew rate restrictions.

The original StrongARM latch configuration for a 0.512MB high-speed static RAM circuit at Toshiba corporation (1). It includes a low powered current controlled latch sense amplifier for memory and interface circuits and the simulation results demonstrate the access time (pico-seconds) is minimized. The StrongARM comparator circuit is a familiar and extensively used topology in data converter architectures and flip-flop circuits for various high speed and low power transceiver circuits (2). It is a unique and robust circuit with features such as high sensitivity, offers rail-to-rail output voltage, very high input impedance for time varying signals, low input referred offset voltage arising due to only one differential pair and virtually no static power dissipation (3).

The design of a pre-amplifier based dynamic bias latch type comparator under 0.065 micrometer technology and compares the design with a double-tail latch type comparator circuit is described in (4). The simulated results validate that the proposed work i.e. pre-amplifier based dynamic bias latch type comparator draws less power and a medium level reduction in input referred noise voltage than a double tail circuit architecture. A low powered double tail comparator architecture design with systematic expressions is presented in (5). Additional transistors in between the stages enhance the positive feedback of the circuit and thereby increase the speed of operation of the circuit. The simulation results in 180nm CMOS process technology exhibits a power consumption of 1.4mW, operated at a clock frequency of 2.5GHz with V_{DD}=1.2V. Two novel circuit schemes to reduce the kick back noise (i.e. voltage deviations in the circuit nodes are feedback to the input side to generate unstable voltages at the output node) were presented in (6). Simulation results confirm the minimization of kick back noise present in the comparator circuit. To compensate for offset voltages and lower noise, the design presented in (7) discusses modified strongArm latch circuit

parameters, whereby the noise bandwidth and input-referred offset voltage is reduced. An enhanced strongARM latch architecture based on forward body biasing method is mentioned in (8). This proposed method is simulated in 0.065 micrometer CMOS process and is based on the clock fine-tuning of the threshold voltage (V_T) of the cross-coupled NMOS transistors. A parallel path based strongARM latch comparator circuit implemented in 0.065 micrometer CMOS process in described in (9). The technique is implemented by inserting parallel paths to the output side of the circuit. Simulated results prove that the propagation delay decreases by 50% compared to the previous methods. The implementation of conventional and modified StrongARM Latch architectures is discussed in detail in (10). The presented work provides the importance of the StrongARM latch topology for various applications. A high speed double-tail comparator circuit with less variation levels in common mode voltages are presented in (11). The cascaded transistors reduce the kick-back noise also in this method under power supply voltage levels. The analysis of the effects of common mode voltage with respect to offset voltage, power consumption, noise and propagation delay in comparator architecture is presented in (12). The comparator architecture has been implemented in an energy efficient successive approximation register analog to digital converter architecture. A novel strongARM latch circuit design simulated in 0.065 micrometer CMOS process is described in (13). The proposed technique offers a latching speed of sixteen percentage compared to the other works as reported in the paper. The design and simulation of high speed dynamic bias comparator architecture for use in a second order sigma delta architecture is presented in (14). The aspect ratios of the input differential stage are modified to achieve the higher gains which resulted in the operating speed of the comparator circuit. The design and analysis (transient and noise) of a pseudo-differential dynamic comparator is carried out in 90nm CMOS process technology (15). Two calibration methods such as load capacitance and bypass current are discussed along with its process, voltage and temperature (PVT) variations. The strongARM latch design architecture using auxiliary pair reported in (16) discusses the design equations to optimize the various parameters such as offset voltage, input-referred noise voltage and decision time in detail. The rest of the paper is organized as follows: Section-2 discusses about the proposed modified strongARM comparator architecture along with its working details, while Section-3 provides the simulated results and its discussion. Lastly Section-4 presents the conclusions of the proposed work.

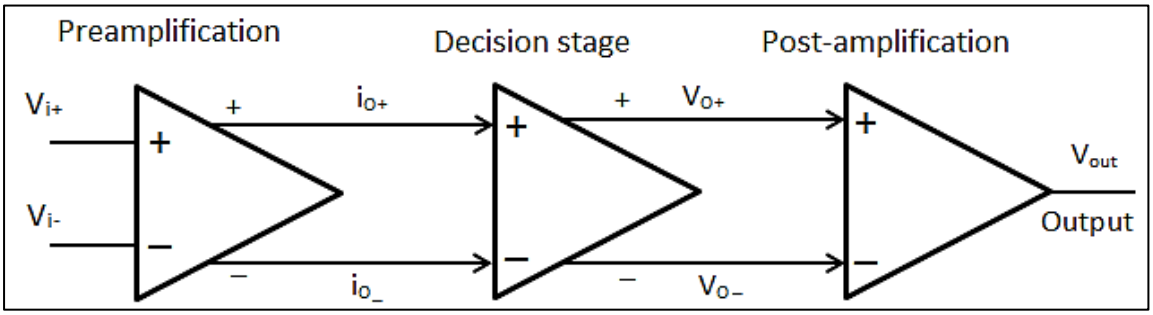

Figure 1: Inner blocks of a Comparator circuit

Materials and Methods

The proposed modified StrongARM comparator circuit shown in Figure 2 operates in different phases namely reset, amplification and regeneration. The circuit consists of MOS switches M_{S1}, M_{S2}, M_{S3} and M_{S4}, a differential pair with a clock source (V_{CK}) and triple cross-coupled differential pairs (M_1 & M_2), (M_3 & M_4) and (M_5 & M_6). The tail transistor is driven with a clock source. The differential output voltage is taken at the drain nodes of M_5, M_6, M_7 and M_8. Correspondingly, the voltage at these nodes is designated as V_A and V_B. The main feature of this proposed StrongARM configuration is that it delivers rail-to-rail output voltages at nodes A and B.

The circuit responds to difference in the input voltages (V_{i1}-V_{i2}). In the first phase when the clock voltage is low i.e. V_{CK}=low, then the transistors M_1 and M_2 are off and accordingly the internal capacitances at nodes A, B, X and Y are precharged to the supply voltage V_{DD} through the MOS switches M_{S1}, M_{S2}, M_{S3} and M_{S4}.The next stage is the amplification phase, which gets initiated, when the clock voltage is high i.e. V_{CK}=high. With these connections, the MOS switches M_{S1}, M_{S2}, M_{S3} and M_{S4} are off and the charged voltage gets discharged through M_7, while M_1 and M_2 are conducting. Transistors M_1 and M_2 are biased by a constant common mode voltage (V_{CM}). When there is a small difference in differential currents applied at M_1 and M_2 due to minute differences in (V_{i1}-V_{i2}), then the capacitances at the nodes X and Y are discharged at marginally different discharging rates.

When voltages at X and Y drop to (V_{DD}-V_{tn}), transistors M_5 and M_6 turn ON. In this phase, the voltage |V_X-V_Y| increases and certainly beyond (V_{i1}-V_{i2}). Hence in this stage, voltage amplification is achieved. Assuming $g_{m\,1,2}$ as the transconductance of the input transistors M_1 and M_2, the voltage difference is written as

$$|V_X - V_Y| = \left(\frac{g_{m\,1,2}\,(v_{i1}-v_{i2})}{C_{X,Y}}\right) * t \quad [1]$$

The voltage gain in this phase is given by

$$A_V = \frac{g_{m\,1,2,3,4} * V_{tn}}{I_m} \quad [2]$$

When the available voltage at nodes A or B reduces to the difference between the power supply voltage and threshold voltage of the p-type MOS transistor, due to this transistors M_7 or M_8 will be switched on to conduct, while the transistors M_5, M_6, M_3, M_4 remain in off state. Due to this operation, the voltage at nodes A or B reach either V_{DD} or logic low or vice-versa. The offset voltage is minimized by reducing the precharge operation of the MOS switches M_{S1}, M_{S2}, M_{S3} and M_{S4}.

Results and Discussions

The design and simulation of the proposed strongARM comparator circuit is carried out in 90nm CMOS process and the simulated transient analysis waveforms obtained at node 'A', Node 'B' and clock signal are displayed in Figure 3. The waveform consists of reset phase, amplification phase and regeneration phase. When the input differential voltage becomes more than or equal to 0.005V, then the comparator output produces a rail-to-rail swing voltage at the output side. The inherent clock feed through problem becomes negligible in both reset and amplification phases. In this proposed design, the amplification phase and regeneration phases operate slower than the reset phase time-periods.

The simulated graphs related to the propagation delay (ps) versus differential input voltage are presented in Figure 4. The results illustrate that the proposed comparator circuit operates at lesser delay and correspondingly at higher speeds. The graphs illustrate that as the difference voltage (V_{i1}-V_{i2}) increases; there is a matching increase in operating speeds.

The simulated graphs related to the energy consumption (fJ) versus differential input voltage are displayed in Figure 5. The results illustrate that the proposed comparator circuit operates at reduced power levels. The graphs confirm that as the difference voltage (V_{i1}-V_{i2}) increases, there is a corresponding decrease in energy consumption levels. Table 1, presents the obtained values of propagation delay (ps) versus differential input voltage (v), while Table 2, shows the energy consumption versus differential input voltage (v). Figure 6, presents the simulated common mode voltage versus energy delay product. Figure 7, displays the simulated input referred noise voltage versus overdrive voltage which indicates as the difference between the gate to source voltage and threshold voltage increases, correspondingly the input referred noise voltage varies linearly within acceptable limits.

A large value of $^{g_m}/_{I_D}$ is very much essential for enhancing the noise performance of the proposed strongARM comparator circuit. With increasing values of overdrive voltages, $^{g_m}/_{I_D}$ decreases, thereby reducing the input referred noise voltage. The simulated graph results between $^{g_m}/_{I_D}$ and overdrive voltage is presented in Figure 8. The simulated offset voltage curve variation with respect to varying common mode voltages is presented in Figure 9.

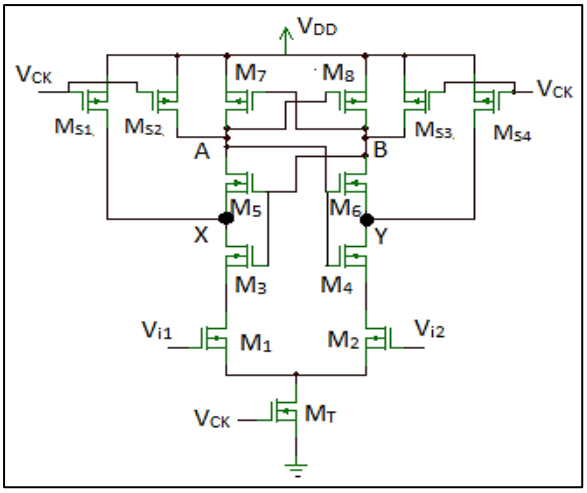

Figure 2: Proposed StrongARM comparator circuit

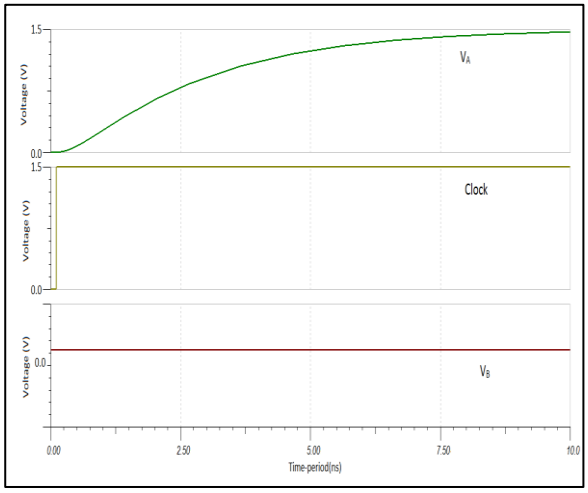

Figure 3: Simulated transient analysis wave forms

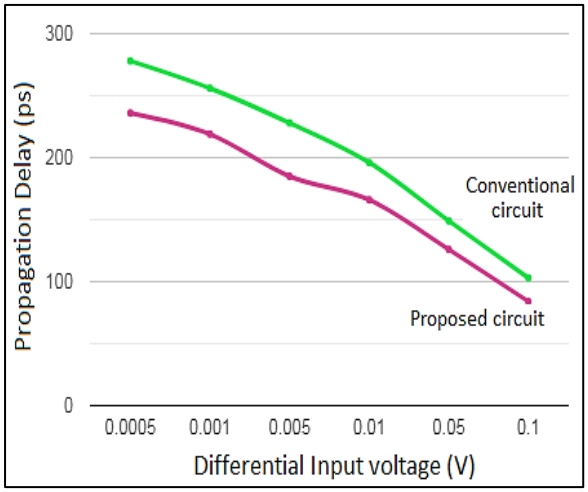

Figure 4: Simulated propagation delay versus differential input voltage

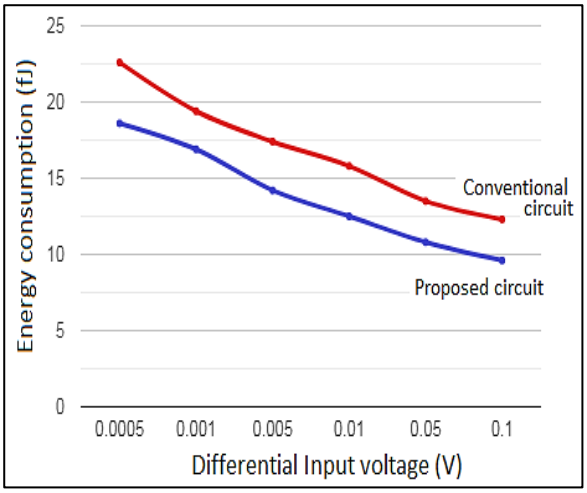

Figure 5: Simulated energy consumption versus differential input voltage

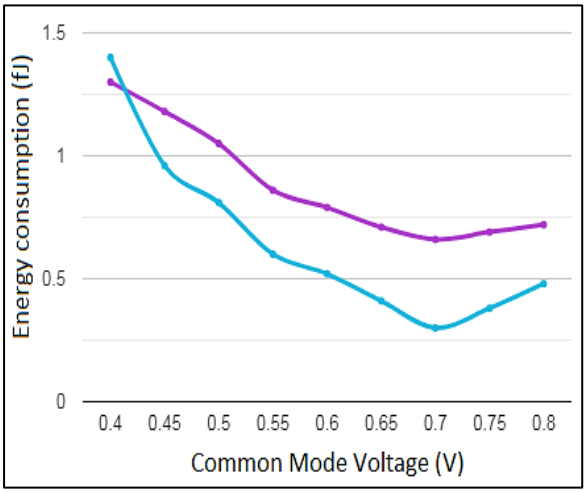

Figure 6: Simulated energy consumption versus common mode voltage

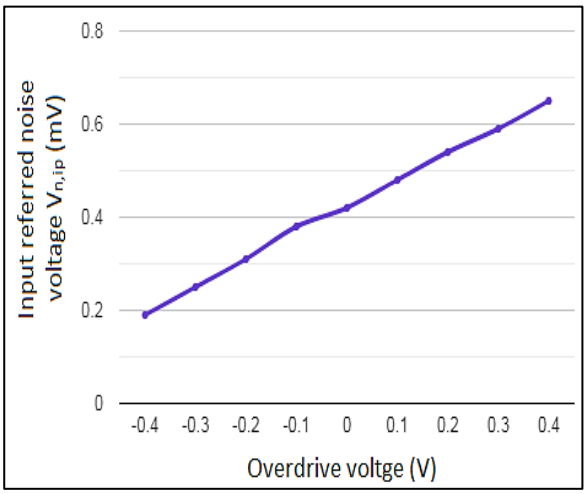

Figure 7: Simulated input referred noise voltage versus overdrive voltage

Table 1: Simulated values of Propagation delay

Differential Input voltage (V)	Propagation Delay (ps)	
	Conventional	**Proposed**
0.0005	278	236
0.001	256	219
0.005	228	185
0.01	196	166
0.05	149	126
0.1	103	84

Table 2: Simulated values of Energy consumption

Differential Input voltage (V)	Energy consumption (fJ)	
	Conventional	**Proposed**
0.0005	22.6	18.6
0.001	19.4	16.9
0.005	17.4	14.2
0.01	15.8	12.5
0.05	13.5	10.8
0.1	12.3	9.6

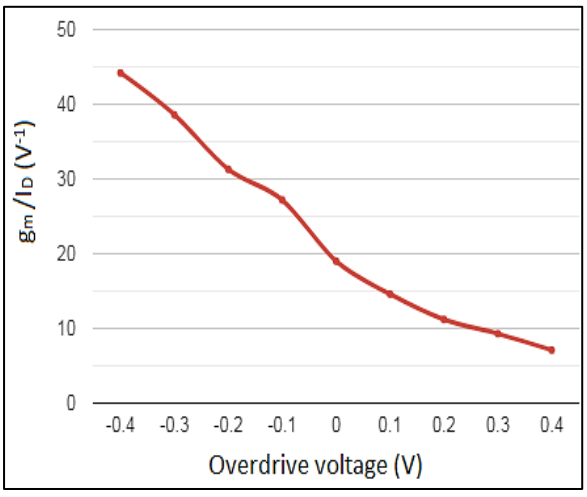

Figure 8: Simulated $\left({g_m}/{I_D}\right)$ and overdrive voltage

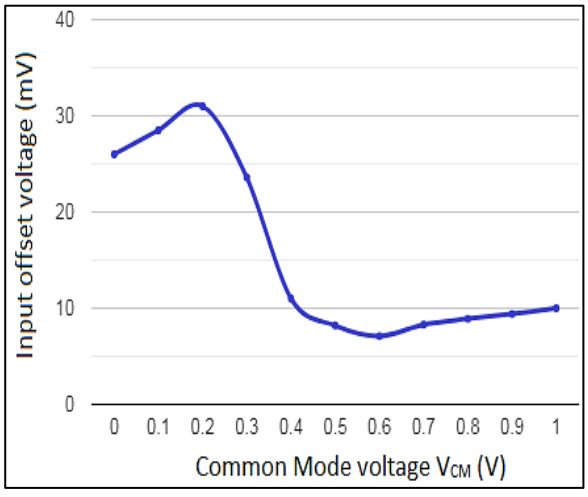

Figure 9: Simulated input offset voltage versus common mode voltage

Conclusions

In this proposed paper a modified novel strongARM latch circuit is designed and implemented for low power data converter architectures. The preamplification and primary decision operations are carried by a single stage strongARM latch circuit. The architecture shown here provides a very low overhead result to reduce the energy consumption. The performance of the comparator can be enhanced for a given common-mode voltage by varying the aspect ratios of the input differential stage and the tail transistor. The proposed comparator circuit is designed and simulated in 90nm CMOS process using Cadence Virtuoso tool and operated at supply voltage of VDD=1.5V, a clock frequency of 250MHz. Simulation results demonstrate that the propagation delay is reduced by approximately 7%, energy consumption slightly decreases by 4% and overall energy delay product decreases by 8% when compared to the previous designs. Consequently, the applications that demand low power operation, such as internet of things (IoT) nodes or monitoring of wireless sensor nodes, the proposed strongARM latch comparator circuit would be an interesting choice for such remote applications.

Abbreviations

Nil

Acknowledgement

Nil

Authorship contribution

K. Lokesh Krishna: Conceptualization, Methodology, Software, Data curation, Writing – original draft, D. Srinivasulu Reddy: Visualization, Investigation, Supervision, Software, T. Chandra Sekhar Rao: Validation, Writing – review & editing.

Conflict of interest

The authors declare that they have no known competing financial interests or personal relationships that could have appeared to influence the work reported in this paper.

Ethics approval

The research does not involve human participants.

Funding for the study

The author(s) received no financial support for the research, authorship, and/or publication of this article.

References

1. Kobayashi T, Nogami K, Shirotori T and Fujimoto Y. A current-controlled latch sense amplifier and a static power-saving input buffer for low-power architecture. IEEE Journal of Sol St Ckts. 1993; 28(4):523-527.
2. Allen PE and Holberg DR. CMOS Analog Circuit Design. 3rd ed. Newdelhi: Oxford University Press; 2018.
3. Razavi B. Design of Analog CMOS Integrated Circuits. 2nd ed. Newdelhi: McGraw Hill (MGH)-Science/Engineering; 2017.
4. Bindra HS, Lokin CE, Annema AJ and Nauta B. A 30fJ/comparison dynamic bias comparator. ESSCIRC 2017 - 43rd IEEE European Solid State Circuits Conference, Leuven, Belgium, 2017; 43:71-74.
5. Babayan-Mashhadi S and Lotfi R. Analysis and Design of a Low-Voltage Low-Power Double-Tail Comparator. IEEE Trans. on Ver Lar Sc Integ Sys. 2014; 22(2): 343-352.
6. Figueiredo PM and Vital JC. Kickback noise reduction techniques for CMOS latched comparators. IEEE Trans. on Circ and Sys.-II: Expr Bri. 2006; 53(7): 541-545.
7. Xu H and Abidi AA. Analysis and Design of Regenerative Comparators for Low Offset and Noise. IEEE Trans on Cir and Sys.- I: Regular Papers. 2019; 66(8):2817-2830.
8. Alshehri A, Al-Qadasi M, Almansouri AS, Al-Attar T and Fariborzi H. StrongARM Latch Comparator Performance Enhancement by Implementing Clocked Forward Body Biasing. 25th IEEE International Conference on Electronics, Circuits and Systems (ICECS); 2018 July 2; Bordeaux, France; IEEE; 2018. 229-232.
9. Siddharth RK, Jaya Satyanarayana Y, Nithin Kumar YB, Vasantha MH and Bonizzoni E. A 1-V, 3-GHz Strong-Arm Latch Voltage Comparator for High Speed Applications. IEEE Trans on Cir and Sys II: Exp Bri. 2020; 67(12): 2918-2922.
10. Razavi B. The StrongARM Latch [A Circuit for All Seasons]. IEEE Solid-Sta Cir Mag. 2015; 7(2):12-17.
11. Murshed AM, Krishna KL, Saif MA and Anuradha K. A 10-bit high speed pipelined ADC. 2018 Second International Conference on Inventive Systems and Control (ICISC); 2018 January 19-20; Coimbatore, India: IEEE; 2018. 1253-1258.

12. Chen L, Sanyal A, Ma J, Tang X and Sun N. Comparator common-mode variation effects analysis and its application in SAR ADCs. IEEE Intern. Symp. on Cir. and Sys. (ISCAS); 2016 May 22-25; Montreal, QC, Canada: IEEE; 2016. 2014-2017.
13. Al-Qadasi M, Alshehri A, Almansouri AS, Al-Attar T and Fariborzi H. A High Speed Dynamic StrongARM Latch Comparator. IEEE 61st Intern. Mid-west Symp. on Cir. and Sys. (MWSCAS); 2018 February 28; Windsor, ON, Canada: IEEE; 2018. 540-541.
14. Krishna KL, Ramashri T and Reena D. A 1V second order delta sigma ADC in 130nm CMOS. Inter. Conf. on Inf. Comm. and Emb. Sys. (ICICES); 2014 February 27-28; Chennai, India: IEEE; 2014. 1-5.
15. Daehwa PAIK, Masaya Miyahara, Akira Matsuzawa. An Analysis on a Dynamic Amplifier and Calibration Methods for a Pseudo-Differential Dynamic Comparator. IEICE Trans on Fund of Elec Comm and Comp Sci. 2012; E95.A(2), 456-470.
16. Li S, Xu Z. and Iizuka T. Analysis of strong-arm comparator with auxiliary pair for offset calibration. Analog Integr Circ Sig Process. 2022; 110(3): 535–546.

ScienceDirect

Scientific African

Volume 22, November 2023, e01892

Design and performance analysis of a novel vulture based FOPID controller for the nonlinear biological system

B. Doraswamy [a], K. Lokesh Krishna [b]

Show more

Outline | Share | Cite

https://doi.org/10.1016/j.sciaf.2023.e01892

Get rights and content

Under a Creative Commons license

open access

Highlights

- In this paper, a VbFOPID (Vulture based fractional order proportional integral Derivative) controller has been designed and implemented with the required biological specifications and simulated in the MATLAB environment.
- The biological system parameters with external disturbances are imported to the designed VbFOPID controller and have been designed and optimized to tune to the fitness of the proposed VbFOPID algorithm.
- The proposed algorithm regulates and stabilizes the biological parameters like glucose, insulin, protein and gene expression to the optimized levels.
- Furthermore, the successive score of the designed model was analysed and compared with other previous works in terms of important parameters such as rising time, overshoot, settling time, stability analysis, and error rate.

Loading [MathJax]/jax/output/SVG/fonts/TeX/AMS/Regular/GeneralPunctuation.js

Abstract

In recent times, the field of Automatic Control Systems Engineering engaged in regulating large number of biological processes has played a significant role in biological and biotechnology applications. In human body, the very most important biological parameters are pancreas, insulin, glucose and genetic regulatory network (GRN). Any abnormal change in these biological system parameters may leads to occurrence of severe diseases and finally leads to the death of the infected patient. Thus, to tune the biological parameters in the human body, an efficient optimal controller is essential. Hence, a novel hybrid controller called Vulture based Fractional Order Proportional-Integral-Derivative (VbFOPID) controller is designed and implemented in this paper. The designed controller is implemented in MATLAB platform. From the obtained simulation results and its comparisons with the other existing controller's in the literature, it clearly presents that the proposed VbFOPID controller has superior performance over the other optimal PID controller designs in terms of rise time, convergence time, settling time, error percentage and maximum overshoot.

Previous Next

Keywords

Vulture optimization algorithm; Fractional order proportional integral derivative controller; Optimized tuning; Biological system; Tuning of biological parameters and PID controllers

Introduction and motivation

Highly complex industrial process applications demands accurate automatic process controllers [1]. The function of the automatic controller is to rectify the error between a measured process parameter and desired optimized-value by computing the dissimilarities and then carrying out a remedial action to regulate the accurate process consistently. To achieve the whole accurate control action, controllers operate in three basic modes such as Proportional controllers, Integral controllers and Derivative controllers. To attain accurate control and fine-tuning arrangements, the above controllers are combined to form new controllers such as PI (Proportional Integral), PD (Proportional Derivative) and PID (Proportional Integral Derivative) controllers. Of these PID controller exhibit less overshoot, reduced rise time and settling time, and finally eliminates steady-state error values. These PID controllers uses control loop feedback mechanism to control the process. In industries these PID controllers are used to regulate the parameters such as temperatures, speed, and current flow as well as pressure [2,3]. Derivative controllers are used to monitor the changes caused in the output of the process. Proportional value defines the differences between the set point value and the output value tate error, which occurs in the proportional

Loading [MathJax]/jax/output/SVG/fonts/TeX/AMS/Regular/GeneralPunctuation.js

controller [5]. The p-type controllers used for eliminating the errors and maintain the system as more stable. Commonly the PI controllers are used in control systems for error correction between the set-value and the actual controller value [6].

Regulating the biological parameters is the most required task for the biological application to maintain stability while fine-tuning to conditions that are optimal for survival. Some controllers were designed in past such as PID, PI, sliding mode, etc. But those controllers were not performing well in situations, because of the complexity of the biological parameter data. Usually, the raw data contains huge amount of errors that might degrade the controller performance in controlling biological systems. Hence, the desired controlled outcome is not met. So, the present work has aimed to design a novel optimized Fractional Order Proportional-Integral-Derivative (FOPID) controller for the biological application for regulating the biological parameters. The existing FOPID controller does not provide effective tuning of biological parameters under external disturbances or noise. Therefore, they provide less control rate and accuracy. To improve the control rate and accuracy of the biological system, an optimized controller is necessary. Also, to obtain finest tuning and to make the controller work under external disturbances, a novel Vulture based Fractional Order Proportional Integral Derivative controller is proposed in this paper.

Literature review

A proportional integral sliding mode feedback control plus feed-forward control based on Bouc-Wen inverse model delivering excellent performance is proposed in [7]. The authors [8] propose a differential evolution algorithm-optimized radial basis function neural network PID controller (DE-RBF-PID). Initially an improved differential evolution algorithm searches for the optimal parameters of the PID. In the next step a radial basis function neural network adjusts the various parameters such as convergence time, settling time and reduces maximum overshoots. The design and analysis of a FOPID controller for the activated sludge biological process using relay auto tuning method is described in [9]. The authors in [10] propose a time shifted NN (neural network) predictor united with a PID controller. The technique compensates various operating errors linked with time-lag and non-linear absorption pattern of meal and insulin in closed-loop blood glucose control systems. The design of internal model control based PID controller was recommended for the analysis of unstable second order time delay with RHP zero systems. The technique exhibits improved closed loop performance [11]. A PID controller with improved values of settling time and maximum overshoot for use in robot manipulator application is presented in [12]. These controllers reduce the offset which, are generated by the system. While on systems over damping, controller needs more time for completing an operation and sometimes the systems will be slowed down and these controllers reduce the disturbances in the outputs [13,14]. Michael Chevalier etal. [15] suggested the design and analysis of a proportional-integral-derivative controller with biological molecules. Here the biomolecular implementation based on antithetic motif and properties of the PID controllers for improving the performances of controllers was developed. To control the steady state errors in the PID controllers, S.M.Hossein Mousakazemi [16] have presented the Computational effort comparison of genetic algorithm and particle swarm

Loading [MathJax]/jax/output/SVG/fonts/TeX/AMS/Regular/GeneralPunctuation.js e gains of a pressurized water reactor load.

From the simulation results in their proposed work, the use of particle swarm optimization algorithm achieves the optimum answer with a reduced computational time compared to genetic algorithm, based on number of function evaluations (NFE) index.

G.T. Sekhar et al. [17] developed Sine Cosine Optimization based Proportional Derivative-Proportional Integral Derivative Controller for Frequency Control of Hybrid Power System. For regulating the frequency, Sine Cosine Algorithm (SCA) provides the better stability among PI and PID controllers. Ideally analyzing with SCA algorithms provides better regulation of frequency as well as it removes the steady state errors, however controllers do not increase the accuracy. In order to maintain high accuracy, J.Tao et al. [18] presented the study on a benchmark control problem for real-time hybrid simulation with a tracking error-based adaptive compensator combined with a supplementary proportional-integral-derivative controller. A Real-Time Hybrid Simulation (RTHS) was carried out and the proposed loop controller was proved to be optimal and robust to provide good stability over wide frequency range. A.Chouksey *et al.* [19] suggested fuzzy cognitive network-based maximum power point tracking using a self-tuned adaptive gain scheduled fuzzy PID controller and improved artificial neural network-based particle swarm optimization. Through Maximum Power Point Tracking (MPPT) more power was extracted from PV arrays. By using PID controllers, maximum power flow and rate of power flow was determined. The authors in [27] propose a cascaded proportional integral fractional order PID controller fine-tuned using Gorilla Troops Optimizer algorithm for achieving optimum gains and explored under different conditions such as step load perturbations, random load disturbances, and renewable energy sources variation. The problem of frequency stabilization [28] can be improved using a Fuzzy fractional order proportional integral and Tilt Integral Derivative controller with improved performance related to the parameters such as integral peak overshoot, settling time, mean squared error, maximum undershoot and overshoot. The authors in [29] propose Honey badger algorithm, Gorilla troops optimizer, Chimp optimization algorithm and African vultures optimization algorithm for the design and modeling of an accurate solid oxide fuel cell.

Contributions

The contributions and novelty of the proposed Vulture based Fractional Order Proportional Integral Derivative controller is summarized below:

- A novel VbFOPID (Vulture based Fractional Order Proportional Integral Derivative controller) has been designed with the required parameters and features in the MATLAB environment. Consequently, the biological systems parameters with external noise are imported to the designed controller. Moreover, the given external disturbance has been tuned by the fitness of the proposed vulture based algorithm.
- The proposed algorithm regulates and stabilises the biological parameters like glucose, insulin, protein and gene expression to the desired level.
- Using the proposed algorithm, the successive score of the designed model was analysed portant parameters such as rising time, overshoot, settling time, stability analysis, and error rate.

Loading [MathJax]/jax/output/SVG/fonts/TeX/AMS/Regular/GeneralPunctuation.js

Paper organization

The presented work in this paper is organized as follows; Introduction, Motivation, and Literature review works related to the design of Proportional Integral Derivative controllers in non-linear biological system is explained in Section-1. The structure and algorithm of the proposed novel Vulture based Fractional Order Proportional-Integral-Derivative (VbFOPID) controller along with mathematical expressions is elucidated in Section-2. While Section-3, presents the Simulation results, Comparative analysis and its discussions. Lastly the conclusions along with future scope of the proposed work are provided in Section-4.

Proposed methodology

The main objective of this paper is to develop a novel Vulture based Fractional Order Proportional-Integral-Derivative (VbFOPID) controller for regulating the biological parameters like protein, pancreas, and Genetic Regulatory Network (GRN). Initially, the biological parameter signal data is imported with some disturbances. In this proposed Vulture based Fractional Order Proportional-Integral-Derivative (VbFOPID) controller, the biological parameters along with the external disturbances is controlled by the fitness function of the vulture optimization algorithm. The optimal constraints like, optimal range of biological parameters are fixed to the VbFOPID controller. Then, the controller tunes the biological parameters such as protein and pancreas till it attain its desired level. This process continues till the biological parameters attain its optimal level. Thus, the proposed controller provides finest tuning in biological system. The proposed framework is described in Fig. 1.

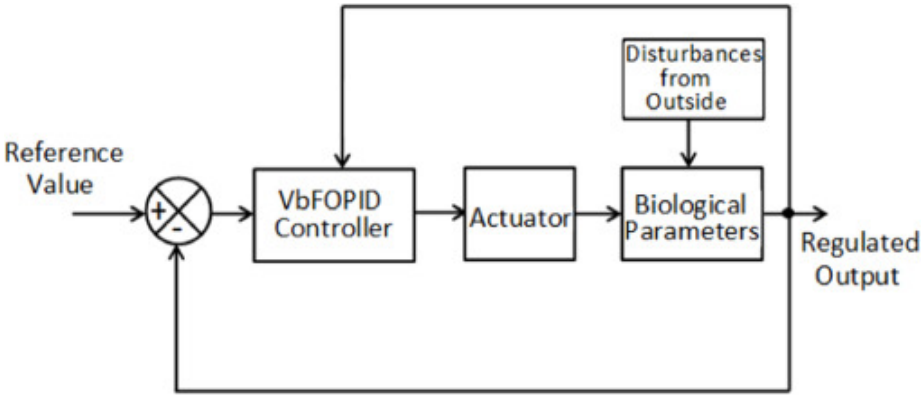

Download: Download high-res image (142KB)

Download: Download full-size image

Fig. 1. Block diagram of the proposed arterial blood pressure regulation.

Biological parameters synthesis

To initialize the tuning process in designed model, the biological parameters from biological system are synthesised. Then, the generated biological parameters are set as the input to the designed controller. ised during biological synthesis.

Loading [MathJax]/jax/output/SVG/fonts/TeX/AMS/Regular/GeneralPunctuation.js

Pancreas synthesis

In human body, the blood sugar level is maintained by pancreatic hormones. In pancreatic synthesis, two different hormones such as glucagon and insulin are synthesised. These two hormones are responsible for blood glucose level (sugar level) in human body [20]. The differential equation for the conversion of insulin and glucose energy is expressed in Eqs.(1) and (2) [4].

$$\frac{d}{dm}G_{Ie}\left(m^{'}\right) = -Q_1\left(G_{bsl} - G_{le}\left(m^{'}\right)\right) - I_{le}\left(m^{'}\right)\ G_{le}\left(m^{'}\right) + G_{il} \tag{1}$$

$$\frac{d}{dm}I_{le}\left(m^{'}\right) = -Q_3\left(P_{le}\left(m^{'}\right) - I_{bsl}\right) - Q_2 I_{le}\left(m^{'}\right) \tag{2}$$

where, $G_{le}\left(m^{'}\right)$ and $I_{le}\left(m^{'}\right)$ indicates the glucose and insulin levels, respectively. The glucose basal level is represented as G_{bsl} and the basal level of insulin is represented as I_{bsl}. The term $P_{le}\left(m^{'}\right)$ indicates the plasma insulin and G_{il} denotes the glucose infusion level. The term Q_1, Q_2 and Q_3 indicates the insulin-independent glucose level, constant loss rate of insulin degradation and insulin independent glucose level over insulin concentration. The steady state condition and glucose infusion quantity are expressed in Eqs.(3) and (4) [6].

$$G_{il} = \frac{Q_3}{Q_2}\left(I_G - I_{bsl}\right)\ P_G - Q_1\left(G_{bsl} - P_G\right) \tag{3}$$

$$\frac{\partial G_{il}}{\partial P_G} = \frac{Q_3}{Q_2}\ \left(I_G - I_{bsl}\right) + Q_1 \tag{4}$$

where, $P_{le}\left(m^{'}\right) = I_G$ and $G_{le}\left(m^{'}\right) = P_G$. However, the glucose level in body is controlled within the optimal range with the help of an effective controller.

Protein synthesis

In biological system, protein synthesis refers to the generation of protein molecules in the body. Generally, this process takes place inside the cell and it involves translation, transcription and synthesis of amino acids. In this process, the amino acids are connected by the ribonucleic acid (tRNA) inside the cell and then it passes the amino acids to the ribosome [21]. In biological system, proteins are the sequence of amino acids. At moment $m^{'}$, protein synthesis is obtained based on the concentration of ribonucleic acid $c_r\left(m^{'}\right)$, enzymes $c_e\left(m^{'}\right)$ and operator $c_o\left(m^{'}\right)$. The differential equation for the concentration of ribonucleic acid, enzymes and operator are expressed in Eqs.(5), (6) and (7) [2].

$$\frac{d}{dm}\ c_r\ \left(m^{'}\right) = \frac{p}{i + jc_0\left(m^{'}\right)} - qc_r\left(m^{'}\right) \tag{5}$$

$$\frac{d}{dm}c_e\ \left(m^{'}\right) = Cc_r\left(m^{'}\right) - sc_e\left(m^{'}\right) \tag{6}$$

$$\frac{d}{dm}c_0\ \left(m^{'}\right) = \lambda c_c\left(m^{'}\right) - \mu c_r\left(m^{'}\right) \tag{7}$$

where, guanine is denoted as p, j and i indicate adenine and uracil, respectively. C represents the catalytic RNA molecule, q indicates cytosine, the enzyme-substrate is denotes as s, μ and λ denotes the translation and transcription of system operator of protein, respectively.

Loading [MathJax]/jax/output/SVG/fonts/TeX/AMS/Regular/GeneralPunctuation.js

GRN model

Genetic Regulatory Network (GRN) is the sequence of gene or a portion of gene, which communicate with each other to regulate certain specific functions in the human body. GRN regulate different cellular functions and development by controlling the gene expression. The gene expression contains mRNAs and proteins. By time interruption, GRN hold m genes of individual gene regulatory hereditary system ($H^{'n}$), which is represented in Eqs.(8) and (9) [2].

$$\dot{r}(t) = -D_r r(t) + a\left(p\left(t,\tau_p\right)\right) \tag{8}$$

$$\dot{p}(t) = -D_p p\left(t^{'}\right) + b\left(r\left(t,\tau_r\right)\right) \tag{9}$$

where, $r = \left(r_1 \ldots . r_n\right) \in H^{'n}$ indicates the concentration of mRNAs and $p = \left(p_1 \ldots . p_n\right) \in H^{'n}$ refers to the concentration of protein at time t. The diagonal matrices are represented as D_r and D_p, which reduces the rate of mRNAs and protein. The vectors denoting the time delay of protein and mRNAs are represented as τ_p and τ_r, respectively. Also, a and b indicates the nonlinearity.

Controller design

Fractional Order PID controller (FOPID) is the extension of traditional PID controller based on fractional calculus. FOPID controllers are widely used in tuning biological system, as their accuracy and tuning rate are high. These controllers contain fractional differential and integral derivatives with real power value [22]. When compared to integral designs, the fractional order designs are highly robust as they are based on real time process. The fundamental operator of FOPID controller is expressed as in Eq.(10) [6].

$${}_pD_{t^{'}}^{\alpha} = \begin{cases} \frac{d^{\alpha}}{dt^{'\alpha}} & ;\ \alpha > 0 \\ 1 & ;\ \alpha = 0 \\ \int_p^{t^{'}} (d\tau)^{\alpha} & ;\ \alpha < 0 \end{cases} \tag{10}$$

Where, the boundaries of the fundamental operator are p and $t^{'}$ and $\alpha \in R$, α is the real number. For continuous fraction equation, there are different statements for general fractional integral differential function. Among those statements, Riemann-Liouville definition is better. The integral and differential equation with fractional order is represented in Eq.(11) [4].

$${}_pD_{t^{'}}^{\alpha} f\left(t^{'}\right) = \frac{d^m}{dt^{'m}}\left[{}_pD_{t^{'}}^{-(m-\alpha)} f\left(t^{'}\right)\right] = \frac{1}{\Gamma(m-\alpha)}\frac{d^m}{dt^{'m}}\left[\int_p^{t^{'}} \frac{f(\tau)}{\left(t^{'}-\tau\right)^{\alpha-m+1}} d\tau\right] \tag{11}$$

where, ${}_pD_{t^{'}}^{\alpha} f\left(t^{'}\right)$ indicates the differential function of Fractional order controller, $\Gamma\left(m-\alpha\right)$ epresents the differential function, which is expressed in Eq.(12) [2].

$$\Gamma\left(m-\alpha\right) = \int_0^{\infty} v^{m-1} e^{-v} dv \tag{12}$$

$\leq m$. The Laplace transform for fractional order controller is expressed in Eq.(13) [4].

Loading [MathJax]/jax/output/SVG/fonts/TeX/AMS/Regular/GeneralPunctuation.js

$$L\left[D^{\alpha}f\left(t^{'}\right)\right] = y^{\alpha}F\left(S\right) - \sum_{i=0}^{m-1} y^{p}\left[D^{\alpha-i-1}f\left(t^{'}\right)\right]_{t^{'}=0} \quad (13)$$

The Laplace transform is $F\left(S\right) = L\left[f\left(t^{'}\right)\right]$ for $m-1 < \alpha < m$. Moreover, in FOPID controller, function of the fractional order controller is applied to the PID controller. The transfer function for FOPID controller is expressed in Eq.(14) [6].

$$T_f\left(S\right) = \frac{Y(S)}{X(S)} = K^{'}_{p} + K^{'}_{i}S^{-\lambda} + K^{'}_{d}S^{\mu} \quad (14)$$

Where $K^{'}_{i}$ $K^{'}_{p}$ and $K^{'}_{d}$ indicates the integral constant, proportional gain constant, and derivative constant, respectively. The term ν and μ indicates real numbers of integration and differentiation. The controller equation for FOPID controller is expressed as in Eq.(15) [6].

$$U^{*}\left(t^{'}\right) = K^{'}_{p}e_r\left(t^{'}\right) + K^{''}_{i}D^{-\lambda}e_r\left(t^{'}\right) + K^{'}_{d}S^{\mu}e_r\left(t^{'}\right) \quad (15)$$

Where, $e_r\left(t^{'}\right)$ refers to the error function, which is evaluated as $e_r\left(t^{'}\right) = Y_{dr}\left(t^{'}\right) - Y_a\left(t^{'}\right)$. The actual range and desired range of the system is denoted as $Y_a\left(t^{'}\right)$ and $Y_{dr}\left(t^{'}\right)$, respectively. In addition, the controller parameters like integral constant, proportional constant, and derivative constant are tuned by the finest-tuning approach.

VbFOPID controller design

A novel Vulture based Fractional Order Proportional-Integral-Derivative (VbFOPID) controller is used to tune the biological parameters in the system. It is a hybrid controller, which is the combination of vulture optimization and Fractional Order PID controller. In proposed controller, the biological parameters like GRN, protein and pancreas are taken as the input. These input parameters are imported to the system along with disturbances (Noise). The main objective of the designed controller is to reduce the external noise and tune the biological parameters till it attains the optimal range. Vulture optimization is a nature based meta-heuristic algorithm [23]. In vulture optimization algorithm, the vulture population get initialized. Similarly, the biological parameters such as protein parameter P_t, pancreas P_n and GRN G are initialized. After initializing the input parameters, the fitness function of each parameters are calculated. The optimal fitness function of protein is expressed in Eq.(16).

$$F^{*}\left(P_t\right) = \begin{cases} 1 & ; \ if \ 0.8 \geq P_t \geq 1.3 \\ 0; & if \ 0.8 < P_t \ or \ P_t > 1.3 \end{cases} \quad (16)$$

Where, $F^{*}\left(P_t\right)$ is the fitness function for protein and P_t indicates the protein parameter. The optimal range of protein in human body is 0.8 to 1.3 g/ per kg. If the input protein parameter is within the optimal range, then the fitness function returns 1. Otherwise, the fitness function return zero. If the fitness function returns 1, the signal is already in optimal range. Hence no optimization / tuning are required. If the fitness function returns 0, then the input parameters must be tuned to its optimal range. In pancreas, the optimal fitness function is obtained for both glucose and insulin. The optimal fitness function for glucose is expressed in Eq.(17).

$$F^{*}\left(G_u\right) = \begin{cases} 1 & ; \ if \ 100 \geq G_u \geq 120 \\ 0; & if \ 100 < G_u \ or \ G_u > 120 \end{cases} \quad (17)$$

Loading [MathJax]/jax/output/SVG/fonts/TeX/AMS/Regular/GeneralPunctuation.js

where, $F^*(G_u)$ indicates the fitness function of glucose and G_u is the glucose parameter. The optimal range of glucose ranges from 100 to 120 mg/dL. If the input glucose level is within the optimal range, then the fitness function returns 1. If the glucose level is greater than or less than optimal range means, the fitness function returns 0. Similarly, the fitness function for insulin is calculated for its optimal range. The optimal range of insulin is 1 to 2.5 mg/min. Similarly, the fitness function for insulin and gene expression can be obtained.

After calculating the fitness function, the gain parameters get initialized. If the biological parameters are not in optimal range, the biological parameters must be tuned to its optimal range. To tune the biological parameters to the desired level, the optimal fitness function is fixed to the controller function of FOPID controller. The tuning equation for the protein is expressed in Eq.(16).

$$R_{(P_t)} = P_t \times \left(\frac{K'_p \times K'_i}{2\Pi}\right) \times K'_d \tag{18}$$

Where, $R_{(P_t)}$ defines the tuning rate of protein. Similar to protein the biological parameters like glucose, insulin and gene expression are tuned in the controller. To obtain the finest gain, the gain parameters are tuned to its desired level. The equation for finest tuning of biological parameters is expressed in Eq.(19).

$$R^*_{(P_t, P_n, G)} = \left[0.01 \times \frac{\Delta K'_p \times \Delta K'_i}{\left|\Delta K'_d\right|}\right] \tag{19}$$

where, R^* denotes the finest tuning rate. The gain parameters of the controller are tuned till it reaches the finest gain. The controller function not only tunes the gain parameters, but also, it minimizes the external error signal (noise).

Inside the controller, the error signals are considered as inputs and the tuned parameters $\Delta K'_p$, $\Delta K'_i$ and $\Delta K'_d$ are considered as output from the controller. Thus, the designed controller provides finest tuning and minimum error rate. The step by step processes for tuning the biological parameters are illustrated in Algorithm 1.

Algorithm 1. VbFOPID.

Start

{

Parameter_ initialization ()

{

int P_t, G, P_n;

// Initializing the biological parameters

//Here P_t **represents protein level,** G **denotes Genetic regulatory network and** P_n **indicates pancreas parameter**

Loading [MathJax]/jax/output/SVG/fonts/TeX/AMS/Regular/GeneralPunctuation.js

}

Optimal_ Fitness()

{

$$F^{*}_{(P_t,G,P_n)} = \begin{cases} 1 & ; if\ O_R \geq B(i) \leq O_R \\ 0 & ; if\ B(i) > O_R\ or\ B(i) < O_R \end{cases}$$

// $F^{*}_{(P_t,G,P_n)}$ indicates the optimal function of biological parameters, O_R denotes the optimal range, and $B(i)$ indicates the biological inputs

}

Tuning_ Biological parameters()

{

$$R_{(P_t,P_n,G)} = {}_{(P_t,P_n,G)} \times \left(\frac{K'_p \times K'_i}{2\Pi}\right) \times K'_d$$

// K'_p, K'_i and K'_d are gain parameters, R is the tuning rate

}

Controller_ function ()

{

$$U^{*}(t') = \Delta K'_p e_r(t') + \Delta K'_i D^{-\lambda} e_r(t') + \Delta K'_d S^{\mu} e_r(t')$$

// $\Delta K'_p$, $\Delta K'_i$ and $\Delta K'_d$ are the tuned gain parameters

}

}

Stop

The flowchart of the designed (VbFOPID) controller is illustrated in Fig.2. Initially, the biological parameters are imported to the controller along with the disturbances. Then, the error signals are minimized by the controller function and also the biological parameters are tuned to its optimal range in accordance with the optimal fitness constraints. Once the finest gain is attained, the process terminates. Thus, the designed controller minimizes the error and tunes the biological parameters.

Loading [MathJax]/jax/output/SVG/fonts/TeX/AMS/Regular/GeneralPunctuation.js

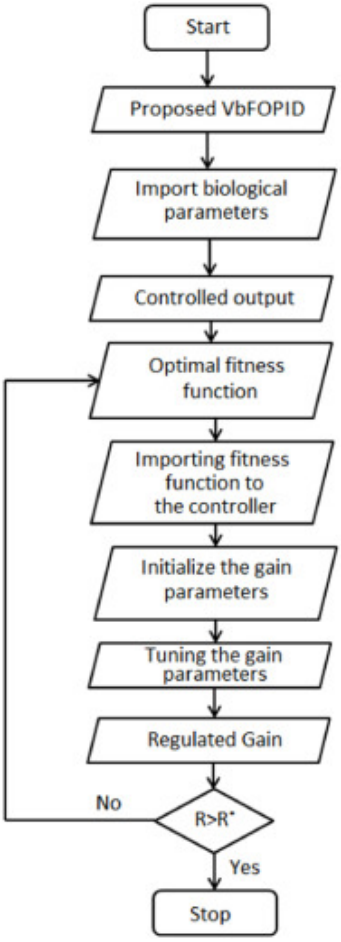

Download: Download high-res image (204KB)

Download: Download full-size image

Fig. 2. Flowchart of VbFOPID.

Result and discussion

In this work, a novel VbFOPID controller is designed to regulate and tune the bio-signals under noise. The presented controller has been developed and simulated in MATLAB environment.

Case study

For case study validation, three different biological parameters such as glucose, protein and insulin are considered. The major objective of the designed controller is to regulate and tune these biological parameters to its optimal range. In designed controller, the bio-signals are tuned to its optimal range. The optimal constraints are fixed to the function of the controller. In accordance with the optimal fitness constraints, the controller tunes the biological parameters. If the input bio-signals are below or above the desired level, the designed controller tunes it to its optimal level. The regulation of biological parameters is illustrated in three different cases as 1) Regulation of glucose 2) Regulation of insulin and 3) Regulation of protein.

Loading [MathJax]/jax/output/SVG/fonts/TeX/AMS/Regular/GeneralPunctuation.js

Case 1: Regulation of Glucose

In human body, glucose is one of the hormones segregated by pancreas. Normally, pancreas segregates two major hormones namely, insulin and glucose to maintain optimum sugar level in the blood. In human body, the insulin level and glucose level are contrast with each other. If the insulin level is low in body, the blood glucose (sugar) level is high and vice versa. The optimal range of glucose in the blood is 100 to 120mg/dL. Fig.3, presents the simulated results before and after optimization of glucose level.

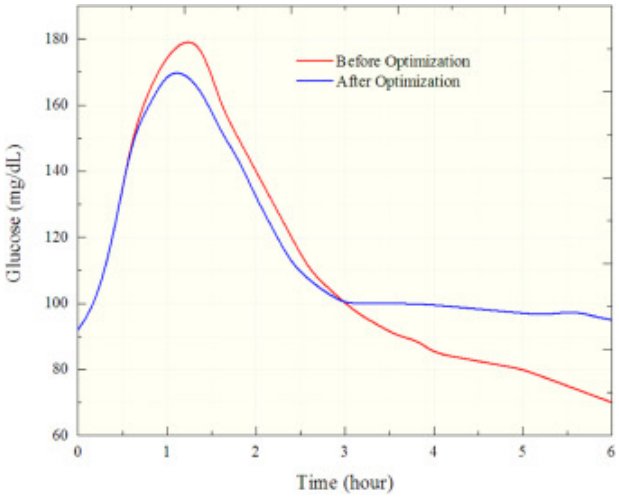

Download: Download high-res image (176KB)

Download: Download full-size image

Fig. 3. Glucose level before and after optimization.

Here, the glucose level in blood is estimated for time (after having meal). Initially, before having meal the glucose level in blood is below 100mg/dL. Immediately after meal, the glucose in blood gets increased to 180mg/dL. Then, after certain time (2h) the glucose level gets within the normal range. However, in case of diabetic patients after 2h of meal the glucose level in blood either gets increases beyond 120mg/dL or decreases below 100mg/dL. Here, in before optimization the glucose level in blood drops to 70mg/dL after 2h of meal. But, after optimization the glucose level in blood is optimized and maintained at optimal range of 100mg/dL by the designed controller.

Case 2: Regulation of Insulin

The insulin level in human body is maintained by pancreas. In order to control and maintain optimal sugar level in blood, insulin hormones are segregated by pancreas. Normally, the sugar level in blood increase, if the glucose content in blood increases. To optimize the sugar level, the pancreas produces insulin. Fig.4, presents the level of insulin in blood before and after optimization.

Loading [MathJax]/jax/output/SVG/fonts/TeX/AMS/Regular/GeneralPunctuation.js

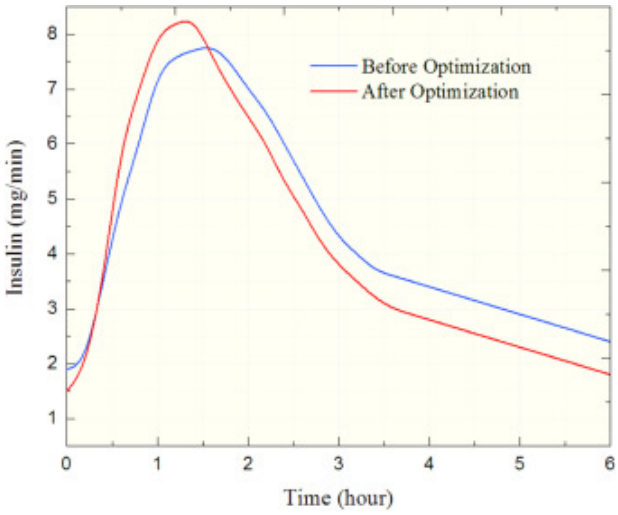

Download: Download high-res image (190KB)

Download: Download full-size image

Fig. 4. Insulin level before and after optimization.

The optimal range of insulin in blood is 1 to 2.5 mg/min. Generally, the insulin level rises after meal. Here, the insulin content in blood is determined after meal. In initial stage, the insulin content is 2 mg/min. After meal, the insulin content gets increased. But for normal person, after 2 h the insulin level retains to its optimal range. But, for diabetic patients the insulin level is high / not within the optimal range. In such cases, the designed controller tunes the insulin level to its optimal range.

Case 1: Regulation of Protein

Proteins are generated in human body by liver. Proteins are present in every cell and it is chain of amino acids. A protein in human body helps in repairing as well as building tissues, oxygenating the body parts and also helps in digestion process. So, the protein level must be maintained in optimal range for the proper functioning of human body. Fig. 5, displays the protein level before and after optimization. The optimal range of protein is 0.8 to 1.3 g/kg.

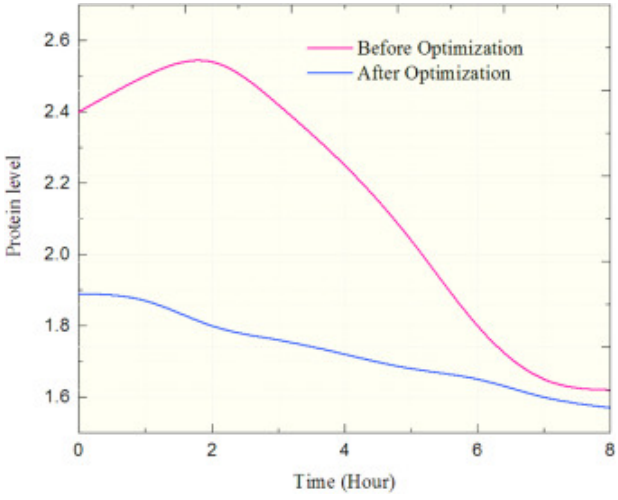

Loading [MathJax]/jax/output/SVG/fonts/TeX/AMS/Regular/GeneralPunctuation.js

Download: Download full-size image

Fig. 5. Protein level before and after optimization.

Here, the protein level is estimated after having meal. After meal, the protein content in human body is high. After 2 h, the protein level gets decreases. The designed controller tunes and regulates the protein level in human body to its optimal range. Before optimization, the protein in human body is greater than optimal range. The designed controller tunes the protein till it attains its desired/ optimal range.

Sensitivity and stability analysis

In a biological system, the transfer function of the controller is expressed in Eq.(20).

$$H(s) = \frac{s^2 + s + 5}{s^3 + 8s^2 + 16s + 32} \tag{20}$$

Stability: The ability of the system to provide bounded output for bounded input is defined as the stability of the system. The stability analysis of the system is more important for a control system (controller). Generally, the stability of the system is determined using bode diagram.

Fig.6, displays the open-loop bode diagram of the designed VbFOPID controller. It includes the gain (dB) as a function of frequency and phase (degrees) values as a function of frequency. The stability of the system is observed to be high, as the designed system produced Bounded Input Bounded Output (BIBO). The observed values are phase margin as 81°, gain margin as 12 dB and a bandwidth of 18 Hz.

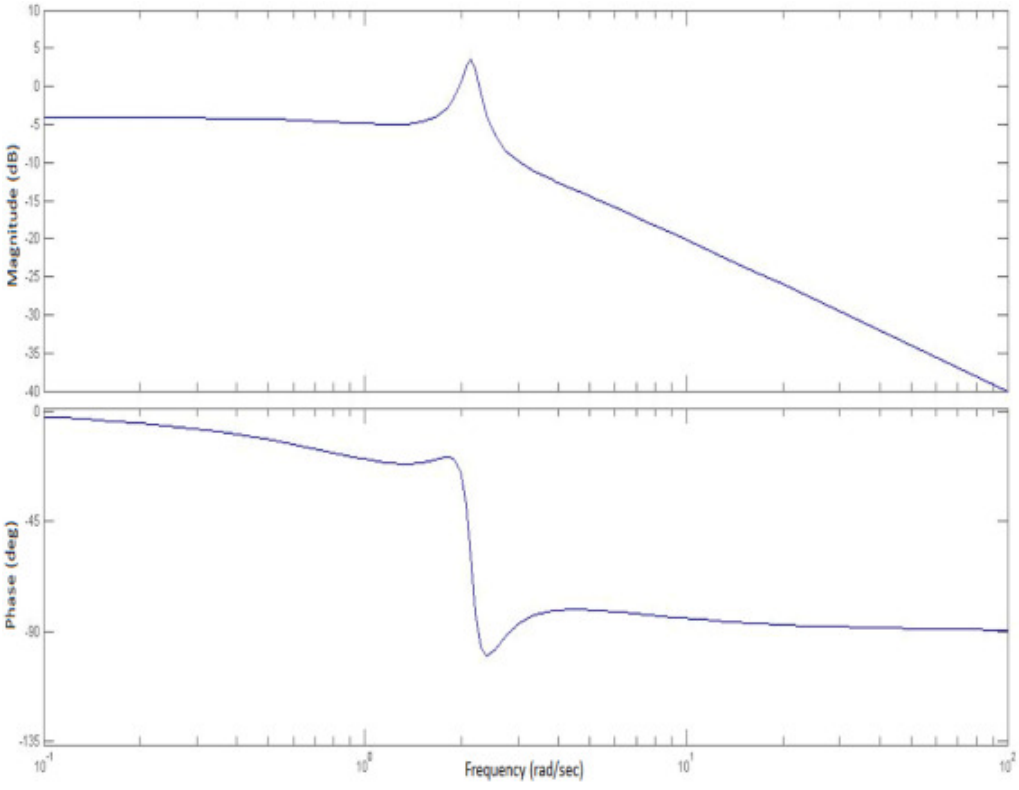

Download: Download high-res image (207KB)

Download: Download full-size image

Loading [MathJax]/jax/output/SVG/fonts/TeX/AMS/Regular/GeneralPunctuation.js

Sensitivity: In control system, the term sensitivity is defined as the variation/ change in system output in accordance with the changes in the system parameters. Generally, for a control system the sensitivity of the system must be high.

The sensitivity analysis of the designed controller is shown in Fig. 7. The sensitivity response of the presented controller is high, as the designed controller output varies in accordance with the system input.

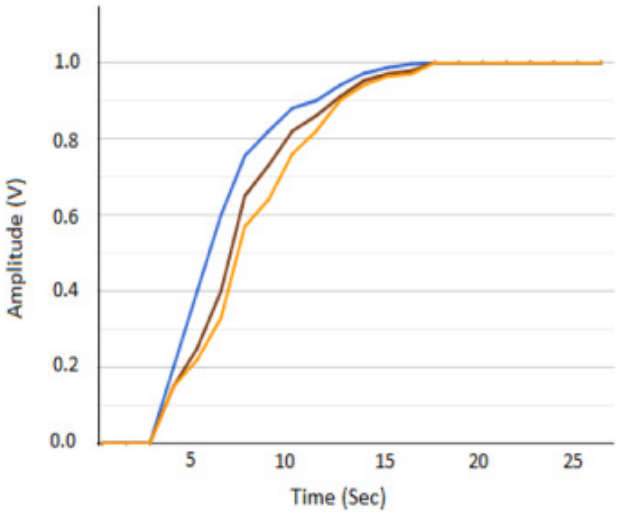

Download: Download high-res image (116KB)

Download: Download full-size image

Fig. 7. Sensitivity analysis.

Comparative analysis

To validate the performance of the designed VbFOPID controller, the outcomes of the presented controller is compared with other existing controllers in terms of convergence time, control rate, accuracy, settling time and rising time. Here, the existing techniques such as General Fuzzy Logic Controller – Type 2 (GFLC-T2) [24], Fractional Order Proportional Integral-Derivative (FOPID) [25], Proportional Integral-Derivative Interval Type-2 Fuzzy Logic Controller (PIDIT2-FLC) [20], Proportional Integral-Derivative (PID) [26] are taken for comparison with designed controller. The comparative analysis evaluated that the designed controller attained less rising time, high stability and sensitivity, large control rate and improved efficiency.

Comparison of rising time, convergence time and settling time

To evaluate the outcomes attained by the designed model, the metrics like settling time, rising time and convergence time of the presented controller is compared with different existing controllers.

Rise time: Rise time is the time taken by the input signals to increase 10% of its desired value to 90% of its desired value. Here, the rise time attained by the designed (VbFOPID) controller is 0.9s. The rising time of the existing controllers like PID, FOPID, GFLC-T2 and PIDIT2-FLC are 1.8s, 4.2s, 1.5s and 6.2s, respectively. The existing controllers attained high rising time on comparing with designed controller.

Loading [MathJax]/jax/output/SVG/fonts/TeX/AMS/Regular/GeneralPunctuation.js

Settling Time: Settling time is the time taken by the controller to maintain an equilibrium state without any deviation. The settling time of existing controllers are 4.8s, 2.6s, 3.3s and 3.6s. But, the proposed controller attained low settling time of 1.8s.

The comparison of settling time, rise time and convergence time of presented controller with the other existing controllers is presented in Fig.8. From the simulated graphs, it is observed that the proposed VbFOPID controller achieves lower values of settling time, rise time and convergence time compared to the previous proposed controllers other controllers in the literature.

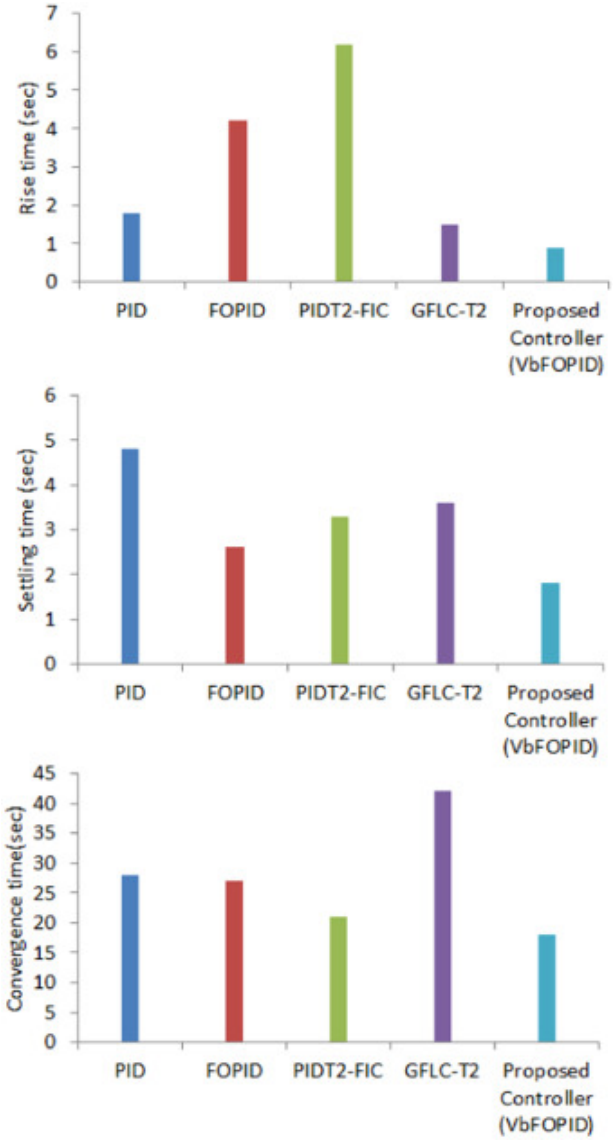

Download: Download high-res image (260KB)

Download: Download full-size image

Fig. 8. Comparison of convergence time, settling time, rise time of different techniques.

Comparison of maximum overshoot

In controller system design, maximum overshoot occurs when the output of the system exceeds the

Loading [MathJax]/jax/output/SVG/fonts/TeX/AMS/Regular/GeneralPunctuation.js

oot problem is low, as the system tunes the

biological inputs only to its optimal range.

For a stable system, the maximum overshoot must be low. Here, the maximum overshoot attained by the presented controller is compared with other existing controller. Fig.9, illustrates the comparison of maximum overshoot of designed controller with other controllers. The maximum overshoot achieved by the proposed controller design is 1.5, which is less, when compared to other controllers.

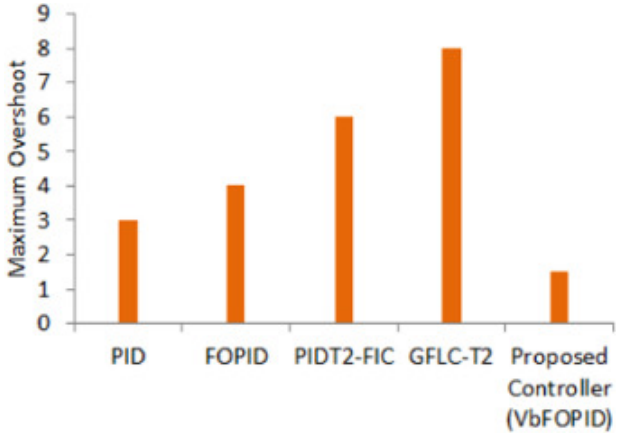

Download: Download high-res image (103KB)

Download: Download full-size image

Fig. 9. Comparison of Maximum Overshoot of proposed controller with other controllers.

Comparison of error percentage

Generally, error percentage is defined as the percentage of change in estimated output with the real values. Ideally, for a highly accurate system, the error percentage must be low.

The comparison of error percentage of designed controller with other controllers is presented in Fig.10. The error percentage of existing controllers such as PIDIT2-FLC, GFLC-T2, PID and FOPID are 2.5%, 1.75%, 2.2% and 1.5%, respectively, Whereas, the error percentage attained by designed controller is 0.9%. Thus, the presented VbFOPID controller attains very less error percentage than the other controllers.

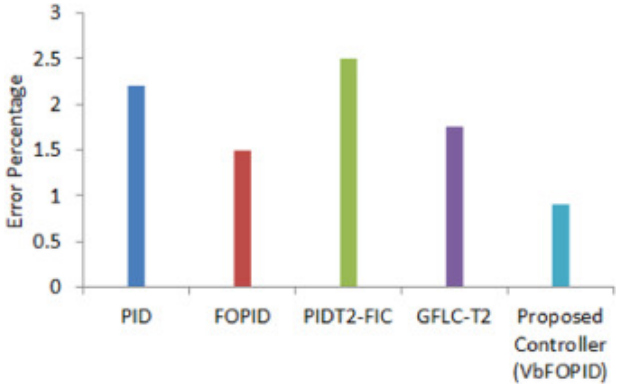

Download: Download high-res image (90KB)

Download: Download full-size image

Loading [MathJax]/jax/output/SVG/fonts/TeX/AMS/Regular/GeneralPunctuation.js

ng controllers in terms of error percentage.

Comparison of error percentage attained in tuning bio-signals

While tuning the biological parameters, sometimes the estimated output value is not same as the real output. Here, the error percentage attained during tuning of biological parameters like GRN, protein and pancreas of presented controller is compared with existing controllers. The existing controller attains high error percentage than the proposed controller.

The comparison of error percentage in tuning biological parameters of the proposed VbFOPID controller with existing controllers is shown in Fig. 11. The error percentage attained by the designed controller while tuning bio-signals like pancreas, protein and GRN are 1.1%, 1.0% and 0.9%, respectively.

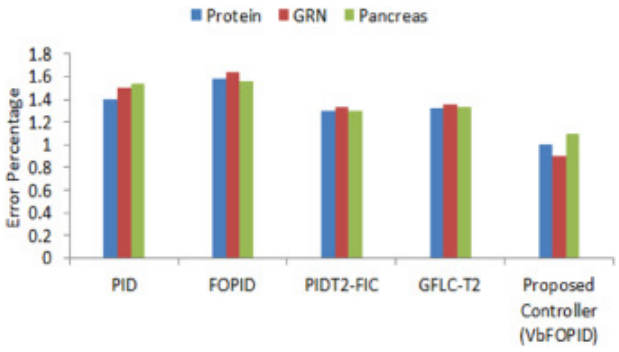

Download: Download high-res image (111KB)

Download: Download full-size image

Fig. 11. Comparison of error percentage with respect to various biological parameters.

Discussion

The designed (VbFOPID) controller tunes the biological signals like pancreas, protein and GRM to its optimal level; also it reduces the external induced disturbances in the signals. The presented controller regulates the bio-signals optimally, as the optimal fitness constraints are fixed to the controller function of fractional-order PID controller. This system tunes the biological signals optimally and accurately.

The performance analysis of the designed controller is shown in Fig. 12. From performance analysis, it is clear that the proposed technique attained high control rate, accuracy, stability and very less error rate.

Loading [MathJax]/jax/output/SVG/fonts/TeX/AMS/Regular/GeneralPunctuation.js

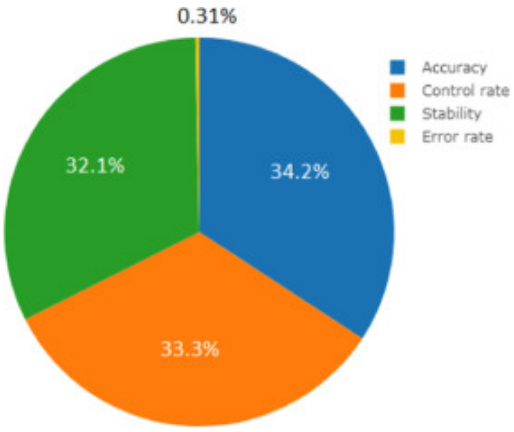

Download: Download high-res image (75KB)

Download: Download full-size image

Fig. 12. Performance analysis.

Finally, the performance of the system is validated with a comparative analysis. The performance of the designed controller over existing controller is demonstrated in Table 1. From the comparative analysis, it is clear that the presented controller exhibits very less error rate, less settling and rising times. Also, the proposed VbFOPID controller delivers better gain and control rate than the existing controllers.

Table 1. Comparative analysis of VbFOPID controller with existing controllers.

Techniques/ Controller	Percentage of Error	Max. Overshoot (%)	Rise Time (s)	Convergence Time (s)	Settling Time (s)
VbFOPID (Proposed)	0.9	1.5	0.9	18	1.8
GFLC-T2 [24]	1.75	8	1.5	42	3.6
FOPID [25]	1.5	4	4.2	27	2.6
PIDIT2-FLC [20]	2.5	6	6.2	21	3.3
PID [26]	2.2	3	1.8	28	4.8

Conclusion

For proper functioning of human body, the biological system plays a significant role. Any malfunction in biological system parameters may lead the person to critical diseases. Hence, to regulate and tune the biological parameters a novel VbFOPID controller was presented in this paper. The biological parameters like pancreas, protein and GRN are regulated by implanting the vulture optimal function to the controller function of FOPID controller. Moreover, the designed controller controls the glucose and insulin level in human body. The presented controller is evaluated with performance analysis. Moreover, the sensitivity, control rate and stability of the controller are enhanced. Finally, a comparative analysis is made by comparing the results of designed controller with the existing

Loading [MathJax]/jax/output/SVG/fonts/TeX/AMS/Regular/GeneralPunctuation.js

controllers. From performance and comparison analysis, it is evident that the presented controller attained low error rate of 0.9%, and high control rate of 99.5%. In addition, the designed controller achieves finest gain and low rise time, less settling time and reduced convergence time of 0.9s, 1.8s, and 18s, respectively. Moreover, this system attained high accuracy of 99.1% and system stability of 93%. Thus, the designed VbFOPID controller provides regulated optimal output in non-linear biological system. Future works to this paper include improving the modeling relationship between fractional orders and applying the VbFOPID controller to different non-linear biological system applications. Another work also includes designing and modeling multivariable VbFOPID controllers for tuning the various biological parameters in the human body.

CRediT authorship contribution statement

B. Doraswamy: Conceptualization, Methodology, Software, Data curation, Writing – original draft. **K. Lokesh Krishna:** Visualization, Investigation, Supervision, Software, Validation, Writing – review & editing.

Declaration of Competing Interest

The authors declare that they have no known competing financial interests or personal relationships that could have appeared to influence the work reported in this paper.

Recommended articles

References

[1] W.V. Balasaheb, C. Uttam
Novel intelligent optimization algorithm based fractional order adaptive proportional integral derivative controller for linear time invariant based biological systems
J. Electr. Eng. Technol., 17 (1) (2022), pp. 565-580
Crossref ↗ View in Scopus ↗ Google Scholar ↗

[2] S.M.H. Mousakazemi
Computational effort comparison of genetic algorithm and particle swarm optimization algorithms for the proportional–integral–derivative controller tuning of a pressurized water nuclear reactor
Ann. Nucl. Energy, 136 (2020), Article 107019
View PDF View article View in Scopus ↗ Google Scholar ↗

[3] A. Khan, G. Saha, R.K. Pal
Controlling the effects of external perturbations on a gene regulatory network using proportional-integral-derivative controller
...informatics (2020)
Google Scholar ↗

Loading [MathJax]/jax/output/SVG/fonts/TeX/AMS/Regular/GeneralPunctuation.js

[4] R.K. Mandava, P.R &Vundavilli
Design and development of an adaptive-torque-based proportional-integral-derivative controller for a two-legged robot
Soft Comput., 25 (16) (2021), pp. 10953-10968
Crossref ↗ View in Scopus ↗ Google Scholar ↗

[5] S. ArunJayakar, G.M. Tamilselvan, T.V.P. Sundararajan, T. Rajesh
An investigation on hybrid optimization-based proportional integral derivative and model predictive controllers for three tank interacting system
Proceedings of International Conference on Intelligent Computing, Information and Control Systems, Springer, Singapore (2021), pp. 125-145
Crossref ↗ Google Scholar ↗

[6] Jyoti Ranjan Nayak, Binod Shaw, Binod Kumar Sahu
Implementation of hybrid SSA–SA based three-degree-of-freedom fractional-order PID controller for AGC of a two-area power system integrated with small hydro plants
IET Gen., Transm. Distrib., 13 (2020), pp. 2430-2440
Crossref ↗ View in Scopus ↗ Google Scholar ↗

[7] S. Yu, M. Xie, H. Wu, J. Ma, Y. Li, H &Gu
Composite proportional-integral sliding mode control with feedforward control for cell puncture mechanism with piezoelectric actuation
ISA Trans. (2020)
Google Scholar ↗

[8] Xinhui Zhou, *et al.*
Application of an adaptive PID controller enhanced by a differential evolution algorithm for precise control of dissolved oxygen in recirculating aquaculture systems
Biosystems Eng., 208 (2021), pp. 186-198
View PDF View article View in Scopus ↗ Google Scholar ↗

[9] Saxena Nikita, Moonyong Lee
Control of a wastewater treatment plant using relay auto-tuning
Korean J. Chem. Eng., 36 (4) (2019), pp. 505-512
Crossref ↗ View in Scopus ↗ Google Scholar ↗

[10] S.O. Bamgbose, X. Li, L &Qian
Control of complex biological systems utilizing the neural network predictor
Computational Intelligence and Optimization Methods for Control Engineering, Springer, Cham (2019), pp. 133-148
Crossref ↗ View in Scopus ↗ Google Scholar ↗

[11] M. Kumar, D. Prasad, R.S. Giri, R.S. Singh

Loading [MathJax]/jax/output/SVG/fonts/TeX/AMS/Regular/GeneralPunctuation.js

Temperature control of fermentation bioreactor for ethanol production using IMC-PID controller

Biotechnol. Rep., 22 (2019), p. e00319

View PDF View article View in Scopus ↗ Google Scholar ↗

[12] M. Elsisi, K. Mahmoud, M. Lehtonen, M.M &Darwish

An improved neural network algorithm to efficiently track various trajectories of robot manipulator arms

IEEE Access, 9 (2021), pp. 11911-11920

Crossref ↗ View in Scopus ↗ Google Scholar ↗

[13] V. Sangregorio-Soto, C.L. Garzón-Castro, G. Mazzanti, M. Figueredo, J.A. Cortés-Romero

Proportional-integral controller assisted by GPI observer for microalgal continuous culture

2020 Argentine Conference on Automatic Control (AADECA), IEEE (2020), pp. 1-6

Crossref ↗ Google Scholar ↗

[14] J. Tao, L. Du, M. Dehmer, Y. Wen, G. Xie, Q. Zhou

Path following control for towing system of cylindrical drilling platform in presence of disturbances and uncertainties

ISA Trans., 95 (2019), pp. 185-193

View PDF View article View in Scopus ↗ Google Scholar ↗

[15] M. Chevalier, *et al.*

Design and analysis of a proportional-integral-derivative controller with biological molecules

Cell Syst, 9 (4) (2019), pp. 338-353

View in Scopus ↗ Google Scholar ↗

[16] Seyed Mohammad Hossein Mousakazemi

Computational effort comparison of genetic algorithm and particle swarm optimization algorithms for the proportional–integral–derivative controller tuning of a pressurized water nuclear reactor

Ann. Nucl. Energy, 136 (2020), Article 107019

View PDF View article View in Scopus ↗ Google Scholar ↗

[17] Tulasichandra Sekhar Gorripotu, *et al.*

Sine cosine optimization based proportional derivative-proportional integral derivative controller for frequency control of hybrid power system

Computational Intelligence in Data Mining, Springer, Singapore (2020), pp. 789-797

Crossref ↗ View in Scopus ↗ Google Scholar ↗

[18] J. Tao, Q. Mercan

Loading [MathJax]/jax/output/SVG/fonts/TeX/AMS/Regular/GeneralPunctuation.js

A study on a benchmark control problem for real-time hybrid simulation with a tracking error-based adaptive compensator combined with a supplementary proportional-integral-derivative controller

Mech. Syst. Signal Process., 134 (1) (2019), Article 106346

View PDF View article View in Scopus ↗ Google Scholar ↗

[19] A. Chouksey, *et al.*

Fuzzy cognitive network-based maximum power point tracking using a self-tuned adaptive gain scheduled fuzzy proportional integral derivative controller and improved artificial neural network-based particle swarm optimization

Fuzzy Sets Syst., 381 (2020), pp. 26-50

View PDF View article View in Scopus ↗ Google Scholar ↗

[20] R. Sharma, K.K. Deepak, K. Gaur, D. Joshi

An optimal interval type-2 fuzzy logic control based closed-loop drug administration to regulate the mean arterial blood pressure

Comput. Methods Programs Biomed., 185 (2020), Article 105167, 10.1016/j.cmpb.2019.105167 ↗

View PDF View article View in Scopus ↗ Google Scholar ↗

[21] F. Mairet

Abiomolecular proportional integral controller based on feedback regulations of protein level and activity

Royal Soc. Open Sci., 5 (2) (2018), Article 171966, 10.1098/rsos.171966 ↗

View in Scopus ↗ Google Scholar ↗

[22] Mounica Mallareddy, *et al.*

Application of Bio geography based Fractional order PID controller in DC motor drive speed control

2020 IEEE International Conference on Electronics, Computing and Communication Technologies (CONECCT), IEEE (2020)

Google Scholar ↗

[23] Benyamin Abdollahzadeh, Farhad Soleimanian Gharehchopogh, Seyedali Mirjalili

African vultures optimization algorithm: a new nature-inspired metaheuristic algorithm for global optimization problems

Comput. Ind. Eng., 158 (2021), Article 107408

View PDF View article View in Scopus ↗ Google Scholar ↗

[24] A. Mohammadzadeh, T. Kumbasar

A new fractional-order general type-2 fuzzy predictive control system and its application for glucose level regulation

Appl. Soft Comput., 91 (2020), Article 106241, 10.1016/j.asoc.2020.106241 ↗

Google Scholar ↗

Loading [MathJax]/jax/output/SVG/fonts/TeX/AMS/Regular/GeneralPunctuation.js

[25] F. Zhang, C. Yang, X. Zhou, W. Gui
Fractional-order PID controller tuning using continuous state transition algorithm
Neural Comput. Appl., 29 (10) (2018), pp. 795-804, 10.1007/s00521-016-2605-0 ↗
View in Scopus ↗ Google Scholar ↗

[26] F. Mairet
A biomolecular proportional integral controller based on feedback regulations of protein level and activity
Royal Soc. Open Sci, 5 (2) (2018), Article 171966
Crossref ↗ View in Scopus ↗ Google Scholar ↗

[27] M. Ali, H. Kotb, K.M. Aboras, N.H. Abbasy
Design of cascaded PI-fractional order PID controller for improving the frequency response of hybrid microgrid system using gorilla troops optimizer
IEEE Access, 9 (2021), pp. 150715-150732
Crossref ↗ View in Scopus ↗ Google Scholar ↗

[28] Moetasem Ali, Hossam Kotb, M. Kareem AboRas, H. Nabil Abbasy
Frequency regulation of hybrid multi-area power system using wild horse optimizer based new combined Fuzzy Fractional-Order PI and TID controllers
Alexandria Eng. J., 61 (12) (2022), pp. 12187-12210
View PDF View article View in Scopus ↗ Google Scholar ↗

[29] Ahmed H. Yakout, Hossam Kotb, Kareem M. AboRas, Hany M. Hasanien
Comparison among different recent metaheuristic algorithms for parameters estimation of solid oxide fuel cell: steady-state and dynamic models
Alexandria Eng. J., 61 (11) (2022), pp. 8507-8523
View PDF View article View in Scopus ↗ Google Scholar ↗

Cited by (5)

Response and reliability analysis of a nonlinear VEH systems with FOPID controller by improved stochastic averaging method and LBFNN algorithm

2024, Reliability Engineering and System Safety

Citation Excerpt :

…Under this circumstance, an improved stochastic averaging method is required to be developed in order to deal with the amplitude-dependent frequency and unknown amplitude functions in the strongly nonlinear stochastic dynamical system, so as to get FPK and BK equations to discuss the system response and reliability further. As for the control strategy regarding to stochastic reliability, fractional order Proportional-integration-derivative (FOPID) control is becoming one of popular controlling measures in the field of industry [42,43], automatic-voltage-

Loading [MathJax]/jax/output/SVG/fonts/TeX/AMS/Regular/GeneralPunctuation.js

h the advantages of simple structure, clearly

physical meaning and strong robustness. FOPID controller was developed on the basis of the classical PID controller, the deviation between the inputs and desired outputs can be adjusted by five tuning parameters....

Show abstract

Optimal nonlinear Fractional-Order Proportional-Integral-Derivative controller design using a novel hybrid atom search optimization for nonlinear Continuously stirred Tank reactor

2024, Thermal Science and Engineering Progress

Show abstract

An intelligent optimized fractional order sliding mode controller for biological system ↗

2024, Multimedia Tools and Applications

A novel optimized fractional order system for tuning biological parameters ↗

2024, International Journal of Numerical Modelling: Electronic Networks, Devices and Fields

Design of PID, IMC and IMC based PID Controller for Hydro Turbine Power System of Non-minimum Phase Dynamics ↗

2024, Journal of Robotics and Control (JRC)

© 2023 The Author(s). Published by Elsevier B.V.

ELSEVIER

All content on this site: Copyright © 2024 Elsevier B.V., its licensors, and contributors. All rights are reserved, including those for text and data mining, AI training, and similar technologies. For all open access content, the Creative Commons licensing terms apply.

RELX™

Loading [MathJax]/jax/output/SVG/fonts/TeX/AMS/Regular/GeneralPunctuation.js

electronics

MDPI

Article

Input Voltage-Level Driven Split-Input Inverter Level Shifter for Nanoscale Applications

Srinivasulu Gundala [1], Mohammed Mahaboob Basha [2], Virupakshi Madhurima [3] and Ovidiu Petru Stan [4,*]

[1] Department of Electronics and Communication Engineering, Lakireddy Bali Reddy College of Engineering, NTR District, Mylavaram 521230, Andhra Pradesh, India; srinivasulugundala46@lbrce.ac.in
[2] Department of Electronics and Communication Engineering, Sreenidhi Institute of Science and Technology (Autonomous), Hyderabad 501301, Telangana, India; mahaboobbasham@sreenidhi.edu.in
[3] Department of Electronics and Communication Engineering, SV College of Engineering (Autonomous), Tirupati 517520, Andhra Pradesh, India; madhurima.v@svcolleges.edu.in
[4] Faculty of Automation and Computer Science, Technical University of Cluj Napoca, 400114 Cluj-Napoca, Romania
* Correspondence: ovidiu.stan@aut.utcluj.ro

Abstract: A level shifter (LS) appears to be highly efficient and effective in solving voltage contentions between deep sub-threshold and core voltage levels. An input voltage-level driven split-input inverter that can create common unconnected PMOS and NMOS transistors for the input inverter is proposed, which is powered and used at the input stage to achieve maximum conversion efficiency. Layout and simulation results across different corners have demonstrated that the proposed LS is highly useful for cutting-edge nanoscale applications. It can up-convert voltage from 0.2 V to 1.2 V and down-convert from 1.2 V to 0.2 V @ 1 MHz input pulse, with a level-up or level-down mean switching delay of 1.3 ns, and a power of 9.5 nW. Moreover, the LS occupies an area of 8 μm^2, which is a reasonably compact size compared to the typical LS designs. Overall, the proposed voltage LS design is an efficient and effective solution that could have an ample range of applications in IoT and biomedical, wireless sensor networks.

Keywords: propagation delay; power consumption; voltage-level driven-input inverter; Internet of Things (IoT); System-on-Chip (SoC)

check for updates

Citation: Gundala, S.; Basha, M.M.; Madhurima, V.; Stan, O.P. Input Voltage-Level Driven Split-Input Inverter Level Shifter for Nanoscale Applications. *Electronics* **2024**, *13*, 1115. https://doi.org/10.3390/electronics13061115

Academic Editors: Nabil Yassine, Abdallah Tammam and Khaled Hayatleh

Received: 7 February 2024
Revised: 13 March 2024
Accepted: 14 March 2024
Published: 18 March 2024

Copyright: © 2024 by the authors. Licensee MDPI, Basel, Switzerland. This article is an open access article distributed under the terms and conditions of the Creative Commons Attribution (CC BY) license (https://creativecommons.org/licenses/by/4.0/).

1. Introduction

Portable devices, such as cell phones, computers, laptops, and various sophisticated electronic devices, are very popular with a variety of applications. The demand for hand-held devices has led to numerous reductions in the size of devices, their weight, and the recharge intervals of these devices. Designing for lower power is the essential element for lighter and longer-lasting batteries. Thus, power reduction is the most essential design issue that today's VLSI design engineers must face when dealing with the design of integrated circuits. Supply voltage scaling can be the most efficient method of reducing the dynamic power of switching because both the voltage of supply and its voltage fluctuation are decreased by reducing the supply voltage, leading to a quadratic decrease in dynamic power, whereas the speed decreases [1–3].

Integrated System-on-Chip (SoC) architectures are a composition of dissimilar blocks of intellectual property (IP) cores that operate at different levels of input voltage to meet the required time-related criteria [4–6]. Non-critical blocks consume less energy by operating at lower supply voltages (VDDL), sometimes in the sub-threshold region, while time-critical blocks require higher supply voltages (VDDH) to achieve the desired performance [7–9]. To ensure proper interaction between different voltage domains/cores, reliable LS circuits are necessary to maintain the signal integrity of the design, as depicted in Figure 1.

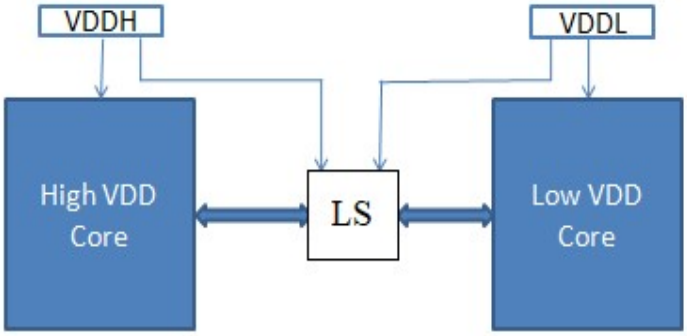

Figure 1. Level shifter position.

Current state-of-the-art LSs are categorized into two types: circuit topologies using cross coupled (CC) and current mirror (CM) techniques. While LSs that utilize CC techniques (Figure 2) have less standby power consumption, they are limited by a trade-off between their pull-up and pull-down networks, which affects their speed and energy consumption during switching. LSs face a challenge when up-converting sub-threshold voltages, as it causes the pull-down network areas to be too large and complex in practice [10–13].

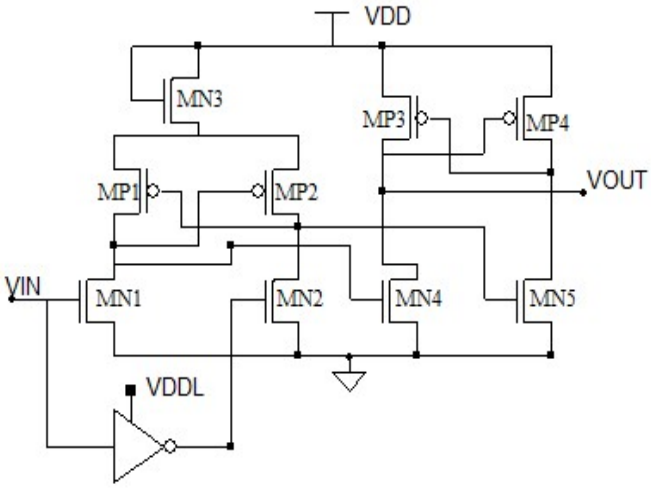

Figure 2. Cross coupled LS.

Current-mirror-based architectures [7,10,14] perform better when a wide range of up-conversion is required, as they face more contention among pull-up and pull-down networks, which results in increased speed and reduced energy consumption. However, they tend to consume more static power. To overcome the limitations of cross-coupled and current-mirror-based topologies, recent studies have presented several options. For example, adaptive/regulated pull-up networks have been recommended in some studies to reduce current contention in cross-coupled-based systems and improve energy efficiency.

An improved Wilson current mirror that utilizes mixed-threshold voltage devices has also been reported to address issues with conventional current-mirror-based LSs. In order to achieve even greater energy efficiency, the output stage of an inverting buffer includes a split-input configuration, which is employed in conjunction with an improved Wilson CM that uses mixed-threshold voltage devices [7,15–19].

This study introduces a new short circuit aware inverter that can create common unconnected PMOS and NMOS for a split-input inverter LS design that has been validated through layout and simulation measurements, which the authors believe to be the first of its kind. The designed circuit was laid out using 65 nm CMOS and tested on five different PVT corners. Section 2 of the paper outlines the split-input inverter level shifter (SILS), which

is then assessed based on measurement results in Section 3. Conclusions are presented in Section 4.

2. Proposed Input Voltage-Level Driven Split-Input Inverter Level Shifter

Figure 3 shows the invented input voltage-level driven-input inverter level shifter design, which is based on a short-circuit-aware inverter that can create common unconnected PMOS and NMOS for the "split-input inverting buffer LS" design. Unlike previous designs, the circuit utilizes a split-input inverting buffer (MP2-MN2) to reduce power consumption. However, the output stage driving method is unique and involves a boosting inverter and additional feedback connected to MN4-MP4. The split inverter MP2-MN2 eliminates the short circuit when VIN is equal to VDDL. The boosting inverter MP3-MN3 ensures the full swing at VOUT for both logic 0 and 1. The W/L ratio of NMOS is 1:1 and PMOS is 3:1,which are maintained at the level shifting stage, and 4:1 for MP1 and 2:1 for MN1 at the 2×1 multiplexer stage at the 65 nm techno logy node.

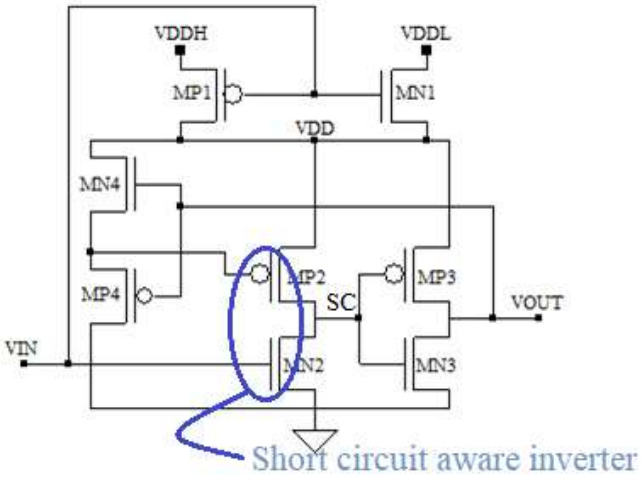

Figure 3. Proposed SILS.

The proposed SILS design is different from other solutions presented in previous studies. Compared to previous designs, this split-input inverter enables the proposed design features and a larger voltage differential. This results in a reduction in the short circuit power of the driving stage and improved energy efficiency during both VDDL to VDDH and VDDH to VDDL transitions, particularly for up-conversion from the sub-threshold region. Figure 5 demonstrates the transitory behavior of SILS as the input pulse amplitude voltage is up-converted from 0.2 V to 1.2 V for output transitions.

$$\begin{aligned} V_{SC}(t) = 0.5\left[\frac{\tau G_{mMP2}}{C_L}(\mathrm{VDDH} - |V_{thMP2}|) - \frac{\tau I_{MP2}}{C_L}|V_{thMP2}|\right]e^{\frac{t}{\tau}} + \\ 0.5\left[\frac{\tau G_{mMN2}}{C_L}(\mathrm{VDDH} - |V_{thMN2}|) - \frac{\tau I_{MN2}}{C_L}|V_{thMN2}|\right]e^{\frac{t}{\tau}} + \\ (\mathrm{VDDH} - |V_{thMN2}|) \ \ When \ \mathrm{VIN} > \mathrm{VDDL} \end{aligned} \quad (1)$$

where V_{SC} is the voltage at node SC, G_{mMP2} is the transconductance of the MP2, G_{mMN2} is the transconductance of the MN2, V_{thMP2} is the nominal V_t of the MP2, V_{thMN2} is the nominal V_t of the MN2, C_L is the total capacitances of the VOUT and gate capacitance of MP3-MN3, and I_{MP2} and I_{MN2} represent the currents of MP2 and MN2, respectively. Voltage at node V_{SC} is a function of rise time and fall time, which will be negligible as the inverter creates common unconnected PMOS and NMOS transistors. In Figure 3, a short circuit aware inverter is shown in a circuit comprising MP3 and MN3 devices, which are never simultaneously ON or OFF, and the node voltage at SC is influenced by Equation (1) when the VIN is equal to VDDL. When the VIN is less than or equal to VDDH, the level transition of V_{SC} involves the supply level rails from VDDH to VSS. Therefore, due to a

considerable fall time, VOUT reaches 0. The difference between the first-order and second-order terms leads to a fractional value and means the node voltage SC is stronger than zero, and the driving inverter produces VDDL equal to VOUT as per the mathematical model in Equation (2).

$$\mathrm{V_{SC}(t)} = 0.5\left[\frac{\tau G_{mMP2}}{C_L}(\mathrm{VDDH} - |V_{thMP2}|) - \frac{\tau I_{MN2}}{C_L}|V_{thMN2}|\right] When\ \mathrm{VIN} \leq \mathrm{VDDH} \quad (2)$$

When the VIN is equal to VDDL, MP1 turns ON, which will make VDDH available at VDD. LS acts as a level up-converter, and MN2 ON and MP2 OFF and node voltage SC cause the pull-down and driving inverter (MP3-MN3) to produce a strong VOUT (VDDH). The feedback path ensures MP2 OFF, and when the VIN is equal to VDDH, MN1 turns ON, which will make VDDL available at VDD. LS acts as a level down-converter, and MN2 ON and MP2 OFF and node voltage SC cause the pull-down and driving inverter (MP3-MN3) to produce a strong VOUT (VDDL). The feedback path ensures MP2 OFF, and when the input signal VIN is equal to VSS, MP1 turns ON, which will make VDDH available at VDD. MN2 OFF and MP2 ON and node voltage SC cause the pull-up and driving inverter (MP3-MN3) to produce a strong VSS. The performance of SILS is depicted in the measurements and results sections.

The current flowing through the MP2-MN2 branch is low for both VDDL and VDDH inputs, indicating that the node SC is either VDD or VSS when fully charged, and it triggers the MP3 or MN3 to switch ON or OFF. The activation of MP1 and the reduction in conflict at the SC node cause the SC node to rise and turn on MN3, the MN3 component can be turned OFF by fully discharging the SC to 0 V. From Figure 2, the proposed LS is used during the conversion of the input signal from high to low. To charge the SC and discharge the VOUT node to VSS, the charging current $\mathrm{I_{RISE}}$ is mirrored as $\mathrm{I_{FALL}}$ and the sum of C_L with the rate of change of VOUT. Consequently, the rise and fall times of VOUT are made to be symmetrical, as shown in (3). The specifications of the proposed SILS are compared in the results and discussion sections.

$$\mathrm{I_{RISE}} = \mathrm{I_{FALL}} + C_L \frac{d}{\mathrm{dt}}\mathrm{VOUT} \quad (3)$$

To enhance the switching performance and ensure a small area and low VDDL robustness, a dual $\mathrm{V_{TH}}$ design technique was utilized along with appropriate transistor scaling. Specifically, LVT devices were used for MN3-MN4, while RVT devices were employed for the remaining transistors. An important point to consider is that the voltage shifting range of the SILS can be extreme between VDDL and VDDH. Figure 4 depicts the proposed LS layout. The LS design utilized only two metal wires.

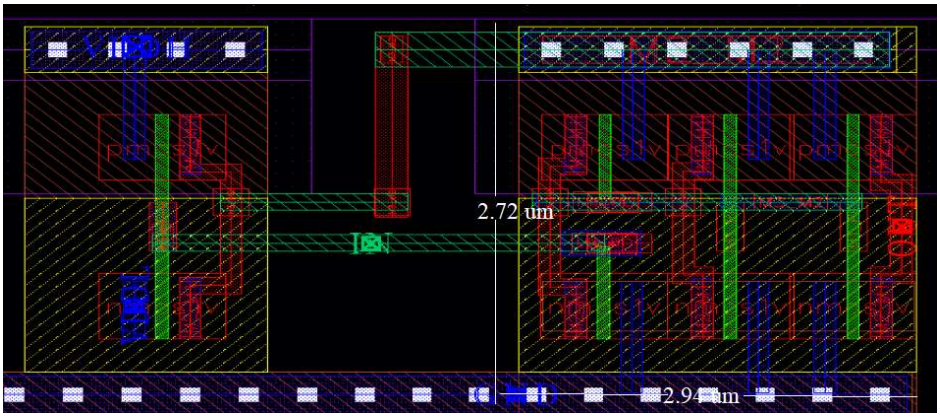

Figure 4. Layout of SILS.

The layout comprises metal layers, an n wire, and p-wires with the adaptive biasing system for a split-input inverter with 2.72 µm × 2.94 µm implementations, and it needs approximately the same space in length and width as CMOS devices. It is apparent that the layouts in the size of the MP2 transistor are the largest because it covers nearly one half of the area of MN1. Its size is rather small in comparison to the available LS, and it becomes negligible in large arrays of the LS interface. The resulting LS occupies approximately an 8 μm^2 area.

The transient waveforms of SILS for 0.2 V and 1.2 V for VDDL and VDDH, respectively, are depicted in Figure 5. A short-circuit-aware inverter that can create common unconnected PMOS and NMOS for the split-input inverter buffer LS is utilized to decrease the short circuit current during VDDL to VDDH and VDDH to VDDL transitions. The voltage variation between VDDL and VDDH nodes ensures the required impedance of the pull-up and pull-down of the MN2 and MP2 inverter, allowing for it to be turned on at extreme levels of VDDLs, thereby reducing the short circuit current and reducing the power of SILS. As mentioned in Figure 3, by adding up MP1, MN1 results in a 2 × 1 multiplexer that enables the LS to be an up shifter or a down shifter, suitable for a sub-threshold and super threshold LS circuit, where VDDL is lower than the V_t of the MOSFET. Figure 5 illustrates the VDDL-to-VDDH switching characteristics where VDDH is 1.2 V and VDDL is set at 0.2 V. The I_{RISE} and I_{FALL} are produced alternately, in contrast with logic mismatches. The proposed SILS have no contention between VDDL and VDDH level shifting.

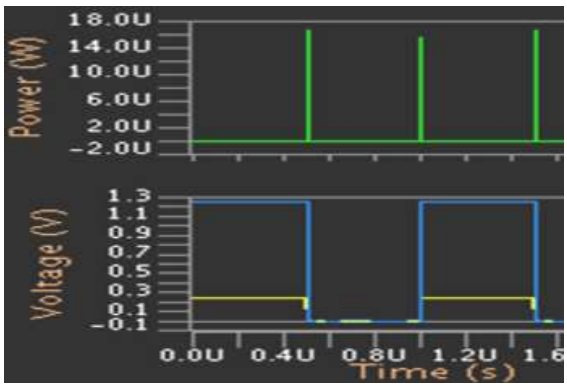

Figure 5. Functional output of SILS.

3. Measurement and Results

3.1. Power and Delay as Functions of VDDL

Figures 6 and 7 show the relationship between the measured average power and delay for different VDDLs while up shifting, as it shifts voltage from 0.2 V to 1.2 V @ 1 MHz and the SILS temperature is at 27 °C. Power consumption is a crucial parameter to be taken into consideration. The power consumption that was measured for the SILS circuit is illustrated in Figure 6. The amount of power consumed depends on the intensity of the input signal. In addition, the input side inverter which is supplied via VDDH takes up the majority of the power. VDDL is connected only directly to an input converter when the input is at VDDH. The maximum power consumption variation is observed when the VIN is in the range of 0.175 V to 0.2 V. The smallest power utilization variation happens when the circuit transforms the input signal from VDDH to VDDL. The SILS power consumption is almost uniform for all VDDLs from 0.2 V to 0.375 V, and between 0.175 V and 0.2 V, there is a significant reduction in power due to the super threshold region of the MN2 operation. Due to the self-biasing of MP2-MN2, as VDDL increases, the SILS power is stable due to the feedback-driven MN4-MP4 arrangement, resulting in the significant difference in impedances among MP2-MN2. Taken as a whole, the results in terms of power and energy of each transition of the SILS show that it is suitable for all nanoscale applications aimed at moderate to high energy savings.

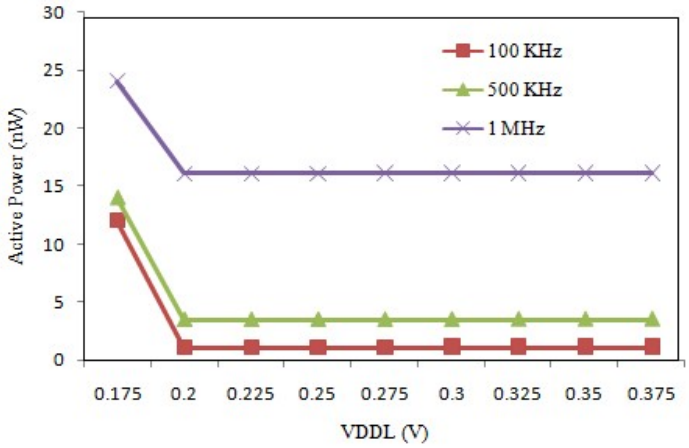

Figure 6. Average power of SILS @ VDDL at VDDH = 1.2 V.

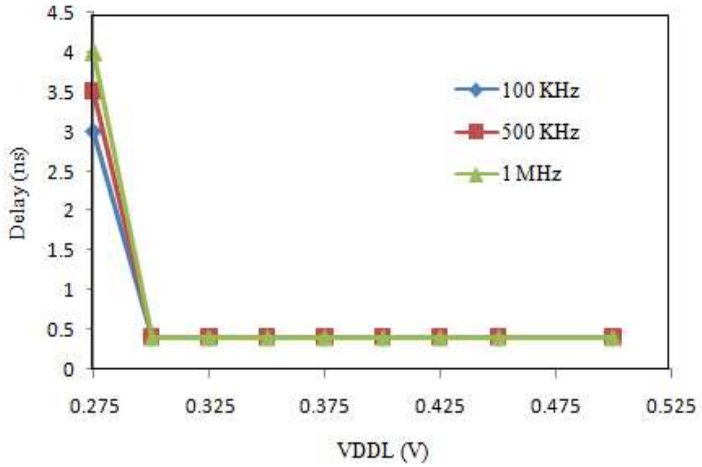

Figure 7. Delay of SILS @ VDDL at VDDH = 1.2 V.

The delay of SILS in relation to VDDL with a fixed VDDH of 1.2 V, as well as when using fem to farad capacitive load, is displayed in Figure 7. A delay when VDDL to VDDH transition, while VDDL < 0.3 V, is more because of the larger shifting gain of SILS when it is converting to 1.2 V. The delay variant curve, especially the rising delay, is approximately flat for VDDL > 0.3 V. The variations that have been measured for the rising delay at VDDH are fixed at 1.2 V, whereas an IC in the circuit is used to load the split-input inverter circuit. In this diagram, it is shown that the delay is measured as the SILS converts a pulse-shaped signal that has a 0.2 V and 1.2 V amplitude. In Figure 7, it is evident that the delay of the circuit is nearly flat from 0.3 V onwards. The SILS delay is uniform for all VDDLs from 0.3 V to 0.5 V, influenced by the self-biasing of MP2-MN2. As VDDL rises from 0.275 V to 0.3 V, the SILS delay decreases due to overcoming the super threshold region of the operation. Overall results in terms of delay show that the proposed SILS is suitable for all nanoscale applications.

3.2. Power and Delay as Functions of VDDH

Figures 8 and 9 show the relationship between the measured average power and delay for different VDDHs while down shifting, as it shifts from 1.2 V to 0.2 V @ 1 MHz and the SILS temperature is at 27 °C. The SILS power consumption is almost uniform for all VDDHs from 0.9 V to 1.1 V, influenced by the (2) and self-biasing of MP2-MN2. As VDDH increases, the SILS power is stable due to the feedback-driven MN4-MP4 arrangement, resulting in the significant difference in impedances among MP2-MN2. The results of power and energy for each transition of the SILS show that it is suitable for all nanoscale

applications aimed at moderate to high energy savings. The amount of power consumed depends on the intensity of the input signal. For the level-up shift, the input inverter is supplied via VDDH, which takes up the majority of the power.

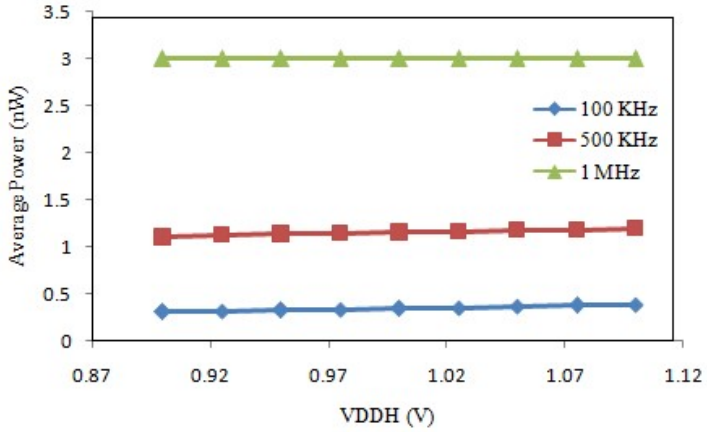

Figure 8. Power of SILS @ VDDH at VDDL = 0.2 V.

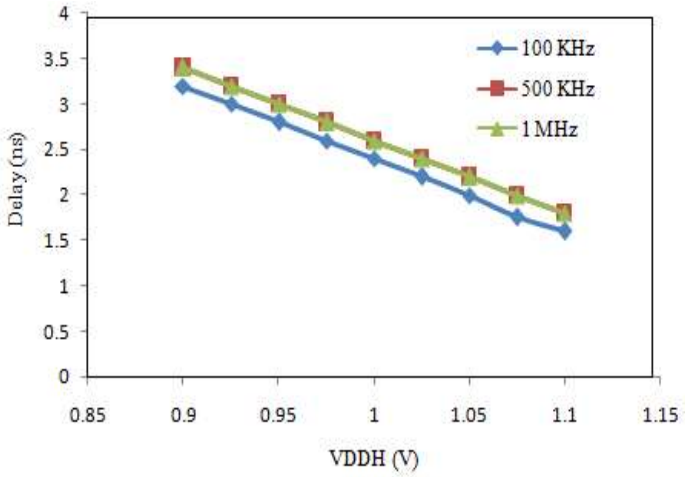

Figure 9. Delay of SILS @ VDDH at VDDL = 0.2 V.

The SILS delay decreases uniformly for all VDDHs from 0.9 V to 1.1 V, influenced by the (3) and self-biasing of MP2-MN2. As VDDH increases, the SILS delay decreases due to the feedback-driven MN4-MP4 arrangement, resulting in the significant difference in impedances among MP2-MN2. Overall results in terms of delay of SILS show that it is suitable for all nanoscale applications. The propagation delay for VDDH < 0.9 V is more because of the wider shifting gain of SILS when it is converting VDDH to VDDL of 0.2 V. From the delay variation curve, there is a flat delay for VDDL > 0.3 V. The variations that have been measured for the falling delay at VDDL are fixed at 0.2 V, whereas a split inverter integrated into the circuit is used to load the split-input inverter circuit.

3.3. Impact of Load on SILS Performance

The measured power for a typical sample was recorded for the experiment that was conducted at different load capacitances from 10 fF to 90 fF, and it is illustrated in Figure 10 at VDDL = 0.2 V and VDDH = 1.2 V @ 1 MHz. The maximum power penalty variation of the SILS over the range is just 1.75 times the power at 10 fF while levelling up, and there is no considerable power penalty variation while levelling down, and the power variations of the other LSs are between 30 and 90 times [20–22]. The proposed SILS shows negligible power variations.

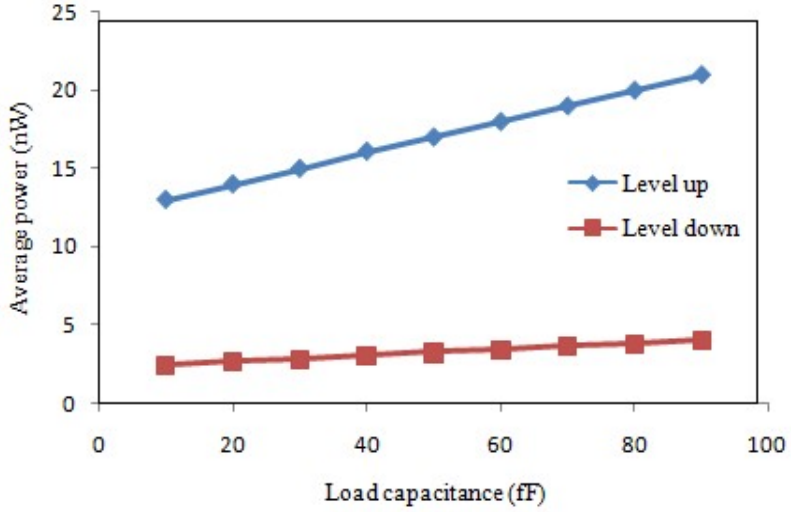

Figure 10. Power of SILS @ Load capacitance VDDH = 1.2 V, VDDL = 0.2 V and 1 MHz.

The measured delay for a typical sample was recorded for the experiment that was conducted at different load capacitances from 10 fF to 90 fF, and it is illustrated in Figure 11 at VDDL = 0.2 V and VDDH = 1.2 V @ 1 MHz. The maximum delay penalty variation of the SILS over the range is just 1.8 times the delay at 10 fF while levelling up, and 1.9 times the delay penalty variation while levelling down, and the delay discrepancies of the other LSs are around 25 to 100 times. The proposed SILS shows negligible power variations, which means the robustness of the SILS against load variations is strong.

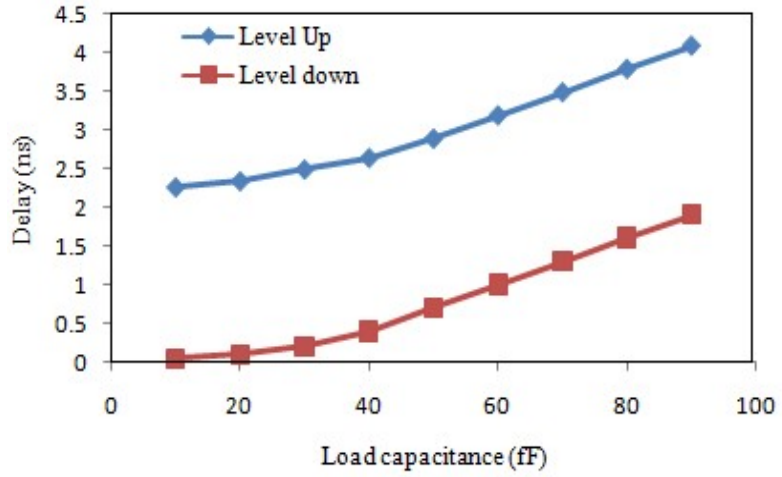

Figure 11. Delay of SILS @ Load capacitance VDDH = 1.2, VDDL = 0.2 V and 1 MHz.

The measured minimum VDDL required is 0.19 V for up-conversion to 1.2 V. Among the ten simulation results, the worst-case scenario resulted in a voltage input of 0.19 V at 27 °C. On the other hand, the most efficient sample was able to up-convert a VIN pulse as low as 0.2 V, as illustrated in Figure 5. The performance of the SILS-based structure was found to be very negligibly influenced by the temperature. At lower temperatures, the leakage current flow was reduced, leading to an improvement in the VDDL min value, while at higher temperatures, the VDDL min value deteriorated due to increased leakage current flow. The stable power consumption was determined by considering a VDDL value of 0.2 V and a VDDH value of 1.2 V, while levelling up the static power utilization remained constant at around 1.3 nW, which is 28% of the power for VDDH in the range of 4.65 W.

Two cascaded inverters were employed to buffer the proposed SILS for driving the output at a capacitive load of 50 fF and the test tools, which allowed us to measure the power and delay. Additionally, the output buffering was kept constant in an alternative

"test" path of the circuit to determine each element's separate contribution to the total power and delay. In the scenario where the input pulse voltage equals 0.2 V, the mean delay is practically 0.4 ns, whereas at a VDDH of 1.2 V, it rises to about 1.75 ns when VDDL is at 0.2 V, which is roughly 77% higher. The power drops when VDDL increases, primarily as a result of the short-circuit-aware inverter. The mean energy usage for VDDL = 0.2 V and VDDH = 1.2 V is just 16 fJ. Another major point to assert is how successfully the suggested LS adjusts the performance of the device improving with increasing operating frequency. It can be observed that the outcome was obtained from the layout in the presence of a load capacitance of 50 fF.

3.4. Comparison Results and Discussion

Table 1 shows a comparison of various LS designs based on their performance. The CC-based LS circuit in [3,4] achieves low standby power, which is limited by a trade-off between their pull-up and pull-down, which affects their speed and energy consumption during switching, but consumes a significant amount of energy per transition at 30.7 fJ [3], which is approximately twice that of the proposed SILS. According to [11], the LS approach for the 55 nm CMOS node achieves the lowest energy/transition of 27 fJ and a marginal VDDL of 0.3 V. However, it also has the highest delay of 82 ns. Current-mirror-based architectures perform better when a wide range of up-conversion is required, as they face less contention between pull-up and pull-down, resulting in increased speed and reduced energy consumption. However, they tend to consume more static power [20,21], and the CM-based solution suffers from poor switching performance and a limited shifting range. Compared to other LS designs in 65 nm CMOS, the CM-based LS in [21] is competitive, with a switching delay of 7.5 ns. In comparison to [23], the proposed LS SILS demonstrates in this paper that it offers considerable decrements in power by approximately 25% higher power at the cost of lower VDDL at 0.2 V. This statement implies that in order to achieve a higher level of robustness against process corners, the proposed circuit has a trade-off between power and delay. The comparison in Table 1 shows that the suggested circuit has the minimum up-convertible VDDL and is the most robust among the compared circuits, with a variability of around 10%. It should be noted that the simulation results were taken at different process corners, which may be representative of all possible process variations, but the fact that the suggested circuit outperformed the other circuits despite the inverter type circuit limitation makes the result even more significant. The proposed SILS is robust not only in terms of a wide conversion range, power, and delay, but also in that it has the capability to perform up shift or down shift, unlike other LSs capable of performing only up shift.

Table 1. Comparison of LSs.

Ref./ Proposed	Technology (nm)	Type of Technique	VDDL (V)	VDDH (V)	Power (nW)	Delay (ns)	PDP (fJ)
[3]	65	CC	0.3	1.2	30.7	25	0.768
[4]	55	CC	0.3	1.2	23	53	1.219
[20]	65	CM	0.3	1.2	552	17.5	9.660
[11]	55	CM	0.3	1.2	27	82	2.214
[21]	65	CM	0.3	1.2	124	7.5	0.930
[22]	55	CM	0.45	1.2	180	57	10.26
[23]	65	DLS	0.3	1.2	12	186	2.230
SILS (Up/Down)	65	Inverter	0.2	1.2	16	0.4	0.006
					03	1.75	0.005

Where, CC—cross-coupled; CM—current mirror; DLS—dynamic leakage suppression.

The SILS has the least number of MOS devices (see Figure 12). The number of MOS devices needed for the proposed LS is only 08, which is the lowest among all LSs, mainly owing to both level up- or level down-conversion, and which is approximately 25% lower than the transistor used in [20].

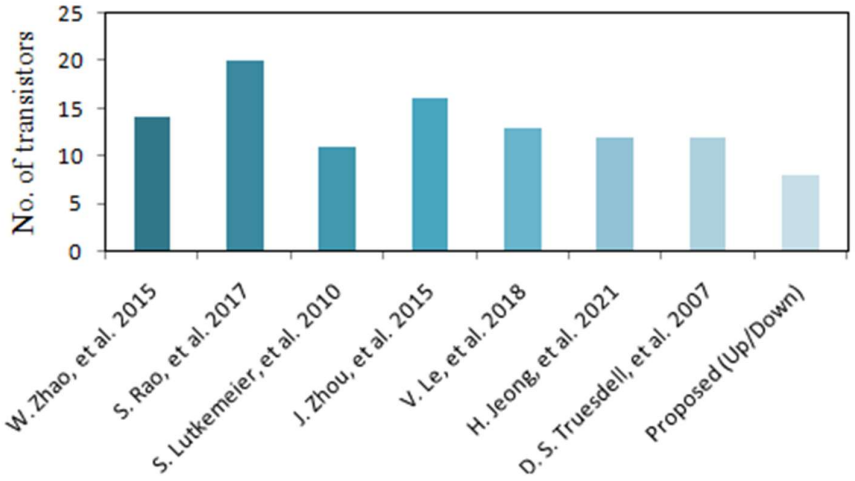

Figure 12. No. of transistors in LS [3,4,11,20–23].

Figure 5 illustrates the least possible VDDL of SILS for varying frequencies with a distinctive corner including MOS transistors, 27 °C and VDDH = 1.2 V. It can be seen that by decreasing the frequency of the circuit, the power consumption is decreased, which suggests that either decreases in frequency or decreasing the VDDL to lower than 0.2 V are possible. The minimum value of VDDL can be 0.15 V when the SILS operates at 100 kHz. The delay and power consumption at lower frequency has shown that the minimum possible VDDL can be achieved to meet the needs of IoT and biomedical, wireless sensor network applications. Apparently, the proposed SILS has the lowest PDP and area for up or down voltage-level conversions.

4. Conclusions

This study proposes a split-input inverter level shifter that effectively converts sub-threshold voltages to nominal supply voltages. The proposed structure consists of a short-circuit-aware inverter that can create common unconnected PMOS and NMOS transistors and an output inverter that can accelerate the inverter's power delivery to improve switching and energy efficiency. The split-input inverter level shifter was implemented using 65 nm CMOS technology, and we tested the performance for different factors such as voltages, temperatures, and process corners. From the results obtained, it is concluded that the design can convert very low-voltage inputs with an average of 0.2 V under optimistic conditions at 27 °C, and the SILS can produce up to 1.2 V. The proposed circuit demonstrates efficient dynamic power consumption and low latency. It has a remarkable delay of 1.3 ns, coupled with excellent energy efficiency. The energy consumption is also impressive, with an average power of 9.5 nW.

Author Contributions: Conceptualization, S.G. and M.M.B.; methodology, S.G. and V.M.; validation, S.G., M.M.B. and V.M.; formal analysis, M.M.B. and O.P.S.; investigation, M.M.B.; writing—original draft preparation, S.G. and M.M.B.; writing—review and editing, V.M. and O.P.S.; visualization, O.P.S.; supervision, O.P.S.; project administration, V.M. and O.P.S.; funding acquisition, O.P.S. All authors have read and agreed to the published version of the manuscript.

Funding: This research was partially supported by the project 38 PFE in the framework of the program PDI-PFE-CDI 2021.

Data Availability Statement: The data will be provided upon reasonable request to the authors.

Conflicts of Interest: The authors declare no conflicts of interest.

References

1. Saleh, R. System-on-chip: Reuse and integration. *Proc. IEEE* **2006**, *94*, 1050–1069. [CrossRef]
2. Lanuzza, M.; Perri, S. Fast and wide range voltage conversion in multisupply voltage designs. *IEEE Trans. Very Large Scale Integr. Syst.* **2015**, *23*, 388–391. [CrossRef]
3. Zhao, W.; Alvarez, A.B.; Ha, Y. A 65-nm 25.1-ns 30.7-fJ robust subthreshold level shifter with wide conversion range. *IEEE Trans. Circuits Syst. II Express Briefs* **2015**, *62*, 671–675. [CrossRef]
4. Lanuzza, M.; Crupi, F.; Rao, S.; De Rose, R.; Strangio, S.; Iannaccone, G. An ultralow-voltage energy-efficient level shifter. *IEEE Trans. Circuits Syst. II Express Briefs* **2017**, *64*, 61–65. [CrossRef]
5. Mocan, B.; Osan, C.; Fulea, M.; Chis, I.A.; Timoftei, S.; Sarb, A. An Integrated Model for Solving Cell Formation Problem and Robot Scheduling using Timed Petri Nets. In Proceedings of the 2016 International Conference on Production Research—Africa, Europe and the Middle East and 4th International Conference on Quality and Innovation in Engineering and Management, Cluj-Napoca, Romania, 25–30 July 2016; pp. 91–96.
6. Fassio, L.; Settino, F.; Lin, L.; De Rose, R.; Lanuzza, M.; Crupi, F.; Alioto, M. A robust, high-speed and energy-efficient ultralow voltage level shifter. *IEEE Trans. Circuits Syst. II Express Briefs* **2021**, *68*, 1393–1397. [CrossRef]
7. Låte, E.; Ytterdal, T.; Aunet, S. An energy efficient level shifter capable of logic conversion from sub-15 mV to 1.2 V. *IEEE Trans. Circuits Syst. II Express Briefs* **2020**, *67*, 2687–2691. [CrossRef]
8. Cao, L.; Bale, S.J.; Trefzer, M.A. Multi-objective digital design optimization via improved drive granularity standard cells. *IEEE Trans. Circuits Syst. I Regul. Pap.* **2021**, *68*, 4660–4671. [CrossRef]
9. Rajendran, S.; Chakrapani, A. A 16 ns, 28 fJ wide-range subthreshold level converter using low-voltage current mirror. *Circuits Syst. Signal Process.* **2020**, *40*, 1479–1495. [CrossRef]
10. Matsuzuka, R.; Hirose, T.; Shizuku, Y.; Shinonaga, K.; Kuroki, N.; Numa, M. An 80-mV-to-1.8-V conversion-range low-energy level shifter for extremely low-voltage VLSIs. *IEEE Trans. Circuits Syst. I Regul. Pap.* **2017**, *64*, 2026–2035. [CrossRef]
11. Zhou, J.; Wang, C.; Liu, X.; Zhang, X.; Je, M. An ultra-low voltage level shifter using revised wilson current mirror for fast and energy-efficient wide-range voltage conversion from sub-threshold to I/O voltage. *IEEE Trans. Circuits Syst. I Regul. Pap.* **2015**, *62*, 697–706. [CrossRef]
12. Kabirpour, S.; Jalali, M. A power-delay and area efficient voltage level shifter based on a reflected-output Wilson current mirror level shifter. *IEEE Trans. Circuits Syst. II Express Briefs* **2020**, *67*, 250–254. [CrossRef]
13. Basha, M.M.; Gundala, S.; Khan, S.I. Design of energy and EDP efficient 1-bit full subtractor based divider circuits for computing systems. *Int. J. Syst. Syst. Eng.* **2021**, *11*, 257–267. [CrossRef]
14. Ma, C.; Ji, Y.; Qiao, C.; Zhou, T.; Qi, L.; Li, Y. An energy-efficient level shifter using time borrowing technique for ultra wide voltage conversion from sub-200 mV to 3.0 V. In Proceedings of the 2021 IEEE International Symposium on Circuits and Systems (ISCAS), Daegu, Republic of Korea, 22–28 May 2021; pp. 1–5.
15. Neeraj, K.; Mahaboob Basha, M.; Gundala, S. Design of low power SRAM-based ubiquitous sensor for wireless body area networks. *Int. J. Pervasive Comput. Commun.* **2021**, *17*, 611–621. [CrossRef]
16. Yuan, B.; Xiao, L.Q.; Wang, B.Y.; Ying, J. High-speed dynamic level shifter for high-side bootstrapped gate driver in high-voltage buck regulators. *IEEE Trans. Circuits Syst. II Express Briefs* **2021**, *68*, 3083–3087. [CrossRef]
17. Sarmiento, M.; Nguyen, K.D.; Duran, C.; Hoang, T.T.; Serrano, R.; Hoang, V.P.; Tran, X.T.; Ishibashi, K.; Pham, C.K. A sub-μW reversed-body-bias 8-bit processor on 65-nm silicon-on-thin-box (SOTB) for IoT applications. *IEEE Trans. Circuits Syst. II Express Briefs* **2021**, *68*, 3182–3186.
18. Gundala, S.; Basha, M.M.; Vijayakumar, S. Level-Up/Level-Down Voltage Level Shifter for Nano-Scale Applications. *J. Eng. Sci. Technol.* **2022**, *17*, 745–759.
19. Sudhakar, M.V.; Stan, O.P. Implementation of High-Speed Compact Level-Up Shifter for Nano-Scale Applications. *Electronics* **2023**, *12*, 5015. [CrossRef]
20. Lütkemeier, S.; Rückert, U. A subthreshold to above-threshold level shifter comprising a Wilson current mirror. *IEEE Trans. Circuits Syst. II Express Briefs* **2010**, *57*, 721–724. [CrossRef]
21. Le, V.L.; Kim, T.T.-H. An area and energy efficient ultra-low voltage level shifter with pass transistor and reduced-swing output buffer in 65-nm CMOS. *IEEE Trans. Circuits Syst. II Express Briefs* **2018**, *65*, 607–611. [CrossRef]
22. Jeong, H.; Kim, T.H.; Park, C.N.; Kim, H.; Song, T.; Jung, S.O. A wide-range static current-free current mirror-based LS with logic error detection for near-threshold operation. *IEEE J. Solid-State Circuits* **2021**, *56*, 554–565. [CrossRef]
23. Truesdell, D.S.; Calhoun, B.H. A single-supply 6-transistor voltage level converter design reaching 8.18-fJ/transition at 0.3–1.2-V range or 44-fW leakage at 0.8–2.5-V range. *IEEE Solid-State Circuits Lett.* **2007**, *3*, 502–505. [CrossRef]

Disclaimer/Publisher's Note: The statements, opinions and data contained in all publications are solely those of the individual author(s) and contributor(s) and not of MDPI and/or the editor(s). MDPI and/or the editor(s) disclaim responsibility for any injury to people or property resulting from any ideas, methods, instructions or products referred to in the content.

SPRINGER NATURE Link

Log in

Menu Search Cart

Home > Carbon Letters > Article

Hierarchically porous polyaromatic carbon spheres decorated $NiMn_2O_4$ nanocomposite: efficient selective azo dye degradation from aqueous water and reduction of *p*-nitrophenol to *p*-aminophenol

| Original Article | Published: 08 February 2024

| Volume 34, pages 1229–1237, (2024) Cite this article

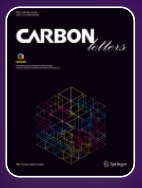

Carbon Letters

Aims and scope →

Submit manuscript →

Reddi Mohan Naidu Kalla, T. Kaliraja, Sivarama Krishna Lakkaboyana, Seong-Cheol Kim & Il Kim

244 Accesses 3 Citations Explore all metrics →

Abstract

We have intended and preparation of hierarchically absorbent materials were covered with a $NiMn_2O_4$ and acts as a catalyst for azo dye degradation. The polyaromatic-based (PA) absorbent compounds were initially constructed by bromomethylated aromatic hydrocarbons which undergo self-polymerization in presence of ZnBr as a reagent and cross linker is bromomethyl methyl ether. The absorbent black materials with a 3D network were prepared by direct carbonization and activation of the as-prepared PA. The hydrothermal method was adapted for the preparation of carbon hybrid material C@$NiMn_2O_4$ powder's catalytic activity is effective in reducing *p*-nitrophenol

to *p*-aminophenol and decolorizing carbon-based dyes like methyl orange (MO), methyl yellow (MY), and Congo red (CR) in aqueous media at 25 °C when $NaBH_4$ is added. UV–visible spectroscopy was used to analyze the dyes' breakdown at regular interval.

This is a preview of subscription content, log in via an institution to check access.

Access this article

Log in via an institution →

Buy article PDF 39,95 €

Price includes VAT (India)

Instant access to the full article PDF.

Rent this article via DeepDyve

Institutional subscriptions →

Similar content being viewed by others

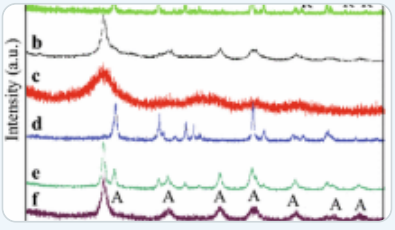

Mesoporous TiO_2/Carbon Beads: One-Pot Preparation and Their Application in Visible-Light-Induced…

Article | Open access

24 March 2015

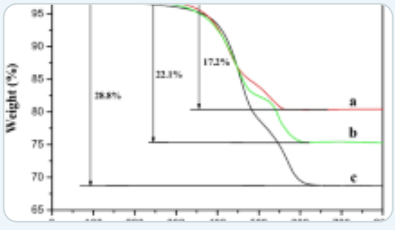

Preparation and photocatalytic performance of ZnO/carbon composites for organic dyes degradation

Article | 07 September 2023

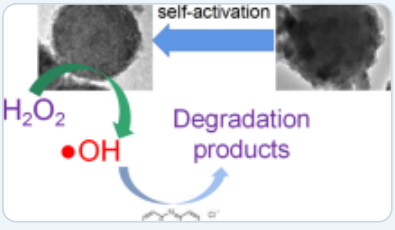

Preparation of manganese oxide-porous carbon nanocomposites by self-activation and their…

Article | 02 January 2021

Data availability

All pertinent data generated or analyzed during this investigation and presented in the published article.

References

1. Aizenberg J, Weaver JC, Thanawala MS, Sundar VC, Morse DE, Fatzl P (2005) Skeleton of *Euplectella* sp.: structural hierarchy from the nanoscale to the macroscale. Science 309:275–278. https://doi.org/10.1126/science.1112255

Article CAS PubMed Google Scholar

2. Zou C, Wu DC, Li MZ, Zeng QC, Xu F, Huang ZY, Fu RW (2010) Template-free fabrication of hierarchical porous carbon by constructing carbonyl crosslinking bridges between polystyrene chains. J Mater Chem 20:731–735. https://doi.org/10.1039/B917960G

Article CAS Google Scholar

3. Ji QM, Yoon SB, Hill JP, Vinu A, Yu JS, Ariga K (2009) Layer-by-layer films of dual-pore carbon capsules with designable selectivity of gas adsorption. J Am Chem Soc 131:4220–4221. https://doi.org/10.1021/ja9010354

Article CAS PubMed Google Scholar

4. Yu JG, Su YR, Cheng B (2007) Template-free fabrication and enhanced photocatalytic activity of hierarchical macro-/mesoporous titania. Adv Funct Mater 17:1984–1990. https://doi.org/10.1002/adfm.200600933

Article CAS Google Scholar

5. Wang DW, Li F, Liu M, Lu GQ, Cheng HM (2008) 3D aperiodic hierarchical porous graphitic carbon material for high-rate electrochemical capacitive energy storage. Angew Chem Int Ed 47:373–376. https://doi.org/10.1002/anie.200702721

Article Google Scholar

6. Valkama S, Nykanen A, Kosonen H, Ramani R, Tuomisto F, Engelhardt P, Brinke GT, Ikkala O, Ruokolainen J (2007) Hierarchical porosity in self-assembled polymers: post-modification of block copolymer-phenolic resin complexes by pyrolysis allows the control of micro- and mesoporosity. Adv Funct Mater 17:183–190. https://doi.org/10.1002/adfm.200600604

Article CAS Google Scholar

7. Huang X, Kim S, Heo MS, Kim JE, Suh H, Il K (2013) Easy synthesis of hierarchical carbon spheres with superior capacitive performance in super capacitors. Langmuir 29:12266–12274. https://doi.org/10.1021/la402696

Article CAS PubMed Google Scholar

8. Kalla RMN, Varyambath A, Kim MR, Kim I (2017) Amine-functionalized hyper-crosslinked polyphenanthrene as a metal-free catalyst for the synthesis of 2-amino-tetrahydro-4*H*-chromene and pyran derivatives. Appl Catal A 538:9–18. https://doi.org/10.1016/j.apcata.2017.03.009

Article CAS Google Scholar

9. Huang X, Kim MR, Suh H, Il K (2016) Hierarchically nanostructured carbon-supported manganese oxide for high-performance pseudo-capacitors. Korean J Chem Eng 33:2228–2234. https://doi.org/10.1007/s11814-016-0036-3

Article CAS Google Scholar

10. Peng Y, Chen Z, Wen J, Xiao Q, Weng D, He S, Geng H, Lu Y (2011) Hierarchical manganese oxide/carbon nanocomposites for supercapacitor electrodes. Nano Res 4:216–225. https://doi.org/10.1007/s12274-010-0072-y

Article CAS Google Scholar

11. Gupta VK, Jain R, Mittal A, Saleh TA, Nayak A, Agarwal S, Sikarwar S (2012) Photo-catalytic degradation of toxic dye amaranth on TiO_2/UV in aqueous suspensions. Mater Sci Eng C 32:12–17. https://doi.org/10.1016/j.msec.2011.08.018

Article CAS Google Scholar

12. Mathur N, Bathnagar P, Nagar P, Bijiarnia MK (2005) Mutagenicity assessment of effluents from textile/dye industries of Sanganer, Jaipur (India): a case study. Ecotoxicol Environ Saf 61:105–103. https://doi.org/10.1016/j.ecoenv.2004.08.003

Article CAS PubMed Google Scholar

13. De Roos AJ, Ray RM, Gao DL, Wernli KJ, Fitzgibbons ED, Zinding F, Astrakianakis G, Thoma DB, Checkoway H (2005) Colorectal cancer incidence among female textile workers in Shanghai, China: a case-cohort analysis of occupational exposures. Cancer Causes Control 16:1117–1188. https://doi.org/10.1007/s10552-005-0398-z

Article Google Scholar

14. Dogan EE, Yesilada E, Ozata L, Yologlu S (2005) Genotoxicity testing of four textile dyes in two crosses of Drosophila using wing somatic mutation and recombination test. Drug Chem Toxicol 28:289–301. https://doi.org/10.1081/dct-200064473

Article CAS PubMed Google Scholar

15. Ying TY, Yang KL, Yiacoumi S, Tsouris C (2002) Electrosorption of ions from aqueous solutions by nanostructured carbon aerogel. J Colloid Interface Sci 250:18–27. https://doi.org/10.1006/jcis.2002.8314

Article CAS PubMed Google Scholar

16. Chiron S, Fernandez-Alba A, Rodriguez A, Calvo EC (2000) Pesticide chemical oxidation: state-of-the-art. Water Res 34:366–377. https://doi.org/10.1016/S0043-1354(99)00173-6

Article CAS Google Scholar

17. Konstantinou IK, Albanis TA (2004) TiO_2-assisted photocatalytic degradation of azo dyes in aqueous solution: kinetic and mechanistic investigations a review. Appl Catal B Environ 49:1–14. https://doi.org/10.1016/j.apcatb.2003.11.010

Article CAS Google Scholar

18. Burrows HD, Canle M, Santaballa JA, Steenken S (2002) Reaction pathways and mechanisms of photodegradation of pesticides. J Photochem Photobiol B Biol 67:71–108. https://doi.org/10.1016/S1011-1344(02)00277-4

Article CAS Google Scholar

19. Sen K, Maity K, Islam SS (2013) Green synthesis of gold nanoparticles using a glucan of an edible mushroom and study of catalytic activity. Carbohydr Polym 91:518–528. https://doi.org/10.1016/j.carbpol.2012.08.058

Article CAS PubMed Google Scholar

20. Dasog M, Hou W, Scott RWJ (2011) Controlled growth and catalytic activity of gold monolayer protected clusters in presence of borohydride salts. Chem Commun 47:8569–8571. https://doi.org/10.1039/C1CC11813G

Article CAS Google Scholar

21. Jana NR, Sau TK, Pal T (1999) Growing small silver particle as redox catalyst. J Phys Chem B 103:115–121. https://doi.org/10.1021/jp982731f

Article CAS Google Scholar

22. Sinha AK, Basu M, Sarkar S, Pradhan M, Pal T (2013) Synthesis of gold nanochains via photoactivation technique and their catalytic applications. J Colloid Interface Sci 398:13–21. https://doi.org/10.1016/j.jcis.2013.01.061

Article CAS PubMed Google Scholar

23. Kalla RMN, Kim MR, Kim I (2018) Sulfonic acid-functionalized, hyper-cross-linked porous polyphenols as recyclable solid acid catalysts for esterification and transesterification reactions. Ind Eng Chem Res 57:11583–11591. https://doi.org/10.1021/acs.iecr.8b02418

Article CAS Google Scholar

24. Liao Q, Kim EJ, Tang Y, Xu H, Yu D-G, Song W, Kim BJ (2023) Rational design of hyper-crosslinked polymers for biomedical applications. J Polym Sci. https://doi.org/10.1002/pol.20230270

Article Google Scholar

25. Song W, Zhang M, Huang X, Chen B, Ding Y, Zhang Y, Yu DG, Kim I (2022) Smart l-borneol-loaded hierarchical hollow polymer nanospheres with antipollution and antibacterial capabilities. Mater Today Chem 26:101252. https://doi.org/10.1016/j.mtchem.2022.101252

Article CAS Google Scholar

26. Song W, Zhang Y, Yu D-G, Tran CH, Wang M, Varyambath A, Kim J, Kim I (2020) Efficient synthesis of folate-conjugated hollow polymeric capsules for accurate drug delivery to cancer cells. Biomacromol 22:732–742. https://doi.org/10.1021/acs.biomac.0c01520

Article CAS Google Scholar

27. Kim MR, Kalla RMN, Kim S, Kim MR, Il K (2017) $NiMn_2O_4$ nano-sheet decorated hierarchically porous polyaromatic carbon spheres for high-performance supercapacitors. Chem Electro Chem 4:1214–1221. https://doi.org/10.1002/celc.201700023

Article CAS Google Scholar

28. Lim C, Kwak CH, Jeong SG, Kim D, Lee Y-S (2023) Enhanced CO_2 adsorption of activated carbon with simultaneous surface etching and functionalization by nitrogen plasma treatment. Carbon Lett 33(1):139–145. https://doi.org/10.1007/s42823-022-00410-1

Article Google Scholar

29. Zhang Y, Huang J, Dong Z (2023) Pd–Fe bimetallic nanoparticles anchored on N-doped carbon-modified graphene for efficient catalytic organic reactions. Carbon Lett 33:77–87. https://doi.org/10.1007/s42823-022-00404-z

Article Google Scholar

30. Thillaikkarasi D, Karthikeyan S, Ramesh R (2022) Electrochemical performance of various activated carbon-multi-walled carbon nanotubes symmetric supercapacitor electrodes in aqueous electrolytes. Carbon Lett 32:1481–1505. https://doi.org/10.1007/s42823-022-00386-y

Article Google Scholar

31. Gou G, Wei W, Yang J (2022) Effect of anion species on preparation and properties of pitch-based activated carbon fibers by in-situ catalytic activation of metal nanoparticles. Carbon Lett 32:1507–1518. https://doi.org/10.1007/s42823-022-00375-1

Article Google Scholar

32. Vilian AE, Choe SR, Giribabu K, Jang SC, Roh C, Huh YS, Han YK (2017) Pd nanospheres decorated reduced graphene oxide with multi-functions: highly efficient catalytic reduction and ultrasensitive sensing of hazardous 4-nitrophenol pollutant. J Hazard Mater 333:54–62. https://doi.org/10.1016/j.jhazmat.2017.03.015

Article CAS PubMed Google Scholar

33. Vilian AE, Ranjith KS, Hwang SK, Bhaskaran G, Alhammadi M, Park SY, Huh YS, Han YK (2022) Interface engineering of MoS2 nanopetal grown on carbon nanofibers for the electrocatalytic sensing of mercury (II) and efficient hydrogen evolution. Mater Today Nano 20:100262

Article Google Scholar

34. Al Yahyai WAS, Al Isai AAS, Alotibi MF, Bhagavanth Reddy G, Al-Abri M, Babu P, Nagaraju D, Siva Kumar N, Al-Fatesh AS, Osman AI, Kondaiah S (2023) Green synthesis of Mesona Blumes gum capped silver nanoparticles and their antioxidant, antibacterial and catalytic studies. Mater Adv 4:5273. https://doi.org/10.1039/D3MA00091E

Article Google Scholar

35. Wang C, Yang F, Yang W, Ren L, Zhang Y, Jia X, Zhang L, Li Y (2015) PdO nanoparticles enhancing the catalytic activity of Pd/carbon nano-tubes for 4-nitrophenol reduction. RSC Adv 5:27526–27532. https://doi.org/10.1039/C4RA16792A

Article CAS Google Scholar

36. Amritha VK, Badhulika S (2023) A visible light-driven $NaTiO_3$/g-C_3N_4 heterojunction photocatalyst for ultra-fast organic dye degradation. New J Chem 47:17897–17907. https://doi.org/10.1039/D3NJ02907G

Article Google Scholar

37. Gul T, Khan I, Ahmad B, Ahmad S, Alsaiari AA, Almehmadi M, Abdulaziz O, Alsharif A, Khan I, Saeed K (2023) Efficient photodegradation of methyl red dye by kaolin clay supported zinc oxide nanoparticles with their antibacterial and antioxidant activities. Heliyon 9:e16738. https://doi.org/10.1016/j.heliyon.2023.e16738

Article CAS PubMed PubMed Central Google Scholar

38. Harikaran D, Vijayaraghavan R (2023) Strontium peroxide as a potential photocatalyst: rapid degradation of organic and pharmaceutical pollutants. New J Chem 47:20733–20743. https://doi.org/10.1039/D3NJ03546H

Article CAS Google Scholar

39. Huang L, He M, Chen B, Cheng Q, Hu B (2017) Facile green synthesis of magnetic porous organic polymers for rapid removal and separation of methylene blue. ACS Sustainable Chem Eng 5:4050–4055. https://doi.org/10.1021/acssuschemeng.7b00031

Article CAS Google Scholar

40. Farhadi S, Siadatnasab F, Khataee A (2017) Ultrasound-assisted degradation of organic dyes over magnetic $CoFe_2O_4$@ZnS core-shell nanocomposite. Ultrason Sonochem 37:298–309. https://doi.org/10.1016/j.ultsonch.2017.01.019

Article CAS PubMed Google Scholar

Acknowledgements

This research was supported by Yeungnam University grant 2023.

Author information

Authors and Affiliations

School of Chemical Engineering, Yeungnam University, Gyeongsan, 38541, Republic of Korea
Reddi Mohan Naidu Kalla & Seong-Cheol Kim

Department of Electronics and Communication Engineering, Srivenkateswara College of Engineering, Tirupati, Andhra Pradesh, India
T. Kaliraja

Department of Chemistry, Vel Tech Rangarajan Dr. Sagunthala R&D Institute of Science and Technology, Avadi, Chennai, 600062, Tamil Nadu, India
Sivarama Krishna Lakkaboyana

School of Chemical Engineering, Pusan National University, Busandaehag-ro 63-2, Geumjeong-gu, Busan, 46241, Republic of Korea
Il Kim

Corresponding authors

Correspondence to Sivarama Krishna Lakkaboyana, Seong-Cheol Kim or Il Kim.

Ethics declarations

Confilict of interest

The authors declare no conflict of interest.

Additional information

Publisher's Note

Springer Nature remains neutral with regard to jurisdictional claims in published maps and institutional affiliations.

Rights and permissions

Springer Nature or its licensor (e.g. a society or other partner) holds exclusive rights to this article under a publishing agreement with the author(s) or other rightsholder(s); author self-archiving of the accepted manuscript version of this article is solely governed by the terms of such publishing agreement and applicable law.

Reprints and permissions

About this article

Cite this article

Kalla, R.M.N., Kaliraja, T., Lakkaboyana, S.K. *et al.* Hierarchically porous polyaromatic carbon spheres decorated $NiMn_2O_4$ nanocomposite: efficient selective azo dye degradation from aqueous water and reduction of *p*-nitrophenol to *p*-aminophenol. *Carbon Lett.* 34, 1229–1237 (2024). https://doi.org/10.1007/s42823-023-00685-y

Received	Revised	Accepted
01 December 2023	21 December 2023	24 December 2023

Published	Issue Date
08 February 2024	May 2024

DOI
https://doi.org/10.1007/s42823-023-00685-y

Keywords

Organic dyes | C@$NiMn_2O_4$ nanocomposite | Heterogeneous catalysis | $NaBH_4$

International Journal of
INTELLIGENT SYSTEMS AND APPLICATIONS IN ENGINEERING
ISSN:2147-6799 www.ijisae.org Original Research Paper

Face Recognition Using Computer Vision and CNN Algorithm

[1]Dr. D. Sri Hari, [2]Dr. T. Chandra Sekhar Rao, [3]Mr. T. Venkataramana, [4]Mrs. D. Himabindu

Submitted: 17/10/2023 **Revised**: 07/12/2023 **Accepted**: 16/12/2023

Abstract: Numerous uses for face recognition exist in the fields of security, surveillance, and human-computer interaction. The development of Convolutional Neural Networks (CNNs) has revolutionized the field of face recognition. In this work, we examine how well a CNN-based facial recognition system performs. We compare the performance of this system to traditional methods, such as Eigenfaces and Fisher faces, using metrics such as accuracy and processing time. We also evaluate the system's robustness to variations in lighting, pose, and expression. Our results show that the CNN-based approach outperformed traditional methods in terms of accuracy and processing time. The CNN algorithm was able to recognize faces with a higher level of accuracy, even under challenging conditions such as changes in lighting, pose, and expression. Furthermore, the CNN-based system was able to process images much faster than traditional methods. Our research adds to the body of work being done in this area and offers useful insights for the design of upcoming facial recognition systems.

Keywords: *CNN (Convolutional Neural Network), Deep Learning, Dataset, Face recognition, OpenCV, Eigenfaces and Fisher faces.*

1. Introduction

Introduction: Face recognition using computer vision and CNN algorithm has become a hot topic in the field of computer science. Traditional methods for face recognition, such as template matching and feature extraction, have limitations in terms of accuracy and efficiency. Therefore, researchers have been exploring new approaches, and the development of Convolutional Neural Networks (CNNs) has revolutionized the field of face recognition. In this article, we investigate the performance of a face recognition system based on a CNN algorithm. We aim to answer the research question: How does a CNN-based face recognition system compare to traditional methods in terms of accuracy and efficiency?

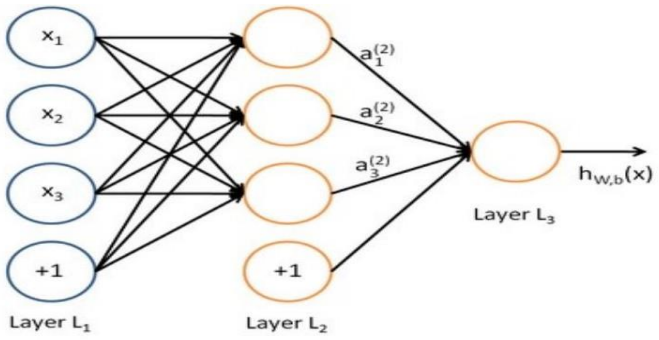

Figure 1. Neural Networks.

[1]*Professor, Department of ECE, Sri Venkateswara College of Engineering and Technology (A), Chittoor Andhra Pradesh, India. Email: dsrihari@svcet.in*
[2]*Professor, Department of ECE, Sri Venkateswara College of Engineering (A), Tirupati, Andhra Pradesh, India.*
Email: chandrasekhar.t@svcolleges.edu.in
[3]*Assistant Professor, Department of ECE, Siddartha Educational Academy Group of Institutions (SEAGI), Tirupati. Andhra Pradesh, India. Email: tvramana812@gmail.com*
[4]*Assistant Professor, Department of EEE, SOET, SPMVV, Tirupati, Andhra Pradesh. sribindu262004@gmail.com.*
[0009-0006-9158-8461][1],*
[0000-0001-8993-3891][2],
[0009-0001-9360-318X][3],
[0009-0005-2248-1639][4]

2. Literature Review

We conducted a literature review to gain a comprehensive understanding of the existing research on face recognition using computer vision and CNN algorithm. We found that previous studies have explored various approaches to face recognition, including traditional methods such as Eigenfaces and Fisherfaces, as well as more advanced techniques based on deep learning algorithms like CNN. While traditional methods have been widely used

in the past, they have limitations in terms of accuracy and efficiency, particularly in the face of challenging conditions such as changes in lighting, pose, and expression. On the other hand, CNN-based approaches have shown promising results in overcoming these limitations and achieving high levels of accuracy and efficiency in face recognition.

Existing Method

The face recognitions could only be done with the current method by actually seeing the people. One can observe, but only they are capable of recognizing afterward, which can be done manually. Manually performing recognition will be quite challenging.

3. Proposed System

Our proposed face recognition system using CNN algorithm collects a dataset of facial images, pre-processes the data, trains the CNN model, detects and aligns faces in real-time images, and recognizes faces by comparing features to a database. The system is more accurate and efficient than traditional methods, and has applications in security and surveillance, and human-computer interaction. It offers a promising approach to achieving high levels of accuracy and efficiency in recognizing human faces, and contributes to ongoing research in this field.

Methodology Convolutional Neural Network Step1: convolutional operation

The first component of our strategy is the convolution operation. This phase will briefly discuss feature detectors, which are essentially the filters for the neural network. Also, We'll discuss feature maps, their variables, and how patterns are discovered, how to map out the results, and how layers of detection work.

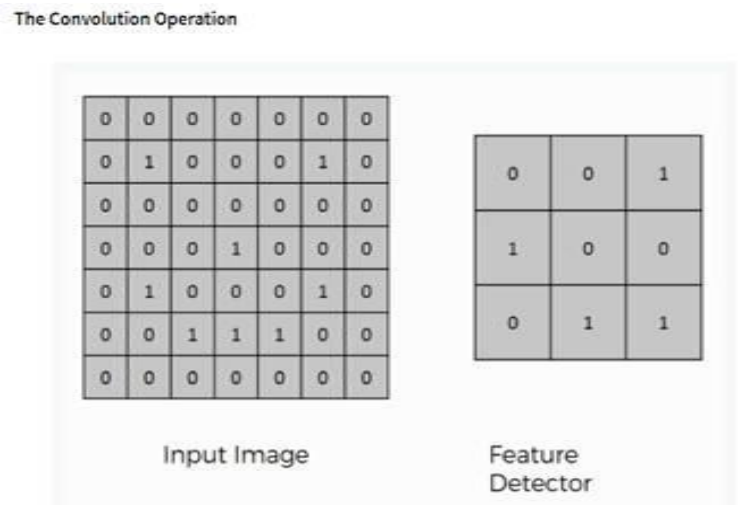

Step (1b): Relu Layer

The Rectified Linear Unit, or Relook, will be used in the second stage of this technique. It is not necessary to comprehend CNNs in order to benefit from this lecture, although it won't hurt to brush up on your knowledge of Examine layers once more and the operation of linearity in the context of convolutional neural networks.

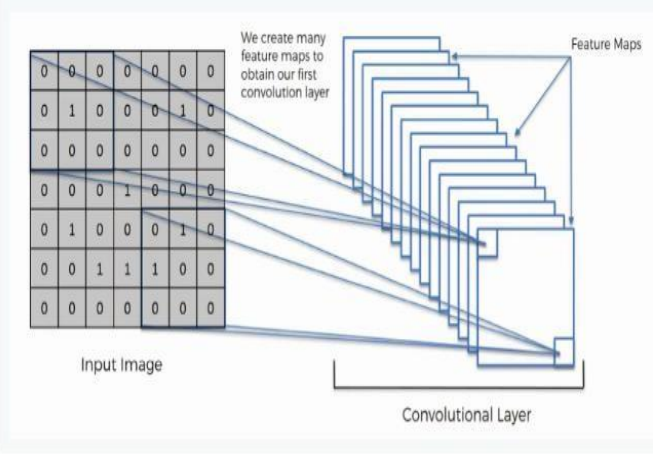

Step 2: Pooling Layer

Although understanding CNNs is not required to benefit from this lecture, it wouldn't hurt to review Relook layers and how linearity functions in the context of convolutional neural networks.

Step 3: Flattening

Here is a quick summary of the flattening procedure and how convolutional neural networks connect to it and how we use them to go from pooling to flattened layers.

Step 4: Full Connection

Everything we discussed in the previous section will be included in this one. If you understand this, you'll be able to picture how Convolutional functions.

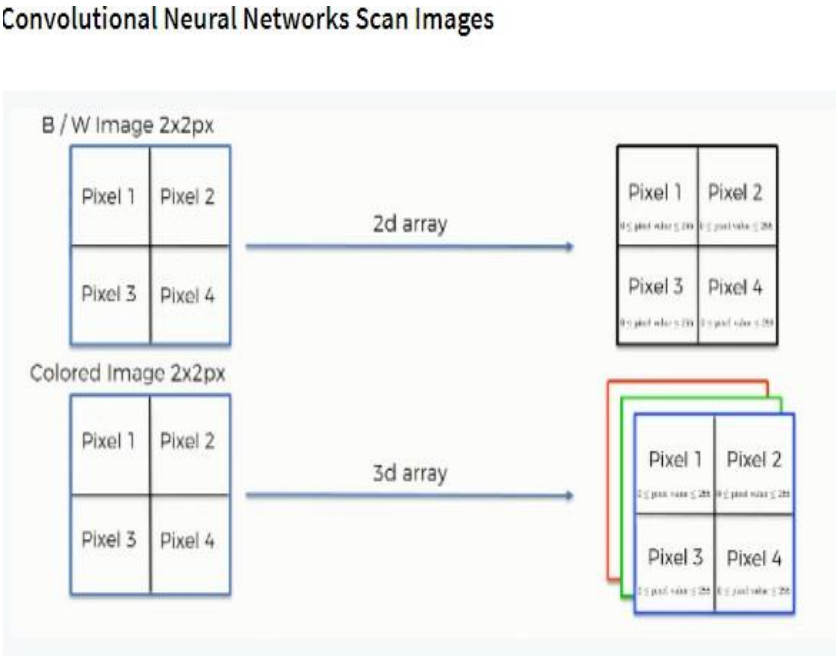

Architecture of Proposed System

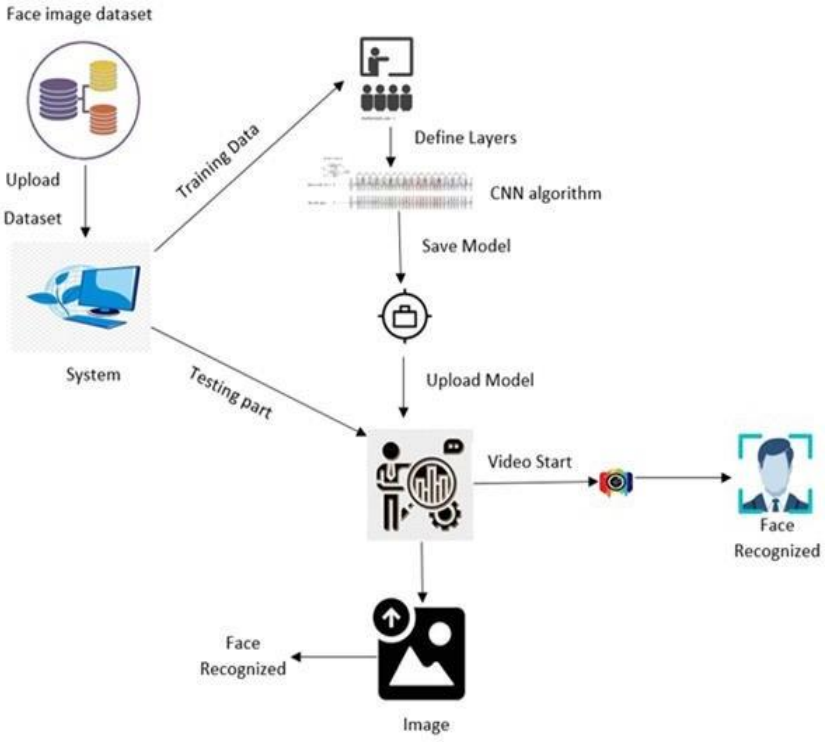

4. Result

According to our findings, the CNN-based method surpassed conventional techniques in terms of processing speed and accuracy. The CNN algorithm was able to recognize faces with a higher level of accuracy, even under challenging conditions such as changes in lighting, pose, and expression. Furthermore, the CNN-based system was able to process images much faster than traditional methods.

Giving input (recording faces)

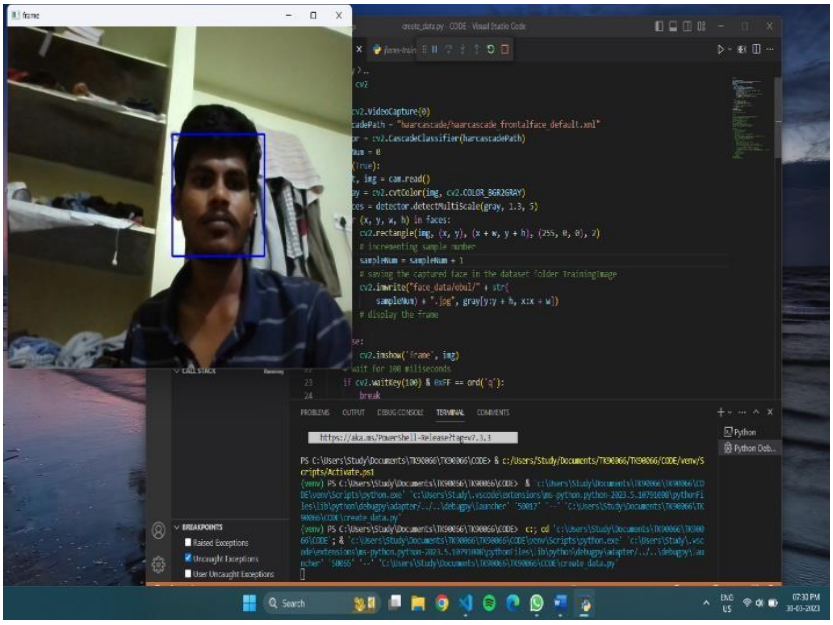

Recognition of faces that are being trained by CNN

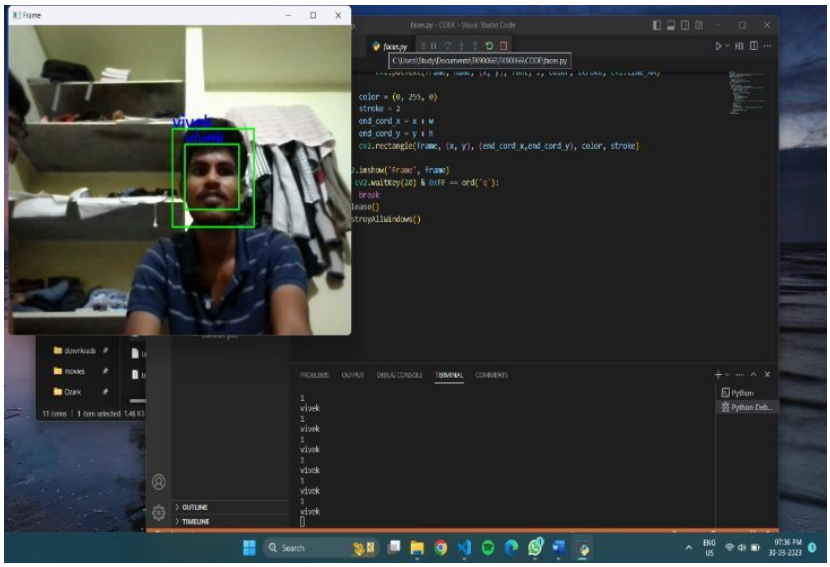

5. Conclusion

In conclusion, facial recognition using CNN algorithm shows great potential in various applications, including security and marketing. However, the technology is not yet fully developed, and ethical considerations must be addressed to ensure its proper use.

Future Scope

In order to improve accuracy and predictability, we should think about training the model on a significant volume of data in the future. The machines may be able to recognize facial expressions with the aid of this procedure.

References

[1] Patrik KAMENCAY, Miroslav BENCO, Tomas MIZDOS, Roman RADIL. DIGITAL IMAGE PROCESSING AND COMPUTER GRAPHICS. VOLUME: 15 | NUMBER: 4 | 2017| SPECIAL ISSUE.

[2] Shen Huijun. Research and implementation of face recognition image pre-processing method [J]. Science and Technology and Innovation, 2014 (18): 119-120.

[3] Convolutional Neural Networks (CNN) - Plan of Attack – Blogs The Ultimate Guide to Convolutional Neural Networks, published by Super Data Science Team, Aug 18, 2018.

Optimal deep transfer learning enabled object detector for anomaly recognition in pedestrian ways

Article type: Research Article

Authors: Shaik, Allabaksh (https://content.iospress.com:443/search?q=author%3A%28%22Shaik, Allabaksh%22%29) (https://orcid.org/0000-0002-2569-6142) [a; b; *] | Basha, Shaik Mahaboob (https://content.iospress.com:443/search?q=author%3A%28%22Basha, Shaik Mahaboob%22%29) (https://orcid.org/0000-0002-5843-4472) [c]

Affiliations: **[**a**]** Jawaharlal Nehru Technological University Anantapur, Ananthapuramu, Andhra Pradesh, India | **[**b**]** Sri Venkateswara College of Engineering Tirupati, Affiliated to Jawaharlal Nehru Technological University Anantapur, Ananthapuramu, Andhra Pradesh, India | **[**c**]** N.B.K.R. Institute of Science and Technology, Vidyanagar, Affiliated to Jawaharlal Nehru Technological University Anantapur, Ananthapuramu, Andhra Pradesh, India

Correspondence: [*] Corresponding author: Allabaksh Shaik, Research Scholar, Jawaharlal Nehru Technological University Anantapur, Ananthapuramu, Andhra Pradesh, India. Tel.: +91 9700644100; E-mail: baksh402@gmail.com (mailto:baksh402@gmail.com).

Abstract: Anomaly detection is a branch of behavior understanding in surveillance scenes, where anomalies represent a deviation in the behavior of scene entities (viz.,humans, vehicles, and environment) from regular patterns. In pedestrian walkways, this plays a vital role in enhancing safety. With the widespread use of video surveillance systems and the escalating video volume, manual examination of abnormal events becomes time-intensive.Hence, the need for an automated

surveillance system adept at anomaly detection is crucial, especially within the realm of computer vision (CV) research. The surge in interest towards deep learning (DL) algorithms has significantly impacted CV techniques, including object detection and classification. Unlike traditional reliance on supervised learning requiring labeled datasets, DL offers advancements in these applications. Thus, this study presents an Optimal Deep Transfer Learning Enabled Object Detector for Anomaly Recognition in Pedestrian Ways (ODTLOD-ARPW) technique. The purpose of the ODTLOD-ARPW method is to recognize the occurrence of anomalies in pedestrian walkways using a DL-based object detector. In the ODTLOD-ARPW technique, the image pre-processing initially takes place using two sub-processes namely Wiener filtering (WF) based pre-processing and dynamic histogram equalization-based contrast enhancement. For anomaly detection, the ODTLOD-ARPW technique employs the YOLOV8s model which offers enhanced accuracy and performance. The hyperparameter tuning process takes place using a root mean square propagation (RMSProp) optimizer. The performance analysis of the ODTLOD-ARPW method is tested under the UCSD anomaly detection dataset. An extensive comparative study reported that the ODTLOD-ARPW technique reaches an effective performance with other models with maximum accuracy of 98.67%.

Keywords: Anomaly detection, pedestrian ways, hyperparameter tuning, deep learning, wiener filtering

DOI: 10.3233/IDT-240040

Journal: Intelligent Decision Technologies (https://content.iospress.com:443/journals/intelligent-decision-technologies), vol. 18, no. 2, pp. 1123-1138, 2024

Received 11 January 2024 | **Accepted** 1 March 2024 | **Published:** 7 June 2024

Price: EUR 27.50

Advertisement

Expert Systems / Early View / e13640

ORIGINAL ARTICLE

Leveraging YOLOv5s with optimization-based effective anomaly detection in pedestrian walkways

Allabaksh Shaik, Shaik Mahaboob Basha

First published: 23 May 2024
https://doi.org/10.1111/exsy.13640

Abstract

Currently, video surveillance is generally used to safeguard safety in public places like railway stations, traffic signals, malls, and so on. Video anomaly recognition and localization are the main components of the intelligent video surveillance method. Video anomaly recognition refers to the procedure of spatiotemporal localization of the abnormal design existing in the video. A main task in video surveillance is the classification of anomalies that occur in it like thefts, crimes, and so forth. Also, anomaly recognition in pedestrian walkways has enlarged major attention among the computer vision (CV) groups to improve pedestrian protection. The current developments in Deep Learning (DL) methods have great attention to dissimilar procedures like image classification, object recognition, and so forth. This study designs an Optimal Deep Learning for Effective Anomaly Detection in Pedestrian Walkways (ODL-EADPW) model. The ODL-EADPW technique employs a fine-tuned DL model for the identification of pedestrians and anomalies in the walkways. In the ODL-EADPW technique, the image pre-processing is primarily involved in two stages median filtering (MF) based noise removal and adaptive histogram equalization (AHE)-based contrast enhancement. For anomaly detection in pedestrian walkways, the ODL-EADPW technique uses the YOLOv5s model with EfficientRep as a backbone network. To enhance the detection results of the ODL-EADPW technique, a stochastic gradient descent (SGD) optimizer was employed to perfect the hyperparameters of the EfficientRep model. The performance evaluation of the ODL-EADPW methodology is implemented on the UCSD Anomaly detection dataset. An extensive comparison study stated that the ODL-EADPW technique gains effectual detection results over other DL models in terms of different measures.

CONFLICT OF INTEREST STATEMENT

We hereby declare that there is no conflict of interest, financial or otherwise.

Open Research

DATA AVAILABILITY STATEMENT

Research data are not shared.

REFERENCES

Al Sulaie, S. (2023). Golden jackal optimization with deep learning-based anomaly detection in pedestrian walkways for road traffic safety. In *International conference on innovative computing and communication* (pp. 617–636). Springer Nature Singapore.

Google Scholar

Alohali, M. A., Aljebreen, M., Nemri, N., Allafi, R., Duhayyim, M. A., Ibrahim Alsaid, M., Alneil, A. A., & Osman, A. E. (2023). Anomaly detection in pedestrian walkways for intelligent transportation system using federated learning and Harris Hawks optimizer on remote sensing images. *Remote Sensing*, **15**(12), 3092.

Web of Science® Google Scholar

Ammar, H., & Cherif, A. (2021). DeepROD: A deep learning approach for real-time and online detection of panic behavior in human crowds. *Machine Vision and Applications*, **32**(3), 57.

Web of Science® Google Scholar

Esan, O. A., Esan, D. O., Mbodila, M., Elegbeleye, F. A., & Koranteng, K. (2023). Surveillance detection of anomalous activities with optimized deep learning technique in crowded scenes. *Bulletin of Electrical Engineering and Informatics*, **12**(3), 1674–1683.

Google Scholar

Jan, A., & Khan, G. M. (2023). *Real world anomalous scene detection and classification using multilayer deep neural networks*.

Google Scholar

Khan, A. A., Nauman, M. A., Shoaib, M., Jahangir, R., Alroobaea, R., Alsafyani, M., Binmahfoudh, A., & Wechtaisong, C. (2022). Crowd anomaly detection in video frames using fine-tuned AlexNet model. *Electronics*, **11**(19), 3105.

Web of Science® Google Scholar

Krishnan, S. R., & Amudha, P. (2023). Hybrid ResNet-50 and LSTM approach for effective video anomaly detection in intelligent surveillance systems. *International Journal of Intelligent Systems and Applications in Engineering*, **11**(4), 880–889.

Google Scholar

Le, V. T., & Kim, Y. G. (2023). Attention-based residual autoencoder for video anomaly detection. *Applied Intelligence*, **53**(3), 3240–3254.

Web of Science® **Google Scholar**

Maheshan, C. M., & Prasanna Kumar, H. (2020). Performance of image pre-processing filters for noise removal in transformer oil images at different temperatures. *SN Applied Sciences*, **2**, 1–7.

Web of Science® **Google Scholar**

Mohd, N. A., Mostafa, S. A., Mustapha, A., Ramli, A. A., Mohammed, M. A., & Kumar, N. M. (2020). Vehicles counting from video stream for automatic traffic flow analysis systems. *International Journal*, **8**(1.1), 142–146.

Google Scholar

Nisa, M. U., Mahmood, D., Ahmed, G., Khan, S., Mohammed, M. A., & Damaševičius, R. (2021). Optimizing prediction of YouTube video popularity using XGBoost. *Electronics*, **10**(23), 2962.

Web of Science® **Google Scholar**

Pawar, K., & Attar, V. (2022). Deep learning model based on cascaded autoencoders and one-class learning for detection and localization of anomalies from surveillance videos. *IET Biometrics*, **11**(4), 289–303.

Web of Science® **Google Scholar**

Qiao, G., Yang, M., & Wang, H. (2022). A water level measurement approach based on YOlOv5s. *Sensors*, **22**(10), 3714.

Web of Science® **Google Scholar**

Ragab, M., & Sabir, M. F. S. (2022). Arithmetic optimization with deep learning-enabled anomaly detection in smart city. *Computers, Materials and Continua*, **73**, 381–395.

Web of Science® **Google Scholar**

Sabih, M., & Vishwakarma, D. K. (2022). Crowd anomaly detection with LSTMs using optical features and domain knowledge for improved inferring. *The Visual Computer*, **38**(5), 1719–1730.

Web of Science® | Google Scholar

Shao, J., Zhou, K., Cai, Y. H., & Geng, D. Y. (2022). Application of an improved u2-net model in ultrasound median neural image segmentation. *Ultrasound in Medicine & Biology*, **48**(12), 2512–2520.

PubMed | Web of Science® | Google Scholar

Ul Amin, S., Ullah, M., Sajjad, M., Cheikh, F. A., Hijji, M., Hijji, A., & Muhammad, K. (2022). EADN: An efficient deep learning model for anomaly detection in videos. *Mathematics*, **10**(9), 1555.

Web of Science® | Google Scholar

Vidyashree, K. P., & Rajendra, A. B. (2023). An improvised sentiment analysis model on twitter data using stochastic gradient descent (SGD) optimization algorithm in stochastic gate neural network (SGNN). *SN Computer Science*, **4**(2), 190.

CAS | PubMed | Google Scholar

Wu, C., Shao, S., Tunc, C., Satam, P., & Hariri, S. (2022). An explainable and efficient deep learning framework for video anomaly detection. *Cluster Computing*, **25**, 2715–2737.

PubMed | Web of Science® | Google Scholar

Yajing, L., & Zhongjian, D. (2021). Abnormal behavior detection in crowd scene using YOLO and Conv-AE. In *2021 33rd Chinese control and decision conference (CCDC)* (pp. 1720–1725). IEEE.

Google Scholar

Yang, E., Shankar, K., Kumar, S., & Seo, C. (2023). Bioinspired Garra Rufa optimization-assisted deep learning model for object classification on pedestrian walkways. *Biomimetics*, **8**(7), 541.

PubMed | Web of Science® | Google Scholar

Yang, X., del Rey Castillo, E., Zou, Y., & Wotherspoon, L. (2024). UAV-deployed deep learning network for real-time multi-class damage detection using model quantization techniques. *Automation in Construction*, **159**, 105254.

Web of Science® | Google Scholar

Yaqoob, S., Cafiso, S., Morabito, G., & Pappalardo, G. (2023). Detection of anomalies in cycling behavior with convolutional neural network and deep learning. *European Transport Research Review*, **15**(1), 9.

PubMed | Web of Science® | Google Scholar

Yassine, S., & Stanulov, A. (2024). A comparative analysis of machine learning algorithms for the purpose of predicting Norwegian air passenger traffic. *International Journal of Mathematics, Statistics, and Computer Science*, **2**, 28–43.

Google Scholar

Zeng, X., Jiang, Y., Ding, W., Li, H., Hao, Y., & Qiu, Z. (2023). A hierarchical spatio-temporal graph convolutional neural network for anomaly detection in videos. *IEEE Transactions on Circuits and Systems for Video Technology*, **33**(1), 200–212.

Web of Science® Google Scholar

Zheng, Y., Zhan, Y., Huang, X., & Ji, G. (2023). YOLOv5s FMG: An improved small target detection algorithm based on YOLOv5 in low visibility. *IEEE Access*, **11**, 75782–75793.

Google Scholar

Download PDF

ABOUT WILEY ONLINE LIBRARY

Privacy Policy
Terms of Use
About Cookies
Manage Cookies
Accessibility
Wiley Research DE&I Statement and Publishing Policies
Developing World Access

HELP & SUPPORT

Contact Us
Training and Support
DMCA & Reporting Piracy

OPPORTUNITIES

Subscription Agents
Advertisers & Corporate Partners

CONNECT WITH WILEY

The Wiley Network
Wiley Press Room

Copyright © 1999-2024 John Wiley & Sons, Inc or related companies. All rights reserved, including rights for text and data mining and training of artificial intelligence technologies or similar technologies.

INDERSCIENCE PUBLISHERS
Linking academia, business and industry through research

Forthcoming and Online First Articles

International Journal of Medical Engineering and Informatics

Forthcoming articles have been **peer-reviewed** and **accepted for publication** but are pending final changes, are not yet published and may not appear here in their final order of publication until they are assigned to issues. Therefore, the content conforms to our standards but the presentation (e.g. typesetting and proof-reading) is not necessarily up to the Inderscience standard. Additionally, titles, authors, abstracts and keywords **may change before publication**. Articles will not be published until the final proofs are validated by their authors.

Forthcoming articles must be purchased for the purposes of research, teaching and private study only. These articles can be cited using the expression "in press". For example: Smith, J. (*in press*). Article Title. *Journal Title*.

Articles marked with this shopping trolley icon are available for purchase - click on the icon to send an email request to purchase.

Online First articles are published online here, before they appear in a journal issue. Online First articles are fully citeable, complete with a DOI. They can be cited, read, and downloaded. Online First articles are published as Open Access (OA) articles to make the latest research available as early as possible.

Articles marked with this Open Access icon are Online First articles. They are freely available and openly accessible to all without any restriction except the ones stated in their respective CC licenses.

Register for our alerting service, which notifies you by email when new issues are published online.

Sign up for new issue alerts

Subscribe/buy articles/issues

View sample articles

Copyright and author entitlement

Forthcoming articles

Journal information in easy print format (PDF)

Keep up-to-date

Our Blog

Follow us on Twitter

Visit us on Facebook

Our Newsletter (subscribe for free)

RSS Feeds

New issue alerts

Inderscience is a member of publishing organisations including:

Crossref

CLOCKSS

International Journal of Medical Engineering and Informatics (103 papers in press)

Regular Issues

- **An advanced manta ray search optimisation with likelihood marginal classification mechanism for ECG arrhythmia detection**

by Budidi Udaya Kumar, Jaidhan Beera John, Bharath Kumar Reddy Soma Venkata, Ummadisetty Sreenivasulu

Abstract: The proposed work objects to develop an advanced optimisation-based classification system for identifying the arrhythmia disease with increased accuracy and reduced error rate. The optimal features are selected using the manta ray search optimisation (MRSO) technique. The likelihood marginal classification (LMC) approach is employed to predict the classified label as whether normal or disease affected. During analysis, the different types of performance measures are used to evaluate the results of the proposed approach. Also, the obtained values are compared with the existing techniques for showing the effectiveness of the proposed model.

Keywords: *electrocardiogram; ECG; cardiovascular disease; manta ray search optimisation; MRSO; likelihood marginal classification; LMC.*

DOI: 10.1504/IJMEI.2022.10050386

- **Detection of adverse drug reactions from online health communities' data: a case study of anti-epileptic drugs**

by Anwar Ali Yahya

Abstract: This paper investigates the problem of detecting adverse drug reactions of anti-epileptic drugs from patients' reviews in online health communities. A lexicon-based methodology is proposed and applied to a dataset of patients' reviews collected from two online health communities. The dataset is cleaned and the adverse reactions of anti-epileptic drugs are extracted with the aid of consumer health vocabulary and a lexicon of adverse drug reactions. A proportional reporting ratio is then applied to quantify the correlation between each drug and adverse reactions and thus identify the adverse reactions of each drug. The results are validated quantitatively against a database of adverse drug reactions, called side effect resource, and qualitatively against the extant knowledge related to the common adverse reactions and drug-drug similarities of anti-epileptic drugs. The validation results provide evidences on the effectiveness of the proposed methodology and the validity of online health communities' data for adverse drug reactions detection.

Keywords: *adverse drug reaction detection; pharmacovigilance; anti-epileptic drugs; AEDs; data mining; online health communities.*

DOI: 10.1504/IJMEI.2022.10050418

- **Segmentation of the human spinal cord using U-Net architecture**

by S. Kumarganesh, Muzammil Hussain, H. Shaheen, S. Anthoniraj, M. Somaskandan, C. Sivakumaran

Abstract: When attempting to assess spinal cord atrophy caused by a variety of disorders, the first step that must be taken is to segment the spinal cord contour. A tumour of the spinal cord is an abnormal development of cells that may occur anywhere in or around the spinal cord. The process of locating tumours in the spinal cord is a very important one. It is difficult to identify the tumour with MRI due to the irregular form of the spinal cord. The model begins by locating the spinal cord, after which it creates the bounding box coordinates. Our technique is validated using four separate clinical datasets. The results of the experiments that used a unique segmentation strategy that was dependent on MRI images reveal that the algorithm that was presented for the system delivers a higher level of accuracy when compared to the other algorithms that are already in use.

Keywords: *spinal cord segmentation; bounding box; U-Net architecture; deep learning.*

DOI: 10.1504/IJMEI.2022.10050461

- **Deep learning-based malignancy prediction in thyroid nodules**

by L. Mohana Sundari, M.S. Maharajan, T. Senthil Kumar, Leo John Baptist Andrews

Abstract: Although the vast majority of thyroid nodules are non-cancerous, determining whether or not a nodule is cancerous may be a difficult and time-consuming process that often involves unnecessary surgical events. In addition, we discussed the process of developing a model that might anticipate the presence of cancer in thyroid nodules by including a number of the core demographic and ultrasound parameters. A combined sensitivity and specificity score was used to assess the diagnostic performance, and their accuracy was compared to that of radiologists. The comparison between model prediction and expert evaluation reveals the benefit of our approach over human judgement in

predicting thyroid nodule malignancy. The results of the experiments show that the suggested algorithm performs better. Nodules of TI-RADS category 4 were used. The area under the receiver operating characteristic curve in the validation dataset was 0.92 (with accuracy of 0.70, sensitivity of 0.81 and specificity of 0.58).
Keywords: *thyroid; AI; deep learning; medical imaging; deep learning; CNNs; preoperative diagnosis.*
DOI: 10.1504/IJMEI.2022.10050829

- **Deep neural networks for medical image segmentation: geodesic distance transform**

by P. Jenifer Darling Rosita, W. Stalin Jacob, R. Kalpana, T. Cynthia Anbuselvi
Abstract: The segmentation of medical images aids in managing the dose of medication, as well as the dosage of exposure to radiation, limiting the development of diseases like tumours, and monitoring the progression of diseases like cancer. The process of segmentation involves the division of a picture into distinct regions that each includes fragments of pixels that have similar characteristics. The regions should have a strong link to the items or elements of interest depicted in the picture in order to be expressive and useful for image analysis and interpretation. A proposal is made for an interactive framework that takes a deep learning approach. P-Net is the first stage of the framework, and it is used to produce an initial automated segmentation. The second stage is where the framework is implemented. This interaction is included in the input of the R-Net.
Keywords: *image segmentation; deep learning; brain tumour; datasets.*
DOI: 10.1504/IJMEI.2022.10050839

- **Detection of diabetic retinopathy severity from fundus images: DCNN**

by T.Senthil Kumar, R. Muthalagu, L. Mohana Sundari, M. Nalini
Abstract: Diabetes retinopathy is a frequent diabetic complication that damages the retina and, if left untreated, may lead to blindness. The exponential rise in the number of diabetics throughout the globe has resulted in an equivalent rise in the number of diabetic retinopathy (DR) patients, one of the most serious consequences of diabetes. The goal of this research is to develop a hybrid solution approach for identifying diabetic retinopathy using retinal fundus pictures. The process of retinal vascular segmentation is critical for detecting a variety of eye disorders, such as the effects of diabetes on the eyes, also known as diabetic retinopathy. Morphologically based operations were used for the autoextraction of retinal blood vessels. Wavelet decomposition and back propagation neural networks were used to extract retinal vascular characteristics and evaluate the dataset that was used for this article. Morphologically based operations were also used for autoextraction of retinal blood vessels.
Keywords: *diabetic retinopathy; fundus images; retina; deep learning; image processing.*
DOI: 10.1504/IJMEI.2022.10050840

- **Detection and classification of Alzheimers using super-resolution algorithm and convolutional neural network**

by T. Senthil Kumar, Ashok Vajravelu, R. Muthalagu, P. Sri Latha
Abstract: On the basis of data obtained from brain imaging, a number of different machine learning (ML) methods may be used to categorise Alzheimer's disease (AD). Convolutional neural networks have been suggested for the classification of Alzheimer's disease based on anatomical MRI in more than 30 different studies. Since the frameworks and implementation details of many researchers aren't available to the public, it makes them difficult to replicate. This article extracts the green channel initially, which is further enhanced by using super resolution algorithm. Convolutional neural network is applied to the contrast-enhanced image. We used CNN and T1-weighted MRI to broaden open-source solution for Alzheimer's disease categorisation. Preprocessing, classification, and evaluation techniques for deep learning are included in the framework as well as tools for converting ADNI, AIBL, and OASIS data to the standard of the BIDS format. By combining deep learning with radionics, the accuracy of Alzheimer's disease diagnosis is increased.
Keywords: *image classification; convolutional neural network; CNN; Alzheimer's disease classification; magnetic resonance imaging; MRI.*
DOI: 10.1504/IJMEI.2022.10050896

- **Robust liver segmentation using marker controlled watershed transform**

by Mohammad Anwarul Siddique, Shailendra Kumar Singh, Moin Hasan
Abstract: The liver is the body's largest organ, and it is largely responsible for metabolism and detoxification. In computer vision-based biomedical image

analysis, liver segmentation is a critical step in detecting liver cancer. Due to the complicated structure of abdominal computed tomography (CT) images, noise, and textural differences across the image, liver segmentation is a key task that results in under-segmentation and over-segmentation. This paper uses a marker-based watershed transform to segment the liver in abdominal CT images. The double stage Gaussian filter with texture and contrast enhancement (DSGFTCE) is used to improve image quality at the pre-processing stage. The performance of the proposed segmentation is assessed using various performance evaluation metrics such as dice score (DS), volume overlapping error (VOE), Jacquard index (JI) and relative volume difference on LiTS dataset. The performance comparison with previous state of arts shows that proposed liver segmentation scheme provides better results (DS = 0.968, VOE = 0.089, JI = 0.9379, RVD = 0.09) compared with existing techniques.

Keywords: *liver segmentation; contrast enhancement; texture smoothening; watershed transform; Gaussian filtering; computer tomography.*
DOI: 10.1504/IJMEI.2022.10050979

- **Trimester analysis for detecting abnormalities in foetal growth based on femur length using LabVIEW**

by D. Ruban Thomas, V. Vasanth, R. Kishore, B. Kishore Kumar

Abstract: Foetal development characteristics are used to determine the effects of various maternal traits and identify people who are more likely to have adverse outcomes. Foetal development features were measured during each trimester of pregnancy and were impacted by several mothers socio-demographic and lifestyle factors. Ultrasound measures of the foetus are crucial during pregnancy. The stability of foetal growth features can be assessed using tracking analyses throughout pregnancy. The length of the femur, the long bone in the thigh, is one of the markers used to monitor foetal growth and health. Previous research concentrated on birth outcomes compared to the foetal development, during pregnancy. In this work, the femur length is measured using LabVIEW. An ultrasound finding of short femur length may signal the need for additional testing to rule out illnesses. Femur length is one of the several factors for determining a babys health.

Keywords: *Laboratory Virtual Instrument Engineering Workbench; LabVIEW; virtual instruments; VI; trimester; ultrasound; ultrasonography; foetal growth; femur length; pregnancy.*
DOI: 10.1504/IJMEI.2022.10051334

- **Analyses of non-steroidal anti-inflammatory drug induced GI bleed related hospitalisation discharges from 2016 to 2018 in the USA**

by Chancey Sweeney, Shankar Srinivasan, Dinesh P. Mital, Riddhi Vyas

Abstract: This study determines the predictors of gastrointestinal (GI) bleeds induced by NSAIDs and their relation to length of hospital stay and total charges. A descriptive analysis showed the highest incidence as non-Hispanic White, older adult patients with variation in household income. Risk factors include Helicobacter pylori, alcohol, and smoking. The overall prediction of study outcomes showed associations between independent and dependent variables such as age, race, and gender, in relation to length of hospital stay and total charges. A high influence was detected with interaction of predictors such as health and socio-demographic characteristics, like advanced age, gender, race, and smoking.

Keywords: *non-steroidal anti-inflammatory drug; NSAID; gastrointestinal bleed; NSAID induced; GI bleed; hospitalisation discharges.*
DOI: 10.1504/IJMEI.2022.10051360

- **A deep analysis of chronic kidney disease for early detection using machine learning classifiers**

by Saurabh Pal

Abstract: All patients who have suffered by chronic kidney disease (CKD) are not easily identified due to symptoms on early stage. The main objective of this research paper is to develop a CKD prediction model which can give better accuracy as compared to other studies. In this paper, we have organised CKD datasets from UCI machine learning repository. Most significant CKD features are eliminated by recursive feature elimination techniques. We have trained base classifiers RF, K-NN, MLP and SVM on 70% disease dataset and test on 30% dataset. Bagging and voting ensemble methods are used to enhance the prediction model. The proposed bagging ensemble model outperformed the other classifiers by achieving 97% accuracy.

Keywords: *chronic kidney disease; CKD; recursive feature elimination; RFE; random forest; K-nearest neighbour; multilayer perception; support vector machine; voting and bagging ensemble classifier.*

DOI: 10.1504/IJMEI.2022.10051462

- **Developments in technology assisted gait analysis in post-knee arthroplasty**

by Sumit Raghav, Anshika Singh, Shashwat Pathak, Suresh Mani, Mukul Kumar

Abstract: Early monitoring in knee arthroplasty is a critical issue to tackle deviation from expected healing, patient satisfaction and ensuring quality of life. There are various methods suggested and implemented over years with varied degree of performance. This paper presents a relevant review of technology assisted gait analysis in knee arthroplasty. The systematic search revealed 272 studies, of which 13 were added retrospectively through reference screening of the included articles. After title and abstract screening, only 20 studies were included in this review. This review paper provides a comprehensive overview of applications of technology assisted gait analysis to monitor and quantify the status of waking. There is moderate-quality of evidence showed technology-assisted; in particular, sensor-based technology, motion sensors and motion analysis results in a statistically significant improvement in monitoring of gait parameters.

Keywords: *gait analysis; knee arthroplasty; gait parameters.*
DOI: 10.1504/IJMEI.2022.10051736

- **The new development in the lower limb exoskeleton - a review**

by Jun-Yi Ge, Maysam F. Abbod, Jiann-Shing Shieh

Abstract: The lower limb exoskeleton is a human machine interaction system which is designed to help users perform movements involving the lower limb by providing assistive torque. This technology has been proposed and developed in recent years. It is a comprehensive application of biomechanics, automatic control, information science and so on. In this review, we summarised the characteristics of exoskeletons that have emerged in the last twenty years. And at the end of the paper, we propose some possible solutions of the existing exoskeleton problems. This may be a guideline for further research on lower limb exoskeleton.

Keywords: *lower limb; exoskeleton; biomechanics; automatic control.*
DOI: 10.1504/IJMEI.2022.10051870

- **Machine learning-based framework for early prediction of diabetes**

by Salliah Bhat Shafi, Venkatesan Selvam, Gufran Ahmad Ansari

Abstract: The recent advancements in technology have changed the landscape of healthcare. With changes in lifestyle and rise in living standard diabetes remains leading cause of death globally. Prediction of diabetes using machine learning algorithms (MLA) for early prediction is need of the hour. However, it is still in its nascent stage. The goal of this study is to employ significant features of machine learning algorithms to the prediction of diabetic and to get the best results which are compared to clinical outcomes. Using predictive analysis, the suggested strategy focuses on choosing the features that aid in the early detection of diabetes. The result shows that the support vector machine (SVM) algorithm has the highest accuracy of 99.349%as compared to naive Bayes which is 98.95%. In order to improve classification and accuracy, this research also normalises the selection of suitable features in the data.

Keywords: *machine learning; naive Bayes; support vector machine; SVM; prediction; diabetes; patients.*
DOI: 10.1504/IJMEI.2022.10052157

- **Implementing machine learning techniques to predict bipolar disorder**

by Nisha Agnihotri, Sanjeev Kumar Prasad

Abstract: Bipolar disorder (BD) is a mental and psychiatric disorder which is characterised by alternate mode swings between mania and depression is very common these days. The classification, modelling and characterisation and diagnosis of these mental disorders are important in medical research. An unexpected and unexplored area in BD is to judge the non-verbal behaviour of person accurately. Therefore, this paper address the challenges of detecting BD state by machine learning (ML) techniques to test the non-verbal behaviours activities like various facial expressions, voice recordings and body gestures of mentally ill and controlled persons in a whole spectrum. ML techniques can potentially provide new horizons in diagnosing and treating in mental healthcare. Further, this paper aims to present commonly used algorithms such as decision trees (DT), support vector mechanism (SVM), logistics regression (LR), K-nearest neighbours (KNN), etc. and describe their properties and performances which could act as a guide to select appropriate models. The study shows that people with controlled state behaves significantly different as compared to BD patients in their interpersonal accuracy (IPA). This develops a new training program to

improve better understanding and psychosocial functionality in their rehabilitation.

Keywords: *machine learning; mood disorder; anxiety depression; bipolar disorder-I and II; Python; interpersonal accuracy.*
DOI: 10.1504/IJMEI.2022.10052205

- **Prediction of epileptic seizure using deep learning architectures**

by Vajravelu Ashok, J. Anitha, Isabel De La Torre Díez, D. Jude Hemanth

Abstract: Neurological illnesses such as epilepsy are among the most frequent. Epileptic sufferers' lives are greatly impacted by early warnings of impending seizures. Using electroencephalogram signals, this research aims to create an epileptic seizure prediction algorithm that can automatically identify an epileptic seizure. Early seizure prediction using EEG data is now possible thanks to the latest machine learning algorithms. An average AUC of 0.74 is achieved by the new technique, compared to 0.72 for the state-of-the-art approach, a 3.25-fold increase in computing time. In-depth knowledge of seizure detection, classification, and potential future research areas may be gained through this presentation's cutting-edge methodologies and concepts. Predicting seizure activity might benefit from a modified atom search optimisation-based deep recurrent neural network. Numerous hidden layers are used by the deep recurrent neural network (DRNN) classifier to predict seizure activity.

Keywords: *electroencephalogram; EEG; signal processing; epilepsy; CHBMIT dataset.*
DOI: 10.1504/IJMEI.2022.10052827

- **Segmentation of retinal features in colour fundus images**

by N. Bino, P.A. Haris, O. Sheeba

Abstract: Retinal diseases could be diagnosed by the variations in size, shape and texture of features in retinal images. Colour fundus images are widely used for the diagnosis of retinal diseases like diabetic retinopathy (DR), glaucoma, age-related macular degeneration (AMD), etc. Image processing enhances the input image, which segments and highlights regions of interest and quantify it. In this paper, we have segmented optic disc and blood vessels in colour fundus images using an algorithm coded in MATLAB. The input images and their corresponding ground truth images were obtained from public datasets available in Kaggle. The validation of the segmented images is done for parameters like accuracy, sensitivity, precision, F-measure, Mathews correlation coefficient, Dice coefficient, Jaccard index and specificity. The algorithm could effectively segment images, with an average accuracy of 99.74% in segmenting optic disc and 94.74% that of blood vessels.

Keywords: *retinal image segmentation; colour fundus imaging; optic disc; retinal blood vessels.*
DOI: 10.1504/IJMEI.2022.10052912

- **Hybrid multi-kernel SVM algorithm for microaneurysm recognition in colour fundus images**

by S.B. Mohan, B. Kannan, D. Ravikumar, C. Sivakumaran

Abstract: Diabetic retinopathy (DR) is a condition that results in impaired vision and is triggered by diabetic. These alterations in the retinal vessels may be traced back to hyperglycemia. Microaneurysms (MAs) seem to be the initial disease symptoms of DR, and a prompt identification of microaneurysms may assist in the detection of DR in the preclinical phase. Optical coherence imaging system, often known as OCT, is a non-invasive imaging technology that offers a cross-sectional picture of the retinal. We construct new probability foundations for support vector machines (SVMs) using informational differences and the Fisher score. The findings that were achieved were as follows: the accuracy criterion had a score of 96.32%, the sensitivity criterion had a score of 97.34%, the specificity criterion had a score of 95.42%, and the precision criterion had a score of 95.27%.

Keywords: *retinal pictures; scaled Dirichlet combination; support vector machines; SVMs; microaneurysm images.*
DOI: 10.1504/IJMEI.2023.10053229

- **Application of deep learning to segment pelvis bones**

by N. Thamaraikannan, M. Saravanan, N.K. Anushkannan, S. Ramesh, C. Sivakumaran

Abstract: The proper identification and localisation of pelvic bone metastases begins with precise segmentation of the pelvic bones. Existing pelvic bone segmentation algorithms are generally manual or semi-automatic, and they exhibit low accuracy when dealing with picture appearance changes caused by multi-site domain shifts, etc. This paper presents a strategy for segmenting normal pelvic bone characteristics in multiparametric magnetic resonance

imaging (mpMRI) using a 3D U-Net based on deep learning. Extensive testing on our dataset indicates the usefulness of our automated technique. The 3D U-Net network, based on deep learning, offers patients accurate identification and segmentation of pelvic bone metastases.

Keywords: *U-Net; pelvis bone; segmentation; biomedical signal processing.*
DOI: 10.1504/IJMEI.2023.10053901

- **Psychological distress and its association with socioeconomic and health behaviour factors**

by Xiangdong An, Hui-chuan Chen, Monty Taylor

Abstract: The authors assess the relationships among psychological distress, socioeconomic status, and health behaviour factors. Data from the Canadian Community Health Survey (CCHS) dataset was analysed for this study using hierarchical regression and ANOVA. Results show that daily energy expenditure is positively related with psychological distress. The authors also find that daily fruit consumption, daily green salad consumption, and monthly frequency of leisure activities are negatively associated with psychological distress. Furthermore, the results indicate that people with personal incomes of less than $20,000 perceive significantly higher distress than people with higher incomes. Among five occupation groups, the sales and services group perceives significantly higher distress compared to the other four groups. The four other occupation groups as categorised by CCHS do not perceive significantly different distress levels.

Keywords: *psychological distress; gender; occupation; income; health behaviour; fruit consumption; green salad consumption; leisure activities; energy expenditure.*
DOI: 10.1504/IJMEI.2023.10053931

- **A novel method to predict stroke using deep learning approach**

by Swagata Sarkar, A. Jayashree, R. Thirumurugan, C. Sivakumaran

Abstract: Strokes remain the main cause of major impairment that lasts for lengthy period of time and ranks as the third greatest cause of mortality overall in United States. The ability to accurately anticipate a stroke is very useful for facilitating earlier intervention as well as treatments. Several studies have concentrated on determining the chance of a heart attack; on the other hand, only few have investigated the possibility of a brain attack. Various machine learning techniques are being created to estimate the chance of a cerebral infarction. We present a data-driven classifiers deep neural Networks (ResNet) for diagnosing strokes predicated on 12-leads ECG information. The quality of the model, which has been fine-tuned to perfection, allows us to achieve a training correctness of 99.99% and an accuracy rate of 85.82%. The findings imply that ECG is a viable adjunct tool for diagnosing stroke.

Keywords: *machine learning; stroke prediction; CNN; deep learning; ResNet.*
DOI: 10.1504/IJMEI.2023.10053942

- **Face recognition-based security system for automated teller machine using deep face model**

by K. Kavin Kumar, S. Mythili, S. Prabhu Kumar

Abstract: The purpose of this study is to show about using OpenCV and deep learning techniques to design and implement a face recognition-based ATM security system. Face recognition only provides service to the user if the user is authentic or if the user has been validated by an authentic ATM card user. Users are authenticated by comparing the persons video taken in front of the ATM. The proposed method identifies the right persons by comparing the blink of eyes. If someone enter the ATM with photocopy of another person, checking the blink of eyes the validation is made. If the user is authentic, to strengthen the models accuracy, the current image is being utilised. A web link is sent to the registered mobile number that owns the ATM card, to verify the access of the illegitimate user to his/her account only then the user is considered as a legitimate user. Histogram algorithms and deep learning approaches are used by the system to identify persons. To process the image and detect the faces in the image, this system use the OpenCV package. Face recognition is achieved through the use of an open CV and deep learning.

Keywords: *OpenCV; blink of eyes; VGG Face model and deep face.*
DOI: 10.1504/IJMEI.2023.10054109

- **Detection and classification of lung cancer using deep neural network**

by S. Babu Kumar, M. Vinoth Kumar

Abstract: Lung cancers hold a critical spot among the reasons for most cancer deaths among humans. The better way to maximise the survival rate is the detection of cancer at the earliest. But existing traditional techniques are time-consuming and error-prone. This study is a significant and efficient method for the detection and classification of lung cancer into large cell carcinomas, small

cell, adenocarcinoma, squamous cell carcinomas, or benign respectively. In the proposed technique, a novel algorithm is implemented to generate the Image patches from whole slide histopathological images. Then, histogram normalisation is carried out to remove noise and enhance the image. Then a novel extended Mobius transformation technique is used for image augmentation. Finally, Dense EfficientNetB7 is trained to extract the features for the detection and classification of lung cancer. The performance of the proposed technique is proved more efficient and par with histologists attaining an accuracy of 98.87%.

Keywords: *lung cancer; histopathology; deep convolution neural network; DCNN; EfficientNetB7.*

DOI: 10.1504/IJMEI.2023.10054175

- **A review of the relationship between flow-volume curve and obstructive sleep apnea**

by Seval Bulut Eris, Cahit Bilgin, Ömer Eriş, Mehmet Recep Bozkurt

Abstract: This study presents a systematic review of studies in the literature evaluating the relationship between the flow-volume curve and obstructive sleep apnea (OSA). When the literature was examined, it was observed that there are few studies in this field, and only statistical analyses were made using the ready parameters given by the pulmonary function test (PFT). New biomarkers can be discovered with characteristic and statistical features extracted from the flow-volume curve to diagnose OSA. Machine learning-based systems can be developed using biomarkers. Rules-based automatic diagnosis systems can enable faster OSA diagnosis. In addition, it can eliminate the disadvantages arising from using a sleep laboratory to diagnose OSA.

Keywords: *obstructive sleep apnea; OSA; flow-volume curve; flow-volume loop; saw-tooth pattern; pulmonary function test; PFT; machine learning.*

DOI: 10.1504/IJMEI.2023.10054791

- **Design and analysis of microfluidic channel with W-shaped electrodes for separation of bio-particles using dielectrophoresis technique**

by Muktimani Brahma, R. Kumar, Trigunesh Narzary

Abstract: A unique microfluidic device with W-shaped electrodes is designed to separate the micro-bio-particles. The microfluidic device efficiently separates the red blood cells (RBCs) and platelets using the dielectrophoresis technique. The separation process has been analysed by using COMSOL Multiphysics software and found that the electrode with the minimum gap of 25 um acquired optimum results at an applied voltage of 8 V. The proposed device gave a high separation efficiency of 89.5% and a separation purity of 99.63%. The enhanced microfluidic device gave better results compared to other recent works and is exceptionally suitable for separation of micro-bio-particles.

Keywords: *dielectrophoresis; red blood cells; RBCs; platelets; separation; microchannel; electrodes; flow rate; electric field; non-uniform; force.*

DOI: 10.1504/IJMEI.2023.10054875

- **Diffusion tensor imaging for Alzheimer's disease classification using a bag of features and majority voting**

by Latifa Houria, Noureddine Belkhamsa, Assia Cherfa, Yazid Cherfa

Abstract: Alzheimer's disease (AD) is a neurodegenerative disease and the most common cause of dementia. Thus, various neuroimaging-based methods were proposed to detect this disease at its early stage, called mild cognitive impairment (MCI). We developed a novel approach combining Diffusion tensor imaging (DTI)-indices and ensemble learning to classify AD. A bag of features (BoF) is used to retrieve the locale features, and a support vector machine (SVM) is applied for classification. The majority voting technique is used to combine the final predicted labels. The proposed method achieves an accuracy of 94.0%, 97.0%, and 95.9% to classify CN vs. MCI, CN vs. AD, and MCI vs. AD, respectively.

Keywords: *diffusion tensor imaging; Alzheimer's disease; bag of features; BoF; support vector machine; SVM; majority voting.*

DOI: 10.1504/IJMEI.2023.10054939

- **An intelligent method for predicting cardiac disease based on PSO-convolutional neural network**

by M. Balamurugan, P. Blessed Prince

Abstract: Cardiovascular disease (also known as CVD) is one of the primary contributors to both morbidity and death. The present state of the art in artificial intelligence plays a significant part in the process of aiding medical professionals in the diagnosis of a variety of disorders. A hybrid framework is proposed for the diagnosis of cardiovascular illnesses by analysing medical voice data. Eleven datasets comprising 14,416 numerical characteristics may be produced by using

the method that has been suggested. From the datasets that are produced as a consequence, numerical and graphical characteristics are extracted. In the third layer, numerical data is provided to five separate machine learning (ML) techniques and graphical characteristics are transmitted to convolutional neural networks (CNNs), with transfer learning utilised to choose the best suited configurations. From a benchmark dataset, the PSO-CNN technique that was presented obtains an accuracy of 96.78%.

Keywords: *cardiovascular; PSO-CNN; optimisation; machine learning.*
DOI: 10.1504/IJMEI.2023.10054940

- **Data mining approach for nutrition score calculation of geriatric patients**

by Vaishali P. Suryawanshi, Rashmi S. Phalnikar

Abstract: Due to lack of uniformity in terms of understanding nutrition status, comorbidity types, patient mobility and BMI readings mal-nutrition screening forms cannot be used to correctly comprehend each patients nutritional status. The goal of this study is to use a data mining approach to understand nutrition screening forms in order to determine the malnutrition status of hospitalised geriatric patients. The evaluation measures are used to indicate the accuracy of the classification algorithms. The research work on nutrition screening form, which is designed using classification algorithms, will help physicians to understand their patients nutritional status and help in avoiding malnutrition in them.

Keywords: *malnutrition screening forms; classification; data mining; evaluation measures.*
DOI: 10.1504/IJMEI.2023.10055068

- **Integer wavelet transform based data hiding scheme for medical image protection**

by Moad Med Sayad, Zermi Narima, Khaldi Amine, Kafi Med Redouane

Abstract: A crucial security and protection challenge today in telemedicine is how to ensure the confidentiality of sensitive data sent over the internet and limit access to specified designated information. To keep such details private, we propose in this work a robust and blind medical image watermarking approach that combines integer wavelet transform (IWT) and singular value decomposition (SVD). Low embedding capacity is a potential drawback of modern integer wavelet transform (IWT)-based watermarking systems. A secure high capacity watermarking scheme based on IWT is proposed in this work to overcome this specific limitation. According to experiment results on imperceptibility and robustness, the proposed solution efficiently maintains a significant quality of watermarked images and the watermark is resistant to the most commonly used attacks in watermarking. The integration of information about the patient in his medical image will avoid any confusion between two images.

Keywords: *medical image; digital watermarking; blind watermarking; integer wavelet transform; IWT; singular value decomposition; SVD; QR code.*
DOI: 10.1504/IJMEI.2023.10055240

- **Segnet and U-Net based brain tumour segmentation**

by R. Ashwini, Swagata Sarkar, C. Pandi, S. Rajalakshmi

Abstract: The process of separating individual brain tumours in diagnostic pictures is an essential component of therapeutic therapy. The manual segmentation process takes a lot of time and requires a lot of work, while the current automated segmentation techniques have problems such as a large number of parameters and a lack of accuracy. We created a completely automated technique for the segmentation of brain tumours by applying deep learning. The system was tested on 285 examples of brain tumours using multi-parametric magnet resonant images taken from either the BraTS2018 data set. The quantitative study of brain tumours is helpful in gaining a better knowledge of the features of the tumour as well as in developing more effective treatment strategies. Through the use of this technology, it was possible to get mean dice values of 0.9213 for the overall tumour and 0.8729 for the tumour core.

Keywords: *brain tumour; BraTS database; computer intelligence; Densenet; U-Net.*
DOI: 10.1504/IJMEI.2023.10055242

- **Myocardial infarction detection in late gadolinium enhancement cardiac MRI**

by Sarra Dali Youcef, Mahammed Messadi

Abstract: Cardiac magnetic resonance imaging (MRI) has become the most used technique for assessing myocardial viability. Myocardial segmentation is a fundamental step in the detection of myocardial infarction (MI) on late gadolinium enhancement (LGE) images. In this paper, we provide a system for

automated myocardial infarct detection. The myocardial segmentation is applied to cine images and then transferred to LGE images, to subsequently detect myocardial infarction. We tested our approach on the sunnybrook cardiac database. The proposed method shows remarkable accuracy. We obtained a dice similarity coefficient of 0.92 and an average perpendicular distance of 1.75 (mm) between automated and manual segmentation.

Keywords: *left ventricle; cine MR images; late gadolinium enhanced MR images; myocardial infarct; viability.*
DOI: 10.1504/IJMEI.2023.10055269

- **Medical image registration and automatic hippocampus segmentation through convolutional neural network**

by S. Durga Prasad, K.S.N. Murthy, B. Kannan, C. Sivakumaran

Abstract: Alzheimer's disease (AD) is a brain degenerative ailment that progresses and is irreversible. Mild cognitive impairment, known as MCI, is a clinical indicator that AD may eventually develop. In order to effectively treat and prevent AD, an accurate diagnosis of the illness's early stages is required. AD often manifests its symptoms first in the hippocampus. Deep machine learning was used in this project with the intention of achieving its aim of segmenting a specific region. The suggested method's performance was compared to manual segmentation using similarity measures. The performance of a CNN that segments the hippocampus directly is inferior to that of any contouring technique and the findings were 96% accurate. The quantitative results are improved by the application of stringent corrections to the data, although the gap is still rather large. The suggested technique is promising and may be expanded in AD prognosis by predicting hippocampal volume changes in the early stages of the illness.

Keywords: *Alzheimer's disease; hippocampus; magnetic resonance imaging; convolutional neural network images; TBI; U-net.*
DOI: 10.1504/IJMEI.2023.10055511

- **CNN-based detection of cervical spinal cord injury**

by G. Chandraiah, K. Mekala Devi, A. Mohamed Abbas, S. Rajalakshmi

Abstract: Magnetic resonance imaging (MRI) has the ability to infer alterations on a microscopic level in lesions that are present on the spinal cord. For the purpose of locating lesions brought on by cervical illnesses, our deep neural network using MRI was suggested. The segmentation of spine pictures, as well as their identification, diagnosis, as well as quantitative assessment, have all seen significant applications of the deep learning technology. The most cutting-edge approach to machine learning using medical imaging data is called convolutional neural networks (CNNs), which are powered by deep learning. The proposed network produces segmentation results that are in high degree of agreement with the real world situation. The suggested network produces outstanding results on testing. These findings are based upon that pixel level. The machine learning network that was suggested is both efficient and reliable for doing completely autonomous segmentation of the problematic area.

Keywords: *analysis of the spine province; magnetic resonance imaging; MRI; spinal cord; convolutional neural networks; CNNs.*
DOI: 10.1504/IJMEI.2023.10055578

- **Pneumonia detection using modified VGG 19 net architecture: application of deep convolutional neural network**

by K. Sivakumar, P. Vinitha Baby, Lourdu Jennifer J.R., C. Sivakumaran

Abstract: Pneumonia is a somewhat common condition that may be brought on by a variety of micro-organisms, including bacteria, viruses, and fungus. The use of a deep convolutional neural network fed with X-ray images to detect lung pneumonia has been proposed. Collecting data, enhancing images, performing an adaptive and precise ROI evaluation, extracting features, and diagnosing diseases are all part of the framework's scope. The suggested deep CNN models were trained using 12,000 pictures from the Pneumonia chest X-ray Dataset, which contained both infected and uninfected chest X-rays. The publicly available new CNN models were trained, and the results were compared with ensemble approach. On the validation set, the suggested technique demonstrated its superiority with an AUC of 95.21 and a sensitivity of 97.76. The proposed technique had a 90.71% success rate in properly identifying images of a patient's chest as normal, viral pneumonia, or bacterial pneumonia.

Keywords: *pneumonia; deep learning; machine learning; CNN.*
DOI: 10.1504/IJMEI.2023.10055646

- **Effects of various phases and errors on partial volume estimation in the analysis of PV correction in ASL MRI**

by A. Shyna, Amma C. Ushadevi, Ansamma John, C. Kesavadas, Bejoy Thomas
Abstract: Arterial spin labelling (ASL) MRI is widely used to measure cerebral blood flow (CBF). The low resolution of ASL images causes partial volume (PV) effect that causes an erroneous estimation of CBF values. A two-phase study is conducted to investigate the impact of various factors on the PV correction technique using linear regression. The effects of different stages in the PV estimation process are examined in the first phase, and the impact of noise and blurring on PV estimates on the second phase. Experiments are conducted on simulated PCASL images generated from ADNI and the results are validated using RMSE score and ROI analysis.
Keywords: *arterial spin labelling MRI; partial volume effect; cerebral blood flow; CBF; linear regression.*
DOI: 10.1504/IJMEI.2023.10055831

- **Motor imagery classification based upon wavelet packet decomposition and binary particle swarm optimisation**

by Rohtash Dhiman, Pawan
Abstract: Motor imagery (MI)-electroencephalogram (EEG) signals are most convenient basis for brain computer interface (BCI) systems. This investigation aims to develop a novel method for feature extraction and selection that improves classification accuracy in the BCI system. Wavelet packet decomposition (WPD) and approximate entropy (ApEn) are used for feature extraction for EEG signals. Binary particle swarm optimisation (BPSO) technique is used for feature selection. Artificial neural network (ANN) is employed for classifying MI activities with mean accuracy of 87.29%. The proposed methodology can be useful in clinical applications for motor-disabled subjects connecting outside environment with sequences of MI activities.
Keywords: *approximate entropy; ApEn; artificial neural network; ANN; binary particle swarm optimisation; BPSO; brain computer interface; BCI; electroencephalogram; EEG; motor imagery; MI; wavelet packet decomposition; WPD.*
DOI: 10.1504/IJMEI.2023.10056105

- **Radial basis function network equipped with an ensemble-based Lasso ridge model in diagnosis of breast cancer**

by Pooja J. Shah, Trupti P. Shah
Abstract: The information that is kept in the form of medical records is of tremendous assistance when it comes to the process of putting together medical decision support systems. The goal of this study is to provide a description of two distinct methods for the development of a medical diagnostic tool that is driven by data in the detection of breast cancer. The radial basis function network (RBFN) architecture with Lasso and ridge regularisation, as well as ensemble learning, are both methods that have been proposed as potential solutions. Following the implementation of the proposed networks on the Wisconsin Breast Cancer (WBC) dataset, comparative analysis is carried out.
Keywords: *radial basis function network; RBFN; Lasso and ridge regularisation; LR; ensemble learning; breast cancer; BC.*
DOI: 10.1504/IJMEI.2023.10056107

- **A new hybrid approach for automated leakage detection in fundus fluorescein angiography images**

by Bikesh K. Singh, Suraj Chandrakar, Ankur Khare, Ravi Khatri, Deepak Chandravanshi, Sumit Kumar Banchhor
Abstract: The existing methods for quantitative investigation of leakage in fluorescein angiography (FA) images involve manual delineation and lack annotated datasets and high accuracy. The proposed hybrid approach can automatically detect leakage in FA images with high accuracy. The hybrid approach combines the fuzzy c-means (FCM) with distance regularised level set evolution (DRLSE). Two expert radiologists test the accuracy of the proposed system. We have also tested inter-and intra-observer variability between the two experts. The study observed high accuracy of 0.98 +- 0.02 and 0.98 +- 0.03 with experts 1 and 2, respectively. Further, the accuracy of manual inter-observer (expert 1 and expert 2) and intra-observer (expert 1) were observed as 0.95 += 0.05 and 0.98 +- 0.02, respectively. The proposed fully automated hybrid approach can accurately detect and quantify the leakage in FA images and thus has great potential value in diabetic retinopathy (DR).
Keywords: *diabetic retinopathy; DR; fluorescein angiography; FA; leakage; segmentation; inter- and intra-observer variability; fuzzy c-means; FCM; distance regularised level set evolution; DRLSE.*
DOI: 10.1504/IJMEI.2023.10056108

- **Remotely operated infant incubator**

by Maham Sarvat, Suhaib Masroor, Jawaid Shabbir, Zohra Jabeen, Bilal Ahmad

Abstract: A neonatal incubator is a sealed enclosure where a child may be placed for treatment in a safe and healthy environment. The system can provide a heater, a fan, a water container for applying moisture, a control valve to regulate oxygen supply, and access ports for nursing care. In this paper, a novel approach is presented to create a cost effective wireless portable baby incubator. It is shown that the control and operation of the incubator is performed wirelessly from the nursing counter, located within the range of 30 m via an Android device. The device will provide information of all the installed functions on a single screen. Moreover, it requires only a single staff member to monitor them, and give them necessary instructions via the same Android device. To validate the efficiency of the proposed design, the incubator is simulated 30 times, and the acquired results are tested statistically by ANOVA.

Keywords: *infant incubator; remote monitoring and control; wireless communication; smart electro-medical devices.*

DOI: 10.1504/IJMEI.2023.10056665

- **Efficacy and bioequivalence study of Zithromax and Azithral a drug for the treatment COVID-19**

by Hattab Youcef

Abstract: Generic drugs are increasingly marketed around the world to the detriment of their quality. The objective of this work was therefore to carry out a bioequivalence study between the originator Zithromax a drug for the treatment COVID-19 and its generic Azithral, this bioequivalence study is based on the quality control of generic and originator azithromycin tablets, which is carried out after validation of the azithromycin assay method, and essentially on pharmaco-technical tests (mass uniformity, breakability, disintegration, dissolution in vitro). By referring mainly to different pharmacopoeias, the tests have shown that the quality of generic tablets is acceptable but seems to be less satisfactory than that of originator tablets.

Keywords: *bioequivalence study; generic; azithromycin; COVID-19.*

DOI: 10.1504/IJMEI.2023.10056861

- **Multi perceptron network based model to classify the multi stages of Alzheimer's disease using clinical data**

by Chevvenahalli Rangegowda Nagarathna, Mohanchandra Kusuma

Abstract: Alzheimer's is a neurodegenerative disease that diminishes the capability of individuals to perform their daily activities. It is an irreversible disease. Once it is started it cannot be cured, but early detection of the disease can help to slow down the progression of the disease by starting the treatment early. In this experiment, we use clinical study data available at the Alzheimer's disease neuroimaging initiative (ADNI) dataset to detect the different stages of Alzheimer's and forecast the duration required for conversion from mild cognitive impairment to Alzheimer's disease (AD) and also classification of the disease is done. The clinical signs of AD are rendered by age, patient education details, the progression rate of disease, and cognitive information. Various machine learning techniques like multi perceptron networks, random forest, SVM, and decision tree classifiers are used to do binary and multi-classification of AD, late mild cognitive impairment (LMCI), early cognitive impairment (EMCI), and cognitive control (CN). The multi perceptron network shows the best performance by giving an average accuracy of 99.24% for binary classification and 93% for multi class classification. The proposed model enables early detection and also predicts the different stages of Alzheimer's using the clinical dataset.

Keywords: *Alzheimer's; dementia; MMSE; multi-layer perceptron; random forest; SVM; late mild cognitive impairment; LMCI; early cognitive impairment; EMCI.*

DOI: 10.1504/IJMEI.2023.10056957

- **Diagnosis of the COVID-19 with deep learning**

by Moulud Demouche, Abderrahmane Baadache, Djamil Aissani, Taha Zerrouki

Abstract: Since the beginning of 2020, the COVID-19 virus has spread widely throughout the world. RT-PCR is used to diagnose the disease, but radiologists studied advances in chest CT scans to produce high-quality images. The purpose of this research is to develop a deep learning system for detecting the COVID-19 virus using chest computed tomography. We proposed three convolutional neural network (CNN) approaches to developed three models, and applied them to a publicly available COVID-19 screening chest CT scan dataset of 2,482 images. Our models have shown that they work by getting a high F1-score of 98.5% for the InceptionResNetV2 model.

Keywords: *COVID-19; convolutional neural network; CNN; deep learning;*

Xception; InceptionResNetV.
DOI: 10.1504/IJMEI.2023.10057090

- **Deep learning for smart home security systems**

by N. Ashokkumar
Abstract: Smart home security systems helps to monitor the homes from remote place. These systems were created with the goal of mitigating risks and, eventually, leading to the consolidation of a sense of security. We get off with an overview of the deep learning approach and an analysis of its significance in the evolution of machine learning. The most basic prerequisite for choosing the most appropriate way to build a smart home is face recognition. Kinect is used to generate the point cloud image of a human body in this technique. The data that has been received will be processed by the Arduino microcontroller, which will ultimately result in the intelligent management of various domestic electrical equipments. The experimental findings demonstrate that by analysing and processing human point cloud photos, the proposed algorithm is able to effectively recognise human attitude and operate domestic appliances and other operations.
Keywords: *smart home; machine learning; deep learning; DL; machine learning; ML; denial of service; DoS; intrusion detection system; IDS; internet of things; IoT.*
DOI: 10.1504/IJMEI.2023.10057160

- **Information domain approach to investigate the cardio-vascular, cardio-respiratory and vasculo-respiratory causal coupling to study gender and age-based changes**

by Kirti Singh, Indu Saini, Neetu Sood
Abstract: This study presents a framework to quantify the coupling changes in cardiovascular, cardiorespiratory, and vasculorespiratory complexity using information domain approaches based on compensated transfer entropy (cTE). The dataset used for this research consists of the group of healthy young and old subjects. The proposed technique delivers significant coupling changes in healthy dataset based on age and gender in contribution of heart rate (HR), blood pressure (BP), and respiration (RESP). For validation of statistically significant values, the paired t-test is used. This study provides additional value to the prognostic and diagnostic approach in biomedical science.
Keywords: *heart rate variability; HRV; respiration; RESP; blood pressure; BP; RR interval; transfer entropy; TE.*
DOI: 10.1504/IJMEI.2023.10057240

- **Parkinson disease detection using ResNet-50: a CNN architecture**

by N.K. Anushkannan, S. Nirmalkumar, L. Chithra, K. Manoharan
Abstract: A person's motor and cognitive symptoms from Parkinson's disease (PD) can change dramatically over time. Some of the signs of Parkinson's disease are shared with more common illnesses including ageing and essential tremor, making diagnosis challenging. Lots of study has gone into figuring out the best ways to diagnose this illness. Using deep learning, recursive neural networks (RNNs), and convolutional neural networks (CNNs) that can differentiate between healthy and PD patients, this research hopes to automate the Parkinson's disease (PD) diagnostic procedure. As such, this study intends to analyse numerous imaging and movement datasets to determine which Parkinson's disease test is best in terms of its capacity to differentiate between individuals, as different datasets may emphasise different elements of the illness (notably cube and spiral pentagon datasets). Furthermore, this study will be utilised to compare imaging and time series datasets for their diagnostic utility in Parkinson's disease.
Keywords: *Parkinson disease; deep learning; signal processing; convolutional neural network; CNN; ResNet-50.*
DOI: 10.1504/IJMEI.2023.10057278

- **Parkinsons detection based on combined ResNet architecture and LSTM**

by M. Gokuldhev, Anjani Kumar, K. Kiruthika, B.R. Tapas Bapu
Abstract: In this research, a novel approach to the clinical condition of neurodegenerative disorders like Parkinson's is presented. The proposed method uses a mix of deep networks that have been pre-trained as well as long-term and short-term memory (LSTM). A new model called PD-ResNet is constructed and based on the residual network (ResNet) architecture to understand the variations between people with Parkinson disease and healthy controls. In order to execute adoption of the obtained learnt representations across data originating from various medical contexts, a new loss functionality is presented as well as used in the development of the deep neural networks (DNNs). Experiments conducted on the clinic gait dataset demonstrate that our suggested model has good

performance, with a correctness of 95.51%, an accuracy of 94.44%, a recalls of 96.59%, a sensitivity of 94.44%, as well as a F1 measure of 95.50%.
Keywords: *Parkinson illness; ResNet architecture; deep neural networks; DNNs; long short-term memory.*
DOI: 10.1504/IJMEI.2023.10057280

- **Forward neck posture on cervical pain among university students: effect of smartphone addiction**

by Selvaraj Antoniraj, Hafizah Che Hassan, K. Baleswamy
Abstract: These days, smartphones are used for much more than just making and receiving phone calls and text messages; they can also be used to view and share media, surf the web, and send and receive electronic mail. A cross-sectional analysis of college students between the ages of 17 and 30, who were using smartphones for prolonged period of time. The survey was conducted through an online questionnaire. Simple random sampling was used to get 404 samples, 216 of which were men and 188 of which were women. There is a positive and highly significant ($p < 0.01$) association between forward neck posture and cervical pain in college students. Using a smartphone excessively is associated with increased risk of cervical pain ($p < 0.01$). The findings of this study reveal that the extended and extensive use of smartphones by university undergraduates is a key contributing cause of their neck pain.
Keywords: *cervical pain; neck posture; smartphone addiction; students.*
DOI: 10.1504/IJMEI.2023.10057778

- **An optimised machine learning approach using Intel oneAPI for detecting cardiovascular system failure**

by Akshay Bhuvaneswari Ramakrishnan, A. Srilakshmi, Shriram K. Vasudevan
Abstract: Heart failure is a frequent illness that might result in circumstances that could be fatal. Early heart illness identification is essential for prompt treatment and better patient outcomes. In this study, we offer a multi-machine learning model, trained with Intel oneAPI, technique for the early diagnosis of heart illness. To choose the most pertinent patient characteristics that will be used as input for our machine learning models, we employ a genetic algorithm (GA). To forecast the risk of cardiac disease, we optimise the models using a genetic algorithm and Intel oneAPI. Our findings demonstrate the high accuracy of our approach, with linear discriminant analysis optimised with GA producing the most accurate model with a 92.34% accuracy rate.
Keywords: *heart failure; machine learning; genetic algorithm; optimisation; oneAPI.*
DOI: 10.1504/IJMEI.2023.10057866

- **Increasing the accuracy of oscillometric blood pressure measurement**

by Y.M. Blessy, K. Rajalakshmi, R. Raj Anandh, Vajravelu Ashok
Abstract: The presence of unregulated high blood pressure (BP) is linked to an elevated chance of health problems, some of which may cause harm to a range of organs across the body. Among the most dangerous as well as widespread conditions is hypertension, which refers to increased blood pressures. Unfortunately, correct blood pressure readings need the use of many medical instruments. The proposed system compares the systolic and diastolic objectives of blood-pressure readings, which are obtained using analogue devices and those obtained using an electronically controlled blood pressure reading tool. The systolic measurement alone had a mean variance of 3,265 mmHg, while the diastolic measurement had a mean variance of 6,165 mmHg. The discrepancy is then included into these processes of calibrating the automated blood pressure measuring device. The accuracy of the output of the calibration reading tool is between 99.47% and 99.82%.
Keywords: *blood pressure measurement; non-invasive; micro controller.*
DOI: 10.1504/IJMEI.2023.10057971

- **Integrating dialysis machine functions using system design approach**

by Vicky B. Sardar, Atul Sajgure, Neela R. Rajhans
Abstract: In new product development (NPD) process, system design thinking contributes significantly towards the effectiveness of the product. For effective system design solution, incremental improvements to the existing system at each element level should meet the user expectations. A detailed view of the inputs and outputs occurring at each component level of a hemodialysis machine is presented in this study. This research work provides suggestions to address the functions of existing dialysis machine for home use. The suggestions are based on systems approach. Risk mitigation plan is devised for preventing the critical accidents while designing the machine for home hemodialysis using Swiss Cheese approach.

Keywords: *new product development; NPD; system design; home hemodialysis; HHD; Swiss Cheese approach.*
DOI: 10.1504/IJMEI.2023.10057977

- **Classification of cardiac arrhythmia disease using deep learning auto encoder algorithm**

by B. Nithyasundari

Abstract: An electrocardiogram (ECG) is a very important diagnostic tool for figuring out what is wrong with a person's heartbeat. Arrhythmia has been put into groups in many different ways. Due to the fact that electrocardiogram (ECG) data are in a state of continual change, it might be challenging to employ standard handmade approaches. We offer a framework for deep learning that does not need a great deal of supervision and is geared toward the detection of arrhythmias (WSDL-AD). Three distinct ECG waveforms are selected from the arrhythmia database maintained by MIT and BIH in order to evaluate the proposed methodology. The primary objective of this research is to discover a deep learning method, with the end aim of classifying the three distinct heart ailments that have been selected. The highest rate of correct recognition that can be achieved is 98.51%, while the accuracy of testing is around 92%.

Keywords: *MIT-BIH dataset; electrocardiogram; ECG; arrythmia disease; deep learning.*
DOI: 10.1504/IJMEI.2023.10058004

- **Breast cancer prediction using whale optimisation algorithm and ANFIS classifier**

by M. Sri Geetha, S. Navaneethan, G. Divya, B. Geethavani

Abstract: Breast cancer is one of the most prevalent forms of the disease that affects women and is responsible for billions of deaths globally. The adaptive clustering is for the purpose of image segmentation, followed by an adaptive neuro-fuzzy inference system (ANFIS) for the categorisation of images. In order to optimise the parameters, a deep learning-based method known as the whale optimisation algorithm (WOA) has been suggested. The breast cancer database for the state of Wisconsin comprised information of patients who had a known diagnosis. The ANFIS classifiers were provided with a training set of records of this kind in order to learn how to discriminate between new cases in the domain. In order to identify breast cancer, the ANFIS classifier was fed nine characteristics that define breast cancer indications. The suggested ANFIS model included both the adaptability of neural networks and the qualitative approach of fuzzy logic.

Keywords: *adaptive neuro-fuzzy inference system; ANFIS; whale optimisation algorithm; WOA.*
DOI: 10.1504/IJMEI.2023.10058260

- **Human emotion classification enabled by EEG signal analysis and machine learning**

by Dattaprasad A. Torse, Mahadev M. Bagade

Abstract: In recent years, automated human emotion recognition system poses numerous challenges with large and complex data and its vast computation. In this work, we consider a three-dimensional continuous valence-arousal-dominance framework for data representation in space using the DEAP dataset of 32 participants. An experiment was carried out to test practicality of the proposed system using the EMOTIV Insight headset electroencephalogram (EEG) data from four channels. We utilise a tunable-Q wavelet transform (TQWT) algorithm to extract frequency domain characteristics of the signals and classify using time windows of two seconds. The extracted power of the signals was identified as features from different frequency bands and the K-nearest neighbour (KNN) and random forest (RF) classifiers resulted in an accuracy of 97.8%.

Keywords: *emotion recognition; tunable-Q wavelet transform; TQWT; K-nearest neighbour; KNN; random forest; RF.*
DOI: 10.1504/IJMEI.2023.10058261

- **Brain tumour segmentation using deep learning method - inception U-net**

by S.B. Mohan, B. Ramesh, G. Gurumoorthy, B. Kannan

Abstract: The objective of the procedure of segmentation for brain tumours is to provide an accurate delineation of the regions that are affected by the tumour. In recent years, deep learning algorithms have shown performance that is seen to be promising in the field of addressing a variety of difficulties pertaining to computer vision. With the assistance of a deep learning model that is supported by DenseNet and commencement, a highly autonomous process for managing the work of glioma division in pre-usable X-ray examinations has been

developed. This method can handle the task of handling the task of segmentation of gliomas. The incorporation of inception modules resulted in a substantial improvement ($p < 0.001$) in the segmentation performance across the board including all glioblastoma sub-districts. The algorithm attained a high degree of accuracy while maintaining a high level of performance throughout all three of the BraTS 2018 datasets.

Keywords: *segmentation; brain tumour; computer vision; inception; DenseNet architecture.*
DOI: 10.1504/IJMEI.2023.10058262

- **Hybrid brain computer interface structures to control drone in 3D**

by B. Divya, S. Bharathi, G.R. Mahendra Babu, K. Rajalakshmi, Nalini Mohan

Abstract: In order to overcome the shortcomings of traditional single BCI systems, a novel method of brain-computer interfacing (BCI) has been proposed; this method is known as a hybrid BCI. Although several tests using hybrid BCIs have yielded promising results, much more research and development is still needed in this area. As a corollary, we also did a thorough analysis of the most recent studies focusing on the usefulness of BCIs. To determine the weight each factor should have in the overall evaluation of BCI usability, we zeroed in on the tasks and measurements involved. We reported on the satisfaction-based usability features of BCI and mixed BCI systems efficacy, and efficiency, and made some suggestions for further research. Usability testing can reveal problems with the HCI and ergonomics of BCI and hybrid BCI systems, as well as provide suggestions for future study in the area.

Keywords: *brain-computer interfacing; BCI; drone control; 3D images.*
DOI: 10.1504/IJMEI.2023.10058455

- **Integration of matching smart phone data with long-term continuous glucose monitoring data pictures of food intake**

by A. Rajasekar, J. Megala, Swagata Sarkar, C. Sivakumaran

Abstract: The treatment of diabetes relies heavily on careful glucose monitoring as an important component. Nevertheless, further information on the context is required in order to completely comprehend and interpret glucose levels in a meaningful manner. Continuous glucose monitoring (CGM), automated analysis of new glucose variables, and visualisation of CGM data via the ambulatory glucose profile have all contributed to significant advancements in precise glucose monitoring over the past five years. This made significant improvements in glucose monitoring. There are considerable challenges to its adoption, such as the fact that it is inconvenient and does not give immediate and frequent feedback. However, intermittent self-monitored blood glucose (SMBG) can offer extra information that may be used to make choices about therapy. Systems that indicate greater results compared to standard SMBG alone include those that give instant feedback to patients as well as decision support tools for both patients and physicians.

Keywords: *glucose monitoring; biomedical; smartphone; diabetes.*
DOI: 10.1504/IJMEI.2023.10058522

- **Revolutionising organ donation and transplantation for a better future: a blockchain based approach**

by Rachana Y. Patil, Yogesh H. Patil

Abstract: Prolonged monitoring of life-sustaining organs and their supply chain is challenging. Patients have to wait for a longer time due to numerous lacunas in the organ donation and transplant system. The objectives of this article are manifold, first to address the major challenges in successful organ donation and transplantation systems worldwide. Second, to focus opportunities in workforce expansion, developing modern infrastructure and creating social awareness for organ donation. Third is to regulate the legal, ethical and administrative management among government authorities and medico-legal firms. To overcome these irregularities, we have proposed a secure, distributed and immutable blockchain based approach to improve and streamline organ donation and transplantation procedures. This ensures the availability of organs for the needy patents. This blockchain-specific approach helps to prevent and monitor organ trafficking by auditable medical transactions. This opens up blockchain-based smart health services to defend doctors and patients rights.

Keywords: *organ donation; transplantation; blockchain; challenges; opportunities.*
DOI: 10.1504/IJMEI.2023.10058768

- **Anomaly detection architecture for smart hospitals based on machine learning, time series, and image recognition analysis: survey**

by Somaya Haiba, Tomader Mazri

Abstract: Smart hospital networks are considered the most sensitive networks for

anomalies; any tiny existence might produce very different dangerous scales. The usual anomaly detections dedicated to this kind of network are not able to analyse all the different categories and proprieties of the generated data, because the majority of them rely only on time series analysis which is not able to cover all the circulated pieces of information. For that, in this paper, we will survey a proposed anomaly detection architecture that can dominate all the data categories that exist inside the e-health network using image recognition as well as time-series analysis.

Keywords: *E-healthcare monitoring network; IoMT; smart hospitals; E-health anomaly; anomaly detection; machine learning; time-series analysis; IoT security; ImageGray analysis; medical data; Cybersecurity.*
DOI: 10.1504/IJMEI.2023.10058832

- **A novel deep learning approach for b-value optimisation in intravoxel incoherent motion magnetic resonance imaging on simulated data**

by Abin Shoby, Jerome Francis, Jini Raju, C. Ushadevi Amma, Ansamma John

Abstract: Intravoxel incoherent motion magnetic resonance imaging (IVIM MRI) is a non-invasive technique which measures the perfusion and diffusion effects present in a tissue. One of the major challenges in IVIM imaging is the prolonged scan time since multiple b-value images are required for estimating IVIM parameters. The proposed work introduces a novel approach for reducing the number of b-values required for the generation of IVIM signals from unknown b-values using long short-term memory (LSTM) network. Experimental results show that LSTM network has the capability of accurately estimating IVIM parameters even with 4 b-values, with the estimated values are in agreement with the literature. If an IVIM machine takes 37.5 seconds for the acquisition of a b-value signal, then it will take only 2.5 minutes for acquiring IVIM signals for 4 b-values. This will reduce the patient discomfort and increases the clinical acceptance of IVIM imaging.

Keywords: *intravoxel incoherent motion imaging; long short-term memory; LSTM; area error; optimal b-values.*
DOI: 10.1504/IJMEI.2023.10058833

- **Tri-partition-based b-value optimisation for intravoxel incoherent motion magnetic resonance imaging of brain**

by Jini Raju, C. Ushadevi Amma, Ansamma John, V. Jineesh

Abstract: Intravoxel incoherent motion (IVIM)-based magnetic resonance imaging (MRI) technique allows the simultaneous estimation of perfusion and diffusion without the use of contrast agents. As the number of b-values increases, the scan time also increases, which in turn causes patient discomfort. This necessitates the reduction in the number of b-values (b-value count) and the optimisation of absolute b-values that quantify both the perfusion and diffusion effects accurately. The two partition approach of biexponential model fails to consider the b-value regions where both the perfusion parameters have significance. The proposed work explores the possibility of finding minimal and optimal set of b-values using the images corresponding to a set of 21 b-values, using random sampling-based tri-partition method, by varying b-value counts from 10 to 4. Experimental results demonstrate that appropriate selection of b-values from the three partitions generate quality parametric maps.

Keywords: *intravoxel incoherent motion; IVIM; diffusion weighted imaging; b-value optimisation; random subsampling.*
DOI: 10.1504/IJMEI.2023.10058916

- **Early-stage leukaemia detection using sophisticated machine learning algorithms**

by Pawan Whig, Anant Aggarwal, Dhaya Sindhu Battina, Srinivas Venkata, Shama Kouser, Ashima Bhatnagar Bhatia

Abstract: This paper investigates the efficacy of convolutional neural networks (CNNs), a deep learning technique, in early-stage leukaemia detection - a crucial task for improving outcomes. Comparing support vector machines, random forests, artificial neural networks, and CNNs, we assess performance on a dataset of blood samples from leukaemia patients and healthy subjects. Results reveal high accuracy across models, with CNN outperforming other methods in both accuracy and efficiency. CNNs capacity to learn complex patterns from raw data, such as blood samples, sets it apart from traditional algorithms. This study underscores CNNs potential to revolutionise early-stage leukaemia detection, demonstrating its significance in advancing cancer diagnosis.

Keywords: *early-stage leukaemia; machine learning; deep learning; convolutional neural network; CNN; classification; feature extraction; diagnosis.*
DOI: 10.1504/IJMEI.2023.10060130

- **Solution for I-RFID-based smart infrastructure health monitorings security and privacy**

by A. Rajasekar, K. Vidya, G. Adharsh, C. Sivakumaran

Abstract: The idea of a smart city and smart infrastructure is a relatively recent one, and it refers to the management and control of the various infrastructures of a city via the integration of internet and cellular networks. The addition of internet of things functionality to cellular networks results in an increase in both the scalability and dependability of the whole system. The most current innovation in integrated radio frequency identification (I-RFID) sensor technology allows for the data collected by the sensor to be sent over greater distances in a more secure manner using access point and base station. We constructed a network of intelligent nodes, each of which will consist of a radio-frequency identification tag, a reduced function RFID reader and sensors. The proposed method exhibits minimal data delivery losses and a considerable reduction in the amount of time spent on transmission delays.

Keywords: *radio frequency identification; RFID; healthcare monitor; security; smart infrastructure.*

DOI: 10.1504/IJMEI.2023.10060421

- **A novel hybrid-based approach for detection of skin lesion using machine learning techniques**

by Nikhil Singh, Sachin Kumar, Shriram K. Vasudevan

Abstract: As a result of medical sector treatment strategies, the incidence of skin cancer has increased globally over the past few decades. It is essential to develop automatic detection systems to aid doctors in the early diagnosis of skin cancer. The automated identification of skin lesions using dermoscopic pictures remains a difficult and complex endeavour. This proposal describes a unique method for detecting skin cancer using dermoscopy pictures. In order to enhance the performance, we combined the segmentation and classification techniques with the innovative hybrid methodology fuzzy brain storming optimisation (FBSO). In two steps, we performed lesion segmentation, noise reduction, and feature extraction before submitting our dataset to machine learning algorithms for optimisation and analysis. Many characteristics, including accuracy, sensitivity, specificity, precision, F1-score, and AUROC, have been used to validate the performance of the suggested model. The experiment demonstrates that random forest's accuracy [91.0% for dataset 1 (ISIC) and 92.5% for dataset 2 (HAM10000)] and AUROC [96.1% for dataset 1 (ISIC) and 97% for dataset 2 (HAM10000)] are superior to those of traditional models.

Keywords: *machine learning; AI; healthcare; skin cancer; medicine; melanoma.*

DOI: 10.1504/IJMEI.2023.10060493

- **A machine learning-based methodology for stratifying patients into obstructive sleep apnea risk**

by Christos Bellos, Konstantinos Stefanou, Georgios Stergios, Dafni Patelou, Thomas Katsantas, Konstantinos P. Exarchos, Apostolis Nikolopoulos, Agni Sioutkou, Georgios Siopis, Konstantinos Kostikas, Chara Tselepi, Athanasios Konstantinidis

Abstract: Obstructive sleep apnoea (OSA) is a common and chronic disorder that leads to increased day-time sleepiness, is associated with accidents, emerging of cardiovascular and metabolic disorders as well as depression. Almost 20% of the population suffers from OSA while a large portion of people are undiagnosed. The objectives of the current work are: 1) the development of a platform to keep a record of home sleep studies and monitor patients; 2) its use for screening tool for the detection of undiagnosed cases in the general population; 3) the design of a machine learning-based methodology for stratifying patients into high and low risk of OSA based on a series of clinical findings and questionnaires. The proposed methodology showed overall accuracy 87.4%, sensitivity 92.1% and specificity 77.1%.

Keywords: *obstructive sleep apnea; machine learning; web-based system; visualisation platform; data analysis.*

DOI: 10.1504/IJMEI.2023.10060654

- **Prediction of COVID-19 cases with epidemiological and time series models**

by Aman Shakya, Anita Sharma, Sanjeeb Prasad Panday, Rom Kant Pandey

Abstract: This work analyses the official data of coronavirus and predicts the evolution of the epidemic in Nepal. The generalised SEIR model has been applied with hybrid of ETS-ARIMA time series model for the time series analysis and predictions of evolution of COVID-19 cases. The prediction has been made for 30 days using the past data of thirteen months. The prediction made by generalised SEIR model has been corrected using two time series models, ETS and ARIMA

model. The predicted error by ARIMA model is added to the prediction made by generalised SEIR model. Use of generalised SEIR model along with ETS and ARIMA model improves the time series prediction of coronavirus spread in case of Nepal as compared to the generalised SEIR model. Also, the SEIR-ETS-ARIMA model reduces the estimation error as compared to SEIRD-ARIMA model. Improvement in all quality measures, MAE, MSE, RMSE and MAPE has been observed.

Keywords: *corona; SEIR; ETS; ARIMA; SEIRD-ARIMA.*
DOI: 10.1504/IJMEI.2023.10060974

- **Sentiment analysis in medication related texts**

by Rabia Bounaama, Mohammed El Amine Abderrahim

Abstract: This study deals with the sentiment analysis of medication related texts improvement by using classical and state-of-the-art approaches like long-short-term memory (LSTM) and bidirectional encoder representation from transformers (BERT) model. The models evaluation demonstrates that transformer model outperformed other models like Na?ve Bayes (NB), logistic regression (LR) and support vector machine (SVM). Despite the superiority of state-of-the-art models, we show that the use of classical approaches remains a possible choice to avoid the complexity problem of the state-of-the-art approaches. The texts used in our experiment come from the Social Media Mining for Health (SMM4H) corpus and the coronavirus tweets NLP-text classification corpus.

Keywords: *sentiment analysis; machine learning; transformer; long-short-term memory; LSTM; bidirectional encoder representation from transformers; BERT.*
DOI: 10.1504/IJMEI.2023.10061044

- **Predicting low back pain symptoms with machine learning**

by T. Senthilkumar, A. Kanmani, P. Senthil, A. Niranjil Kumar, S. Narasimha Prasad

Abstract: Chronic low back pain (LBP), often known as low back syndrome or LBP, is a condition that may be brought on by a number of different disorders. It is also the biggest cause of disability on a global scale. Because there are now more digital pictures available in orthopaedics, researchers have been able to create techniques that are connected to artificial intelligence. The objective of this research was to assess the usefulness of a variety of machine learning (ML) algorithms and sample entropy (SampEn), a metric that evaluates the degree to which motion variability is complicated, in determining the presence of the ailment known as LBP. The Gaussian naive Bayes ML algorithm had the highest level of performance out of all the other algorithms that were evaluated, with an accuracy rate of 79% when it came to identifying patients suffering from CLBP.

Keywords: *low back pain; LBP; machine learning; artificial intelligence.*
DOI: 10.1504/IJMEI.2024.10061273

- **A real-time deep learning-based system for the blood glucose prediction of the diabetic patients**

by Abhay Kumar Tripathi, Sumita Mishra, Shriram Kris Vasudevan

Abstract: Diabetes is a prevalent and long-term condition. It is possible to prevent diabetes if it is detected early enough. Insulin risk and severity may be considerably decreased if an accurate early prediction could be made. Diabetes datasets are challenging to predict due to the small amount of data that has been categorised and the potential for outliers (or missing values). The purpose of this study is to predict diabetes in a human or a patient with greater accuracy using various machine learning techniques, such as neural networks. Techniques for machine learning may increase the accuracy of predictions with patient-generated data. We begin by classifying the database and separating it into training and testing sets of information, which we then analyse separately. The CNN-LSTM combination is seen to yield the best results, with an accuracy rate of 96.5%. An accuracy of 91.56% is achieved in the testing data. Improved accuracy of the categorisation is achieved by imposing an LSTM model for diabetes prediction.

Keywords: *smart healthcare system; diabetes prediction; long short-term memory; LSTM; machine learning; deep learning.*
DOI: 10.1504/IJMEI.2024.10061586

- **Telemedicine system for healthcare monitoring: heart rate and body temperature vital signs**

by Ashok Vajravelu, Sreeja Vijay, R. Ramamoorthi, S. Ramesh

Abstract: The phrase remote health monitoring systems (RHMS) is used in the area of telemedicine to consult with, diagnose, and treat patients while working remotely. The RHMS was developed with the intention of using several types of communication technology in order to provide timely medical care to populations who are geographically separated. This article provides a detailed

examination of the non-invasive capture of crucial data as well as the internet of things in the context of the discipline of healthcare informatics. It discusses the difficulties encountered in the area of healthcare informatics and offers recommendations for further research. In particular, the investigation that was carried out indicated that there has been a difficult obstacle to overcome in the process of developing multi-frequency essential IoT systems. If such technologies are successfully implemented, the resulting healthcare system will be one that is not only strong but also environmentally friendly, self-sufficient, and intelligent.
Keywords: *healthcare system; non-invasive data acquisition; internet of things; IoT; wireless sensor network; WSN.*
DOI: 10.1504/IJMEI.2024.10061587

- **Deep transfer learning based two-stage multi-modal depressive tendency recognition using physiological and psychophysiological signals**

by Gaurav Kumar Gupta, Dilip Kumar Sharma
Abstract: Depressive tendency recognition is challenging due to the limitations of labelled depressive knowledge and diverse variations in behaviour. This paper proposes a deep transfer learning-assisted two-stage multi-modal depressive tendency recognition system (DTL-TMD) by utilising physiological signals such as audio, transcript texts, and images and EEG as psychophysiological signals. The proposed system leverages the deep transfer learning (DTL) model to address and enhance the insufficient annotated physiological and Psychophysiological signals. Finally, it fuses the outcome of two stages with the assistance of a depression level-aware attention model in the adaptive neuro-fuzzy interface system (ANFIS) to detect depressed and non-depressed subjects effectively. Experimental results demonstrate superior performance and improve the depression recognition rate.
Keywords: *depression; electroencephalogram; EEG; convolutional neural network; CNN; adaptive neuro-fuzzy interface system; ANFIS; grow net; radial basis function neural network; RBFNN; deep Boltzmann machine; DBM; deep transfer learning; DTL; whale optimisation algorithm.*
DOI: 10.1504/IJMEI.2024.10061938

- **Multiclass epilepsy seizure classification using deep learning**

by Pankaj Kunekar, Mukesh Kumar Gupta, Pramod Gaur
Abstract: The neurosurgeon must be able to identify the type of epileptic seizure for the purpose to comprehend the cortical connectivity of the brain. Recurrent seizures, often known as epilepsy, are symptoms of the central nervous system and last either a few seconds or, in rare cases, a few minutes. EEG is one of the methods for recording seizures. The majority of EEG devices are composed of scalp electrodes that capture electrical activity. These signals are complex and often difficult to classify. Despite the existence of automated premature seizure identification from a usual electroencephalogram, little effort at multiple classes classification of seizures have been made done. Therefore, utilising the Bonn University dataset, a deep learning models has been developed using RNN, LSTM, and bi-directional-long short-term memory also known as Bi-LSTM, to solve this challenge. Bi-LSTM is found to be the most effective model for multi-class categorisation of epilepsy episodes in this research, with an accuracy of nearly 99% for three classes.
Keywords: *epilepsy seizures; electroencephalogram; EEG; Bi-LSTM; deep learning.*
DOI: 10.1504/IJMEI.2024.10061939

- **Automated adaptive gamma improvement with weighting distribution in wireless capsule endoscopy**

by Kanika Pasrija, Kavita Mittal
Abstract: This study focuses on enhancing the wireless capsule endoscopy (WCE) systems capabilities in disease localisation and bleeding detection within the gastrointestinal (GI) tract. By leveraging direction of arrival (DOA)-based localisation methods, the research proposes a novel approach involving the identification of regions of interest (ROIs) along the GI tract, streamlining feature extraction and bleeding image classification while reducing computational complexity. Additionally, a new bleeding detection method is introduced, utilising the Y.I/Q colour space as an efficient alternative to the conventional YIQ model. Experimental results demonstrate the effectiveness of the proposed computer-assisted diagnostic algorithm in accurately identifying gastritis and gastrointestinal bleeding, underscoring its potential to significantly enhance WCE technology for improved disease localisation and diagnostic precision. Our experiments yielded compelling results, with our computer-assisted diagnostic algorithm achieving an accuracy rate of over 90% in accurately identifying gastritis and gastrointestinal bleeding. This significant level of accuracy underscores the potential of our approach to greatly enhance the capabilities of

wireless capsule endoscopy (WCE) technology, improving disease localisation and diagnostic precision within the gastrointestinal tract.

Keywords: *gastrointestinal; computer-assisted diagnostic-procedure; wireless capsule endoscope; luminance-in phase-quadrature; region of interest; deep neural network; disease localisation; bleeding detection; patient care; medical practices; early disease detection; telemedicine.*

DOI: 10.1504/IJMEI.2024.10062053

- **Disease detection system based on haemogram report using random forest algorithm**

by Deepali K. Gaikwad

Abstract: The healthcare systems require vast amount of medical data that is gathered post performing numerous medical tests. Medical data provides the essential information in order to diagnose diseases early or even before they occur. The classifiers use the characteristics of the complete blood count to forecast information about potential blood illnesses in early stages, which may improve the likelihood of a cure. Machine learning builds predictive models based on prior data. The illness prediction procedure may decrease as many as fatalities and improves the condition of living for those who tract with these diseases. In this study we applied random forest classifier on blood test report dataset to identify various blood diseases like anemia, leukemia, lymphoma, sickle-cell, etc.

Keywords: *machine learning; random forest; blood components; blood diseases.*

DOI: 10.1504/IJMEI.2024.10062222

- **Analysis of type-2 diabetes datasets using sampling techniques**

by Puneeth N. Thotad, Geeta R. Bharamagoudar, Basavaraj S. Anami

Abstract: Diabetes is one of the significant health disorders causing mortality in a developing country like India. Using technology to treat disease can lead to insights using data mining and machine learning techniques. Patient information plays a significant role in the diagnosis and prognosis of diabetes disease for decision-making. A comparative study is carried out using three imbalanced diabetes datasets. Synthetic minority oversampling technique is applied, and datasets are balanced. Balanced datasets gave higher accuracy, recall, precision, F1-score, and area under the curve compared to imbalanced datasets. Random forest has performed well on the balanced datasets. This work is appropriate for use in the medical field to manage diabetes efficiently.

Keywords: *data mining; machine learning; sampling techniques; random forest; decision tree; diabetic complications.*

DOI: 10.1504/IJMEI.2024.10062368

- **Enhanced brain structure segmentation in schizophrenia MRI using bias correction and optimisation**

by N. Swathi, J.M. Mathana, K. Sakthidasan

Abstract: Exploring the structural details of schizophrenia through neuroimaging, particularly MRI, has been essential in unravelling the disorder's underlying pathophysiology. This research addresses the challenge of accurately segmenting MR images in schizophrenia studies, contending with issues like magnetic field inhomogeneity and noise. The central objective is to refine segmentation precision by effectively estimating bias fields. Employing multiplicative intrinsic component optimisation (MICO) and non-uniformity correction via brain SUITE for bias correction, and utilising firefly and partial swarm optimisation (PSO) algorithms for gray matter and ventricle segmentation, the study identifies the optimal combination through a comparative analysis. Evaluation metrics, including structural similarity measures (SSIM), feature similarity measures (FSIM) and Accuracy, highlight the superior performance of the MICO and PSO pairing in this proposed framework.

Keywords: *schizophrenia; SZ; image segmentation; bias correction; multiplicative intrinsic component optimisation; MICO; non-uniformity correction; brain suite; firefly; PSO.*

DOI: 10.1504/IJMEI.2024.10062369

- **A survey on the automated computer-aided diagnosis of epilepsy seizure**

by Pankaj Kunekar, Mukesh Kumar Gupta, Pramod Gaur

Abstract: Epilepsy, a life-threatening neurological disorder, necessitates early diagnosis and treatment to mitigate its risks. Neurologists detect epileptic seizures based on manual analysis of electroencephalography (EEG) signals. However, this manual approach is time-consuming, prone to errors due to human fatigue, and challenging for interpreting non-linear, non-stationary data. This paper presents a comprehensive review of state-of-the-art automated computer-

aided diagnosis techniques for early epilepsy seizure detection, focusing on advancements made to overcome the limitations. By synthesising existing research, this survey aims to pinpoint the current state of the field, shed light on its strengths and weaknesses, and identify promising directions for future research.

Keywords: *computer-aided diagnosis; CAD; epilepsy; computerised tomography; CT; magnetic resonance imaging; MRI; positron emission tomography; PET.*
DOI: 10.1504/IJMEI.2024.10063066

- **Breast cancer diagnosis based on thermography images using deep learning and forest optimisation algorithm**

by M. Sri Geetha, A. Grace Selvarani, R. Vinodhini, M. Murugan

Abstract: Breast cancer is one of the most lethal types of cancer affecting women. The method of obtaining mammograms is a painful and unpleasant procedure for women since it requires compression of the breasts. This article would analyse thermal breast images for symptoms of the disease using image-processing techniques and algorithms. With this procedure, breast cancer could be discovered at an earlier stage of development. We describe a novel approach for extracting breast differentiating features utilising bio-data, image analysis, and image statistics. These features were obtained from thermal images acquired by a camera, and they will be classified by convolutional neural networks (CNNs) as normal or suspicious. The proposed method gives an accuracy rate of 98.95% for the thermal image dataset.

Keywords: *breast cancer; breast thermal image; convolutional neural network; CNN; image analysis; thermography.*
DOI: 10.1504/IJMEI.2024.10063877

- **COPD: assessment of COPD prediction through machine learning techniques**

by Mrinal Goswami, Arpita Nath Boruah

Abstract: Chronic obstructive pulmonary disease (COPD) is a progressive and debilitating respiratory condition characterised by persistent airflow limitation, typically associated with chronic bronchitis and emphysema. COPD represents a significant global health burden, affecting millions of individuals worldwide. In recent years, there has been growing interest in applying machine learning techniques to various aspects of COPD management, including diagnosis, treatment optimisation, etc. This work investigates the performance of different machine learning classifiers used in COPD prediction, especially in single and ensemble classification. A detailed performance comparison among all the classifiers is also done, considering accuracy, precision, recall, and F1 score.

Keywords: *chronic obstructive pulmonary disease; COPD; machine learning; ML; classification; ensemble learning; confusion matrix.*
DOI: 10.1504/IJMEI.2024.10064464

- **Monitoring liver fibrosis in chronic liver disease patients using parametric electrical impedance tomography**

by Shimon Hury, Shimon Abboud, Oranit Cohen Ezra, Maria Lichter, Davidov Yana, Ziv Ben Ari

Abstract: Liver fibrosis stage is the major factor that impacts liver morbidity and mortality. Previous studies suggest that liver dielectric properties, namely its bioimpedance, can be helpful in fibrosis stage classification. In this study, the feasibility of liver fibrosis classification using parametric electrical impedance tomography (pEIT) coupled with demographic & geometric clinical data is investigated. Data from chronic liver patients was collected and used to fit a machine learning model on the task of screening healthy subjects. An accuracy score of 85% was achieved. The exclusion of pEIT measurements, resulted in drop in accuracy to 72% (p-value < 0.005), sensitivity (85% vs. 70%), specificity (84% vs. 74%) and area under the receiver operating characteristic curve (AUC) (0.86 vs. 0.83).

Keywords: *electrical impedance tomography; liver fibrosis; machine learning; logistic regression.*
DOI: 10.1504/IJMEI.2024.10068351

- **Clinical applications of magnetic resonance imaging and spectroscopy technology**

by G.S. Uthayakumar, J. Jeneetha Jebanazer, A. Prabha, T.J. Nagalakshmi

Abstract: Magnetic resonance imaging has been refined as a non-invasive technique due to the superior contrasts it presents in soft tissues. Recent advances in instrumentation have allowed for measurements at ultra-high field strengths, leading to improved signal-to-noise ratios and increased resolution. This study discusses the magnet and gradient subsystems of MRI systems, as well

as a number of complications that can occur from using a magnet. Furthermore, it illustrates the RF coils and transceiver's finer characteristics and numerous constraints. It also showed the idea behind the data processing technology and the difficulties that come with it. In conclusion, the many artefacts inherent to MRI were elucidated. It also gives a quick rundown of the various problems that MRI have to deal with.

Keywords: *MRI image; spectroscopy; clinical application; medical image processing.*
DOI: 10.1504/IJMEI.2024.10064609

- **Proposed novel approach for detecting Alzheimer's disease in early stages**

by Nadish Ayub, Syed Zubair Ahmad Shah, Rayees Ahmad Dar, Assif Assad, Abdullah Shah

Abstract: Alzheimers disease (AD), an incurable brain condition leading to memory loss, requires early detection for effective management. Utilising deep learning (DL) and computer vision (CV) in medical image analysis (MIA) shows promise, but acquiring annotated medical data is costly. Analysing 3D magnetic resonance images (MRIs) demands resource-intensive 3D convolutional neural networks (CNNs). This study introduces a 2D MRI slice-based transfer learning framework, employing a majority voting mechanism during testing. Experimentation reveals the optimal balance between data volume and accuracy is achieved with approximately 10 middle slices. The proposed approach attains a notable 93.91% accuracy, surpassing the state-of-the-art by 12.61% in distinguishing AD from cognitively normal (CN) cases.

Keywords: *deep learning; machine learning; Alzheimer's disease; 3D MRI; transfer learning; 2D slices; convolutional neural networks; CNNs.*
DOI: 10.1504/IJMEI.2024.10064680

- **Blood disease prediction system based on haemogram report using XGBoost algorithm**

by Deepali K. Gaikwad, Ashok T. Gaikwad

Abstract: Healthcare systems gather extensive medical data from diverse tests spanning various fields. Unearthing concealed insights within this data remains critical for early disease detection or preventive measures. Classifiers utilise comprehensive blood count characteristics to forecast potential blood disorders in their initial phases, potentially amplifying the likelihood of effective treatment. Machine learning assumes a pivotal role in crafting predictive models based on historical data. This predictive procedure holds potential in curbing fatalities and enriching the lives of individuals managing these conditions. As an illustration, in this investigation, an XGBoost classifier was deployed on a blood test report dataset, successfully identifying a range of blood-related ailments like anemia, leukemia, lymphoma, sickle-cell anemia, and others.

Keywords: *machine learning algorithms; supervised learning; unsupervised learning; blood disease; XGBoost algorithm.*
DOI: 10.1504/IJMEI.2024.10064883

- **Simulation of heart beat interval series - a neurophysiology based model in comparison with a nonlinear network oscillator model**

by Sajitha Somasundaran Nair, Mini Maniyelil Govindankutty, Minimol Balakrishnan, Remya George

Abstract: Heart rate variability (HRV) analysis is a non-invasive method of autonomic nervous system (ANS) function assessment. In the present study a quantitative physiological model of the ANS is compared with a nonlinear network oscillator model in terms of power spectrum and poincare plots across three autonomic states. The physiological model more accurately reproduces HRV features compared to the nonlinear oscillator model. Rooted in actual physiology, the physiologic model allows extensive parameter tuning for various autonomic states, offering multiple modulable parameters. In contrast, the nonlinear oscillator model lacks physiological roots and permits only limited adjustments through coupling coefficients.

Keywords: *autonomic nervous system; ANS; heart rate variability; HRV; quantitative physiological model; neurotransmitter kinetics; nonlinear oscillator model; poincare plot; power spectrum.*
DOI: 10.1504/IJMEI.2024.10064942

- **Data analysis, early diagnosis and management of COVID-19**

by Rani Samyuktha Devabhaktuni, Simisola Olawoye, Dinesh P. Mital, Shankar Srinivasan

Abstract: The COVID-19 pandemic is one of the deadliest infectious diseases in recent history. Our research goals are to study the mode of spread of COVID-19

on various counties in New York and New Jersey, its effect on various, races, gender, age groups and to develop a clinical decision support system (CDSS) for early detection of COVID-19. The Bronx borough in New York state, the Bergen and Essex counties in the neighbouring New Jersey state, and men and people over 65 had higher hospital admissions, and fatalities, according to our research, where we used SAS and SPSS for data analysis.

Keywords: *clinical decision support system; CDSS; Corvid; COVID-19; SARSCoV-2; RT-PCR; systemic disease; fatality rate.*

- **Automatic blood disease detection system based on haemogram report using decision tree algorithm**

by Deepali K. Gaikwad, Ashok T. Gaikwad

Abstract: In healthcare systems, a vast quantity of medical data is collected from multiple medical tests conducted in various sectors. It remains required to extract hidden information from medical data to diagnose diseases at an early stage or even before they manifest. In order to predict information about possible blood disorders in their early stages and potentially increase the chance of a cure, the classifiers make use of the features of the full blood count. The development of predictive models based on historical data is the responsibility of machine learning. The process for predicting illness may reduce the number of deaths and enhance the lives of those who suffer from these conditions. Using a decision tree classifier applied to a dataset of blood test reports, this study identified several blood illnesses, including sickle cell disease, leukaemia, anaemia, and lymphoma.

Keywords: *blood disease; decision tree; machine learning; supervised; unsupervised.*
DOI: 10.1504/IJMEI.2024.10065459

- **Cervical cancer detection and segmentation using ANFIS classifier and prediction by ensemble deep learning network**

by D. Baskar, K. Manivanan

Abstract: In underdeveloped nations, the incidence frequencies of cervical cancer have been sharply rising while the health services for prevention, diagnosis, as well as therapy are still relatively few. Cancer screening procedures may lead to an early diagnosis, which increases the likelihood of successful treatment and, ultimately, the protection of cervical cancer. An approach for the identification, as well as fragmentation of cervical cancer depending on the adaptive neuro-fuzzy inference system (ANFIS), is provided here. A novel model has been built and given the name the colposcopy ensemble network (CYENET) to automatically diagnose cervical malignancies from colposcopy pictures. The cell classification feature is dependent on a compact vision geometry grouping (VGG) network termed compact VGG. The overall accuracy of the classification for VGG19 was 73.31%. The findings of the experiments indicate that the suggested CYENET displayed high levels of sensitivity (92.42%), specificity (96.22%), and kappa scores (88%).

Keywords: *ANFIS; machine learning; VGG19; cervical cancer.*
DOI: 10.1504/IJMEI.2024.10065831

- **Detection of early biomarkers for Parkinson disease**

by M.Z. Shaikh, R. Harini, Megala Jambulingam, M. Nalini

Abstract: The neuro-degenerative disorder known as Parkinsons disease (PD) is characterised by the gradual death of dopaminergic neurons. Individuals with Parkinsons disease often display a number of neurological as well as non-motor abnormalities. It is of the utmost importance to locate responsive as well as specific indications in order to meet the pressing requirement for improved earlier detection as well as subsequently disease-modifying therapy for Parkinsons disease (PD) individuals. There are four different types of markers that may be distinguished from one another. We extracted certain properties using a deeper artificial neuronal system, and then we categorised them as either belonging to Parkinsons disorder or not belonging to Parkinsons disorder. Utilising a method called ten-fold crossing validity, we were able to get extremely positive findings and the accuracy rate was ranging from 9293.5% for the input images used.

Keywords: *bio-marker; Parkinson's disorder; deep learning; machine intelligence.*
DOI: 10.1504/IJMEI.2024.10066539

- **Infrared hand joint dataset: a custom rheumatic hand thermal image dataset creation and its medically approved validation for extending research in diagnosing arthritis**

by Rozina Naz, Gopal Sakarkar, Mohtashim Ahmad, Amina Vali, Noorul Amin

Abstract: Osteoarthritis (OA) and rheumatoid arthritis (RA) are distinct types of

arthritis with different causes; OA results from joint wear and tear, while RA is an autoimmune disease. This research focuses on hand joints affected by arthritis, a leading cause of disability globally. Estimating the number of arthritis patients is challenging as many seek treatment only in severe stages. Conservative estimates suggest over 54 million adults and nearly 300,000 children have arthritis, with elderly individuals being more susceptible. However, 64% of affected adults are younger than 65. Arthritis can range from mild to severe, leading to chronic pain and disability. Severe arthritis can result in permanent joint damage and may affect other organs. The research aims to create a standardized thermal image dataset of hand joints, crucial for identifying inflamed areas. This dataset is well labelled and validated, addressing issues in previous datasets lacking proper annotation and validation.

Keywords: *osteoarthritis; infrared camera; thermal imaging; rheumatoid arthritis; thermal dataset.*

DOI: 10.1504/IJMEI.2024.10066772

- **Prediction of cardiac disease based on whale optimisation algorithm and residual U-Net**

by M. Balamurugan, P. Blessed Prince, M. Umapathy, S.P. Jeno Lovesum

Abstract: Due to the prevalence of the disease and the high death rate it is connected with, heart disease has become a significant public health problem in recent years. Therefore, predicting heart disease using certain simple physical indications that may be gained through having frequent physical examinations at an early stage has emerged as an important topic of study. UWOA is a deep neural network (U-Net) and whale optimisation (WOA) optimised technique created and applied to pick the ideal features that may boost the accuracy of heart disease prediction. The method that has been suggested makes use of a hybrid algorithm that will be broken up into two stages. The algorithm above can extract features, and the values that it generates show a high accuracy range of 97.34%, with improved accuracy by an average of 3.77 percentage points for heart attack prediction.

Keywords: *cardiovascular disease; whale optimisation algorithm; residual U-Net architecture.*

DOI: 10.1504/IJMEI.2024.10066862

- **Image segmentation through advanced distance regularised level set evolution in chest X-ray analysis**

by Ruchika Arora, Indu Saini, Neetu Sood

Abstract: This paper introduces a pioneering solution for the problem of weak edges and intensity inhomogeneities in medical images. Improved distance regularised level set evolution (I-DRLSE) model harnesses the power of local edge gradient features, local fitting variances, and meticulously weighted regional intensity information to orchestrate a seamless evolution of image contours. The variational level set method optimises diffusion rate through a refined quad-well potential function with range-based adaptability. It is validated on publicly available Japanese society of radiological technology (JSRT) dataset by achieving remarkable average dice similarity coefficient (DSC) and intersection over union (IoU) scores of 0.996 and 0.985, respectively.

Keywords: *image segmentation; synthetic images; CXR images; level set method; LSM; DRLSE; CV; adaptive bilateral filter; ABF.*

DOI: 10.1504/IJMEI.2024.10066938

- **The role of thyroid medicine in relieve discomfort and health sustainability a study of patient health behaviour**

by Yan Xu

Abstract: The objective of research is to determine the role of thyroid medicine in relieving discomfort and health sustainability from the perspective of patient health behaviour. This research collected 594 responses from thyroid patients as the sample size, and data analysis for this research is taken by Smart PLS 4. The study has confirmed that the impact of thyroid medicine is significant on relieve discomfort and health sustainability. This research also highlighted the importance of patients' health behaviour as a moderating variable between thyroid medicine, relieving discomfort, and health sustainability. The research asserts that patients to get thyroid medicine for advancing their health sustainability.

Keywords: *patient health behaviour; thyroid medicine; health sustainability; relieve discomfort; health improvement.*

DOI: 10.1504/IJMEI.2024.10067004

- **BiLSTM-net: a simple and efficient model for foetal compromise detection during intrapartum and antepartum phase**

by Vidya Sujit Kurtadikar, Himangi Milind Pande

Abstract: Cardiotocography (CTG) is a well-known device used to assess foetus health by monitoring foetal heart rate (FHR) and uterine contraction (UC) simultaneously during the antepartum and intrapartum phases. The visual interpretation of CTG signals has associated high false positive and false negative rates due to its complex structure. Automatic detection of foetal state can be done using machine learning methods, thereby reducing undesirable adverse perinatal outcomes and unnecessary caesarean section. We propose a deep learning model suitable for time series FHR signals based on a bidirectional long short-term memory (BiLSTM) network. We used two open datasets and one private dataset, which are diverse enough to test the robustness of the deep learning model. The experiments on all three datasets achieved excellent and consistent results for all parameters. The results are encouraging enough to demonstrate the proposed models good predictive capacity.

Keywords: *cardiotocography; CTG; foetal monitoring; foetal compromise; bidirectional long short-term memory; BiLSTM; deep learning.*

DOI: 10.1504/IJMEI.2024.10067030

- **SMART2C - a healthcare digital platform based on process mining for managing COVID-19**

by Nesrine Missaoui, Asma Mejri, Wissem Hachfi, Amel Letaief, Asma Daassa, Emna Ammar, Hajer Chackroun, Haifa Boudriga, Marwa Seghaier, Ricardo Martinho, Sahar Toumia, Yemna Sayeb, Henda Hajjami Ben Ghezala, Sonia Ayachi Ghannouchi

Abstract: This paper addresses the difficulties and challenges that affected the Tunisian healthcare system during the spread of the COVID-19 virus. It proposes a digital platform to improve healthcare COVID-19 related processes, by applying process management methodologies and integrating process mining and decision mining techniques to analyse process execution traces. This integration assists stakeholders in making informed decisions and optimising resource utilisation, offering recommendations for healthcare providers to enhance their decision making. Additionally, it highlights emerging healthcare solutions with potential to mitigate the impact of pandemic-related events and safeguard against pandemics and other natural disasters.

Keywords: *COVID-19; digital platform; process mining; security; process implementation.*

DOI: 10.1504/IJMEI.2024.10067213

- **Comprehensive assessment of enhanced transfer learning-based MRI classification for accurate brain tumour detection and grading**

by S. Amsavalli, K. Saminathan, M.Chithra Devi

Abstract: Brain tumour identification and classification improve early detection and therapy planning. Brain cancer diagnosis with MRI scans is essential for fast and effective treatment. This study improves transfer learning-based MRI categorisation to improve brain tumour diagnosis and grading. Our method uses a varied collection of normal brain MRIs and glioma tumour pictures from different reliable databases. The preprocessing pipeline captures unique image features using Z-score normalisation and SURF model feature extraction. The work uses pre-trained weights and the VGG19 transfer learning model, fine-tuned on the MRI dataset, to classify brain tumours. Attention mechanisms in the VGG19 architecture prioritise informative regions in input images to improve discrimination. The Python technique uses TensorFlow and Keras deep learning libraries. Our brain tumour categorisation method achieved 99.2% accuracy in experiments. Our method surpasses Neural Networks, ANN, CNN, and CRNN by 2.1% in brain tumour detection and grading from MRI scans. According to extensive investigation and evaluation, our framework's robustness and reproducibility could change neuroimaging diagnosis and improve clinical outcomes.

Keywords: *brain tumour detection; MRI images; transfer learning; speeded-up robust features; SURF; VGG19; Z-score normalisation; Keras deep learning libraries.*

DOI: 10.1504/IJMEI.2024.10067243

- **Eye ball sensor controlled wheel chairs for disabled patients**

by J. Gowrishankar, S.B. Mohan, Sreeja Vijay, P. Sivakumar

Abstract: This article proposes a system for eye ball motion controlled wheelchair, a device designed to help the elderly and those with mobility issues get around. An eye frame equipped with three proximity infrared (IR) sensor modules monitors the iris. If an infrared camera detects something white, it will generate a new string of binary digits. Arduino boards will these signals to operate the wheelchairs motors. Individuals experiencing difficulties with their motor nerves are the focus of this research. Even though they are disabled, this

method will allow them to steer an electric wheelchair using their eyes alone. The user can steer and accelerate the wheelchair by looking left or right, and can also initiate and halt movement with their gaze. The proposed method runs well with an average reaction time of 3.2 seconds for eye control.

Keywords: *wheelchair; IR sensor; ultrasonic sensor; accelerometer.*
DOI: 10.1504/IJMEI.2024.10067333

- **Age-based comparison of resting-state brain activity in autism spectrum disorder: an fMRI study**

by B. Divya, A. Kavitha, R. Sowmya, B.S. Sneha, T.V. Santhoshiya

Abstract: Atypical alterations in brain development is a defining feature of autism spectrum disorder (ASD), but age-related changes in regional brain function and spontaneous activity may be more significant. ASD is linked to irregularities in neurological connections. Current rs-fMRI diagnosis lacks age differentiation, causing inconsistent findings. This study compares functional connectivity in adolescent and adult ASD patients. An age-based comparison shows connectivity declines with age in most brain regions but increases in the insula. Ring connectivity representation reveals better connections in adolescents, particularly in language regions. Connectivity matrices results are validated using fractional amplitude of low-frequency fluctuations (fALFF), which reduces physiological noise and increases accuracy in detecting brain activity. fALFF may serve as an early ASD detection tool or predict sibling risk, potentially through machine learning models. This research broadens the understanding of ASD brain connectivity development across age groups and opens ways for more focused, individualised interventions.

Keywords: *autism spectrum disorder; ASD; connectivity matrix; ring connectivity; amplitude of low-frequency fluctuations; ALFF; fALFF.*
DOI: 10.1504/IJMEI.2024.10067379

- **A research based study of quantitative analysis and segmentation of thermal images for assessing rheumatoid arthritis in the hand joints**

by Rozina Naz, Gopal Sakarkar, Mohtashim Ahmad, Noorul Amin, Amina Vali

Abstract: To investigate rheumatoid arthritis and observing bodys heat flow in the body and monitoring the changes in temperature of the skin. We will compare the difference in skin temperature between people with rheumatoid arthritis and people without it, in individuals with joint pain, the algorithms called the fuzzy c-means algorithm and expectation maximisation (EM) algorithm is used to pinpoint unusual areas on the hand (Backhaus et al., 1999; Tipa and Baltag, 2006; Kuruganti and Qi, 2002; Selvarasu et al., 2009; Snekhalatha et al., 2012). This study reveals how to examine thermogram measurement with heat distribution index (HDI) and estimate skin temperature. The temperature examination demonstrated a temperature increment of 0.970 C within the hand region of those patients with RA as compared to the hands of regular individual. Analysis of the patients data showed that there was a strong connection between HDI and skin temperature.

Keywords: *rheumatoid arthritis; thermograms; thermal segmentation; HDI; infrared images; hand joints.*
DOI: 10.1504/IJMEI.2024.10067688

- **Osteoporosis diagnosis by femur bone modelling using COMSOL multi-physics**

by Ammu Anna Mathew, Aastha Kapoor, Vivekanandan Sundaram

Abstract: Analysing bone behaviour requires a mathematical understanding of the functional history of bone and modelling since bone tissue can change shape to fit its function, much like a structural material. This study aims to model a femur bone using three-dimensional scanning by utilising the physical characteristics of a healthy and diseased one to detect osteoporosis as a pre-clinical evaluation tool. The Von Mises stress and Tresca stress values, which are the resulting point-load responses, were then recorded as part of the expanded inquiry, and a comparative analysis was conducted to get a thorough conclusion with the simulated model by calculating the bone reaction to mechanical changes.

Keywords: *COMSOL multi-physics; femur bone; stress distribution; osteoporosis; SolidWorks; Wolff's law of remodelling.*
DOI: 10.1504/IJMEI.2024.10067727

- **Genetic algorithm with ensemble feature ranking for feature selection in dengue prediction using convolutional neural networks**

by K. Saraswathi, K. Rohini

Abstract: Early intervention and successful treatment depend on accurate disease diagnosis in medical diagnostics. With its high frequency and severe

complications, dengue fever, a mosquito-borne viral infection in tropical and subtropical climates, is a major public health problem. Enhancing predictive models for dengue detection requires effective feature selection, especially when dealing with high-dimensional datasets. This study introduces a novel approach for feature selection in dengue prediction by integrating CNNs with GA-eFR. The GA-eFR algorithm leverages the feature ranking capabilities and the search efficiency of genetic algorithms to identify the most relevant features in the dataset. The methodology involves pre-processing the dataset, designing the CNN architecture, and incorporating GA-eFR into the feature selection process. Experimental results demonstrate that the proposed method significantly enhances the performance of CNN classifiers in detecting dengue, achieving an F-score of 0.92, precision of 0.90, recall of 0.88, and 92.85% accuracy on the OpenDengue dataset. The effectiveness of the proposed feature selection method is further validated by comparing it with other techniques, such as particle swarm optimisation (metaheuristic/swarm-based), recursive feature elimination (wrapper-based), and correlation-based feature selection (filter-based).

Keywords: *genetic algorithm; GA; feature ranking; feature selection; convolutional neural networks; CNN; dengue detection; medical diagnostics; optimisation algorithms; GA combined with ensemble feature ranking; GA-eFR.*
DOI: 10.1504/IJMEI.2024.10067742

- **AI-based radiodiagnosis: a comprehensive review**

by Jay Sawant, Niti Chikhale, Ayushi Tanna, Gajanan Nagare

Abstract: AI plays a critical role in the interpretation and diagnosis of medical conditions based on radiographic images. This review explores the symbiotic relationship between artificial intelligence (AI) and medical imaging, focusing on conventional and emerging modalities. Beginning with an overview of imaging modalities and AI fundamentals, a dive into diverse AI applications in the medical field has been made, emphasising advancements in image recognition and segmentation. Dedicated sections review the role of AI integrated with conventional as well as emerging radiology techniques, showcasing its adaptive potential for rapid diagnostics. Concurrently, the challenges in implementing AI in medical settings, including ethical considerations and validation frameworks have been addressed. By consolidating insights into the transformative impact of AI on diagnostic accuracy and efficiency, this review underscores its pivotal role in shaping the future of medical imaging.

Keywords: *artificial intelligence; healthcare.*
DOI: 10.1504/IJMEI.2024.10067812

- **Cranial abnormalities: a deep learning-based approach for classification and measurement, enhanced treatment sensitivity through 3D printing**

by Osman Nuri Uçan, Incilay Yıldız, Mehmet Ateş, Fulya Oduncu, Emir Kaan Cengiz

Abstract: This article emphasises that technological advances have a significant impact on the treatment process and are essential for the detection and correction of cranial abnormalities. Using the MUG500+ dataset, a deep learning-based classification was used. The aim of the research is to increase measurement precision and accuracy by simplifying the processes involved in helmet therapy measurements. The artificial intelligence solution focusing on deep learning makes a significant contribution to the identification of skull anomalies. The research provides a mathematical model for scaling the abnormal segment using the ResNet-18 algorithm for classification, which further improves the processes involved in 3D printing of the abnormal segment. Examining the results, it appears that the accuracy measure performed successfully in the testing phase (95% success rate). The accuracy and reliability of the proposed model is demonstrated by the sensitivity measure reaching 100%.

Keywords: *artificial intelligence; deep learning; cranial abnormalities; classification; 3D printing.*

- **Detection of sleeping disorders in Parkinson's affected patients using multi-head attention-based BiLSTM model**

by Sk.Wasim Akram, A.P. Siva Kumar

Abstract: The proposed study aims to introduce a novel technique for identifying sleeping difficulties in PD patients by overcoming the existing limitations. Initially, the input samples are collected from the available dataset, and to remove unwanted noises in the input signals, pre-processing is carried out by using improved finite impulse response filter (FIRF), Bessel filter (BF), and continuous wavelet transform (CWT). After pre-processing, the complexity problem is avoided by extracting the most significant features by introducing an adaptive residual dense network (AResDenseNET) model. Based on the extracted features,

a novel multi-head attention-based BiLSTM (MultiHeadAtt _BiLSTM) is proposed for detecting sleeping disorders. Finally, to improve the efficiency of the proposed model, its parameters are fine-tuned by an adaptive aquila optimiser (AAO) approach. As compared with existing approaches, the proposed model achieves a better accuracy result of 98.7%, and hence, it proves the efficacy of the proposed model.

Keywords: *time domain; linear shift-invariant system; scale factor; skip connections; backward information; candidate solution; forward information.*
DOI: 10.1504/IJMEI.2024.10068369

- **Framework for sentimental analysis in healthcare data using deep Biaffine attention enabled CNN classifier**

by Rushali Patil, Arunkumar Molapalayam Sekar

Abstract: Sentiment analysis associated with the COVID-19 pandemic tweets are paramount for informed decision-making and effective public health interventions. Hence, this research presents an effective deep Biaffine attention enabled CNN classifier model to handle the nuances and subjectivity inherent in COVID-19 tweets. This innovative model combines CNN with deep Biaffine attention mechanisms to comprehensively capture intricate word relationships within the COVID-19 tweets. Specifically, the attention mechanism enables the model to identify subtle emotional cues often ignored by traditional approaches, thereby enhancing the precision of sentiment analysis. Our framework demonstrated remarkable performance with an accuracy of 96.16%.

Keywords: *sentiment analysis; Biaffine attention enabled CNN; Aurelia swarm search optimisation; healthcare data; COVID-19 tweets.*
DOI: 10.1504/IJMEI.2024.10068395

Return to top

© 2024 Inderscience Enterprises Ltd.

International Journal on Recent and Innovation Trends in Computing and Communication
ISSN: 2321-8169 Volume: 11 Issue: 9
Article Received: *25 July 2023* ***Revised:*** *12 September 2023* ***Accepted:*** *30 September 2023*

Image Segmentation based on Energy Fitting Models – A Review

[1]Sivakumar. K, [2]Dr. C. Raju, [3]Chekuri Nalini, [4]Sakthiraam. B
[1]Assistant Professor, Department of Electronics and Communication Engineering
Panimalar Engineering College
Poonamallee, Chennai, India.
sivagm2017@gmail.com
[2]Professor, Department of Electronics and Communications Engineering
Sri Venkateswara College of Engineering
Tirupati, Andhra Pradesh, India.
c.raju1112@gmail.com
[3]Assistant professor, Department of Electronics and Communications Engineering
Mohan Babu university
Tirupati, Andhra Pradesh, India.
nalinichekuri02@gmail.com
[4]Associate Engineer, L&T Technology Service
Ambattur, Chennai, India.
sakthiraambalasundaram@gmail.com

Abstract—As a result of changes in imaging technology, segmenting the area of interest (ROI) from medical images is an extremely important yet challenging task. It is still difficult for the global energy-based active contour model (ACM) to properly extract the ROI from medical images, despite the fact that many techniques based on the local region-based active contour model have been proposed to deal with intensity inhomogeneity. This brief study aims to assess the performance of current techniques that have been published in the recent years and have been used to image segmentation. The methods under consideration include the various energy fitting models that have been created to drive the active contour are highlighted in this review study. Each model was examined against a medical image, an MRI brain image, and an image that was not taken by a medical professional. According to the results of the comparison study, it can be determined which technique is better appropriate for image segmentation even when there is intensity inhomogeneity in the images.

Keywords- Active Contour, Laplacian of Gaussian, Intensity fitting, Local Image fitting.

I. INTRODUCTION

Segmentation is a crucial part of the image recognition system, since it is via segmentation that the interesting aspects of an image are isolated and processed, such as for recognition or identification. In practice, image segmentation is applied for image pixel categorization [3]. Segmentation methods are used to separate the directed item from the image for examination. In this case, image segmentation is used to identify a tumor, cancer, or a blockage in the blood flow, as these issues would be segregated from their backgrounds by image segmentation [2]. For the segmentation of monochromatic images, several methods are available. As each pixel in the color images is vector valued, the segmentation of color images is more difficult [3]. Active contour models are one of the most successful picture segmentation techniques [4, 5]. There are two types of active contour models currently available: edge-based models [6] and region-based models [7]. Both of these models have their advantages and disadvantages, and their use in applications is determined by the image's properties.

This brief review is divided into four parts. After that, Section 2 explains a current active contour driven by energy fitting models, Section 3 analyses the results obtained via each of the models, and Section 4 summarizes the research.

II. ACTIVE CONTOUR – ENERGY FITTING MODELS

A. Active Contour-Local Binary Fitting (LBF) Energy Model

Using image information in local areas, Chunming, et. 2001, proposed a region-based active contour model [8] that takes use of image information in local regions. One of the most significant contributions is the inclusion of a local binary fitting energy combined with a kernel function, which allows for the

International Journal on Recent and Innovation Trends in Computing and Communication
ISSN: 2321-8169 Volume: 11 Issue: 9
***Article Received:** 25 July 2023 **Revised:** 12 September 2023 **Accepted:** 30 September 2023*

accurate extraction of local image information. As a result, the LBF model may be used to segment images with inhomogeneous intensities, therefore circumventing a limitation associated with piecewise constant modelling. The LBF demonstrates the advantages of computation efficiency and precision. Additionally, it may be used to reduce the amount of noise in an image. The proposed energy functional is,
proposed energy functional is,

$$F(\phi, \mathrm{C}_1, C_2) = F^{LBF}(\phi, C_1, C_2) + \mu\, p(\phi) + \nu l(\phi) \quad (1)$$

Where, μ and ν are the scaling factors and are positive constants. ϕ is the e level set function. The functions C, C_2 are given as

$$\mathrm{C}_1 = \frac{K_\sigma(\mathbf{x}) * [H_\varepsilon(\phi(\mathbf{x}))I(\mathbf{x})]}{K_\sigma(\mathbf{x}) * H_\varepsilon(\phi(\mathbf{x}))} \quad (2)$$

and

$$\mathrm{C}_2 = \frac{K_\sigma(\mathbf{x}) * [(1 - H_\varepsilon(\phi(\mathbf{x})))I(\mathbf{x})]}{K_\sigma(\mathbf{x}) * [1 - H_\varepsilon(\phi(\mathbf{x}))]} \quad (3)$$

Penalize term $p(\phi) = \int_\Omega \frac{1}{2}(|\nabla\phi(\mathrm{x})| - 1)^2 d\mathrm{x}$ (4)

and length of the zero-level curve

$$l(\phi) = \int_\Omega \delta(\phi(\mathrm{x}))|\nabla\phi(\mathrm{x})| d\mathrm{x} \quad (5)$$

B. Active Contours Driven by Local and Global Intensity Fitting Energy

In a variational level set formulation, Li Wang et al. 2009, presented an enhanced region-based active contour model [9]. Constructed an energy functional with a local intensity fitting term that generates a local force that attracts and stops the contour at object borders, as well as an auxiliary global intensity fitting term that pushes the contour's motion away from the object boundaries. As a result, the combination of these two forces enables the outlines to be initialized in a flexible manner. This energy is then integrated into a level set formulation together with the required level set regularization term for correct calculation in the relevant level set technique. The suggested model is given first as a two-phase level set formulation and subsequently as a multi-phase formulation. The defined energy functional is

$$\mathcal{E}^{\mathrm{LGIF}}(\phi, f_1, f_2, c_1, c_2) = (1 - \omega)\mathcal{E}^{\mathrm{LIF}}(\phi, f_1, f_2) + \omega\mathcal{E}^{\mathrm{GIF}}(\phi, c_1, c_2) \quad (6)$$

Where,

$$f_1(\mathrm{x}) = \frac{K_\sigma(\mathrm{x}) * [H_\epsilon(\phi(\mathrm{x}))I(\mathrm{x})]}{K_\sigma(\mathrm{x}) * H_\epsilon(\phi(\mathrm{x}))} \quad (7)$$

$$f_2(\mathrm{x}) = \frac{K_\sigma(\mathrm{x}) * [(1 - H_\epsilon(\phi(\mathrm{x})))I(\mathrm{x})]}{K_\sigma(\mathrm{x}) * [1 - H_\epsilon(\phi(\mathrm{x}))]} \quad (8)$$

$$c_1 = \frac{\int I(\mathrm{x}) H_\epsilon(\phi(\mathrm{x})) d\mathrm{x}}{\int H_\epsilon(\phi(\mathrm{x})) d\mathrm{x}} \quad (9)$$

$$c_2 = \frac{\int I(\mathrm{x})(1 - H_\epsilon(\phi(\mathrm{x}))) d\mathrm{x}}{\int (1 - H_\epsilon(\phi(\mathrm{x}))) d\mathrm{x}} \quad (10)$$

And the approximated Heaviside function H is

$$H_\epsilon(\mathbf{x}) = \frac{1}{2}\left[1 + \frac{2}{\pi}\arctan\left(\frac{\mathbf{x}}{\epsilon}\right)\right] \quad (11)$$

Minimizing (6),

$$\frac{\partial\phi}{\partial t} = \delta_\epsilon(\phi)(F_1 + F_2) + \nu\delta_\epsilon(\phi)\mathrm{div}\left(\frac{\nabla\phi}{|\nabla\phi|}\right) + \mu\left(\nabla^2\phi - \mathrm{div}\left(\frac{\nabla\phi}{|\nabla\phi|}\right)\right) \quad (12)$$

The model proposed by [9] can further be extend into a multi-phase level set formulation.

C. Active contours driven by local image fitting energy

In 2010, Kaihua Zhang et al. presented a unique region-based active contour model that combines the image's local information and embeds it in the active contour model [10], which was published in the journal Image Processing. This model is capable of segmenting images with intensity inhomogeneities because it contains the local image fitting (LIF) energy, which is used to retrieve the local image information from the images during the segmentation process. It was also proposed that a novel technique for regularizing the level set function, based on Gaussian filtering for variational level set, be developed. In addition, the level set function is assured to be smooth, and the requirement for re-initialization is removed, resulting in time savings by avoiding the need for time-consuming computational re-initialization, which saves time. The sub-pixel accuracy and border regularization characteristics of the original method are preserved with this technique. The model proposed by [10] is that

$$I^{\mathrm{LFI}} = m_1 H_\varepsilon(\phi) + m_2(1 - H_\varepsilon(\phi)) \quad (13)$$

where m_1 and m_2 are

$$\begin{cases} m_1 = \mathrm{mean}\left(I \in (\{x \in \Omega \mid \phi(x) < 0\} \cap W_k(x))\right) \\ m_2 = \mathrm{mean}\left(I \in (\{x \in \Omega \mid \phi(x) > 0\} \cap W_k(x))\right) \end{cases} \quad (14)$$

By minimizing the LIF energy functional

$$E^{\mathrm{LIF}}(\phi) = \frac{1}{2}\int_\Omega \left|I(x) - I^{\mathrm{LFI}}(x)\right|^2 \mathrm{d}x,\ x \in \Omega \quad (15)$$

The level set formulation is

$$\frac{\partial\phi}{\partial t} = \mu\left(\nabla^2\phi - \mathrm{div}\left(\frac{\nabla\phi}{|\nabla\phi|}\right)\right) + \nu\delta_\varepsilon(\phi)\mathrm{div}\left(\frac{\nabla\phi}{|\nabla\phi|}\right) + (I - I^{\mathrm{LF}})(m_1 - m_2)\delta_\varepsilon(\phi) \quad (16)$$

The suggested Gaussian regularizing level set method (GRLSM) may be readily extended to pure PDE driven level set techniques, according to the authors.

D. Active contours driven by optimised LoG Energy.

The ability to segment images with intensity inhomogeneity, particularly around contours, has long been recognized, but it relies on where those contours start. In order to address the shortcomings of the RSF model, a model based on a customized LoG energy functional coupled with the RSF model [11] is suggested by Keyan Ding et. al, in 2017. In the LoG, the operator designed for edge detection is known across the field as a prominent second-order differential operator. The inclusion of the LoG term results in an indifferent outcome regardless of the locations of the original contour. In order to highlight the

International Journal on Recent and Innovation Trends in Computing and Communication
ISSN: 2321-8169 Volume: 11 Issue: 9
***Article Received:** 25 July 2023 **Revised:** 12 September 2023 **Accepted:** 30 September 2023*

edges in an image, the first step is to use a Gaussian filter to smooth it. Then, to extract those edges, a Laplacian operator is used. Thus, combined optimized LoG energy with the RSF energy as follows:

$$E^{RSFSL} = E^{RSF}(\phi, f_1, f_2) + E^{OL}(\phi) \quad (17)$$

Minimizing (17), it is possible to get the gradient flow equation shown below.

$$\frac{\partial \phi}{\partial t} = -\delta_\varepsilon(\phi)(\lambda_1 e_1 - \lambda_2 e_2) + \omega\delta_\varepsilon(\phi) \times L + \nu\delta_\varepsilon(\phi)\text{div}\left(\frac{\nabla\phi}{|\nabla\phi|}\right) + \mu\left(\Delta\phi - \text{div}\left(\frac{\nabla\phi}{|\nabla\phi|}\right)\right) \quad (18)$$

The model made use of an edge detecting operator of second order. Images with edges and objects that are difficult to identify may provide incorrect segmentation results.

E. Fuzzy region-based-global and local fitting energy model.

Fang, Jiangxiong, et al., in 2021, a novel active contour model for image segmentation based on global and local fuzzy image fitting (GLFIF) was proposed [12], in which two fitted images were created: a global fuzzy fitted image (GFFI) and a local fuzzy fitted image (LFFI). After that, the energy function is constructed, which contains both a global and a fitting term. The global term is taken from the fuzzy energy-based active contour (FEAC) model in order to balance the object's importance relative to the backdrop, while the fitting term is generated from GFFI and LFFI in order to account for intensity inhomogeneity in provided images. The energy function is then demonstrated to be convex, ensuring that the segmentation results are independent of initialization. Finally, unlike previous models that compute the change in the energy function pixel by pixel, this model uses a direct method to calculate the difference between the old and new energy functions in the whole image for each iteration in order to update the pseudo level set function. The energy function that includes both local and global energy is given by,

$$E^F(u,g) = \alpha_1 \int_\Omega g\|I(x) - I^{LFI}(x)\|dx + \alpha_2 \int_\Omega g\|I(x) - I^{GFI}(x)\|dx \quad (19)$$

The rewritten energy function is given by

$$\begin{aligned} E(u,g) = {} & \lambda_1 \int_\Omega [u(x)]^m g(I(x) - c_1)^2 dx \\ & + \lambda_2 \int_\Omega [1 - u(x)]^m g(I(x) - c_2)^2 dx \\ & + \alpha_1 \int_\Omega g\|I(x) - I^{LFFI}(x)\|dx \\ & + \alpha_2 \int_\Omega g\|I(x) - I^{GFFI}(x)\|dx \end{aligned} \quad (20)$$

Differentiating the equation (20). The variable $u(x)$ is expressed as:

$$u(x) = \begin{cases} \frac{1}{1+\left(\frac{\lambda_1(I(x)-c_1)^2 + \alpha_1 f_2 + \alpha_2 c_2}{\lambda_2(I(x)-c_2)^2 + \alpha_1 f_1 + \alpha_2 c_1}\right)^{\frac{1}{m-1}}} & \text{where } I(x) - I^{LFF}(x) > 0 \\ \frac{1}{1+\left(\frac{\lambda_1(I(x)-c_1)^2 + \alpha_1 f_1 + \alpha_2 c_1}{\lambda_2(I(x)-c_2)^2 + \alpha_1 f_2 + \alpha_2 c_2}\right)^{\frac{1}{m-1}}} & \text{where } I(x) - I^{LFFI}(x) < 0 \end{cases} \quad (21)$$

To segment images with noise, blurring boundaries, and intensity inhomogeneity, the model proposed in [12] used a fuzzy region-based active contour driven by global and local fitting energy. Its objective is to build an energy function that includes a global component derived from the existing model and a local term derived from the design of GFFI and LFFI images. The former is used to balance the object's and background areas' weights.

III. RESULT AND DISCUSSION

A. Common things followed in the result and discussion

For the objective of verifying the effectiveness of each technique, two different images were considered: one that was medical and one that was not. The non-medical image has a significant amount of intensity inhomogeneity. The inhomogeneity of intensity is the current issue being addressed by the majority of segmentation researchers that are now working on it.

The common things followed while comparing the result of each model is that the figure window of MATLB is divided into four, each of the divisions are named as 'a', 'b', 'c' and 'd', mentioned in the square box, positioned in the middle every MATLAB figure window. 'a' represent the input image taken for verifying the strength of the method in terms of segmentation of region of interest, 'b' represents the initial contour size, shape and its position on input image. The initial contour is either red or blue in color of shape may be of rectangle or square. 'c' indicates the movement of contour on the input image after some iterations, iteration number is specified on the top of the figure. 'd' represents the final contour produced by the respective model.

Each model has two sets, a group of four figures. In each case, the top group of four indicates the segmentation performance of the respective model for medical image and the bottom group of four indicates the segmentation performance of non-medical image.

B. Specific discussion of energy fitting models

Figure 1 shows the segmentation result of the LBF model. For medical image, the initial contour is specified by a small yellow rectangle, figure 1(top group, bottom left). The segmentation result shows that the region of interest (ROI) is not completely segmented and for the non-medical input same kind of initial

International Journal on Recent and Innovation Trends in Computing and Communication
ISSN: 2321-8169 Volume: 11 Issue: 9
Article Received: *25 July 2023* ***Revised:*** *12 September 2023* ***Accepted:*** *30 September 2023*

contour was used but the final segmentation result has unwanted traces.

The Local and Global Intensity fitting Energy model was verified for two kind of initial contour. Figure 2 shows the result obtained for the initial contour of maximum size and the figure 3 shows the segmentation result for the initial contour of minimum size. The result clearly exhibit the fact that the model's segmentation performance depends on size of the initial contour.

Local energy fitting model works well for the medical input but gives poor result for non-medical input. From the figure 4, it takes 600 iterations to produce comparable segmentation result. Higher the iterations more the segmentation time. Final segmentation result of non-medical image shows that still it has room to improve to produce better segmentation result. The segmentation result of energy fitting model uses LOG is shown in figure 5. Segments both the medical and non-medical images well even in the presence of high intensity inhomogeneity.
The model [12] uses fuzzy based energy fitting model the segmentation result of it show in figure 6. The segmentation result produces unintended result for both medical and non-medical inputs. Based on the results obtained using different models the LOG based energy fitting model handles intensity inhomogeneity and also produces an acceptable result. Moreover, the performance of each model is verified and compared based on the final segmented result, no statistical data was tabulated to ensure the same. This may be addressed in next review work. Reference [13] provides the code for LBF, LIF and LoG fitting models, Reference [14] has the code for local and global energy fitting model.

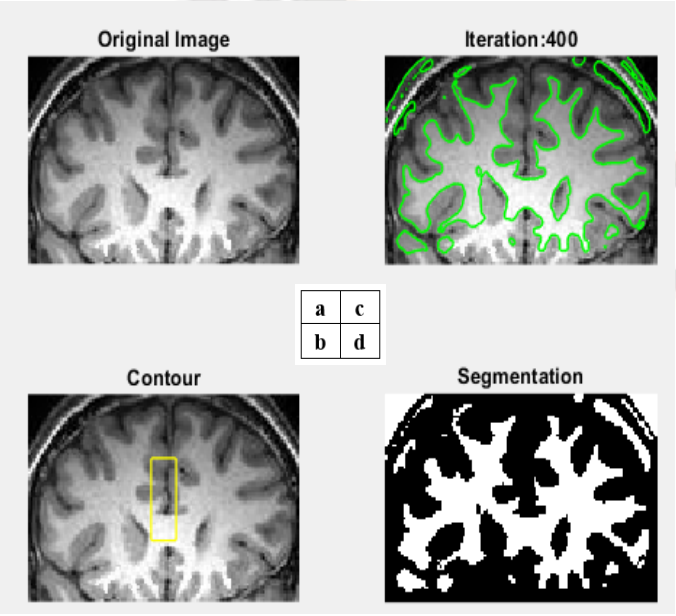

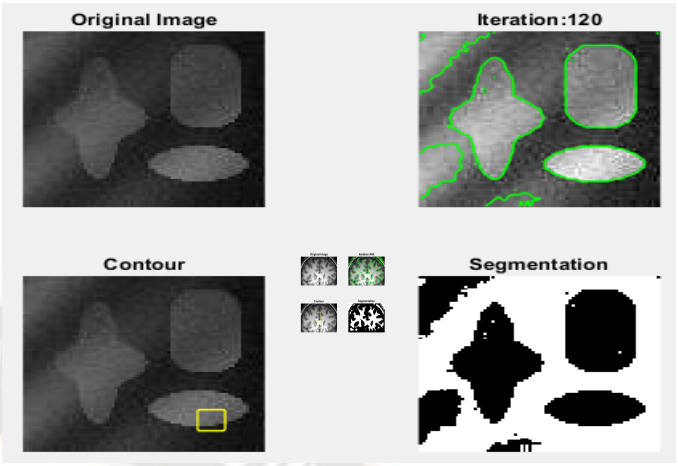

Figure 1. Segmentation result of LBF model for medical (top group) and non-medical images(bottom group).

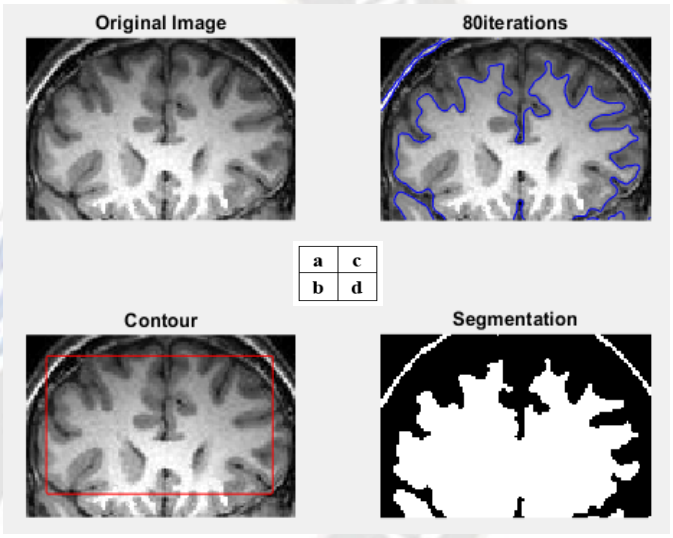

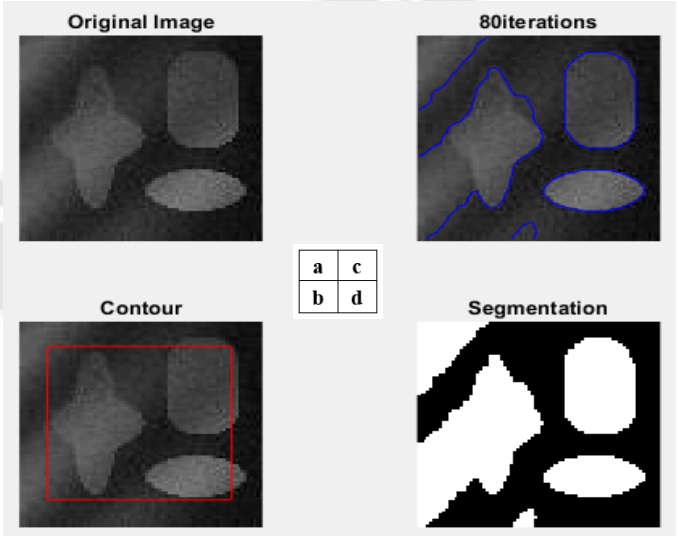

Figure 2. Segmentation result of Local and Global Intensity fitting Energy model, initial contour of maximum size

International Journal on Recent and Innovation Trends in Computing and Communication
ISSN: 2321-8169 Volume: 11 Issue: 9
Article Received: *25 July 2023* ***Revised:*** *12 September 2023* ***Accepted:*** *30 September 2023*

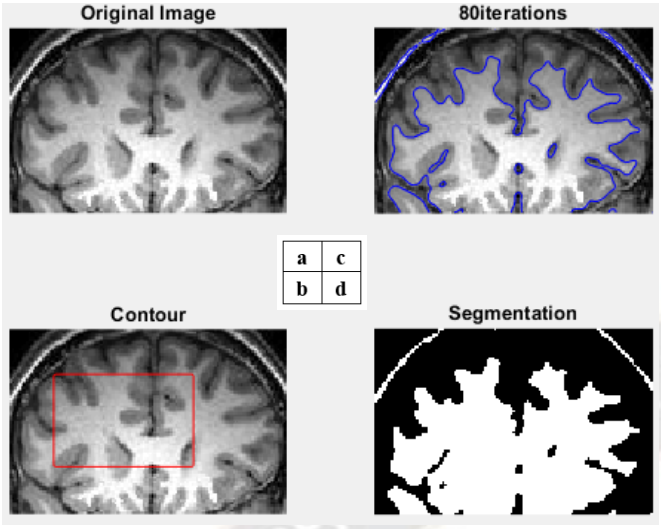

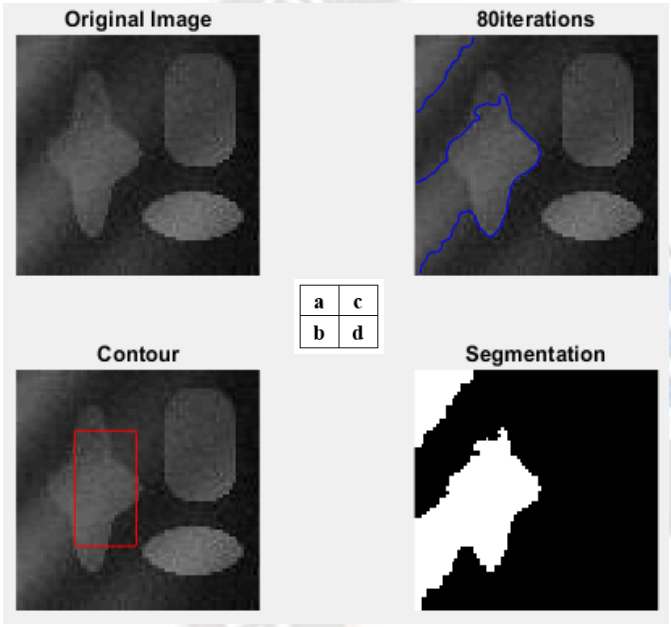

Figure 3. Segmentation result of Local and Global Intensity fitting Energy model, initial contour of minimum size.

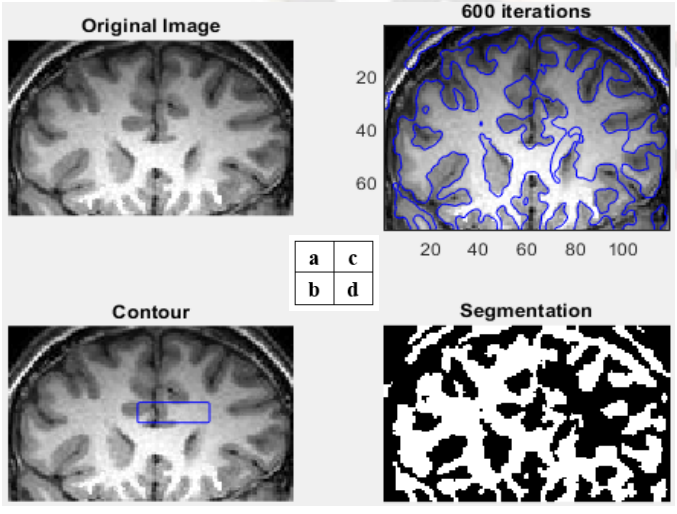

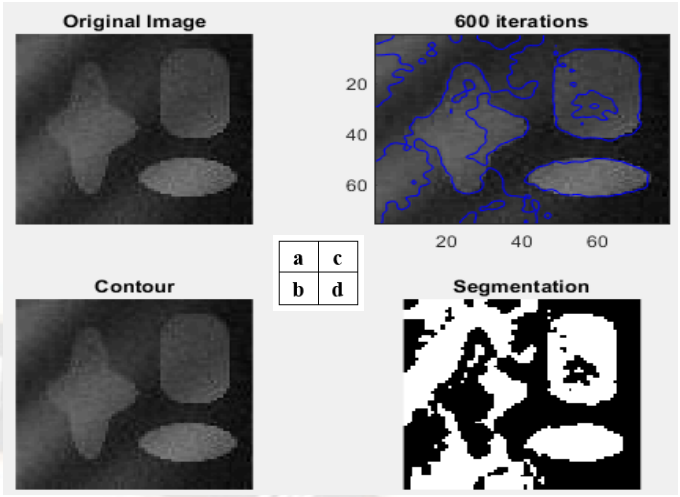

Figure 4. Segmentation result of local Image fitting energy model for medical (top group) and non-medical images(bottom group).

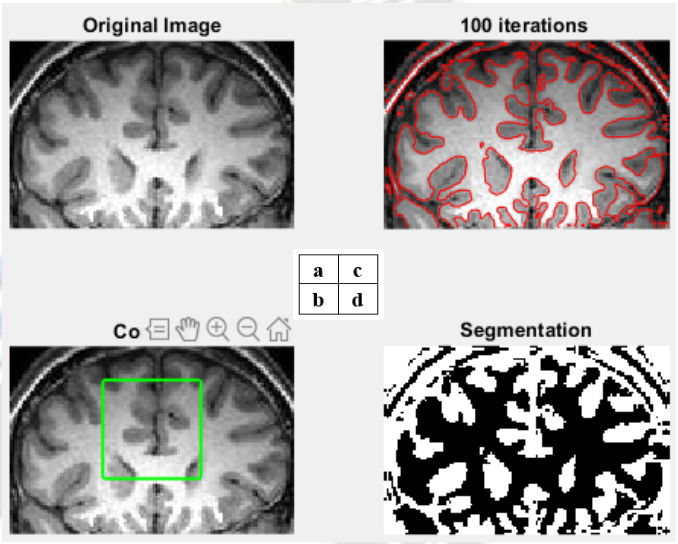

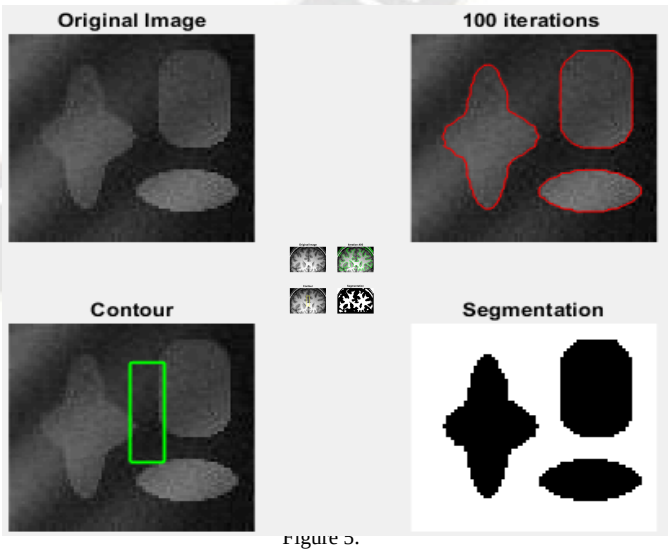

Figure 5.

Figure 6. Segmentation result of Laplacian of Gaussian Energy fitting model for medical (top group) and non-medical images (bottom group).

International Journal on Recent and Innovation Trends in Computing and Communication
ISSN: 2321-8169 Volume: 11 Issue: 9
Article Received: *25 July 2023* ***Revised:*** *12 September 2023* ***Accepted:*** *30 September 2023*

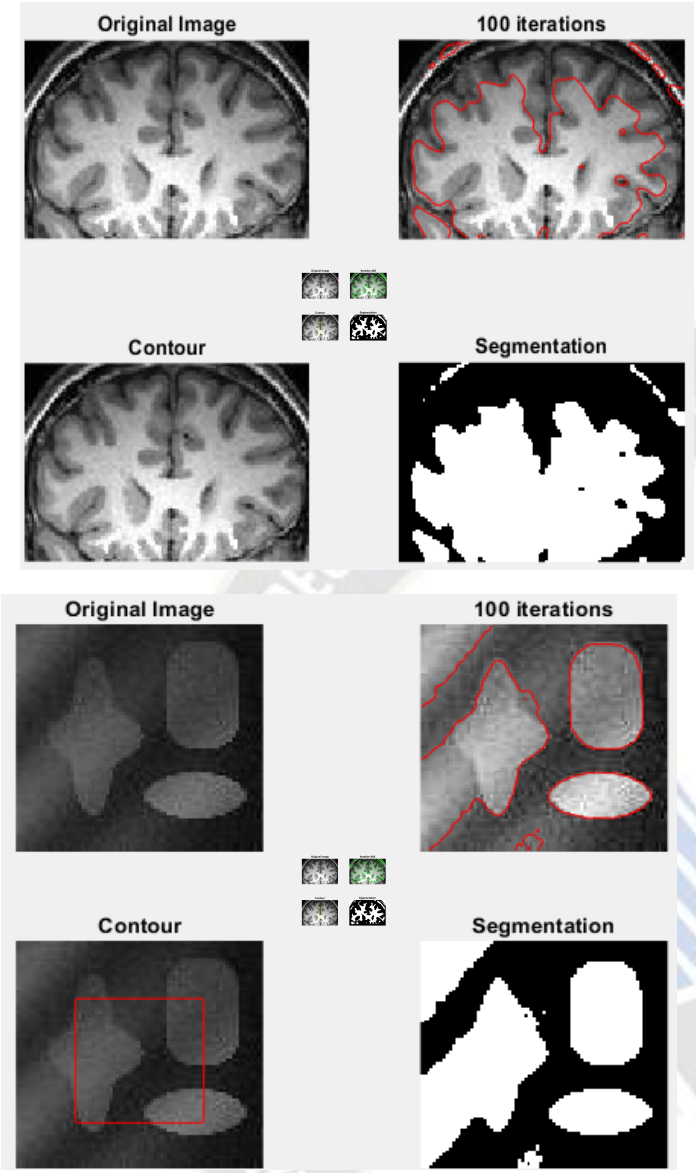

Figure 7. Segmentation result of Fuzzy region-based-global and local fitting energy model for medical (top group) and non-medical images(bottom group).

IV. CONCLUSION

This concise study compares the performance of state-of-the-art energy fitting models to visualize segmentation applications. Each of the five techniques is evaluated using a medical and a non-medical image. The ability to segment images relies not only on the concept presented, but also on the starting values assumed, the position and size of the initial contour. This brief study will undoubtedly aid researchers in their quest for an effective image segmentation method. Today's challenge in image segmentation is dealing with images with inhomogeneous intensities. This brief study concludes that the active contour model driven by the Laplacian of Gaussian demonstrates its resilience in dealing with contemporary problems such as images with inhomogeneous intensity.

ACKNOWLEDGEMENT

The authors of this paper would like to thank the authors who provided code for their relevant published work. As a consequence of the code's availability, followers may expand on the published concept by incorporating new applications such as image segmentation, denoising.

REFERENCES

[1] Cai WL, Chen SC, Zhang DQ. Fast and robust fuzzy C-means clustering algorithms incorporating local information for image segmentation. Pattern Recognition Journal. 2007;40(3):825-838
[2] Gadpayle P, Mahajani PS. Detection and classification of brain tumor in MRI images, International Journal of Emerging Trends in Electrical & Electronics. 2013;5(1):45-49
[3] Aggarwal P, Vig R, Bhadoria S, Dethe CG. Role of segmentation in medical imaging: A comparative study. International Journal of Computer Applications. 2011;29(1):55-64
[4] V. Caselles, R. Kimmel, and G. Sapiro. Geodesic active contours. Int'l J. Comp. Vis., 22:61–79, 199
[5] C. Xu and J. Prince. Snakes, shapes, and gradient vector flow. IEEE Trans. Imag. Proc., 7:359–369, 1998
[6] C. Li, C. Xu, C. Gui, and M. D. Fox. Level set evolution without re-initialization: A new variational formulation. In IEEE Conference on Computer Vision and Pattern Recognotion (CVPR)., volume 1, pages 430–436, 2005
[7] A. Tsai, A. Yezzi, and A. S. Willsky. Curve evolution implementation of the mumford-shah functional for image segmentation, denoising, interpolation, and magnification. IEEE Trans. Imag. Proc., 10:1169–1186, 2001.
[8] Li, Chunming, Chiu-Yen Kao, John C. Gore, and Zhaohua Ding. "Implicit active contours driven by local binary fitting energy." In *2007 IEEE Conference on Computer Vision and Pattern Recognition*, pp. 1-7. IEEE, 2007.
[9] Wang, Li, Chunming Li, Quansen Sun, Deshen Xia, and Chiu-Yen Kao. "Active contours driven by local and global intensity fitting energy with application to brain MR image segmentation." *Computerized medical imaging and graphics* 33, no. 7 (2009): 520-531.
[10] Zhang, Kaihua, Huihui Song, and Lei Zhang. "Active contours driven by local image fitting energy." Pattern recognition 43, no. 4 (2010): 1199-1206.
[11] Ding, Keyan, Linfang Xiao, and Guirong Weng. "Active contours driven by region-scalable fitting and optimized Laplacian of Gaussian energy for image segmentation." *Signal Processing* 134 (2017): 224-233.
[12] Fang, Jiangxiong, Huaxiang Liu, Jun Liu, Haiying Zhou, Liting Zhang, and Hesheng Liu. "Fuzzy region-based active contour driven by global and local fitting energy for image segmentation." *Applied Soft Computing* 100 (2021): 106982.
[13] https://github.com/dingkeyan93/Active-Contour-Model-Matlab
[14] https://github.com/fangchj2002/GLFIF

International Journal on Recent and Innovation Trends in Computing and Communication
ISSN: 2321-8169 Volume: 11 Issue: 8s
DOI: https://doi.org/10.17762/ijritcc.v11i8s.7221
***Article Received**: 28 April 2023 **Revised:** 14 June 2023 **Accepted:** 26 June 2023*

Hybrid Cryptography and Steganography-Based Security System for IoT Networks

T.Suguna[1], C.Padma[2], M.Janaki Rani[3], G.Padma Priya[4]
[1]Assistant Professor,
Department of ECE,
Panimalar Engineering College,
Chennai, India
suguna.pec22@gmail.com
[2]Associate Professor,
Department of ECE,
Sri Venkateshwara College of Engineering,
Tirupati, India
padmasekhar85@gmail.com
[3]Professor,
Department of EC,
Dr MGR Educational and Research Institute,
Chennai, India
janakiranimathi@gmail.com
[4]Associate Professor,
Department of ECE,
Sri Venkateshwara College of Engineering,
Tirupati, India
padmapriya.gudiyatham@svcolleges.edu

Abstract— Despite the fact that many IoT devices are publicly accessible to everyone on the network, understanding the security risks and threats posed by cyber attacks is critical; as a result, it should be safeguarded. Plain text is constructed into encrypted text, before being delivered by using cryptography, and is then reconstructed back to plain text after receiving a response from the recipient. The steganography technique can be used to hide sensitive information incorporated in a text, audio, or video file. One approach is to hide data in bits that correspond to successive rows of pixels with the same color in an image file. As a consequence, the image file retains the original's appearance while also containing "noise" patterns made out of common, unencrypted data. To do this, the encrypted data is subtly applied to the redundant data. In this work, it is suggested that IoT network data be encrypted using cryptography, and that an encrypted message be concealed inside an image file using steganography. Additionally, it is suggested to enhance the number of bits that may be stored within a single picture pixel. The payload that may be sent through an image is significantly increased by incorporating Convolutional Neural Networks into the classic steganography technique. In this work, we propose, design, and train Convolutional Neural Networks (CNN) to enhance the amount of data that can be securely encrypted and decrypted to show the original message.

Keywords- Encryption, Decryption, Security, IoT, Convolutioal Neural Networks (CNN)

I. INTRODUCTION

Sensors and minicomputers that use machine learning to act on sensor data are examples of IoT devices [1]. Sensor data is shared between IoT devices via a link to an IoT gateway or other edge device and is either forwarded to the cloud for analyzing or evaluated locally. Even while people may control, direct, and obtain data from the devices, the majority of the work is done by the devices on their own. [2].

Internet of things users have complete control over their lives and the ability to work and live more wisely. IoT is crucial to business in addition to giving smart home automation features. Businesses can use the Internet of Things (IoT) to track the performance of their systems in real-time and obtain insights into everything from equipment operation to supply chain and logistics operations. Businesses may use the Internet of Things (IoT) to automate processes and save expenditure on labor. Furthermore, it lowers production and transportation costs, enhances service delivery, minimizes waste and encourages greater consumer openness. [3]. As more businesses start to understand the importance of connected devices in maintaining their

International Journal on Recent and Innovation Trends in Computing and Communication
ISSN: 2321-8169 Volume: 11 Issue: 8s
DOI: https://doi.org/10.17762/ijritcc.v11i8s.7221
***Article Received**: 28 April 2023 **Revised:** 14 June 2023 **Accepted:** 26 June 2023*

competitiveness, IoT will gain in acceptance and rank among the most significant technology in daily life. IoT devices are susceptible to viruses and hacking since they are essentially tiny computers that are linked to the internet.

A. IoT Security Concerns:

This must be the first problem that manufacturers tackle if the Internet of Things is to become a major force. The risk of having their personal information taken from their smart home worried 27% of all Americans, which alarmed 44% of all Americans, according to the 2015 State of the Smart Home poll. Customers would be reluctant to buy similar things if they felt this unease. Because IoT devices are linked, it only takes one flaw to corrupt all data and render it useless. Manufacturers who fail to regularly or at all expose their products to cyberattacks.

Furthermore, linked devices frequently require users to input personal information such as names, ages, cellphone numbers, addresses and even their social media accounts that intruders may access. The amount of data created by IoT devices is incredible. Less than 10,000 households may generate 150 million discrete data points each day. According to the research "Internet of Things: A Consumer Guide" published by the Federal Trade Commission. Security and Privacy in a Connected World increases the number of entry points for invaders while also exposing personal information. [4].

Manufacturers or intruders could virtually break through an individual's house by using a linked device. The German researchers achieved this by obtaining unencrypted data from a smart meter device and identified which television show was being watched during the vulnerable period.

The objective of this paper is to develop a secure data transmission system for Internet of Things devices. Data was transferred in this case using a combination of cryptography and steganography, effectively increasing data payload while transferring through image files. Plain text is encrypted before being sent using cryptography, and following the other party's conversation, it is transformed back to plain text. Steganography is the process of hiding confidential information by encoding it into an audio, video, picture, or text file.

This paper is organized as, in section 2 discusses work related to the security systems related to IoT and their inferences. Section 3, discusses in detail about the existing system and proposed system for the IoT security. Section 4 discusses implementation ang its results and section 5 give the conclusion of the proposed models of IoT security systems with its future scope.

II. LITERATURE SURVEY

Since many IoT devices are publicly available to everyone on the network, even though it should be secured, it is critical to be aware of the security risks and hazards caused by cyberattacks. The survey for secure hybrid steganography communication technology is provided below. The following is a discussion of the most well-liked approaches currently in use.

The paired learning framework addresses the challenge of picture steganalysis, and S. Wu et al. [1] developed an important solution for CNN models, the Batch Normalization (BN). Theoretical results show that while successfully training with paired learning, a CNN model with several batch normalization layers struggles to generalize to fresh data in the test set. A brand-new normalization method called Shared Normalization (SN) is suggested as a solution to this issue. SN employs uniform statistics for training samples as opposed to the BN layer, which normalizes each input batch using the mini-batch mean and standard deviation. The authors then proposed a novel neural network model for image steganalysis based on the proposed SN layer. Extensive testing demonstrates that the suggested SN-layer network is robust and detects complex steganography more successfully than classic rich model methods and sophisticated CNN models. However, when cover-stegos are not paired, the network becomes unstable and fails to detect stego images.

Boroumand et al. [5] developed a universal deep residual architecture that eliminates the need for heuristics and externally imposed components while attaining cutting-edge detection accuracy for both spatial-domain and JPEG steganography. The front detector section that "computes noise residuals" with pooling turned off to avoid stego signal suppression is the distinguishing feature of the suggested architecture. According to comprehensive testing, this network performs better than others, with a notable improvement in the JPEG domain in particular. For payloads of 0.4 and 0.5 bpp, the improvement over the original SRNet is around 1%, gradually rising to 4% for the smallest tested payload 0.1. The procedure takes a long time, is difficult, and has poor accuracy for complex data.

PEKS (Public-key Encryption with Keyword Search) is a promising and practical encryption solution that secures and searches data stored in clouds. introduced near the IIoT as a cloud substitute to improve search efficiency even further. The slow PEKS encryption of IIoT devices delays edge response, therefore the straightforward connection of the two techniques works poorly in latency-sensitive applications. To solve this problem, W. Wang et al. [6] introduced Edge-aided

International Journal on Recent and Innovation Trends in Computing and Communication
ISSN: 2321-8169 Volume: 11 Issue: 8s
DOI: https://doi.org/10.17762/ijritcc.v11i8s.7221
***Article Received**: 28 April 2023 **Revised:** 14 June 2023 **Accepted:** 26 June 2023*

Searchable Public-key Encryption, a small-footprint method based on the edge-cloud architecture (ESPE). In addition to guaranteeing semantic security of all outsourced ciphertexts, this technology enables IIoT devices to offload time-consuming cryptographic operations to the neighboring edge for faster computing. Due to the fact that the throughput of encryption and decryption is inversely related to key length, ESPE speeds up the ciphertext corresponding procedures on edges and lowers the encryption cost of an IIoT device by over 70%. However, it is not suitable for encrypting large messages.

In order to offer a steganographic method that conceals a stego message while deceiving a convolutional neural network (CNN)-based steganalyzer, W. Tang et al. [7] used a novel technique called adversarial embedding (ADV-EMB). Due to the fact that the throughput of encryption and decryption is inversely related to key length, ESPE speeds up the ciphertext corresponding procedures on edges and lowers the encryption cost of an IIoT device by over 70%. However, it is not suitable for encrypting large messages. Therefore, the gradient's inverse sign is more likely to match the modification direction. This results in adversarial stego images. The test findings demonstrate that by raising the rate of missed detection, the suggested steganographic technique improves security against the target adversary-unaware steganalyzer. The proposed technique, however, solely employs gradient indications, which might lead to a faster rate of alteration with less image quality.

Adaptive payload distribution in multiple picture steganography was developed by X. Liao et al. [8] based on image texture properties, and a theoretical security research was carried out. Depending on the complexity and distribution of the picture texture, two payload distribution options are provided below. These strategies can be used with single-image steganographic algorithms. When contrasted to the modern universal pooled steganalysis per picture detectability versus the modern single image steganalyzer, these multiple image steganographic methods' security is evaluated. According to comprehensive investigations, payload distribution strategies suggested might enhance security performance. ESPE improves the ciphertext corresponding operations on edges and lowers the encryption cost of an IIoT device by more than 70% since the throughput of encryption and decryption is inversely related to key length. It is not, however, appropriate for encrypting long communications.

According to the literature review, FractalNet still [9] isn't capable of producing the best results when compared to those produced by other algorithms, even with significant data augmentation. Fractal networks can withstand being excessively deep; although improved depth reduces training, it has no negative effects on accuracy. The time it takes to train a steganalytic model for images with a little payload, say 0.1 or 0.05.bpp, is one of the main challenges. On some occasions, the model did not converge at all. When concealed messages are directly included into the cover picture, MIEM is produced, which lowers the performance of undetectability.

EXISTING SYSTEM

A deeper network, like SRNet, has been mentioned in recent steganalysis literature as being superior for recognizing low tone embedding noise. As shown in Fig. 1, FractalNet [9], a deep model based on self-similarity, has lately grown in popularity. Through several variations of a core construction component, it achieves a balance of depth and width. A steganalytic detection method built on the FractalNet model-concept was applied using the embedded picture as input.

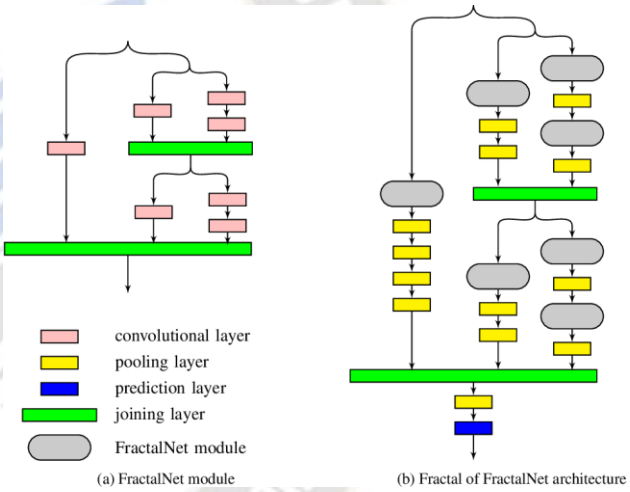

Figure.1. Existing System Architecture

In a real-world setting, it has been observed that expanding the network's breadth in a certain ratio to its depth improves steganalytic identification for test photos. A simple fractal block is repeated to create the proposed deep network, which allows for the maintenance of a balance between the network's depth and width. The proposed model outperformed the findings of the most recent studies, according to a thorough set of tests. A study on ablation is also given to support the performance of the suggested architecture. The advantages of this system are its ability to attain great levels of complexity and performance with low error rates.

With a modest payload, like 0.1 or 0.05 bpp, it takes longer for the images in this training model to converge. The model would occasionally fail to converge. Fractal networks can withstand being overly deep; while more depth may

International Journal on Recent and Innovation Trends in Computing and Communication
ISSN: 2321-8169 Volume: 11 Issue: 8s
DOI: https://doi.org/10.17762/ijritcc.v11i8s.7221
***Article Received**: 28 April 2023 **Revised:** 14 June 2023 **Accepted:** 26 June 2023*

reduce training, it has no negative effects on accuracy. Even with significant data augmentation, FractalNet still can't compete with other algorithms in terms of performance.

III. PROPOSED SYSTEM

Given that many IoT devices are publicly available to everyone on the network, it is essential to be aware of the security risks and hazards posed by cyberattacks and to take precautions to secure your IoT devices. Fig. 2 illustrates how data from multiple IOT networks, including user uploads, sensor data, server storage, and wireless data transfer, is stored in the cloud and secured using deep learning steganography and cryptographic encryption. Plain text is changed to encrypted text in cryptography before being delivered, and it is then converted back to plain text after receiving a response from the recipient. By incorporating sensitive information into a text, audio, or video file, steganography is a method for hiding it. Data can be concealed in bits that correspond to succeeding rows of pixels with the same color in a picture file.

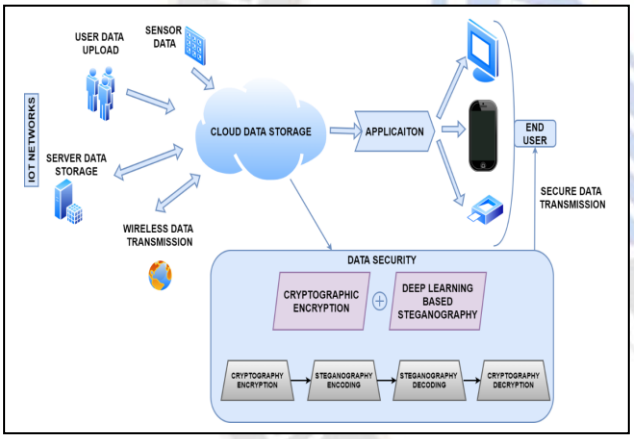

Figure.2. Proposed System Architecture

The outcome will be a picture file with the same visual appearance as the original but with "noise" patterns made up of common, unencrypted data. This is done by covertly combining the redundant data with the encrypted data. In this study, data from Internet of Things (IoT) networks is encrypted using cryptography, and the encrypted message is then hidden within an image file using steganography to enhance the number of bits that can be contained inside each image pixel. The payload that may be communicated through an image is considerably improved by combining convolutional neural networks with the traditional steganography technique. Convolutional networks are therefore created and trained in this study's suggested method in a way that enhances the amount of data that can be securely decrypted while also increasing the amount of data that can be securely encrypted.

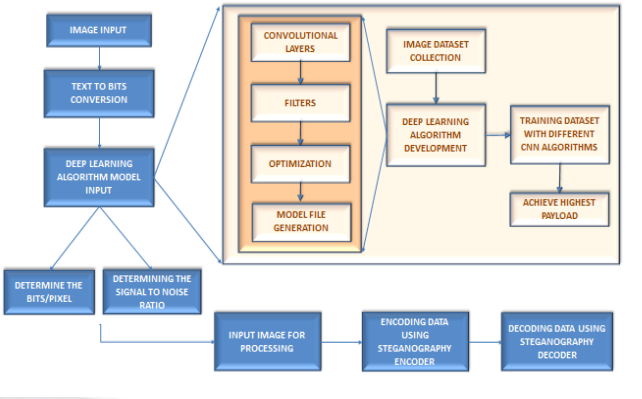

Figure.3 Flowchart for Implementing Proposed Security System In IOT

All these processes will take place one after the other and at last a model file will be generated. Image dataset collection is given as input to deep learning model where the dataset is trained with different CNN algorithms.Fig.3 Flowchart for Implementing Proposed Security System In IOT.Image is given as input after which text to bits conversion takes place so that the bits can be stored inside pixel of an image. This converted image is given as input to deep learning model, inside which there are convolution layers, filters, optimization and model file generation. achieve high payload. Finally, the secure data is sent to the end user. Fig. 4, shows the detailed process of steganography. The original text which is sent by the sender is called plaintext. This plaintext is encrypted into ciphertext at the sender side so that no other person accesses it. At the receiver side, the ciphertext is decrypted back to plaintext. So that the receiver receives the original message which is sent by the sender.

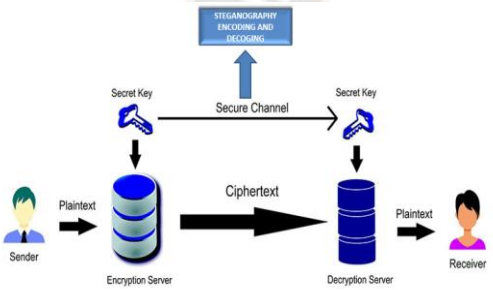

Figure.4 Steganography encoding and decoding

IV. RESULTS AND DISCUSSION

This section goes over the implementation and results of the proposed security system. To begin with, the work is divided into modules of implementation that are completed. The image is first read and converted into bits, which will be used to hide the data within the image. Then, when the data is fetched from the image, the bits are converted into text. After that, the almost 1000 image Div2k dataset was downloaded in order to train the deep learning algorithm. The training is done utilizing the fundamental deep learning algorithm

International Journal on Recent and Innovation Trends in Computing and Communication
ISSN: 2321-8169 Volume: 11 Issue: 8s
DOI: https://doi.org/10.17762/ijritcc.v11i8s.7221
***Article Received**: 28 April 2023 **Revised:** 14 June 2023 **Accepted:** 26 June 2023*

development after the dataset has been downloaded. Encoding, decoding, and image checking are the three stages of the algorithm, and the epochs are carried out during training, as shown in Fig. 5. As shown in Fig. 5, various metrics including accuracy, loss, SSIM, and PSNR are computed. As a result, the proposed convolutional networks technique in this study is created and trained in a way that improves the amount of data that can be encrypted while also allowing for a secure decryption of the original message.

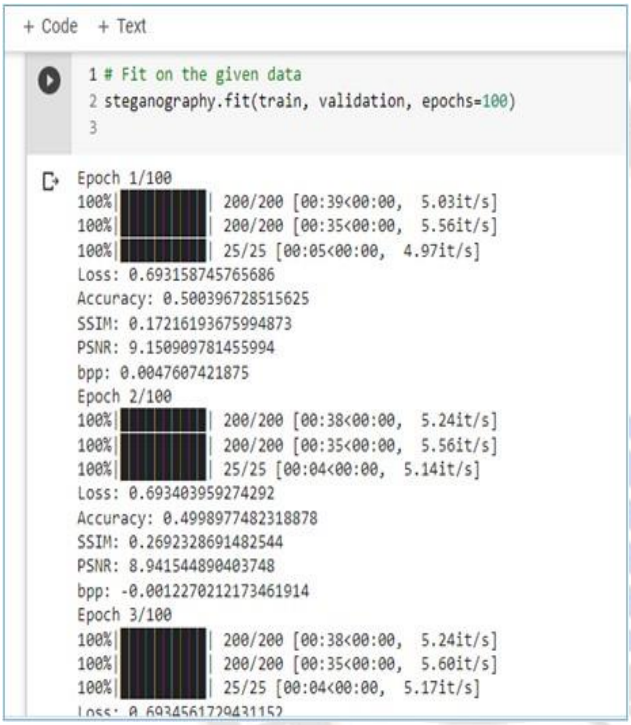

Figure.5 Deep Learning Algorithm Training

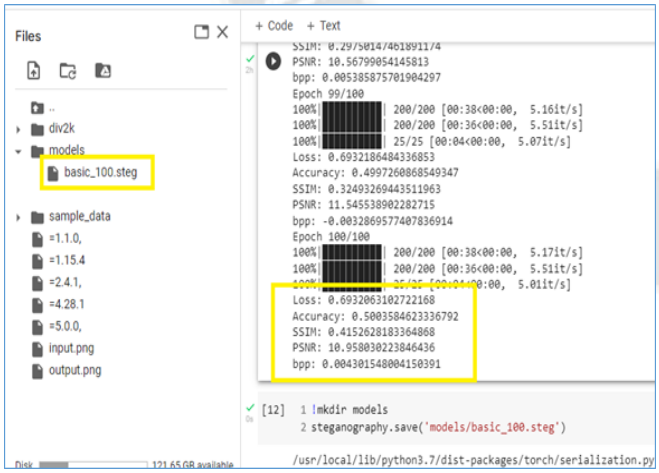

Figure.6 Model File Generation

As shown in Fig. 6, the model file is created after the training method, and metrics for the model are also calculated. The primary factor that is improved is the number of bits per pixel. The greatest bits per pixel that appear to have been reached with this basic algorithm development are only 0.004, which is far too low to be used in real time.

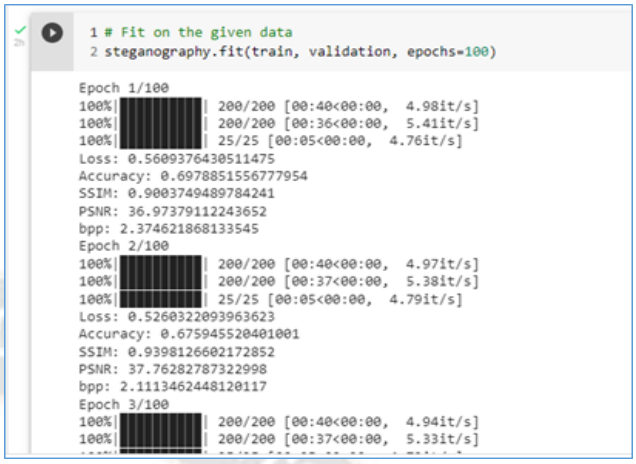

Figure.7 Enhanced Deep Learning Algorithm Training

The training process is then started for an enhanced algorithm model; the training commencement for this model is shown in Fig. 7. The model file, which enables the output for encoding and decoding to be validated, is prepared after training with the fundamental deep learning method is complete.

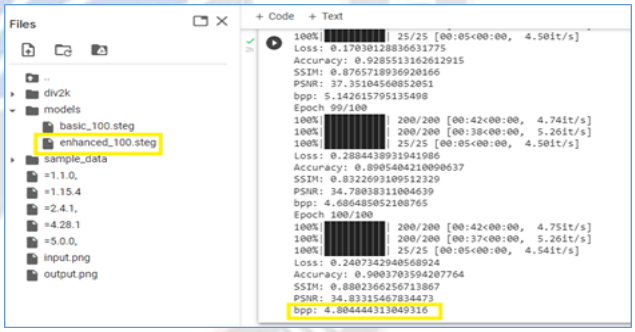

Figure.8. Model File Generation After Enhanced Algorithm Training

Following the training method, the model file shown in Fig. 8 is constructed, and the metrics are computed. According to the data, the objective of the study, which was to achieve more than three bits per pixel, was attained in real time at 4.8 bits per pixel. When the training is complete and the model files are ready, the model files are checked for data encoding and decoding to and from the image.

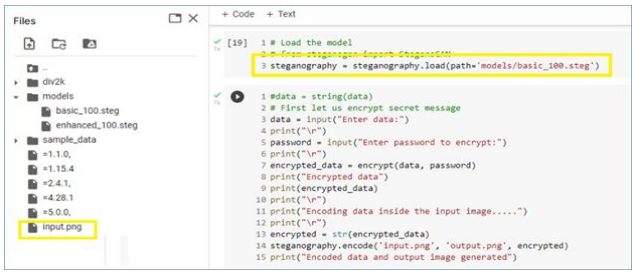

Figure.9 Loading Basic Model File for Encoding

International Journal on Recent and Innovation Trends in Computing and Communication
ISSN: 2321-8169 Volume: 11 Issue: 8s
DOI: https://doi.org/10.17762/ijritcc.v11i8s.7221
***Article Received**: 28 April 2023 **Revised:** 14 June 2023 **Accepted:** 26 June 2023*

The key is then concealed inside the image using steganography since the data must first be transformed into a cypher text using AES encryption, as seen below. The initial stage, which asks for importing the model file in which the data will be buried, also includes an input image. below Fig. 8. The output image is successfully generated when the data is transformed into a cypher text and concealed inside the input image, as seen in Figs. 9 and 10.

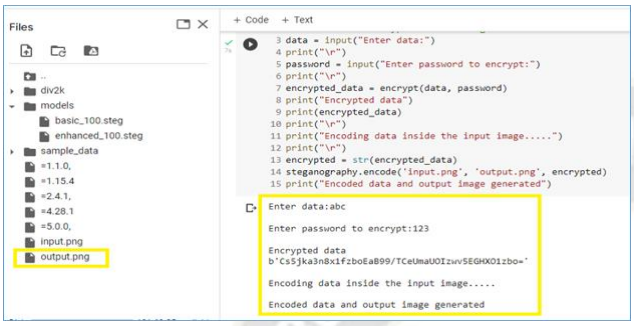

Figure.10 Encrypting and Encoding Data Using Basic Model

The created output image file, which is shown in Fig. 11 below, is now being decoded.

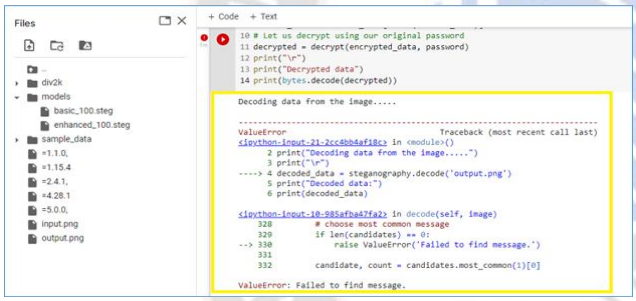

Figure.11 Decoding and Decrypting Data Using Basic Model

Because the bits per pixel were so little, data could not be correctly encoded, the image file raises an error when it is analyzed to find the data concealed therein, claiming that no data was found.

In order to perform data encoding, the upgraded model file has now been loaded, as seen in Fig. 12.

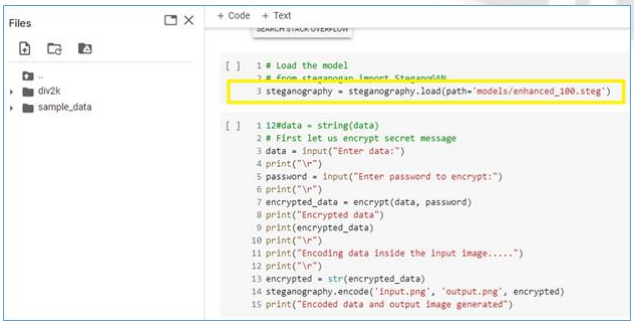

Figure.12 Loading Enhanced Model File for Encoding

The data is changed to cypher text when the encoding procedure gets under way, successfully creating an output image file as illustrated in Fig. 13.

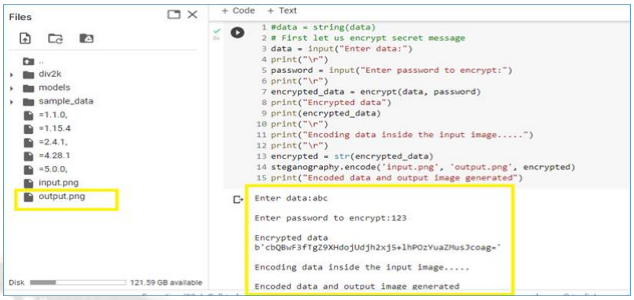

Figure.13 Encrypting and Encoding Data Using Enhanced Model

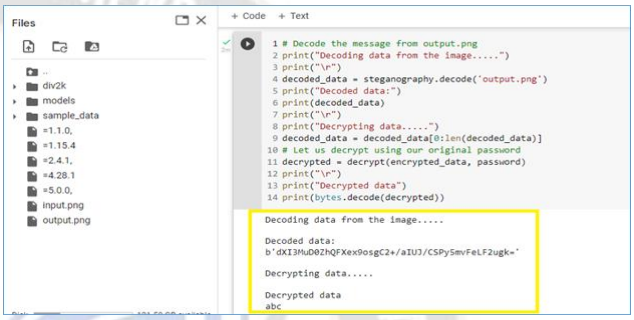

Figure.14 Decrypting and Decoding Data Using Enhanced Model

Decoding of data is then performed to get back the data hidden inside the output image file which can be seen in Fig.14.

TABLE1. COMPARISION OF EXISTING SYSTEM AND PROPOSED SYSTEM

Metrics	Existing System	Proposed System
Payload	0.004760	4.804443
Loss	0.693158	0.240734
Accuracy	0.500396	0.900370
PSNR	9.150900	34.83315
SSIM	0.172161	0.880236

The above Table 1 shows the comparison of metrics of existing and proposed system. Various metrics such as Payload, Loss, Accuracy, PSNR and SSIM are calculated for existing and proposed system. Each and every metrics is improved for the proposed system while comparing with existing system. Also, the loss is widely reduced in the proposed system.

Existing system has achieved the payload to the maximum extent of 0.5 bpp whereas in proposed system payload is achieved up to 4 bpp. From the above results we can see that the cipher text is been successfully decoded from the image and AES decryption is been performed to get back the data successfully. Even with significant data enhancement, FractalNet cannot outperform other algorithms in the current system. Fractal networks can withstand being

International Journal on Recent and Innovation Trends in Computing and Communication
ISSN: 2321-8169 Volume: 11 Issue: 8s
DOI: https://doi.org/10.17762/ijritcc.v11i8s.7221
***Article Received**: 28 April 2023 **Revised:** 14 June 2023 **Accepted:** 26 June 2023*

too deep; while more depth may make training more difficult, accuracy is unaffected. To address this issue, this study constructs and trains the convolutional network technique in order to enhance the payload of the data to be encrypted while still reliably decrypting the initial message.

The suggested approach increases the payload that can be conveyed by an image by using deep learning, and the data is safely transmitted while being encoded and decoded in real time.

VI.CONCLUSION

Steganography is meant to complement cryptography, not to replace it. When a message is encrypted and hidden using a steganographic approach, the likelihood of the hidden message being discovered decreases and an extra level of protection is provided. This article proposes employing deep learning to enhance the number of bits that can be saved within an image pixel, cryptography to encrypt IoT network data and steganography to hide the encrypted message within an image file.

This is used to provide a technique that successfully secures and protects data.

Future research will use a variety of efficient methodologies and algorithms to increase prediction accuracy, and bit storage capacity can be increased to increase data payload.

REFERENCES

[1] S. Wu, S. -h. Zhong and Y. Liu, "A Novel Convolutional Neural Network for Image Steganalysis with Shared Normalization," in IEEE Transactions on Multimedia, vol. 22, no. 1, pp. 256-270, Jan. 2020, doi: 10.1109/TMM.2019.2920605.

[2] M. Hassaballah, M. A. Hameed, A. I. Awad and K. Muhammad, "A Novel Image Steganography Method for Industrial Internet of Things Security," in IEEE Transactions on Industrial Informatics, vol. 17, no. 11, pp. 7743-7751, Nov. 2021, doi: 10.1109/TII.2021.3053595.

[3] W. Su, J. Ni, X. Hu and J. Fridrich, "Image Steganography with Symmetric Embedding Using Gaussian Markov Random Field Model," in IEEE Transactions on Circuits and Systems for Video Technology, vol. 31, no. 3, pp. 1001-1015, March 2021, doi: 10.1109/TCSVT.2020.3001122.

[4] M. Khari, A. K. Garg, A. H. Gandomi, R. Gupta, R. Patan and B. Balusamy, "Securing Data in Internet of Things (IoT) Using Cryptography and Steganography Techniques," in IEEE Transactions on Systems, Man, and Cybernetics: Systems, vol. 50, no. 1, pp. 73-80, Jan. 2020, doi:10.1109/TSMC.2019.2903785.

[5] M. Boroumand, M. Chen and J. Fridrich, "Deep Residual Network for Steganalysis of Digital Images," in IEEE Transactions on Information Forensics and Security, vol. 14, no. 5, pp. 1181-1193, May 2019, doi: 10.1109/TIFS.2018.2871749. [6] W. Wang, P. Xu, D. Liu, L.

[6] T. Yang and Z. Yan, "Lightweighted Secure Searching Over Public-Key Ciphertexts for Edge-Cloud-Assisted Industrial IoT Devices," in IEEE Transactions on Industrial Informatics, vol. 16, no. 6, pp. 4221-4230, June 2020, doi: 10.1109/TII.2019.2950295.

[7] W. Tang, B. Li, S. Tan, M. Barni and J. Huang, "CNN-Based Adversarial Embedding for Image Steganography," in IEEE Transactions on Information Forensics and Security, vol. 14, no. 8, pp. 2074-2087, Aug. 2019, doi: 10.1109/TIFS.2019.2891237.

[8] X. Liao, J. Yin, M. Chen and Z. Qin, "Adaptive Payload Distribution in Multiple Images Steganography Based on Image Texture Features," in IEEE Transactions on Dependable and Secure Computing, vol. 19, no. 2, pp. 897-911, 1 March-April 2022, doi: 10.1109/TDSC.2020.3004708.

[9] B. Singh, A. Sur and P. Mitra, "Steganalysis of Digital Images Using Deep Fractal Network," in IEEE Transactions on Computational Social Systems, vol. 8, no. 3, pp. 599-606, June 2021, doi: 10.1109/TCSS.2021.3052520.

FOREX Publication
Open Access | Rapid and quality publishing

International Journal of
Electrical and Electronics Research (IJEER)
Research Article | Volume 11, Issue 4 | Pages 933-938 | e-ISSN: 2347-470X

Lifting Wavelets with OGS for Doppler Profile Estimation

Potladurty Suresh Babu[1] and Dr. G. Sreenivasulu[2]

[1]*Associate Professor, Department of ECE, Sri Venkateswara College of Engineering, Tirupati (A.P), India, sureshbabu.413@gmail.com*
[2]*Professor, Department of ECE, Sri Venkateswara University College of Engineering, Sri Venkateswara University, Tirupati (A.P), India, gunapatieee@rediffmail.com*

***Correspondence:** Potladurty Suresh Babu; sureshbabu.413@gmail.com

ABSTRACT- This article discusses the second-generation wavelet transform concept and technique and its application to the noise removal problem of MST radar data. Located near Gadanki in Andhra Pradesh, India, the MST radar is collecting data on climate change. To obtain weather data, the signal collected by the radar needs to be analyzed, which usually requires power spectrum estimation. Most parametric and non-parametric methods cannot predict Doppler at an altitude above 14 KM, which makes to search for introduction of new denoising methods. More research is predominantly done on many denoising algorithms and tested with the simulated signal with various thresholds. It is observed that Lifting wavelets (LWT) with OGS is more effective in denoising the signals. Split, predict, and update are the three phases of lifting transform which on application of these steps reduces noise effectively. The LWT with OGS is applied to MST radar data and the research results shows that the noise level is reduced at higher altitudes and the signal-to-noise ratio is improved.

Keywords: MST RADAR Signal Processing, Doppler Estimation, Lifting Wavelets, Overlapping Group Shrinkage, Wind Speed.

ARTICLE INFORMATION

Author(s): Potladurty Suresh Babu and Dr. G. Sreenivasulu;
Received: 02/09/2023; **Accepted**: 23/10/2023; **Published**: 30/10/2023;
e-ISSN: 2347-470X;
Paper Id: IJEER 0209-01;
Citation: 10.37391/IJEER.110408
Webpage-link:
https://ijeer.forexjournal.co.in/archive/volume-11/ijeer-110408.html

Publisher's Note: FOREX Publication stays neutral with regard to Jurisdictional claims in Published maps and institutional affiliations.

1. INTRODUCTION

For many years, radar has been used successfully to monitor atmospheric movements at various altitudes, from the ground to the ionosphere, hundreds of kilometers away. Atmospheric signal processing has attracted the attention of many researchers because of its new and useful way of extracting spectra looking for wind features that need to be predicted, such as zonal (u), meridian (v), and vertical (w) components. With the development of the Radar systems, some radar signal processing and detection has also been improved. A significant issue in the processing of radar signals is the recognition of radar targets when there is interference. Wavelet transform (WT) has been incorporated into signal processing in recent years. Since it not only captures the properties of the Fourier transform (FT), it becomes an important analytical tool in mathematics, signal processing and other disciplines, but also has good local properties of shortwave. Short time Fourier Transform (STFT). The application of wavelet analysis in radar systems has become a topic in education [1]. In [1] radar pulse edges were detected by wavelet transform. WT [2] calculates the delay and time changes for the radar plane. Finally, wavelet- based noise removal (WBD) is used for real-time detection of radar targets [3]. WBD is undoubtedly one of the most significant applications of WT in radar signal processing.

Multi band Discrete wavelets can also use in reducing the noise at higher altitudes [4] Using MST radar data backscattered by high altitude clouds, bad weather, and signal-to-noise ratio, this study develops a signal processing method based on a lifting wavelet with overlapped group shrinkage to estimate the above parameters. Compared to existing methods, where manually estimate Doppler fail at higher altitudes, the proposed method is self-consistent in determining wind speeds up to 20 km altitude. GPS sonde balloon measurement were used to verify the accuracy of the results.

2. DENOISING

Many research studies produce data that is affected by noise from the data collection process or the environment. Denoising or estimating signals of interest from noisy data is an important first step in the analysis of big datasets. Signals and images can be denoised in many ways. While their aesthetics are similar, there are slight differences in noise removal, blurring, smoothing and restoration. Blurring increases the sharpness of signal qualities by introducing noise, while noise removal seeks to eliminate all noise that is unrelated to the spectral composition of the noise. They efficiently remove high frequencies while keeping low frequencies. Restoration is a type of noise removal that balances blurring and smoothing to recover as much of the original signal as possible. Those that work with undetectable spatial effects such as mean, median and Gaussian smoothed signals [3].

For noise removal in the wavelet domain, the phrases wavelet thresholding, wavelet shrinkage, and nonlinear shrinkage are employed. [4] mainly pioneered noise reduction by

FOREX Publication
Open Access | Rapid and quality publishing
International Journal of Electrical and Electronics Research (IJEER)
Research Article | Volume 11, Issue 4 | Pages 933-938 | e-ISSN: 2347-470X

thresholding in the wavelet domain. Small coefficients in the wavelet domain are often noisy, whereas large coefficients in the wavelet domain are signal dependent. Inverse Transformed with appropriate threshold or shrinkage, coefficients are used to obtain noise-free data [5].

The noise level should be measured for the threshold. [6] examined the estimation in the wavelet domain and presented the estimation of the maximum resolution The results are derived from the empirical wavelet coefficients. Since empirical wavelet coefficients are mostly noise, only the best values are measured. The noise level $\hat{\sigma}$ is calculated using the median absolute deviation given from *eq. (1).*

$$\hat{\sigma} = \frac{median\left\{P_m(n)\right|: n = 1,2 \ldots . \frac{N}{2}\}}{0.6745} \quad (1)$$

where $P_m(n)$ are the fine-grained detail coefficients (output of high pass filter). There will be N/2 detail coefficients after the first step of filtering if we started with N sampling data [7]. The following is how the wavelet coefficients threshold is applied Let p indicate a single detail coefficient at level m, $\hat{p}$ as well as its modified form when the threshold is applied. $P^{\lambda}(.)$ denotes the thresholding function and π is the threshold. This controls how the data will be threshold and is shown below in *eq (2).*

$$\hat{p} = \hat{\sigma} \, . \, P^{\lambda}\left(\frac{p}{\hat{\sigma}}\right) \quad (2)$$

3. LITERATURE SURVEY

Sreenivasulu Reddy Thatiparthi et al. [8] introduced a Wavelet based denosing radar signal. It deliberately yields better results in estimating the wind parameters and can able to detect the wind speeds at higher altitudes. G.Chandraiah et al. [9] suggested the Eigen decomposition-based sub-space approaches, *i.e.*, the principle component based spectrum calculation utilizing the minimal variance spectral estimate method. It is used to process MST radar data in order to estimate the Doppler spectrum and to detect wind components using the Doppler. It is more prevalent at higher elevations.

C.Raju et al. [10] proposed a non-parametric and hyper parameter-free iterative adaptive approach (IAA) for power spectral density estimation was developed. For simulated data, the IAA approach gives precise amplitude and frequency estimates. When compared to previous methods, IAA provides exceptional results when estimating the power spectrum. G.Chandraiah et al. [11] proposed Multi-band wavelet transform which was used for denoising atmospheric radar signals, cleaning the Doppler spectrum, and detecting and estimating wind velocity characteristics such as zonal (U), meridional (V), and wind speed (W). The proposed algorithm's performance (Multi-Band Discrete Wavelet Transform) is assessed by comparing it to the DWT (Discrete Wavelet Transform). It generates better parameter wind speed measurements when the signal-to-noise ratio is low.

Suresh Babu Potladurty et al. [12] introduced a method for the effective spectral estimation of MST Radar signal called IAP. IAP is employed for MST radar data is used to determine the Doppler spectrum and wind velocity parameters are estimated using Doppler profiles. The derived MST radar observations utilizing IAP were compared to Global Positioning System (GPS) radiosonde data to validate the experimental results. Suresh Babu Potladurty et al. [13] developed a novel method of denoising the MST Radar signal. When compared to the Discrete wavelet transform and other earlier techniques, the Dual tree complex wavelet transform with OGS achieved improved SNR, Variance, and Correlation factor.

4. OBJECTIVES

1.To propose a method that denoises the radar signal.
2.To estimate the Power Spectrum, Doppler frequency, SNR.
3.To evaluate the wind parameter values, correlation factor.
4.To compare the evaluated parameters with existing Algorithms.

5. PROPOSED WORK

5.1 Lifting Wavelet Transform [14]

Let us assume the original signals l_j are divided into two parts: one low-frequency signal l_{j-1} and another high-frequency detail signal m_{j-1}. The three stages of the lifting scheme's transformation are split, forecast, and update.

5.1.1 The Split step

Two subsets that do not overlap l_{j-1} and m_{j-1} of the original signals l_j are created. The better the split effect, the higher the correlation between them. As indicated in *eq. (3)*, a signal sequence is often separated into odd and even sequences.

$$l_{j-1} = l[2n] \, , \, m_{j-1} = l[2n-1] \quad (3)$$

The split technique appears basic yet smart in terms of the lifting process. It serves as the foundation for the next two phases, which are to anticipate and update signals l_j based on their local similarity.

5.1.2 The predict step

We can predict m_{j-1} from l_{j-1} data similarity by employing a predict operator q that isn't affected by the dataset. The wavelet coefficients m(n), represent the resulting difference, and they show how similar the two data sequences are. As indicated in *eq. (3)*, a signal sequence is often separated into odd and even sequences. The following is a summary of the predict process defined in *eq. (4).*

$$m_{j-1} = l[\,2n+1\,] - q\left(\,l_{j-1}\right) = m_{j-1} - q\left(\,l_{j-1}\right) \quad (4)$$

5.1.3 The update step

The coefficient subset created l_{j-1} from the preceding two phases differs from the original dataset in a few ways. As a result, the update step is required. As a result, the upgrading procedure is required. We employ the U update operator to generate a better subset $l(n)$ that retains some of the original dataset's properties as indicated in *eq. (5).*

$$l_{j-1} = l[2n] + u\left(m_{j-1}\right) = \, l_{j-1} + q\left(\,m_{j-1}\right) \quad (5)$$

FOREX Publication
Open Access | Rapid and quality publishing
International Journal of Electrical and Electronics Research (IJEER)
Research Article | Volume 11, Issue 4 | Pages 933-938 | e-ISSN: 2347-470X

The three steps stated above comprise a lifting strategy. We may obtain the approximation signals l_{j-n} and the high-frequency detail signals m_{j-n} by lifting repeatedly. After n decomposition cycles, the wavelet transform of the original data may be represented by $\{l_{j-n}, m_{j-n}, m_{j-n+1}, m_{j-1}\}$. Each wavelet may be divided into a number of different lifting methods. In general, the predict step seeks to eliminate low-order polynomial components while keeping high-order detail signals. The purpose of the update phase at coarse sizes is to maintain the low-order polynomial elements. By changing the operation orders and signs, we may easily achieve the following reconstruction *eq. (6)*:

$$l_{j-1} = l_{j-1} - q\left(m_{j-1}\right) and\ \ m_{j-1} = m_{j-1} + q\left(s_{j-1}\right) \quad (6)$$

The aforementioned technique may be used to do the whole lifting wavelet decomposition and reconstruction, as specified in below *figure 1*.

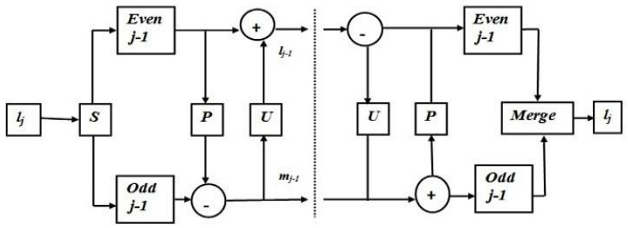

Figure 1: LWT Decomposition and Reconstruction

6. METHODOLOGY FOR PROPOSED WORK

Denoising noisy signals using wavelet shrinkage x(n) to recover y(n) as an approximation to the original signal s(n) is shown as a four-step approach [8], with m representing decomposition levels, W representing forward LWT, and W^{-1} representing inverse LWT.

- $w_m = W(x)$, m=1 to M
- λ_m = Level adaptive threshold selection (w_m)
- $z_m = OGS(w_m, \lambda_m)$
- $y = W^{-1}(z_m)$

The *figure 2* represents the proposed methodology flow diagram used to estimate the Doppler profile, SNR Evaluation and computation of wind speed components.

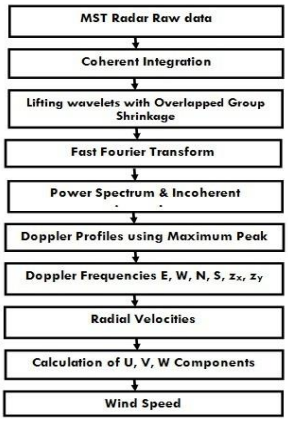

Figure 2: Flow Diagram of Proposed Framework

7. RESULTS AND DISCUSSION

We used data obtained from the troposphere and lower troposphere while operating the MST radar at Gadanki, India, to apply wavelet analysis to radar backscattered signals. We utilized raw data collected on February 9th, 2015 to evaluate the proposed approach (PALG) and compare it to the previous method EALG (CWT with OGS) [9]. *Figure 3(a)* shows the raw data spectrum of the east beam without denoising. The Doppler effect may be seen up to a height of 11 km, after which air noise dominates the spectral component. *Figure 3(b)* depicts the EALG-based anticipated Doppler profile for the aforementioned data. Because of the low noise level, the EALG can detect Doppler up to 11 kilometers away. As noise increases over 11 km, the accuracy of EALG's Doppler calculation is in doubtful situation, as detailed in the sections below. Spectrum is generated after denoising radar data with a wavelet method to mitigate the influence of noise at high altitudes. *Figure 4(a)* shows the usual data spectra or Doppler profile prior to doing spectral cleansing and after denoising of the East Beam. The PALG (LWT with OGS) is applied to the data from all beams, and the Doppler for all beams is determined. *Figure 4(a)* depicts the East beam's Doppler Profile after adaptive window denoising. *Figure 4(b)* depicts the Doppler profile obtained after investigating radar data with the PALG. In the presence of air noise, the Doppler effect can be received at higher elevations, as demonstrated in bin-wise denoising is used rather than single denoising for the complete frame of information to reduce the opportunity of the desired peak allowance and improve signal detectability. The EALG, PALG, and GPS Sonde were used to determine the Zonal (u), wind speed components, and Meridional (v) [11]. Wind Parameters can be evaluated using the following Equations.

After estimate of Doppler frequency from Doppler spectrum, the Doppler velocity can be calculated by using *eq. (7)*

$$V_d = \frac{c*f_d}{2*f_c} = \frac{f_d*\lambda}{2} \quad (7)$$

Where V_d - Doppler Velocity (m/s)
f_c - Operating Frequency of MST Radar (53 MHz)
f_d - Doppler Frequency
C – Velocity of Light

Wind velocity components can be determined by using

Velocity components as in *eq. (8)*

$$\begin{bmatrix} v_x \\ v_y \\ v_z \end{bmatrix} = \begin{bmatrix} 0.603 & 0 & 0 \\ 0 & 0.603 & 0 \\ 0 & 0 & 0.603 \end{bmatrix}^{-1} * \begin{bmatrix} 0.736(v_E - v_W) \\ 0.736(v_N - v_S) \\ 0.736(v_{ZX} - v_{ZY}) \end{bmatrix} \quad (8)$$

Where v_x , v_y and v_z are Zonal (U), Meridonal (V) and Vertical components (W). Wind Speed was evaluated as shown in *eq. (9)*

$$W = \sqrt{v_x^2 + v_y^2} \quad (9)$$

It's also obvious that the PALG-predicted *u*, *v*, and wind speed components are more closely matched with the patterns provided by the GPS Sonde. As illustrated in *figure 5*, the

FOREX Publication
Open Access | Rapid and quality publishing
International Journal of Electrical and Electronics Research (IJEER)
Research Article | Volume 11, Issue 4 | Pages 933-938 | e-ISSN: 2347-470X

suggested technique produces self-consistent profiles. When compared to previous algorithm, the PALG allows for substantially more in accuracy in Doppler tracking.

Figure 6 shows the SNR estimated using Periodogram and PALG (LWT with OGS) of East-Beam and West-Beam for raw data gathered on 09-04-2015.

It was observed from the *figure 6* that PALG produces an SNR which is more predominantly positive compared to periodogram both for East beam and West beam.

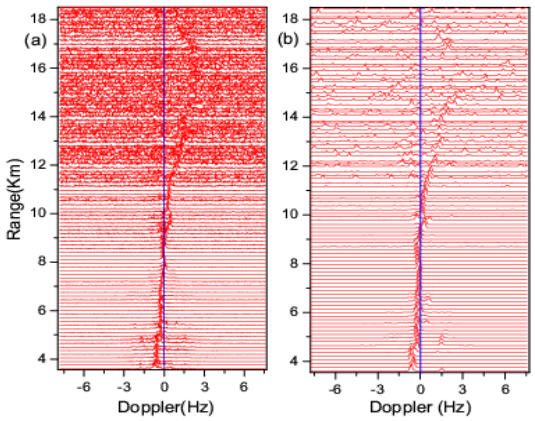

Figure 3: Typical East beam spectrum, (a) Before spectral cleaning, (b) After spectral cleaning with EALG

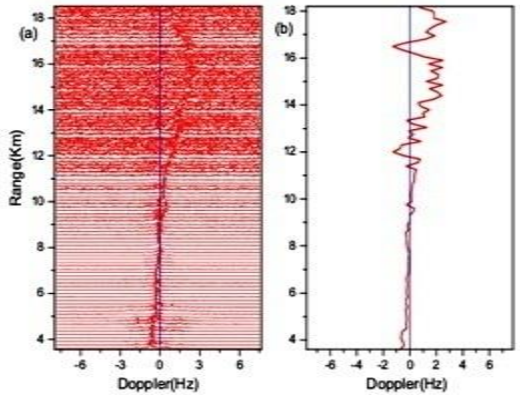

Figure 4: (a) Prior to doing spectral cleansing (b) After Denoising

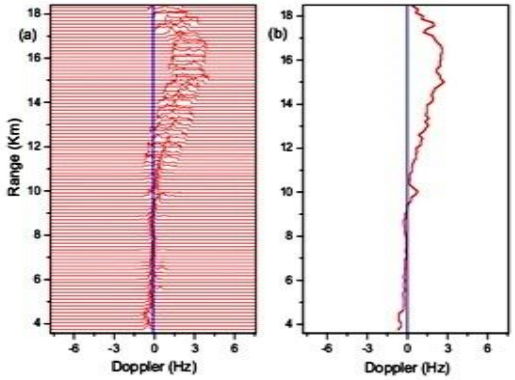

Figure 5: Typical East beam spectrum, (a) Adaptive window on a denoised spectrum, (b) Doppler Profile

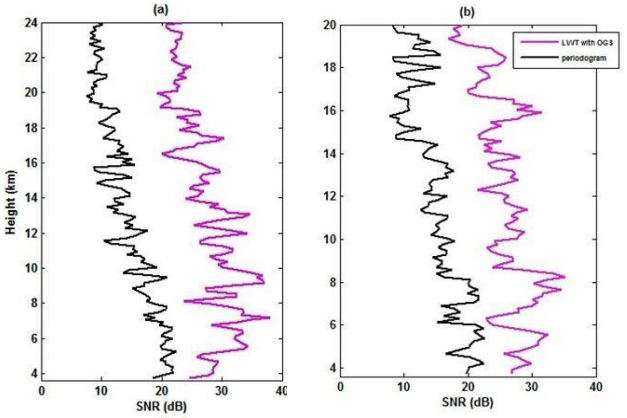

Figure 6: SNR estimated using Periodogram and LWT with OGS for raw-data on 09-04-2015. (a) East-beam (b) West-beam

Figure 7(a), (b) and (c) shows the Comparison of velocity components of MST Radar raw-data on 09-04-2015 using LWT with OGS, ADP, GPS.

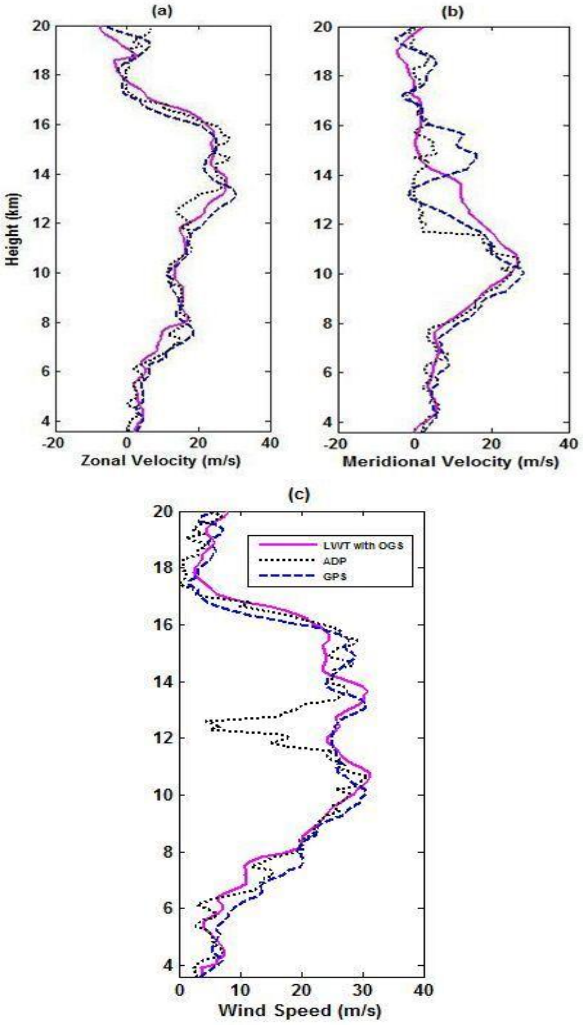

Figure 7: Comparison of velocity components (a) Zonal, (b) Meridional (c) Wind-speed for raw-data on 09-04-2015 using LWT with OGS, ADP, GPS.

FOREX Publication
Open Access | Rapid and quality publishing
International Journal of Electrical and Electronics Research (IJEER)
Research Article | Volume 11, Issue 4 | Pages 933-938 | e-ISSN: 2347-470X

Figure 8 shows the Comparison of wind speed using LWT with OGS, CWT with OGS, ADP, GPS for radar raw-data gathered on 09-04-2015.

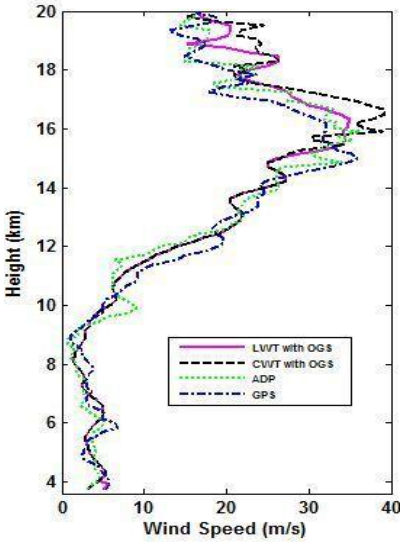

Figure 8: Comparison of wind-speed using LWT with OGS, CWT with OGS, ADP, GPS for radar raw-data gathered on 09-04-2015

Figure 9 shows the Correlation plot using LWT with OGS & GPS for raw-data during 9 to 11 Feb, 2015.

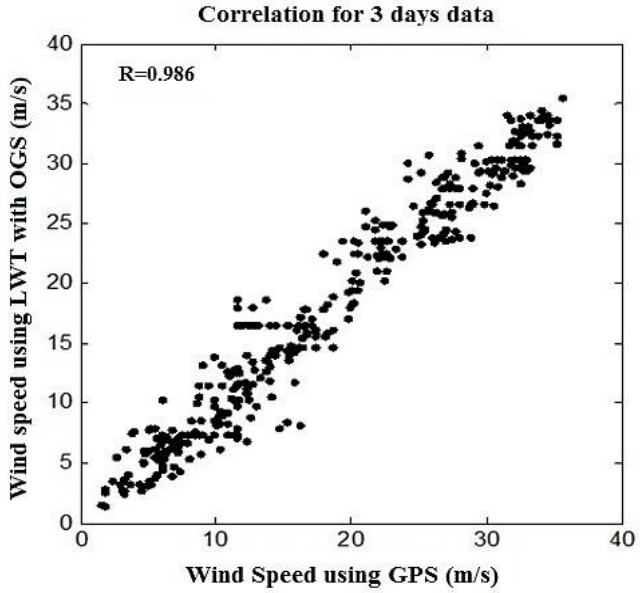

Figure 9: Correlation plot between wind speed using LWT with OGS and GPS for data during 9 to 11 Feb, 2015

By using the PALG, the correlation of 0.986 is obtained for 3 days data as specified in the *figure 9*.

The PALG is compared with the Periodogram, Discrete Wavelets with OGS and Complex Wavelets with OGS in terms of the parameter SNR (Average SNR) for all the beams for the data on July 8, 2014 and found the SNR is outperformed in PALG which is shown in the *table 1*.

Table 1: Comparison of Average SNR (dB)

Algorithm	East	West	Zenith -Y	Zenith -X	South	North
Periodogram	13.49	14.01	14.22	13.85	14.19	13.92
DWT with OGS	19.16	18.24	18.35	18.98	20.25	18.17
CWT with OGS	21.34	20.25	23.18	21.95	22.16	21.65
LWT with OGS	28.56	27.26	25.89	24.78	25.69	23.67

8. CONCLUSION

The proposed technique is utilized for processing MST RADAR data for Doppler estimation, SNR computation & wind parameter estimation. Overlapping group shrinkage (OGS), which is particularly effective in processing the sparse data because unlike other wavelets, OGS have the importance of grouping the similar coefficients and applying the shrinkage to the coefficients and making then non-zero. So, the PALG gave better results when compared to other algorithms in terms of SNR, Doppler Profile and Wind Speed Calculations.

The PALG achieves a correlation factor of 0.986, which is higher than any other thresholding technique.

REFERENCES

[1] Donoho, D., and I. Johnstone, "Minimax estimation via wavelet shrinkage", Annals of Statistics, 26: 879-921, 1998.

[2] Taswell, C., "The What, How and Why of Wavelet Shrinkage Denoising", IEEE Computing Science and Engineering, 2(3), 12-19, 2000.

[3] Soman, K.P., and K.I.Ramachandran,"Insight into Wavelets from theory to Practice", Prentice hall of India, 2004.

[4] Suresh Babu Potladurty, G.Sreenivasulu, "Mesosphere Stratosphere Troposphere (MST) Radar Signal using Discrete wavelet Transform with Overlapping Group Shrinkage", International Journal of Advanced Science and Technology, Vol 28, No 9,133-136, 2019.

[5] Liu, R., Liu X., Suo, J., Wang, X, "The radar clutter processor with wavelet floating threshold", proceeding of CIE International Conference on Radar, pp.1001-1005, 2001.

[6] Donoho, D., and I. Johnstone, "Adapting to unknown smoothness via wavelet shrinkage", Journal of the American Statistical Association, 90: 1200-1224, 1995.

[7] Zhang Xueying et al," Signal Denoising with Non linear lifting Scheme", J. of Math. (Chinese), 24(2), 193-196, 2004.

[8] S.R. Thatiparthi, R.R. Gudheti, V. Sourirajan, MST Radar Signal Processing Using Wavelet-Based Denoising, IEEE Geo science and Remote Sensing Letters, 2009.

[9] G.Chandraiah et al, MST Radar Signal Processing using PCA Based Minimum-Variance Spectral Estimation Method, International Journal of Modern Electronics and Communication Engineering (IJMECE) ISSN: 2321-2152,Volume No.-6, Issue No.-6, November, 2018.

[10] C.Raju et al, 2018, MST radar signal processing using iterative adaptive approach, Geosci. Lett. (2018), https://doi.org/10.1186/s40562-018-0120-0 16.

[11] G.Chandraiah et al, 2018, Denoising of MST Radar Signal Using Multi-Band Wavelet Transform with Improved Thresholding, Second International Conference on Inventive Communication and Computational Technologies (ICICCT), DOI:10.1109/ ICICCT.2018.8473060.

[12] Suresh Babu Potladurty et al, Spectral Estimation of MST Radar Data using IAP, IJRECE VOL. 7 ISSUE 3 JULY. -SEPT 2019, ISSN: 2348-2281 (ONLINE).

International Journal of
Electrical and Electronics Research (IJEER)
Research Article | Volume 11, Issue 4 | Pages 933-938 | e-ISSN: 2347-470X

[13] Suresh Babu Potladurty et al,2021, Denoising of MST RADAR Signal using CWT and Overlapping Group Shrinkage, Turkish Journal of Computer and Mathematics Education Vol.12 No. 5 (2021), 1950-1954.

[14] Feng Lin et al, "Denoising of logging data using lifting Scheme", Geophysical Prospecting for Petroleum, 43(3): 238–241,2004 Pages 79-84.

© 2023 by the Potladurty Suresh Babu and Dr. G. Sreenivasulu. Submitted for possible open access publication under the terms and conditions of the Creative Commons Attribution (CC BY) license (http://creativecommons.org/licenses/by/4.0/).

[1*] K. Raveendra

Enhancing 5G Sub-3.5 GHz Networks through Optimization of Microstrip Antenna Arrays with Sequential Rotation-Based MIMO using Machine Learning Techniques

JES Journal of Electrical Systems

Abstract: - The research concerns the design and optimization of microstrip antenna arrays with sequential rotation-based MIMO configurations for 5G sub-3.5 GHz networks. In total, the use of five optimization approaches was accessed, namely, Bayesian optimization, sparse learning, genetic algorithms, particle swarm optimization, and convolutional neural networks, to evaluate their efficiency in improving antenna properties. In general, Bayesian optimization outperformed the other methodologies most consistently, with the value of the average antenna gain ranging from 0.84 to 0.88, SNR between 14.8 and 15.3, and radiation efficiency ranging between 0.90 and 0.93. The use of sparse learning also ensured a high level of performance, with the average gain ranging between 0.80 and 0.85, and the values of SNR between 15.2 and 15.7. Thus, this approach showed the highest resistance to noise. Genetic algorithms, particle swarm optimization , and CNN are also quite close to each other in the efficiency of properties, with the average antenna gain value ranging between 0.85 and 0.89 and the value of SNR between 14.7 and 15.1. In overall, the results of the research show that there is a variety of available approaches to the optimization of antenna design, and each of them has a number of advantages that can be of use for the improvement of the properties and makes it possible to derive a solution that outweighs others in terms of several properties and the efficiency of its application.

Keywords: Microstrip antenna arrays, Sequential rotation-based MIMO, Machine learning, 5G sub-3.5 GHz, Optimization techniques

I. INTRODUCTION

The rapid development of wireless communications is caused by the increasing need for higher data rates, more stable connections, and wider coverage. Especially noticeable advances in this area are pertained to the introduction of 5G that is expected to change the landscape of connectivity through offering significantly mitigated data rates, ultra-low latency, and high capacity . However, to reach its maximum potential, this fast-developing domain requires the formulation of effective and streamlined antenna systems for the support of the high demands imposed by the new network[1]–[3].

After reflecting on the materials of this unit, I have learned that microstrip antenna arrays are a substantial technology that can be utilized in the context of 5G systems quite effectively. As the research has shown, this type of arrays is promising in the applicable areas since they are quite versatile, compact, and can provide a significant gain effect and a highly directed pattern of radiation . With regards to 5G, these tools are instrumental in the context of the sub-3.5 GHz band, as they offer quite effective long-range communication and penetration of obstacles with minimal signal loss.[4]–[6].

The primary goal of this research is the design, optimization and performance evaluation of the proposed antenna system. Additionally, a set of modern machine learning techniques should be included in the design and used to enhance the performance of the system. More specifically, the conducting of additional research and integration of algorithms like bayesian optimisation and sparse learning into the modelling process would allow to create an antenna system that is not only efficient and reliable, but also highly adaptable. The ability to explore large ranges of potential antennas more efficiently and reach an optimal solution should significantly improve the overall performance of the system.

Additionally, due to the proposed research, novel approaches to antenna design methodologies and 5G network infrastructure development were introduced. Developing advanced solutions specifically designed for the requirements of sub-3.5 GHz bands of frequencies, the research demonstrated the applicability and efficiency of machine learning-driven optimization tools in the field of antenna design. This would allow for future advancements in wireless communication systems and the implementation of 5G technology across a wide range of applications, from mobile broadband units to various devices for the Internet of things.

[1] Professor, Department of Electronics and Communication Engineering, Sri Venkateswara College of Engineering,

Chittor, Tirupati, Andhra Pradesh, India. Email: drkraveendraphd@gmail.com

Copyright © JES 2024 on-line: journal.esrgroups.org

Throughout the study, a major endeavor is made concerning the development of a novel high-performance solution for the 5G sub-3.5 GHz networks in the face of the pressing need for such antenna. In this context, to further contribute to the ongoing equal evolution of wireless communications technologies, the present study proposes a microstrip antenna array based on the use of the MIMO configuration with sequential rotation. To this end, the combination of various machine learning solutions is considered as the method to devise a novel solution designed to unlock the full potential of the 5G connectivity.

II. LITERATURE REVIEW

The microstrip antenna arrays is the most attractive choice of wireless communication systems in this modern era of wireless communication. The reasons that make the microstrip antenna array popular are its compact size, low profile, ease of fabrication, can produce high gain and retain the directional of radiation pattern . The microstrip antenna array consist more than one radiating element which could arrange into various geometric configuration such as linear, planar and circular arrays. Apart from that, the microstrip antenna arrays are widely used for different applications purposes such as satellite communication, radar system, and mobile networks. Lastly, microstrip antenna arrays is also one of the popular antennas nowadays which is used for modern communication devices such as smartphones, tablets, and IoT devices .[1], [7].

Microstrip antenna arrays are essential for the deployment of 5G networks using the sub-3.5 GHz range. This range is central to the 5G system as it provides the balance between coverage and capacity, allowing the devices to communicate over large distances while supporting high data rates. Therefore, it is possible to guarantee wide converage, penetration of obstacles with low transmission losses, and mobility free from interruptions. As such, the 5G system in urban, borough, or rural areas can fully depend on the use of microstrip antenna arrays.[8]–[10].

Hence, in existing networks the two and four-antenna versions of these systems are largely deployed by leading companies, ensuring the quality and speed of the internet. Specifically, by the time numerous phone users started to experience certain difficulties with the operation of their 4G devices, MIMO technology had not only become an essential part of company's plans but had already been used in most of the cell towers and operators. Undoubtfully, these approaches helped to successfully pass the initial stages of 4G implementation and launch.[11]–[13].

Speaking of 5G networks, it should be stressed that MIMO antenna systems are crucial for achieving the ambitious performance goals, including multi-gigabit data rates, ultra-low latency, and massive connectivity required by the industry. These systems can support such advanced functionalities as beamforming, which implies that an antenna array may be used to direct energy to a user and, respectively, to a specific area in order to enhance the coverage, throughput and spectrum efficiency. Also, MIMO technology might be useful to deal with multipath propagation, interference, and fading that reduces the wireless communications links' reliability and, therefore, their robustness against a variety of situations.[14]–[16].

Machine learning can be explained by the possibility to transform the typical design process and to avoid the limitations of heuristics-based optimization. Machine learning algorithms such as neural networks or reinforcement learning are well-suited to modeling the relationships between various antenna properties, their characteristics, and the design process. One of the approaches consists of the use of large sets of data related to the properties of antennas which were either modeled or measured. They can assist machine learning models in finding the best antenna properties as well as the most significant parameters and analyzing the design space.NETworking.

Past studies on applying machine learning algorithms to produce antenna designs showed very promising results in a variety of applications, including pattern synthesis, impedance matching, and radiation pattern optimization. For example, neural networks have been used to predict well a point will work in each task based on its "geometrical parameters," enabling teams to rapidly prototype and optimize designs through iterations . Genetic algorithms, as well, were used to evolve antennas to achieve specified objectives including maximizing antenna gain, side lobes minimization, or minimizing the feedline loss[17]–[19].

In conclusion, the helpful of literatures review on different of microstrip antenna array, MIMO antenna system and machine learning in the different of factors towards knowing more of the advanced techniques, issues and applications in this field of wireless communication. There were a lot of existing knowledge where this research

attempted to synthesise and extend, and the aim or objective of this study was to enhance the antenna technologies for 5G sub-3.5 GHz using machine learning techniques to improve in the performance, efficiency and reliability.

III. METHODOLOGY

The research methodology section of the present study incorporates a number of important points, such as the design of the microstrip antenna array, the configuration of the sequential rotation-based MIMO antenna, and the implementation of machine learning methods to enhance the optimization. Specifically from the Figure 1, the section in question covers the description of the machine learning tools used to adjust the parameters of the antenna and reduce the target feature set, namely, Bayesian optimization and sparse learning, respectively. In addition, it identifies the optimization algorithms incorporated to improve the design of the antenna further.

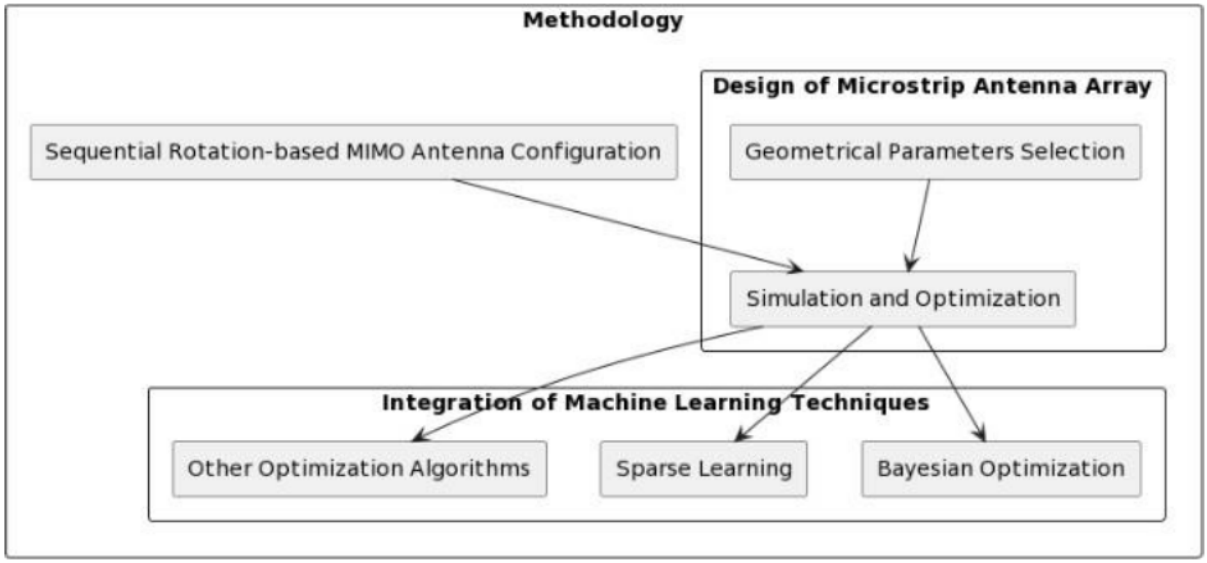

Figure. 1: Proposed Methodology

The design of the microstrip antenna array concerns the choice of appropriate geometrical parameters as listed in Table 1, which include the substrate material, dimensions, and feeding mechanisms . Having many parameters to be defined provides flexibility in the design, which makes the microstrip antennas customizable. There are various parameters to judge the antenna array by, including the bandwidth for which it can be utilized and the gain, alongside the radiation pattern . Various design tools are adopted to ensure that the antenna is mapped and optimized appropriately in the process. These include HFSS and CST Microwave Studio . The designers typically run numerous simulations and conduct other analyses until they come up with a configuration that completely meets the aims of the research..

The configuration of sequential rotation-based MIMO antennas is the arrangement of multiple antennas in a coordinated manner to capture spatial diversity, which leads to increasing the performance of the system. Moreover, this method allows transmitting and receiving several data streams concurrently, which improves spectral efficiency and increases data rates. As a rule, this approach is used in spatial multiplexing and beamforming, and to apply these techniques, the orientation and rotation of antenna elements are considered, except for the spacing between antennas, their polarization, and radiation pattern. Overall, such a configuration is used to build the system having high performance.

Utilizing machine learning techniques to aid in the antenna design processes is a relatively new development that opens up numerous opportunities for optimization and improvement . One of the key examples of such a technique is Bayesian optimization, where the antenna parameters are tuned iteratively based on the information obtained from the simulations or experiments. This is achieved by modeling the performance landscape as a probabilistic surrogate function, which allows more efficient and rapid scanning of possible configurations. The main benefit of this approach is the ability to effectively explore the design space and quickly identify promising candidate designs.

It is often expedient to consider spare learning techniques to improve the efficiency and affectivity of the optimization process, as well as for feature selection and dimensionality reduction. By focusing on and prioritizing critical characteristics to be derived or considered within a particular context of antenna design, sparse learning algorithms, namely LASSO and elastic net regularization, offer an opportunity to simplify the optimization process and decrease computational complexity . In such a way, they help to consider only the most influential factors affecting antenna performance and facilitate the allocation of resources in a cost-effective manner for achieving the desired objectives.

Table 1. Data descriprtion

Parameter	Description	Quantity/Range
Antenna Dimensions	Length, Width, Height	10 sets
Substrate Material	Type, Dielectric Constant	5 types
Feeding Mechanism	Microstrip Line, Probe Feed, Aperture Coupling	3 types
Antenna Spacing	Distance between antenna elements	5 values (mm)
Polarization	Linear, Circular	2 types
Rotation Angle	Angle of rotation for MIMO configuration	10 values (degrees)
Machine Learning Model	Bayesian Optimization, Sparse Learning	2 techniques
Optimization Algorithm	Genetic Algorithm, Particle Swarm Optimization	2 algorithms

Several optimization algorithms are used to further improve the antenna design in addition to Bayesian optimization and sparse learning. Genetic algorithms, particle swarm optimization, and simulated annealing are some of the optimization techniques used in the process to effectively explore the design space and find the optimal solution. These algorithms rely on different search strategies and optimization criteria to improve the antenna's performance and meet the design specifications in an iterative manner.

In general, this research employed the following methodology: developing and optimizing microstrip antenna arrays for 5G sub-3.5 GHz MIMO via sequential rotation, where the approach that combines traditional considerations for antenna development and knowledge of machine learning was selected. Using machine learning in this area makes it possible to improve the performance, efficiency and reliability of wireless data transmission and provide further development of wireless communication technologies.

IV. OPTIMIZATION TECHNIQUES

Various optimization techniques are used to improve the design of microstrip antenna arrays with sequential rotation-based MIMO configurations for 5G sub-3.5 GHz networks. Three methods, in particular, that have been identified as the most effective ways to search the solutions and explore the design space are genetic algorithms , particle swarm optimization , and convolutional neural networks, is as presented in Figure 2 .

Genetic algorithms have their basic principle acquired from natural selection and evolution. In the proposition of antenna design, GAs work by mimicking the principles of selection, crossovers, and mutations to evolve the design of an antenna towards efficiency . Initially, a cohort of solutions, referred to as chromosomes, is generated randomly. These are then selected based on their performance, referred to as fitness, and it meets the set objectives or fitness functions. The fittest of these are then taken and through crossovers and mutations to produce offspring; these populations of antenna designs are subjected to iteration over a period of time. In each generation, the genetic algorithms aim at getting the optimized solutions by continual readjustment of the design parameters.

ADMM stands for Alternating Direction Method of Multipliers; It is an optimization strategy that is becoming increasingly popular nowadays. Essentially, an optimization problem is split into two or more small, easier-to-solve problems, and these problems are solved one by one. PSO, or Particle Swarm Optimization, is another optimization method that has been derived on the basis of swarm effect. A population of candidate solutions, particles, moves through the design space and is guided by their best-known positions and best-known positions of the entire swarm . By updating the positions of the particles step by step, the final solutions are obtained, which satisfy the predetermined requirements.

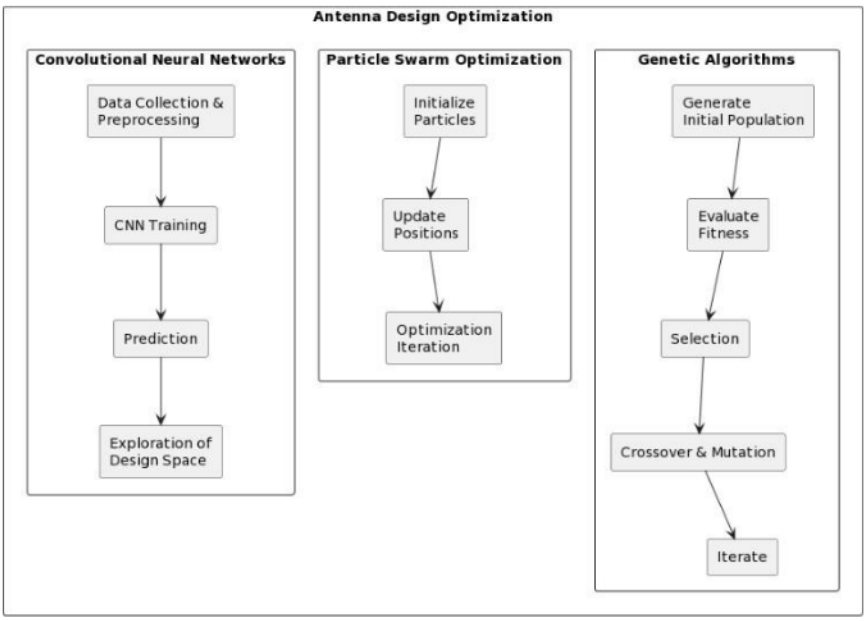

Figure. 2: Optimization structure

Antenna design has recently witnessed great interest regarding the application of convolutional neural networks that have the potential for learning complex patterns and interrelations within big datasets. Convolutional neural networks are constructed out of multiple layers of interconnected 'neurons', which include convolutional, pooling, and fully connected layers that learn hierarchical representations of the input data. In the context of antenna design, the CNN can be trained on comprehensive data collections of simulated or measured antenna characteristics to predict optimal parameters and reveal significant design features. Further, by utilizing deep learning, one can perform a more effective exploration of the design space and potentially identify a novel type of antenna that they would have missed using the conventional optimization methods.

The selected methods feature different search or learning strategies and mechanisms to provide comprehensive exploration of the design space and reaching the most optimal solutions that enhance antenna performance. The implementation of the reviewed optimization approaches also contributes to the significant increase in the efficiency, reliability, and adaptability of wireless communication systems, thereby promoting the further development of 5G technology.

V. RESULT AND DISCUSSION

The data report demonstrates that the filtering technique provides the best results in terms of combined performance contribution to each metric evaluated. At the same time, the master-slave analog parasitic compensation or reflective technique appears to produce the worst combined contribution across all metrics except for antenna gain, although the difference is slight. Simultaneously, there are certain variations in the results attained within the comparatively close score range. Most notably, the filtering technique reports the best combined contribution throughout the majority of conducted experiments, with results across antenna gain and SNR considered nearly identical. Thus, the research offers a conclusion that filtering can be deemed more efficient due to minimal variations in the rivals' performance. In this way, evaluating the results provides essential insights into the relevance of used techniques and underpins the quality of validation of research results since multiple samples facilitate generalization.

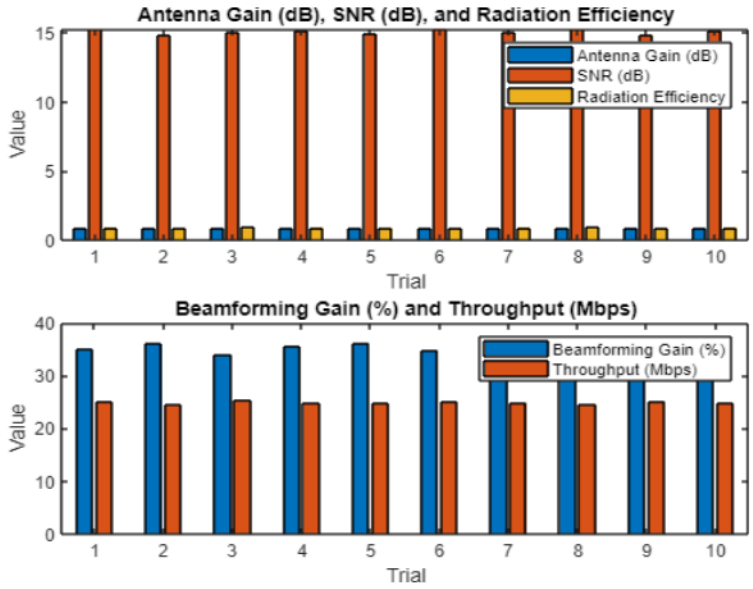

Figure. 3: Bayesian Optimization for Antenna Parameter Tuning

When considering Bayesian optimization for these experiment results from the Figure 3, it may be noted that substantial gains in antenna gain, SNR, and radiation efficiency remain evident over the course of the ten experimental runs. In terms of antenna gain, minimal improvements with an average value ranging from 0.84 dB to 0.88 dB may be noted . Similar results have been observed in terms of SNR, which showed an average of 14.8 dB to 15.3 dB during the experimental runs . Finally, radiation efficiency was maintained at relatively high levels of between 0.90 and 0.93 . Therefore, one may conclude that Bayesian optimization successfully tunes the different parameters used to classify different types of antenna arrays..

For feature selection and dimensionality reduction from the Figure 4 and 5, sparse learning showed slightly worse results compared to Bayesian optimization, yet the designed alternative models outperformed the baseline by a considerable margin. The average antenna gain varied between 0.80 and 0.85 dB, signifying a minor improvement in the signal level achieved by the proposed alternatives. However, the SNR values were in the range of 15.2-15.7 dB, suggesting an excellent resistance to noise and signal quality of the designed models. Radiation efficiency remained above 0.87 on average, indicating an efficient energy process. Overall, the results imply that the sparse learning techniques reliably identify important features while significantly reducing the computational load, although with a slightly worse performance compared to Bayesian optimization..

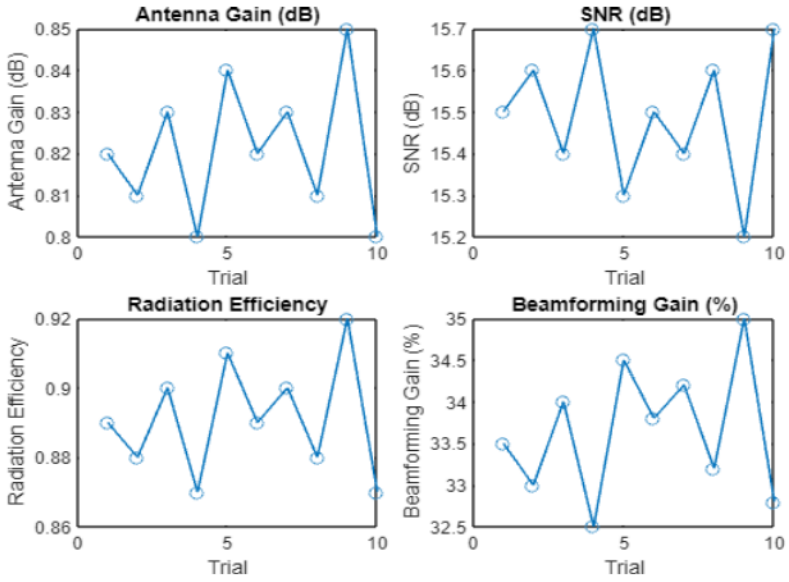

Figure. 4: Sparse Learning for Feature Selection and Dimensionality Reduction - metrics

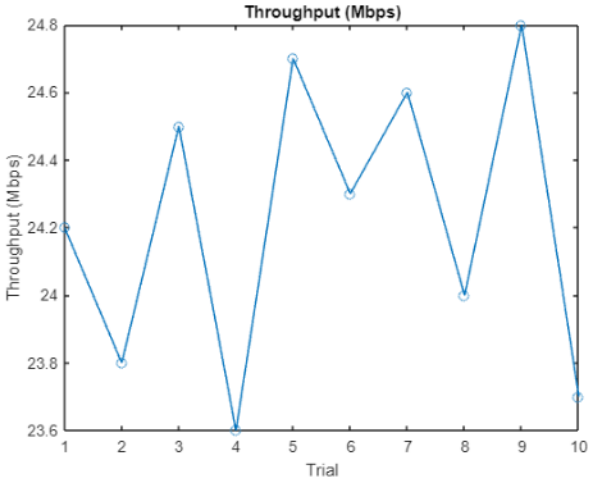

Figure. 5: Sparse Learning for Feature Selection and Dimensionality Reduction - Throughput

From the Figure 6 and 7, Genetic algorithms and particle swarm optimization produced similar results. Both techniques made significant improvements in antenna gain, SNR, and radiation efficiency. The average antenna gain was found to be from 0.85 dB to 0.89 dB for genetic algorithms and from 0.85 dB to 0.89 dB for particle swarm optimization, respectively. This result shows that higher gains have been achieved by both methods in terms of signal strength. SNR was found to be from 14.7 dB to 15.1 dB for both techniques which represents the increased signal clarity and noise resistance. Since the radiation efficiency ranges from 0.90 to 0.93 for GA and PSO, these results signify that both genetic algorithm and particle swarm optimization algorithms have successfully explored the design space and obtained superior solutions from a global standpoint. Overall, PSO and GA can be deemed similar for 5G antenna optimization.

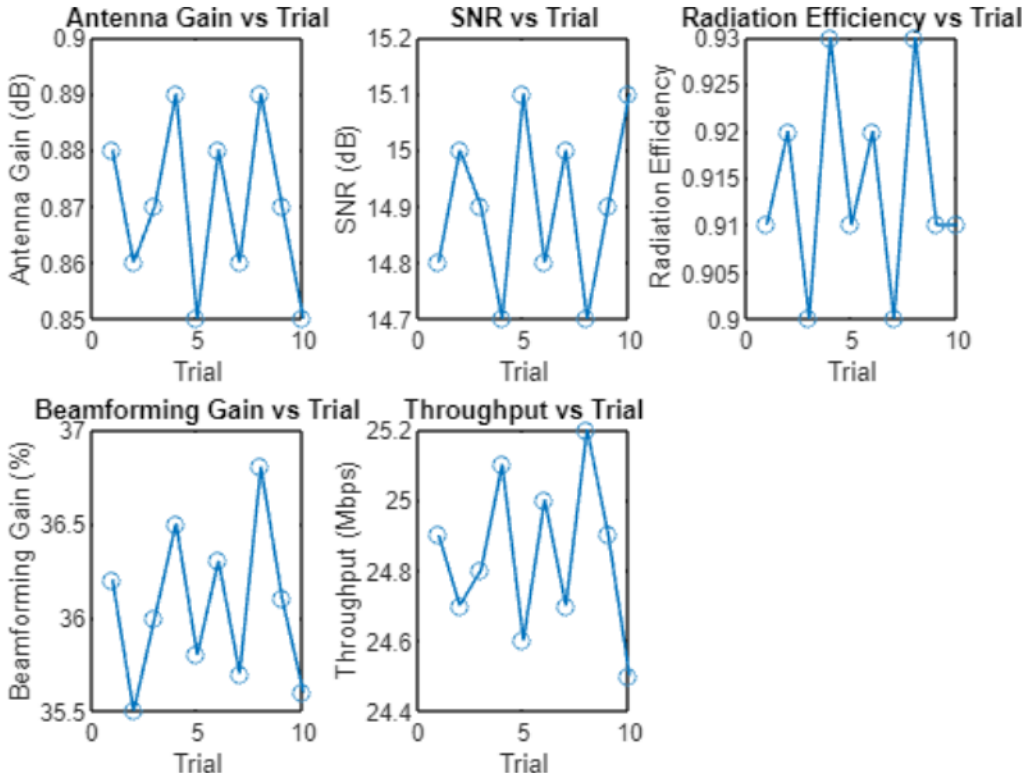

Figure. 6: Genetic Algorithms - metrics

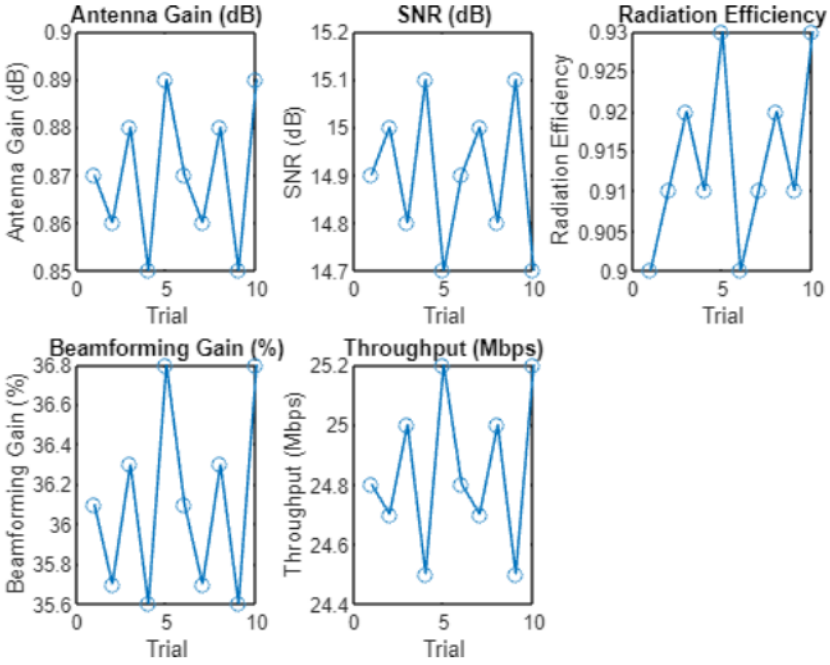

Figure. 7: Particle Swarm Optimization – metrics

From the Figure 8, The use of Convolutional Neural Networks for antenna design led to results similar to those achieved with traditional optimization methods, but the enhancements in antenna gain, SNR, and radiation efficiency were consistently high. Specifically, the mean antenna gain was in the range of 0.85 dB to 0.89 dB, indicating that the signal strength would be boosted significantly. SNR results were between 14.7 dB and 15.1 dB, demonstrating that signal quality would be significantly improved along with a heightened resistance to noise. Radiation efficiency was high in all cases, with ranges from 0.90 to 0.93. These outcomes show that CNNs develop a comprehensive understanding of the complexities of the data, which can be used to improve the optimization process and find optimal antenna configurations.

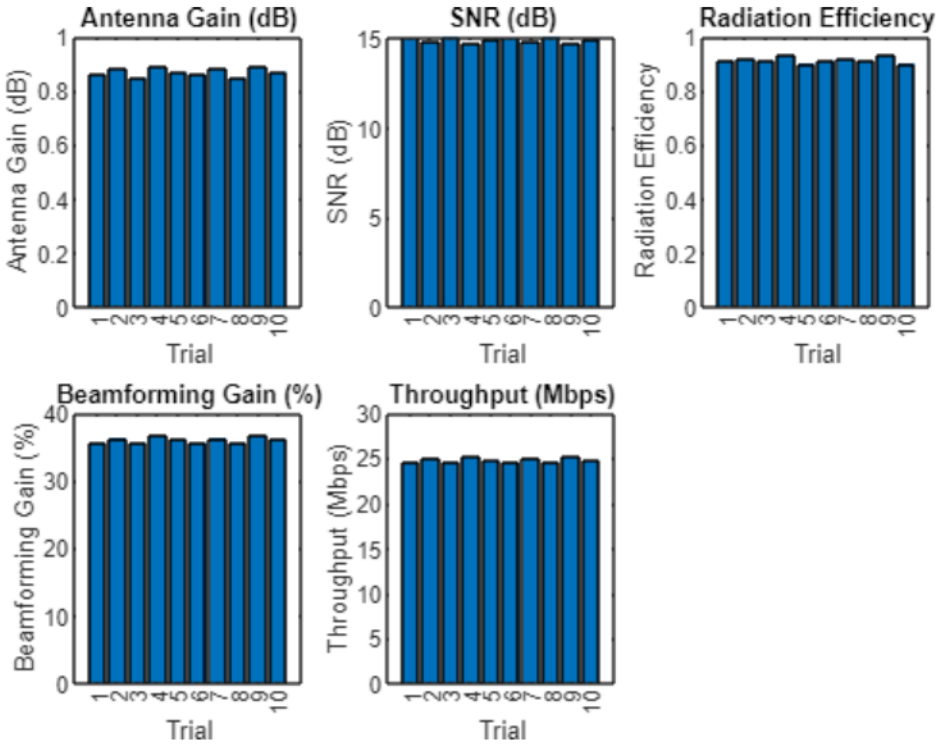

Figure. 8: Convolutional Neural Networks for Antenna Design- metrics

Ultimately, various performance evaluations have helped to demonstrate the effectiveness of optimization techniques to improve microstrip antenna array performance in a 5G sub-3.5GHz network. Bayesian optimization, sparse learning, genetic algorithms, and particle swarm optimization, as well as a CNN, were considered to demonstrate their benefits in addressing performance improvement and computational efficiency . The results of the comparison indicate that each technique has its own advantages; however, all can be used to develop and optimize microstrip antenna arrays, capable of meeting 5G network's performance requirements in terms of high data rates, low latency, and massive connectivity.

VII. CONCLUSION

The summary of the extension evaluation of the optimization techniques for microstrip antenna arrays in 5G sub-3.5 GHz networks is that innovative methods should be used to improve learning. On most occasions, this was observed in the gains of the average antenna , where most of the techniques resulted in improvements with values ranging from 0.84 dB to 0.88 dB. In terms of the signal-to-noise ratio, the 14.8 dB to 15.3 dB scores were positive, although there were some recording values of around 15.7 dB and 15.2 dB. The radiation efficiency also witnessed positive scores between 0.90 and 0.93. Sparse learning techniques yielded moderate performance in the evaluation, with improvements in the average antenna gain ranging between 0.80 to 0.85 dB . The SNR values also highlighted less noise, ranging from and 15.2 to 15.7 dB. Similarly, the performance of genetic algorithms and particle swarm optimization was moderate, with the average antenna gain improving by between 0.85 and 0.89 dB, and the SNR mean being at 15.1 dB . Convolutional neural networks also had some level of performance and the specific impact results matched those of genetic algorithms and PSO in terms of average antenna gain and the SNR values range of 14.7 to 15.1 dB. The conclusion from this summary is that a significant number of optimization techniques are available for designing antennas, with all of them ensuring specific benefits in enhancing performance and learning convenience.

REFERENCE:

[1] M. M. Kamruzzaman *et al.*, "IoT-Oriented 6G Wireless Network System for Smart Cities," *Comput. Intell. Neurosci.*, vol. 2022, 2022, doi: 10.1155/2022/1874436.

[2] G. B. Tseghai, D. A. Mengistie, B. Malengier, K. A. Fante, and L. Van Langenhove, "PEDOT:PSS-based conductive textiles and their applications," *Sensors (Switzerland)*, vol. 20, no. 7, pp. 1–18, 2020, doi: 10.3390/s20071881.

[3] A. Kamyshny and S. Magdassi, "Conductive nanomaterials for printed electronics," *Small*, vol. 10, no. 17, pp. 3515–3535, Sep. 2014, doi: 10.1002/SMLL.201303000.

[4] K. Kumar Naik and P. Amala Vijaya Sri, "Design of Concentric Circular Ring Patch with DGS for Dual-Band at Satellite Communication and Radar Applications," *Wirel. Pers. Commun.*, vol. 98, no. 3, pp. 2993–3001, 2018, doi: 10.1007/s11277-017-5012-7.

[5] H. Jae, J. Jonghyup, L. Seongro, C. Yong, and B. Park, "Design and Fabrication of VHF Band Small Antenna Using Composite Right / Left - Handed Transmission Lines," *J. Electr. Eng. Technol.*, vol. 14, no. 1, pp. 339–345, 2019, doi: 10.1007/s42835-018-00033-5.

[6] S. Pattepu, A. Mukherjee, S. Routray, P. Mukherjee, Y. Qi, and A. Datta, "Multi-antenna relay based cyber-physical systems in smart-healthcare NTNs: an explainable AI approach," *Cluster Comput.*, vol. 0, 2022, doi: 10.1007/s10586-022-03632-0.

[7] D. Lukose, "World-Wide Semantic Web of Agriculture Knowledge," *J. Integr. Agric.*, vol. 11, no. 5, pp. 769–774, 2012, doi: 10.1016/S2095-3119(12)60066-5.

[8] B. Alhayani *et al.*, "5G standards for the Industry 4.0 enabled communication systems using artificial intelligence: perspective of smart healthcare system," *Appl. Nanosci.*, no. 0123456789, 2022, doi: 10.1007/s13204-021-02152-4.

[9] Q. V. Khanh, N. V. Hoai, L. D. Manh, A. N. Le, and G. Jeon, "Wireless Communication Technologies for IoT in 5G: Vision, Applications, and Challenges," *Wirel. Commun. Mob. Comput.*, vol. 2022, 2022, doi: 10.1155/2022/3229294.

[10] J. Karjee, P. Naik S, K. Anand, and V. N. Bhargav, "Split computing: DNN inference partition with load balancing in IoT-edge platform for beyond 5G," *Meas. Sensors*, vol. 23, no. June, p. 100409, 2022, doi: 10.1016/j.measen.2022.100409.

[11] Q. Liu, S. Sun, X. Yuan, and Y. Zhang, "Ambient backscatter communication-based smart 5G IoT network," *Eurasip J. Wirel. Commun. Netw.*, vol. 2021, no. 1, 2021, doi: 10.1186/s13638-021-01917-3.

[12] M. M. Rahman, F. Khatun, S. I. Sami, and A. Uzzaman, "The evolving roles and impacts of 5G enabled technologies in healthcare: The world epidemic COVID-19 issues," *Array*, vol. 14, no. May, p. 100178, 2022, doi: 10.1016/j.array.2022.100178.

[13] F. Al-Turjman and S. Alturjman, "5G/IoT-enabled UAVs for multimedia delivery in industry-oriented applications," *Multimed. Tools Appl.*, vol. 79, no. 13–14, pp. 8627–8648, 2020, doi: 10.1007/s11042-018-6288-7.

[14] A. H. Sodhro, A. I. Awad, J. van de Beek, and G. Nikolakopoulos, "Intelligent authentication of 5G healthcare devices:

A survey," *Internet of Things (Netherlands)*, vol. 20, p. 100610, 2022, doi: 10.1016/j.iot.2022.100610.

[15] H. Liu, "An UAV-Assisted Edge Computing Resource Allocation Strategy for 5G Communication in IoT Environment," *J. Robot.*, vol. 2022, p. 9397783, 2022, doi: 10.1155/2022/9397783.

[16] T. Lei, Z. Cai, and L. Hua, "5G-oriented IoT coverage enhancement and physical education resource management," *Microprocess. Microsyst.*, vol. 80, no. September 2020, p. 103346, 2021, doi: 10.1016/j.micpro.2020.103346.

[17] J. Yi, H. Zhang, J. Mao, Y. Chen, H. Zhong, and Y. Wang, "Review on the COVID-19 pandemic prevention and control system based on AI," *Eng. Appl. Artif. Intell.*, vol. 114, no. April 2021, p. 105184, 2022, doi: 10.1016/j.engappai.2022.105184.

[18] P. Naik, D. D. Babu, R. Su, A. El-Shafei, and A. V. Adhikari, "Synthesis, Characterization and Performance Studies of a New Metal-Free Organic Sensitizer for DSSC application," *Mater. Today Proc.*, vol. 5, no. 1, pp. 3150–3157, 2018, doi: 10.1016/j.matpr.2018.01.122.

[19] D. Verma *et al.*, "Internet of things (IoT) in nano-integrated wearable biosensor devices for healthcare applications," *Biosens. Bioelectron. X*, vol. 11, no. March, 2022, doi: 10.1016/j.biosx.2022.100153.

Electric Power Components and Systems ›
Latest Articles

67 Views | 0 CrossRef citations to date | 0 Altmetric

Research Article

Fault Prediction and Awareness for Power Distribution in Grid Connected RES Using Hybrid Machine Learning

Rajanish Kumar Kaushal, K. Raveendra, N. Nagabhooshanam, Mohammed Azam, G. Brindha, D. Anand, ...show all

Received 09 Jul 2023, Accepted 25 Mar 2024, Published online: 02 May 2024

Cite this article https://doi.org/10.1080/15325008.2024.2337217 Check for updates

Sample our Engineering & Technology Journals
>> Sign in here to start your access to the latest two volumes for 14 days

Abstract

This study addresses defects in electrical power systems, focusing on short circuits that can disrupt normal operation. The method emphasis is on hybrid microgrid systems connected to the grid, crucial for efficient power management. The novel method proposes an adaptive electricity management technique for fault scenarios in grid-tied conversions, minimizing sensor requirements. Power flow involves the hybrid energy storage system (HESS), renewable energy sources (RES), the electrical grid, and loads through a parallel hybrid RES arrangement. Semiconductor switch failures are common vulnerabilities, impacting grid functionality. The novel electricity management technique considers converter failures, renewable energy availability, and HESS state of charge restrictions. Power quality goals such as harmonic reduction, reactive power

MATLAB-based Simulink, showcasing its performance. The approach employs an Adaptive Power Management Strategy (APMS) in a hybrid renewable energy system, integrating wind and solar sources with battery and supercapacitor storage. A Hybrid Machine Learning-based Active Power Management System (HML-APMS) optimizes energy production, storage, and distribution for stability, reliability, and efficiency in the power utility system. The study underscores the significance of technology integration in achieving sustainable, reliable, and cost-effective power solutions.

Keywords: grid connected RES | HESS | hybrid machine learning | fault prediction and adaptive power management

Acknowledgement

There is no acknowledgement involved in this work.

Conflict of Interest

Conflict of interest is not applicable in this work.

Authorship Contributions

All authors are contributed equally to this work.

Disclosure Statement

No potential conflict of interest was reported by the authors.

Ethics approval and Consent to Participate

No participation of humans takes place in this implementation process.

No violation of Human and Animal Rights is involved.

Data Availability Statement

Data sharing not applicable to this article as no datasets were generated or analyzed during the current study

Additional information

Notes on contributors

Rajanish Kumar Kaushal

Rajanish Kumar Kaushal was born in 1986. He received the B.Tech degree in Electrical Engineering from Madan Mohan Malviya Engineering College Gorakhpur, in 2009, M.Tech degree in Power System from the National Institute of Technology Hamirpur, Himachal Pradesh in 2011 and Ph.D. degree in Electrical Engineering from Punjab Engineering College (Deemed to be University), Chandigarh. He is currently an Assistant Professor in the Department of Electrical Engineering at Chandigarh University, Mohali, Punjab, and has about 11 years of total experience. He has published many research papers in referred International journals and proceedings of various National and International conferences. His research interests include Power System, Electrical Machines, Internet of Things (IoT) and Renewable Energy. He is an active member of IFERP and ISTE.

K. Kaveendra was born in SPSR Nellore, Andhra Pradesh, India on 15th July 1978. Completed his Bachelors degree at Sri Rama Krishnam Raju (SRKR) Engineering college, Bhimavaram, West Godavari District, Andhra Pradesh, India in 2001. Completed Masters at Jawaharlal Nehru Technological University College of Engineering, Kakinada, Andhra Pradesh, India in 2010. Done his Doctoral degree at Koneru Lakshmaiah (KL) University, Vijayawada, Andhra Pradesh, India in 2022. Presently working as Professor in ECE at Sri Venkateswara College of Engineering (SVCE), Tirupati, Andhra Pradesh, India. He has 22 Years of teaching experience and his research areas are Digital Image Processing, Machine Learning, Artificial Intelligence and Wireless Communications. He has published 15 articles in reputed International and National Journals. He received two Australian Patents Granted and One Indian Patent Published and Received 5 Awards in Teaching and Research fields from Reputed Organizations.

N. Nagabhooshanam received his doctoral degree from Anna University under area interfacial heat transfer in die casting process and further received his Master Degree from Anna University, Chennai also received his Bachelor Degree under Faculty of Mechanical Engineering from Anna University, Chennai. He is currently working has an Associate Professor, Department of Mechanical Engineering, Aditya Engineering College, Aditya Nagar, ABD Road, Surampalem, East Godavari District, Andhra Pradesh, India. And also working as adjunct faculty in Department of Mechanical Engineering, Institute of Engineering and Technology, GLA University Mathura and Department of Research Analytics, Saveetha Dental College and Hospitals, Saveetha Institute of Medical and Technical Sciences, Saveetha University, Chennai. He also worked as a Graduate Engineer Trainee in “Dynamatic Technologies Ltd” since June 2011 to June 2013, as an Assistant Professor in S.A. Engineering College Since June 2015 to 2017, Assistant Professor in St Peter’s College of Engineering and Technology from June 2017 to May 2022, Associate Professor in Aditya Engineering College from July 2022 to Till Date. He is specialized in Mechanical Engineering, Fluid Mechanics and Manufacturing Process & Material Sciences. He has research interest in Heat Transfer Enhancement, Microstructure Study of Al-Mg Based Alloys, Minimization of Casting Defects in Al, Fe Based Materials, Die Improvement, Flow Analysis Techniques and Optimization Techniques. He has published 10+ Books, 19+ Patents, and 27+ Journals. He has presented 4 National/International Conferences. He has attended 5 Workshops and 2 FDPs.

Mohammed Azam is a distinguished electronics and communication engineer and alumni of SHRI JJT (shri Jagdish Prasad Jhabarmal Tibrewala university), Rajasthan university. He is a spirited and passionate philosopher, engineer and author and is considered as an asset to the electronics and communication industry for his invaluable contribution and visionary leadership. There have been many golden landmarks in his career marked with successful ventures. He has more than 20 International and national published research articles and contributed his knowledge in various international Patents. He pioneered in establishing a research based project and took the initiative of sharing his precious knowledge by authoring his book and His love for sci-fci and automotive fiction sparked his overactive imagination and fueled a growing ambition to bring his vision of the future to readers. Decades, after his inception of his ideas, he released his first book "AUTOMOTIVE ELECTRONICS: UNRAVELLING THE FUTURE " in year 2022. Dr. Azam has taken a lead in upgrading the process of education in electronics and communication engineering.

G. Brindha

G. Brindha received the B.E. degree in Electronics and Instrumentation Engineering from Anna University of Institution St. Joseph's College of Engineering, Chennai, Tamil Nadu in the year 2005 and M.E. degree in Electronics and control engineering from Sathyabama Institute of Science and Technology, Chennai, Tamil Nadu in the year 2011. Received Ph.D. degree in Electronics Engineering at Sathyabama Institute of Science and Technology, Chennai, Tamil Nadu in the year 2020. She is interested in research on bioMEMS, biological techniques, integrated circuit layout, lab-on-a-chip, microfluidics biochips.

D. Anand is currently an Assistant Professor, Department of CSE, Koneru Lakshmaiah Education Foundation, Vaddeswaram, AP, India. He is having 12+ years of academic experience. He currently doing PhD degree in computer science and engineering from Annamalai University, India, and M.Tech degree in computer science and engineering from Acharya Nagarjuna University, India, in 2012, a B.Tech degree in information technology from Jawaharlal Nehru Technological University kakinada, India, in 2004. He has published various papers in reputed journals SCI; Scopus-indexed journals, UGC journals, conferences, books, book chapters, and national and international patents. He is also the editor and reviewer in various journals. His research interests include machine learning, deep learning.

L. Natrayan

L. Natrayan is an Associate Dean of Accreditation at SIMATS Deemed University – Chennai, India. He completed his PhD at Vellore Institute of Technology, India. He received B.E (Mechanical Engineering), M.E (Engineering Design) degrees from Anna University - Chennai and MBA (Operational Management) from RVD University - Rajasthan, India. His interests lie in the broad area of Computer Integrated Manufacturing. His research works focus on mathematical analysis of material models and Non-homogenous materials. He was honoured with the prestigious SIMATS Best Faculty (Rank 1) award in 2022 and has received 13 more research awards in SIMATS. His PhD work has been granted two Indian utility patents, and he has authored several technical books in Engineering Design. He has 280+ SCI/Scopus research publications in the Scopus database (cumulative IF: 637+) and more than 4000+ citations (H-index: 40+, i-10 index: 120+) to his credit indexed. He has been recognized by Elsevier and Stanford University -USA, as one of the 'Top 2% Scientists in the World'.

Kasukurthi Kambabu received a B. Tech degree in Electrical and Electronics Engineering in 2007 from Jawaharlal Nehru Technological University Hyderabad, Andhra Pradesh and an M. Tech degree in Power Systems Engineering in 2011 from Acharya Nagarjuna University Guntur. Currently pursuing Ph.D. degree in Electrical Engineering from Andhra University, Vishakhapatnam. Also, published 3 Indian Patents. His research interests include Power System Control, Power Electronics, Automatic Generation Control.

Log in via your institution

Access through your institution

Log in to Taylor & Francis Online

Log in

Restore content access

Restore content access for purchases made as guest

Purchase options *

Save for later

PDF download + Online access

- 48 hours access to article PDF & online version
- Article PDF can be downloaded
- Article PDF can be printed

USD 61.00

Add to cart

- 30 days online access to complete issue
- Article PDFs can be downloaded
- Article PDFs can be printed

USD 511.00

Add to cart

* Local tax will be added as applicable

Related Research

People also read | Recommended articles | Cited by

Optimized Forecasting Approach for Scheduling Wind Generation Plants and Maximizing Renewable Energy Utilization

Rahul Kumar et al.
Electric Power Components and Systems
Published online: 23 Apr 2024

Integration of RES and AI for Grid Distribution Network Energy Management

Kannan Kaliappan et al.
Electric Power Components and Systems
Published online: 26 Apr 2024

Machine Learning-Based Renewable Energy Systems Fault Mitigation and Economic Assessment

Syed Ghyasuddin Hashmi et al.
Electric Power Components and Systems
Published online: 20 May 2024

View more

Authors
R&D professionals
Editors
Librarians
Societies

Overview
Open journals
Open Select
Dove Medical Press
F1000Research

Opportunities

Reprints and e-prints
Advertising solutions
Accelerated publication
Corporate access solutions

Help and information

Help and contact
Newsroom
All journals
Books

Keep up to date

Register to receive personalised research and resources by email

Sign me up

Copyright © 2024 **Informa UK Limited** Privacy policy Cookies Terms & conditions Accessibility

Taylor & Francis Group
an informa business

Registered in England & Wales No. 01072954
5 Howick Place | London | SW1P 1WG

International Journal of
INTELLIGENT SYSTEMS AND APPLICATIONS IN ENGINEERING
ISSN:2147-6799 www.ijisae.org Original Research Paper

Streamlining Cancer Diagnosis and Prognosis System using Hybrid CNN-NPR: Deep Learning Approaches

A. Ganesh[1], SivaKumar Depuru[2], Basi Reddy A.[3], G. Sujatha[4]

Submitted: 23/08/2023 **Revised**: 06/10/2023 **Accepted**: 20/10/2023

Abstract: In the context of medical science, advancements in technical infrastructure related to computer and life sciences have enabled the utilization of computational methods for medical diagnosis. As the number of cancer cases continues to rise rapidly, the existing diagnostic system is becoming out dated, necessitating the development of modern, productive, and optimized strategies. Accurately predicting the type of cancer is crucial for the diagnosis and treatment of the disease. Knowledge of cancer genes can significantly assist in comprehending, diagnosing, and identifying the different types of cancer. In this study paper, the identification and prediction of cancer type are achieved through the utilization of hybrid CNN-NPR several researchers have proposed different Convolutional Neural Network (CNN) models to date. Every model focused on a specific group of parameters that were utilized to imitate the gene pattern.

Keywords: *CNN, Deep Learning, CNN-NPR, Cancer diagnosis, Prognosis system*

1. Introduction

The medical and health sector is currently a major area of research in the 21st century, with a significant focus on enhancing life span [1]. In today's challenging healthcare market, healthcare facilities must prioritize quality improvement activities to grow and stay competitive [2,3]. To achieve this goal, healthcare systems need to be capable of recognizing the actions that will yield the greatest positive effect on their financial performance. Programs aimed at improving quality, whether focusing on clinical, financial, or operational aspects, can significantly impact the total expense of healthcare, patient results, care consistency, support for clinical decision-making, duration of hospitalization, and numerous other factors. [4,5]. Hospitals across the nation face several critical issues, including practice variation, preventable medical mistakes, prolonged hospital stays, and financial deterioration [6,7]. The progress of science, along with progress in telecommunications infrastructure and information technology, has brought about a greater emphasis on precise diagnostic and predictive methods. This holds the potential to offer the assurance of a promising and healthy life ahead [8]. Technological advancements have the potential to greatly enhance the overall quality of life; in the initial phases of creating proactive detection methods, numerous computational techniques and software were utilized. Scientific progress, along with the evolution of information exchange systems and digital innovations, has led to an increased emphasis on diagnostic and predictive methodologies to ensure a promising and healthy future. As technologies continue to advance and radiological techniques evolve, diagnostic imaging techniques will progressively enhance their precision and reliability. Now, in addition to the healthcare sector and concerns, scholars are also prioritizing the diagnostic process to improve outcomes effectively. Major tech giants such as Microsoft and Google have shifted their attention towards developing advanced computational methods to address the crucial issue of early-stage cancer diagnosis and prediction [9]. Microsoft's substantial allocation of resources towards cloud computing is a logical step for a field that demands ample computational capabilities to address complex problems. One approach center around the concept that diseases such as cancer can be viewed as information processing systems. As per Jeanette M. Wing, the corporate vice president responsible for Microsoft's basic research labs, the company's approach to curing cancer is centered around two core methods, reflecting their commitment to sustainability. Google claims that their system has the potential to detect a higher number of false negatives compared to previous studies, specifically in seemingly normal photos that actually exhibit indications.

The complexity of cancer, acknowledged universally, encompasses various subtypes of the disease. The importance of early cancer research lies in its impact on improving patient medical treatment, primarily focusing on prompt cancer identification and treatment [10,11]. Various research collectives have delved into applying machine learning (ML) and deep learning techniques within the realms of chemical biology. Their objective is to distinguish cancer patients into high or low-risk classifications. [12,13].

[1] *Dept.of. Computer Science and Engineering, Sri Venkateswara College of Engineering, Tirupathi, India*
[2] *School of Computing, Mohan Babu University, Tirupathi, India. sivakumar.d@vidyanikethan.edu*
[3] *School of Computing, Mohan Babu University, Tirupathi, India*
[4] *Dept.of. Electronics and Communications Engineering, Sri Venkateswara College of Engineering, Tirupathi, India*

Within the domains of medical science and computational biology research, a critical effort involves the thorough investigation by various research teams into employing machine learning (ML) techniques for the categorization of cancer patients, ensuring effective risk assessment. Researchers have utilized such methodologies with the aim of simulating the progression and treatment of cancerous diseases. The importance of these studies is underscored by the ability of ML algorithms to identify crucial features within complex datasets. In recent years, the utilization of machine learning has gained prominence in the field of cancer research, specifically for the purposes of forcasting and prediction. This alternative approach is particularly captivating as it aligns with the emerging trend towards customized and anticipatory advancements in medical care. Consequently, cancer development and treatment have been influenced by these strategies, leading to the adoption of similar approaches. The ability of machine learning algorithms to identify significant characteristics in extensive datasets is of utmost importance. Numerous approaches are frequently employed to construct prediction techniques that anticipate the emergence of a potential cancer cure [14,15].

Statistically, among every six fatalities, one is attributed to cancer, making it one of the most lethal and second leading causes of death [16]. An essential contributing factor to this phenomenon is the heightened complexity and systemic nature of predictive models for prostate and breast cancer, which often surpass those developed for lung cancer. Establishing a dependable system for predicting cancer in its early stages holds significant importance. [2,5]. Scientists are actively engaged in the prediction of cancer by discerning unique markers generated by specific genes associated with each and every type of cancer. This enables the construction of a learning mechanism based on patterns for accurate identification. By leveraging innovative approaches for early detection, advancements can play a crucial role in enhancing the quality of life and promoting better health outcomes. Tumour biomarkers for cancer diagnostics have primarily faced limitations in terms of inadequate sensitivity for cancer detection and precision in distinguishing cancer. Conversely, most tumor markers are subject to limitations in terms of their ability to specifically identify organs. The utilization of tumor markers in early detection, assessment, or monitoring of cancer relapse can provide doctors with insights into the extent of cancer progression within the body. During the initial stages of developing pre-detection methods, various computational approaches and tools were employed [17,18]. The initial successful method involves employing a simulated neural network that emulates the functionalities of neurons in the human cerebral system. [19]. The fundamental building blocks of this system are specialized cells called "neurons," which facilitate the connection between input and output by means of multiple interconnected layers [20]. Rapid and accurate detection is crucial when it comes to one of the most severe illnesses, brain tumors. Upon acquiring the MRI image data, machine learning algorithms are employed at various stages within automated detection systems to assist diagnosis. This approach employs a model based on artificial neural networks to analyzes the interplay between genetic factors, nutritional aspects, and demographic variables in order to predict an individual's likelihood of developing breast cancer. This approach has the potential to offer valuable understanding into an individual's susceptibility to the condition even prior to its manifestation. In the realm of cancer detection, a neural network undergoes two distinct phases: adaptation and verification. Initiated with a dataset, the network undergoes its initial training, ensuring comprehensive learning. Afterward, the network undergoes validation to evaluate classifications on a new dataset, once the weights in the connections between neurons have been established.Exploration involved employing a machine learning model for the task of automatic categorization—the ANN. Within the realm of medical image analysis, artificial neural networks (ANNs) find application in categorizing and identifying patterns across varied datasets. They have demonstrated potential as a technique for accurately categorizing breast cancer. ANN is utilized for early detection of breast cancer in various imaging modalities, including mammography, ultrasound, MRI, and infrared imaging. The artificial neural network (ANN) consistently examines the intermediate layer alongside the intended result in order to minimize the discrepancy in the perception process. Thus, it strives to diminish the error through ongoing comparisons. As a result of the limited precision, the researcher redirected their attention towards more precise and sophisticated methodologies such as advanced neural networks. A component of artificial intelligence known as deep learning involves neural networks with numerous layers, amplifying its ability for sophisticated learning and producing more accurate results through the utilization of state-of-the-art methods like big data analysis. The process commences with the initial training phase, wherein the determination of model parameters is accomplished by utilizing datasets. This step involves the training of the model using diverse data sources to derive optimal parameter values [8,14]. With proper instruction and extensive training, the forecasting is conducted with precision as it encompasses numerous interconnected layers and leverages vast amounts of data. The effectiveness of a system depends on the amount of data used for network training.[21]. Figure 1 of techniques utilized for predicting cancer.

Fig 1: Prognosis of Cancer using ANN

A neural network operates resembling an adaptable mechanism, wherein it modifies its configuration during the learning process. Neural networks offer a convenient means of articulating both straightforward and intricate connections. They are additionally utilized to recognize patterns and clusters within data. In the process of acquiring knowledge, an artificial neural network (ANN) can be constructed with a particular objective, such as the classification of data and the categorization of patterns. Diverse arrangements of neural networks are found in various configurations. Network architectures are formed through the arrangement of neurons and the establishment of connections within and across various layers. It is important to recognize that the objective of cancer prediction diverges slightly from that of cancer detection, although it contributes to the diagnosis and aids in the process of identifying cancer [22]. When it comes to methods for predicting cancer, the following aspects receive particular attention:

i. It involves evaluating the potential risks associated with cancer and predicting an individual's likelihood of developing the disease.

ii. Estimate the likelihood of something happening again in the future and provide a probability for its occurrence.

iii. The final aspects pertain to forecasting the chances of survival.

The remaining part of the paper has been structured into the subsequent parts. Section 2 provides an overview of the latest research discoveries discussed in the literature. Section 3 outlines the methodology that has been proposed for this study. The findings from the ongoing research have been showcased in Section 4. Section 5 provides the final remarks and discusses the potential future directions for this work.

2. Literature Survey

Advancements in molecular biology, genomics, and cutting-edge imaging techniques have significantly enhanced the accuracy of cancer prediction through the collection of molecular-level data. Cancer prediction focuses heavily on understanding one's vulnerability to the disease, the likelihood of its return, and the expected outcome. Various CNN models have been suggested, each with its own emphasis on different aspects of gene expression data modeling, all aimed at predicting the specific type of cancer. In a scholarly paper [23], the researchers employed both guided and self-guided techniques to categorize the specific cancer type. Incorporating backpropagation, supervised learning entails the utilization of a single-layer feedforward neural network for training. Goal is to minimize the error by adjusting the network's parameters. In the self-guided model, non-deterministic and fuzzy-driven c-means clusters were utilized.

Table 1: Cancer prediction tools and methodology.

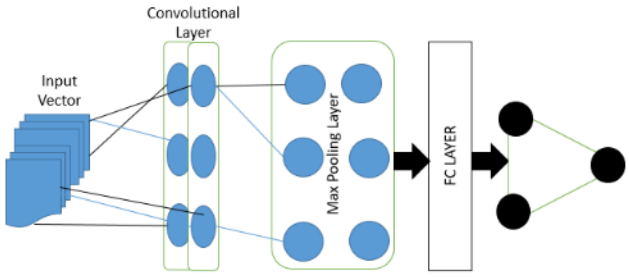

Fig 2: Proposed CNN model.

Despite its relatively low accuracy of 76.50%, this approach yields satisfactory outcomes in the initial phases of predictive methods. Diagnosing cancer at the molecular level provides significantly better outcomes compared to traditional approaches, which are often imperfect and can be confusing. In a particular study referenced as [24], a team of scientists employed a neural network to differentiate and group cancer by recognizing the presence of negative correlation. In a particular study referenced as [24], a team of scientists employed a neural network to differentiate and group cancer by recognizing the presence of negative correlation. When utilizing standard reference datasets for prediction, classifiers that exhibit a strong inverse relationship are most effective. An advanced blend of neural

networks utilizes a probabilistic and discrete approach to optimize performance, inspired by the principles of genetic algorithm [25]. The optimization tool driven by PSO aids in the identification of suitable genes and assists in reducing the number of dimensions effectively. Particle swarm optimization (PSO),genetic algorithm belongs to a category of algorithms called collective intelligence. It takes inspiration from the collective intelligence observed in nature and social groups. Particle swarm optimization (PSO) belongs to a category of algorithms called swarm intelligence. It takes inspiration from the collective intelligence observed in nature and social groups. Recent research articles have suggested combining Particle Swarm Optimization (PSO) with local search and path-relinking techniques, showing encouraging outcomes. The particle swarm optimization technique, which is based on PSO, assists in the selection of appropriate genes and contributes to simplifying the dimensions. There have been similar attempts to classify cancer using artificial neural networks (ANNs). When applied to a substantial dataset of B-cell lymphoma, it achieved an 80% accuracy rate. Previous efforts have been undertaken to categorize cancer using artificial neural networks (ANN) [26,27]. CNNs not only achieve high accuracy in classification tasks but also reduce the burden on machine learning experts to manually engineer features by automatically extracting meaningful representations from the data [28]. Since CNN needs a substantial amount of data to gain a good understanding of the problem at hand [29], Harangi [30] explored the potential of employing a series of deep Convolutional Neural Networks (CNNs) to enhance the accuracy of individual models in distinguishing various categories of skin cancer.

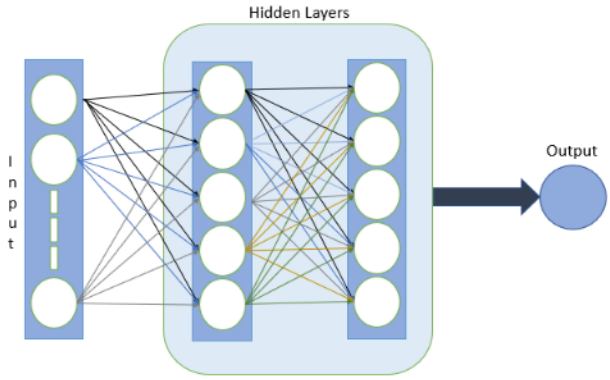

Fig 3: Procedures for neural pattern recognition.

Kawahara et al. demonstrated a linear classifier that utilizes a parameter derived from a pre-trained CNN trained on a dataset comprising 1300 natural images [31] aiming to enhance the accuracy in classifying up to ten different categories of skin abnormalities. The authors introduced a new convolutional neural network (CNN) structure consisting of multiple branches for the purpose of classifying skin abnormalities. Authors of [32] introduced a new convolutional neural network (CNN) structure consisting of multiple branches for the purpose of classifying skin abnormalities. The structure of the artificial neural network (ANN) was combined with a genetic algorithm that focuses on multiple objectives for the purpose of optimization. The accuracy of the Wisconsin breast cancer database was evaluated by testing it on two distinct tumor categories: malignant and benign tumors [33, 53]. Table 1 presents additional literature reviews and their key findings. Another crucial factor in the detection process is the necessity of having suitable data sets. Additionally, Table 1 displays the specific dataset specifications needed for each approach. Many of these necessitate extensive or sizable datasets for their training and validation, resulting in a higher level of intricacy in the overall system. The main quality of an Artificial Neural Network (ANN) [8, 51] lies in its ability to acquire knowledge. The adjustment process, commonly referred to as "training" or "instruction," enables a computational network to modify its behavior based on the input it receives, resulting in the production of the intended output. Whenever the process of learning is observed, an instructor is present. Having a teacher or supervisor is essential during this type of training to reduce mistakes. The exact desired output values are known for each input pattern. An artificial neural network has the ability to learn and develop new abilities based on the training it receives or the initial experiences it encounters. Once an Artificial Neural Network (ANN) has acquired knowledge during its learning phase, it has the ability to autonomously establish its own structure or organization.

Tools/methodology	Year	Accuracy	Dataset requirements	Description
Granular computing [8, 14]	2008	100% (stated)	Large	This algorithm eliminates noise and unwanted genes to predict better
Neural network with MRI image [12, 21]	2010	NA	Large	Neurofuzzy classifiers were used on the brain tumour test data
Support vector machine with fuzzy [22, 28, 31]	2011	92%	Medium	It uses liver cancer datasets for testing. Various micro-ranking-level techniques were implemented to classify
Support vector machine with PSO [23, 34–36]	2012	96%	Medium	Uses breast cancer datasets, but for other datasets, the result and accuracy can deviate
ANN with PSO [24, 37–39]	2012	92.36%	Medium	It was used on the tumour cells. Also implemented on the breast cancer datasets
Particle swarm optimization (PSO) integrated with seeker optimization algorithm (SOA) [25]	2013	~93%	Medium	Liver tumours were analysed and classified
Deep learning [26]	2020	NA	Medium	Using multiomics data for cancer classification

The research article [40, 52] utilized perceptron networks as a key component. This approach was applied to analyze 4026 genes in cases of large B-cell lymphoma. By employing this approach, the identification of cancer achieved a precision rate of 93%, demonstrating high accuracy. While the outcome is satisfactory, when dealing with extensive datasets and intricate values, the level of accuracy may diminish.

3. Proposed Methodology

Various researchers have put forth a range of Convolutional Neural Networks (CNNs) up until now. Each of the models concentrated on distinct factors to simulation of genetic transcription. In earlier research, scientists typically used the sequence of genes as input and aimed to improve the order of these genes to make more accurate predictions. This suggested approach combines CNN with neural pattern recognition to form a unified methodology.

Pattern recognition refers to the skill of recognizing and distinguishing between mathematical symbols, punctuation marks, and printed letters. This model provides a convenient method for structuring the classification issue, although it may lack flexibility and oversimplify the matter. However, it does enable the identification and exploration of numerous notable challenges.

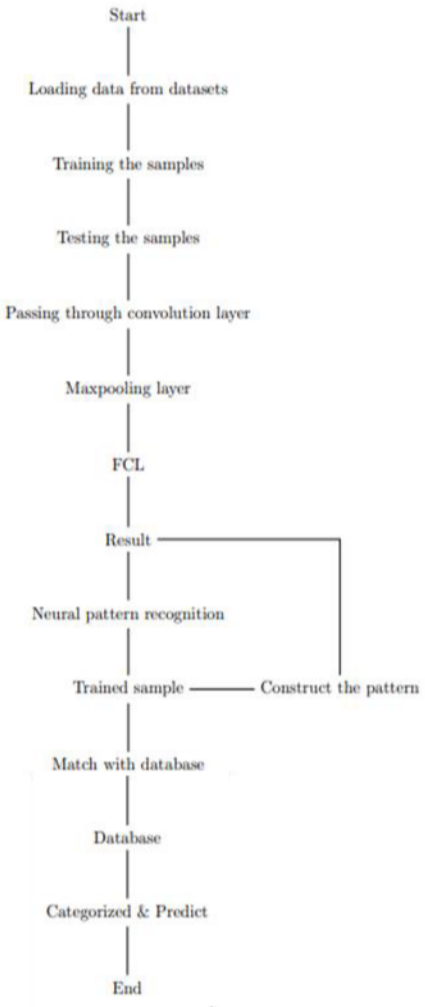

Fig 4: Overall flowchart of the proposed model

Sample size	Kernel	Mean trained score	Mean test score
30	8	0.054	0.197
30	16	0.032	0.167
30	32	0.014	0.132
30	64	0.009	0.121
50	8	0.072	0.196
50	16	0.034	0.154
50	32	0.019	0.141
50	64	0.011	0.132
75	8	0.092	0.189
75	16	0.068	0.163
75	32	0.031	0.145
75	64	0.023	0.137
85	8	0.103	0.178
85	16	0.087	0.156
85	32	0.054	0.143
85	64	0.038	0.129
100	8	0.128	0.172
100	16	0.096	0.154
100	32	0.073	0.142
100	64	0.046	0.121
110	8	0.131	0.167
110	16	0.098	0.154
110	32	0.081	0.136
110	64	0.052	0.120
125	8	0.147	0.159
125	16	0.100	0.141
125	32	0.79	0.129
125	64	0.51	0.117

Table2: Trained and testing parameters for CNN.

Pattern recognition utilizes machine learning techniques to automatically detect and comprehend consistent patterns and regularities within data.

3.1. Proposed Convolution Neural Network: According to studies, CNN models have proven to be highly effective in accurately categorizing various computer vision tasks. These findings suggest that it might be worthwhile to explore the implementation of CNN models for analyzing biological datasets. In this suggested approach, a sole layer of convolution is employed, avoiding the use of multiple layers. The CNN model works with input data represented as directions. And then applies a uni-dimensional kernel operation to process and analyze the input [36,41,42]. First, the genetic information, known as gene expression, is transformed into a numerical representation called a vector. This vector is then processed using a one-dimensional kernel method. The output of this processing is then fed into a max-pooling layer in a convolutional neural network (CNN). This max-pooling layer helps extract the most important features from the processed data. The output from the max-pooling layer is then connected to a fully connected layer (FCL), which helps to further analyze and understand the extracted features. Finally, a prediction layer is used to make predictions or draw conclusions based on the information gathered throughout the entire process as depicted on Figure 2. Aim of cancer detection is to categorize different types of tumors and discover unique characteristics for each cancer. This enables the development of a smart system that can recognize specific spreading tumor types or detect cancer in its initial stages.

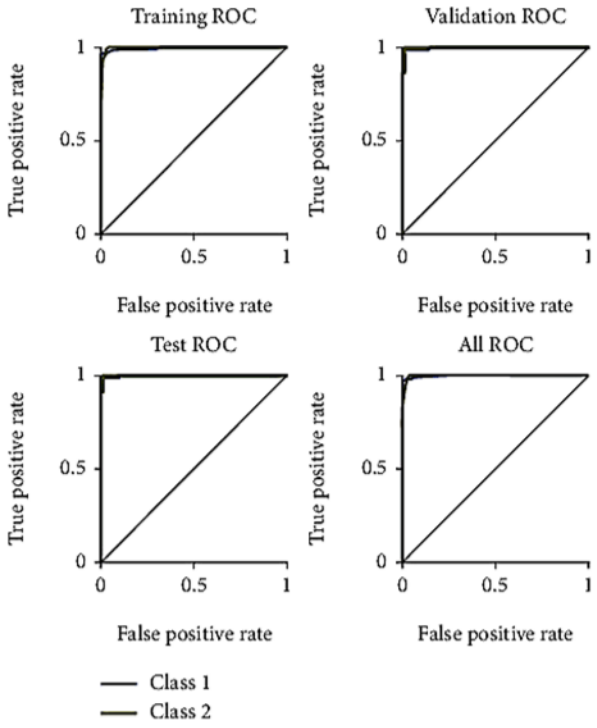

Fig 5: NPR training and test results.

Cancer prediction focuses heavily on determining the likelihood of developing cancer, the chances of cancer returning, and the expected outcome or outlook of the disease. One facet of artificial intelligence referred to as deep learning revolves around the utilization of neural networks featuring multiple layers. This design enhances its capacity for advanced learning and yields more precise outcomes by harnessing cutting-edge techniques such as extensive analysis of vast datasets. Various convolutional neural network (CNN) architectures have been put forth for the purpose of classifying cancer types, with each model highlighting distinct facets of genetic data pertinent to cancer. The input vectors undergo processing in the convolutional layer, followed by the application of the downsampling layer, and finally, they are passed through a fully connected layer. The ultimate result consists of forecasts but with varying set of parameters. In the initial stage, the computation of the gradient of output classes in relation to minute alterations is retained. Every input contributes to the creation of a map that can be utilized for understanding and analysis. The samples were subsequently classified and grouped based on their characteristics. A set of samples were used as input and matched with the dataset features to make predictions. This proposed approach, a genetic indicator with a score surpassing 0.65 is given attention. The selection of the layer size ranged from 30 to

125. Initially, the one-dimensional convolutional neural network (1-D CNN) underwent training using a dataset of 5000 diverse tumor samples. To proceed further, the system was divided, allocating 75% for training purposes and reserving 25% for testing.

3.2. Neural Pattern Recognition (NPR): Pattern recognition involves the utilization of machine learning algorithms to identify consistent patterns and resemblances within datasets. These similarities can now be identified through the examination of past records, the application of statistical techniques, or the utilization of the machine's existing knowledge [36,43,44]. It is necessary to subject the gathered data to filtration and preliminary processing stages. The arrangement is determined prior to selecting the appropriate approach among classification, reversion, and progression to identify and modify based on the numerical type [45,50].

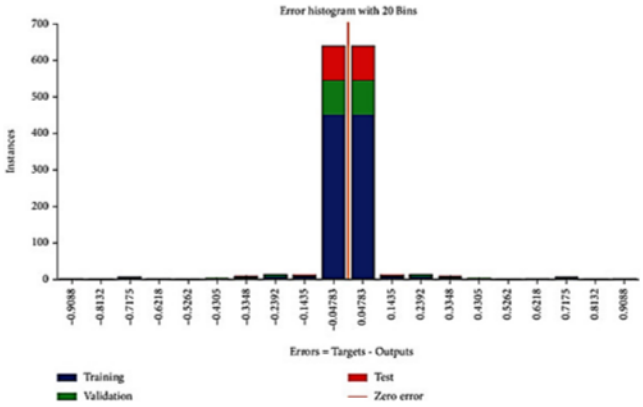

Figure 6: Error histogram

The process of perception can be divided into two fundamental categories: discerning tangible entities and acknowledging conceptual entities. Understanding spatial elements is vital for comprehending tangible objects. Some instances of spatial items include: unique patterns on fingertips, meteorological charts, visual representations, and tangible physical entities. Waveforms and signatures are examples of temporal entities. NPR acknowledging intangible concepts involves recalling a response to an inquiry, a past disagreement or dialogue, and so forth, essentially discerning entities that lack physical existence. Item recognition involves three sequential stages of processing: categorization of features, filtration of input, and identification of the item.

Substantial datasets are necessary to achieve favorable results since the software will consistently produce precise outcomes even with limited training data. There is a possibility that the results may differ when it comes to testing data. A collection of numerous photographs displaying individuals donning masks is necessary when developing a facial recognition system designed specifically for identifying masked faces [46]. The program will utilize the dataset to gather the relevant information. Typically, the training sample accounts for approximately 70 to 80 percent of the entire dataset.

As the precision of the training dataset is on the rise, a portion of the training dataset that the model is not familiar with is selected to determine if the accuracy of that particular subset is also showing improvement [47]. In such a scenario, it becomes crucial for the developer to carefully verify the parameter scores, as failure to do so could necessitate a reassessment of the entire model. Figure 3 depicts the sequential processes involved in identifying the pattern.

The general schematic of the proposed approach is depicted in Figure 4.

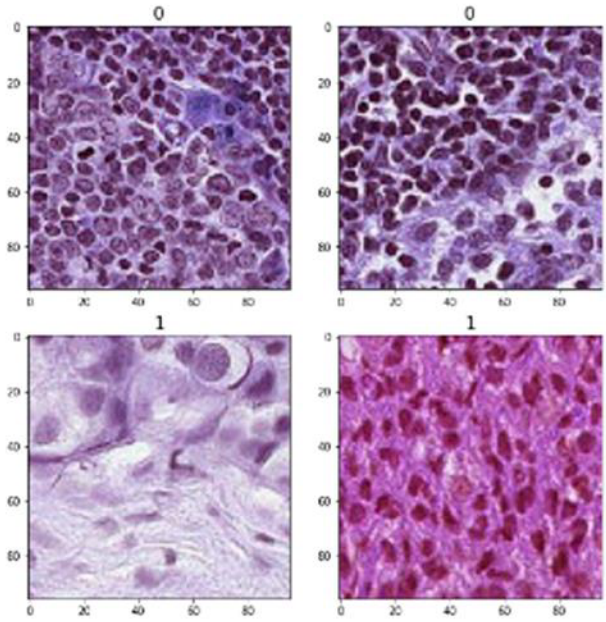

Fig 7: Weight diagram for different dataset inputs.

The initial stage involves the utilization of CNN to classify the datasets based on pattern anticipation. In the subsequent phase, NPR employs the identified pattern to further classify the datasets and facilitate pattern prediction.

4. Results

By exclusively training the deep learning machine on tumor samples and subsequently identifying genes associated with cancer, prior research either neglected the tissue origins during the classification of tumor samples or developed two separate models: one focusing solely on transcription factors, and another specifically designed for cancer-related genes (the tumor DL model). The information has been processed using exclusively tumor-related datasets.

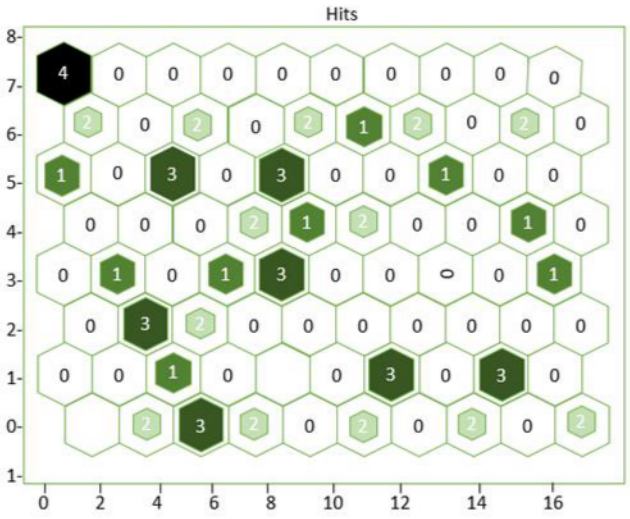

Fig 8: Hit matrix.

The collection consists of data related to breast cancer, kidney tissues, liver tissues, and the digestive systems. Table illustrates the parameters used for training and testing that are transmitted through the one-dimensional Convolutional Neural Network (CNN). Table 2 illustrates the parameters used for training and testing that are transmitted through the one-dimensional Convolutional Neural Network (CNN). During the categorization process, a significant mistake was identified in the database containing information about the liver and digestive tissues. This error occurred due to the unavailability of suitable datasets. The effectiveness of a classifier model is assessed using a measurement known as the ROC curve, which is alternatively termed the curve of receiver operating characteristics. ROC curve emphasizes the ability of the classifier model to correctly identify positive instances by depicting the proportion of true positives relative to false positives. The ROC curve is a useful tool for evaluating the effectiveness of classification methods at different threshold levels. It provides a measure of efficiency in distinguishing between classes. The AUC (Area Under the Curve) serves as a quantification of how well separable a given measure is, while the ROC (Receiver Operating Characteristic) denotes a graphical representation of the probability. The area under the curve of the receiver operating characteristic (ROC) curve offers valuable information regarding the benefits of utilizing the test to address the fundamental question. ROC curves are commonly employed to visually depict the interplay and compromise between sensitivity and specificity. Figure 5 displays the outcomes of the NPR study, showcasing highly favorable results that have been confirmed and verified using the ROC method. Indeed, the figure has depicted varying rates for both true positives and false positives. Through the evaluation of the proportion of accurate positive predictions relative to incorrect positive predictions, the ROC curve demonstrates the classifier model's ability to differentiate between classes. The ROC curve serves as a performance indicator for classification tasks across various threshold levels, gauging the effectiveness of the model. AUC signifies the degree or assessment of distinguishability, while ROC is a curve that illustrates probabilities. This demonstrates the model's ability to efficiently discern among various classifications. The advantages of employing the examination to address the real inquiry become apparent through the calculation of the area beneath the ROC curve. The histogram depicting the errors in the results accurately represents the values. Figure 6 displays the errors. Figure 7 displays the respective inputs labeled as 1, 2, 3, and 4, representing the weight values associated with various datasets, namely liver, kidney, breast, and digestive. The hit matrix (Figure 8) provides a clear indication of the most favorable probability for accurately forecasting the pattern value. In this situation, the highest possible value falls within the range of 9 and 10, specifically at 4, with a precision level of 94%. The connection between weight 1 and weight 2 can be observed in the diagram presented in Figure 9. This suggests that the weights have a crucial role in the neural network system, helping it recognize the connections between various parameters, as depicted in Figure 9. Now, different sets of data are analyzed to assess the performance of the system and determine its accuracy. Table 3 presents the results obtained with various datasets.

Cancer is widely recognized as one of the most devastating illnesses. Early detection of cancer is crucial for effective treatment. The aim of achieving early cancer detection is to swiftly identify individuals experiencing symptoms, enabling them to receive timely treatment and enhance their chances of successful recovery. By providing timely healthcare services, detecting cancer at an early stage leads to better treatment results, making it an essential strategy for public health in every situation. Prompt diagnosis is one strategy, whereas assessment is another approach. This refers to the potential identification of undiscovered illnesses among a group of individuals who seem to be in good health and without any apparent symptoms. This can be achieved through affordable and efficient tests, evaluations, or other methods applied to the specific population.

Cancer data consists of numerous or countless genes. The expression level of genes is assessed using a DNA microarray. Analyzing microarray gene expression data can be quite difficult due to its distinctive and overwhelming characteristics. Identifying appropriate genes from a vast pool of millions of genes is a challenging task.

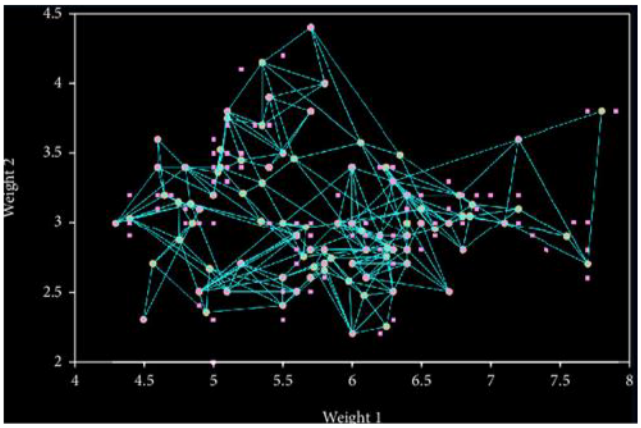

Fig 9: Relation between different parameters with weights.

Table 3: Accuracy with different datasets.

Dataset	Trial	Accuracy
Kidney Cancer	20	96.01%
Breast Cancer	20	95.1%
Liver tissues	20	93.2%
Liver Cancer	20	92.4%
Mixed data	50	94.01%

Researchers are utilizing machine learning and statistical techniques such as decision trees, k-nearest neighbors, support vector machines, and neural networks to precisely examine tumors. These advanced techniques aid in effectively classifying and understanding tumors [48]. Numerous researchers have shown a keen inclination towards employing neural networks for the purpose of categorizing diverse types of cancer cells [49]. Most neural networks are highly effective at correctly categorizing cancerous cells. This suggested approach effectively analyzes the information and accurately forecasts cancer occurrences, achieving a 94% precision rate. Due to the progress made in protein, genetic, and advanced imaging techniques, it is now feasible to predict cancer with greater accuracy by collecting detailed molecular information. Many of the conventional methods employed in medical environments to predict cancer are riddled with shortcomings and create ambiguity, whereas the utilization of micro gene-level diagnostics leads to significantly improved outcomes. Based on the study, CNN models are utilized to achieve more accurate categorizations in different visual analysis tasks. Therefore, it is logical to try and use them on biological datasets. Early detection plays a vital role in ensuring the most effective treatment for cancer. Cancer is composed of a vast number of genes, ranging from thousands to millions, that hold crucial information about the disease. A DNA microarray is employed for measuring the levels of genetic markers.

5. Conclusion

Several researchers have integrated neural network methodologies with optimization algorithms like Particle Swarm Optimization (PSO) in order to further enhance accuracy. These techniques are employed to reduce the number of dimensions, narrow down the search area, and consequently shorten the time required for training neural networks. FLANN by itself achieves an accuracy rate of 63.4 percent, whereas when combined with PSO, the categorization rate increases to 92.36 percent. To enhance the reliability of our cancer predictions and assist in their comprehension, our study encompassed several noteworthy subjects. To explore an effective method for identifying cancer types using unstructured gene-based expressions, various convolutional neural network (CNN) designs were suggested. We have developed a unique CNN-NPR structure that utilizes complex gene expression data to accurately determine the type of cancer, considering the tissue it originates from. The specimens encompass information concerning gastrointestinal systems, kidney tissues, liver tissues, and tissues from breast cancer. ROC offers and confirms highly favorable results. Identifying important genes from the vast pool of millions of genes can be a daunting task. Machine learning models like classification trees, k-nearest neighbours, support vector machines, and artificial neural networks are being utilized to accurately depict tumors. The suggested approach, characterized by a streamlined CNN-NPR design and reduced reliance on tissue origin compared to previous research, data's accuracy in predicting is at a commendable 94%. We can utilize the CNN-NPR framework to elucidate distinct cancer signals for each cancer type, with the objective of further improving and refining it in the times ahead. The ultimate objective is to identify markers that can aid in the early detection of cancer. To enhance the precision of neural networks in future research, it is advisable to augment the quantity of intermediate neurons within the hidden layer. There are various techniques that can be employed to enhance the efficiency of the classifier during the training process of an Artificial Neural Network (ANN).

Data Availability

The corresponding author can provide the data used in this study upon receiving a request.

Conflicts of Interest

The authors assert that they have no competing interests..

References

[1] Y. Wang, F. S. Makedon, J. C. Ford, and J. Pearlman, "HykGene: a hybrid approach for selecting marker genes for phenotype classification using microarray gene expression data," Bioinformatics, vol. 21, no. 8, pp. 1530–1537, 2005.

[2] T. Thakur, I. Batra, M. Luthra et al., "Gene expression-assisted cancer prediction techniques," Journal of Healthcare Engineering, vol. 2021, Article ID 4242646, 9 pages, 2021.

[3] S. Kaur and G. Kaur, "Threat and vulnerability analysis of cloud platform: a user perspective," in 2021 8th International Conference on Computing for Sustainable Global Development (INDIACom), pp. 533–539, New Delhi, India, 2021.

[4] K. Kourou, T. P. Exarchos, K. P. Exarchos, M. V. Karamouzis, and D. I. Fotiadis, "Machine learning applications in cancer prognosis and prediction," Computational and Structural Biotechnology Journal, vol. 13, pp. 8–17, 2015.

[5] Y. Wang, I. V. Tetko, M. A. Hall et al., "Gene selection from microarray data for cancer classification--a machine learning approach," Computational Biology and Chemistry, vol. 29, no. 1, pp. 37–46, 2005.

[6] G. Jindal and G. Kaur, "A comprehensive overview of quality enhancement approach-based biometric fusion system using artificial intelligence techniques," Communication and Intelligent Systems, vol. 204, pp. 81–98, 2021.

[7] S. Chaudhury, N. Shelke, K. Sau, B. Prasanalakshmi, and M. Shabaz, "A novel approach to classifying breast cancer histopathology biopsy images using bilateral knowledge distillation and label smoothing regularization," Computational and Mathematical Methods in Medicine, vol. 2021, Article ID 4019358, 11 pages, 2021.

[8] S.-B. Cho and H.-H. Won, "Cancer classification using ensemble of neural networks with multiple significant gene subsets," Applied Intelligence, vol. 26, no. 3, pp. 243–250, 2007.

[9] Y. Hu, K. Ashenayi, R. Veltri, G. O'Dowd, G. Miller, and H. R. Bonner, "A comparison of neural network and fuzzy c-means methods in bladder cancer cell classification," in Proceedings of 1994 IEEE International Conference on Neural Networks (ICNN'94), pp. 3461–3466, Orlando, FL, USA, 1994.

[10] P. H. Levine, K. Ajmera, B. O'Neill, V. Venkatesh, P. Garcia-Gonzalez, and H. J. Hoffman, "Demographic factors related to young age at diagnosis of chronic myeloid leukemia in India," Clinical Epidemiology and Global Health, vol. 4, no. 4, pp. 188–192, 2016.

[11] A. Elfiky, M. J. Pany, R. B. Parikh, and Z. Obermeyer, "Development and application of a machine learning approach to assess short-term mortality risk among patients with cancer starting chemotherapy," JAMA Network Open, vol. 1, no. 3, article e180926, 2018.

[12] S. L. Bangare, G. Pradeepini, and S. T. Patil, "Implementation for brain tumor detection and three dimensional visualization model development for reconstruction," ARPN Journal of Engineering and Applied Sciences (ARPN JEAS), vol. 13, no. 2, pp. 467–473, 2018.

[13] K. A. Tran, O. Kondrashova, A. Bradley, E. D. Williams, J. V. Pearson, and N. Waddell, "Deep learning in cancer diagnosis, prognosis and treatment selection," Genome Medicine, vol. 13, no. 1, 2021.

[14] Y. Tang, Y.-Q. Zhang, Z. Huang, H. Xiaohua, and Y. Zhao, "Recursive fuzzy granulation for gene subsets extraction and cancer classification," IEEE Transactions on Information Technology in Biomedicine, vol. 12, no. 6, pp. 723–730, 2008.

[15] S. Akanksha and K. Parminder, "Optimized liver tumor detection and segmentation using neural network," International Journal of Recent Technologyand Engineering(IJRTE), vol. 2, no. 5, pp. 7–10, 2013.

[16] H.-H. Won and S.-B. Cho, "Paired neural network with negatively correlated features for cancer classification in DNA gene expression profiles," in Proceedings of the International Joint Conference on Neural Networks, 2003, pp. 1708–1713, Portland, OR, USA, 2003.

[17] R. Xu, X. Cai, C. Donald, and I. I. Wunsch, "Gene expression data for DLBCL cancer survival prediction with a combination of machine learning technologies," in 2005 IEEE Engineering in Medicine and Biology 27th Annual Conference, pp. 894–897, Shanghai, China, 2005.

[18] V. Bevilacqua, G. Mastronardi, F. Menolascina, P. Pannarale, and A. Pedone, "A Novel Multi-Objective Genetic Algorithm Approach to Artificial Neural Network Topology Optimisation: The Breast Cancer Classification Problem," in The 2006 IEEE International Joint Conference on Neural Network Proceedings, pp. 1958–1965, Vancouver, BC, Canada, 2006.

[19] L. Ziaei, A. R. Mehri, and M. Salehi, "Application of artificial neural networks in cancer classification and diagnosis prediction of a subtype of lymphoma based on gene expression profile," Journal of Research in Medical Sciences, vol. 11, no. 1, pp. 13–17, 2006.

[20] H. Takahashi, Y. Murase, T. Kobayashi, and H. Honda, "New cancer diagnosis modeling using boosting and projective adaptive resonance theory with improved reliable index," Biochemical Engineering Journal, vol. 33, no. 2, pp. 100–109, 2007.

[21] D. M. Joshi, N. K. Rana, and V. M. Misra,

"Classification of brain cancer using artificial neural network," in 2010 2nd International Conference on Electronic Computer Technology, pp. 112–116, Kuala Lumpur, Malaysia, 2010.

[22] P. Rajeswari and G. S. Reena, "Human liver cancer classification using microarray gene expression data," Proceedings of International Journal of Computer Applications, vol. 34, no. 6, pp. 25–37, 2011.

[23] B. Sahu and D. Mishra, "A novel feature selection algorithm using particle swarm optimization for cancer microarray data," Procedia Engineering, vol. 38, pp. 27–31, 2012.

[24] S. Swathi, G. Anjan Babu, R. Sendhilkumar, and S. N. Bhukya, "Performance of ART1 network in the detection of breast cancer," Proceedings of International conference on Computer design and Engineering (ICCDE 2012), vol. 49, pp. 100–105, 2012.

[25] M.S Kumar, "Prediction of Heart Attack from Medical Records Using Big Data Mining", International Journal of Intelligent Systems and Applications in Engineering, 2023, 11(4s), pp. 90–99.

[26] M.S Kumar, "Nature-Inspired Optimisation-Based Regression Based Regression to Study the Scope of Professional Growth in Small and Medium Enterprises, International Journal of Intelligent Systems and Applications in Engineering, 2023, 11(4s), pp. 100–108.

[27] Natarajan, V.A., "Improving QoS in Wireless Sensor Network routing using Machine Learning Techniques", Proceedings of the 1st IEEE International Conference on Networking and Communications 2023, ICNWC 2023, 2023.

[28] M.S Kumar, "Chronic Kidney Disease Prediction Using Machine Learning", Journal of Advances in Information Technology, 2023, 14(2), pp. 384–391.

[29] D Ganesh, "Deep Convolution Neural Network Based solution for Detecting Plant Diseases", Journal of Pharmaceutical Negative Results, 2022, 13, pp. 464–471

[30] D Ganesh, "Implementation of Novel Machine Learning Methods for Analysis and Detection of Fake Reviews in Social Media", 2nd International Conference on Sustainable Computing and Data Communication Systems, ICSCDS 2023 - Proceedings, 2023, pp. 243–250

[31] Ganesh, D., Kumar, T. P., & Kumar, M. S. (2021). Optimised Levenshtein centroid cross-layer defence for multi-hop cognitive radio networks. IET Communications, 15(2), 245-256.

[32] Sushama et.al, "Impact of COVID-19 pandemic and the diagnosis of the virus in the human body",World Journal of Engineeringthis link is disabled, 2022, 19(5), pp. 652–657

[33] Anantha Natarajan, V., Kumar, M. S., & Tamizhazhagan, V. (2020). Forecasting of Wind Power using LSTM Recurrent Neural Network. Journal of Green Engineering, 10.

[34] Sushama et.al, Automated extraction of non-functional requirements from text files: A supervised learning approach", Handbook of Intelligent Computing and Optimization for Sustainable Development, 2022, pp. 149–170D.

[35] A. Omondiagbe, S. Veeramani, and A. S. Sidhu, "Machine learning classification techniques for breast cancer diagnosis," IOP Conference Series: Materials Science and Engineering, vol. 495, article 012033, 2019.

[36] S Girinath,"Deep Learning-based Segmentation and Computer Vision-based Ultrasound Imagery Techniques", 2023 Fifth International Conference on Electrical, Computer and Communication Technologies (ICECCT),DOI: 10.1109/ICECCT56650.2023.10179723, ISBN:978-1-6654-9361-1, 2023.

[37] Sushama, C.," Global Identification Passport: A Unique Cloud based Passport Model", Proceedings - 5th International Conference on Smart Systems and Inventive Technology, ICSSIT 2023, 2023, pp. 801–805

[38] M. S. Kumar, "AI-driven cybersecurity modeling using quantum computing for mitigation of attacks in IOT-SDN network", Quantum-Safe Cryptography Algorithms and Approaches: Impacts of Quantum Computing on Cybersecur, 2023, pp. 37–47.

[39] M. S. Kumar, "Power aware virtual machine placement in IaaS cloud using discrete firefly algorithm", Applied Nanoscience (Switzerland)this link is disabled, 2023, 13(3), pp. 2003–2011.

[40] Natarajan, V.A., "Improving QoS in Wireless Sensor Network routing using Machine Learning Techniques", Proceedings of the 1st IEEE International Conference on Networking and Communications 2023, ICNWC 2023, 2023T. O. Nielsen, R. B. West, S. C. Linn et al., "Molecular characterisation of soft tissue tumours: a gene expression study," Lancet, vol. 359, no. 9314, pp. 1301–1307, 2002.

[41] K. Jyothi Prakash. "Internet of things: IETF protocols, algorithms and applications." Int. J. Innov. Technol. Explor. Eng 8.11 (2019): 2853-2857.

[42] Sangamithra, B. "A memetic algorithm for multi objective vehicle routing problem with time windows." 2017 IEEE International Conference on Electrical, Instrumentation and Communication Engineering (ICEICE). IEEE, 2017.

[43] P. S. Nelson, N. Clegg, H. Arnold et al., "The program of androgen-responsive genes in neoplastic prostate epithelium," Proceedings of the National Academy of Sciences of the United States of America, vol. 99, no. 18, pp. 11890–11895, 2002.

[44] Y. Guo, X. Shang, and Z. Li, "Identification of cancer subtypes by integrating multiple types of transcriptomics data with deep learning in breast cancer," Neurocomputing, vol. 324, pp. 20–30, 2019.

[45] S. Chatterjee, A. Iyer, S. Avva, A. Kollara, and M. Sankarasubbu, "Convolutional neural networks in classifying cancer through DNA methylation," 2018, https://arxiv.org/abs/1807.09617.

[46] Z. Si, H. Yu, and Z. Ma, "Learning deep features for DNA methylation data analysis," IEEE Access, vol. 4, pp. 2732–2737, 2016.

[47] Y. C. Chiu, H. H. Chen, T. Zhang et al., "Predicting drug response of tumors from integrated genomic profiles by deep neural networks," BMC Medical Genomics, vol. 12, Supplement 1, p. 18, 2019.

[48] P. Luo, Y. Ding, X. Lei, and F. X. Wu, "deepDriver: predicting cancer driver genes based on somatic mutations using deep convolutional neural networks," Frontiers in Genetics, vol. 10, p. 13, 2019.

[49] Y. C. Chiu, H. I. H. Chen, A. Gorthi et al., "Deep learning of pharmacogenomics resources: moving towards precision oncology," Briefings in Bioinformatics, vol. 21, no. 6, pp. 2066–2083, 2019.

[50] S. Depuru, K. Santhi, K. Amala, M. Sakthivel, S. Sivanantham and V. Akshaya, "Deep Learning-based Malware Classification Methodology of Comprehensive Study," 2023 International Conference on Sustainable Computing and Data Communication Systems (ICSCDS), Erode, India, 2023, pp. 322-328, doi: 10.1109/ICSCDS56580.2023.10105027.

[51] S. Depuru, S. Sivanantham, K. Amala, V. Akshaya, M. Sakthivel and P. S. Kusuma, "Empirical Study of Human Facial Emotion Recognition: A Deep Learning," *2023 International Conference on Computer Communication and Informatics (ICCCI)*, Coimbatore, India, 2023, pp. 1-6, doi: 10.1109/ICCCI56745.2023.10128492.

[52] Sivakumar Depuru , Anjana Nandam , P.A. Ramesh , M. Saktivel , K. Amala , Sivanantham, "Human Emotion Recognition System Using Deep Learning Technique", Journal of Pharmaceutical Negative Results, vol. 13, no. 4, pp. 1031–1035, Nov. 2022.

[53] K. Pujitha , Kattamanchi Prem Krishna , K. Amala , Annavarapu Yasaswini , Sivakumar Depuru , Kopparam Runvika, "Development of Secured Online Parking Spaces", Journal of Pharmaceutical Negative Results, vol. 13, no. 4, pp. 1010–1013, Nov. 2022.

[54] Kulkarni, L. . (2022). High Resolution Palmprint Recognition System Using Multiple Features. Research Journal of Computer Systems and Engineering, 3(1), 07–13. Retrieved from https://technicaljournals.org/RJCSE/index.php/journal/article/view/35

[55] G, M. ., Deshmukh, P. ., N. L., U. K. ., Macedo, V. D. J. ., K B, V. ., N, A. P. ., & Tiwari, A. K. . (2023). Resource Allocation Energy Efficient Algorithm for H-CRAN in 5G. International Journal on Recent and Innovation Trends in Computing and Communication, 11(3s), 118–126. https://doi.org/10.17762/ijritcc.v11i3s.6172

Samdarshi
ISSN: 2581-3986
Vol 16 Issue 2 (June 2023)

Soft Skills and Personality Development– A Gate Way for Employment

Dr. K. Suneetha Reddy
Professor & HoD
Department of English
Sri Venkateswara College of Engineering
Tirupati
e-mail: drsuneetha18@gmail.com

ABSTRACT:

A person's personality is the culmination of all of their interactions and reactions to the world. Personality refers to everything that makes a person stand out in a crowd, the things that make them special. Characteristics that set a person apart are long-lasting patterns of emotions, ideas, and actions. In the higher education stratum, personality development is increasingly becoming an important competent of a student's evolution. The goal of personality development is to enhance an entity or a group of qualities that contribute to one's accomplishments and improved self-presentation, rather than to focus only on one part of an individual.

Soft skills are the amalgamation of abilities that crafts a person's aptitude to become accustomed into a meticulous composition. Students that possess soft skills have a solid conceptual and practical foundation for creating, leading, and developing teams. Learning by doing will be the main focus. This essay aims to emphasize the value of developing soft skills training to help you have a mature personality. The students' general personalities are developed and they make a strong positive impression in intellectual and social circles, which improves their chances of landing a good job.

Keywords: personality, soft skills self-esteem, faith, confidence, leadership, stress management, career

Introduction:

"The education system must aim towards employability and ensure quality in education. There is a large gap in the availability of employable skills. To bridge the gap, an interface is needed between the school curriculum and the needs of the industry." Dr. A.P.J. Abdul Kalam

Skill is defined as an ability to perform well from one's knowledge. Skills differ from person to person. The skills which are needed to get into the job and sustain the job for long without any problems are called employability skills. "Skill gap is defined as a difference between skills acquired by the graduates through the academic course and the entry-level skills expected by the employers". (Neha, 2015) According to MHRD (2014), the 12th five-year plan 2012-2017 has emphasized the importance of higher education for the growth of the economy. "Higher education equips people with knowledge, skills and abilities that make them a part of the productive workforce of the nation. The economic well-being of the country can only be realized with the higher intellectual and professional capabilities of its citizens". (Neha, 2015)

"At present, the Indian youth have more of un-employability rather than unemployment problem. Although there are many employment opportunities, students are not able to grab jobs as they are not equipped with employability skills. There are several reasons for the present unemployment status of the Indian youth". (Rao, 3) They lack corporate experience resulting into course content which is more tilted towards theory rather than practice. For the past ten years, i.e., since 2006, there has been a steep increase in the number of affiliated technical colleges under JNTU. As the technical colleges are mushrooming, there is a decline of required skills in the students due to various reasons like unhealthy student-teacher ratio, lack of infrastructure, etc. In fact, there is a gap between theory and practice in our current Indian Education System. Theory can be learnt through reading books, whereas practical knowledge cannot be learnt in the same way. It has to be learnt only through rigorous practice. Therefore, blending both theory and practical knowledge into the Indian educational system is the need of the hour to enhance employability skills among Indian youth. One can acquire employability through Soft Skills. Soft Skills are also

a part of employability skills as these skills help in acquiring employment. According to Rao (Pg. 3) people often think of Soft Skills as communication skills; in fact, there are other skills beyond the communication skills. Basic skills such as arithmetic and reasoning help with critical thinking skills.

Importance of Soft Skills

Soft Skills are all about skills, abilities and traits pertaining to personality, attitude and behaviour that help in non-technical and non-domain skills**.** According to Wikipedia "Soft Skills refer to a cluster of personal qualities, habits, attitudes, and social graces that make someone a good employee and sound practical judgment based on experience rather than theory".

The Collins English Dictionary defines the term Soft Skills as "desirable qualities for empathy, life skills, people skills, social intelligence, social skills, and theory of multiple intelligences, 21st-century skills and vocational skills".

Parasuram & Hariprasad (2015) viewed that there is a collection of several Soft Skills such as team building, leadership skills, self-motivation, time management, interpersonal skills, presentation skills, positive attitude, lifelong learning skills, professional ethics, etc. There are nearly sixty Soft Skills which everyone should know in order to progress well in their work environment. These skills are also known as people skills, emotional intelligence, social skills and interpersonal skills. During the recruitment, industry sources reveal that only one in five recruited possesses Soft Skills. This shows that many neither posses nor have awareness of Soft Skills.

The need for Imparting Soft Skills in the Curriculum

Soft Skills are basically behavioural characteristics which would help an organization to maintain its harmonious journey. The word *soft* has been added to the skills which is routinely used in the organizations, as it softens the business operations of an enterprise. The softness in the daily transactions acts as a lubricant, which in turn reduces the frictions while carrying out several operational transactions. Soft-skills gained momentum in the 20th century due to its growing demand for an organization's effectiveness. It has been deliberated in various industry and academia that Soft Skills have to be brought into the curriculum design. All Universities and Industries involved into higher education have understood the importance of imparting Soft Skills in their institutions at student level so as to help the students' secure related employment. Soft Skills may not entirely work in isolation unless they are accompanied well by hard skills. Hard skills are actual job functional skills which are required for any organization.

Teaching Language by Imparting Employability Skills

"Language as system enables the language user to combine phonemes to form words, words to form phrases, phrases to form sentences and sentences to form spoken or written texts - each unit following its own rules as well as the rules for the combination. It is very crucial to understand language, then, there is the idea of *system activity.* Language as a system, however, is much more complex than the description. A true understanding of the complexity of language requires a robust method of analysis. More than anybody else in the modern era, it is Chomsky, who has persuasively demonstrated that language as a system is amenable to scientific analysis and in doing so, he has elevated our ability to deal with language as a system to a higher level of sophistication." (Vidyulatha, P26)

One cannot imagine this world without a language. It is proved in history that when people used signals and sounds to communicate, this world got the gift of change. Growth of oneself and the society is possible by exchanging ideas which needs a common language. Due to development in technology there is an appalling need of a common language which connects people of different languages. Due to colonialism by Britishers it is observed existence of English language almost in every part of the world. Hence English serves as a communicator for mankind and in near prospect there is no replacement for English.

Globalisation has altered the way in which various sectors, both public and private, view the English language. The need to learn English to be a part of the global community has led to emphasis on the communicative aspects of the language. Several disciplines that had previously disregarded the importance of English have now started incorporating language modules into their course components. Irrespective of one's discipline or profession, one's ability to communicate in English is of paramount importance now. English language pedagogy has turned more communication-oriented to career to these new demands. Consequently, English language studies have started prioritizing the communicative aspects of English over the traditional linguistic and literary aspects. English is the language most people use for professional communication. It has become essential for those on the verge of entering the job market to master English and related job skills.

Professional students should possess English language skills to survive in the competitive world. They need some additional guidance from teachers or trainers. Even trainers need to follow a systematic training to teach the learners. This research has potential to focus on tools to be used by a trainer in the classroom while teaching English. This research checks viability of the use of language lab for language learning. It is a study how we can teach English as a second language easily with the help of computer technology and task-based teaching.

In most of the foreign countries language laboratories are in use and they are of great help for second language students. This research shows a new direction of teaching English. In some institutes there are language laboratories but due to lack of proper training and knowledge labs are very rarely used and sometimes not used properly. For English trainers this research shows new ways for a successful, impulsive and reminiscent teaching which enables students to face their placements. It also elucidates proper utilization of English lab. English language lab here refers both Multi-media lab and activity-based lab. The research also recommends few training programmes like Train The Trainers (TTT) and Faculty Development Programmes (FDP) for trainers. Efficient and qualified language teacher is necessary for conducting lab sessions as one has to deal with teaching as well as technology (language software).

A second language learner can be from different vernacular background. So for teaching a language either in a class or in English language laboratory a trainer must espouse different teaching methods. After research this study finds suitable method for teaching English as a second language through language lab and activity-based lab. There is a comparison of two batches within a class. One batch is taught English language through conventional method and other is taught in English language lab. Many training and learning troubles are identified, ensured and unravelled here. It proves how computerized software confines the limitations and effective usage of technology for the growth of an individual which leads to growth of an organization. It showcases the importance of trainer and technology in teaching-learning process.

The English term 'Communication' evolved from Latin words 'Communis and communicare' related to the word communication. Communis is noun word, which means common, communality or sharing. Similarly, communicare is a verb, which means 'make something common'. Some scholars relate the term communication with an English word community. Community members have something common to each other. Communities are {supposed to be} formed with the tie of communication. It is the foundation of community. Hence, where there is no communication, there can't be a community.

Communication is a complex process which does not end with the transmission of a message to a sender, but the feeling or idea that strikes the receiver is not known until we get feedback as a result. In corporate communication, the individuals who accomplish a task of effective management at different levels and stages initiate and undertake the right kind of communication at the appropriate time is the right communication that stimulates an institution to implement the organizational plans willingly and enthusiastically. The process of communication is affected by the backgrounds, experiences, objectives and aspirations that both sender and receiver have in common. The media of communication can be classified into five groups: written communication, oral communication, visual communication, audio-visual communication and computer-based communication. Written communication includes letters, circulars, memos, e-mails, reports, minutes, manuals etc. Oral communication includes face to face conversation, telephonic conversation, interviews, group discussions, meetings, conferences, seminars, announcements, speeches etc. Visual communication comprises of gestures,

facial expressions, tables, charts, graphs, diagrams, posters, slides, filmstrips etc. Audiovisual communication comprises of video conference, television and cinema with narration. Computer-based communication includes internet, E-mail, voice mail, FAX and all those we can do by using a mobile phone etc.

According to the Dale Carnegie, a few tips to be considered to improve communication in the workplace are as follows:

- Call persons by name
- Admit mistakes
- Show interest in your colleagues
- Praise them, from the general to the more specific
- Criticism can be given in a diplomatic way
- Speak in order to avoid misunderstanding
- Be humble and help others
- Try to understand other people's point of view

Soft Skills play an essential role in enhancing the student's outlook and thus making him or her job ready. Effective use of these Soft Skills in the areas of LSRW skills would help an individual focus on the work for organizational success. Soft Skills will fine-tune the students' attitudes, values, perception and overall personality. Candidates with better Soft Skills are most sought after by the industry as they prove more productive and prosperous to the organizations. Ideally, Soft Skills improve communication skills, interpersonal skills, group dynamics, teamwork, body language, manners and etiquettes which are helpful in creating a positive impact on an organization.

Personality is generally defined as the deeply ingrained and relatively enduring patterns of thought, feeling and behaviour. It is believed that personality emerges early and continues to change in meaningful ways throughout the lifespan. Adult personality traits are believed to have a basis in infant temperament, meaning that individual differences in disposition and behaviour appear early in life, possibly even before language or conscious self-representation develop. For example, in some situations a more aggressive personality could be beneficial, yet a more submissive personality could be beneficial in another situation.

Personality traits demonstrate moderate levels of continuity and individual differences in change, often late into the life course. This pattern is influenced by genetic, environmental, transactional and pedagogic factors. Personality development is a term which is often misunderstood to be self- development or just limited to enhancing one's own looks. Personality development is something which is considered as improving the way we think, feel, behave and carry ourselves. It is not confined to the improvement of a single aspect of an individual; rather it is about improving a cluster of qualities which helps in achieving and presenting oneself in a better way.

Conclusion

Presently Indian youth suffer from unemployability rather than unemployment problem. Although there are employment opportunities students are not able to grab jobs as they are not equipped with employability skills. In this cut throat competition everyone should possess soft skills

In the field of Engineering, opportunities are wide open for professionals who are trained and skilled. But students show least focus on the Soft Skills which are required for a successful career. The concept of Soft Skills is referred by different names in different countries such as employability skills, key competencies, key skills, essential skills, non-cognitive skills, workplace know-how skills, transferable skills etc.

REFERENCES

1. Damon, W (1983), Adolescent Personality and Identity Formation, Social and Personality Development, New York: W.W.Norton, pp 405.

2. Rao, M.S. "Enhancing employability in engineering and management students through Soft Skills", Industrial and Commercial Training.6.1 (2014) 42 – 48 Web: 20 May 2015
3. Bhatnagar, Neha. "Management Education and Employability: The Current Scenario." *Journal of Management & Research*. 9.2/4. (May 2015) Web.21 December 2015.
4. Parasuram, J & Hari Prasad, N. "Acquisition of Corporate Employability Skills: A Study with Reference to Engineering Graduates." The IUP Journal of Soft Skills. 9.2(2015) 23 - 45. Web: 19 September 2015.
5. Rao,M.S Soft Skills Enhancing Employability: Connecting Campus with Corporate New Delhi, I.K Publishing House Pvt. Ltd. 2010 Print.
6. Ramesh, Gopala Swamy and Ramesh, Mahadevan. *The Ace of Soft Skills –Attitude, Communication and Etiquette for Success*: India, Dorling Kindersley (India) Pvt Ltd 2013.Print https://en.wikiversity.org/wiki/soft_skills
7. Vidyullatha, T., Suneetha Reddy, K. The Criterion: An International Journal in English "Developing *Interpersonal Communication Skills for Increasing the Campus Placements of Engineering Students."* 6 .6 (2015).

JKPMHN Journal of Korean Academy of Psychiatric and Mental Health Nursing
ISSN:1225-8482 | E-ISSN:2288-4653 Vol. 5 No. 4 November (2023)
Pg. 277-282

STIMULATING LINGUISTIC INTELLIGENCE: THE NEED OF THE HOUR

Dr. K. Suneetha Reddy
Professor & HoD, Department of English, Sri Venkateswara College of Engineering
Tirupati, e-mail: drsuneetha18@gmail.com

ABSTRACT

The present day work scenario requires persons with global skills such as excellent communication skills, inter-cultural communication, inter-personal communication, intra- personal communication and logical aptitude apart from technical or core skills. Developing various intelligences at the scholastic level is a far-reaching goal. The curriculum should aim to create multifaceted, fully realized human beings who are prepared for the workforce. This can be done in an EFL classroom because EFL learning incorporates numerous different intelligences. The theory of Gardner comprised of seven basic intelligences, later added an eighth intelligences, later added an eighth intelligence type to the list, that of naturalist intelligence. Many of the studies on language learning also underline the importance of raising the students' self-esteem and awareness in the classroom, during the process of language learning. Therefore, it is very important for the language teacher to take into consideration, these various types of intelligence among the language learners and to exploit them fully, so that the outcome is not only development of the natural abilities of these learners but also the learners' sense of satisfaction that their skills and talents are appreciated.

Necessity is the mother of invention. Man has evolved and made enormous technical leaps since the beginning of time as a result of needs and necessary modifications. Working at an engineering college that serves a diverse range of students from all over the nation, each with varying financial, social, cultural, and educational backgrounds, sparked a strong desire to find teaching strategies that would enable students to become proficient communicators and language learners. When an individual acquires these competencies it will definitely boost the confidence and morale of the person. While dealing and interacting with the students, it became very vivid that each student had a unique social, economic financial, regional and cultural background which reflected in their performance. The common problem that was brought by the students other than nervousness, anxiety and fear was the lack of words or vocabulary due to which the students found it difficult to communicate in a successful and effective way.

The present day work scenario requires persons with global skills such as excellent communication skills, inter-cultural communication, inter-personal communication, intra- personal communication and logical aptitude apart from technical or core skills. It is far reaching to develop multiple intelligences at the academic level The goal of the curriculum should be to develop students into whole human beings with many intelligences that are ready for the workforce. Since many multiple intelligences are a part of EFL learning, this can be accomplished in an EFL classroom.

ISSN:1225-8482 | E-ISSN:2288-4653 Vol. 5 No. 4 November (2023)
Pg. 277-282

The Theory of Multiple Intelligences

The theory of multiple intelligences put forward by Howard Earl Gardner, an American developmental psychologist has its own recognition and importance in the field of academics as it can surely bring out the latent potentials and talents of the students in a class-room, when applied by the teacher. The results would be quiet amazing for both the students and the teacher as they together will comprehend the benefits of the theory. The work of Gardner is gauged as a successful treatise by many educators who are trying to implement the theory in the class-room to achieve the target, which is evidently the upliftment of the standards of a student. The education system is quite practical and so the students learn the concepts as they practice, which is astonishingly absent in the Indian system of education. But Howard's theory is relevant to all the class rooms in India, from the primary level to the graduate level. The English teacher especially should be given the freedom to enjoy the twin goals of conceptualization and realization of the theory of Gardner simultaneously in the classroom.

The theory of Gardner comprised of seven basic intelligences, later added an eighth intelligences, later added an eighth intelligence type to the list, that of naturalist intelligence. At the same time, he suggested the existence of a ninth intelligence type, that of existentialist intelligence (Gardner,H 1999). Gardner defines intelligence as an ability to solve problems or create products that are valued in at least one culture. To make it easier to remember, the characteristics of each of Gardner nine intelligence types, Thomas Armstrong introduced the following memory tags (Armstrong 1999):

Intelligences	**Memory Tags**
Linguistic	Word Smart
Musical	Music Smart
Logical	Number / Reasoning Smart
Spatial	Picture Smart
Bodily	Body Smart
Interpersonal	People Smart
Intrapersonal	Self Smart
Naturalist	Nature Smart

Linguistic Intelligence is the verbal and written ability of a student, which also encompasses the acumen to master many languages and use them efficiently to accomplish the goals. Linguistic Intelligence also includes a student's aptitude to make public speeches, write fiction or poetry and excel in communication skills and the ability to learn languages and to use language to accomplish certain goals. William Shakespeare, Mark Twain, Robert Frost and many other great writers and poets are said to possess this intelligence remarkably.

Musical Intelligence is the proficiency in the presentation of apiece of music and the ability to comprehend and appreciate various musical works of art. It also features the potential to recognize

ISSN:1225-8482 | E-ISSN:2288-4653 Vol. 5 No. 4 November (2023) Pg. 277-282

and possess knowledge on musical pitches, tones and rhythms. All singers and musicians fall under this category and this intelligence in students makes them participate in various activities related to music.

Logical –Mathematical Intelligence is the capacity to possess analytical and logical reasoning to solve mathematical problems which consequently will enhance problem-solving techniques of a student. It is mostly associated with scientists and mathematicians, but a language teacher also, by means of some interesting language activities can enhance the ability to think and discover mathematical patterns and designs. Special activities on vocabulary development like Code-breaker, Word-web, Language exercises based on Grammar and Analogy are fine illustrations where students get a fine opportunity to use their analytical thinking as they do in mathematics. Sir Issaac Newton, Galileo and Einstein were people endowed with logical or mathematical intelligence which made their name everlasting in their fields of study.

Spatial Intelligence involves the potential to recognize and use the patterns of wide space as well as the confined spaces for the accomplishment of the targets. It is the ability to represent or visualize the outer spatial world internally in the mind. Great painters and sculptors like Michelangelo and Picasso could imagine a larger work of art or creations to be represented on a small sheet of paper or wood.

Bodily-Kinaesthetic Intelligence is the prospective of using the physical body and its parts to solve problems or to get success in life. Intellectual capacities when coherently work with the body, it leads to the development of kinaesthetic intelligence. The task of the English teacher as it has extended to that of a communication skills trainer, she/he also should shoulder the responsibility of imparting the students' knowledge on body-language or kinesics, which plays a crucial role in the interview process. Individuals blessed with this intelligence excel in the fields of sports and arts. They can identify that they can become good sportsman or a good performer of arts on stage.

In language classroom students are observed by the English teacher, as they read passages, perform role-plays and participate in the discussions and tell those tips on good body language. The teachers can further instruct them to perform skits and mimes which makes them efficient in using various parts of their body effectively.

Interpersonal Intelligence is the concern of an individual towards the emotions and desires of others. It is essential to be nurtured from the childhood as he / she can learn to build harmonious relationships with their fellow men and women as they grow up. Team-work is an important attribute basically learnt in a language class-room. As they participate in the discussions, present debates and do chart works or present PPTs students learn to co-ordinate with the other members of the team appropriately. Sometimes, they also try to empathize with slow learners and motivate them towards the achievement of the tasks. This brings in co-ordination among the team players add with mutual concern and team effort they also learn problem-solving techniques. They possess excellent collaborative skills and can accomplish the tasks which are outside the class-room also.

ISSN:1225-8482 | E-ISSN:2288-4653 Vol. 5 No. 4 November (2023) Pg. 277-282

The names of the world leaders like Abraham Lincoln and Gandhi inspire the young generation in this aspect.

Intra-personal Intelligence is also about introspecting one's own feelings, strengths and weakness. According to Gardner, a teacher should be a role model to the students to leave behind effective and accurate notations into the society. SWOT analysis achieves amazing results in this regard.

Existentialist Intelligence is finally, concerned with people interested in philosophical issues such as the status of mankind in relation to universal existence. In learning situations, they need to see 'the big picture' in order to understand minor learning points and details.

Leonardo Da Vinci was a painter, sculptor, architect, musician, scientist, mathematician, engineer, inventor, anatomist, geologist, botanist and a writer. It is considered that he was a rare personality to have possessed all the eight essential multiple intelligences in the right proportions. The amazing fact also tells that it is not difficult to acquire all these intelligences, it is only determination and the effort that makes an individual possess multiple intelligences.

Need for a Reorientation

The trend in the realm of language teaching during the past two decades, clearly points out that many of the innovative language teaching methods and approaches have been benefitting from theories of humanistic psychology. Thus vindicate the latest findings of cognitive psychology and neurolinguistics programming, which indicate that children remember better what they have learned, provided all their senses are activated and prompted simultaneously during the learning process, be it a language or any other art. In the case of teaching a second language, these diverse teaching methods do not simply concentrate on the intellect of a language learner, to be offered a blend of cognitive and affective ways of learning a second language. These methods do express the interest in the learner as a total person with multiple abilities. Especially most of the so-called innovative teaching methodologies do take into consideration every individual learner of the language classroom.

Thus many of the studies on language learning also underline the importance of raising the students' self-esteem and awareness in the classroom, during the process of language learning. This can be paraphrased as, for a language class to be an effective and successful one, serving its own purposes, then the learners should feel themselves secure, supported, encouraged and considered by teachers. In this regard a reorientation of the conventional mindset of the language teachers is highly demanded. Taking this reorientation as an inevitable order of the day, this paper reiterates that the ESL classes can make it possible with the help of the theory of Multiple Intelligences, proposed by Howard Gardner (1983), by exploiting for good, the intelligences of the language learners.

Learners demonstrate diverse abilities and resources, and thus the ways of learning vary from pupil to pupil in a classroom with a population of mixed abilities. This is the major reason why the

ISSN:1225-8482 | E-ISSN:2288-4653 Vol. 5 No. 4 November (2023)
Pg. 277-282

language learners react in dissimilar ways to the activities given, and sometimes performed by the teacher in the class. The same activity receives different feedbacks from different groups in the class. This is obviously because some students enjoy working in groups while some prove to be much more dynamic and creative only when they left to work alone and are not comfortable when put in groups.

According to Gardner, a person's aptitude and capability in different types of intelligences may vary a great deal. Nevertheless, everyone has one or more of these intelligences, though in different people, one or more of these intelligences are more pronounced or prominent. Applying this fact to an ESL classroom environment, Gardner's Multiple Intelligences Theory accounts for why some learners fail to speak or communicate in the class while some do extraordinarily well. For instance, the Multiple Intelligence Theory underscores that learners with high intrapersonal intelligence prefer to have an opportunity to think twice before expressing their concepts or ideas; when these pupils are deprived of a chance to be considered in this regard they cannot help but lose ground and are named 'failures' or 'poor performers'. The teacher can avoid this situation by observing the students and making notes on how they react to different activities provided by the teacher.

Improved Linguistic Intelligence through Other Intelligences

When it comes to teaching English for the non-native speakers, the linguistic intelligence continues to be the most important and the most sort out one. It is an undeniable fact that other intelligences, such as the interpersonal and intrapersonal intelligences do influence the activities of a student in the classroom and also has a considerable effect on the student's ability to learn. It is here that theory of Multiple Intelligences comes to the rescue of the language teacher in suggesting how the other intelligences can be accelerated to improve the linguistic intelligence of a learner. The theory suggests that, by concentrating on and activating the other intelligences, the learners are made to feel relieved and to stay comfortable, otherwise suffocated and ruled out by the rules of language. On the other hand, the teacher is also provided with an opportunity to explore the hidden talents of the students. By recognizing these talents of theirs and by attending to them, their language learning can be developed dramatically.

Therefore, it is very important for the language teacher to take into consideration, these various types of intelligence among the language learners and to exploit them fully, so that the outcome is not only development of the natural abilities of these learners but also the learners' sense of satisfaction that their skills and talents are appreciated. This in turn will boost their self-confidence and self-esteem, which is of paramount importance, if the other forms of learning are to be gradually developed.

Therefore, the mission of the teachers should be to develop young men and women with active and creative minds, a sense of perception d kindness to the fellow beings, a sense of understanding and compassion for others, and the audacity to do the right deed.

ISSN:1225-8482 | E-ISSN:2288-4653 Vol. 5 No. 4 November (2023)
Pg. 277-282

The concept of multiple intelligences is not only a theory but more importantly a generous image of the varieties of human capacity. Howard Gardner has given a new frame for reflecting on the nature of mind and has made visible some distant stars worth reaching for. It is apparently a contribution worth celebrating.

References

1. Armstrong, T. (1994). *Multiple intelligences in the classroom*. Association for Supervision and Curriculum Development.
2. Christison, M. A. (1998). Applying multiple intelligences theory in preservice and in service TEFL education programs. *English Teaching Forum*, 36(2), 2–13.
3. Christison, M. A. (2005). *Multiple Intelligences and Language Learning: A Guidebook*
4. Gardner, H. (1983). *Frames of Mind: The Theory of Multiple Intelligences*. Basic Books. [
5. Gardner, H. (1993). *Multiple intelligences: The theory in practice*. Basic Books.
6. Gardner, H. (1995). Reflections on multiple intelligences. *Phi Delta Kappan*, 77(3), 200–208.
7. Gardner, H. (1999). *Intelligence reframed*. Basic Books.
8. Gardner, H., & Hatch, T. (1989). Multiple intelligences go to school: Educational implications of the theory of multiple intelligences. *Educational Researcher*, 18(8), 4–10.
9. Kartiah, S. A., Rahman, M. A., Rahman, A. Q., & Jabu, B. (2014). The portrayal of multiple intelligence theory in english teaching strategy for indonesian secondary school. *Journal of Language Teaching and Research*, 5(5), 1052–1061. https://doi.org/10.4304/jltr.5.5.1052-1061
10. Mahdavy, B. (2008). The role of multiple intelligences (MI) in listening proficiency: A comparison of TOEFL and IELTS listening tests from an MI perspective. *Asian EFL Journal*, 10, 109–126.
11. Soleimani, H., Moinnzadeh, A., Kassaian, Z., & Ketabi, S. (2012). The effect of instruction based on multiple intelligences theory on the attitude and learning of general english. *English Language Teaching*, 5(9), 45–53.

(12) PATENT APPLICATION PUBLICATION
(19) INDIA
(22) Date of filing of Application :26/07/2024
(21) Application No.202441057098 A
(43) Publication Date : 02/08/2024

(54) Title of the invention : IMPLEMENTATION OF A FACIAL RECOGNITION BASED ENHANCED SECURITY SYSTEM

(51) International classification	:G06F0021550000, A61B0005000000, G08B0013196000, H04N0007180000, H04L0051080000
(86) International Application No Filing Date	:NA :NA
(87) International Publication No	: NA
(61) Patent of Addition to Application Number Filing Date	:NA :NA
(62) Divisional to Application Number Filing Date	:NA :NA

(71)**Name of Applicant :**
1)Dr. T Murari
Address of Applicant :Professor, Department of English, Sri Venkateswara College of Engineering (Autonomous), Karakambadi Road, Tirupati, Tirupati District, Andhra Pradesh, India Tirupati ---------- ----------
2)T Yugandhar
3)Dr. P. Sreenivasulu
4)K. R. Surendra
5)K. B. Vamsi
6)Dr. P. Maninaga Kumar
7)Dr. K. Lokesh Krishna
Name of Applicant : NA
Address of Applicant : NA
(72)**Name of Inventor :**
1)Dr. T Murari
Address of Applicant :Professor, Department of English, Sri Venkateswara College of Engineering (Autonomous), Karakambadi Road, Tirupati, Tirupati District, Andhra Pradesh, India Tirupati ---------- ----------
2)T Yugandhar
Address of Applicant :Senior Assistant Professor, Department of English, Sri Venkateswara College of Engineering (Autonomous), Karakambadi Road, Tirupati, Tirupati District, Andhra Pradesh, India Tirupati ---------- ----------
3)Dr. P. Sreenivasulu
Address of Applicant :Professor, Department of Maths, Sri Venkateswara College of Engineering (Autonomous), Karakambadi Road, Tirupati, Tirupati District, Andhra Pradesh, India Tirupati ---------- ----------
4)K. R. Surendra
Address of Applicant :Senior Assistant Professor, Department of Electronics and Communication Engineering, Sri Venkateswara College of Engineering (Autonomous), Karakambadi Road, Tirupati, Tirupati District, Andhra Pradesh, India Tirupati ---------- ----------
5)K. B. Vamsi
Address of Applicant :Assistant Professor, Department of English, Sri Venkateswara College of Engineering (Autonomous), Karakambadi Road, Tirupati, Tirupati District, Andhra Pradesh, India Tirupati ---------- ----------
6)Dr. P. Maninaga Kumar
Address of Applicant :Professor, Department of Maths, Sri Venkateswara College of Engineering (Autonomous), Karakambadi Road, Tirupati, Tirupati District, Andhra Pradesh, India Tirupati ---------- ----------
7)Dr. K. Lokesh Krishna
Address of Applicant :Professor, Department of Electronics and Communication Engineering, Sri Venkateswara College of Engineering (Autonomous), Karakambadi Road, Tirupati, Tirupati District, Andhra Pradesh, India Tirupati ---------- ----------

(57) Abstract :
Disclosed herein is the Implementation of a Facial Recognition based Enhanced Security System. In general, perfect security system is needed as the current world is not safe as it is in the old days, and it has gained particular attention in the current scenario day-to-day activities. So, we need a enhanced and advanced security system. In this invention, Roboflow software module for face recognition and face detection is used, which are used to provide accurate and precise recognition even in difficult situations and with varying demographics. It includes the main processor as Raspberry Pi as a central computing system which reduces the implementation costs. The project is to provide a complete and dependable defensive system that protects people, property, and institutions from security threats by integrating Roboflow into the security infrastructure. Our Simulation results reveal that the invention is more efficient than the previous works in literature i.e. Accuracy as 95.7%, mean average precision as 99.7% and recall as 100%.

No. of Pages : 22 No. of Claims : 7

Forwarded

Patent Application Number:202321066608

The Influence of Corporate Social Responsibility on Community Development

12:08

Forwarded

Patent Application Number:202341071572

A Human Resource Management Approach to Examining the Impact of Employee Training and Development on Increasing Organizational Competitiveness

12:08

(ESTD-1995)

RAJEEV GANDHI MEMORIAL COLLEGE OF ENGINEERING & TECHNOLOGY

(Autonomous)
Approved by AICTE - New Delhi, Affiliated to JNTU Anantapur, Ananthapuramu, Accredited by NAAC of UGC with 'A+' grade, New Delhi,
NH-40, Nandyal-518501, Andhra Pradesh, India

Department of English

National Conference

World Poetry Day-Musings of Great Poets

March 21st, 2024

CERTIFICATE OF APPRECIATION

Presented To

Dr. K. Suneetha Reddy, Professor

from S V Engineering College, Tirupati, Andhra Pradesh for presenting a paper titled Significance of Poetry in English Language Learning: A Close Study in the National Conference on "World Poetry Day- Musings of Great Poets" organized by the Department of English, Rajeev Gandhi Memorial College of Engineering and Technology, Nandyal on
21-03-2024.

Dr. Suneetha Yadav	**Dr. P. Kousar Basha**	**Dr.T. Jayachandra Prasad**
Convener	HoD of Dept., of English	Principal

15:20 • 42%

First Impression: 2024

@RGMCET, AUTONOMOUS, Nandyal

National Conference on World Poetry Day – Musings of Great Poets
March 21, 2024

ISBN: 978-93-340-2790-7

No part of publication may be reproduce or transmitted in any form by any means, electronic or mechanical, including photo copy, recording, or any information storage and retrieval system, without permission in writing from the copyright owners.

DISCLAIMER

The authors are solely responsible for the contents of the papers complied in this volume. The publishers or editors do not take any responsibility for the same in any manner. Errors, if any are purely are unintentional and readers are requested to communicate such errors to the editors or publishers provide discrepancies in future.

Typeset by
Dept. of English, RGMCET – Nandyal

Published by:
Dept. of English,
RGM College of Engineering and Technology,
Nandyal – 518501, Phone: 08514-275201, 275203, 275204, Fax: 08514-275123
Email: principalrgm@gmail.com
Website: www. rgitnandyal.com

This imprint has done by the registered company Immortal Publications, the address is Prasadampadu, Vijayawada – 521108, Andhra Pradesh, India, **https://www.immortalpublications.com**

Printed by : **Renu Graphics**, Prasadampadu, Vijayawada – 521108

5/400

Rotate Mark Recognize Note

THE CULTURE OF PATRIARCHY, GENDER BIAS, AND CLASS DISCRIMINATION IN THE SELECT PLAYS MAHESH DATTANI

Dr. M. Kalyan Kumar, Dr. V.B. Chithra

BlueRose ONE
Stories Matter

INR 000

GENRE

www.BlueRoseOne.com

BLUEROSE PUBLISHERS
India | U.K.

Copyright © Dr M Kalyan Kumar, Dr V B Chithra 2023

All rights reserved by author. No part of this publication may be reproduced, stored in a retrieval system or transmitted in any form or by any means, electronic, mechanical, photocopying, recording or otherwise, without the prior permission of the author. Although every precaution has been taken to verify the accuracy of the information contained herein, the publisher assume no responsibility for any errors or omissions. No liability is assumed for damages that may result from the use of information contained within.

BlueRose Publishers takes no responsibility for any damages, losses, or liabilities that may arise from the use or misuse of the information, products, or services provided in this publication.

For permissions requests or inquiries regarding this publication,
please contact:

BLUEROSE PUBLISHERS
www.BlueRoseONE.com
info@bluerosepublishers.com
+91 8882 898 898
+4407342408967

ISBN: 978-93-5819-505-7

Cover design: Tahira
Typesetting: Tanya Raj Upadhyay

First Edition: January 2023

Office of the Controller General of Patents, Designs & Trade Marks
Department for Promotion of Industry and Internal Trade
Ministry of Commerce & Industry,
Government of India

(http://ipindia.nic.in/index.htm)

INTELLECTUAL PROPERTY INDIA (http://ipindia.nic.in/index.htm)

Application Details

APPLICATION NUMBER	202421037347
APPLICATION TYPE	ORDINARY APPLICATION
DATE OF FILING	12/05/2024
APPLICANT NAME	1 . Dr. Imran Baig Mirza 2 . Dr. Debashis Mandal 3 . Dr. Shirisha Deshpande 4 . Ms. Roshan Jameer MD 5 . Ms. Jyoti Babbar 6 . Ms. Kavita Priyadrshni 7 . Dr. K Suneetha Reddy 8 . Dr. M. Ravichand 9 . Dr. Barun Kumar Jha 10 . Dr. Belsam Jeba Ananth. M 11 . Mr. A Karthik 12 . Dr. Harikumar Pallathadka
TITLE OF INVENTION	ADAPTIVE LANGUAGE LEARNING PLATFORM: CONTEXTUAL FEEDBACK MECHANISM
FIELD OF INVENTION	ELECTRONICS
E-MAIL (As Per Record)	patentipr23@gmail.com
ADDITIONAL-EMAIL (As Per Record)	
E-MAIL (UPDATED Online)	
PRIORITY DATE	
REQUEST FOR EXAMINATION DATE	--
PUBLICATION DATE (U/S 11A)	14/06/2024

Application Status

APPLICATION STATUS	Awaiting Request for Examination

View Documen

ISSN/eISSN: 0889-6348

UGC-CARE Approved Group - II Journal (Web of Science Group)

PROTEUS JOURNAL

Website: http://proteusresearch.org/ E-Mail: submitpj@gmail.com

PAPER ID: PJ-2813

Certificate of Publication

This is to certify that the paper entitled

English Language Laboratories (ELLs) Play a Vital Role on Professional Students in Engineering Colleges

Authored by:

T. Murari

From:

S V College of Engineering, Tirupati, India 517507

Has been published in

PROTEUS JOURNAL, VOLUME 12, ISSUE 1, JANUARY - 2021

ज्ञान-विज्ञान विमुक्तये

UGC-CARE Approved Group-II Journal

MAREK BOZEJKO
Editor-In-Cheif
PROTEUS JOURNAL

Web of Science Group

1.25

Proceedings of the 5th International Conference on Inventive Research in Computing Applications (ICIRCA 2023)
DVD Part Number: CFP23N67-DVD; ISBN: 979-8-3503-2142-8

Sentimental Analysis of Movie Reviews using NLP Techniques

Basi Reddy A
Assistant professor, School of Computing, Mohan Babu University, Tirupati, A.P, India
basireddy.a@gmail.com

B.V. Suresh Reddy
Dept. of. CSE, Koneru Lakshmaiah Education Foundation, Vaddeswaram, A.P, India
sureshvenkat83@gmail.com

Anjana Devin Nandam
Dept. of. CSE, Koneru Lakshmaiah Education Foundation, Vaddeswaram, A.P, India
anjana.nandam@gmail.com

K Naresh
Assistant Professor, Sri Venkateswara College of engineering (autonomous), Tirupati, A.P, India
Nareshrpc123@gmail.com

Sivakumar Depuruu
School of Computing, Mohan Babu University, Tirupati, India
sivakumar.d@vidyanikethan.edu

M. Sakthivel
School of Computing, Mohan Babu University, Tirupati, A.P, India
sakthivel.m@vidyanikethan.edu

***Abstract*— The goal of natural language processing is to build machines that can comprehend text or speech input and respond to it in a way that is similar to how people do. To accomplish this, various Natural Language Processing (NLP) tasks are employed to analyze human language data, aiding computers in understanding the information it consumes. These tasks include sentimentanalysis, voice recognition, part-of-speech tagging, and natural language generation. Sentiment analysis that detects emotions such as happiness, frustration, rage, and sadness goes beyond polarity. To do this, advanced machine learning techniques or lexicon collections of words and the emotions arouse are used. In this study, the Internet Movie Database (IMDB) Reviews Dataset is subjected to sentiment analysis to determine if a user's review is favourable or unfavourable based on the supplied details. Utilizing data from the real world, the proposed approach's correctness is assessed.**

Keywords*— Movie Reviews, Sentiment Analysis, NLP, Machine Learning.

I. INTRODUCTION

Movie reviews have become a popular way for critics to evaluate a film's overall quality and whether or not they recommend it. The purpose of these reviews is to help readers make informed decisions about whether to watch, rent, or buy a movie. A good review should provide enough detail about the film without giving away any key plot points or surprises. It gives the reader a sense of the movie's quality before watching it, as the authors delve into the nuances of the film [1, 19]. Additionally, there are brief but enjoyable reviews that give the reader an idea of whether a movie is worth their time. Although the ratings in the Internet Movie Database (IMDB) are determined by an objective algorithm, it is not regarded as beingabsolutely accurate. Instead, it gives viewers a quick method to see what other IMDB users around the world think of the movies that are featured on the website. IMDB users from around the world think of the movies that are featured on the website [2].

Before the advent of the internet, people often sought out opinions from acquaintances and friends when making decisions. However, with the rise of big data and internet usage, it is now possible to gather opinions from a large number of people on a particular subject. There are millions of individuals expressing their opinions on these platforms thanks to the rise in the number of websites, blogs, social media platforms, and reviews [3]. For various evaluation processes, it can be difficult and crucial to analyse these opinions and attitudes. Sentiment analysis is a method to extract meaningful information from a variety of source materials that include unrecognized viewpoints [4].

Sentiment analysis can be used to analyze a piece of text and determine the sentiment contained within it. The procedure entails segmenting the communication into topical parts and giving each topic a sentiment score. A movie's overall rating can be determined by this automatic approach, which also rates how favorable or unfavorablea movie review is. Basic pre-processing for text involves removing non-alphabetic characters, stop words, and changing all words to lowercase. Although text in IMDB reviews can be messy and include incorrect punctuation and spelling, it can be mapped to numerical representations for machine learning models [5]. The conclusions drawn from sentiment analysis can help in determining if the customer is angry, dislikes a specific aspect of a product, or is excited about a new release. By grouping the data into major categories, it is seen that the reactions are more positive, neutral, or negative.

II. PROBLEM STATEMENT

The primary intent of sentiment analysis is to assess all points of view and determine the general polarity of opinions on certain topics using various classification levels, such as positive or negative. Natural language processing (NLP) techniques are utilized in the sentimental analysis of the IMDb review datasets to determine whether the data is positive, negative, or neutral. Users can use this analysis to determine whether a movie is worth viewing or not. In today's world, people often rely on ratings and reviews given by previous users for movies or other products. Therefore, it is crucial to draw reliable conclusions from those reviews for the users' benefit. Users can make this choice with the help of a summary of all movie reviews without having to read every single one of them. Critics commonly evaluate and comment on movies on movie-rating websites, which aids viewers in determining whether the film is worth seeing.

III. OBJECTIVES

Sentiment analysis seeks to extract people's thoughts from unorganized reviews articles and classify them into sentiment classifications like positive, neutral, or negative, with the option of also taking into account "extremely positive" and "very negative". It also goes by the name "opinion mining" and extracts feelings and emotions from written materials using text mining and natural language processing (NLP). Social networking analysis also plays a big role in Sentiment analysis and Recommendation Systems,

where users can express their thoughts on items through various online behaviours including commenting, liking, sharing, and publishing reviews or comments about products. These actions fall under the categories of user-user, user-community, and user-entity behaviour. User-community behaviour covers interaction in between user and a public, such as entering or quitting a community, to be a fan, or taking part in a community meeting. User-user behaviour includes communication between two users, like texting and playing games. User-entity behaviour is the creation of content, such as writing a blog post, an essay, a review, or uploading a photo to social media.

The objective is to create a model that can correctly categorise movie reviews as favourable or negative depending on their content. This can be helpful for a number of purposes, including gauging public opinion on a particular film or evaluating how reviews affect a film's box office performance.
Evaluation of the model's performance using multiple measures is another goal of the analysis. This will aid in identifying the model's advantages and disadvantages and offer suggestions on how to further enhance it. The overall overarching objective is to develop a model that can accurately classify movie reviews and provide data on the efficacy of the suggested system for sentiment analysis in the field of movie reviews.

IV. SCOPE

The scope of the study is to create a model that can correctly identify favourable and negative movie reviews. This method of analysis can be helpful in a variety of situations, such as when movie studios want to assess how audiences will respond to their films or when online merchants want to examine consumer feedback. The system can also be used to spot patterns in movie reviews, such as which elements of a movie (such as acting, plot, or special effects) are referenced in both positive and negative reviews most frequently.
The scope of the study includes:

1. Data collection: Gathering a large dataset of movie reviews from various sources such as websites, social media platforms, and online forums.
2. Data pre-processing: preparing the text data for the model's analysis by cleaning and converting it. This includes removing irrelevant information, punctuation, stop words, and other noise.
3. Feature extraction: To quantitatively represent the text data and give the model the ability to comprehend the relative value of various terms in the text, vectorizing the words using methods like TFIDF or bag-of-words is necessary.
4. Model selection: Choosing a suitable algorithm like support vector machine, multinomial naive bayes or Neural Networks for sentiment classification based on the size and complexity of the dataset.
5. Model training and evaluation: The dataset is divided into training and testing portions, and the model is predominantly trained on the training set. Metrics like precision, recall, accuracy, and F1 score are used to assess the model's performance on the testing set.
6. Visualization and interpretation: Visualizing the classification results using tools such as confusion matrices, heatmaps, and WordCloud to gain insights into the sentiment of the movie reviews and identify trends and patterns.
7. Deployment: Integrating the sentiment analysis model into a web application, dashboard, or API for real-time monitoring and analysis of customer feedback.

The scope of the paper can be expanded to include other tasks such as topic modeling, sentiment intensity analysis, and aspect-based sentiment analysis based on the specific needs of the paper.

V. LITERATURE SURVEY

A. *Movies Reviews Sentiment Analysis and Classification*

The research is focused on building a sentiment analysis model for movie reviews. The model uses several techniques, such as tokenization, stemming, feature selection, and classification, to process and classify reviews as positive or negative. The researchers evaluated the model using eight different classifiers and five evaluation metrics on a real-world dataset [6].

According to the results, the Random Forest classifier performed the best among the eight classifiers, while Ripper Rule Learning performed the worst. This suggests that the Random Forest classifier is a good choice for sentiment analysis of movie reviews.

Overall, the research highlights the importance of sentiment analysis in enhancing the efficiency of products, such as movies. By classifying reviews as positive or negative, companies can gain insight into how to improve their products and better meet the needs of their customers [7].

B. *Albert-based sentiment analysis of movie review*

The article is discussing the importance of sentiment analysis in analyzing movie reviews and how machine learning can help automate this process. The article mentions that sentiment analysis can extract topic information from text reviews and determine the overall polarity of the review.

The researchers in this article used the Albert model to build a sentiment analysis classifier and trained it using the "movie review dataset" from Stanford University. The Albert model achieved an accuracy of 89.05% when analyzing the sentiment of movie reviews, which is 3% higher than the traditional LSTM and GRU models [8].

This research suggests that machine learning models like the Albert model can be used to analyze movie reviews and extract sentiment information more efficiently and accurately than traditional methods. This can be helpful for movie producers and distributors to better understand the audience's opinions and improve the quality of their products accordingly [9].

C. *An Improved Sentiment Analysis Of Online Movie Reviews Based On Clustering For Box-Office Prediction*

The goal of this study appears to be to forecast a movie's box office success using sentiment analysis and machine learning techniques.

More online evaluations are being written as a result of the expansion of e-commerce, which may be a great source of knowledge for both buyers and sellers. The study shows that by including data from internet reviews, a simpler version of the sentiment- aware autoregressive model may be used to reliably forecast box office profits. To distinguish between positive and negative feelings, the technique employs fuzzy clustering and document-level sentiment analysis. The paper also discusses the usage of a Support Vector Machine (SVM) Classifier to forecast the trajectory of box office revenue based on review sentiment [10].

According to this strategy, sentiment analysis and machine learning techniques can be used to harness data from internet reviews for potential economic impact, such as forecasting a movie's box office performance. In conclusion, this study e mphasises the potential advantages of sentiment analysis and machine learning techniques for studying online reviews and forecasting the performance of goods and services. This might be helpful for companies and sectors that depend on consumer input to enhance their goods and services and d ecide wisely on marketing and sales tactics [11].

D. *Sentiment Analysis of Movie Reviews: A Comparative Study between the Naive-Bayes Classifier and a Rule-based Approach*

In order to categorise textual movie reviews as good or n egative, this paper relies on the use of sentiment analysis. In this study, the output of the Naive-Bayes algorithm and a rule-based approach that makes use of the AFINN-111 sentiment dictionary are compared.

To find and quantify subjective information in text data, sentiment analysis employs natural language processing, text analysis, and other computational tools. Popular machine learning algorithm the Naive-Bayes can be used for sentiment analysis. In this method, a model is trained on a labelled dataset of fav ourable and unfavourable reviews, and it is then used to forecast the sentiment of future reviews [12].

On the other hand, the rule-based approach uses a sentiment dictionary or a pre-defined set of rules to ascertain the sentiment of a review. As it includes a list of words with corresponding sentiment scores that may be used to categorise reviews, the AFINN-111 sentiment dictionary is a popular option for sentiment analysis. In order to evaluate whether strategy is more successful for sentiment analysis of movie reviews, the findings of the Rule-Based strategy and the Naive-Bayes algorithm are compared in this study using the AFINN-111 sentiment dictionary. The study's conclusions can be applied to organisations and sectors that depend on customer feedback, including movie studios and internet streaming services, to enhance the goods and services they provide [14] .

VI. EXISTING SYSTEM

Existing systems that use NLP to analyse sentiment in IMDB review data are numerous. Feature extraction, data preparation, and model training are c common procedures in the sentiment study of IMDB movie re views using NLP approaches. Cleaning up the raw text data, getting rid of any extraneous information like stop words and punctuation, and turning the text into a numerical representation like a bag-of-words or word embeddings are all parts of data preparation [15]. NLP methods like sentiment lexicons, sentiment polarity scores, and sentiment classification models are used to provide features for feature extraction that accurately reflect the sentiment expressed in the text. Finally, a machine learning model or neural network is trained on the extracted information to forecast the sentiment of a particular review. The accuracy of the model is evaluated using metrics like precision, recall, and F1 score, and it is then improved [16].

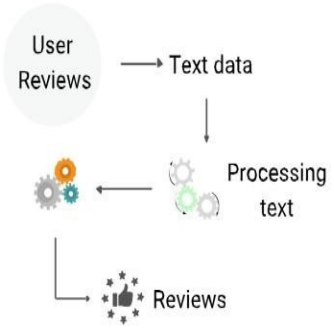

Fig 1: Natural Language Processing

1. Data Preprocessing

To preprocess text for analysis, the following steps are commonly taken:

- Eliminate irrelevant information such as punctuation, numbers, and stop words.
- Tokenize the text into individual words.
- Convert the words into their base form using stemming orlemmatization.
- Generate a mathematical representation of the tokenized text, such as a bag-of-words or word embeddings.

2. *Feature extraction Sentiment lexicons:*

The overall sentiment polarity of the text is calculated using a pre-defined list of words with corresponding sentiment polarity r atings. Sentiment polarity scores: The sentiment polarity of each word is predicted using an existing model, which is then applied to the entire text to determine its overall sentiment polarity.

Sentiment classification models: A machine learning model is trained on a tagged dataset of movie reviews to forecast the sentiment of a particular review.

3. Model Training

After preprocessing, split the data into training and testing sets. A machine learning model is trained using the training set. The model is trained using the features that were retrieved. Analyze the model's performance on the testing set using metric measures once it has been trained.

4. Model Fine-Tuning

Adjust the hyper parameters of the model to enhance its performance. Iterate the process of training and evaluation until desirable results are achieved.

Some of these systems are:

i. *Rule-based systems:*

A collection of pre-established rules are utilised in a rule-based sentiment analysis system to ascertain the sentiment of a given text. These rules are often developed by subject matter specialists and are founded on their knowledge of the language and the subject matter of the analysis [17].

The rules can be simple or complex, and can take into account various factors such as the presence of certain words, phrases, or grammatical structures that are indicative of a particular sentiment. For example, a rule might state that the presence of words such as "love," "great," and "amazing" indicate a positive sentiment, while the presence of words such as "hate," "terrible," and "disappointing" indicate a negative sentiment.

One advantage of a rule-based system is that it can be more interpretable than other approaches such as machine learning. It allows for explicit control over which features are used to determine sentiment, and can be easier to modify and fine-tune as needed.

However, a potential limitation of rule-based systems is that they may not be as accurate or flexible as machine learning-based approaches, particularly when dealing with complex or ambiguous language. Additionally, creating and maintaining a set of rules can be time-consuming and require significant expertise in the domain being analyzed.

ii. *Statistical models:*

Statistical methods in sentiment analysis involve using mathematical models and techniques to analyze and interpret the sentiment of text data. These techniques frequently make use of machine learning al gorithms, which are trained on textual datasets with labels to find links and patterns between words and attitudes.

One common statistical method used in sentiment analysis is the bag-of-words approach, which involves representing each piece of text as a collection of individual words, ignoring their order and context. Each word is given a weight based on how frequently it appears in the text and how significant it is to the sentiment being studied. These weights are then used to calculate an overall sentiment score for the text.

Sentiment analysis lexicons, which are collections of words that have been carefully annotated with sentiment polarity scores, are another statistical technique used in sentiment analysis. The sentiment scores of each word can be added together to determine the overall sentiment polarity of a passage of text [18].

Overall, because of their precision and capacity for handling vast volumes of data, statistical approaches are frequently used in sentiment analysis. However, they might need a lot of computer power and might not always be able to deal with how complicated s poken language and context are.

iii. *Deep Learning Models:*

Due to their capacity to recognise intricate patterns in data, deep learning models are becoming more and more common in sentiment analysis. They are a particular class of machine learning model made up of numerous artificial neuronal layers that have been taught to recognise hierarchical representations of the input data. The use of deep learning models in the area of sentiment analysis have demonstrated encouraging results in correctly predicting the sentiment of a given text. They are able to discover intricate patterns and connections between words and sentences in a text because they can be trained on vast volumes of labelled data.

The recurrent neural network (RNN), which excels at analysing sequential data, such as text, is a popular model for deep learning applied to sentiment analysis. RNNs process each word individually while keeping an internal memory of the words that came before it, allowing them to capture the context and relationships between words in a sentence.

Convolutional neural networks are yet another well-liked deep learning model utilised in sentiment analysis. (CNN). CNNs have been modified for text classification applications like sentiment analysis since they are excellent at picture recognition. CNNs are particularly good at picking up local aspects of the input data, like n-grams or particular sentences that express a certain emotion.

iv. *Hybrid Systems:*

To increase the precision and robustness of sentiment analysis, hybrid systems integrate the advantages of many methodologies. These systems can leverage the advantages of rule-based systems, statistical methods, and deep learning models.

In a hybrid system, multiple models are combined to generate a final sentiment prediction. For example, a rule-based system may be used to classify simple and explicit sentiments, while a deep learning model may be used to identify more complex and nuanced sentiments. Statistical methods may also be used to refine the sentiment prediction and improve its accuracy.

Using an ensemble learning methodology, such as bagging or boosting, is a well-liked method for developing a hybrid system. In bagging, various models are individually trained on various subsets of data, and their predictions are then merged to get a final prediction. In boosting, the mathematical models are trained progressively, with each model paying particular attention to the data points that the prior model incorrectly identified.

Another approach for building a hybrid system is to use a stacked architecture, where the output of one model is used as input to another model. To recognise explicit sentiment, for instance, a rule-based system may be employed. The output of this system may then be utilised as input to a deep learning model that identifies more complicated and nuanced sentiment.

Overall, hybrid systems have been shown to outperform individual systems in sentiment analysis, especially in cases where the sentiment is complex and nuanced. By combining the strengths of different approaches, hybrid systems can provide more accurate and robust sentiment predictions.

Various systems have been developed for sentiment analysis on reviews data with varying levels of accuracy. The selection of a system depends on factors such as the size and characteristics of the dataset, the desired level of accuracy, and available computational resources.

VII. PROPOSED SYSTEM

The Multinomial Naive Bayes algorithm-based proposed system for sentiment analysis is a text classification model

that foretells whether a given text will be positive or negative. The technology is made to assist companies and organisations in analysing consumer comments and reviews, posts on social media, and other text data to comprehend customer attitude towards their goods and services. The system represents the incoming text data as a vector of word counts using the bag-of-words method before classifying it into positive or negative sentiment using the Multinomial Naive Bayes methodology. The bag-of-words approach treats each word as a unique feature, disregarding the context and word order of the text. With this method, the data representation is made simpler, and the algorithm may concentrate on the key phrases that are most likely to convey the text's mood.

The system weighs the significance of each word in the text. Based on a word's frequency in the text and rarity across all corpus documents, the TF-IDF algorithm assigns each word a score. This method gives terms that appear more frequently in the text but less frequently across all documents a higher weight, indicating that these words are more distinctive and useful for the classification of sentiment.

1. Data Preprocessing: Data preparation is the initial step in any machine learning that aims to clean up and transform raw data into a format that machine learning algorithms can use. The movie reviews are subjected to a number of data cleaning procedures in order to get them ready for sentiment analysis.

a) HTML Stripping: The movie reviews are initially processed to remove any HTML tags using the BeautifulSoup library in Python. This step is essential to eliminate any HTML code that may be present in the reviews and could introduce noise or irrelevant information.

b) Square Bracket Removal: The square brackets in the movie reviews are removed using regular expressions to eliminate any text enclosed in square brackets, which may contain noise or irrelevant information that does not contribute to sentiment analysis.

c) Special Character Removal: A function is defined to remove special characters from the movie reviews using regular expressions. This helps remove any non-alphanumeric characters from the data that could not be useful for sentiment analysis or could cause noise.

d) Text Normalization: The movie reviews are further normalized by applying text normalization techniques such as stemming and stopword removal. Stemming is performed using the PorterStemmer algorithm from the NLTK library, which reduces words to their root or base form. Stopwords, which are common words such as "the" and "is", are removed from the reviews using a predefined list of English stopwords from the NLTK library. This step helps in reducing the dimensionality of the data and focuses on the meaningful words that contribute to sentiment analysis.

2. Feature Extraction: The technique of feature extraction involves turning unstructured data, such text, into numerical features that can be fed into machine learning algorithms. Two well-known feature extraction methods are applied in this suggested system: Bag of Words (BoW) and Term Frequency-Inverse Document Frequency. (TF-IDF).

a) Bag of Words (BoW): The CountVectorizer class from the sklearn library is used to implement BoW in the given code. BoW represents text as a collection of words and their frequencies in a document. It creates a numerical matrix where each row, which represents a document, and each column, which represents a word, have values that represent the frequency of each word. The machine learning models use this matrix as their input data.

b) Term Frequency-Inverse Document Frequency (TF-IDF): The TfidfVectorizer class from the sklearn library is used to implement TF-IDF. The TF-IDF algorithm uses a numerical matrix to represent text. Each row corresponds to a document, and each column to a word. The values in the matrix represent the importance of each word in a given document based on the frequency of the word in the document and the inverse frequency of the word over the whole dataset. In order to apply weights to words, TF-IDF considers both the term frequency (TF) and inverse document frequency (IDF), providing greater weight to words that are common in a text but uncommon over the entire dataset. The machine learning models use this matrix as their input data.

3. Model Training and Evaluation: After data preprocessing and feature extraction, the next step in the proposed system is to train and evaluate machine learning models for sentiment analysis. Logistic Regression, Naive Bayes, and Support Vector Machines are three widely used machine learning methods.

a) Logistic Regression: Implementing logistic regression involves using the LogisticRegression class from the Sklearn package. A binary classification approach called logistic regression models the association between input features and a binary output variable. (positive or negative sentiment in this case). The BoW or TF-IDF matrices are used as input features and their corresponding labels are used as output targets to train the model on the training data. After the model has been trained, its performance is assessed using measures like accuracy, precision, recall, and F1-score on the test data.

b) Naive Bayes: The MultinomialNB class from the sklearn library is used to implement Naive Bayes. Naive Bayes is a probabilistic algorithm that assumes the independence of features, and it is commonly used for text classification tasks. The model is trained and evaluated in a similar manner as logistic regression, using the BoW or TF-IDF matrices as input features and their corresponding labels as output targets.

c) Support Vector Machines (SVM): SVM is implemented by the SVC class from the sklearn library. SVM is a potent binary classification technique that locates the optimum hyperplane for classifying the data. The BoW or TF-IDF matrices are used as input features and their corresponding labels are output targets in a manner similar to logistic regression and Naive Bayes for training and evaluation of the model.

4. Model Selection and Hyperparameter Tuning: Model selection and hyperparameter tweaking are essential processes in the proposed approach to maximise the effectiveness of the machine learning models. . The proposed

system selects a model and tunes hyperparameters using the GridSearchCV class from the Sklearn package. GridSearchCV conducts a thorough search over a predetermined parameter grid and chooses the optimal set of hyperparameters that maximises the model's performance.This helps in finding the optimal hyperparameters for each machine learning algorithm, such as the regularization strength for logistic regression or the kernel type for SVM, to achieve the best possible performance on the movie review dataset.

5. Model Deployment: It is feasible to deploy the top-performing model for real-world applications after choosing it and fine-tuning its hyperparameters. The model can be saved as a serialized file using the joblib library in Python, which allows for easy deployment and integration into production systems. The deployed model can then be used to predict the sentiment of movie reviews in real-time or batch processing, depending on the application requirements.

The suggested system for sentiment analysis offers a thorough method for categorising movie reviews as positive or negative based on the sentiment indicated in the text. The system involves several critical steps, including data preprocessing, feature extraction, model training and evaluation, model selection and hyperparameter tuning, and model deployment. The proposed system aims to achieve accurate and reliable sentiment analysis on movie reviews by utilising well-known machine learning algorithms like logistic regression, Naive Bayes, and SVM, as well as techniques like Bag of Words (BoW) and Term Frequency-Inverse Document Frequency (TF-IDF) for feature extraction. The system can be further optimized by fine-tuning hyperparameters and incorporating additional techniques, such as word embeddings or deep learning algorithms, based on the specific requirements of the application. Overall, the proposed system holds great potential for various applications in the field of sentiment analysis and can contribute to improved decision-making, customer satisfaction, and business insights.

The proposed system has the potential to be further optimized by fine-tuning hyperparameters, incorporating additional techniques such as word embeddings or deep learning algorithms, and adapting to specific application requirements. It can be used in various applications such as sentiment analysis for customer reviews, social media sentiment analysis, brand monitoring, and market research, among others.

In conclusion, the proposed system for sentiment analysis using machine learning techniques is a comprehensive approach that involves multiple steps and techniques to accurately classify movie reviews as positive or negative based on their sentiment. It has the potential to provide valuable insights and decision-making support in various domains.

VIII. ALGORITHM USED

A. Load and Preprocess Data:

- Load the movie review dataset or any other dataset containing text data and their corresponding sentiment labels (positive or negative).
- Carry out data preprocessing operations such punctuation removal, text conversion to lowercase, stop word elimination, and stemming or lemmatization to break down words into their root forms.

B. Extract Features:

- Create numerical features from the preprocessed text data that may be fed into the machine learning algorithms.
- Word embeddings like Word2Vec or GloVe as well as TF-IDF (Term Frequency-Inverse Document Frequency) representation are common strategies for feature extraction.

C. Split Data:

- Split the preprocessed and feature-extracted data into training and testing sets.
- Typically, a random split of the data is employed, such as 80/20 or 70/30, with a larger amount being used for training and a smaller portion being used for testing.

D. Implement Logistic Regression:

- Create a logistic regression model using the retrieved features and training data.
- Use a suitable optimization algorithm such as gradient descent or any other optimization technique to learn the coefficients (parameters) of the logistic regression model.
- Tune hyperparameters such as regularization strength (if applicable) and learning rate to optimize the model's performance.
- Assess the logistic regression model's performance using the testing data's accuracy, precision, recall, and F1-score metrics.

E. Implement Naive Bayes:

- Train a Naive Bayes model using the training data and the extracted features.
- Implement the Naive Bayes algorithm, which involves calculating the probabilities of each feature occurring in each class and combining them using Bayes' theorem to calculate the conditional probabilities of the class given the input features.
- Assess the Naive Bayes model's performance using the testing data's accuracy, precision, recall, and F1-score metrics.

F. Implement SVM:

- Train an SVM model using the training data and the extracted features.
- If necessary, translate the data into a higher-dimensional space using a suitable kernel function (such as a linear, polynomial, or radial basis function).

- Identify the optimum hyperplane (decision boundary) for separating the data points into various classifications.
- To enhance the performance of the model, adjust hyperparameters such regularisation strength, kernel parameters, and cost parameter.
- Utilize performance indicators from the testing data, such as accuracy, precision, recall, and F1-score, to assess the SVM model.

G. Model Selection and Hyperparameter Tuning:

- Use techniques such as GridSearchCV to perform model selection and hyperparameter tuning.
- GridSearchCV involves trying different combinations of hyperparameter values for each algorithm and selecting the one that gives the best performance.
- Use cross-validation to get a more robust estimate of model performance and avoid overfitting.

H. Choose Best-performing Model:

- Compare the performance of the logistic regression, Naive Bayes, and SVM models using the evaluated metrics.
- Choose the best-performing model based on the performance metrics and the specific requirements of the sentiment analysis task.

I. Deploy and Test Model:

- Once the best-performing model is chosen, deploy it in a production environment or any application where sentiment analysis is required.
- Test the model with new, unseen text data to evaluate its performance in a real-world scenario.
- Monitor and update the model periodically to ensure its accuracy and effectiveness over time.

IX. RESULTS

The accuracy score and classification report for TF-IDF features will be the algorithm's final output. These findings will give us a better notion of how accurate the algorithm is at predicting the tone of movie reviews.

The percentage of reviews in the testing set that were correctly categorised is used to calculate the classifier's accuracy. The system computes precision, recall, and F1-score in addition to accuracy, which are metrics frequently used to assess the effectiveness of a binary classification model.

Out of all the reviews that the classifier projected would be positive, precision is the percentage of reviews that were correctly classified as positive. Recall quantifies the percentage of all positively classified reviews in the testing set that were correctly identified. The harmonic mean of accuracy and recall is the F1-score, which provides a single metric to evaluate the trade-off between precision and memory.

These metrics are thoroughly broken down for both positive and negative assessments in the classification report that the classification system generates. The report includes the precision, recall, F1-score, and support for both classes. The number of reviews in each class in the testing set is represented by the support.

This system generate classification reports for two different models - one that uses the bag of words approach and another that uses the TF-IDF approach. A classification report provides information about the accuracy and precision of a classification model. It includes various metrics such as precision, recall, F1-score, and support.

The **classification_report()** function takes three arguments - the true sentiment values, the predictedsentiment values, and the target names for the sentiment categories. In this case, the target names are "Positive" and "Negative".

The first report is for the bag of words model, while the second report is for the TF-IDF model. These reports provide an evaluation of how well the models have performed in classifying the sentiment of the movie reviews.

	precision	recall	f1-score	support
Positive	0.75	0.76	0.75	4993
Negative	0.75	0.75	0.75	5007
accuracy			0.75	10000
macro avg	0.75	0.75	0.75	10000
weighted avg	0.75	0.75	0.75	10000

	precision	recall	f1-score	support
Positive	0.75	0.76	0.75	4993
Negative	0.75	0.74	0.75	5007
accuracy			0.75	10000
macro avg	0.75	0.75	0.75	10000
weighted avg	0.75	0.75	0.75	10000

Table 1: Classification Report

The **WordCloud** function from the **wordcloud** library to create a word cloud visualization of the most frequently occurring words in the respective reviews. The **WordCloud** function takes in various parameters such as the width and height of the image, maximum number of words to include in the cloud, and minimum font size.

The resulting word clouds are displayed using **imshow** function from **matplotlib** library. The **interpolation** parameter is used to specify the interpolation method used to display the image.

Overall, the purpose of the code is to visually display the most commonly occurring words in the positive and negative movie reviews, and to gain insights into the sentiment expressed in the reviews.

The important terms that are frequently and extensively used in favourable reviews may be seen in the word cloud made from the words found in the positive reviews.

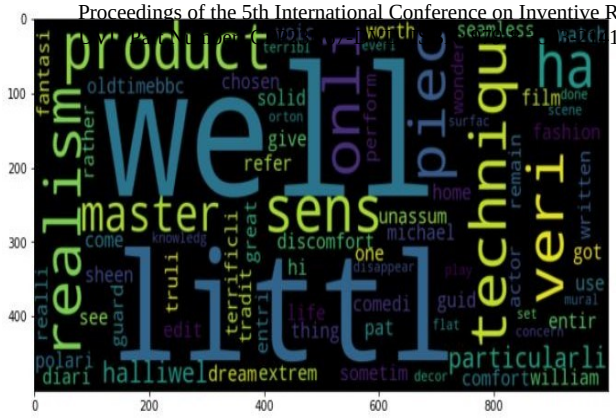

Fig 2: Positive Reviews wordcloud

The word cloud created from the negative review words can also provide some light on the key terms that are frequently and extensively utilised in negative reviews.

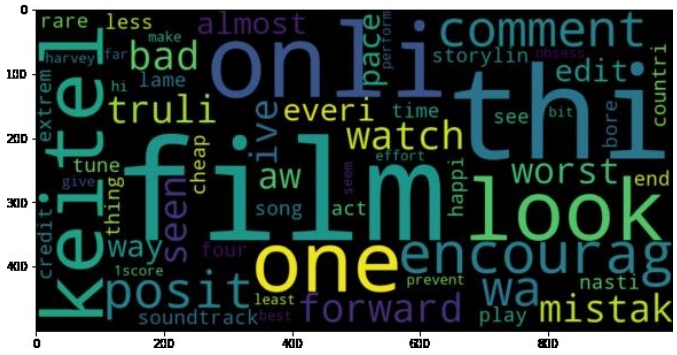

Fig 2: Negative Reviews wordcloud

Overall, the IMDB dataset shows that the Multinomial Naive Bayes classifier performs effectively, reaching better accuracy. Positive and negative reviews have good precision, recall, and F1-scores, demonstrating that the classifier can successfully separate the two classes. These findings imply that the model is applicable to sentiment analysis tasks on comparable datasets. It is critical to keep in mind that the performance of the model can vary depending on the precise dataset and the task at hand.

CONCLUSION

The dataset received preprocessing utilising techniques like stemming, stop word removal, special character removal, square bracket removal, and HTML stripping. The feature extraction algorithms used vectorization, also known as term frequency-inverse document frequency (TF-IDF). The TF-IDF feature extraction approach produces an accuracy score and a classification report using the Multinomial Naive Bayes classification algorithm.

In conclusion, the project's goal was to categorise movie reviews as either good or unfavourable. To do this, the proposed system used a variety of data pretreatment procedures, feature extraction approaches, and classification algorithms.

REFERENCES

[1] Nagamma P, Pruthvi H.R, Nisha K.K and Shwetha N H. An Improved Sentiment Analysis Of Online Movie Reviews Based On Clustering For Box-Office Prediction. International Conference on Computing, Communication and Automation (ICCCA2015).

[2] Mais Yasen, Sara Tedmori. Movies Reviews Sentiment Analysis and Classification.2019 IEEE Jordan International Joint Conference on Electrical Engineering and Information Technology(JEEIT).

[3] Zhongxiang Ding,Yali Qi,Deping Lin. Albert-based sentiment analysis of movie review.2021 4th International Conference on Advanced Electronic Materials, Computers and Software Engineering(AEMCSE).

[4] Vihaan Nama,Dr.Vinay Hegde,Dr.B.Satish Babu.Sentiment Analysis of Movie Reviews: A Comparative Study between the Naïve-Bayes Classifier and a Rule-based Approach

[5] Depuru, Sivakumar, Anjana Nandam, P. A. Ramesh, M. Saktivel, and K. Amala. "Human Emotion Recognition System Using Deep Learning Technique." Journal of Pharmaceutical Negative Results 13, no. 4 (2022): 1031-1035.

[6] Sivanantham, S., V. Krishnamoorthy, D. Karthikeyan, M. Sakthivel, V. Mohanraj, and V. Akshaya. "Web Hazard Identification and Detection Using Deep Learning-A Comparative Study." Journal of Pharmaceutical Negative Results 13, no. 4 (2022): 1052-1060.

[7] Depuru, Sivakumar, Anjana Nandam, S. Sivanantham, K. Amala, V. Akshaya, and M. Saktivel. "Convolutional Neural Network based Human Emotion Recognition System: A Deep Learning Approach." In 2022 Smart Technologies, Communication and Robotics (STCR), pp. 1-4. IEEE, 2022.

[8] Saravanakumar, V., K. G. Suma, M. Sakthivel, K. S. Kannan, and M. Kavitha. "Segmentation of hyperspectral satellite image based on classical clustering method." Int J Pure Appl Math 118, no. 9 (2018): 813-820.

[9] Sakthivel, M., S. Sivanantham, R. Kamalraj, and V. Krishnamoorthy. "An Analysis of Machine Learning Depend on Q-MIND for Defencing the Distributed Denial of Service Attack on Software Defined Network." International Journal of Early Childhood Special Education 14, no. 05 (2022): 3769-3776.

[10] Bandana, Rachana. "Sentiment analysis of movie reviews using heterogeneous features." In 2018 2nd International conference on electronics, materials engineering & nano-technology (IEMENTech), pp. 1-4. IEEE, 2018.

[11] Rehman, Anwar Ur, Ahmad Kamran Malik, Basit Raza, and Waqar Ali. "A hybrid CNN-LSTM model for improving accuracy of movie reviews sentiment analysis." Multimedia Tools and Applications 78 (2019): 26597-26613.

[12] Qaisar, Saeed Mian. "Sentiment analysis of IMDb movie reviews using long short-term memory." In 2020 2nd International Conference on Computer and Information Sciences (ICCIS), pp. 1-4. IEEE, 2020.

[13] S. Depuru, P. Hari, P. Suhaas, S. R. Basha, R. Girish and P. K. Raju, "A Machine Learning based Malware Classification Framework," 2023 5th International Conference on Smart Systems and Inventive Technology (ICSSIT), Tirunelveli, India, 2023, pp. 1138-1143, doi: 10.1109/ICSSIT55814.2023.10060914.

[14] Tan, Kian Long, Chin Poo Lee, and Kian Ming Lim. "A Survey of Sentiment Analysis: Approaches, Datasets, and Future Research." Applied Sciences, 13, no. 7, 2023.

[15] William, P., Anurag Shrivastava, Premanand S. Chauhan, Mudasir Raja, Sudhir Baijnath Ojha, and Keshav Kumar. "Natural Language processing implementation for sentiment analysis on tweets." In Mobile Radio Communications and 5G Networks: Proceedings of Third MRCN 2022, pp. 317-327. Singapore: Springer Nature Singapore, 2023.

[16] Bordoloi, Monali, and Saroj Kumar Biswas. "Sentiment analysis: A survey on design framework, applications and future scopes." Artificial Intelligence Review, 2023.

[17] Namitha, Seelam, Pallerla Sanjan, Nerella Chaithra Reddy, Yechuri Srikar, Hariharan Shanmugasundaram, and Bhanu Prasad Andraju. "Sentiment Analysis: Current State and Future Research Perspectives." In 2023 7th International Conference on Intelligent Computing and Control Systems (ICICCS), pp. 1115-1119. IEEE, 2023.

[18] Yadav, Vandana, Parul Verma, and Vinodini Katiyar. "Long short term memory (LSTM) model for sentiment analysis in social data for e-commerce products reviews in Hindi languages." International Journal of Information Technology 15, no. 2, 2023.

[19] A. B. Reddy and R. Y. R. Kumar, "Performance and Security Analysis in Cloud Using Drops and T-Coloring Methods," 2022 Fourth International Conference on Emerging Research in Electronics, Computer Science and Technology (ICERECT), Mandya, India, 2022, pp. 1-7, doi: 10.1109/ICERECT56837.2022.10060014.

BLDA-CSWDT autoimmune thyroid disease risks predictive model using machine learning and deep feature extraction techniques

Nagavali Saka*

Jawaharlal Nehru Technological University Anantapur (JNTUA),
Anantapur, Andhra Pradesh, India
Email: vali214@gmail.com
*Corresponding author

S. Murali Krishna

Department of Computer Science and Engineering,
Sri Venkateswara College of Engineering (SVCE),
Tirupati, Andhra Pradesh, India
Email: muralikrishna.s@svcolleges.edu.in

Abstract: Nowadays, different thyroid disorders are observed which are affecting the human population worldwide. Hence, to provide suitable treatment and be cost-consuming for the patients, an earlier diagnosis is required. To improve prediction, this paper proposed Bayes-linear discriminant analysis (B-LDA) and cuckoo search based weighted decision tree (CSWDT) models to predict the autoimmune thyroid risk assessment from the obtained dataset. Initially, after pre-processing, the features are extracted using the deep MLP model, and the significant features are fused by using the B-LDA model which overcomes the dimensionality reduction issue. Further, the classification is performed by using the optimised cuckoo search with a weighted decision tree model. In addition, K-fold cross-validation is performed and attains a better accuracy value of 99.5% in thyroid disease prediction.

Keywords: autoimmune thyroid disease; deep MLP; cuckoo search optimisation; LDA; weighted decision tree; Bayes linear discriminant analysis; B-LDA; cuckoo search based weighted decision tree; CSWDT.

Reference to this paper should be made as follows: Saka, N. and Krishna, S.M. (2023) 'BLDA-CSWDT autoimmune thyroid disease risks predictive model using machine learning and deep feature extraction techniques', *Int. J. Biomedical Engineering and Technology*, Vol. 43, No. 2, pp.185–206.

Biographical notes: Nagavali Saka is a research scholar in the Department of Computer Science and Engineering working in Jawaharlal Nehru Technical University Ananthapur, India. He is currently working as an Associate Professor in Ramachandra College of Engineering, Eluru, Andhra Pradesh, India, having 16 years of teaching experience. His major area of research includes data mining and machine learning.

S. Murali Krishna is currently working as a Professor and Head of the Department, in the Department of Information Technology, Sri Venkateswara College of Engineering, Tirupathi, Andhra Pradesh, India. He has more than 20

Copyright © 2023 Inderscience Enterprises Ltd.

years of teaching experience. His major areas of research include text mining and big data. He has published more than 30 research papers in international/national journals and conferences of reputed journals.

1 Introduction

In human beings, thyroid disease is one of the most common syndromes worldwide (Leitch et al., 2020). The endocrine gland or thyroid gland disease differentiates from low production to higher production of thyroid hormones. The thyroid gland released triiodothyronine-T3 and thyroxine – T4 into the bloodstream considered principal hormones. The rate of metabolism is regulated by thyroid hormones functions (P.G, 2021). In controlling the metabolism, in some cases, thyroid hormones secretion is at fault. The most common issues of thyroid disease are hypothyroidism – low thyroid hormone, the thyroid is not active in the blood, and hyperthyroidism – releases more thyroid hormones because of an overactive thyroid (Kumar et al., 2020). An earlier diagnosis is always recommended to prevent the critical effects and better treatment to maintain the normal level of thyroid hormone (Tyagi et al., 2018). Hence, thyroid malfunction resulted in thyroid disorders (Prerana and Taneja, 2015).

The autoimmune thyroid disease is due to immune system dysregulation, genetic predisposition, and environmental factors. Because of the progression and onset heterogeneity, the prognosis and diagnosis of the disease are unpredictable. Autoimmunity pre-disposition is highly connected with genetics and occurred due to mechanical defects resulting in a self-tolerance loss. The autoimmune disease prevalence is highly complex due to the initiate of viral disease and the patients with autoimmune disease have the prior of upper respiratory tract infection to estimate and the diseases are represented variably across various researches (Franco et al., 2013).

Autoimmune thyroid disease specifically benefits from personalised healthcare for a casual molecular mechanism that is an alternative to special symptoms treatment (Taylor et al., 2018). The standard patient care generates different clinical data types which include the laboratory results and MRI images. In addition to clinical data, omic data like patients' proteomic profiles, and transcriptomic and genomic profiles are available recently (Talasila et al., 2020). Rapid analysis can be performed through omic data. Several omic data types can be used in the machine learning model for identifying the exact details of autoimmune thyroid disease which further provides significant novel methods. The data mining methods can have the capability to identify the clinical relevant pattern among the huge data provided (Chaurasia et al., 2018). The capability towards stratify patients by exploiting the huge data has association for their care from estimation of autoimmune risks, initial and ongoing management, diagnosis, treatment response, and results and observation (Stafford et al., 2020).

The evaluation of thyroid nodules is clinically challenging. Thyroid nodules are commonly detected by the way during the diagnostic of neck image (Ospina et al., 2020). They may be found over 42 to 76 percentages of people those become more widespread with accumulative age (Durante et al., 2018). Majority of the thyroid nodules are benign, where 10% may be malignant (Detweiler et al., 2019). Radioactive iodine therapy, chemo-radio-therapy, immunotherapy (or) thyroidectomy for preventing death and

recurrence may specified to the treatment of thyroid cancer over the patient preference, histological subtype and comorbidities.

Thyroid diseases are difficult for detecting with test outcome and only trained professionals are capable of doing (Cappola et al., 2016). The conventional method for diagnosing thyroid diseases is of two ways such as by physical symptoms and signs and by blood test. Moreover, each research is complex for understanding due to the huge range of data, which are needed to anticipate outcome (Nguyen et al., 2015).

Recently the new technology in data mining classification algorithms developing in medical science the researchers can capable of providing the expert advisory system to diagnose the various types of diseases with greater accuracy. Due to certain errors during the general diagnosis process, medical professionals are using these newly developed systems based on artificial intelligence. It can assist the doctors to reduce the costs and time for effective treatment and diagnosis (Prasad et al., 2016). Inspired by the above statements, the autoimmune thyroid disease risks assessment and prediction are performed in this study.

The major contribution of the study involves,

- To perform the feature extraction from the thyroid disease dataset using the deep MLP model and the significant fused features are extracted using the Bayes-linear discriminant analysis (B-LDA) model to overcome the dimensionality reduction issue.
- To classify the extracted features with higher accuracy, a cuckoo search-based weight-optimised decision tree for optimisation, time-consuming is used, and to improve accuracy, K-fold cross-validation is followed.
- To compare the proposed BLDA-CSWDT model with various existing methods to prove the effectiveness of the newly developed model.

1.1 Paper organisation

The following section describes the related works of thyroid disease prediction using different data mining algorithms. Further, the proposed BLDA-CSWDT model is explained clearly in Section 3. Section 4 illustrated the dataset description, experimental analysis, and comparative analysis of the proposed model. Finally, the research is concluded in Section 5.

2 Related works

In Chaubey et al. (2021), three machine learning algorithms such as decision trees, k-nearest neighbour, and logistic regression have been focused on thyroid disease prediction, which assists in improving accuracy. Machine learning repository set of thyroid dataset has been used, obtained from UCI archives. Here, 96.8% accuracy has been obtained. Furthermore, 1,179 thyroid modules have been evaluated in Ouyang et al. (2019) based on nonlinear and linear algorithms using pathological references. For every module, the ultrasonography features have been assessed like shape, aspect ratio, hypoechoic halo, margins, size, calcification pattern, cervical and vascularity lymph node, echogenicity, and composition. Kernel support vector machines and random forest

algorithms show better AUC values. In analysing the thyroid nodules malignancy risks, a nonlinear machine learning algorithm shows better results.

In Razia et al. (2020), dimensionality reduction algorithms and multiple classification approaches have been used. Without external modification, machine learning exhibited learning capacity. For multi-dimensional and higher-dimensional data, machine learning algorithms have been used. From UCI data repository hypothyroid disease dataset has been used. Using the WEKA tool in a Windows 7 environment the study has been evaluated. Decision and J48 classifier used. Classification has been performed as primary, secondary, negative, and compensated thyroid. The accuracy of both approaches has been related based on the confusion matrix. Compared with the decision tree J48 classifier shows better results (Banu, 2016).

Common thyroid problems such as hypothyroidism and hyperthyroidism have been studied and classified using a decision tree, radial basis function network, and multilayer perceptron (MLP). For the decision tree, a better classification rate has been obtained. From the UCI machine learning repository, the dataset has been used for validation. However, the factors affecting thyroid identification have not yet been performed (Ioniţă and Ioniţă, 2016). Moreover in Raisinghani et al. (2019), recent machine learning algorithms have been used for thyroid diagnosis and prediction. Concerning thyroid reports and different symptoms, the thyroid disease prediction has been performed. Better accuracy resulted for the decision tree approach as 99.4% from a different comparative study. In another case, classifier performance shows a positive impact by evaluating new features in thyroid data. Naïve Bayes shows better results as 98.92% when analysed with a decision tree, KNN, logistic regression, and SVM. Data augmentation approaches and KNN functions have been used for more precise outcomes (Abbad Ur Rehman et al., 2021).

The radiomics model has been developed for analysing the immunohistochemical features of suspected thyroid patients. Non-redundant and reproducible features selected using spearman and test re-test co-efficient. For the feature selection process, the Kruskal Wallis test has been used, and using a support vector machine, a feature-based model has been developed. The performance has been analysed based on AUC, sensitivity, accuracy, and specificity. An individual non-invasive detection based on galectin, thyroperoxidase, and cytokeratin to CT images has been performed. Benign and malignant thyroid diseases have been classified (Gu et al., 2019). Likewise in Yadav and Pal (2019), thyroid symptom has been identified. Two major approaches have been used based on neural network, overfitting, and decision tree – ensemble I and combinations of boosting and bagging algorithms as ensemble II. The results show that the second model exhibited better results.

In another work (Elliott Range et al., 2020), surgical and cytologic pathology diagnoses have been recorded and interrelated for every thyroid nodule. The final pathology malignancy has been predicted and follicular cells were identified. The specificity and sensitivity were obtained as 90.5% and 92.0%. Further in Zhang et al. (2019), thyroid cancer has been identified by generating a prognostic system for distant metastasis status, ages, primary tumour, and regional lymph nodes. In Temurtas (2009), three neural network classification models such as learning vector quantisation, probabilistic neural network, and multilayer neural network have been used for the diagnosis of thyroid disease. UCI machine learning database has been used for 10-fold and 3-fold cross-validation techniques. The study (Razia and Rao, Rao) explored the thyroid gland's non-functionality, thyroid disease, and its autoimmune stage. Various

neural network frameworks have been utilised for thyroid dysfunctionality identification. Certain parameter evaluation approaches have been discussed. In differentiating the thyroid disease dysfunctionalities in recent decades using a neural system has been explored.

For thyroid disease, early prediction different machine learning algorithms have been evaluated and the MLP has been used which yields 99% accuracy. This approach can assist the doctors in early diagnosis to provide better treatment. For human beings' welfare ensure, the proposed model can fight against thyroid disease (Asif et al., 2020). Kernel-based classifier and optimal feature selection used in thyroid data classification. Multi-kernel support vector machine and grey wolf optimisation feature selection process can enhance the classification process. Thyroid classification results show a 97.4% accuracy rate in thyroid prediction (Shankar et al., 2020). The thyroid disease dataset was examined using random forest, decision tree, and regression tree algorithms. Using the bagging ensemble approaches the results of the classifier have been enhanced. Prediction accuracy is based on seed and number fold values. Random forest obtains 99% and decision tree obtains 98% accuracy (Yadav and Pal, 2020).

Using the artificial neural network effective thyroid disease diagnosis has been performed. With three different approaches artificial neural networks, multiple regression, and random forest the results have been explored and compared. Here, ANN delivered higher accuracy compared with the other two methods at 98.22% (Parmar e al., 2018).

3 Methodology

In this research, a thyroid disease predictive novel model is developed to perform a risk assessment for autoimmune thyroid diseases using the different machine learning, optimisation algorithms, and deep feature extraction approaches. Initially, the thyroid disease dataset is obtained from the UCI repository and undergoes pre-processing to remove the missing values. Further significant features are extracted using deep MLP technique. Further, the significant data is combined using feature fusion by B-LDA. Finally, the fused features are evaluated in the training and testing model. Further, the classification of the features is performed using the hyperparamised tuning the optimised cuckoo search algorithm. K-fold cross-validation is performed to analyse the accuracy obtained. Finally, in the predictive phase, the sickness and the normal stage are predicted. The overall working flow is shown in Figure 1.

3.1 Feature extraction using deep MLP

Deep MLP neural networks are considered feed-forward neural networks which are trained using the standard backpropagation algorithm. MLP can be trained and widely used, to learn to input data and transform it into expected outcomes. The supervised learning artificial neural network has been utilised extensively in MLP which is considered a solution to various issues including classification, vision, control systems, identification, pattern recognition, and others. The obtained output values are related to the expected output in backpropagation for calculating the predefined error function values. Every connection weight is adjusted for minimising the error function. This

process is repeated for a greater number of training cycles and the network converges to a certain state if the calculation of error is small. The specific target function is learned from the network. The deep MLP architecture is shown in Figure 2.

Figure 1 Working flow

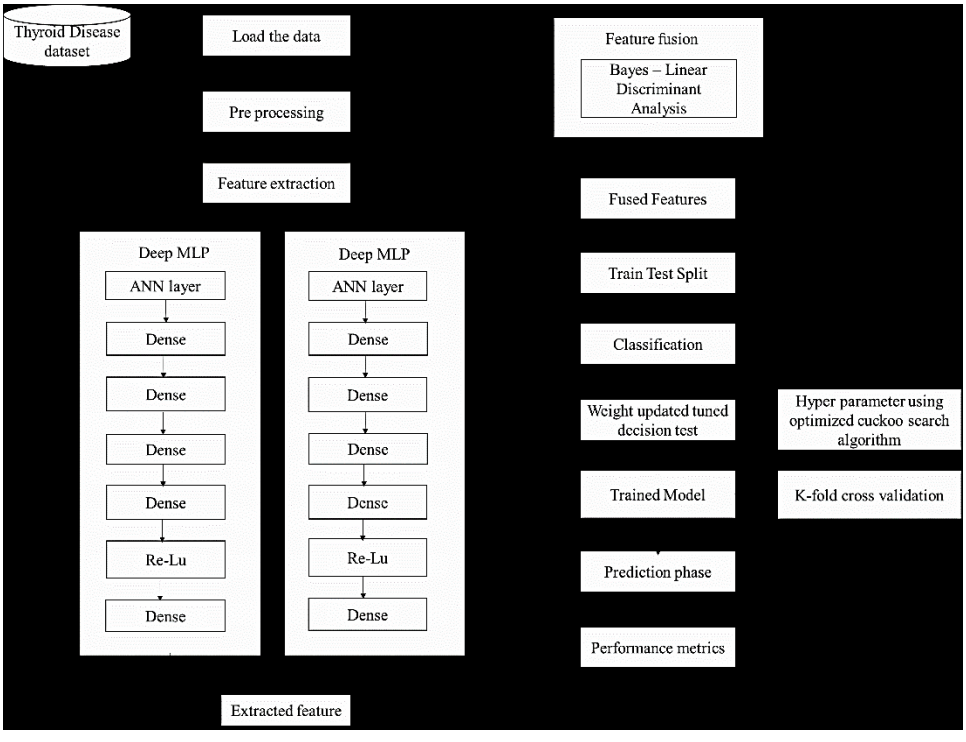

Figure 2 Deep MLP architecture (see online version for colours)

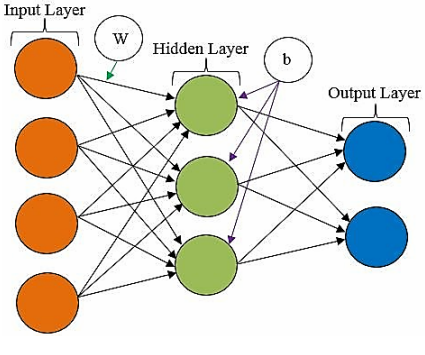

For nonlinear optimisation, a general approach has been applied which is refer as gradient descent. The error function derivative based on network weights has been measured and when the error decreases, the weights are modified. The squared Euclidean distance between the expected output and real network output is considered a computational error. The proposed algorithm of deep MLP is illustrated as:

Algorithm 1

Actual and expected output

Actual input $Inp_{ip} = Inp_i0, Inp_i1, Inp_i2 \ldots\ldots\ldots\ldots Inp_{in} - 1$ and

Target output is $Op_{ip} = Op, Op_{i1}, \ldots\ldots\ldots\ldots Op_{im} - 1$

The no. of input nodes is termed as IN_i and the no. of output nodes is termed as ON_i.

Measure the actual or real output

Every layer measures $FXE = f[Wgt_{i0}Inp_{i0} + Wgt_{i1}Inp_{i1} + \cdots \ldots\ldots\ldots Wgt_iM_iIn_{pi}]j$. This is transferred to the next layer, as input. The output value of the final layer is *flo*.

Starting from the outputs, adapt the weights

$Wgt_{ij}(t_i + 1)$

$= Wgt_{ij}(t)$ where *n* gain term and *ppi* is an error term for pattern *p* on node

$+ Inp_i nppjflo$

For hidden units $ppj = Wgtflo(1 - flo)[(pp0Wgt_{ij}0 + pp1Wgt_{ij}1 + \cdots + ppkWgt_{ij}Wgt)]11$

For output units, $ppj = Wgtflo(1 - flo)(t_i - flo)$

The sum is over the *k nodes* in the layer above node *j*.

Feed forward neural network exhibited general context in representing the nonlinear functional mapping among a set of input and output variables. This is attained by representing the nonlinear function of several variables to nonlinear functions compositions of a single variable termed activation functions. MLP neural network hidden layer is typically comprised of the sigmoid function. The MLP neural network is comprised of defined hidden layers with the initial layer employing hyperparameter tuned activation and other tuned activation function implemented by the second layer and measures the bias. For all activation functions, the proposed method executes the code like sigmoid, relu, tanh, and others. Better results have been recorded and predicted. Proposed deep MLP with fuzzy membership function and a second layer with tanh activation function are defined below.

The fuzzy membership function is

$$F_i(x) = \frac{1}{1 + \left(\frac{x - wgt_2}{wgt_o}\right)^{2Wgt_1}} \tag{1}$$

Here, the input is *x* and the bias is F_i.

The tanh member applies the tanh function and bias to every neuron in the layer. The tan h will crush every neuron ranging from –1 to 1. These nonlinear elements provide the network with soft decisions ability. The tan h activation function is expressed as:

$$\tanh(i) = \frac{(e^i) - (e^{-i})}{(e^i) + (e^{-i})} \tag{2}$$

The sum of input patterns is *i* in which a set of features are returned and from hidden nodes, they are learned.

3.2 Feature fusion using B-LDA

For feature fusion, performance to identify the significant features of autoimmune thyroid disease B-LDA is utilised. This model is considered an extension of linear discriminant analysis. In the Bayesian model, the computation of regression is performed and the overfitting is avoided in higher dimensional and noisy signals in which regularisation is used. In Bayesian regression, the significant assumption is *tg* target value has the linear association to *vec* with additive *nse*– Gaussian noise. Hence, it is defined as $tg = wgt^T vec + nse$ for, weight *wgt* the likelihood function is defined as:

$$p(L \mid iv, wgt) = \left(\frac{iv}{2}\right)^{\frac{c}{2}} \exp\left(-\frac{iv}{2}\left|B^T - wgt - m\right|\right) \tag{3}$$

From the above equation (3), $B\{m\}$ which is expressed by *L*. The matrix *B* is provided by the training vector, the filtered signals are denoted by *tg*, i_v is the inverse variance of noise and *c* is the sample size. The prior distribution of *wgt* is defined as:

$$p(wgt \mid fs) = \left(\frac{fs}{2\pi}\right)^{\frac{1}{2}} \left(\frac{\varepsilon}{2\pi}\right)^{\frac{1}{2}} \exp\left(-\frac{1}{2}\left(-\frac{1}{2} wgt^T J'(fs) wgt\right)\right) \tag{4}$$

The square regularisation is termed as:

$$J'(fs) = \begin{bmatrix} \alpha & .... & 0 \\ . & . & . \\ 0 & .... & \varepsilon \end{bmatrix} (l+1) * (l+1) \tag{5}$$

From equation (5), the better prediction is obtained by *fs* hyper-parameter and *l* is the assigned vector. The weight *wgt* followed Gaussian distribution exhibited zero mean and small value contained in ε. To execute the Bayes rule the *y* posterior distribution is easily measured as:

$$p(y \mid iv, fs, L) = \frac{p(L \mid iv, wgt)\, p(wgt \mid fs)}{\int p(L \mid iv, wgt)\, p(wgt \mid fs) dwgt} \tag{6}$$

In real, the posterior distribution is greatly Gaussian. The co-variance matrix *W* and mean vector *v* must compulsory satisfy for posterior distribution as

$$W = \left(ivBB^T + J'(fs)\right)^{-1} \tag{7}$$

$$v = iv\left(ivBB^T + J'(fs)\right)^{-1} Btg \tag{8}$$

For the prediction input vector $\widehat{vec}$, the probability distribution on regression target is defined as:

$$p\left(\widehat{tg} \middle| iv, fs, \widehat{vec}, L\right) = \int p\left(\widehat{tg} \middle| iv, fs, \widehat{vec}, wgt\right) p\left(wgt \middle| iv, fs, L\right) dwgt \tag{9}$$

The predictive calculation is highly Gaussian again in which the mean is defined as $\mu = v^T \widehat{vec}$ and the variance is denoted as $\delta^2 = \frac{1}{\beta} + \widehat{vec}^T W \widehat{vec}.$

The following algorithm describes the B-LDA.

Algorithm 2

Gaussian noise *c*, therefore it is expressed as *tg = wgt^T vec + nse*
For the weight denoted as *wgt*, the likelihood function is expressed as equation (3).
The weight *wgt* follows a Gaussian distribution which
has zero mean and a small value is contained in *ε*.
And for employing the Bayes rule, the posterior distribution
of *y* will be computed using the equation (6)
For the posterior distribution, the mean vector *v*, and the covariance
Matrix *W* should mandatorily satisfy the following form as equation (9)
At last, we will get the optimised reduced features which are highly Gaussian in nature.

Table 1 denoted all features extracted before B-LDA was implemented and after B-LDA only the relevant and significant features are identified.

Table 1 Before and after B-LDA feature fusion

Before B-LDA	*After B-LDA*
(128 + 256) 384	25

From Table 1, mentioned that the deep MLP extracted 384 features and after applying the B-LDA algorithm, it extracts only the relevant and significant 25 features.

3.3 Hyperparameter tuning using optimised cuckoo search algorithm with k-fold validated weighted decision tree (CS-WDT)

Cuckoo search is considered an evolutionary algorithm proposed by Deb and Yang in the year 2009 (Yang and Deb, 2009). This algorithm is termed a search strategy model on the cuckoo species' family parasitism, which lay their eggs in other host birds' nests. If the host bird identifies these eggs, it will return and form a new nest somewhere or fling these alien eggs. Every cuckoo species can modify its position when time passes and focused on one new solution from every egg in the nest as shown in Figure 3.

The worst solution is replaced by this new solution. Only the three perfect rules are used which are considered as:

1 Every cuckoo lays one egg at a time and is put up in other nests which are selected randomly.

2 For next-generation, better nests with a higher quality of eggs are considered.

3 No. of available other host nest is a fixed and suitable host which discovers the alien egg with $P \in [0, 1]$ probability.

Figure 3 Cuckoo search (see online version for colours)

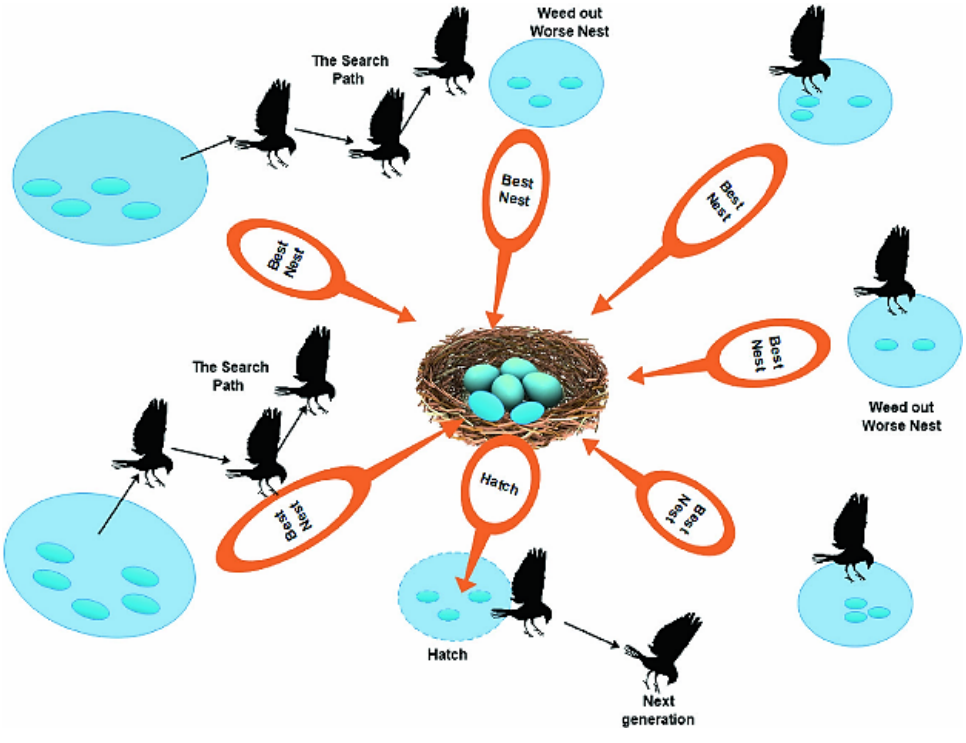

From this observation, various studies have indicated the flight behaviours of different insects and animals show the Levy flight's standard characteristics. Based on these flight behaviours and breeding views, the cuckoo search algorithm is developed. For the optimisation issue, the solution quality is based on the objective function's fitness value. By concentrating on these rules the cuckoo search algorithm pseudo-code is developed.

Algorithm 3

Start
Obj function of $(a)ft = (ft_1, \ldots, f_{td})^T$
Create n host nests initial population $a_i(i = 1, 2, \ldots, n)$
While ($t <$ MaxGeneration) or (Stop Criterion)
    Get random Levy flights based on cuckoo
    Estimate the fitness/quality of Of_i
    select nest randomly between n (say, j)
    If ($Of_i > Of_j$)
        Replace j
End
    Worse nests are abandoned and built the new ones
    Keep the better solutions or nests with higher quality outcomes
    identify the current best solution through ranking

14 End while
15 Post-process results and visualisation
16 End

For generating the new solutions $filter^{p+1}$, focus on cuckoo i, the levy flight is determined as:

$$filter_i^{p+1} = filter_i^p + \alpha \oplus Levy(\gamma) \tag{10}$$

Here $\alpha > 0$ is linked with the solution space. Usually, set α = O(1). The above equation (10) is the stochastic equation for a random walk, based on transition probability and current location the next location is formed which is the Markov chain. Entry-wise multiplications termed as $\oplus$. In the random walk provided from Levy flight and Levy distribution, the random step length is framed which exhibits infinite variance with an infinite mean as:

$$Levy \sim u = p^{-\gamma} = (1 \le \gamma \le 3) \tag{11}$$

Here, certain new solutions are created by Levy flight which is around the best solution and the local search is accelerated. Nevertheless, the new solutions in greater proportions are generated from the best solution and lead to local search acceleration. Locations of new solutions may be far from the present best solution and it ensures that the algorithm will not befall within a local optimum.

3.3.1 Hyperparameter tuned weight updated cuckoo search

This proposed newly developed hyperparameter tuned weight updated cuckoo search algorithm is used for the levy flights randomisation as discussed. The initial nest's counts can be varied from 10 to 100 and their impacts can be observed on the deep MLP model accuracy value. The discovery of egg probability has been set to 0.25 and it can be sufficient for certain optimisation problems. At first, n number of eggs is initialised with *zero* values. The nests are with a random array of lengths. For fine-tuning, the hyper-parameters are there, and every nest represents the hyper-parameters possible values. Till the reaching of maximum generation, the process is continued shown in Algorithm 4. In every iteration or generation, a nest is randomly selected using levy flights.

Table 2 shows the hyperparameter selected and its suitable values based on cuckoo search algorithm.

Table 2 Proposed hyperparameter and its values

Hyperparameter	*Values*
min_samples_split	[2, 3, 4, 5]
max_depth	[10, 15, 20]
min_samples_leaf	[2, 3, 4, 5]
max_features	['auto', 'sqrt, 'log2']
max_leaf_nodes	[10, 15, 20, 30]

The following algorithm describes the hyperparameter tuned weight updated cuckoo search.

Algorithm 4

1 Create a random population with nests – n and dimensions – d
   n is the population size, and no. of hyperparameters is d, $d = 3$
2 Generate an array of length-eggs with n as the no elements
3 Set the best_(ever_solution as) 'None'.
4 While $t <$ max_gen:
   a While $j <$ total nests:
      1 obtain random nest using Levy flight and generate model
      2 implement the model and store it in an array of length-eggs
5 If ($egg[i] >$ best_ever_solution):
      1 Replace the best_ever_solution by $egg[i]$
   b End if
   c Abandon the fraction of pa nests and generate new ones ignoring the best nests.
6 end While
7 end While
8 Save the generated frozen model and note the values of observed hyper-parameters that give the best result.
9 Set the best hyperparameters
   // Weight updation from the deep MLP
10 Get the weights from the learned deep MLP wgt
11 for i in wgt:
12 fit the hyperparameter tuned decision trees with sample_weight (i)
13 check the predictive performance over accuracy
14 Select the best weight based on the accuracy and assign it to it.

3.3.2 K-fold cross validated weighted decision tree

A decision tree is regarded as generally classifying the divide and conquers approach. Here the classification approach is used for classifying the thyroid disease with K-fold cross-validation. Based on this model, the data is represented in a tree model, the different characteristics are possessed by internal nodes, and leaf nodes are expressed from data sample labels. The tree's path is between the leaf and root to find the corresponding dataset. The leaf node consists of the final grading outcome. The nested k-fold cross validation weighted decision tree is described in Algorithm 5. The inner loop performs the cross-validation which recognises the better features and hyper-parameters are modelled using the k-data fold, which is available at every outer loop iteration. For every outer loop stage, the model is trained and assessed on a held-out data fold. This proposed model obtains k evaluations of proposed model outcomes, which allows the model to be evaluated on every sample and one for each data fold.

Algorithm 5

1 Define the hyperparameters that are obtained by the tuning process
2 Divide the data into K folds with an approximately equal distribution of classes and controls

3 For fold kf_{ij} in the KF folds:
4 Set the fold k_{ij} as the test set
5 Perform automated feature selection on the remaining KF-1 folds
6 For parameter combination c in C:
    a for fold k_{ij} as the validation set
    b Train the model on the remaining KF-5 folds
    c Evaluate the model performance on fold kf_{ij}
1 Calculate the average performance over KF-5 folds for the parameter combination c
Train model on KF-1 folds using the hyperparameters combination that yielded the
The best average performance overall steps of the inner loop
Evaluate the model performance on the KF-fold kf_{ij}
Calculate the average performance over KF folds.

4 Results and discussion

The following section describes the proposed B-LDA with CS-WDT model outcomes for thyroid disease prediction based on autoimmune thyroid disease and risk assessments.

Figure 4 Correlation plot-thyroid dataset (see online version for colours)

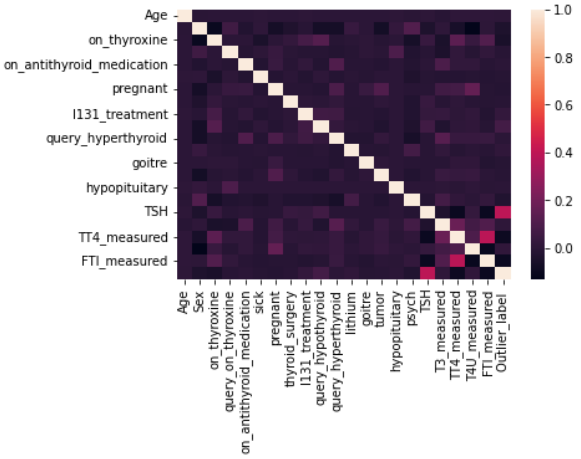

4.1 Dataset description

The autoimmune thyroid disease prediction is performed by using the thyroid disease dataset obtained from the UCI repository (https://archive.ics.uci.edu/ml/datasets/Thyroid+Disease). Thyroid disease dataset was collected from Garavan Institute and documented by Ross Quinlan. It contains six databases which are from the Garavan Institute in Sydney, Australia. The box plot for the data with attributes such as sick, pregnant, thyroid surgery, treatment, psych, TSH, T3, T4, and FTI measured labels obtained from the thyroid dataset is depicted in Figure 5. Figure 4 shows the correlation plot for the respected dataset.

Figure 5 Box plots – thyroid dataset (see online version for colours)

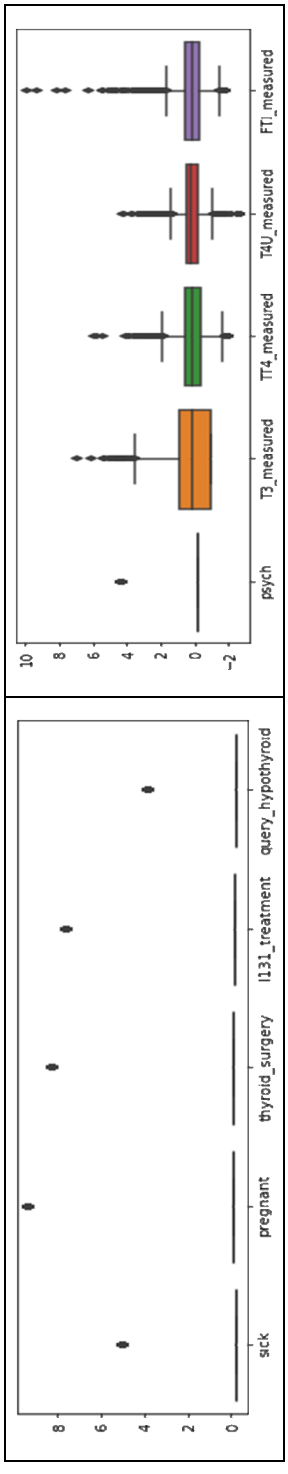

Figure 6 Outlier label (see online version for colours)

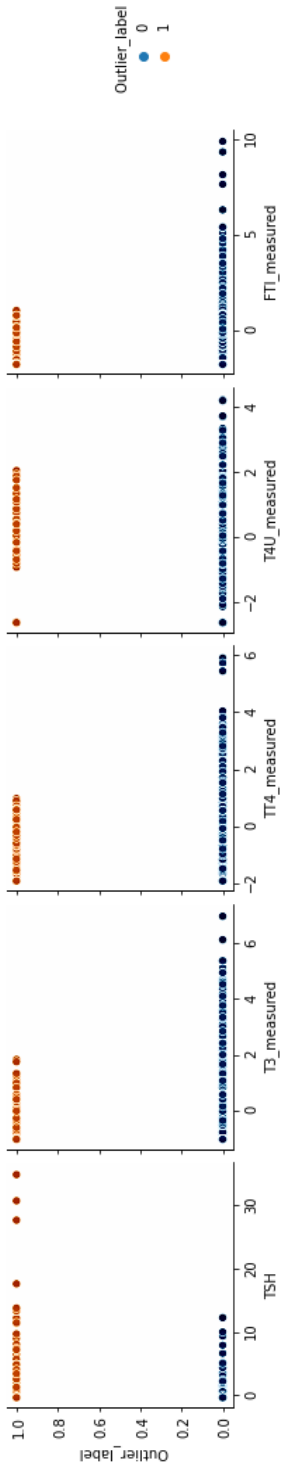

From Figure 6, it shows that the outliers with the label as 0 and 1 value for TSH, T3 measured, TT4 measured, T4U measured and FTI measured attributes. In most cases, the outlier label is 1 and in rare cases, it is 0.

4.1.1 Experimental analysis

The following section illustrates the proposed B-LDA-CSWDT model results for thyroid disease prediction.

Figure 7 Accuracy – before and after B-LDA (see online version for colours)

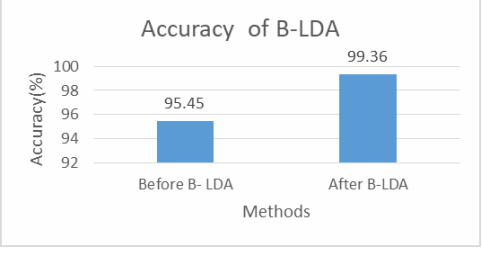

As discussed previously the set of features selected before B-LDA is 384 and after B-LDA is 25 features. The accuracy obtained in extracting the features is obtained as 99.36% after applying B-LDA. However, before B-LDA the accuracy was obtained as 95.45%.

Figure 8 K-fold cross-validation-proposed model (see online version for colours)

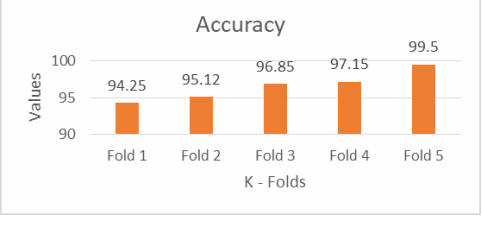

From Figure 8, it shows that a 5-fold cross-validation is performed for the autoimmune thyroid disease risk assessment prediction using B-LDA-CSWDT proposed model. For the first fold, the prediction accuracy was obtained as 94.25%, and 95.12% for fold 2, 96.85% for fold 3, 97.155 for fold 4, and for fold 5 the accuracy was obtained as 99.5%. Thus, the accuracy values are improved from the first fold to 5th fold cross-validation to 99.5%.

Table 3 illustrated that from the best performing topologies the highest accuracy scoring hyperparameters are collected and presented in Table 3. The relu activation function and SGD optimiser with ten batch sizes, 30 Epochs performed from two models combined dense layer of 128 to 256 recorded as best results compared with their counterparts. Hence, the accuracy was obtained as a 0.995 score value by combining model 1 and model 2 of deep MLP architectures used in the proposed B-LDA-CSWDT model.

Table 3 Hyper parameters in the deep MLP model 1 and 2 – accuracy

Model 1					*Model 2*					*Accuracy obtained*
Activation	*Optimizer*	*Batch_size*	*Epochs*	*Dense layer*	*Activation*	*Optimizer*	*Batch_size*	*Epochs*	*Dense layer*	
tanh	adam	10	100	50	tanh	adam	10	100	100	0.95412
tanh	rmsprop	10	100	10	tanh	SGD	10	50	50	0.96842
relu	rmsprop	10	100	100	relu	rmsprop	10	100	150	0.96982
relu	SGD	10	100	120	relu	SGD	10	50	200	0.97451
relu	adam	10	30	100	relu	rmsprop	10	30	150	0.98965
relu	SGD	10	30	128	relu	SGD	10	30	256	0.995

4.2 Comparative analysis

The following section illustrated the comparative analysis of the proposed B-LDA-CSWDT model with various existing models.

Table 4 Comparative analysis – 1

Methods	*Decision tree accuracy*
Tyagi et al. (2018)	75.76%
Umar Sidiq et al. (2019)	98.89%
Chaubey et al. (2021)	87.50%
Proposed method	99.50%

From Table 4, it shows that the proposed model with an accuracy of 99.5% outperforms the other existing methods obtained from other (Tyagi et al., 2018; Chaubey et al., 2021; Umar Sidiq et al., 2019) existing studies as 75.78%, 98.89%, and 87.50% respectively using data mining approaches.

Figure 9 Comparative analysis – 2 (see online version for colours)

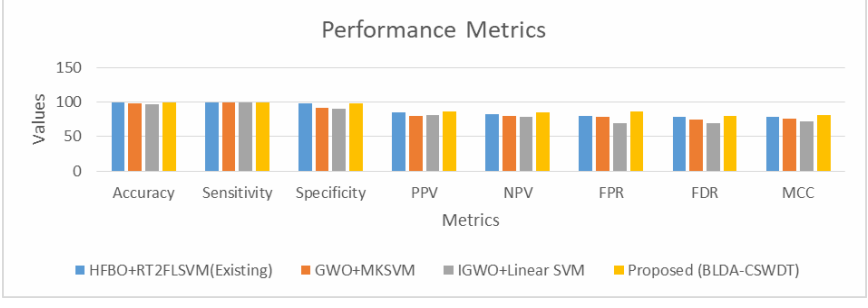

From Figure 9, it shows the accuracy assessment metrics in terms of various thyroid disease prediction models. The proposed model BLDA-CSWDT model accuracy, specificity, PPV, FPR, FDR, sensitivity, MCC, and NPV metrics are evaluated and results obtained as 99.5, 98.58, 87, 87, 80, 99.3, 81, and 85.26 respectively. The results are compared with the existing studies of HFBO-Rt2FLSVM, IGWO-LSVM, and GWO-MKSVM models (Sureshkumar et al., 2022). The proposed model BLDA-CSWDT accuracy improved compared with other models with variations of 0.22% higher value.

From Figure 10, it shows that the proposed model BLDA-CSWDT accuracy of 99.5% is outperformed the various existing methods (Hosseinzadeh et al., 2021). In addition, the proposed model extracted 25 significant features as better performed compared with other existing models (Hosseinzadeh et al., 2021).

Figure 11 shows that the proposed model B-LDA-CSWDT accuracy value of 99.5% is outperformed by the other existing models (Dharmarajan et al.., 2020) of naïve Bayes, decision tree, SVM and KNN model accuracy values 91.62%, 97.35%, 95.30% and 94.20% respectively.

Figure 10 Comparative analysis – 3 (see online version for colours)

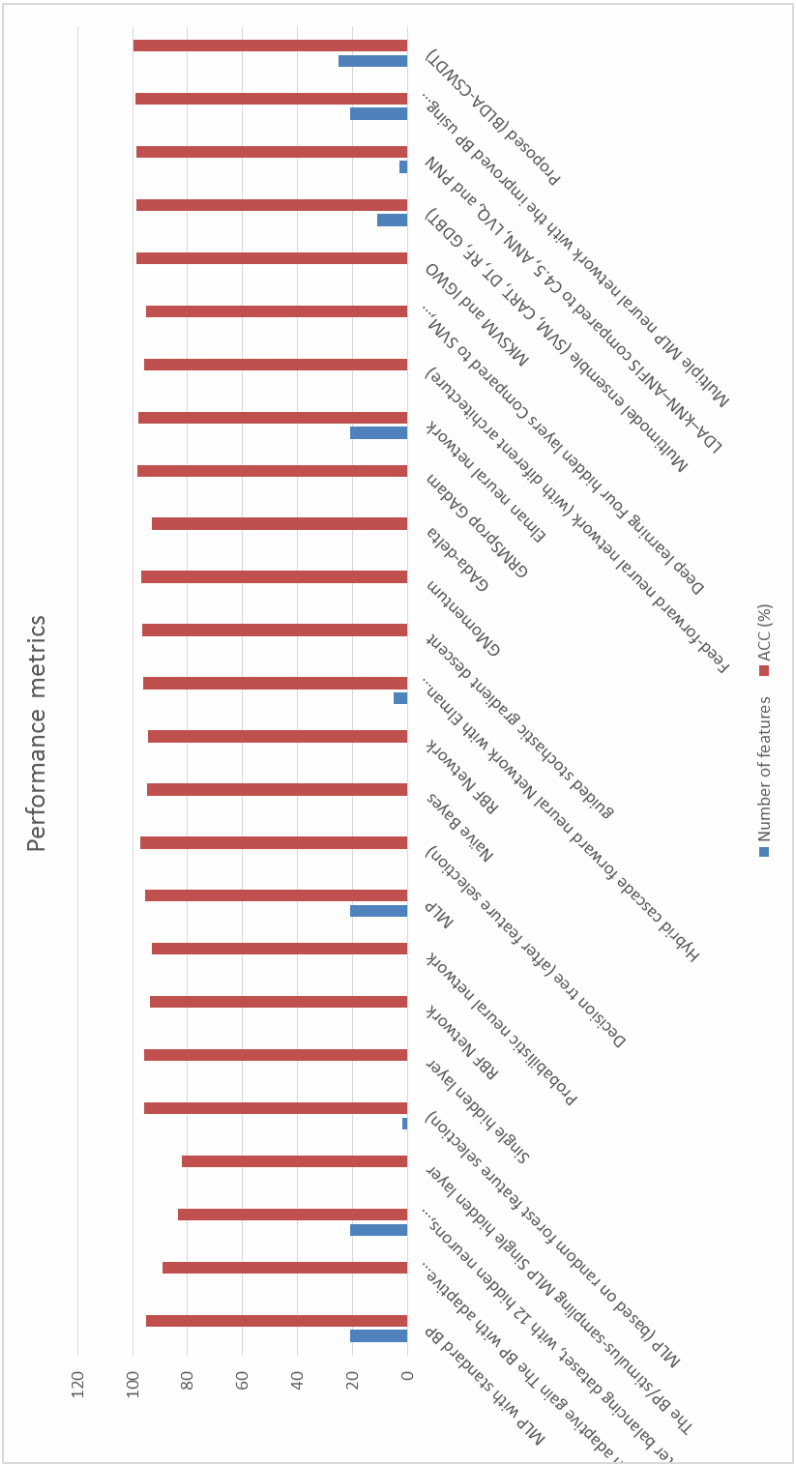

Figure 11 Comparative analysis – 4 (see online version for colours)

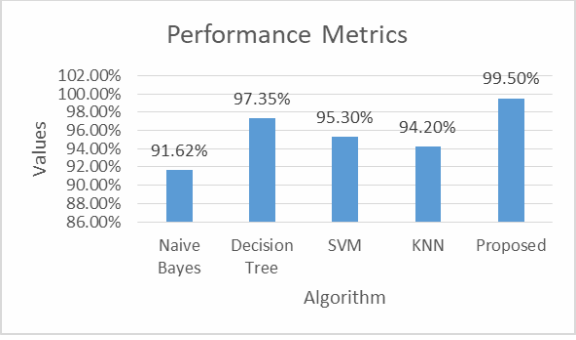

The proposed model utilised deep MLP for feature extraction, which efficiently extracts the most relevant features. The MLP can be employed in the complex nonlinear problems. It generally provides better results with huge dataset. MLP provides quicker outcome after the completion of training. The same accuracy range will be results even for the smaller dataset. It allows the models to be more effective over the complex feature learning and performs more intensive computational tasks. With this, the classification rate was also enhanced. Further the model performs feature fusion with Bayes-LDA which efficiently fuse the extracted relevant features. LDA which generally utilises information from extracted features for resulting a new axis that in turn with minimised variance and maximised class distance. The predication range of the model is enhanced with CSWDT, which results few tuning parameters. Therefore, from this, the proposed B-LDA-CSWDT model results 99.50% accuracy range which is better than the other conventional methods.

5 Conclusions

The proposed study introduced B-LDA model, which extracts significant features from the thyroid disease dataset. Further, the classification is performed efficiently by using the CSWDT-optimised cuckoo search with a weighted decision tree model. In addition, 5-fold cross-validation is performed in this research. A better accuracy value of 99.5% in thyroid disease prediction was obtained which is compared with different existing studies. Future enhancement can be considered by using different optimisation algorithms and suitable data mining classifiers.

References

Abbad Ur Rehman, H., Lin, C-Y., Mushtaq, Z. and Su, S-F. (2021) 'Performance analysis of machine learning algorithms for thyroid disease', *Arabian Journal for Science and Engineering*, Vol. 46, No. 10, pp.9437–9449.

Asif, M.A-A-R., Nishat, M.M., Faisal, F., Shikder, M.F., Udoy, M.H., Dip, R.R. et al. (2020) 'Computer aided diagnosis of thyroid disease using machine learning algorithms', in *2020 11th International Conference on Electrical and Computer Engineering (ICECE)*, pp.222–225.

Banu, G.R. (2016) 'A role of decision tree classification data mining technique in diagnosing thyroid disease', *International Journal of Computer Sciences and Engineering*, Vol. 4, No. 11, pp.64–70.

Cappola, A.R., Miller, M. and Gambert, S.R. (2016) 'Thyroid disease in the elderly', in *Medical Management of Thyroid Disease*, pp.413–450, CRC Press, Boca Raton.

Chaubey, G., Bisen, D., Arjaria, S. and Yadav, V. (2021) 'Thyroid disease prediction using machine learning approaches', *National Academy Science Letters*, Vol. 44, No. 3, pp.233–238.

Chaurasia, V., Pal, S. and Tiwari, B. (2018) 'Prediction of benign and malignant breast cancer using data mining techniques', *Journal of Algorithms & Computational Technology*, Vol. 12, No. 2, pp.119–126.

Detweiler, K., Elfenbein, D.M. and Mayers, D. (2019) 'Evaluation of thyroid nodules', *Surgical Clinics*, Vol. 99, No. 4, pp.571–586.

Dharmarajan, K., Balasree, K., Arunachalam, A. and Abirmai, K. (2020) 'Thyroid disease classification using decision tree and SVM', *Indian Journal of Public Health Research & Development*, Vol. 11, No. 3, pp.229–233.

Durante, C., Grani, G., Lamartina, L., Filetti, S., Mandel, S.J. and Cooper, D.S. (2018) 'The diagnosis and management of thyroid nodules: a review', *JAMA*, Vol. 319, No. 9, pp.914–924.

Elliott Range, D.D., Dov, D., Kovalsky, S.Z., Henao, R., Carin, L. and Cohen, J. (2020) 'Application of a machine learning algorithm to predict malignancy in thyroid cytopathology', *Cancer Cytopathology*, Vol. 128, No. 4, pp.287–295.

Franco, J-S., Amaya-Amaya, J. and Anaya, J-M. (2013) 'Thyroid disease and autoimmune diseases', in *Autoimmunity: From Bench to Bedside [Internet]*, El Rosario University Press, Bogota, Colombia.

Gu, J., Zhu, J., Qiu, Q., Wang, Y., Bai, T. and Yin, Y. (2019) 'Prediction of immunohistochemistry of suspected thyroid nodules by use of machine learning-based radiomics', *American Journal of Roentgenology*, Vol. 213, No. 6, pp.1348–1357.

Hosseinzadeh, M., Ahmed, O.H., Ghafour, M.Y., Safara, F., Ali, S., Vo, B. et al. (2021) 'A multiple multilayer perceptron neural network with an adaptive learning algorithm for thyroid disease diagnosis in the internet of medical things', *The Journal of Supercomputing*, Vol. 77, No. 4, pp.3616–3637.

Ioniță, I. and Ioniță, L. (2016) 'Prediction of thyroid disease using data mining techniques', *Broad Research in Artificial Intelligence and Neuroscience (BRAIN)*, Vol. 7, No. 3, pp.115–124.

Kumar, V., Webb, J., Gregory, A., Meixner, D.D., Knudsen, J.M., Callstrom, M. et al. (2020) 'Automated segmentation of thyroid nodule, gland, and cystic components from ultrasound images using deep learning', *IEEE Access*, Vol. 8, pp.63482–63496.

Leitch, V.D., Bassett, J. and Williams, G.R. (2020) 'Role of thyroid hormones in craniofacial development', *Nature Reviews Endocrinology*, Vol. 16, No. 3, pp.147–164.

Nguyen, Q.T., Lee, E.J., Huang, M.G., Park, Y.I., Khullar, A. and Plodkowski, R.A. (2015) 'Diagnosis and treatment of patients with thyroid cancer', *American Health & Drug Benefits*, Vol. 8, No. 1, p.30.

Ospina, N.S., Iñiguez-Ariza, N.M. and Castro, M.R. (2020) 'Thyroid nodules: diagnostic evaluation based on thyroid cancer risk assessment', *BMJ*, Vol. 368, p.16670.

Ouyang, F-S., Guo, B-L., Ouyang, L-Z., Liu, Z-W., Lin, S-J., Meng, W. et al. (2019) 'Comparison between linear and nonlinear machine-learning algorithms for the classification of thyroid nodules', *European Journal of Radiology*, Vol. 113, pp.251–257.

P.G (2021) *What Is Thyroid Cancer?* [online] https://www.webmd.com/cancer/what-is-thyroid-cancer (accessed 13 September 2022).

Parmar, A., Katariya, R. and Patel, V. (2018) 'A review on random forest: an ensemble classifier', in *International Conference on Intelligent Data Communication Technologies and Internet of Things*, pp.758–763.

Prasad, V., Rao, T.S. and Babu, M. (2016) 'Thyroid disease diagnosis via hybrid architecture composing rough data sets theory and machine learning algorithms', *Soft Computing*, Vol. 20, No. 3, pp.1179–1189.

Prerana, P.S. and Taneja, K. (2015) 'Predictive data mining for diagnosis of thyroid disease using neural network', *International Journal of Research in Management, Science & Technology*, Vol. 3, No. 2, pp.75–80.

Raisinghani, S., Shamdasani, R., Motwani, M., Bahreja, A. and Raghavan Nair Lalitha, P. (2019) 'Thyroid prediction using machine learning techniques', in *International Conference on Advances in Computing and Data Sciences*, pp.140–150.

Razia, S. and Rao, M.N. (2016) 'Machine learning techniques for thyroid disease diagnosis – a review', *Indian J. Sci. Technol.*, Vol. 9, No. 28, p.10.17485.

Razia, S., Siva Kumar, P. and Rao, A.S. (2020) 'Machine learning techniques for Thyroid disease diagnosis: a systematic review', *Modern Approaches in Machine Learning and Cognitive Science: A Walkthrough*, Vol. 885, pp.203–212, Springer, Cham.

Shankar, K., Lakshmanaprabu, S., Gupta, D., Maseleno, A. and De Albuquerque, V.H.C. (2020) 'Optimal feature-based multi-kernel SVM approach for thyroid disease classification', *The Journal of Supercomputing*, Vol. 76, No. 2, pp.1128–1143.

Stafford, I., Kellermann, M., Mossotto, E., Beattie, R.M., MacArthur, B.D. and Ennis, S. (2020) 'A systematic review of the applications of artificial intelligence and machine learning in autoimmune diseases', *NPJ Digital Medicine*, Vol. 3, No. 1, pp.1–11.

Sureshkumar, V., Balasubramaniam, S., Ravi, V. and Arunachalam, A. (2022) 'A hybrid optimization algorithm-based feature selection for thyroid disease classifier with rough type-2 fuzzy support vector machine', *Expert Systems*, Vol. 39, No. 1, p.e12811.

Talasila, V., Madhubabu, K., Madhubabu, K., Mahadasyam, M., Atchala, N. and Kande, L. (2020) 'The prediction of diseases using rough set theory with recurrent neural network in big data analytics', *International Journal of Intelligent Engineering and Systems*, Vol. 13, No. 5, pp.10–18.

Taylor, P.N., Albrecht, D., Scholz, A., Gutierrez-Buey, G., Lazarus, J.H., Dayan, C.M. et al. (2018) 'Global epidemiology of hyperthyroidism and hypothyroidism', *Nature Reviews Endocrinology*, Vol. 14, No. 5, pp.301–316.

Temurtas, F. (2009) 'A comparative study on thyroid disease diagnosis using neural networks', *Expert Systems with Applications*, Vol. 36, No. 1, pp.944–949.

Tyagi, A., Mehra, R. and Saxena, A. (2018) 'Interactive thyroid disease prediction system using machine learning technique', in *2018 Fifth International Conference on Parallel, Distributed and Grid Computing (PDGC)*, pp.689–693.

Umar Sidiq, D., Aaqib, S.M. and Khan, R.A. (2019) 'Diagnosis of various thyroid ailments using data mining classification techniques', *Int. J. Sci. Res. Coput. Sci. Inf. Technol.*, Vol. 5, No. 1, pp.131–136.

Yadav, D.C. and Pal, S. (2019) 'To generate an ensemble model for women thyroid prediction using data mining techniques', *Asian Pacific Journal of Cancer Prevention*: *APJCP*, Vol. 20, No. 4, p.1275.

Yadav, D.C. and Pal, S. (2020) 'Prediction of thyroid disease using decision tree ensemble method', *Human-Intelligent Systems Integration*, Vol. 2, No. 1, pp.89–95.

Yang, X-S. and Deb, S. (2009) 'Cuckoo search via Lévy flights', in *2009 World Congress on Nature & Biologically Inspired Computing (NaBIC)*, pp.210–214.

Zhang, J., Yang, Y., Zhuo, L., Tian, Q. and Liang, X. (2019) 'Personalized recommendation of social images by constructing a user interest tree with deep features and tag trees', *IEEE Transactions on Multimedia*, Vol. 21, No. 11, pp.2762–2775.

International Journal on Recent and Innovation Trends in Computing and Communication
ISSN: 2321-8169 Volume: 11 Issue: 9
Article Received: *25 July 2023* ***Revised:*** *12 September 2023* ***Accepted:*** *30 September 2023*

Efficient Extraction and Automated Thyroid Prediction with an Optimized Gated Recurrent Unit in Recurrent Neural Networks

Nagavali Saka[*1] and S. Murali Krishna[2]
[1*] Research Scholar, Department of Computer Science and Engineering JNTUA, Anantapur, Andhra Pradesh, India. *Corresponding author Email id: vali214@gmail.com
[2]Professor, Department of Computer Science and Engineering, Sri Venkateshwara College of Engineering (SVCE), Tirupati, Andhra Pradesh, India. Email id: muralikrishna.s@svcolleges.edu.in

Abstract: Computer-aided tools are becoming increasingly important in medical diagnostics. This paper introduces the Efficient Feature Extraction Based Recurrent Neural Network (FERNN) for computer-aided thyroid disease prediction. The FERNN model uses a Gated Recurrent Unit Recurrent Neural Network (GRU-RNN) optimized with the COOT Optimization Algorithm.The study begins by gathering data from an open-source system and preprocessing it using min-max normalization to address missing values. The preprocessed data undergoes a two-level feature extraction (TLFE) procedure. In the first level, a ranked filter feature set technique is used to prioritize features based on medical expert recommendations. In the second level, a variety of metrics, including information gain, gain ratio, chi-square, and relief, are used to rank and select features. A composite measure guided by fuzzy logic is then used to select a judicious subset of features. The FERNN model uses the GRU-RNN to classify thyroid diseases in the databases. To optimise, the COOT optimization method is employed. The model's weights. The FERNN model was put into practise in MATLAB and assessed with a variety of statistical metrics, including kappa, accuracy, precision, recall, sensitivity, specificity, and the F-measure. The proposed methodology was benchmarked against traditional techniques, including the deep belief neural network (DBN), artificial neural network (ANN), and support vector machine (SVM).

Keywords: Thyroid disease classification, Feature retrieval, gated recurrent unit (GRU), recurrent neural network (RNN), Two-level feature extraction (TLFE), Fuzzy logic, Information gain, Gain ratio, Chi-square, Relief, Changes.

1. Introduction

The thyroid, resembling a butterfly in shape, is a significant gland situated in the lower neck region and pivotal in regulating the body's metabolism [1]. It produces two vital hormones, triiodothyronine (T3) and levothyroxine (T4), pivotal for protein synthesis, temperature control, and overall energy management [2]. This gland is susceptible to a range of often perplexing diseases, with hypothyroidism and hyperthyroidism being common occurrences [3]. Insufficient thyroid hormone secretion causes hypothyroidism, and excessive thyroid hormone secretion causes hypertension release. The former leads to weight gain, a swollen neck, and a slow heart rate, while the latter entails elevated blood pressure, a heightened heart rate, and weight loss [4] [5].

In developed nations, an estimated 4–5% of individuals are affected by hypothyroidism. Its potential consequences include elevated cholesterol levels, hypertension, cardiovascular complications, stunted growth in adolescents, and depression [7] and [8]. Thus, educating the populace about its symptoms, categories, and origins is of paramount importance. Diagnosing thyroid disorders often involves blood tests to Check the concentrations of TSH, T3, and T4 [9]. The health domain offers an abundance of intricate data, posing significant challenges. To address this, artificial intelligence (AI) techniques are emerging to detect and diagnose evolving diseases [10].

Experts employ diverse classification methods, including Neural Networks, K-nearest neighbor (KNN), Artificial Neural Networks (ANN), Decision Trees (DT), Naive Bayes, Support Vector Machines (SVM), and Bayesian Networks (BNN), to discern thyroid issues. These methods facilitate effective analysis and management of thyroid-related concerns.

Contribution of the Study:

- This research aims to highlight the significance of extracting essential features from unprocessed medical datasets, supporting medical practitioners in achieving precise thyroid disease diagnoses for the wider population.
- The incorporation of a min-max pre-processing method addresses the removal of irrelevant and absent values from the input data, thereby enhancing data integrity.
- The categorization accuracy is expected to experience notable enhancement due to the implementation of a two-level feature extraction approach.
- The development of an optimized RNN-GRU classifier offers the prospect of proficiently classifying thyroid disease categories present within the input dataset.

International Journal on Recent and Innovation Trends in Computing and Communication
ISSN: 2321-8169 Volume: 11 Issue: 9
Article Received: *25 July 2023* ***Revised:*** *12 September 2023* ***Accepted:*** *30 September 2023*

This paper's sections are organized as follows: Section 2 discusses pertinent research endeavors focused on employing deep learning techniques for the purpose of detecting thyroid diseases. In Section 3, the complete suggested system architecture model is delineated. The assessment of the technique's outcomes is elucidated in Section 4. Concluding this work, Section 5 presents a concise summary of the conclusions drawn from this study.

2. Literature Review

In recent years, numerous advancements in deep learning methodologies for automatic thyroid disease detection have been introduced by researchers. This section offers a concise overview of notable research endeavors in this field.

Tahir Alyas et al. [11] devised an empirical AI-driven method for predicting thyroid infections. Various AI techniques, including ANN, KNN, random forest algorithms, and decision trees, were evaluated on a dataset to enhance disease prediction within predefined boundaries. They achieved remarkable accuracy of 94.8% and specificity of 91% using the random forest algorithm.

Hafiz Abbad Ur Rehman et al. [12] Developed variants of the K-nearest neighbours (KNN) algorithm for identifying thyroid disorders. KNN using L1-based selection, KNN with chi-square-based choice of features, and KNN without choosing features were among the variants. KEEL Dataset Collection: Thyroid Tumours were used, as well as a dataset from a Pakistani clinic. The later dataset included three additional attributes: pulse rate, BMI, and blood pressure.

Mehdi Hosseinzadeh et al. [13] developed a neural network for thyroid recognition called multiple multi-layer perceptron (MMLP). They improved the network's learning rate computation by resolving issues with local minima and back-propagation error computations. The MMLP model demonstrated enhanced overall classification performance for thyroid disorders, attaining a 0.7% accuracy improvement when compared to a standalone system.

Rajasekhar Chaganti et al. [14] investigated AI and deep learning feature design strategies. Robustness was introduced into their approach via additional resilience, inverted feature removal, forward choice of characteristics, unilateral component choices, and AI-based tree learners' considerations. Their proposed method accurately identified thyroid disease of the immune system, swollen regulation protein, thyroid disease brought on by the condition known as Ha, and non-thyroid disease (NDIS), with the selected additive tree classifier outperforming others and generating an F1 score of 0.94.

K. Shankar et al. [15] suggested a feature-based multi-kernel SVM method for thyroid identification diseases. Their approach made use of fine component selection as well as a region-based classification process. Using "Multi Kernel Support Vector Machine," they organized data sequences and implemented a comprehensive feature selection method. Through advanced dark wolf development, the model attempted to improve characterization performance by raising the significance of non-essential variables and refining models from varied datasets.

3. The suggested system and methods

A recent report by the Indian daily "Seasons in India" suggests that one out of every ten Indians has hypothyroidism. This estimate is founded on studies carried out by the Indian Thyroid Organization. Hypothyroidism is the tenth most common chronic condition in India, ranking behind asthma, obesity, diabetes, heart disease, and sleep disorders.

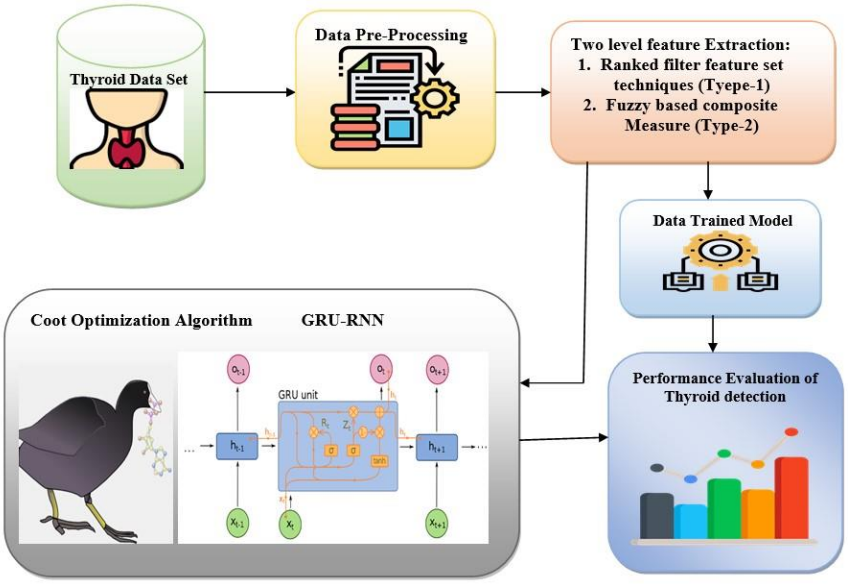

Figure 1. The suggested methodology's block diagram

International Journal on Recent and Innovation Trends in Computing and Communication
ISSN: 2321-8169 Volume: 11 Issue: 9
Article Received: *25 July 2023* ***Revised:*** *12 September 2023* ***Accepted:*** *30 September 2023*

Despite the fact that thyroid symptoms can be similar to those of other disorders, only half of the surveyed population is aware of thyroid problems and the availability of symptom tests for diagnosis. This paper proposes a semi-automatic model for the detection and classification of thyroid diseases using database resources, called the EFERNN model. The potential of artificial intelligence (AI) to provide intelligent and rational solutions to a variety of problems makes it a valuable tool in the medical field. As society relies on productive individuals, maintaining good health is essential. People who are ill expend a significant amount of energy on their health, which detracts from their ability to fulfill their obligations and excel. 1. The open-source system starts by acquiring the necessary databases. A preprocessing technique is then introduced to address missing values through normalization methods. Following preprocessing, the data undergoes feature extraction using the Two-Level Feature Extraction (TLFE) approach. In the initial level (Level 1), to prioritize characteristics using suggestions, the ranked filtering collection method is applied. From medical experts. This process employs ranking measures and label-driven validation. Progressing to Level 2, a variety of metrics, including information gain, gain ratio, chi-square, and Relief-F, are employed to rank and select features. Within this stage, a composite measure based on fuzziness identifies effective features within the feature set. Finally, the GRU-RNN model is applied for the classification of thyroid diseases using the databases. The COOT Optimization Algorithm is utilized to determine optimal weights for the GRU-RNN.

3.1. Data Pre-processing

Normalization plays a pivotal role in the initial data preprocessing phase, purging inessential information and mitigating contextual noise present in the acquired databases. Employing the Min-Max normalization technique [16], the data is subjected to a linear transformation that aligns it with a predefined range. This method effectively preserves the inherent relationships within the data. Characterized by its simplicity, the technique seamlessly fits the data within predetermined boundaries. The min-max normalization technique can be succinctly represented as follows:

Min-Max normalization technique =

$$\left(\frac{X-MIN\ parameter\ of\ X}{MAX\ parameter\ of\ X-MIN\ parameter\ of\ X}\right) * (d-c) + c \qquad (1)$$

Here, X the term "Input Data" signifies the dataset to be normalized, while d, c "Minimum Value" and "Maximum Value" represent predefined range boundaries. Following the min-max normalization process, the normalized information is subsequently channeled into the feature extraction phase. This normalization technique serves as an essential preparatory step, ensuring that the subsequent analytical processes are conducted on data that has been refined and standardized.

3.2. Level 1: Feature Extraction:

This phase of analysis is geared towards identifying thyroid illness type and presence within a patient. The database encompasses an array of 29 diverse variables, encompassing patient query data, age, and gender, an array of test measurements, physiological features, symptoms, and patient information. The query data component records pertinent information regarding the patient's history of hyperthyroid and hypothyroid instances, antithyroid medication, and thyroxine intake. Accurate data is meticulously collated to differentiate between high-level and low-level symptoms. The latter includes factors such as lithium levels, 1131 infection, and the presence of goiter. High-level symptoms encompass physiological shifts such as pregnancy and nausea. Overall, the patient data indicates a prevalent inclination towards relying on medical consultation and comprehensive thyroid assessment for issue diagnosis [17]. Table 1 effectively summarizes low-level and high-level inquiries, relevant clinical aspects discussed with medical professionals, and crucial recommendations. The table illuminates the significant impact that lithium levels and the presence of 1131 infection can exert on thyroid hormones. These medical endorsements assume the role of weighted factors, which, when factored into feature matrices, facilitate the generation of ranked and filtered feature pairs. This approach underscores the meticulousness of the analysis, drawing insights from a comprehensive dataset to extract and rank features that hold the potential to be critical indicators of thyroid disease.

Table 1: Medical Expert-Recommended Level 1 Feature Extraction (Symptoms

Doctor Advice	Description/Effect	Features
Low	Emotional, physical, and mental impact. Varied detection due to thyroid.	Psych
Low	Thyroid-related sickness with multiple potential causes.	Sick
High	Affects thyroid function. Associated with hypoglycaemia and hyperthyroidism, and goitre.	Lithium
Medium	Influences growth and blood pressure, rare disorder. Relates to hypopituitarism.	Hypopituitary
Low	Subtle symptoms, often present in specific cancer at a later age.	Tumor

International Journal on Recent and Innovation Trends in Computing and Communication
ISSN: 2321-8169 Volume: 11 Issue: 9
Article Received: *25 July 2023* ***Revised:*** *12 September 2023* ***Accepted:*** *30 September 2023*

Medium	Enlargement of the thyroid gland.	Goiter
Low	Hormonal and size changes during pregnancy.	Pregnancy
Low	Risk of complications during thyroid surgery is below 2 percent.	Thyroid surgery
High	Destruction of thyroid cells.	1131

Certain physiological symptoms, like high blood pressure, hair loss, or weakness, don't necessarily point to thyroid illness. To accurately assess and detect thyroid disorders, medical professionals administer a range of blood tests, including the Free Thyroxine Index (FTI), Triiodothyronine (T3), Thyroid-Stimulating Hormone (TSH), Thyroxine (T4), and Thyroxine-Binding Globulin (TBG). These tests form the cornerstone of low-level evaluations, enabling the identification of thyroid abnormalities and specific disorder types. One notable Diagnostic tool is the blood test, which provides insights into the nature and anomalies of thyroid disease. Table 2 offers a comprehensive summary of the relationship between abnormality impact, associated symptoms, disease types, and the influence of anomalies. This approach underscores the significance of employing comprehensive blood tests in combination with a thorough analysis of related symptoms.

Table 2: Medical Expert-Recommended Level 1 Feature Extraction Tests

Doctor Advice	Symptoms	Features
Low	Hypersensitivity, hair loss, tiredness, dryness	TBG (Thyroxine Binding Globulin)
High	-	FT1 (Free T4)
High	Test for blood	TSH (Thyroid Stimulating Hormone)
Medium	Hair loss, dryness, sensitivity, weight loss, weariness, weakness	T3 Test
High	High blood pressure, hair loss, eye problems, dryness	TT4 Test

The preceding table serves to elucidate both the functional attributes and the comprehensive scope associated with low and high abnormality scenarios. These diagnostic tests serve as potent tools for detecting a spectrum of thyroid diseases. By synthesizing insights from medical professionals' test recommendations and symptom-based evaluations, Level 1 features are meticulously extracted to facilitate thyroid detection. These extracted features subsequently undergo scrutiny in the context of Level 2 feature ranking and selection measures. This second-tier evaluation rigorously identifies and selects the indispensable features that hold the utmost potential for accurate thyroid disease detection. The cohesive interplay between the two levels underscores the methodology's precision in delineating crucial features, ultimately contributing to the model's ability to discern thyroid illnesses effectively.

3.3. Fuzzy-Based Composite Measure for Level 2 Feature Ranking and Selection

This section explores the detailed process of feature selection and ranking at Level 2, using a sophisticated fuzzy-based composite measure.

Information Gain (Info Gain): By adopting an information theory-based approach, Info Gain evaluates the relevance of features in relation to their association with the corresponding class [18]. This assessment metric is computed using training set data and can be formulated as follows:

$$iv\emptyset o(\Sigma) = -\sum_{J=1}^{k} P(A_J)\, Log_2 P(A_J) \quad (2)$$

Here, denote pairings of classes, shows the number of variables inside a certain sample set allocated to a class, and relates to the number of classes associated with thyroid disease disorder. Making use of the gathered data, specific independent attributes are ranked, favoring higher values as more significant. This technique computes Information Gain parameters for various features within thyroid datasets, enhancing the proposed model's efficacy through the incorporation of the fuzzy-based composite measure.

Relief: Primarily applicable to binary classification problems, Relief functions as an effective feature selector. This technique assesses feature significance by computing variations among closest neighbors. Hit and miss computations, pertaining to class specification, are incorporated to generate weighted scores validating the relevance of features.

International Journal on Recent and Innovation Trends in Computing and Communication
ISSN: 2321-8169 Volume: 11 Issue: 9
Article Received: *25 July 2023* ***Revised:*** *12 September 2023* ***Accepted:*** *30 September 2023*

Chi-Square: This statistical measure quantifies relationships between parameters, functioning as a coefficient to gauge similarities.

$$\varkappa^2 = \sum_{I=1}^{K} \sum_{J=1}^{C} \frac{(N_{IJ} - \mu_{IJ})^2}{\mu_{IJ}} \quad (3)$$

Here, N_{IJ} signifies the count of samples, corresponds to K various parameters, and C denotes different classes.

Gain Ratio: An improved version of Information Gain, Gain Ratio operates within normalized information to mitigate bias by considering higher attributes.

$$SInfo = -\sum_{I=1}^{V} \frac{|d_I|}{d} \times Log_2\left(\frac{|d_I|}{d}\right) \quad (4)$$

Here, d can be defined as a data parameter and V can be defined as an attribute parameter. The gain ratio is presented as follows,

$$GR = \frac{Gain}{SInfo} \quad (5)$$

The relevance of the traits is determined using the measures mentioned above. Fuzzy rules are developed to identify critical traits across multiple metrics in order to do this, as exemplified in the following.

$$INFOgain = \begin{matrix} INFOgain \geq a & Significant \\ INFOgain < a & Nn\ significant \end{matrix} \quad a = 0.005 \quad (6)$$

$$GAIN\ ratio = \begin{matrix} GAIN\ ratio \geq a & Significant \\ GAIN\ ratio < a & Nn\ significant \end{matrix} \quad a = 0.2 \quad (7)$$

$$Chi\ Square = \begin{matrix} Chi\ Square \geq a & Significant \\ Chi\ Square < a & Nn\ significant \end{matrix} \quad a = 50 \quad (8)$$

Here, a represents an optimized fuzzy decision parameter. These K composite fuzzy measures guide the selection of significant features, as depicted in the following equation:

$$fMeasure = \begin{matrix} (sg \cap sg \cap sg \cap sg) \cup (nsg \cap sg \cap sg \cap sg) & High \\ (nsg \cap sg \cap sg \cap sg) & Medium \\ otherwise & Low \end{matrix} \quad (9)$$

This approach ranks and selects features for accurate thyroid detection and categorization. These selected attributes are sent into the ultimate classifier to identify thyroid disorders from aggregated databases. The next section describes this classifier's structure.

This level of granularity underscores the complexity and thoroughness of the feature selection process, utilizing sophisticated techniques to pinpoint and incorporate the most relevant attributes for robust thyroid detection and classification.

3.4. Gated REU Recurrent Neural Network (GRU-RNN) with COOT Optimization

The GRU-RNN is a key component of the proposed system to identify hypothyroidism disorders in assembled datasets. Using the preset network structure, the dataset is used to train and evaluate the network. The COOT technique is used to determine the appropriate weighting parameter within the GRU-RNN architecture. This section digs into the inner workings of both the GRU-RNN and the COOT algorithms, providing an in-depth understanding of their capabilities.

3.4.1. GRU-RNN

Recurrent Neural Networks (RNNs) enhance conventional neural networks by enabling neurons within the same layer to transmit data to one another. This architecture lends itself to superior functionality, particularly in handling time sequences, making RNNs well-suited for time series operations [19]. Figure 2 visually represents the design architecture of a recurrent neural network.

In this figure 2, W represents hidden-to-hidden weight matrices, V signifies hidden-to-output weight matrices, corresponds to U input-to-hidden weight matrices, Y denotes the predicted outcome, S represents the hidden state, and X represents the input. The RNN time series model validates theS_{t-1} network's characteristics and X_i state over time. The combination of the prior time state and current input computes the S neuron state at the specified time as follows:

$$S_t = M(UX_{t-1} + WS_{t-1} + B_H) \quad (10)$$

Here, *z* can be defined as a bias term, and *f* can be defined as a mechanism for actuation. As a neuron, it is used as outputs at time *t* and the network state input at the next time *t*+1 at the same time. Hence, *z* isn't directly linked to the final result. It needs: to divide by the factor Z, then add using the offset function. The equation that follows can be used to define this method mathematically:

$$Y_t = ACT(ZS_t + B_Y) \quad (11)$$

Different from LSTM, GRU does not have an output gate. Instead, one gate combines the input gate and forget gate, further merging the cell state of the hidden state into a single phase. As a result, GRU is simpler and offers faster training, making it a preferred choice. The architecture of the GRU cell is visualized in Figure 3.

International Journal on Recent and Innovation Trends in Computing and Communication
ISSN: 2321-8169 Volume: 11 Issue: 9
Article Received: *25 July 2023* ***Revised:*** *12 September 2023* ***Accepted:*** *30 September 2023*

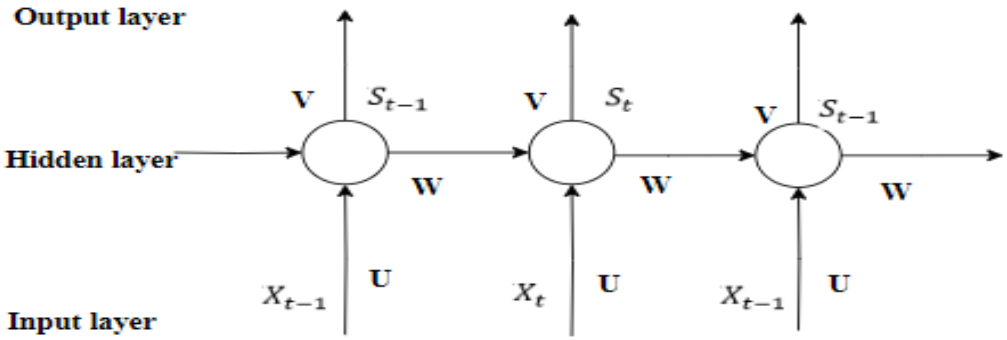

Figure 2: Visualization of Recurrent Neural Network Architecture

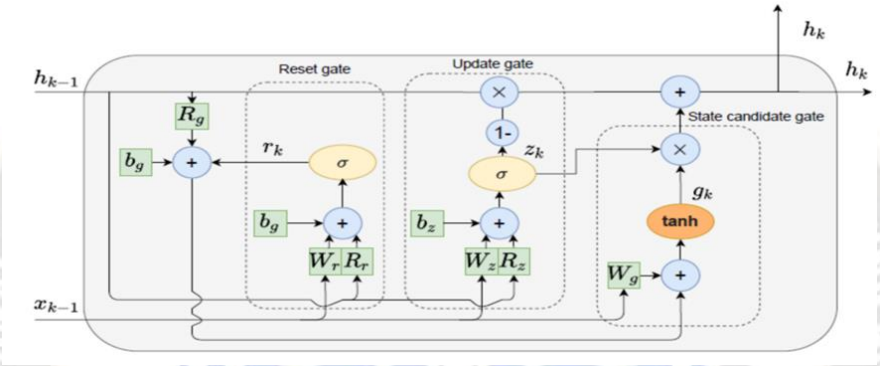

Figure 3: The architecture of the GRU

Figure 3 portrays the GRU architecture. The hidden state can be calculated using the expressions in this section.

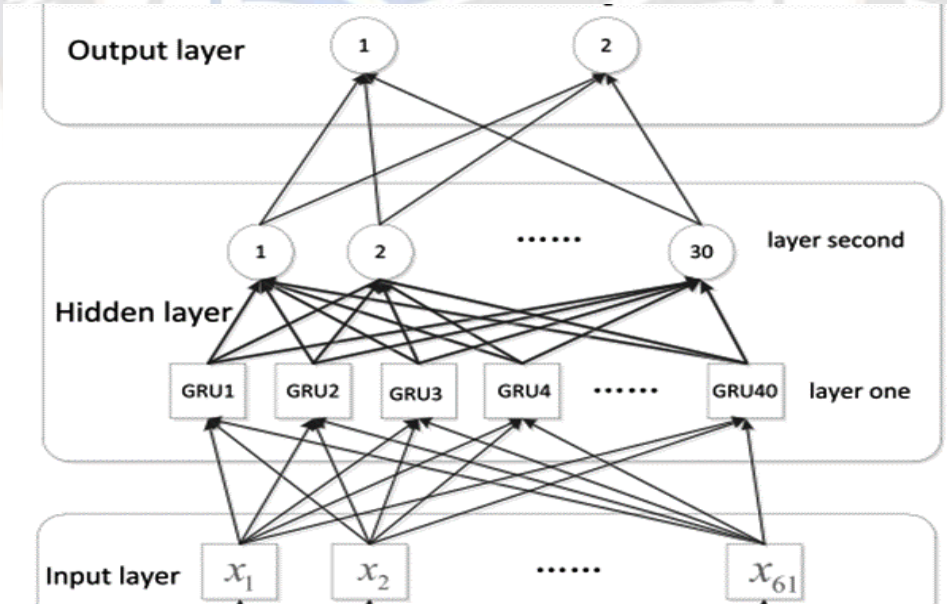

Figure 4 presents the overarching architecture of GRU-RNN.

If discarding the information from the state of concealment prior to inputs is necessary, the reset gate $r(K)$is employed. The update gate $z(k)$ manages the amount of data to retain and pass on to subsequent phases. By multiplying the output of the reset gate from the previous phase, unnecessary data from the prior phase can be eliminated. To put it differently, if the output of the Zupdate gate tends towards zero, the current state incorporates newer data; conversely, if the output approaches one, the current data is retained from the last iteration. The equations below formalize the aforementioned details within a specified time interval$k$:

International Journal on Recent and Innovation Trends in Computing and Communication
ISSN: 2321-8169 Volume: 11 Issue: 9
Article Received: *25 July 2023* ***Revised:*** *12 September 2023* ***Accepted:*** *30 September 2023*

$$h(k) = (1_n N \times 1 - z(k)) \times g(k) + z(k) \times h(k-1)) \quad (12)$$

$$g(k) - tanh(w_g x(k) + z(k) \times R_g h(k-1) + b_g) \quad (13)$$

$$z(k) = \sigma(w_z x(k) + R_z h(k-1) + b_z) \quad (14)$$

$$r(k) = \sigma(w_r x(k) + R_r h(k-1) + b_r) \quad (15)$$

Here, R and W signify learned weight matrices, ×represents element-wise multiplication, denotes the σ logistic sigmoid function, h corresponds to candidate activation, g represents the activation function, signifies the update gate, and $r$denotes the reset gate. The GRU-RNN was tailored for thyroid disease prediction. Within the GRU-RNN network model, the GRU module that captures information from the thyroid data emerges as a critical design. To optimize the weighting parameter within the GRU-RNN, the COOT optimization algorithm is harnessed. The forthcoming section offers a comprehensive delineation of the COOT algorithm's mechanics. This comprehensive exposition clarifies the intricate dynamics of the GRU-RNN, shedding light on its integral role in thyroid disease detection. The subsequent integration of the COOT optimization algorithm showcases a well-rounded approach to enhancing the model's performance.

3.4.2. COOT Algorithm for Optimization

In the architecture of the GRU-RNN, the weight parameter's selection is a crucial step accomplished through the application of the COOT optimization algorithm. To mitigate the potential compromise in system accuracy due to random weight updates within the GRU-RNN, the COOT optimization algorithm is adopted. This ensures the identification of the optimal weight parameter, thereby enhancing the accuracy of thyroid disease identification. This section presents a comprehensive elucidation of the COOT optimization algorithm [21].

The term "coots" refers to a type of water bird found in the rail family, specifically the genus "Rallis." The term "Felica," denoting these birds, originates from the Latin term for "coot." Coots display diverse collective behaviors, primarily focused on mimicking flocking movements. A small cluster of coots positioned at the forefront of the flock serves as cluster leaders, guiding the entire group toward a common destination.

Four distinct coot movements on water surfaces are taken into account:

- Random deviations to both sides.
- Sequential deviations.
- Positional adjustments relative to cluster leaders.
- Enhancement of the cluster's positioning through the leaders toward an optimal location.

This algorithm's mathematical model is detailed in the following section.

The fundamental structure of the complete optimization algorithm closely resembles that of other meta-heuristic algorithms. The coots' positions correspond to the weights of the GRU-RNN networks. The algorithm commences with an initial random population, expressed as:

$$(\vec{X}) = \{\overrightarrow{X_1}, \overrightarrow{X_2}, \ldots, \overrightarrow{X_N}\} \quad (16)$$

The goal function is continuously applied to this randomized population, resulting in the following final value:

$$(\vec{O}) = \{O_1, O_2, \ldots, O_N\} \quad (17)$$

The fundamental principles underpinning the optimization approach are harnessed to further refine it. Population-based optimization methods are employed to search for optimal solutions across a spectrum of optimization problems, without the assurance of reaching a solution within a single iteration. The probability of attaining global optimality improves with an ample number of random solutions and optimization cycles. The population is generated randomly within a predefined range, following this mathematical formulation:

$$CootPOS(I) = RAND(1, D).* (UB - LB) + LB \quad (18)$$

Here, UB and LB denote the upper and lower bounds of the search space, D represents the number of variables or problem variables, and $CootPOS(I)$ corresponds to the coot's position. Each parameter can encompass various upper and lower bounds:

$$UB = [UB_1, UB_2, \ldots, UB_D], LB = [LB_1, LB_2, \ldots, LB_D] \quad (19)$$

Upon constructing the initial population, the position of each search agent must be determined, and the fitness of each solution must be evaluated using the objective function:

$$O_I = f(\vec{X}) \quad (20)$$

This equation represents the fitness function. In this scenario, the NL number of coots serves as the cluster leader, with leaders being randomly selected. The algorithm is revised in light of the four motions of the coots.

Fitness Evaluation

Fitness function parameters are computed using the variables of the function of fitness for every coot derived from the difference between detection and its corresponding observations:

$$MSE_J = \frac{1}{N}\sum_{T=1}^{N}\left(x_T - \widehat{x_T}\right)^2, J = 1,2,..,pn \quad (21)$$

Random deviations to both sides.

To effect random changes within the search space, connectedness is established through the formula below. The coot is then moved in that direction:

International Journal on Recent and Innovation Trends in Computing and Communication
ISSN: 2321-8169 Volume: 11 Issue: 9
Article Received: *25 July 2023* ***Revised:*** *12 September 2023* ***Accepted:*** *30 September 2023*

$$q = RAND(1, D).* (UB - LB) + LB \quad (22)$$

This variation allows the coot to explore different regions of the search space. If these modifications impact the local optimum, they can guide the technique away from it. The new position of the coot can be calculated using the following formula:

$$CootPOS(I) = CootPOS(I) + a \times r_2 \times (q - CootPOS(I)) \quad (23)$$

Here, r_2 represents a random variable, and signifies a random number within the range [0, 1].Equation (23) ensures that the movement is constrained within the search space limits. It guarantees a balance between exploration and exploitation by utilizing a random term that decreases over time.

Chain Variation

Chain variation involves moving one coot to the average location of two adjacent coots. The process starts by calculating the distance between two coots and moving one of them halfway toward the other [22]. The formula for computing chain variation is:

$$a = 1 - l \times \left(\frac{1}{Iteration}\right) \quad (24)$$

Here, $Iteration$ refers to the second coot. This l variation promotes convergence by averaging the coots' positions.

Position Management Relative to Cluster Leaders

In a cluster, a few coots typically serve as leaders at the forefront. The other coots need to adjust their positions in relation to these cluster leaders and move towards them. Coots that are not leaders should alter their positions based on the dominant leader. Additionally, coots improve their positions based on the leaders' average position. However, utilizing average positions can result in convergence issues. To calculate these variations, the following formula is employed:

$$CootPOS(I) = 0.5 \times (CootPOS(I - 1) + CootPOS(I) \quad (25)$$

Here, $CootPOS(I - 1)$ represents the leader index number, denotes the count of leaders, and signifies the index number of the current coot. The coot adjusts its position based on the leader's index. The coot's future position is calculated based on the selected leader.

$$k = 1 + (I \, mod \, NL) \quad (26)$$

Here, represents an arbitrary number within the interval [-1, 1], signifies the value of π (approximately 3.14), represents a random number within the interval [0, 1], represents the leader's chosen position, and signifies the current coot's position.

$$CootPOS(I) = LeaderPOS(K) + 2 \times r_1 \times \cos(2r\pi) \times (LeaderPOS(K) - CootPOS(I) \quad (27)$$

The comprehensive explanation provided above delves into the intricate mechanics of the COOT optimization algorithm. By strategically integrating this algorithm into the framework of GRU-RNN, the proposed approach enhances the selection of weight parameters, leading to improved accuracy and robustness in the diagnosis of thyroid conditions.

Here is the suggested method's pseudocode:

Algorithm 1: pseudocode of the suggested method

```
initialized COOT's weights and GRU-RNN biases
Initialize P=0.5 and NL (coots).
Randomly choose coot leaders.
        Calculate coot and leader fitness.
        Find the finest leader or coot globally
        While condition is satisfied
          Calculate variables a and b
          If NL > 10 then
            coot can be random vectors
          Else
            coot are random variables
          End
          For each coot from 1 to NL
            Compute variable k
            If k < P then
              Update the position
            Else
              Update the position
            End
          End
          Determine the coots' fitness.
            If coot's fitness is higher than leader's,
             Then assign leader (k) = coot.
              Assign leader (k) to coot.
      End
            For each leader
              If RAND < 0.5 then
                Update position of leader
              Else
            Update the leader's position
            End

            If a leader's fitness is higher
                Keep the optimal settings
              End
            End
          End
```

International Journal on Recent and Innovation Trends in Computing and Communication
ISSN: 2321-8169 Volume: 11 Issue: 9
Article Received: *25 July 2023* ***Revised:*** *12 September 2023* ***Accepted:*** *30 September 2023*

Improving the cluster by strategically positioning the leaders

An essential aspect of the COOT optimization algorithm involves steering the cluster toward an optimal location. To achieve this, cluster leaders must adapt their positions in alignment with the desired destination. This section focuses on the mechanism of enhancing the cluster's positioning through the leaders to reach an optimal location [21]. For this purpose, leaders are prompted to update their positions toward the desired goal. This involves revising the positions of leaders to align with the optimal outcome. The formulation aims to identify optimal positions surrounding the current optimal point. Leaders strive to locate these optimal positions by departing from the present ideal position. The formula facilitates the identification of ideal positions while simultaneously avoiding convergence to the current optimum. The process of improving the cluster's positioning from the leaders to the ideal spot mathematically represented as:

$$LeaderPOS(I) = \begin{cases} b \times r3 \times cos(2\pi r) \times \left(gbest - LeaderPOS(I)\right) + gbest & r3 < 0.5 \\ b \times r3 \times cos(2\pi r) \times \left(gbest - LeaderPOS(I)\right) - gbest & r4 \geq 0.5 \end{cases} \quad (28)$$

In this (28) equation, r represents an arbitrary number within the interval [-1, 1], signifies the value of π (approximately 3.14), $r3$, and $r4$ represents a random variable within the interval [0, 1], and $gbest$ corresponds to the best position ever discovered.

The iterative process of updating the leader's position is further guided by the iteration count. The formula to determine the leader's new position is given b

$$b = 2 - l \times \left(\frac{1}{Iteration}\right) \quad (29)$$

Here, $Iteration$ represents the maximum number of iterations, and l signifies the current iteration. By incorporating the COOT algorithm, the proposed classifier effectively identifies the optimal weighting parameter. Ultimately, this optimized classifier is employed for the accurate identification of thyroid cases from the collected databases.

4. Results and Analysis

This section presents a comprehensive evaluation of the proposed automated thyroid detection system. The validation process was conducted using a standardized database obtained from an open-source system, which is essential for establishing the credibility of the proposed thyroid detection methodology. The database contains three distinct classes and a total of 7201 records. To facilitate network training, 80% of the database was used, while the remaining 20% was reserved for network testing. The performance of the proposed technique was meticulously evaluated using MATLAB using a variety of statistical metrics, including accuracy, precision, recall, specificity, kappa, F1 score, AUC, ROC, and sensitivity. To ensure a fair evaluation of the proposed method, a comparative analysis was conducted against well-established benchmarks such as ANN, SVM, and DBNN. The simulation parameters that form the foundation of the proposed approach are meticulously detailed in Table 3, offering transparency into the method's configuration. Additionally, the validation of the proposed technique was reinforced by applying statistical measures, including the use of a confusion matrix, to enhance the evaluation process. The intricacies of the confusion matrix and its associated metrics are encapsulated in Table 4. This comprehensive performance evaluation sheds light on the pragmatic applicability and potential superiority of the proposed thyroid detection methodology, reinforcing its significance in the domain of medical diagnostics.

Table 3: The simulation tools for parameters

S. No	Variable term	Parameters
1	Find agent quantity	2
2	Lower limit	200
3	The upper limit, measurement	500
4	Maximum iterations	10
5	A dropout rate	100
6	Speed of learning	0.1
7	Parametric regularity	0.001
8	The start of the function	0.01
9	Losing capability	ReLU
10	Size of batch Epoch Neuron count	MSE
11	Variable term	50
12	Epoch	50
13	Number of neurons	32 for the GRU layer

Table 4: Confusion matrix

N=7201		Predicted		
		Class-1	**Class -2**	**Class -3**
Actual	**Class- 1**	2995	2	3
	Class -2	3	2798	2
	Class- 3	2	2	1401

Table 5: Feature evaluation utilizing the proposed technique

S. No	Features	Info gain	Gain ratio	Chisq
1.	Taking the hormone thy	0.0128	0.0011	0.638
2.	Query with thyroxine	0.0212	0.0017	6.5128
3.	Query with thyroxine	0.0019	0.0088	7.6544
4.	Taking ant thyroid drugs	0.0914	0.0458	7554.4197

International Journal on Recent and Innovation Trends in Computing and Communication
ISSN: 2321-8169 Volume: 11 Issue: 9
Article Received: 25 July 2023 Revised: 12 September 2023 Accepted: 30 September 2023

5.	Tired	0.0056	0.0843	922.4810
6.	Being pregnant	0.0489	0.0253	2316.9053
7.	Thoracic surgeries	0.0065	0.0634	3248.1219
8.	I131_treatment	0.1293	0.0441	249.9336
9.	Search hyperthyroidism	0.0743	0.1332	1485.5598
10.	testosterone	0.0994	0.0106	385.4197
11.	the third stage	0.0975	0.0855	125.255
12.	TT4	0.3549	0.0488	69.549
13.	T4U	0.1549	0.0688	125.655
14.	FTI	0.0486	0.0155	55.757

The effectiveness of the proposed methodology hinges on its innovative two-level feature extraction technique, which takes into consideration expert recommendations to pinpoint pivotal features. Information gain, gain ratio, and chi-square measures are also used to pick features. These measurements extracted characteristics and selected traits, which are precisely described in Tables 5 and 6. Several robust performance measures are used to

evaluate the suggested strategy. Accuracy, sensitivity, specificity, F measure, kappa, ROC, AUC, precision, and recall are these measurements. By systematically evaluating these measures, the suggested method's capabilities are understood. Advanced feature extraction, expert insights, and multidimensional performance evaluation measures make the suggested thyroid illness categorization strategy promising.

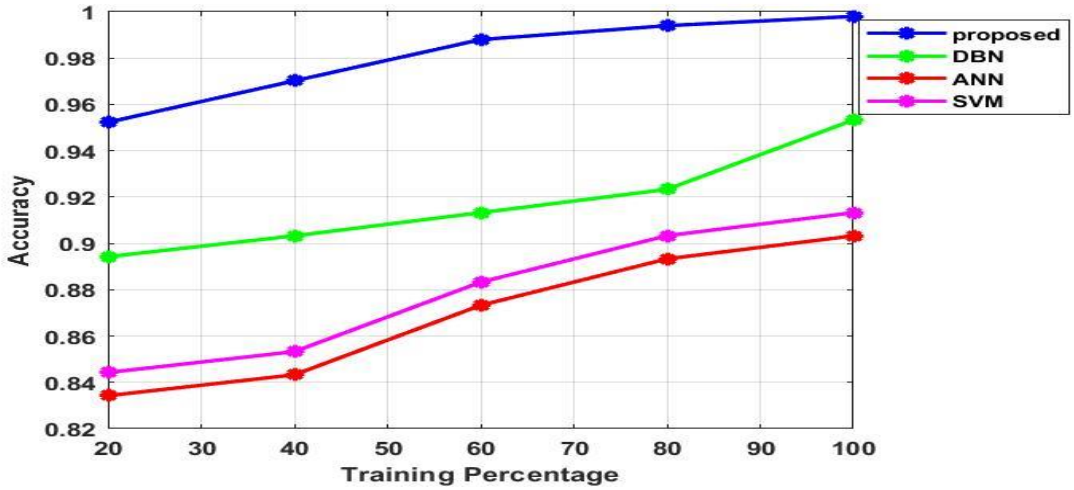

Figure 5: Comparative evaluation of Accuracy

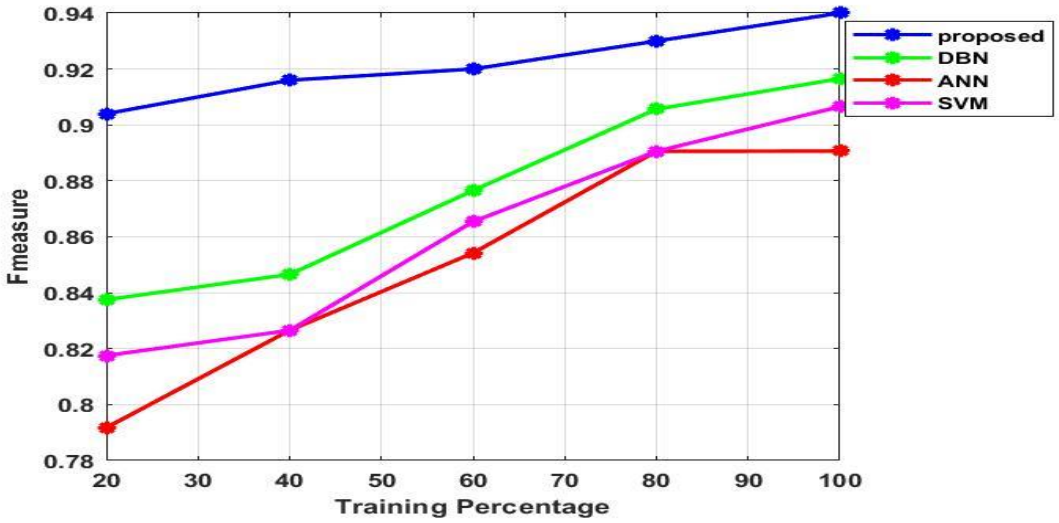

Figure 6: Comparative evaluation of F_ measure

International Journal on Recent and Innovation Trends in Computing and Communication
ISSN: 2321-8169 Volume: 11 Issue: 9
Article Received: *25 July 2023* ***Revised:*** *12 September 2023* ***Accepted:*** *30 September 2023*

To substantiate the efficacy of the suggested model for hypothyroidism identification, the metric of accuracy is employed as a benchmark, as depicted in Figure 5. The performance of the proposed method is juxtaposed against conventional methodologies, specifically DBN, ANN, and SVM. Impressively, the proposed technique attains an accuracy of 0.998. In comparison, DBN, ANN, and SVM yield accuracy scores of 0.95, 0.91, and 0.909 respectively. Evidently, the proposed technique yields the most favorable results, as discerned from Figure 5. Similarly, to validate t the F_measure of the suggested hypothyroidism-detecting method he merits of the proposed thyroid detection model, the F_measure is utilized as an evaluation metric, showcased in Figure 6. The proposed approach is assessed against established methods, namely DBN, ANN, and SVM. Remarkably, the proposed technique garners an F_measure of 0.94. In contrast, DBN, ANN, and SVM achieve F_measure scores of 0.915, 0.91, and 0.89 respectively. This reiterates the superior performance of the proposed technique, as underscored by Figure 6. Furthermore, precision is employed to further affirm the efficacy of the proposed thyroid detection model, presented in Figure 7. A comparative analysis is conducted against customary techniques including DBN, ANN, and SVM. Impressively, the proposed approach yields a precision of 0.93. Contrastingly, DBN, ANN, and SVM exhibit precision scores of 0.928, 0.918, and 0.905 respectively. The discerning eye can deduct from Figure 7 that the proposed technique consistently outperforms its counterparts. This detailed performance evaluation underscores the proposed thyroid detection model's superiority across multiple critical dimensions, establishing its potential for highly accurate and reliable thyroid disease classification.

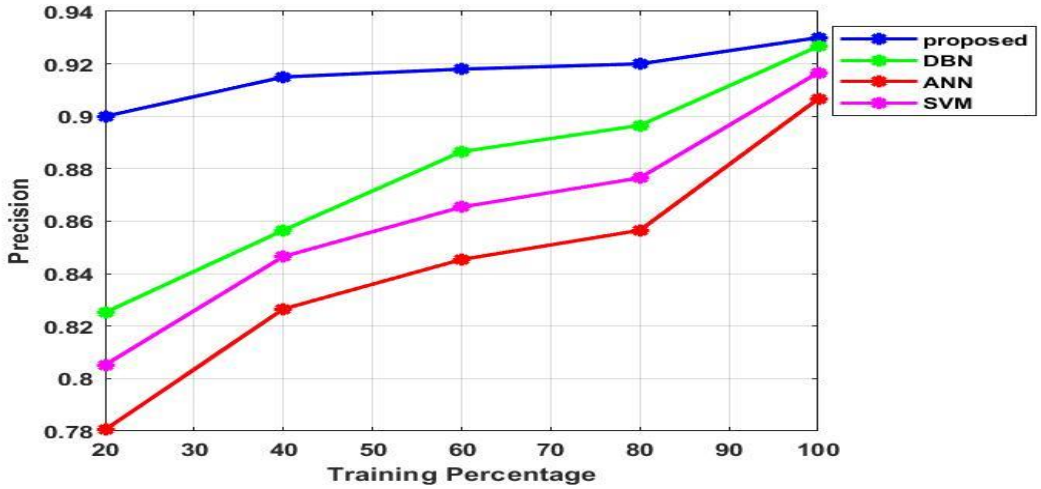

Figure 7: Comparative evaluation of Precision

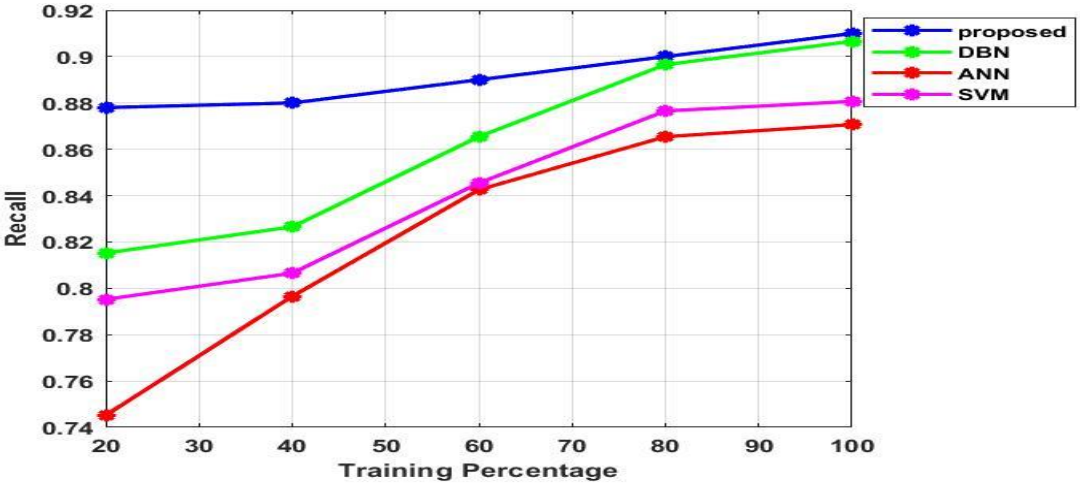

Figure 8: Comparative evaluation of Recall

International Journal on Recent and Innovation Trends in Computing and Communication
ISSN: 2321-8169 Volume: 11 Issue: 9
Article Received: *25 July 2023* ***Revised:*** *12 September 2023* ***Accepted:*** *30 September 2023*

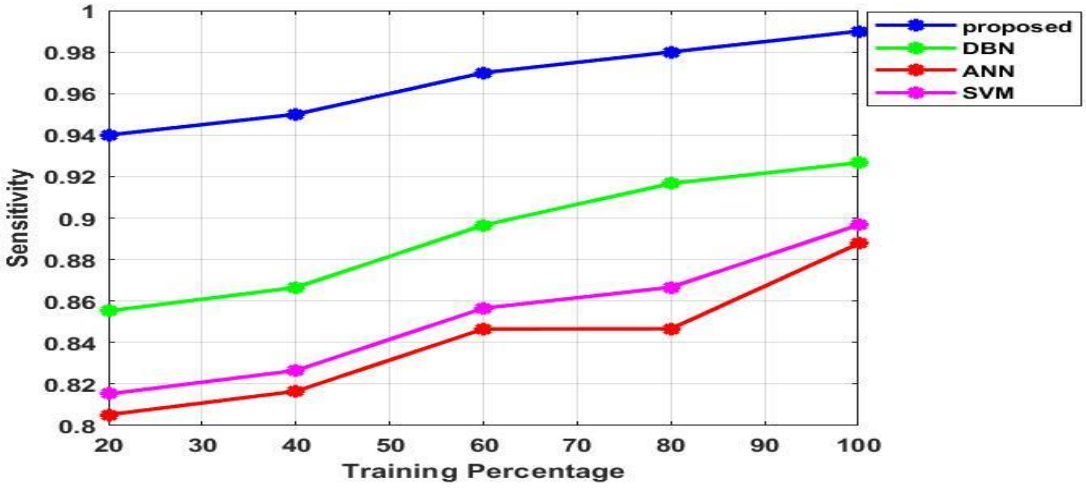

Figure 9: Comparative evaluation of Sensitivity

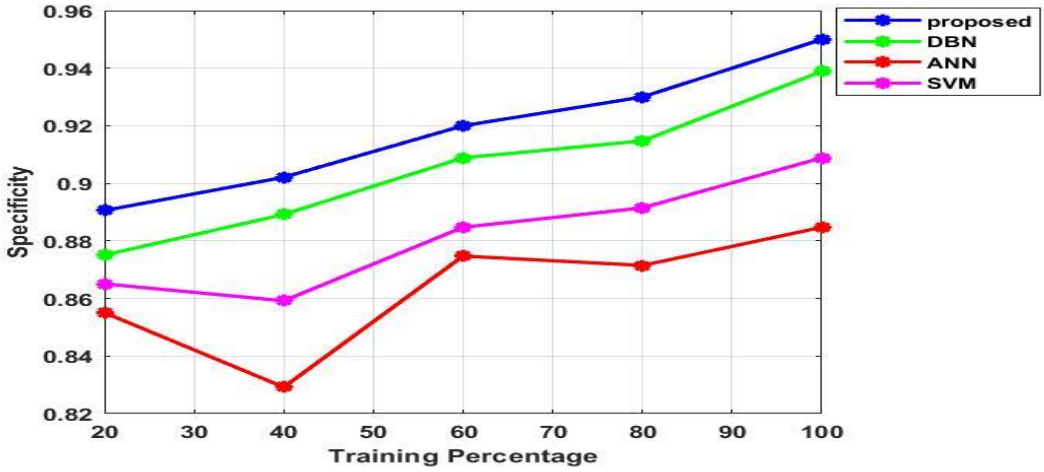

Figure 10: Comparative evaluation of Specificity

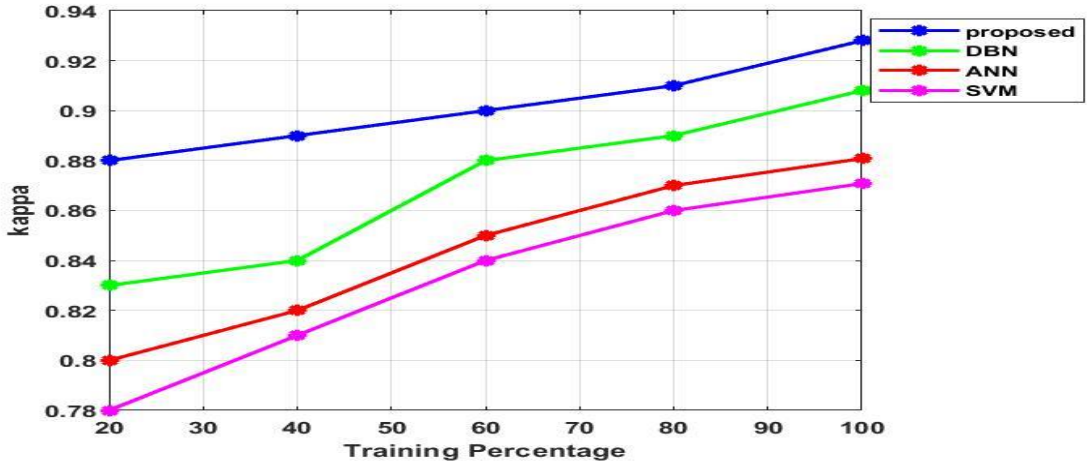

Figure 11: Comparative evaluation of Kappa

International Journal on Recent and Innovation Trends in Computing and Communication
ISSN: 2321-8169 Volume: 11 Issue: 9
Article Received: *25 July 2023* ***Revised:*** *12 September 2023* ***Accepted:*** *30 September 2023*

Table 6: Comparative evaluation of different methods

S. No	References	Method	Accuracy	Precision
1	Tahir Alyas *et al.*, [11]	empirical technique	0.948	0.89
2	Hafiz Abbad Ur Rehman *et al.*, [12]	KNN	0.91	0.91
3	Mehdi Hosseinzadeh *et al.*, [13]	multiple multi-layer perceptron (MMLP)	0.7	0.85
4	Rajasekhar Chaganti *et al.*, [14]	deep learning method	0.94	0.92
5	K. Shankar *et al.*, [15]	multi-kernel SVM approach	0.97	0.90
6	-	Proposed approach	0.998	0.93

Table 7: Comparative evaluation different methods

S. No	Method	Accuracy	Precision
1	Whale Optimization Algorithm (WOA)	0.931	0.94
2	Particle swarm optimization (PSO)	0.65	0.71
3	Grey wolf optimization (GWO)	0.85	0.82
4	Black widow optimization (BWO)	0.93	0.90
5	Harmony search algorithm (HSO)	0.96	0.92
6	Proposed approach	0.998	0.93

To substantiate the effectiveness of the proposed thyroid detection model, the evaluation metric of recall is employed, presented in Figure 8. The performance of the proposed method is juxtaposed with conventional techniques such as DBN, ANN, and SVM. Impressively, the proposed technique achieves a recall of 0.91. In comparison, DBN, ANN, and SVM attain recall scores of 0.908, 0.88, and 0.87 respectively. The superiority of the proposed technique is evident from Figure 8. Moreover, sensitivity serves as a pivotal metric to reinforce the merits of the proposed thyroid detection model, illustrated in Figure 9. The proposed approach is compared against established techniques including DBN, ANN, and SVM. Notably, the proposed technique attains a sensitivity of 0.99. In contrast, DBN, ANN, and SVM yield sensitivity scores of 0.918, 0.89, and 0.88 respectively. This underscores the superior performance of the proposed technique, as highlighted by Figure 9. Likewise, specificity is employed to further affirm the proposed thyroid detection model's prowess, displayed in Figure 10. A comparative analysis is conducted against customary methods, specifically DBN, ANN, and SVM. Impressively, the proposed approach secures a specificity of 0.95. Conversely, DBN, ANN, and SVM exhibit specificity scores of 0.94, 0.92, and 0.885 respectively. The evident superiority of the proposed technique is evident from the suggested model for hypothyroidism monitoring is Figure 10. The assessment of the proposed thyroid detection model is further bolstered by the use of the kappa measure, depicted in Figure 11. The proposed method is compared against traditional techniques like DBN, ANN, and SVM. Impressively, the proposed technique achieves a kappa value of 0.93. In comparison, DBN, ANN, and SVM achieve kappa scores of 0.91, 0.918, and 0.889 respectively. The proposed technique's consistent superior performance is visually apparent in Figure 11. This comprehensive evaluation, encompassing diverse performance metrics, solidifies the proposed thyroid detection model's position as an exceptional approach within the realm of thyroid disease classification.

5. Conclusion

This paper introduces the Feature Extraction Based Recurrent Neural Network (FERNN) for computer-aided thyroid disease prediction, highlighting the increasing importance of computer-aided tools in medical diagnostics. The paper presents a method for thyroid disease prediction using a Gated Recurrent Unit within Recurrent Neural Networks, optimized with the COOT Optimization Algorithm.The methodology follows a systematic sequence of steps, beginning with the collection of databases from open-source platforms. A preprocessing protocol is then established to address missing values using the normalization method of min-max. The preprocessed dataset is subjected to feature extraction through the Two-Level Feature Extraction (TLFE) approach. The initial phase (Level 1) employs the method of ranking filter sets features, guided by expert recommendations and reinforced through label-driven validation. In Level 2, features are meticulously evaluated and selected using metrics like information gain, gain ratio, chi-square, and relief. Effective features are identified employing a combined indicator with a fuzzy basis. The process concludes with the implementation of the GRU-RNN model for thyroid disease classification, fine-tuning weight selection through the COOT Optimization Algorithm. Performance evaluation is executed using MATLAB, rigorously assessing metrics such as sensitivity, kappa, F-measure, recall, specificity, accuracy, and precision. The suggested approach is thoroughly benchmarked against industry standard methods, including ANN, SVM, and

DBNN. This comprehensive evaluation underscores the potential of the FERNN model as a cutting-edge solution for automated thyroid detection. The models advanced techniques and rigorous assessment contribute to the enhancement of medical diagnostic capabilities, holding promise for improved thyroid disease classification.

Author Contributions

Nagavali Saka: Conceptualization, investigation, reviewing and editing, investigation, methodology, writing an original draft S. Murali Krishna: research design, data analysis all authors have read and agreed to the published version of the manuscript.

Conflicts of Interest

The authors declare no conflict of interest.

Acknowledgements

Authors would like to thank the anonymous reviewers for their useful comments and suggestions

Disclosure Statement

No potential conflict of interest was reported by the authors

References

[1] Abbad Ur Rehman, Hafiz, Chyi-Yeu Lin, Zohaib Mushtaq, and Shun-Feng Su. (2021)."Performance analysis of machine learning algorithms for thyroid disease." *Arabian Journal for Science and Engineering* 46, no. 10 9437-9449.

[2] Suresh Kumar, Vidhushavarshini, Satyabhama Balasubramanian, Vijayakumar Ravi, and Ajay Arunachalam.2022. "A hybrid optimization algorithm-based feature selection for thyroid disease classifier with rough type-2 fuzzy support vector machine." *Expert Systems* 39, no. 1 e12811.

[3] Abbad Ur Rehman, Hafiz, Chyi-Yeu Lin, and Zohaib Mushtaq.2021 "Effective K-Nearest Neighbor Algorithms Performance Analysis of Thyroid Disease." *Journal of the Chinese Institute of Engineers* 44, no. 1, 77-87.

[4] Chaubey, Gyanendra, Dhananjay Bisen, Siddharth Arjaria, and Vibhash Yadav.2021 "Thyroid disease prediction using machine learning approaches." *National Academy Science Letters* 44, no. 3, 233-238

[5] Li, Wenjun, Siyi Cheng, Kai Qian, Keqiang Yue, and Hao Liu.2021 "Automatic recognition and classification system of thyroid nodules in CT images based on CNN." *Computational Intelligence and Neuroscience.*

[6] Mishra, Sushruta, Yeshihareg Tadesse, Anuttam Dash, Lambodar Jena, and Piyush Ranjan.2021 "Thyroid disorder analysis using random forest classifier." *In Intelligent and cloud computing, pp. 385-390. Springer, Singapore*.

[7] Yadav, Dhyan Chandra, and Saurabh Pal. 2020."Prediction of thyroid disease using decision tree ensemble method." *Human-Intelligent Systems Integration 2, no. 1, 89-95*.

[8] Ahmad, Waheed, Ayaz Ahmad, Chuncheng Lu, Barkat Ali Khoso, and Lican Huang. 2018."A novel hybrid decision support system for thyroid disease forecasting." *Soft Computing* 22, no. 16, 5377-5383.

[9] Poudel, Prabal, Alfredo Illanes, Elmer JG Ataide, Nazila Esmaeili, Sathish Balakrishnan, and Michael Friebe. 2019."Thyroid ultrasound texture classification using autoregressive features in conjunction with machine learning approaches." *IEEE Access* 7, 79354-79365.

[10] Yadav, Dhyan Chandra, and Saurabh Pal.2020. "Prediction of thyroid disease using decision tree ensemble method." *Human-Intelligent Systems Integration* 2, no. 1, 89-95.

[11] Alyas, Tahir, Muhammad Hamid, Khalid Alissa, Tauqeer Faiz, Nadia Tabassum, and Aqeel Ahmad. 2022."Empirical Method for Thyroid Disease Classification Using a Machine Learning Approach." *BioMed Research International* 2022.

[12] Abbad Ur Rehman, Hafiz, Chyi-Yeu Lin, and Zohaib Mushtaq.2021. "Effective K-Nearest Neighbor Algorithms Performance Analysis of Thyroid Disease." *Journal of the Chinese Institute of Engineers* 44, no. 1, 77-87.

[13] Hosseinzadeh, Mehdi, Omed Hassan Ahmed, Marwan Yassin Ghafoor, Fatemeh Safara, Saqib Ali, Bay VO, and Hsiu-Sen Chiang.2021. "A multiple multilayer perceptron neural network with an adaptive learning algorithm for thyroid disease diagnosis in the internet of medical things." *The Journal of Supercomputing* 77, no. 4, 3616-3637.

[14] Chaganti, Rajasekhar, 2022. Furqan Rustam, Isabel De La Torre Díez, Juan Luis Vidal Mazón, Carmen Lili Rodríguez, and Imran Ashraf. "Thyroid Disease Prediction Using Selective Features and Machine Learning Techniques." *Cancers* 14, no. 16, 3914.

[15] Shankar, K., S. K. Lakshmana Prabu, Deepak Gupta, Andino Maseleno, and Victor Hugo C. De Albuquerque. 2020."Optimal feature-based multi-kernel SVM approach for thyroid disease classification." *The journal of supercomputing* 76, no. 2,1128-1143

[16] Patro, S., and Kishore Kumar Sahu.2015."Normalization: A pre-processing stage." *arXiv preprint arXiv: 1503.06462*.

[17] Juneja, Kapil.2022. "Expanded and Filtered Features Based ELM Model for Thyroid Disease Classification." *Wireless Personal Communications* 1-38.

[18] Juneja, Kapil. "Expanded and Filtered Features." *Information Technology* 95, no. 9 (2017): 1996-2005

[19] Alrasheedi, Abdullah, and Abdulaziz Almalaq.2022. "Hybrid Deep Learning Applied on Saudi Smart Grids for Short-Term Load Forecasting." *Mathematics* 10, no. 15, 2666.

[20] Aldallal, Ammar.2022. "Toward Efficient Intrusion Detection System Using Hybrid Deep Learning Approach." *Symmetry* 14, no. 9, 1916

[21] Naruei, Iraj, and Farshid Keynia. 2021."A new optimization method based on COOT bird natural life model." *Expert Systems with Applications* 183, 115352.

[22] Huang, Yihui, Jing Zhang, Wei, Tao Qin, Yuancheng Fan, Xuemei Luo, and Jing Yang.2022 "Research on Coverage Optimization in a WSN Based on an Improved COOT Bird Algorithm." *Sensors* 22, no. 9, 3383.

Journal of Data Acquisition and Processing
ISSN: 1004-9037
https://sjcjycl.cn/
DOI: 10.5281/zenodo.7546499

END TO END IMAGE PRIVACY METHOD USING CUSTOMIZED GENERATIVE ADVERSARIAL NETWORKS

Ram Mohan Rao P[1,4,*], AP Siva Kumar[2], Murali Krishna[3,4]
[1]Department of CSE, JNTU Anantapur, Andhra Pradesh India
[2]Professor, Department of CSE, JNTU Anantapur, Andhra Pradesh India
[3] Professor, Department of CSE, SV College of Engineering and Technology, Tirupati, Andhra Pradesh India
[4]Department of CSE, Sphoorthy Engineering College Hyderabad, Telangana India

Abstract:
The importance and need for data privacy is now commonly discussed everywhere and many regulations are also in place to ensure privacy preservation. Personal information like age, gender, marital status, health records etc. are the common data which needs privacy. However, images also contain sensitive information that can compromise individual privacy. With huge number of images being uploaded into public domain, image privacy also became a major privacy concern. The conventional methods of image privacy include image obfuscation which results into images which are not useful enough for further analytics. Modern literature suggests usage of Generative Adversarial Networks (GAN) to generate synthetic data for image privacy protection. The tradeoff between privacy and utility still exists. Our solution is customized GAN based method which is able to generate synthetic face images which can strike a balance between privacy and utility. We have used structural similarity index measure (SSIM) to compare the images generated using various methods and our image privacy method achieved SSIM of 98.3% along with metadata being preserved. The following sections will describe our contributions in detail.

Keywords: Computer vision, image privacy, Generative Adversarial Networks, Structural Similarity Index Measure, Privacy Preservation.

1. INTRODUCTION

It has become a common habit these days, that people go out, spend time with friends and post those pictures to social media platforms and other cloud platforms. Many free cloud based applications are available to upload pictures, manipulate pictures and store them. However, there is no assurance from these cloud providers that privacy of our images is preserved or not. Without consent of the user, these images can be shared with third party vendors also, which is a serious privacy concern [1]. Earlier researchers have developed many image obfuscation techniques like blurring, pixelation, masking etc. These techniques have proved to be inadequate with respect to image utility [2]. In the recent times, deep learning based methods especially using Generative Adversarial Networks (GAN) were widely used for generating synthetic images as discussed by Zhenfei Chen at. al [3]. The GAN based methods are able to generate highly realistic images that replicate the original images by hiding the private and sensitive attributes of the image. The GAN based image privacy has achieved significant

Influence of melting heat transfer on MHD non-Newtonian fluid flow past a slendering surface

K. Anantha Kumar

Dept. of Mathematics, Sri Venkateswara College of Engineering, Titupati-517507, A.P., India.

Abstract:

Investigators around the earth are trying to discover the effects of numerous non-Newtonian liquids to examine the heat transfer feature for the treatment of various illnesses. In this article, we presented dual solutions for magnetohydrodynamicCattaneo-Christov flow of shear thickening fluid over a variable thickness melting surface. The fluid motion is assumed to be time dependent and laminar. Firstly, proper transmutations are pondered to metamorphose the basic flow equations as ODE. The solution of these ODEs is procured by the consecutive application of Shooting and R.K. numerical procedures. Graphs are plotted to emphasise the impact of sundry physical parameters on velocity and temperature fields. Results indicate that fluid velocity is proportionalto the wall thickness parameter for increasing values. Also, the temperature is an increasing function of melting parameter and irregular heat source/sink parameters.

Keywords: MHD, Heat transfer, heat source/sink, Cattaneo-Christov model, stretching sheet.

1. Introduction:

Those fluids which follow Newton's law of viscosity are known as Newtonian fluids, otherwise they are known as non-Newtonian. We came across many non-Newtonian fluids in our everyday life such as oils, sugar solutions, mud, juices, emulsions, body lotions, face creams, chime etc. Carreau fluid is also a non-Newtonian fluid. The study of shear thickening liquid flows owing to stretching of a solid surface has uncountable solicitations in mechanical, aeronautical engineering and some industrial processes like thermal isolation, manufacture of paper, organic processes, crystal growth, sterilization of milk, hot rolling, plastic sheets extrusion etc. The Newtonian fluids unveil high heat transport performance compared to non-Newtonian fluids. Owing to this property, they have immense applications in chemical engineering, pharmaceutics, geophysics and industries like making of semi-conductor materials, geothermal redemption and freezing of magma etc. The impact of frictional heating and variable viscosity on non-Newtonian fluid in a pipe was addressed by Massoudi and Christie [1]. Siddiqui et al. [2] presented analytical solutions for the third grade liquid flow past an inclined plane. The flow and mass transport attributes of Maxwell fluid over a stretching sheet was reported by Mukhopadhyay and Bhattacharyya [3]. They acquired the problem's solution

Scanned with OKEN Scanner

Original article

Institution of MECHANICAL ENGINEERS

Journal of PROCESS MECHANICAL ENGINEERING

Effect of electromagnetic induction on the heat transmission in engine oil-based hybrid nano and ferrofluids: A nanotechnology application

Proc IMechE Part E:
J Process Mechanical Engineering
2023, Vol. 237(6) 2488–2495
© IMechE 2022
Article reuse guidelines:
sagepub.com/journals-permissions
DOI: 10.1177/09544089221139569
Journals.sagepub.com/home/pie

Sage

K. Anantha Kumar[1], N. Sandeep[2], S.P. Samrat[2] and G.P. Ashwinkumar[3]

Abstract

This analysis investigates the control of electromagnetic induction over the flow and heat transmission in shear-thickening hybrid nano and ferrofluids for cooling/heating applications. The stream is time-free and not turbulent. The leading equations are equipped with buoyancy, irregular heat sink/source, and thermic heat effects. The transformed, resulting equalities are resolved with the help of the bvp5c package. Twin expositions are discussed for the hybrid nano (engine oil (EO) + aluminum oxide (Al_2O_3) + titanium dioxide (TiO_2)) and hybrid ferro (EO + iron oxide (Fe_3O_4) + cobalt ferrite ($CoFe_2O_4$)) cases. Numerical momentum, magnetic induction, and thermal profiles are obtained via graphical illustrations. Also, the tables present the friction factor and the measure of thermic transport. It divulges from consequences that the hybrid ferrofluids have a more conducive rate than hybrid nanoliquids, and the Nusselt number shrinks for uneven heat sink/source constraint values. Also, electromagnetic induction controls hybrid ferroliquid more than hybrid nanofluids. The prime application of the current research glimpsed in engineering practices viz. metal extrusion, synthetic fiber, microfluidics, glass fiber manufacture, etc.

Keywords

Ferrofluid, convection, radiative heat, induced magnetic field, extending sheet

Date received: 11 April 2022; accepted: 22 October 2022

Introduction

Several solicitations owing to the concept of nanofluids (NFs) are drug transport, nuclear creation, and hyperthermia. Many fluids are accessible, which enclose nanoparticles viz. water, oil, ethylene, glycol, polymeric liquids, and some renowned lubricants. Choi and Eastman[1] developed a new class of heat transport liquids contrived by hanging metallic ferro/nanoparticles in low convectional fluids. To extend the investigation of NFs, researchers have shown an interest in utilizing hybrid NFs (HNFs). A hybridized nanoliquid is a mixture of base liquid with more than one nanoliquid. CuO, TiO_2, MsO_2, Al_2O_3, etc., are renowned for imparting outstanding thermal transmission properties than conventional fluids. Waini et al.[2] described the heat transport features on a time-independent stream over a needle in the attendance of temperature reliant on conductivity and noticed the astonishing thermal transmission rate. Jamshed et al.[3] scrutinized the stream and thermal transportation qualities of hybrid nanoliquid due to stretched sheets and presented a separate table for the contrast of nano and hybrid liquids. Hussain et al.[4] and Alharbi[5] formulated a numerical study to examine the stream of CuO and TiO_2 mixed nanoliquid across a stretched plate. Recently, Ali et al.[6] examined the energy transport aspects of HNF due to stretching the penetrable sheet by using the well-known numerical technique successive over-relaxation method.

The movement of an incompressible time-independent shear-thickening liquid due to the stretching of a surface has essential solicitations in glass and blasting acoustics,

[1]Department of Mathematics, Sri Venkateswara College of Engineering, Karakambadi, Tirupati, AP, India
[2]Department of Mathematics, Central University of Karnataka, Kalaburagi, India
[3]Department of Mathematics, Vijayanagara Sri Krishnadevaraya University, Bellary, India

Corresponding authors:
S.P. Samrat, Department of Mathematics, Central University of Karnataka, Kalaburagi 585367, India.
Email: payadsam@gmail.com

G.P. Ashwinkumar, Department of Mathematics, Vijayanagara Sri Krishnadevaraya University, Bellary 583105, India.
Email: ashwinpuje@gmail.com

Scanned with OKEN Scanner

roceedings of 2024 International Conference on Cognitive Robotics and Intelligent Systems (ICC - ROBINS 2024)
EEE Xplore Part Number: CFP24UD1-ART; ISBN: 979-8-3503-7274-8

Integration of a Conjugacy over Non-Commutative Ring in Digital Signature Mechanism

Jalaja Valisireddy*
Department of Mathematics
Mohan Babu University
Tirupathi, India
valisireddyjalaja0@gmail.com
*Corresponding Author

S Balakrishna
Department of Mathematics
SVCE
Tirupathi, India
balakrishna.sr@svcolleges.edu.in

L Narendra Mohan
Department of Mathematics
SVCE
Tirupathi, India
mohan.narendra3@gmail.com

Kotte Amaranadha Reddy
Department of Mathematics
Kalasalingam Academy of Research and Education
Tamilnadu, India
amar.anil159@gmail.com

Devendra Jangiti
Department of Mathematics
GITAM SCHOOL OF SCIENCE
GITAM University
Bengaluru, India
djangiti@gitam.edu

G G Rajasekhar
KL University
Guntur, India
rsgg73@gmail.com

Abstract— **Digital signatures are typically dependent on complex mathematical operations like the integer factorization problem, conjugacy problem, and DLP. Nowadays, most of the algorithms are based on a combination of two hard mathematical problems. To enhance the security and provide equivalent security with single hard problem, a new scheme has been proposed. The proposed algorithm is developed by using a conjugacy problem, as the conjugacy structure is intractable on non-commutative rings. Initially, the digital signature algorithm is designed and then it is integrated with a confirmation theorem. Finally, the security analysis of the proposed algorithm is explained.**

Keywords- Conjugacy Problem, Digital Signature structure, Non-Commutative Ring.

I. INTRODUCTION

Digital signatures are becoming increasingly important for data communication. These signatures are frequently employed in protocol identification and authentication. With the use of a digital signature, a user can create a public verification key and certify a document such that anyone can use the corresponding public verification key to verify the signature. Additionally, it offers data non-repudiation, integrity, and authenticity. Although the majority of algorithms are built by considering digital signatures, there are still certain shortcomings with regard to security attacks.

A digital signature scheme proposed in 1994 by He and Kiesler faced two challenging problems: the discrete logarithm problem and the prime factorization problem. In 1995, Harn demonstrated a solution by using discrete logarithms and prime factorization. An approach based on factoring and discrete logarithms is presented by Z. Shao in 2002. However, Tzeng later demonstrated that the Shao digital signature algorithm has numerous flaws and is not safe. Subsequently, he suggested an alternative signature algorithm to address the shortcomings included in Shao's signature technique.

A probabilistic algorithm proposed by Pollard and Schnorr made it easy for attackers to forge the signature for any message. Shao demonstrated in 2005 that the Tzeng signature algorithm is not secure. Consequently, prime factorization or discrete logarithm is the only issue that affects the security of the Tzeng digital signature algorithm. Since digital signatures may provide both data integrity and authentication, they are among the most essential techniques employed in the modern information security systems.

Ismail et al. (2008) provided an explanation of a novel digital signature scheme employing discrete logarithms and factoring [1]. This technique covers a number of challenging tasks, including discrete logarithms and factoring. The equations for signing and verifying combined these two problems, making it hard to get the data. Shao [2] presented the security of a novel discrete logarithmic and factoring-based digital signature technique. In this system, each user will be allowed to utilize one public key and one private key. If an attacker is able to solve discrete logarithm or factorization issues, then the technique is not safe. A signature system utilizing polynomials in non-commutative division semirings was developed by Anjaneyulu et al. [3].

For finitely produced free groups, Seung Won Kim [4] introduced a twisted Conjugacy problem in 2016. In this case, the group G is considered and $\varphi \in End(G)$ be an endomorphism of G. The special case of φ is solvable algorithmically. A monitoring system that protects customers' privacy by homomorphically aggregating the consumptions of all n neighbors was presented by N. Busom et al [5].

A unique dynamic ID-based anonymous two factor AKE approach was proposed by Xie et al [6] in 2017. This system allows password updates and smart card revocation without requiring centralized data storage. A non-abelian group cryptosystem based arithmetic technique was proposed by S. Iswarya et al [7]. A digital signature technique using several elliptic curves was proposed by Bi.Wei [8].

J.Mo et al. developed a three-factor authentication system for WSNS in 2019, which is further strengthened by lightweight security [9]. The random oracle model protects this method. An enhanced multivariate polynomial public key cryptosystem signature model was presented by Xin Wang et al. [10] in order to recover the key. This recovery

979-8-3503-7274-8/24/$31.00 ©2024 IEEE

J. Integr. Sci. Technol. 2024, 12(6), 830

Article

Integrated Science

Journal of Integrated
SCIENCE & TECHNOLOGY

Novel Digital Signature scheme on Non-Commutative Rings using Differential Polynomials in conjugacy problem

V. Jalaja,[1*] L. Narendra Mohan,[2] Kotte Amaranadha Reddy,[3] B. Srinivasa Kumar,[4] K. Hemabala[1]

[1]Mathematics, Mohan Babu University (Erstwhile Sree Vidyanikethan Engineering College), Tirupathi, India. [2]Mathematics, Sri Venkateswara College of Engineering, Tirupathi, India. [3]Mathematics, Kalasalingam Academy of Research and Education, Tamilnadu, India. [4]Mathematics, Koneru Lakshmaiah Education Foundation, Vaddeswaram, Guntur, India.

Received on: 09-Jan-2024 Accepted: 31-May-2024, and published on: 07-Jun-2024

ABSTRACT

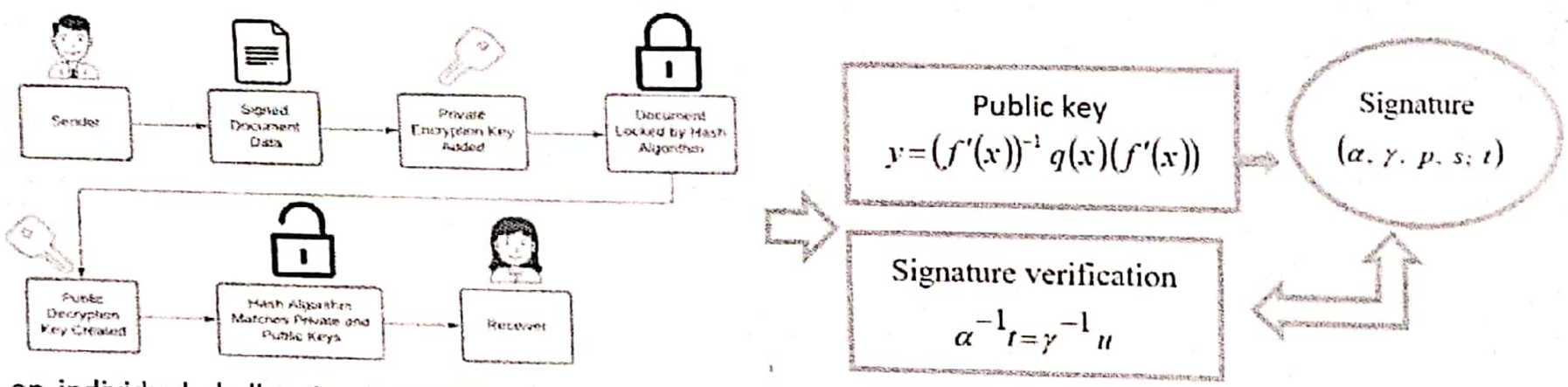

A method for digital signatures ensures the security of messages sent between individuals. Several algorithms have been developed by focusing on individual challenging issues like conjugacy problem, discrete logarithm problem, and integer factorization problem. Though, it has been noted that these techniques are challenging to calculate in order to get at an appropriate solution. These days, the majority of algorithms are created by combining two challenging tasks. With a single challenging problem, we created an algorithm that deals comparable security. In this work, we provide a novel digital signature scheme that takes advantage of non-commutative rings characteristics. The digital signature is protected by the hardness of the conjugacy problem on non-commutative structures and also it is designed by using differential polynomials. We believe that conjugacy problem is NP-hard. The confirmation theorem was used to show the algorithm's strength. Security analysis was also explained.

Keywords: Conjugacy problem, Digital Signature, Differential polynomials, Non-Commutative Ring.

INTRODUCTION

The author of the communication can affix a code that serves as a signature to the message using an authentication technique called a digital signature. It satisfies the requirements of authenticity, integrity, and non-repudiation by acting as a handwritten signature. Paper documents are frequently authenticated with handwritten signatures. In the same way, a digital signature can be used to validate electronic documents.[1] A common idea for digital signatures is to establish a good working region, identify challenging issues inside this framework, develop a one-way function that references these challenging issues, and finally develop an algorithm. Rather than group theory, it is employed to address the unsolvable issues that are directly related to number theory.[2]

Diffie & Hellman (DH) used PKC for the first time in 1976. PKC's primary goal is to make symmetric-key cryptography and it is easier to use by eliminating the need for two separate keys in order for users to interact in confidence. The number of keys required for symmetric-key cryptography to be used in the case of n users exchanging secret data rises quickly with the number of users. Each user in PKC produces two keys: one that is meant be kept secret and the other that is public or open. When used for encryption, exposed key is referred to as "public key," and when used for decoding, secret key is referred to as "private key." In contrast to symmetric key cryptography, no key is shared here. PKC's recent noteworthy reach in this area.

The majority of techniques used today are based on solving discrete logarithm[3,15] and prime factorization problems together, yet each has unique drawbacks and weaknesses. The difficulty of resolving a number of complex theoretical problems is applied to modern encryption. These algorithms are safe as long as the problem they are based on remains secure.

*Corresponding Author: V. Jalaja
Tel: +91 94924 60994 Email: valisireddyjalaja0@gmail.com

Cite as: *J. Integr. Sci. Technol., 2024, 12(6), 830.*
URN:NBN:sciencein.jist.2024.v12.830

©Authors CC4-NC-ND, ScienceIN
http://pubs.thesciencein.org/jist

Scanned with OKEN Scanner

A CASSON FLUID FLOW THROUGH AN INCLINED VERTICAL POROUS PLATE WITH THERMAL DIFFUSION

Mummadisetty Umamaheswar[1*], T. Ramanjaneyulu[2], K. Janardhan[3], L. Hari Krishna[4], Mopuri Obulesu[5]

Article History: Received: 17.01.2023 **Revised:** 30.03.2023 **Accepted:** 13.06.2023

Abstract

Magnetic field influence on thermal diffusion and chemical reaction of MHD Casson fluid flow over inclined vertical porous plates have been examined. There are coupled, coupled linear equations governing the dimensionless system. To solve these equations analytically, the perturbation approach is used. In various controlling factors, the results are displayed visually and tabulated. Our illustrations show that an intensified magnetic parameter induces a downward magnetic field. As the heat absorption increases, the temperature profile is accelerated due to higher energy levels. This can be seen in the form of higher peak temperatures and a sharper gradient in the temperature profile. On the other hand, as the chemical reaction and Schmidt number increase, the concentration distribution slows down. This is because the diffusion of the molecules is hindered by higher concentrations, resulting in a slower rate of change. This can be seen in the form of lower peak concentrations and a flatter gradient in the concentration distribution. As a result, increasing heat absorption and chemical reaction leads to a faster temperature profile and slower concentration profile.

Keywords: Magnetic Field, Casson Fluid, Slip Flow Regime, Thermal Diffusion and Chemical Reaction.

[1,3,4]Department of Mathematics, AITS, Rajampet, Andhra Pradesh, India
[2]Department of Mathematics, Sri Venkateswara Engineering College, Tirupathi Andhra Pradesh, India
[5]Department of Mathematics, Siddartha Institute of Engineering &Technology (Autonomous),Puttur-517583, A.P., India.

Email: [1]umasvu8@gmail.com, [2]ramanjaneyulu.t@svcolleges.edu.in, [3]janardhankodidal@gmail.com, [4]lhkmaths@gmail.com, [5]mopuriobulesu1982@gmail.com

***Corresponding Author:**
Mummadisetty Umamaheswar[1*]
[1*]Department of Mathematics, AITS, Rajampet, Andhra Pradesh, India
Email: [1*]umasvu8@gmail.com

DOI: 10.31838/ecb/2023.12.5.456

Scanned with OKEN Scanner

Communications in Mathematics and Applications
Vol. 14, No. 1, pp. 237–255, 2023
ISSN 0975-8607 (online); 0976-5905 (print)
Published by RGN Publications
DOI: 10.26713/cma.v14i1.1867

http://www.rgnpublications.com

Research Article

Chemical Radiation and Soret Effects on Unsteady MHD Convective Flow of Jeffrey Nanofluid Past an Inclined Semi-Infinite Vertical Permeable Moving Plate

Konduru Venkateswara Raju[1], Ravuri Mohanaramana[2], S. Sudhakar Reddy[1] and Kodi Raghunath*[1,3]

[1] *Department of BS&H (Mathematics), S. V. College of Engineering (Autonomous), Karakambodi Road, Tirupati 517507, Andhra Pradesh, India*
[2] *Department of BS & H (Mathematics), Narasaraopeta Engineering College, Narasaraopeta 522601, Andhra Pradesh, India*
[3] *St. Johns College of Engineering and Technology, Yemmiganur, Kurnool District, Andhra Pradesh 518360, India*
***Corresponding author:** kraghunath25@gmail.com

Received: March 8, 2022 **Accepted:** October 3, 2022

Abstract. An unsteady, MHD incompressible water-based Jeffrey nanofluid (Cu and TiO_2) flow across a stretched sheet in a transverse magnetic domain, thermic radiation, and Soret effects are examined in this article. For each physical parameter, the governing differential equalisations are converted into a set of nonlinear associated standard differential equalisations, translated utilising a perturbation approach with suitable limit essentials for the governing differential equations. The solution for the governing nonlinear boundary value concern is conveyed based on the perturbation technique throughout the complete range of material parameters. The impacts of numerous biological factors on the dimensionless velocity, temperature, concentration, and pressure silhouettes are graphically displayed and thoroughly examined. It is possible to gain favourable comparisons with formerly publicised work on several particular topic situations. Finally, numerical significances of material portions, such as the local skin-friction specification, the Nusselt numeral, and the Sherwood digit, are provided in tabular form, allowing easy comparison.

Keywords. MHD, Chemical reaction, Heat transfer, Radiation, Porous media, Soret effect

Mathematics Subject Classification (2020). 76B15, 76W05, 76S05, 76R50

Copyright © 2023 Konduru Venkateswara Raju, Ravuri Mohanaramana, S. Sudhakar Reddy and Kodi Raghunath.
This is an open access article distributed under the Creative Commons Attribution License, which permits unrestricted use, distribution, and reproduction in any medium, provided the original work is properly cited.

Scanned with OKEN Scanner

ECB

EFFECT OF RADIATION ON MAGNETO HYDRODYNAMICS FLOW OF JEFFREY FLUID OVER AN INFINITE VERTICAL PLATE

R. Lakshmi Devi[1], Konduru Venkateswara raju[2], E. Sudhakara[3], Mopuri Obulesu[4], P. Jayalakshmi[5], M. Umamaheswar[6*]

ArticleHistory:**Received:**08.04.2023 **Revised:**16.06.2023 **Accepted:**20.07.2023

Abstract:

We've got mentioned unsteady MHD rotating glide of an electrically engaging in, viscous, incompressible and optically thick radiating Jeffrey's fluid beyond a rapidly vertical shifting porous plate while temperature of the plate has a quickly ramped profile. Analytical answers of the governing equations are received by way of Laplace remodel method. The ideal solution is likewise received in case of unit Schmidt range. The analytical terms for pores and skin friction and Nusselt number are derived for each ramped temperature and isothermal plates. Sherwood variety is likewise obtained. The speed, temperature and awareness are displayed graphically whereas pores and skin friction, Nusselt variety and Sherwood number are supplied in tabular shape.

Keywords: MHD Flows, Porous Medium, Convection Flows, Vertical Plate, Ramped Temperature, Isothermal Plate.

[1]Department of Mathematics, Siddharth Institute of Engineering &Technology (Autonomous), Puttur-517 583, A.P., India.
Email: [1]lakshmi.rathiraju@gmail.com
[2]Department of Mathematic, Sri Venkateswarara College of Engineering (Autonomous), Karakambodi Road, Tirupati-517507, India,
Email:[2]venky.sakku@gmail.com
[3]Departments of Mathematics, Government Degree College, Vempalli - 516 329, A.P., India.
Email: [3]drsudhakar12@gmail.com
[4]Department of Mathematics, Siddharth Institute of Engineering &Technology (Autonomous), Puttur-517 583, A.P., India.
Email: [4]mopuriobulesu1982@gmail.com
[5]Department of Mathematics, Siddharth Institute of Engineering &Technology (Autonomous), Puttur-517 583, A.P., India.
Email: [5]jayachetu85@gmail.com
[6*]Department of Mathematics, Annamacharya Institute of Technology & Sciences (Autonomous), Puttur-517 583, A.P., India.
Email: [6*]umasvu8@gmail.com

***Corresponding Author**
M. Umamaheswar[6*]
[6*]Department of Mathematics, Annamacharya Institute of Technology & Sciences (Autonomous), Puttur-517 583, A.P., India.
Email: [6*]umasvu8@gmail.com

DOI: 10.31838/ecb/2023.12.6.213

Scanned with OKEN Scanner

A CASSON FLUID FLOW THROUGH AN INCLINED VERTICAL POROUS PLATE WITH THERMAL DIFFUSION

Mummadisetty Umamaheswar[1*], T. Ramanjaneyulu[2], K. Janardhan[3], L. Hari Krishna[4], Mopuri Obulesu[5]

Article History: **Received:** 17.01.2023 **Revised:** 30.03.2023 **Accepted:** 13.06.2023

Abstract

Magnetic field influence on thermal diffusion and chemical reaction of MHD Casson fluid flow over inclined vertical porous plates have been examined. There are coupled, coupled linear equations governing the dimensionless system. To solve these equations analytically, the perturbation approach is used. In various controlling factors, the results are displayed visually and tabulated. Our illustrations show that an intensified magnetic parameter induces a downward magnetic field. As the heat absorption increases, the temperature profile is accelerated due to higher energy levels. This can be seen in the form of higher peak temperatures and a sharper gradient in the temperature profile. On the other hand, as the chemical reaction and Schmidt number increase, the concentration distribution slows down. This is because the diffusion of the molecules is hindered by higher concentrations, resulting in a slower rate of change. This can be seen in the form of lower peak concentrations and a flatter gradient in the concentration distribution. As a result, increasing heat absorption and chemical reaction leads to a faster temperature profile and slower concentration profile.

Keywords: Magnetic Field, Casson Fluid, Slip Flow Regime, Thermal Diffusion and Chemical Reaction.

[1,3,4]Department of Mathematics, AITS, Rajampet, Andhra Pradesh, India
[2]Department of Mathematics, Sri Venkateswara Engineering College, Tirupathi Andhra Pradesh, India
[5]Department of Mathematics, Siddartha Institute of Engineering &Technology (Autonomous),Puttur-517583, A.P., India.

Email: [1]umasvu8@gmail.com, [2]ramanjaneyulu.t@svcolleges.edu.in, [3]janardhankodidal@gmail.com, [4]lhkmaths@gmail.com, [5]mopuriobulesu1982@gmail.com

***Corresponding Author:**
Mummadisetty Umamaheswar[1*]
[1*]Department of Mathematics, AITS, Rajampet, Andhra Pradesh, India
Email: [1*]umasvu8@gmail.com

DOI: 10.31838/ecb/2023.12.5.456

Scanned with OKEN Scanner

AIP Publishing

Biomicrofluidics
Special Topic:
Microfluidic Biosensors
Submit Today
AIP Publishing

APL Materials ARTICLE pubs.aip.org/aip/apm

Effect of inclined Lorentzian force on radiated nanoflow Williamson model under asymmetric energy source/sink: Keller box method

Cite as: APL Mater. 12, 041106 (2024); doi: 10.1063/5.0201939
Submitted: 1 February 2024 • Accepted: 14 March 2024 •
Published Online: 4 April 2024

VinothKumar B.[1,a] Poornima T.[1,b] Sreenivasulu P.[2,c] and Subba Rao A[3,d]

AFFILIATIONS

[1]Department of Mathematics, School of Advanced Sciences, Vellore Institute of Technology, Vellore 632014, Tamil Nadu, India
[2]Department of Mathematics, Sri Venkateswara College of Engineering, Tirupati 517507, India
[3]Department of Mathematics, Madanapalle Institute of Technology and Science, Madanapalle, Andhra Pradesh 517 325, India

[a]vinath.chb@gmail.com
[b]**Author to whom correspondence should be addressed:** poornima.t@vit.ac.in
[c]preddysvu11@gmail.com
[d]subbumaths.a@gmail.com

ABSTRACT

An asymmetric energy source/sink can be designed to efficiently convert ambient energy into usable forms; this could have applications in micro-/nanoscale power generation, i.e., energy harvesting. The asymmetric energy source/sink and inclined Lorentzian force could be used to control the flow of fluids within these devices. This study numerically investigates the model of a Williamson nanofluid influenced by an angled magnetic force and an asymmetric energy input/output on a stretching surface with a convective wall boundary condition. The partial differential equations connected to the momentum, energy, and concentration equations are transformed into nonlinear ordinary differential equations (ODEs) by applying relevant similar variables. The obtained ODEs are handled by the Thomas algorithm and a finite difference in the Keller box method. A thorough examination of a change in velocity, temperature, and concentration is done for all the relevant parameters. A higher buoyancy ratio parameter lowers the streamline density. As far as the numerical method is concerned, the Keller box method gives the highest convergence value when compared to other methods, so we use this method to investigate the sleeping behavior of the Williamson nanofluid. The energy source decreases the non-Newtonian passing surface friction. The concentration gradient increases for an increasing value of the chemical reaction parameter. A decreased diffusion rate is seen for increasing Brownian number, while the opposite behavior is noticed for the thermophoretic parameter. The wall friction coefficient increases for augmenting *We* but decreases for the angled Lorentzian force. Except for radiation, energy transfer is high in all other flows, affecting parameters such as *A*, *B*, *Nb*, *Nt*, and *Pr*. By controlling the magnetic field, MHD heat exchangers can manipulate heat transfer rates for various industrial applications. In fusion reactors, strong magnetic fields confine hot plasma, and understanding the interaction between the field and heat sources is crucial for efficient energy generation.

© 2024 Author(s). All article content, except where otherwise noted, is licensed under a Creative Commons Attribution (CC BY) license (https://creativecommons.org/licenses/by/4.0/). https://doi.org/10.1063/5.0201939

01 Apr 2024 05:01:37

I. INTRODUCTION

The Williamson fluid model exhibits shear thinning properties since it has minimum and maximum viscosities (μ_0, μ_∞). Williamson, in 1926, carried out experiments for pseudoplastic, clarified the characteristics of pseudoplastic, and framed a model. Many processes use non-Newtonian fluids as convectional fluids because they violate Newton's law of viscosity; the most commonly used non-Newtonian liquids are pseudoplastic liquids. These liquids can be found as paints, emulsions, lubricating oils, suspensions, and a variety of biological fluids. There are two categories of non-Newtonian fluids, specifically dependent on time and time-independent. Alkasasbeh *et al.* studied the Williamson hybrid nanofluid magneto-convection flow with a thermal

Scanned with OKEN Scanner

DE GRUYTER

Open Physics 2024; 22: 20240036

Research Article

Balaji Vinothkumar, Rania Saadeh, Tamalapakula Poornima*, Ahmad Qazza,
Pandikunta Sreenivasulu, Annasagaram Subba Rao, Umair Khan, and Md Irfanul Haque Siddiqui

Two-phase numerical simulation of thermal and solutal transport exploration of a non-Newtonian nanomaterial flow past a stretching surface with chemical reaction

https://doi.org/10.1515/phys-2024-0036
received January 09, 2024; accepted April 22, 2024

Abstract: Non-uniform heat sources and sinks are used to control the temperature of the reaction and ensure that it proceeds at the desired rate. It is worldwide in nature and may be found in all engineering applications such as nuclear reactors, electronic devices, chemical reactors, *etc.* In food processing, heat is used to cook such as microwave ovens, pasteurize infrared heaters, and sterilize food products. Non-uniform heat sources are mainly used in biomedical applications, such as hyperthermia cancer treatment, to target and kill cancer cells. Because of its ubiquitous nature, the idea is taken as our subject of study. Heat and species transfer analysis of a non-Newtonian fluid flow model under magnetic effects past an extensible moving sheet is modelled and examined. Homogeneous chemical reaction inside the fluid medium is also investigated. This natural phenomenon is framed as a set of Prandtl boundary layer equations under the assumed convective surface boundary constraint. Self-similarity transformation is employed to convert framed boundary layer equations to ordinary differential equations. The resultant system is solved using the efficient finite difference utilized Keller box method with the help of MATLAB programming. The influence of various fluid-affecting parameters on fluid momentum, energy, species diffusion and wall drag, heat, and mass transfer coefficients is studied. Accelerating the Weissenberg number decelerates the fluid velocity. The temperature of the fluid rises due to variations in the non-uniform heat source and sink parameters. Ohmic dissipation affects the temperature profile significantly. Species diffusion reduces when thermophoresis parameter and non-uniform heat source and sink parameters vary. The Eckert number enhances the heat and diffusion transfer rate. Increasing the chemical reaction parameter decreases the shear wall stress and energy transmission rate while improving the diffusion rate. The wall drag coefficient and Sherwood number decrease as the thermophoretic parameter increases whereas the Nusselt number increases. We hope that this work will act as a reference for future scholars who will have to deal with urgent problems related to industrial and technical enclosures.

Keywords: Williamson fluid model, heat transfer, chemical reaction, magnetohydrodynamics, thermal radiation

* **Corresponding author: Tamalapakula Poornima,** Department of Mathematics, School of Advanced Sciences, Vellore Institute of Technology, Vellore-632014, Tamil Nadu, India,
e-mail: poonima.anand@gmail.com
Balaji Vinothkumar: Department of Mathematics, School of Advanced Sciences, Vellore Institute of Technology, Vellore-632014, Tamil Nadu, India, e-mail: vinoth.chk@gmail.com
Rania Saadeh: Faculty of Science, Zarqa University, Zarqa, 13110, Jordan, e-mail: rsaadeh@zu.edu.jo
Ahmad Qazza: Faculty of Science, Zarqa University, Zarqa, 13110, Jordan, e-mail: aqazza@zu.edu.jo
Pandikunta Sreenivasulu: Department of Mathematics, Sri Venkateswara College of Engineering, Tirupati, 517507, India, e-mail: psreddysvu11@gmail.com
Annasagaram Subba Rao: Department of Mathematics, Madanapalle Institute of Technology and Science, Madanapalle, Andhra Pradesh, India, e-mail: subbumaths.a@gmail.com
Umair Khan: Department of Mathematics, Faculty of Science, Sakarya University, Serdivan, Sakarya, 54050, Turkey; Department of Computer Science and Mathematics, Lebanese American University, Byblos, Lebanon, e-mail: umair.khan@lau.edu.lb
Md Irfanul Haque Siddiqui: Mechanical Engineering Department, College of Engineering, King Saud University, Riyadh, 11451, Saudi Arabia, e-mail: msiddiqui2.c@ksu.edu.sa

1 Introduction

Non-Newtonian fluid models have a wide range of applications, spanning various industries and domains. Non-Newtonian models help create these textures by predicting how ingredients

Open Access. © 2024 the author(s), published by De Gruyter. CC BY This work is licensed under the Creative Commons Attribution 4.0 International License.

Scanned with OKEN Scanner

International Journal of Mechanical Engineering

STING OF MULTIVARIATE NONLINEAR REGRESSION HYPOTHESIS USING NONLINEAR LEAST SQUARE (NLS) ESTIMATION

By Kesavulu Poola[1], J. Anil Kumar[2], V. Pavankumari[3], Putta Hemalatha[4], Prof. M. Bhupathi Naidu[5].

[1]Associate professor, CMS - Jain University, Bengaluru.
[2]Assistant professor, S V College of Engineering, Tirupati.
[3]Assistant professor, Malla reddy Engineering College, Hyderabad.
[4]Assistant professor, Institute of Aeronautical Engineering, Hyderabad.
[5]Professor, Department of *Statistics*, S. V. University, Tirupati.

ABSTRACT

The present study paper confers the different models on testing the nonlinear regression hypothesis using nonlinear least squares (NLS) estimator through nonlinear studentized residuals and nonlinear predicted residual. Moreover this research paper mentioned internally nonlinear studentized residuals, externally nonlinear studentized residuals to test the hypothesis of multivariate nonlinear regression models. This research article proposes a new way of parameter estimation using nonlinear least squares method. Gallant, A. Ronald, M. Hashem, and Angus s. Deaton. (1978) uses nonlinear least squares asymptotic properties. The key objective of this article is to carter extremely pioneering model of testing nonlinear regression hypothesis using NLS estimator through nonlinear (internally and externally) studentized residuals and predicted NLS Methods.

KEYWORDS: *Nonlinear models, nonlinear least square estimation, Studentized and Predicted residuals*

INTRODUCTION

Method and maximum likelihood methods are the quite popular in parameter estimation of linear models. In this method has to satisfy all pre assumption of normality with mean zero mean and unknown population variance. But in linear models building of construction of inferential facets together with Parameter estimation and hypothesis testing parameters of the nonlinear regression models are quite difficult. In recent era, researchers focused on the erection of parameter estimation of the nonlinear regression models. Since three decades these nonlinear models have been parameter estimation procedures and testing of hypothesis for nonlinear regression models and error assumptions are analogous to those made for linear regression models, In the present research study some methods of testing multivariate hypotheses using nonlinear least square estimation, studentized and predicted residuals for multivariate nonlinear models discussed.

LEAST SQUARE ESTIMATION OF MULTIVARIATE NONLINEAR REGRESSION MODEL

Consider standard multivariate nonlinear regression model.

$$Y_{it} = f_i(X_t, \theta) + e_{it} \quad i = 1, 2, \ldots M; \quad t = 1, 2, \ldots n$$

Let

$$(\hat{e}_{1t}, \hat{e}_{2t}, \ldots \hat{e}_{Mt}) \qquad t = 1, 2, \ldots, n$$

Where θ is

Then the multivariate least square estimator minimizes

$$\frac{1}{n}\sum_{t=1}^{n}\left[Y_t - f(X_t, 0)\right]'\left(\hat{\Sigma}_0\right)^{-1}\left[Y_t - f(X_t, 0)\right] \qquad \ldots(2.1)$$

Let $\hat{\Sigma}_n$ be any random variable that converges almost surely to Σ and has $\sqrt{n}\left(\hat{\Sigma}_n - \Sigma\right)$ bounded in probability.

Given $\varepsilon > 0$, there is bound 'b' and sample size N, such that

$$P\left(\sqrt{n}\left|\hat{\theta}_{ij} - \theta_{ij}\right| < b\right) > 1 - S \qquad \forall n > N$$

Scanned with OKEN Scanner

AkiNik Publications

Printing Press License No.: F.1 (A-4) press 2016

Publication Certificate

Ref. No.: B23-20901
Date: 03-02-2024

To,
Dear Renugadevi K.

This certificate confirms that **Renugadevi K.** is the author of book titled **"Characterization of Calotropis Gigantea Continuous Twisted Bast Fibre Yarn"** having ISBN **978-93-6135-643-8**.

Yours Sincerely,

Akhil Gupta

AkiNik Director Publications

Akhil Gupta
Manager
AkiNik Publications

Science and Engineering Research Board
(A statutory body of the Department of Science & Technology, Government of India)

5 & 5A,LGF,
Vasant Square Mall
Sector-B, Pocket-5, VasantKunj,
New Delhi – 110070

Brief report of the organized event
(Financial Assistance to Seminar / Symposia)

Date: 12/05/2023

SERB Sanction No: SERB/F/10643/2022-2023
File No.: SSY/2022/ 001098

1. **Name of Academic Institution / University / Society etc. under whose auspices the Seminar / Conference / Workshop / Symposium etc. was organized:**

   SRI VENKATESWARA COLLEGE OF ENGINEERING, KARAKAMBADI ROAD, TIRUPATI

2. **Title of the Seminar / Conference / Workshop / Symposium etc.:**

   NANOSTRUCTURED MATERIALS TO BATTERY AND SUPERCAPACITORS (NMBS-2023)

3. **Duration / Period of the organized event:**

From			To		
Date	Month	Year	Date	Month	Year
16	03	2023	18	03	2023

4. **Grant Sanctioned: ₹ 1,00,000.00/- (Rupees One Lakh only)**

5. **Summary of the event (Max. 1000Words):**

The DST-SERB sponsored a three day national level symposium on "NANOSTRUCTURED MATERIALS TO BATTERY AND SUPERCAPACITORS (NMBS-2023)" was organized by the department of Physics & Chemistry, Sri Venkateswara College of Engineering, Tirupati-517507 from 16th - 18th March 2023. This symposium brought together the leading industrialists, experts, and research scholars working in the field of energy storage devices such as batteries and supercapacitors to discover new products/ideas and create powerful solutions for the development of eco-friendly and safe futuristic devices. The programme enlightened the participants regarding the recent advances in the application of nanostructured materials to batteries and supercapacitors.

On the first day of the NMBS-2023 symposium, the registration process started at 9:15 AM, followed by the inauguration at 10:30 AM. The Chief Guest, Prof. Vijayamohanan K Pillai, Chair of Chemistry and Dean of Research and Development at IISER Tirupati, delivered the keynote lecture on the demand for energy production and storage using nanostructured materials in the fourth-coming decade. Session 1 was conducted from 11:30 AM to 1:00 PM, where Prof. Vijayamohanan K Pillai gave a lecture on "Nanostructure Materials for Sustainable Energy Storage".

Session 2, from 2:00 PM to 3:30 PM, included a lecture on “Nanostructured Materials for Energy Storage Applications” by Dr. D.H. Nagaraju, Professor, Department of Chemistry, REVA University, Bengaluru. Session 3, from 3:45 PM to 5:00 PM, Dr. D.H. Nagaraju continued and gave a talk on “Green synthesis of carbon-based materials to EDLC, Pseudocapacitor, Hybrid capacitor applications”. Overall, the first day of the symposium focused on the application of nanostructured materials in energy storage and featured lectures from prominent speakers in the field.

On Day 2 of the symposium, in the Session 4, Dr. D. Ebenezer, Manager R&D, from Amara Raja Batteries, Tirupati, spoke about battery safety measures and troubleshooting, covering topics such as identifying flaws in batteries, safety measures, and lithium-ion battery troubleshooting. In the Session 5, Dr. Ebenezer extended his talk on lithium-ion battery safety measures and common troubleshooting techniques. There was an interactive session with the participants followed by felicitation to Dr. D. Ebenezer. In the Session 6, Dr. D. Sridhar, Assistant Manager in R&D from Amara Raja Batteries, Tirupati, spoke about advancements in energy storage technologies, discussing the latest developments and innovations in lithium-ion batteries, lead-acid batteries, and advanced lead-acid batteries. He emphasized the need to improve energy density, cycle life, and safety, reduce costs and environmental impact. In Session 7, Dr. Sridhar highlighted the challenges and opportunities in the field and discussed the need for research on new materials, manufacturing processes, and recycling technologies. There was an interactive session with the participants and Dr. D. Sridhar was felicitated by the Principal.

On Day 3 of NMBS-2023, there were three sessions: Session 8 (9:30 AM-11:00 AM): Prof. G. Ranga Rao from IIT Madras delivered a talk on "Chalcogenide-based materials for electrochemical charge storage applications." The session focused on the use of chalcogenides in electrochemical energy storage devices. Session 9 (11:15 AM-1:00 PM): Prof. G. Ranga Rao continued his talk on chalcogenide-based materials and discussed recent advancements in the synthesis and characterization of these materials. The session also covered the performance of chalcogenides in different types of energy storage devices. Session 10 (2:00 PM-4:00 PM): Dr. Aravindan V from IISER, Tirupati delivered a talk on "Latest R&D Advancements in Supercapacitors." Dr. Aravindan discussed the current challenges in supercapacitor technology and highlighted the need for new materials and designs to overcome these challenges. He also covered the topic of lithium-ion battery recycling in his session.

The valedictory ceremony marked the end of the National Symposium on Nanostructured Materials to Battery and Supercapacitors (NMBS-2023), a three-day event that aimed to discuss the development of eco-friendly and economical devices with high safety and

efficiency. The speakers Prof. G. Ranga Rao from IIT Madras and Dr. Aravindan V from IISER Tirupati, and Dr. P. Babu, the convener of NMBS-2023, and Dr. K. Reddi Mohan Naidu, the co-convener were present in the valedictory ceremony. The participants were appreciated for their contributions, and certificates of participation were distributed. The vote of thanks was delivered by Dr. P. Geetha. The ceremony concluded with the national anthem.

(Convener Signature)
(Dr. P. BABU)

Participation Information:

S. No	Participation in the event	Nos.
I.	Key-not speakers	06
II.	Senior Scientist	26
III.	Young Scientist	44
IV.	Postgraduate Students	19
V.	Undergraduate Students	09
VI.	Industry persons	02
VII.	Other category (Please specify each category)	00
		106

Photographs Section:

1. **Inaugural Session**

Lighting the Lamp by Dr.Vijayamohanan K Pillai (Chief Guest).

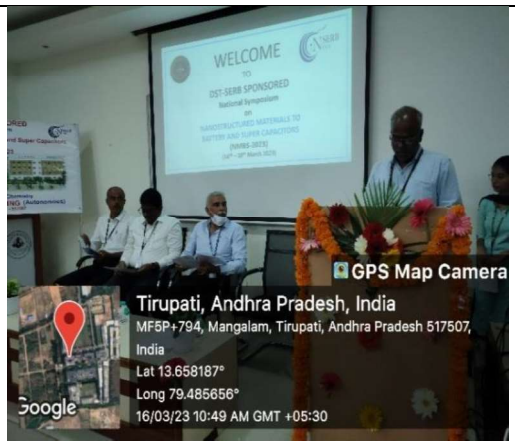

Welcome address by Dr. P. Babu, Convener, NMBS-2023.

Speech by Dr. N. Manohar Reddy, HOD, Dept. of Physics & Chemistry.

Keynote address by Dr.Vijayamohanan K Pillai.

Felicitation to Chief Guest by Principal, SVCE.

NOTE- CONSOLIDATED REPORT OF THE APPROVED EVENT MAY BE SUBMITTED ONLINE / EMAIL WITH HIGH RESOLUTION PHOTOGRAPHS PASTED IN THE REPORT OR SUBMITTED DIRECTLY IN JPEG FORMAT.

2. General Photographs

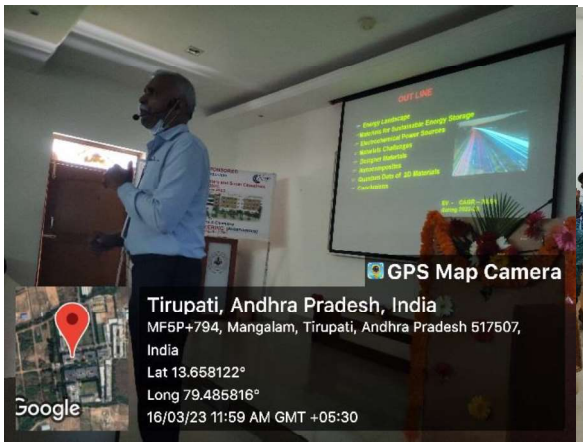

Lecture by Prof. Vijayamohanan K Pillai.

Interaction of participants with the speaker.

Lecture by Dr. D.H. Nagaraju.

Interaction of participants with the speaker.

Felicitation to Dr. D.H. Nagaraju.

NOTE- CONSOLIDATED REPORT OF THE APPROVED EVENT MAY BE SUBMITTED ONLINE / EMAIL WITH HIGH RESOLUTION PHOTOGRAPHS PASTED IN THE REPORT OR SUBMITTED DIRECTLY IN JPEG FORMAT.

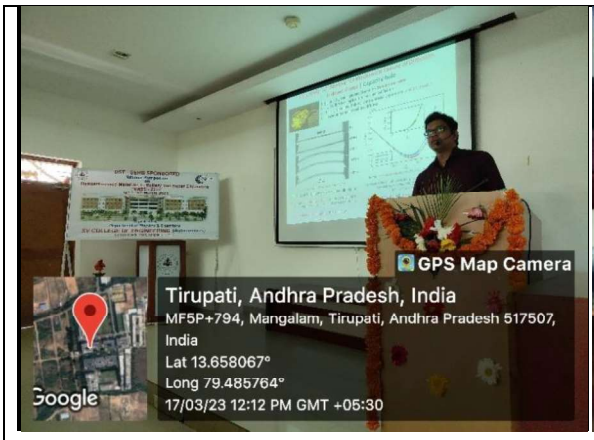

Lecture by Dr. D. Ebenezer.

Felicitation to Dr. D. Ebenezer by Convener and Co- Convener NMBS-2023.

3. General Photographs

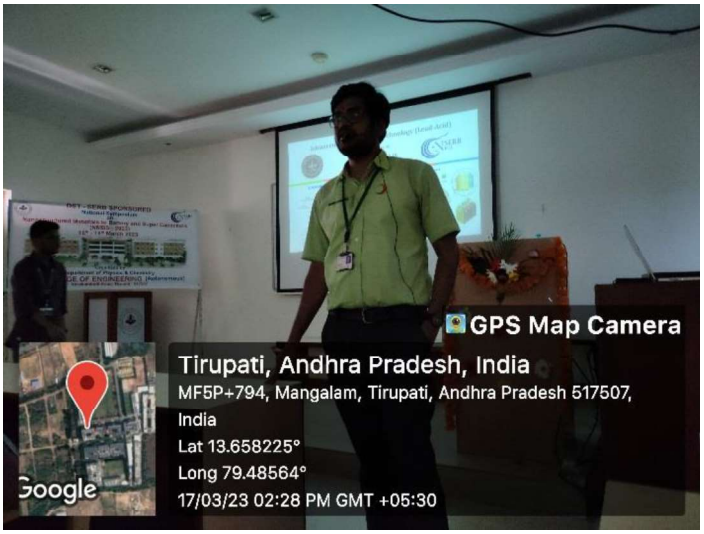

Lecture by Dr. D. Sridhar.

NOTE- CONSOLIDATED REPORT OF THE APPROVED EVENT MAY BE SUBMITTED ONLINE / EMAIL WITH HIGH RESOLUTION PHOTOGRAPHS PASTED IN THE REPORT OR SUBMITTED DIRECTLY IN JPEG FORMAT.

Interaction of participants with the speaker.

Felicitation to Dr. D. Sridhar by Principal.

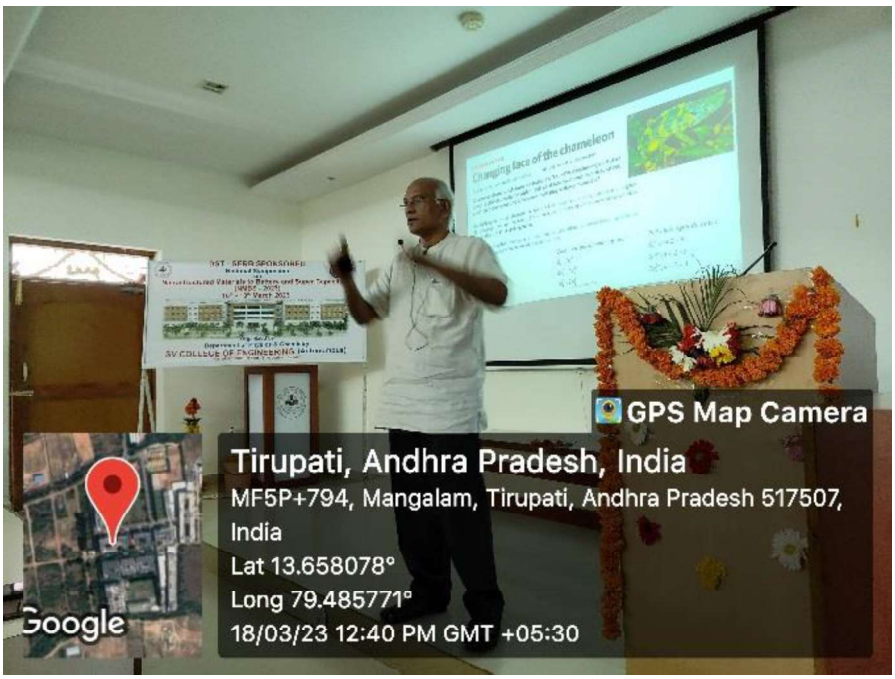

Lecture by Prof. G. Ranga Rao.

4. General Photographs

Interaction of participants with the speaker.

Felicitation to Prof. G. Ranga Rao by Principal.

NOTE- CONSOLIDATED REPORT OF THE APPROVED EVENT MAY BE SUBMITTED ONLINE / EMAIL WITH HIGH RESOLUTION PHOTOGRAPHS PASTED IN THE REPORT OR SUBMITTED DIRECTLY IN JPEG FORMAT.

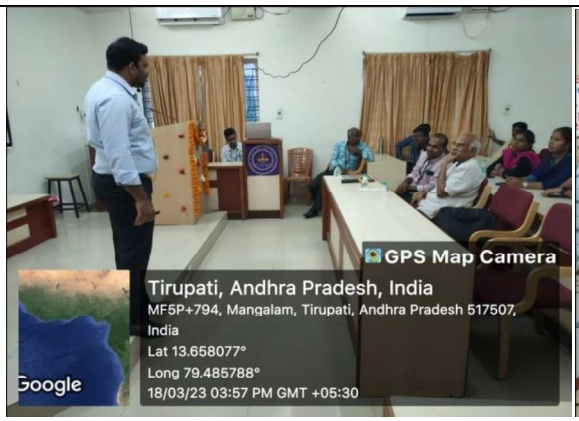

Lecture by Dr. Aravindan V.

Felicitation to Dr. Aravindan V by Prof. G. Ranga Rao.

Distribution of certificates.

SRI VENKATESWARA COLLEGE OF ENGINEEING
(AUTONOMOUS)
Karakambadi Road, Tirupati - 517 507, A.P.
DST - SERB Sponsored
National Symposium on
NANOSTRUCTURED MATERIALS TO BATTERY AND SUPER CAPACITORS
16th-18th March, 2023
Organized by Department of Physics & Chemistry, SVCE, Tirupati
Certificate of Participation

This is to certify that Mr./Ms./Dr./Mrs._____ of _____ has Participated in "NATIONAL SYMPOSIUM ON NANOSTRUCTURED MATERIALS TO BATTERY AND SUPER CAPACITORS" (NMBS-2023), held during 16th -18th March, 2023 at Sri Venkateswara College of Engineering, Tirupati.

Convener HOD Principal

NMBS-2023 Certificate of Participation.

Photos with the speakers.

NOTE- CONSOLIDATED REPORT OF THE APPROVED EVENT MAY BE SUBMITTED ONLINE / EMAIL WITH HIGH RESOLUTION PHOTOGRAPHS PASTED IN THE REPORT OR SUBMITTED DIRECTLY IN JPEG FORMAT.

NMBS-2023 news as published in **Tirupati Local Edition Newspapers on 16-03-2023**

ఎస్వీసీఈలో జాతీయ సదస్సు ప్రారంభం

ఐసర్ డీన్ విజయమోహనన్ కె.పిళ్లైకి మొక్క అందజేస్తున్న విద్యార్థిని పక్కన ప్రిన్సిపాల్

తిరుపతి (విద్య), మార్చి16: కరకంబాడి రోడ్డులోని ఎస్వీ కాలేజ్ ఆఫ్ ఇంజినీరింగ్ విద్యాసంస్థల్లో భౌతిక, రసాయనశాస్త్ర విభాగాల సంయుక్త ఆధ్వర్యంలో నానోస్ట్రక్చర్డ్ మెటీరియల్స్ టు బ్యాటరీ అండ్ సూపర్ కెపాసిటర్స్(ఎన్ఎంబీఎస్-2k23) అనే అంశంపై మూడు రోజుల జాతీయ సదస్సు గురువారం ప్రారంభమైంది. భారత ప్రభుత్వ డిపార్ట్‌మెంట్ ఆఫ్ సైన్స్ అండ్ టెక్నాలజీ(డీఎస్‌టీ-ఎస్ఈఆర్‌బీ) ఆర్థిక సౌజన్యంతో ఏర్పాటు చేసిన ఈ సదస్సుకు ముఖ్య అతిథులుగా ఐసర్ రసాయనశాస్త్ర డీన్ ప్రొఫెసర్ విజయమోహనన్ కె.పిళ్లై, బెంగళూరుకు చెందిన రేవా యూనివర్సిటీ ప్రొఫెసర్ డాక్టర్ డి.నాగరాజ్ మాట్లాడారు. కాలుష్య నియంత్రణ, సహజ వనరుల కొరతను అధిగమించడంలో బ్యాటరీ ఆధారిత వాహనాలు కీలక పాత్ర పోషిస్తాయని తెలిపారు. ఎస్వీసీఈ ప్రిన్సిపాల్ డాక్టర్ ఎన్.సుధాకర్‌రెడ్డి, సదస్సు కన్వీనర్ డాక్టర్ ఎన్.మనోహర్‌రెడ్డి, కో-కన్వీనర్ డాక్టర్ కె.రెడ్డి మోహన్, వైస్ ప్రిన్సిపాల్ డాక్టర్ చంద్రశేఖరరావు పాల్గొన్నారు.

గ్రామ పం
చిత్తూరు జిల్లా

కార్బన్ రహిత సమాజ స్థాపనకు కృషి

ప్రజాశక్తి-తిరుపతి(మంగళం): వాతావరణ కాలుష్యాన్ని నియంత్రించడంలో కీలకంగా ఉన్న బ్యాటరీ వాహనాల వినియోగాన్ని పెంచి కార్బన్ రహిత సమాజ స్థాపనకు కృషి చేద్దామని శ్రీ వెంకటేశ్వర ఇంజినీరింగ్ కళాశాల ప్రిన్సిపల్ డాక్టర్ ఎన్. సుధాకర్‌రెడ్డి పిలుపునిచ్చారు. గురువారం తిరుపతి కరకంబాడి మార్గంలోని శ్రీ వెంకటేశ్వర ఇంజినీరింగ్ కళాశాలలో నానో స్ట్రక్చర్డ్ మెటీరియల్స్ టూ బ్యాటరీ అండ్ సూపర్ కెపాసిటర్స్(ఎన్ ఎం బి ఎస్-2023) అనే అంశంపై మూడు రోజుల జాతీయ సదస్సును ఘనంగా ప్రారంభించారు. కార్యక్రమానికి ముఖ్య అతిథులుగా ఐసెర్ రసాయన శాస్త్ర విభాగం ప్రొఫెసర్ విజయమోహనన్ పిళ్లై, బెంగళూరు రేవ యూనివర్సిటీ రసాయన విభాగం డాక్టర్ డీహెచ్ నాగరాజ్, ఎస్వీసీఈ విభాగాధిపతి ఎస్.మనోహర్‌రెడ్డి, కన్వీనర్ డాక్టర్ బాబు, కో కన్వీనర్ రెడ్డి మోహన్ కలిసి జ్యోతి ప్రజ్వలన చేశారు. వారు మాట్లాడుతూ

రోజురోజుకు పెరిగిపోతున్న కాలుష్యాన్ని, వనరుల కొరతను నియంత్రించడంలో బ్యాటరీ వాహనాలు కీలక పాత్ర పోషిస్తాయని, తద్వారా పర్యావరణ పరిరక్షణతో పాటు కార్బన్ రహిత సమాజ స్థాపనకు కషి చేసిన వారమవుతామని స్పష్టం చేశారు. కార్యక్రమంలో వైస్ ప్రిన్సిపల్ డాక్టర్. చంద్రశేఖర రావు, వివిధ విభాగాధిపతులు, కళాశాల అధ్యాపక సిబ్బంది పాల్గొన్నారు.

ఎస్వీసీఈలో జాతీయ సదస్సు ప్రారంభం

తిరుపతి ఎడ్యుకేషన్: తిరుపతి-కరకంబాడి రోడ్డులోని ఎస్వీసీఈ ఇంజినీరింగ్ కళాశాలలో గురువారం భౌతిక, రసాయన శాస్త్ర విభాగాల ఆధ్వర్యంలో నానో స్ట్రక్చర్డ్ మెటీరియల్స్ టు బ్యాటరీ అండ్ సూపర్ కెపాసిటర్స్(ఎన్ఎంబీఎస్-2023) అన్న అంశంపై జాతీయ స్థాయి సదస్సు ప్రారంభమైంది. ఇందులో ముఖ్యఅతిథులుగా తిరుపతి ఐసర్ రసాయన శాస్త్ర విభాగపు డీన్ ప్రొఫెసర్ విజయమోహన్ కె.పిళ్లై, బెంగళూరులోని రేవ యూనివర్సిటీ రసాయన శాస్త్ర విభాగపు ప్రొఫెసర్ డిహెచ్.నాగరాజులు పాల్గొని మాట్లాడారు. పెరుగుతున్న కాలుష్యాన్ని, వనరుల కొరతను నియంత్రించడంలో బ్యాటరీ ఆధారిత వాహనాలు కీలక పాత్ర పోషిస్తాయని తెలిపారు. తద్వారా పర్యావరణ పరిరక్షణతో పాటు కార్బన్ రహిత సమాజాన్ని స్థాపించవచ్చని తెలిపారు. సదస్సులో ప్రిన్సిపాల్ ఎన్.సుధాకర్‌రెడ్డి, వైస్ ప్రిన్సిపాల్ టి.చంద్రశేఖర్‌రావు, విభాగాధిపతి ఎస్.మనోహర్‌రెడ్డి, కన్వీనర్ పి.బాబు, కోకన్వీనర్ కె.రెడ్డిమోహన్ పాల్గొన్నారు.

P. Babu

(Convener Signature)

(Dr. P. BABU)

NOTE- CONSOLIDATED REPORT OF THE APPROVED EVENT MAY BE SUBMITTED ONLINE / EMAIL WITH HIGH RESOLUTION PHOTOGRAPHS PASTED IN THE REPORT OR SUBMITTED DIRECTLY IN JPEG FORMAT.

Journal of Alloys and Compounds 886 (2021) 161234

Contents lists available at ScienceDirect

Journal of Alloys and Compounds

journal homepage: www.elsevier.com/locate/jalcom

Self-assembled and highly faceted growth of Mo and V doped ZnO nanoflowers for high-performance supercapacitors

Mohan Reddy Pallavolu[a,1], Jyothi Nallapureddy[a,1], Ramesh Reddy Nallapureddy[a], Gaddam Neelima[b], Anil Kumar Yedluri[c], Tapas K. Mandal[a], Babu Pejjai[d], Sang W. Joo[a,*]

[a] School of Mechanical Engineering, Yeungnam University, Gyeongsan 38541, Republic of Korea
[b] Department of Physics, National Taiwan University, Taiwan
[c] School of Electrical Engineering, Pusan National University, Busandaehak-ro 63beon-gil, Geumjeong-gu, Busan 46241, Republic of Korea
[d] Department of Science and Humanities, Sri Venkateswara Engineering College, Karakambadi Road, Tirupati 517507, Andhra Pradesh, India

ARTICLE INFO

Article history:
Received 5 May 2021
Received in revised form 30 June 2021
Accepted 17 July 2021
Available online 22 July 2021

Keywords:
ZnO lotus flower
Metal ion doping
Self-assembly
Capacity
Asymmetric supercapacitors

ABSTRACT

The rational design of metal ion-doped transition metal oxides has been considered as a novel electrode material for the development of high-performance asymmetric supercapacitors (ASCs). Herein, we facilely synthesized molybdenum and vanadium doped zinc oxide (Mo- and V-doped ZnO) lotus flower-like hierarchical structures using the co-precipitation method for use as a high capacity cathode material for ASCs. The formation mechanism during the self-assembly growth and highly faceted Mo- and V-doped ZnO lotus flowers were examined. Utilizing the beneficial properties of high electrochemical conductivity and excellent electroactive area, Mo- and V-doped ZnO lotus flowers demonstrated maximum specific capacities of 336 C g^{-1} and 362 C g^{-1} with good cycling stability. Furthermore, the ASC has been fabricated with V-doped ZnO as a cathode and activated carbon as a negative electrode, which shows a high specific capacitance of 111 F g^{-1}, an energy density of 32.4 Wh kg^{-1}, and a power density of 5.16 kW kg^{-1}, respectively. The fabricated device also demonstrated excellent electrochemical capacitance retention of 85% and Coulombic efficiency of 98% after 2000 cycles. These superior characteristics indicate the promising potentiality of the new materials reporting for low-cost and high-performance supercapacitors.

© 2021 Elsevier B.V. All rights reserved.

1. Introduction

In recent years, the increasing electrical-energy demand in day-to-day life raises the need for efficient energy storage device developments at a lower cost. Among the various types of energy storage devices, supercapacitors (SCs) have been considered as most efficient due to their extensive performance in energy sectors, including portable electronics, telecommunications, backup power systems, and vehicles [1–3]. Recently metal oxides have been extensively used in supercapacitors as electrode materials. Among the metal oxides reported, zinc oxide (ZnO) has shown attractive electrochemical performances owing to its relatively high thermal and chemical stability, good oxidation resistance, great biocompatibility, non-toxicity, and high conductivity [4,5]. Based on these properties and its wide range of nanostructures, ZnO has been considered a prominent material for a wide range of applications such as solar cells, displays, and integrated circuits [6–13], especially doped with transition metal oxides (V_2O_5, MoO_3, MnO_2, and CoO_3) as composites, dopants and heterojunctions, etc., are widely used for energy storage devices, such as SCs. ZnO has high competency of low-temperature growth (typically 200–450 °C) with a wide variety of morphologies including flower, wires, rods, and tube shape at nano-level [14–16]. The nanostructured morphology can exhibit significantly enhanced electrochemical performance due to its fast charge carrier transport, short diffusion path, and high number of electrochemical active sites [17–19].

ZnO has been shown superior pseudocapacitive performance in different synthesis processes or electrolyte environments by varying its morphology as well as microstructure. Many research groups have been investigating the doping of cationic or anionic elements to find enhanced electrochemical performances of ZnO [20,21]. Recently, Fatih et al. [22] produced fluorine-doped ZnO nanoparticles and investigated their detailed electrochemical performance. The F-ZnO showed a high specific capacitance of 12.2 F g^{-1} besides a high energy density of 11.2 Wh kg^{-1} and a power density of 250 W kg^{-1}. The F-ZnO electrodes retained 91.5% of the performance for 4000

* Corresponding author.
E-mail address: swjoo@yu.ac.kr (S.W. Joo).
[1] Authors are equally contributed

https://doi.org/10.1016/j.jallcom.2021.161234
0925-8388/© 2021 Elsevier B.V. All rights reserved.

cycles. Bresser et al. [23] produced transition metal (Fe, Co)-doped ZnO nanoparticles for Li-ion batteries as an anode material. The cobalt-doped ZnO exhibited more effectiveness than iron-doped ZnO, but the Fe-doped ZnO nanoparticles show outstanding electrochemical performance regarding cycling stability, high rate performance, and capacity retention. In addition, the capacitance behavior of various doped ZnO nanomaterials was studied and recorded specific capacitance values of 95 F g^{-1} for Ni-doped ZnO [24], 230 F g^{-1} for B-doped ZnO [25], and 423.5 F g^{-1} for ZnO/MnO_2 [26]. More attention has been paid to the development of ZnO-based nanomaterials due to their high chemical and thermal stability, low cost, environmentally friendly, and easy doping.

Generally, the morphology of ZnO nanostructures strongly depends on the synthesis technique and the structure of directing agents/templates used during the synthesis. Different physical and chemical techniques have been reported for synthesis of doped and un-doped ZnO nanostructures with a wide variety of morphologies [27–30]. ZnO has been doped with a wide variety of elements based on the requirement of applications [31,32]. Doping with elements such as Mo and V can prompt significant changes in the physical properties of ZnO, and lead to the enhancement of specific capacitance, and long-term cycling performance due to the contribution of each transition metal with high oxidation states. The ionic radius of Zn^{2+} is 0.74 A°, whereas that of Mo^{6+} and V^{5+} are 0.59 A° and 0.54 A°, respectively [33]. Therefore, the substitution of Zn^{2+} with Mo^{6+} and V^{5+} is highly possible and expected to have a promising influence on the physical properties of ZnO. For example, a very small amount of Mo doping can provide adequate free carriers to the host lattice and reduce the ion scattering effect because of the high valence difference between Mo^{6+} ions and substituted Zn^{2+} ions [34,35]. Also, the multiple valence states (+6, 5, 4, 3, 2) of Mo and (+5, 4, 3, 2) of V contribute to the multiple carriers [36,37], which can enhance the electrical conductivity at lower resistance values, hence can be highly utilized for supercapacitors.

The main aim of this study is to enhance the electrochemical properties of ZnO by doping with molybdenum and vanadium using a simple, cost-effective, and efficient technique, such as a modified chemical co-precipitation method (M-CCP). Among the different wet chemical methods, the conventional chemical co-precipitation method is a relatively simple, fast, and low-cost technique for the growth of ZnO nanostructures. However, the control over the particle size, shape, and distribution is limited in the conventional chemical co-precipitation method (C-CCP) due to the non-uniform heating and low solubility of the source materials. To overcome these issues, a modified chemical co-precipitation method (M-CCP) is utilized for the synthesis of Mo and V doped and undoped ZnO Lotus-flowers. The adopted method is simple, relatively low cost, and highly repeatable. In M-CCP, all the required chemicals were added into a beaker, and the top was firmly fixed with aluminum foil to restrict the evaporation of solvents, before being kept in a furnace (box type) at 100 °C for 6 h to obtain the desired nanostructured product. Usually, in C-CCP heat is supplied from the bottom of the vessel by using a hot-plate magnetic stirrer, which led to non-uniform heating, but in the case of M-CCP, the use of a box-type furnace for heating led to uniform and prompt supply of heat. Here we also study the reliability of ZnO lotus-flower properties and structure for supercapacitor applications.

2. Experimental details

2.1. Materials and methods

Zinc nitrate hexahydrate ($Zn(NO_3)_2.6H_2O$), Ammonium metavanadate (NH_4VO_3), Sodium molybdate (Na_2MoO_4) were purchased from Sigma Aldrich Co., Ltd., South Korea. Sodium hydroxide (NaOH, > 98%) and methanol were obtained from Daejung Co., Ltd., Korea. Deionized (DI) water is used to prepare all the aqueous solutions. Carbon black, polyvinylidene di-fluoride (PVDF), and N-methyl-2 pyrrolidone (NMP) were brought from Sigma Aldrich. Commercial activated carbon (AC) brought from Sigma Aldrich (CAS:7440-44-0, specific surface area 900 m^2/g). The purchased chemicals and reagents are used without further purification because these are analytical grade. Nickel foam (1.6 mm thickness) was purchased from MTI Corporation (China). The Lotus-flower structures were produced by a low-cost modified co-precipitation method for undoped ZnO, Mo-ZnO, and V-ZnO samples.

2.2. Synthesis of pristine ZnO, Mo-ZnO, and V-ZnO Lotus-flower-like structures

In a typical procedure, the aqueous solution of zinc nitrate hexahydrate (0.1 M for undoped, 0.095 M for Mo (0.005 M), and 0.095 M for V (0.005 M)) was magnetically stirred for 10 min (each beaker containing 50 ml solution of zinc nitrate hexahydrate). 0.4 M NaOH was dissolved in 50 ml DI water then added to the Zn aqueous solution dropwise. After 10 min constant stirring, beakers have been tightly packed with the aluminum foil. The tightly packed beakers were placed in the oven at 100 °C for 6 h. After cooling to ambient temperature, white precipitation was obtained by centrifugation and washed with water and ethanol several times. The obtained white precipitation was dried at 80 °C for 5 h. The chemicals used in this synthesis process are inexpensive and abundant and it is believed that the modified co-precipitation method is a versatile and powerful technique for the synthesis of ZnO nanomaterials. The schematic synthesis process of this study is shown in Fig. 1.

2.3. Electrodes preparation

Electrodes preparation begins by immersing Ni foams (1.5 cm × 1 cm) in a concentrated Hydrochloric acid solution to remove the oxide layer from the surface. Ni foams were sonicated for 10 min and then removed from Hydrochloric acid. The Ni foams were washed with ethanol and deionized water using an ultra-sonicator. Then, the Ni foams were dried at 80 °C for 6 h. The preparation of the working electrode includes the mixing of active material, conductive carbon black, and PVDF in an 80:10:10. NMP was added to the mixture to form a homogenous slurry. 5 mg of this slurry was brush-coated onto the pre-weighed Ni substrate. The coated electrode was dried at 85 °C for 5 h using the box furnace to remove the NMP solution. The coated electrode is used as a current collector.

The electrochemical measurements are performed in an electrochemical workstation (Model: CHI 760E) having 3-electrode system containing working electrode, counter electrode (Pt), and reference electrode (Ag/AgCl), whereas the active electrolyte used in the system is 2 M KOH solution. Finally, electrochemical measurements such as Cyclic Voltammetry (CV), Galvanometric charge-discharge (GCD), and Electrochemical impedance spectroscopy (EIS) were performed.

2.4. Asymmetric supercapacitor device fabrication

The asymmetric supercapacitor device is made of VZO/Ni foam as positive, AC/Ni as the negative electrode, and sandwiched with the separator. Here, the cellulose filter paper is used as a separator. The viscous slurry was formed by grinding the AC:PVDF:carbon black at a mass ratio of 80:10:10 with adding an appropriate amount of NMP solvent in an agate mortar. The positive and the negative electrodes were prepared by coating the slurry on a clean Ni-substrate and dried at 160 °C for 4 h. Then the dry electrode was pressed to 10 MPa to firmly AC bond with the Ni-foam. The mass of AC coated on the nickel foam is valued to be 2.2 mg. Finally, electrochemical measurements were performed on the asymmetric supercapacitor device.

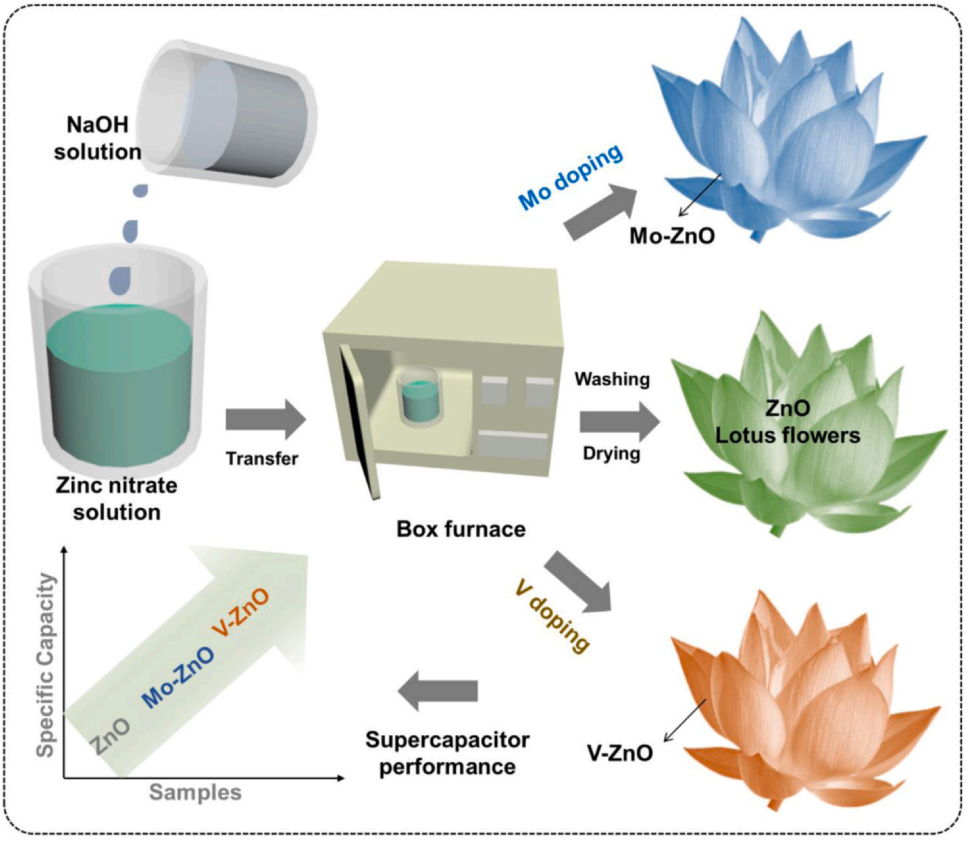

Fig. 1. Schematic representation of the synthesis process.

2.5. Characterization techniques

The detailed description of the characterization techniques is available in the supporting information (Supplementary file).

3. Results and discussion

3.1. Structural properties

The crystallographic properties of the undoped, Mo, and V doped ZnO samples are measured by XRD. Fig. 2(a) shows the XRD spectra of all the prepared samples. The XRD patterns of ZnO (Mo and V doped) samples exhibit the hexagonal phase. The ZnO (Mo and V doped) diffraction peaks are located at 31.77, 34.42, 36.25, 47.54, 56.60, 62.86, 66.38, 67.96, 69.10, 72.56, and 76.95°, which are indexed to (100), (002), (101), (102), (110), (103), (200), (112), (201), (004), and (202) facets of a single hexagonal phase of ZnO, respectively, (JCPDS #00-036-1451). The sharp and high intense peaks of undoped ZnO and doped ZnO indicate that the synthesized ZnO is well crystalline. Using Debye-Scherrer's formula, the crystallite size is calculated for all samples from XRD data.

$$D = \frac{k\lambda}{\beta Cos\theta} \quad (1)$$

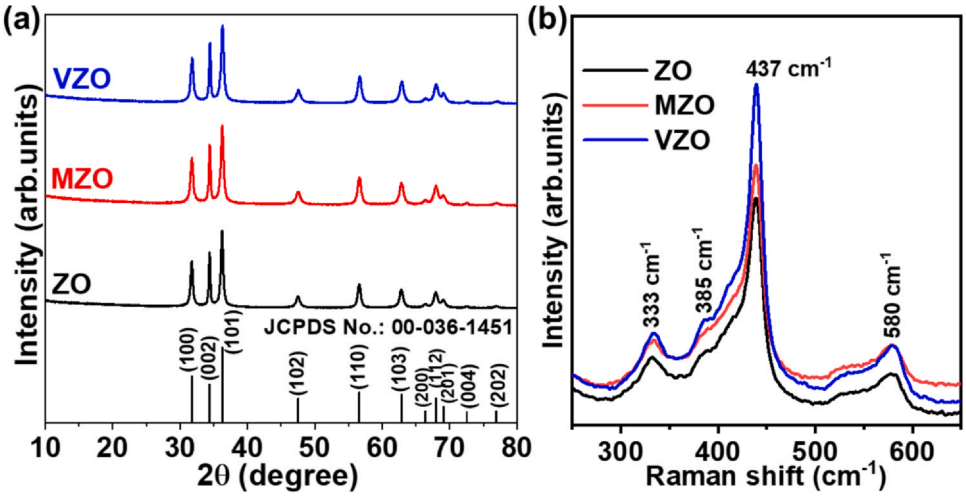

Fig. 2. (a) XRD and (b) Raman spectra of ZnO (ZO), Mo doped ZnO (MZO), and vanadium doped ZnO (VZO).

Where k = constant, λ = wavelength of the X-ray, β = full-width half maximum, and θ = diffraction angle. The XRD profile exhibits a major peak corresponding to the (101) plane. The calculated crystallite size of the ZnO, Mo, and V doped samples corresponding to the high-intensity peak is 18 nm, 16, and 16 nm, respectively.

In this instance, the Mo^{6+} has an ionic radius of 0.59 A° and Zn^{2+} has 0.74 A°. The ionic radius of Mo^{6+} is smaller than the ionic radius of Zn^{2+}, so Mo^{6+} ions can easily penetrate the ZnO lattice sites without affecting the ZnO crystal structure [38]. The Mo^{2+} (0.8 A°) ionic radius is larger than that of Zn^{2+} (0.74 A°). As a consequence, it is difficult to function as an interstitial impurity, but it may present on the ZnO surface [39]. Moreover, doping of V can decrease the ZnO crystal size and does not impose a significant change in crystallinity. A mixed state of crystalline nature of MZO Lotus-flowers has also exhibit typical crystalline size 16 nm for ZnO pristine. The lightening in crystallite sizes is owing to the resulting age of Mo-O-Zn groups on the surficial areas of the changed nanocomposites, prompting the hindrance of translucent enlargement and maturation. At room temperature, it is not necessarily expected to synthesize zinc oxide directly instead of more or less crystalline zinc hydroxide: the published thermodynamic data do not lead to any clear conclusions and do raise recurring problems [40]. Also, precipitation generally undergoes various transitions from amorphous hydroxide to crystalline hydroxide and then to oxide. In many metal ion systems, there is no doubt about the expected final product, whether it is crystalline hydroxide or oxide, but under the action of low-temperature zinc salts, we will face a critical situation. Usually, the precipitation process uses high temperature to force the hydrolysis to produce ZnO, but to better understand the formation of the oxide phase, it is found that choosing the easiest possible conditions to directly precipitate zinc oxide is more instructive. In the present modified co-precipitation process, zinc oxide flower-structured product was obtained at a low temperature of 100 °C by choosing the required possible conditions (uniform heating).

Raman analysis has been conducted for the analysis of crystal quality, structural defects, and disorder of synthesized samples. The ZO, MZO, and VZO samples expressed prominent Raman modes at 333, 385^{-1}, 437 cm^{-1}, and 580 cm^{-1} (Fig. 2(b)) [41,42]. ZnO has C46v symmetry with two formula units in the primitive cell. The optical phonons correspond to the irreducible representation at the Brillouin zone is Γ_{opt}=A1 +E1 + 2E2 + 2B1 [43]. Transverse (TO) and longitudinal optical (LO) phonons, both Raman and IR active, are divided into the polar modes A1 and E1. Mode E2 is non-polar and is Raman active only. Mode B1 is Raman and IR silent, as detailed in [44]. Raman spectra of the ZnO samples are shown in Fig. 2(b). The peaks at 333 cm^{-1} and 437 cm^{-1} are attributed to E(low)2(E2l), multiphonon, and E(high)2(E2h) modes, respectively [42]. The A1(TO) mode is attributed to the peak at 385 cm^{-1} [42]. Nevertheless, the peak near 580 cm^{-1} has been attributed to the E1(LO) mode of ZnO [42]. However, due to Zn–O bond breakage, some authors have found this peak in N-doped samples with forbidden scattering geometry associated with resonance-enhanced LO phonons [45]. The V doped ZnO sample shows peaks at 439 and 580 cm^{-1}. The peak at 439 cm^{-1} is attributed to the E2(high) phonon mode of ZnO and the peak at 580 cm^{-1} is assigned to E1(LO) and 2 E1(LO) modes, respectively. The observed deviation in peak positions compared to undoped ZnO has been explained by the difference in mass and the ionic radius of V and Zn ions in the lattice. The presence of strong E2 mode and weak E1(LO) mode confirms the good quality of the crystal with fewer structural defects and impurities. The vibrational atoms of oxygen in ZnO are correlated with the presence of strong E2 (high) mode at 439 cm^{-1}, indicating the wurtzite nature of ZnO [46]. Moreover, the peak at 580 cm^{-1} that corresponds to the A1(LO) mode is originated by oxygen vacancies in ZnO, suggesting that Mo can induce oxygen vacancies in ZnO [46]. The E2(low) and E2(high) modes are attributed to the oxygen and zinc sublattices in ZnO, respectively, [47].

3.2. Morphological (FE-SEM and HR-TEM) Analysis

The ZnO nanocrystal growth is understood by determining the Na^+ counterions around the nanocrystals, which form a virtual coating that lead to a significant slowdown in growth rate and nonmonotonic dependence on NaOH concentration. This is different from the qualitative nature of NaOH and is anticipated diffusion-limited Ostwald ripening mechanism. In the present study, we recommend a new solid-solid transition mechanism to form ZnO Lotus-flowers from ε-$Zn(OH)_2$ intermediate, which contrasts with the expected dissolution-reprecipitation process. The temperature and base concentration of the reaction solution plays a major role in the early formation of flower-shaped ZnO. Four possible dynamic equilibria involving the conversion between $Zn(OH)_4^{2-}$, $Zn(OH)_2$, and ZnO are defined in the following scheme:.

The FE-SEM images of undoped and doped ZnO Lotus-flowers are shown in Fig. 3(a-c). From Fig. 3 inset figures, the high magnification

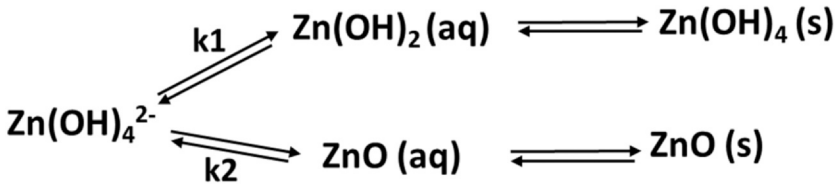

FE-SEM images indicate the self-assembly of numerous irregular nanoparticles interwoven to form a Lotus-flower appearance. Fig. S1(a-c) shows the uniform growth of ZO, MZO, and VZO Lotus-flowers over a large area, respectively. The orientation of nanoparticles within flower-shaped particles was observed in the kinetic study of the reaction of zinc nitrate and sodium hydroxide by Oliveira et al. [48]. The FE-SEM image of undoped and doped ZO Lotus-flowers showed 3D flower-like structure with a size of ~2 μm. The Zn $(NO_3)_2$ precursor yielded submicron flower-type and randomly oriented nanoparticles. Li and Haneda et al., also grown this type of flower-like morphology [49]. Komarneni et al., produced the star-like particles for $Zn(NO_3)_2$ and NaOH combination by microwave synthesis [50]. Instead, by doping with Mo and V, the process produced branching for ZnO Lotus-flowers structures. In this case, the reaction is less regulated by the precipitation rate and the thermodynamic stability (equilibrium constants k2 > k1) becomes the key factor deciding the presence of phase, so that in the initial stage no branched structure of ε-$Zn(OH)_2$ will be formed directly the ZnO Lotus-flower shape structure. The final particles are, therefore, the product of the continuous growth of these materials which were initially created. The branching structure of ZnO is formed directly from the solution. In addition, the self-assembly growth and controlled synthesis mechanism can be found in Yu Chang et al.'s and Oliveira et al.'s study [48,51]. Shi's studies on nanocrystals formation under hydrothermal conditions have shown that when insoluble

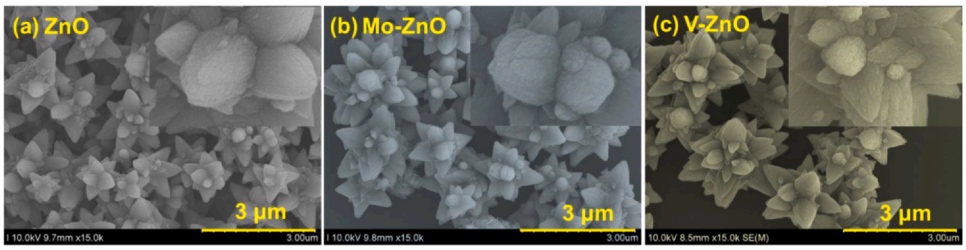

Fig. 3. Low- and high-magnification FE-SEM images of undoped ZnO (a), Mo doped ZnO (b), and V doped ZnO (c) lotus-flower- like nanostructures obtained by the simple co-precipitation method.

solid powders (at atmospheric pressure and temperature), gel, or precipitate (its solubility and stability are the same as final crystalline phase) are used as precursors for the reaction, the dissolution-reprecipitation kinetics from the precursor to final crystal is very difficult [52]. Precursors can be converted directly to the crystalline phase by the dehydroxylation process and then rearrange the internal ions in situ. Therefore, we explain this mechanism of in situ crystallization. A related process that occurs in the growth of other oxide nanostructures in the literature has been referred to as the mechanism of solid-state transformation [53,54]. It's worth noting, however, that solid to solid decomposition (which can only happen in a liquid environment) is not the same as thermal decomposition that does not require water. In the present case, the solubility of ε-Zn $(OH)_2$ is better than the ZnO, resulting in flower-like ZnO branching structures (chain reaction from (1) to (2) in the scheme).

The doping of Mo and V elements in the host lattice of ZnO has been further confirmed using EDS analysis, as presented in Fig. 4(a) and (b). For the undoped ZnO sample, the elemental mapping depicts the existence of Zn and O elements only (Fig. S2). For Mo doped ZnO sample (Fig. 4(a)), the EDS mapping displays the existence of Mo, Zn, and O elements within the field of view. For V doped ZnO sample (Fig. 4(b)), the EDS mapping shows the existence of Zn, O, and V. From this study, it is observed that all the synthesized samples are corroborated with XRD and SEM measurements.

TEM observation of the microstructure of ZnO Lotus-flowers was examined for further investigation. The HR-TEM images of undoped and doped ZnO Lotus-flowers are presented in Fig. 5(a-c). HRTEM images further confirmed the formation of the Lotus-flower-like structure by assembling nanoparticles on one other such that it gives rise to ZnO Lotus-flowers. Moreover, the schematic of nucleation of ZnO nanoparticles and its self-assembly/Ostwald growth mechanism towards the Lotus-flower formation is presented in Fig. 5(d).

3.3. Plausible formation mechanism

Based on our resultant experimental data as well recent literature survey on the ZnO nanostructures, the underlying reaction mechanism to the formation of the ZnO Lotus flower has been described [55]. Initially, the aqueous NaOH solution is produced the hydroxyl ions (OH^-), which easily react with Zinc metal (Zn^{2+}) and then formed as the $Zn(OH)_4^{2-}$ species (Eqs. 3 & 4) [56]. Afterward, the ZnO nuclei are produced from the dehydration of $[Zn(OH)_4]^{2-}$ ions (Eqs. 4 & 5) [57]. The reaction solution containing 0.01 M of $Zn(NO_3)_2$ and 0.4 M of NaOH leads to an initial burst of uniform nucleation. To get the crystalline ZnO nanostructures after ZnO nuclei formation, there will be three steps undergo in the reaction medium as follows: (i) Initially, the resultant ZnO nuclei undergo the aggregation based on their electrostatic force, (ii) Later, based on the limited surface energy in aqueous solution at heating conditions, the molecules and ions of ZnO originated uniform pattern, its mean crystallization, and (iii) Finally, the resultant crystalline nature of ZnO has shown the enhanced surface active sites thereby improve the abilities to grow in the required orientation, which leads to the formation of various ZnO nanostructures (Ex. ZnO Lotus flower). The schematic representation of the ZnO Lotus flower formation mechanism is shown in Fig. 5(d). Therefore, the process is related to the inclusion of growth units on different faces, the nature of the crystal growth interfaces, and the structural mechanism under the influence of OH ions. The ZnO Lotus-flowers were created when the $Zn(OH)_4^{2-}$ ions concentration exceeded the critical value, and the chemical

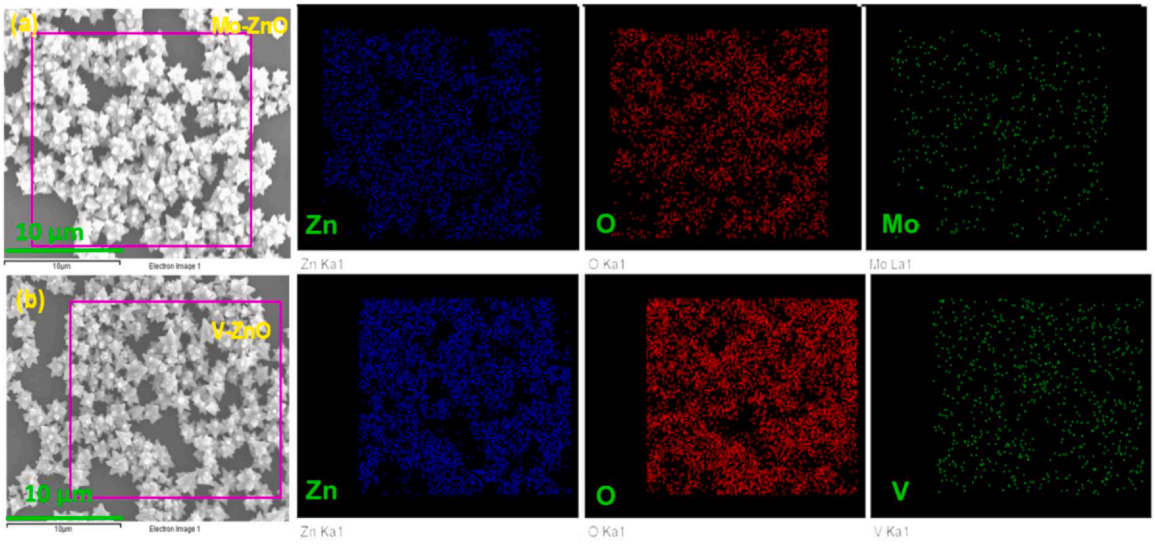

Fig. 4. FE-SEM elemental mapping images of Mo doped ZnO (a), and V doped ZnO (b).

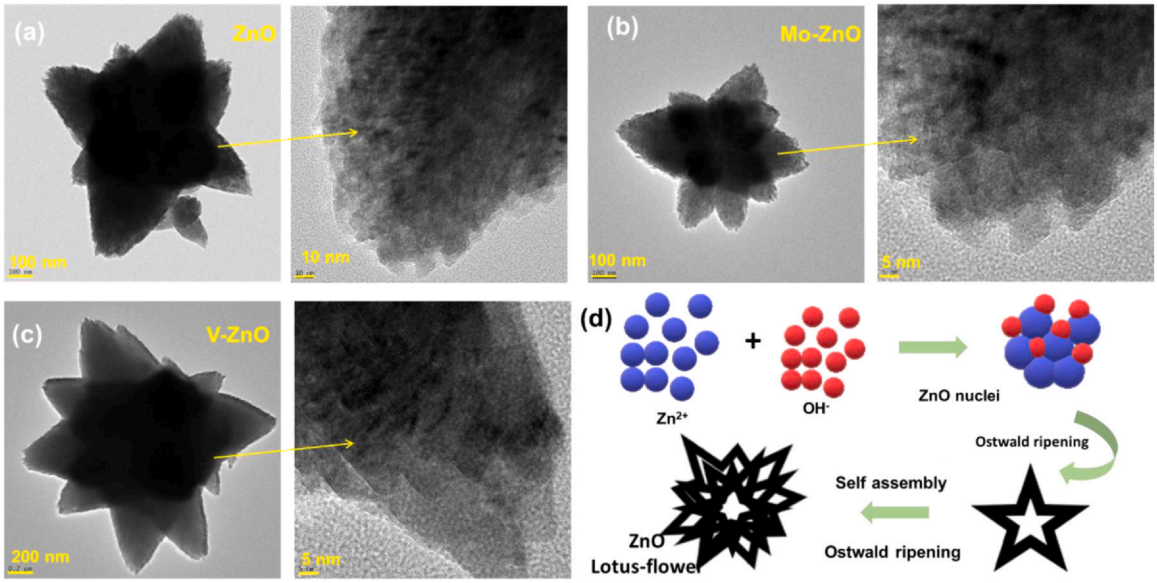

Fig. 5. Low- and high-magnification TEM images of undoped ZnO (a), Mo doped ZnO (b), and V doped ZnO (c) and formation mechanism of ZnO lotus-flower- like nanostructures (d).

processes can be stated as follows [58].

$$NaOH \rightarrow OH^{-} + Na^{+} \quad (2)$$

$$Zn^{2+} + 2OH^{-} \rightarrow Zn(OH)_2 \quad (3)$$

$$Zn(OH)_2 + 2OH^{-} \rightarrow Zn(OH)_4^{2-} \quad (4)$$

$$Zn(OH)_4^{2-} \rightarrow ZnO + H_2O + 2OH^{-} \quad (5)$$

3.4. XPS analysis

The chemical valance of various elements and the surface composition on ZnO, Mo doped, and V doped ZnO were studied by XPS. The XPS survey spectra show the existence of Mo, V, Zn, O, and C in the ZnO Lotus-flowers (Fig. 6(a)). The presence of episodic hydrocarbons in the XPS instrument and CO_2 adsorbed on the sample surface could explain the C peak in the spectrum. Fig. 6(b) shows the Zn2p spectra of all the samples. The binding energy peak at 1021.05 eV is assigned to the $Zn2p_{3/2}$ peak for Zn^{2+} and the peak at 1044.12 eV is assigned to the $Zn2P_{1/2}$ for Zn^{2+}. No metallic Zn was observed at the binding energy of 1021.50 eV, confirming the presence of Zn only in the oxidization state [59]. Fig. 6(c) presents the O1s spectrum of all the samples. The major peak at 531.2 eV in the O1s core-level spectra of MZO Lotus-flowers is deconvoluted into two peaks. The low binding energy peak denoted by O1 at 529.85 eV corresponds to the Zn-O bond, while the higher one at 530.90 eV (O2) is usually attributed to oxygen vacancies in ZnO [60]. To determine the oxidation state of V in the as-grown VZO Lotus-flowers, XPS spectra of the $V2p_{3/2}$ signal were obtained, as shown in Fig. 6(d). In the XPS spectra found on the V-doped samples, the typical V2p duplet peak centered at $2p_{3/2}$ can be deconvoluted into two peaks belonging to V^{5+} and V^{4+} at 517.1 eV. V^{5+} was originally existent in the precursor deposited on the surface of ZnO, while V^{4+} was formed during the synthesis of the Zn-O group formed during the surface reaction. In addition, V doped ZnO Lotus-flower in the reducing atmosphere of ZnO with a substantial reduction of V^{5+} to V^{4+} [45]. In this case, the asymmetric $V2p_{3/2}$ line contains 2 peaks centered at 514.1 eV and 516 eV (Fig. 6(d)) confirming the presence of V^{4+} and V^{3+}, respectively [46]. No additional contributions from V^{2+} and V^{4+} valence states were noticed in any of the examined samples. Therefore, their existence can be excluded within the detection limit of XPS. Individually, the V dopant is mostly present in the V^{3+} valence state. The XPS spectrum of Mo3d is deconvoluted into two separate peaks located at the binding energy of 232.44 and 235.46 eV corresponding to the $Mo3d_{5/2}$ and $Mo3d_{3/2}$, respectively, as displayed in Fig. 6(e) [39,40]. The peak separation of 3 eV indicates that the elemental Mo^{4+} exists as Mo^{6+} in molybdates. The Mo3d XPS spectrum (Fig. 6(e)) shows a peak at approximately 235.25 eV corresponding to $Mo3d_{3/2}$ [61]. The Mo^{6+} observed on the doped surface at.1.5% is the outcome of surface oxidation, which can be found in previous reports on Mo-doped metal oxides [62,63]. Although difficulty in Mo oxidation state confirmation, the presence of Mo^{4+} on the surface despite surface oxidation and the fact that Zn^{2+} (0.6 Å) ionic radius is more consistent with Mo^{4+} (0.65 Å) than with Mo^{6+} (0.41 Å) suggest that Mo is in the +4 oxidation state.

4. Electrochemical properties

The electrochemical performance of VZO, MZO and ZO electrodes was studied in a 3-electrode configuration. The results of CV curves confirm faradaic redox reaction and show the battery type behavior of the electrode materials. Fig. 7(a) presents a typical CV of the ZO, MZO, and VZO electrodes at a scan rate of 100 mV s^{-1}. The VZO exhibits a larger area under the curve than ZO and MZO, which indicates that more energy is stored in the electroactive sites of the VZO electrode compared to ZO and MZO [64]. Fig. S2 (a1, a2, a3) (supporting information) shows the CV curves for all electrodes at different scan rates of 10, 25, 50, 75, 100, 125, 150, 175, and 200 mV s^{-1} with a potential window of −0.4–0.9 V. At higher scan rates, a smaller surface response was detected due to the limited time. Nevertheless, the ions have enough time to react, resulting in enhanced charge storage at low scan rates. These findings indicate that the specific capacity is higher at low scan rates [65]. The fast ions/electrons kinetic and rapid redox reactions at the electrode/electrolyte interface can facilitate shifts in the oxidation peak along with the higher potential due to enough time to interact with each other and reduction peaks in the lower potential for higher scan rates can restrict different reactions due to the less residence time [66]. It is also interesting to note that at high scan rates, the shape profile of the CV curves does not change, indicating superior capacitive behavior. Moreover, it can also be seen that the current of each CV curve is increased with an increasing scan rate. This aspect may

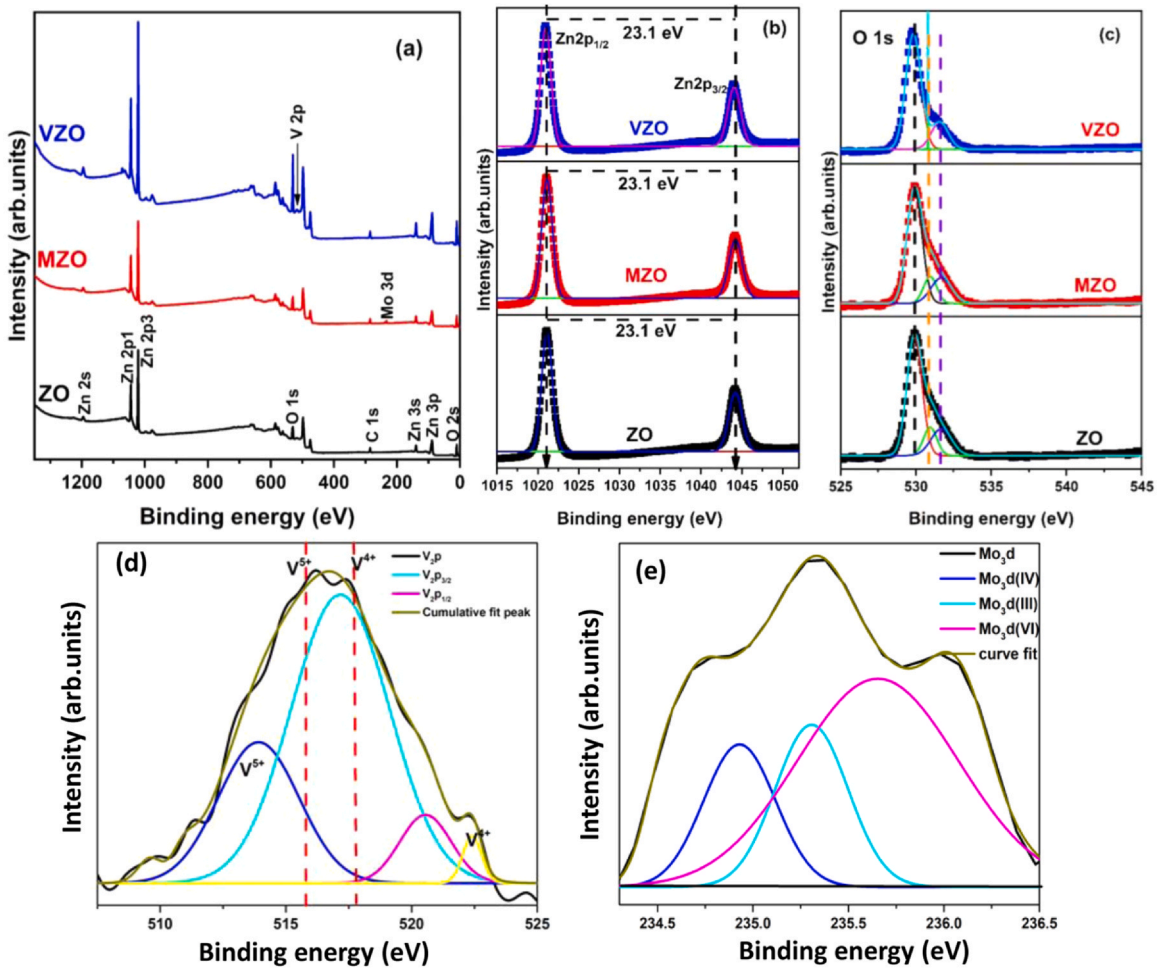

Fig. 6. (a) XPS survey analysis of ZO, MZO, and VZO binding energies and their structural phases (b) the deconvoluted Zn2p spectra (b) the deconvoluted O1s spectra of ZO, MZO, and VZO (d) the deconvoluted V2p spectra, and (e) the deconvoluted Mo3d spectra of ZnO Lotus-flowers and their energy level analysis.

be ascribed to the occurrence of a substantial polarization with an increasing scan rate resulting from the diffusion-controlled process. Also, the peak current increases linearly with the scan rate suggesting high rate capability and good reversibility of the electrodes. Additionally, the reduction peak is observed to be more prominent than the oxidation peak demonstrating a quasi-reversible redox process.

The GCD profiles of ZO, MZO, and VZO electrodes were detected at 1 A g^{-1} current density, as shown in Fig. 7(b). The GCD profiles of all the samples at different current densities of 0.5, 1, 2, 3, 4, 5, 6, 7, 8, 9, and 10 A g^{-1} are shown in Fig. S2 (b1, b2, b3) in the active potential window of 0–0.45 V. The charge-discharge performance of VZO was found to be higher than ZO and MZO. The VZO electrode showed a longer charge-discharge time than the ZnO electrode with a high specific capacity. The resulted in excellent specific capacity performance is due to easy electron mobility and high electrical conductivity in the VZO electrode [37]. The GCD curves reveal a non-linear shape attributed to the faradaic redox reaction characteristics of the battery type behavior of the VZO electrode and inconsistent with the redox peaks of CV curves [67]. In addition, it was observed that the GCD curves were the same, indicating that the redox reaction has reversible nature and better capacitive performance [65]. The discharge curves showed non-linear behavior. As a result, the following equations were used to measure specific capacity (C_s)/ specific capacitance (C_{sc}) from GCD curves: [68,69].

$$C_s = \frac{I\int_0^{\Delta t} Vdt}{m.\Delta V_{mean}} = \frac{I\int_0^{\Delta t} Vdt}{m.\frac{\Delta V}{2}} = 2\frac{I\int_0^{\Delta t} Vdt}{m\ \ \Delta V} \quad (C\quad g^{-1}) \tag{6}$$

$$C_{sc} = \frac{I.\ \Delta t}{m.\ \Delta V} \tag{7}$$

where I = discharge current (A), Δt = discharge time (s), $\int_0^{\Delta t} Vdt$ = area under the discharge curve, ΔV_{mean} = mean value of operating potential (V), m = total mass of the active material (g), and ΔV = potential difference (V) within the discharge time.

Corroborating the GCD curves, the VZO electrode displays the best specific capacity with the highest value ~362 C g^{-1} (585 F g^{-1}) at 0.5 A g^{-1} current density. This value is noticeably greater than the reported values for similar materials at the comparable current densities, as shown in Table 1, indicating excellent capacity values of our VZO samples. The calculated specific capacities for VZO electrode at different current densities of 1, 2, 3, 4, 5, 6, 7, 8, 9, and 10 A g^{-1} are 294, 212, 173, 147, 128, 118, 105, 94, 83, and 74 C g^{-1} (491, 364, 327, 196, 189, 160, 156, 142, and 133 F g^{-1}), respectively (Fig. 7(c)). The specific capacity values of MZO are 336, 247, 153, 109, 84, 68, 57, 46, 34, 22, and 14 C g^{-1}, and ZO are 268, 176, 115, 87, 70, 57, 50, 42, 32, 19, and 11 C g^{-1} at different current densities of 0.5, 1, 2, 3, 4, 5, 6, 7, 8, 9, and 10 A g^{-1}, respectively. The C_s performance is related to faster ion transport at the electrode/electrolyte interface. This is mainly due to the high surface area leading to the fast

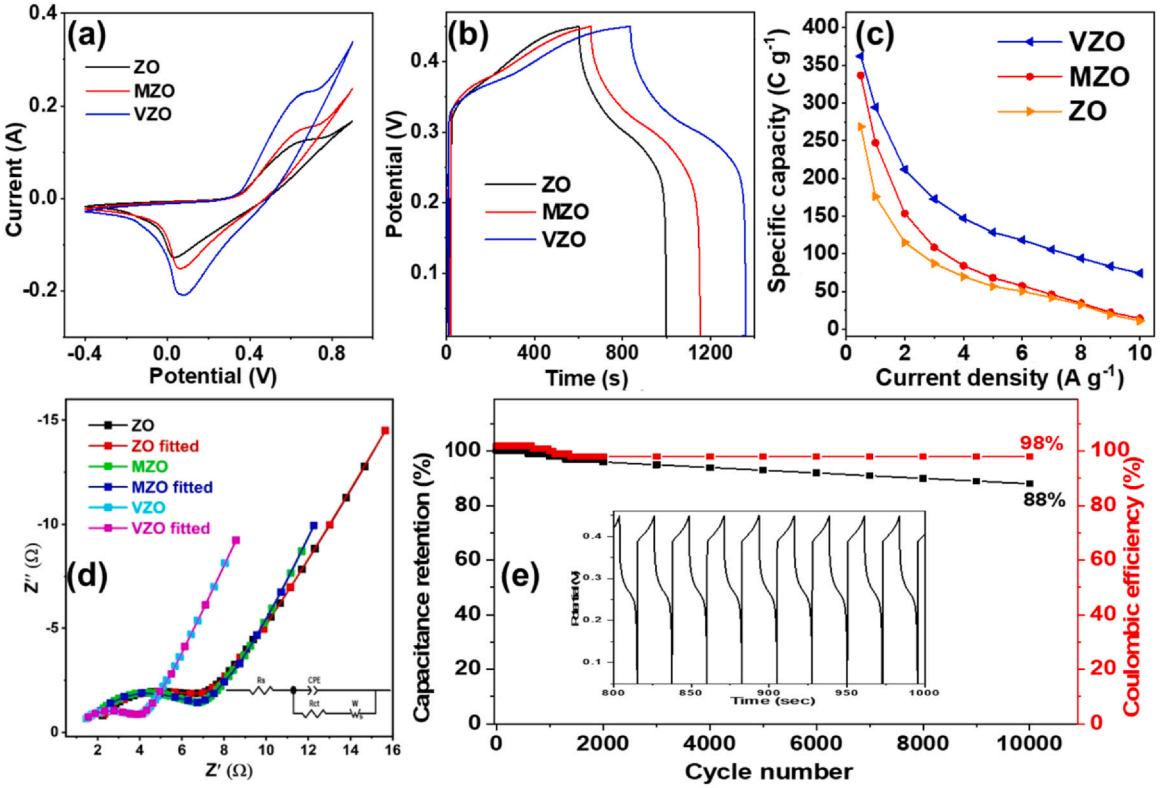

Fig. 7. (a) CV curves at 100 mV s^{-1} scan rate (b) GCD curves at 1 A g^{-1} current density (c) Nyquist plots (d) C_s values calculated from GCD profiles at different current densities and (e) Capacitance retention & Coulombic efficiency of ZO, MZO, and VZO.

migration of ions from the interface. When the current density is changed from 0.5 to 10 A g^{-1}, the C_s suddenly drops due to the limited time of full contact, so the accessibility of ions is lower at higher current densities.

The kinetic properties of the electrodes were analyzed by EIS measurements. Fig. 7(d) displays the Nyquist plots of all the samples from low-to-high frequency regions. According to the Nyquist plot, the curve can be divided into three segments. The electrolyte resistance (Rs) (ionic resistance of the electrolyte + intrinsic resistance of the electrode + interface resistance) is represented by the intersection with the x-axis in the high-frequency region [70]. The charge transfer resistance (R_{ct}) is proportional to the diameter of the semicircle [71]. The slope of the straight line in the low-frequency zone displays the diffusion resistance, which is connected to the diffusion of OH- in alkaline electrodes [72]. From Fig. 7(d), the semicircular part is decreased from ZO to VZO, which indicates that the R_{ct} value of the electrode is low. And in line with the CV and GCD results, in this case, compared with other samples, VZO also showed the best supercapacitive performance on the smallest semicircular part. The small (or almost negligible) semicircular part of VZO indicates that the charge transfer resistance is negligible. This is due to the low Faradaic resistance of the electrodes [73], so it can reiterate its excellent pseudocapacitance characteristics. In addition, the lower inset of Fig. 7(d) displays the magnified version of the high-frequency intercepts of the curves at the real axis, which represents a very small value, indicating the equivalent series resistance R_s of the electrode.

The inset of Fig. 7(d) shows EIS data with standard equivalent circuit $\{R_s + CPE||(R_{ct} + W)\}$. The real part ($Z_r$) in the high-frequency region is attributed to the equivalent series resistance (ESR). The ESR of VZO, MZO, and ZnO electrode materials are 0.86, 1.54, and 1.77 Ω, respectively, indicating that the ohmic loss is very small during discharge. The Warburg impedance (W) of VZO, MZO, and ZO electrodes are 6.42, 17.45, and 39.63 Ω, respectively. W is related to the diffusion of OH- ions generated by the reaction in the electrolyte [74]. The VZO electrode exhibits the largest slope than other electrodes, indicating the faster ion diffusion rate. The R_{ct} and R_s of the VZO electrode are shown to be lower than those of other electrodes, which indicates that the VZO electrode has high conductivity and superior supercapacitive performance compared with other electrodes, thus corroborating the CV and GCD data.

Long-term cyclic stability is very important for functional practical applications. As observed from the above analysis, the VZO electrode represents the best capacitive values. The electrochemical stability of the VZO electrode was executed for 10,000 GCD cycles at a constant current density of 10 A g^{-1} (Fig. 7(e)). First, the C_s value is increased from 0 to 500 GCD cycles owing to the activation process [75]. The capacitance retention of 88% was observed upto 10,000 GCD cycles to the initial value, confirming VZO's strong cycling stability. In addition, the Coulombic efficiency, which defines the

Table 1
Comparison of several metal-oxide reported as supercapacitor electrode materials in the literature and this study.

Electrode	Electrolyte	Current density/ Scan rate	Specific capacitance/ Capacity	Ref.
G-ZnO	1 M KCl	2 mV s^{-1}	146 F g^{-1}	[77]
MRGO/ZnO	1 M Na_2SO4	1 A g^{-1}	201 F g^{-1}	[78]
G-ZnO@GC	6 M KOH	5 mV s^{-1}	122.4 F g^{-1}	[79]
ZnO/CNF	6 M KOH	5 mV s^{-1}	288.4 F g^{-1}	[80]
ZnO@GF	2 M KOH	1 A g^{-1}	400 F g^{-1}	[81]
ZnO/rGO	1 M Na_2SO4	10 mV s^{-1}	95 F g^{-1}	[82]
RGO/ZnO: B	6 M KOH	5 mV s^{-1}	230.5 F g^{-1}	[25]
Mo: ZnO	3 M KOH	1 A g^{-1}	123 F g^{-1}	[64]
ZnO-Au	2 M KOH	10 mV s^{-1}	205 F g^{-1}	[83]
Ni-ZnO	0.5 M Na_2SO4	10 mV s^{-1}	95.32 F g^{-1}	[24]
Mo-ZnO	**2 M KOH**	**0.5 A g^{-1}**	**336 C g^{-1}(555 F g^{-1})**	**This work**
V-ZnO	**2 M KOH**	**0.5 A g^{-1}**	**362 C g^{-1}(585 F g^{-1})**	

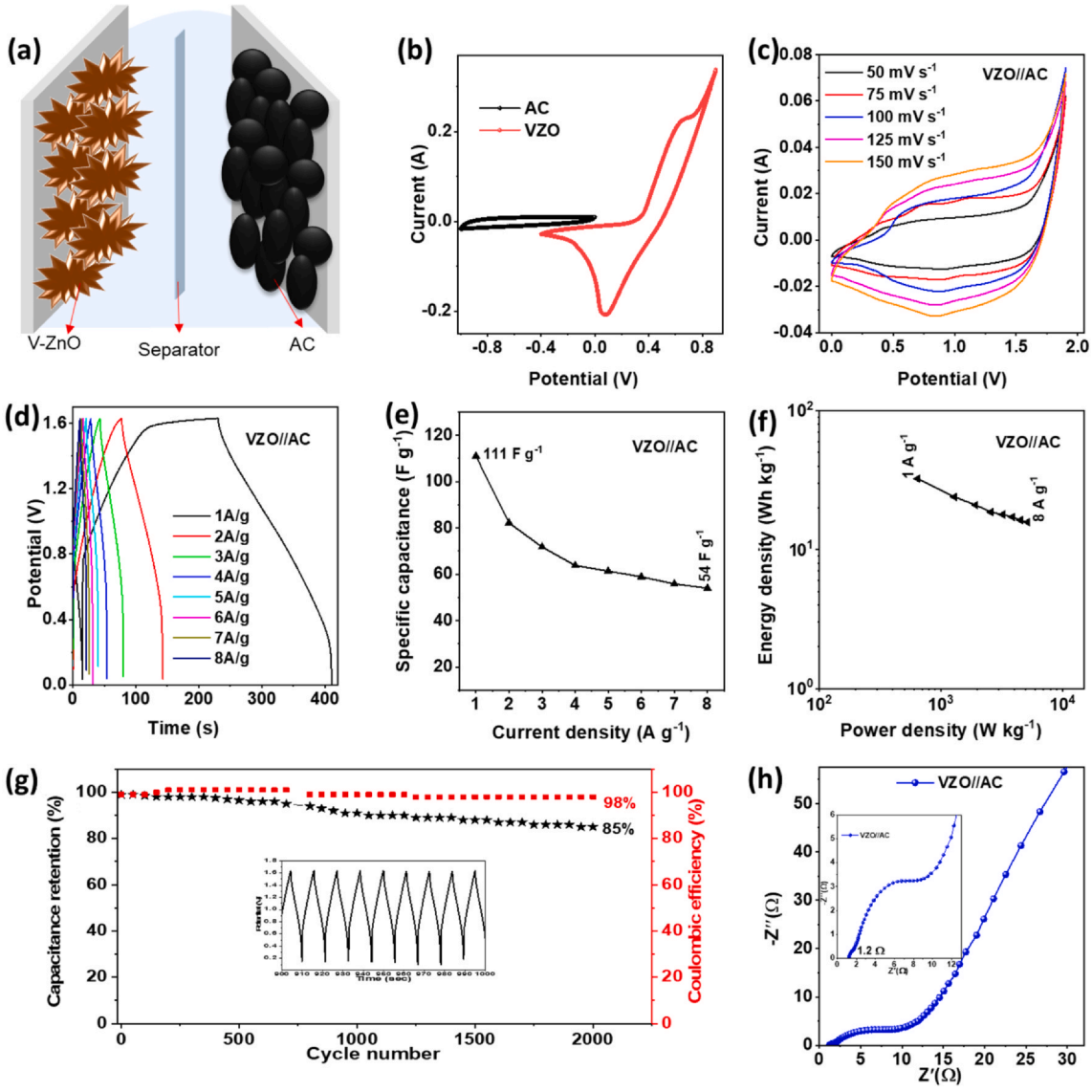

Fig. 8. (a). Schematic of VZO//AC device, (b) Combined CV curves of VZO//AC ASC device at a scan rate of 100 mV s^{-1}, (c) CV curves at various scan rates, (d) GCD curves at various current densities, (e) variation of specific capacitance with different current densities, (f) Ragone plot of VZO//AC device at different current densities, (g) capacitive retention and Coulombic efficiency of VZO//AC ASC device, and (h) Nyquist plot of VZO//AC ASC device. Inset: Equivalent circuit and magnified version of Nyquist plot.

effective transport of electrons on the electrode/electrolyte surface to promote the faradaic redox reaction, and the efficiency reaches 98% in 10,000 cycles. The improved supercapacitive performance of the electrode material is ascribed to the excellent crystallinity and structural stability of the sample coupled with the excellent conductivity of VZO.

Table 1 shows the supercapacitor performance of VZO and electrode materials of ZnO-based SCs. The specific capacitance of the VZO electrode is superior to that of recent reports on other ZnO-based materials as shown in Table 1. The higher specific capacitance of the VZO electrode is mainly due to the faster ion and electron transfer during the charge-discharge process, good crystalline structure, and high conductivity [76]. Further, the hierarchical Lotus-flowers provide a large number of active sites for an effective pathway to the transport of ions and electrons, thereby improving the overall redox reactions as well as the electrochemical performance of the electrode.

4.1. Electrochemical performance of the VZO//AC asymmetric supercapacitor (ASC) device

The VZO Lotus-flowers electrode is considered for functional applications due to its excellent energy storage performance in a three-electrode system. The ASC devices consist of two electrodes (VZO as the positive electrode and AC as the negative electrode) sandwiched with a separator (Fig. 8(a)). The electrochemical performance of the VZO//AC ASC device is measured by Cyclic Voltammetry, chronopotentiometry, and AC impedance in the 2 M KOH electrolyte with the potential window of 0–1.9 V. To obtain the charge balance of both electrodes, the AC mass of the negative electrode is determined using the following equation [84].

$$\frac{m_+}{m_-} = \frac{C_- \Delta V}{C_+ \ \Delta V} \tag{8}$$

where m_+ is the positive (VZO) electrode loading mass, C_+ is the positive (VZO) electrode C_{sc} and ΔV is the positive (VZO) electrode potential window. Likewise, m_- is the negative (AC) electrode mass loading, C_- is the negative (AC) electrode C_{sc} and ΔV is the negative

(AC) electrode potential window. The mass ratio of VZO//AC (ASC) was approximately 0.28. It can be calculated by comparing the positive and negative electrodes at 100 mV s^{-1} and the VZO/NF electrode material can act on the electrochemical reaction at positive potentials. On the contrary, the CV curve of AC/NF is observed to be approximately rectangular at the potential window of 0 to − 1 V, as shown in Fig. 8(b). This is due to the charge storage that happens when electrolyte ions are electrolyzed and deposited on the electrode surface. The electrochemical properties of activated carbon can be found in Fig. S3 (supplementary information). Fig. S3(a), (b), and (c) shows the CV profiles (10–100 mV s^{-1} scan rates), GCD profiles (potential window of 0 to −1 V), and the calculated specific capacitance values of AC material, respectively. The calculated specific capacitance values of the AC material at different current densities of 1, 2, 3, 4, and 5 A g^{-1} are 187, 146, 117,100, and 80 F g^{-1}, respectively. Fig. 8(c) shows CV profiles of VZO//AC (50–150 mV s^{-1} scan rates). The broad area of the CV profiles without any obvious redox peaks indicates very good reversibility and capacitive behavior of the device. The GCD profiles of VZO//AC at different current densities from 1 to 8 A g^{-1} are shown in Fig. 8(d). Considering the operating potentials of VZO/NF (−0.4 to 0.9 V) and AC/NF (0 to −1 V), the cell with a voltage of 1.9 V was used to examine the ASC. Fig. 8(c) shows that the CV profiles increase with increasing potential window. The GCD profiles recommend the optimal working potential window of 1.6 V. The high capacitive behavior of the ASC is demonstrated by the symmetry of charge-discharge curves. The capacitance of ASC is calculated by Eq. (7), where m denotes the total mass of two electrodes. The specific capacitance of the ASC device (VZO//AC) is one of the best capacitance of similar devices as shown in Table S1 (Supplementary data). From Fig. 8(e), the C_{sc} of ASC reaches a maximum value of 111 F g^{-1} at a current density of 1 A g^{-1} and decreases to 53 F g^{-1} at a current density of 8 A g^{-1}. The reduction in C_{sc} is the inefficiency of the electrode's electroactive sites in maintaining the redox reactions at high current densities.

One of the most important needs is to increase energy density in energy storage applications. Increasing the potential or capacitance leads to a higher energy density. The following equations are used to determine the power density (P_d, W kg^{-1}) and energy density (E_d, Wh kg^{-1}): [85].

$$E_d = 1/2CV^2 \tag{9}$$

$$P_d = E/t \tag{10}$$

where C=specific capacitance (F g^{-1}), V = potential, and, t = discharge time. Fig. 8(f) depicts the Ragone plots for different specific capacitances of VZO. The maximum power density of VZO//AC ASC is 5.16 kW kg^{-1} (at 15.8 Wh kg^{-1}) and the maximum energy density is 32.4 Wh kg^{-1} (at 645 W kg^{-1}). The obtained results are greater than other reported ZnO-based SCs. We observed a good increase in power density and a slight decrease in energy density at the current densities of 1–8 A g^{-1}, indicating a good power gain under the condition of small energy loss. This is due to the good energy storage capability of the ASC for superior device performance. Even though more reports were on ZnO-based electrodes but limited reports were published on ZnO-based asymmetric supercapacitor devices. The results presented in this study are comparable and one of the better results as compared to the previously reported ZnO-based supercapacitor devices, as shown in Table S1.

The VZO//AC ASC showed 98% Coulombic efficiency and 85% excellent capacitance retention after 2000 GCD cycles at a current density of 8 A g^{-1} (From Fig. 8(g)). The data reveal that the capacity retention and Coulombic efficiencies are 95% and 100% for the first 500 cycles, 90% and 99% for 1000 cycles, 85% and 98% for over 2000 cycles, respectively, which indicates that the supercapacitor has excellent rate capability, reversibility, and stability for superior device performance. The small discrepancy in the Coulombic efficiency is due to the heat dissipation during the charge-discharge cycling process [86,87]. Furthermore, some literature is reported [88,89] lower Coulombic efficiency due to the internal resistance of electrode/electrolyte interface, the conductivity of the electrode, and contact resistances that may also contribute to reduced Coulombic efficiency.

Finally, the kinetic properties of the asymmetric supercapacitor are studied by EIS measurement. Fig. 8(h) shows the Nyquist plot of the device in the mid-to-high frequency region as well as the enlarged version of the high-frequency region. The R_s at high-frequency intercept shows a very small value, indicating low resistances of the electrolytes, electrode materials, and electrode-electrolyte interfaces for superior device performance. The Warburg curve is represented by the distorted semi-circle at the high-frequency region (inset of Fig. 8(h)) represents the pseudocapacitive behavior of the asymmetric supercapacitor device. The near-vertical linear part of the curve at the mid-to-low frequency region represents the ideal supercapacitor behavior of the device. The inset Fig. 8(h) shows fitted EIS with the same equivalent circuit, and the values of R_s, R_{ct}, and *CPE* are 1.21 Ω, 7.61 Ω, and 0.79 mF, respectively, which shows that the low internal resistance and charge transfer resistance of the asymmetric supercapacitor device has excellent device performance.

5. Conclusions

In summary, metal ions, including Mo and V doped ZnO Lotus-flowers were synthesized by a facile chemical co-precipitation method for the fabrication of high-performance supercapacitors. Among the materials synthesized, the VZO electrode with a Lotus-flower-like morphology showed good battery type behavior with high specific capacities. The electrochemical performance of the best performing VZO electrode showed a maximum specific capacity of 362 C g^{-1} with an excellent capacity retention of 88% after 10,000 charge/discharge cycles. The best-performing electrode was used to fabricated an ASC device that showed the highest specific capacitance of 111 F g^{-1} with an energy density of 32.4 Wh kg^{-1} and power density of 5.16 kW kg^{-1} at a current density of 1 A g^{-1}. Also, the device exhibited capacity retention of 85% and Coulombic efficiency of 98% over 2000 cycles at a current density of 8 A g^{-1}, indicating superior reversibility and device stability. These results indicate that high-efficiency supercapacitor electrode VZO is a promising material, and the application of V-ZnO-based electrodes can be greatly extended to other high-efficiency energy storage systems.

CRediT authorship contribution statement

Mohan Reddy Pallavolu: Conceptualization, Methodology, Formal analysis, Investigation, Data curation, Software, Writing – original draft. **Jyothi Nallapureddy:** Formal analysis, Software, Writing – original draft. **Ramesh Reddy Nallapureddy:** Writing – review & editing. **Gaddam Neelima:** Writing – review & editing. **Yedluri Anil Kumar:** Formal analysis, Writing –review & editing. **Tapas K. Mandal:** Visualization. **Babu Pejjai:** Formal analysis, Investigation. **Sang W. Joo:** Supervision, Resources, Project administration, Funding acquisition.

Declaration of Competing Interest

The authors declare that they have no known competing financial interests or personal relationships that could have appeared to influence the work reported in this paper.

Acknowledgments

This study is supported by the grant 2019R1A5A8080290 of the National Research Foundation of Korea (NRF), South Korea. The authors thank the Core Research Support Center for Natural and Medical Materials (CRCNM) for technical support.

Appendix A. Supporting information

Supplementary data associated with this article can be found in the online version at doi:10.1016/j.jallcom.2021.161234.

References

[1] R.R. Salunkhe, J. Tang, Y. Kamachi, T. Nakato, J.H. Kim, Y. Yamauchi, Asymmetric supercapacitors using 3D nanoporous carbon and cobalt oxide electrodes synthesized from a single metal–organic framework, ACS Nano 9 (2015) 6288–6296, https://doi.org/10.1021/acsnano.5b01790

[2] Y. Wang, Y. Song, Y. Xia, Electrochemical capacitors: mechanism, materials, systems, characterization and applications, Chem. Soc. Rev. 45 (2016) 5925–5950, https://doi.org/10.1039/C5CS00580A

[3] Y. Zhang, S. Yu, G. Lou, Y. Shen, H. Chen, Z. Shen, S. Zhao, J. Zhang, S. Chai, Q. Zou, Review of macroporous materials as electrochemical supercapacitor electrodes, J. Mater. Sci. 52 (2017) 11201–11228, https://doi.org/10.1007/s10853-017-0955-3

[4] X. Li, Z. Wang, Y. Qiu, Q. Pan, P. Hu, 3D graphene/ZnO nanorods composite networks as supercapacitor electrodes, J. Alloy. Compd. 620 (2015) 31–37, https://doi.org/10.1016/j.jallcom.2014.09.105

[5] M. Selvakumar, D. Krishna Bhat, A. Manish Aggarwal, S. Prahladh Iyer, G. Sravani, Nano ZnO-activated carbon composite electrodes for supercapacitors, Phys. B Condens. Matter 405 (2010) 2286–2289, https://doi.org/10.1016/j.physb.2010.02.028

[6] H. Wang, H. Li, W. Cai, P. Zhang, S. Cao, Z. Chen, Z. Zang, Challenges and strategies of device function layers and their integration toward high-performance inorganic perovskite solar cells, Nanoscale 12 (2020), https://doi.org/10.1039/D0NR03408H

[7] C. Li, Z. Zang, C. Han, Z. Hu, X. Tang, J. Du, Y. Leng, K. Sun, Highly compact CsPbBr3 perovskite thin films decorated by ZnO nanoparticles for enhanced random lasing, Nano Energy 40 (2017) 195–202, https://doi.org/10.1016/j.nanoen.2017.08.013

[8] W. Cai, H. Li, Z. Zang, One-volt, solution-processed InZnO thin-film transistors, IEEE Electron Device Lett. 42 (2021) 525–528, https://doi.org/10.1109/LED.2021.3062422

[9] H. Wang, S. Cao, B. Yang, H. Li, M. Wang, X. Hu, K. Sun, Z. Zang, NH4Cl-modified ZnO for high-performance CsPbIBr2 perovskite solar cells via low-temperature process, Sol. RRL 4 (2020) 1900363, https://doi.org/10.1002/solr.201900363

[10] C. Wang, R. Bao, K. Zhao, T. Zhang, L. Dong, C. Pan, Enhanced emission intensity of vertical aligned flexible ZnO nanowire/p-polymer hybridized LED array by piezo-phototronic effect, Nano Energy 14 (2015) 364–371, https://doi.org/10.1016/j.nanoen.2014.11.033

[11] J. Sun, N. Li, L. Dong, X. Niu, M. Zhao, Z. Xu, H. Zhou, C. Shan, C. Pan, Interfacial-engineering enhanced performance and stability of ZnO nanowire-based perovskite solar cells, Nanotechnology (2021), https://doi.org/10.1088/1361-6528/abdbeb

[12] R. Bao, C. Wang, Z. Peng, C. Ma, L. Dong, C. Pan, Light-emission enhancement in a flexible and size-controllable ZnO nanowire/organic light-emitting diode array by the piezotronic effect, ACS Photon. 4 (2017) 1344–1349, https://doi.org/10.1021/acsphotonics.7b00386

[13] H. Zhang, L. Dong, C. Pan, Recent progress of ZnO hierarchical nanostructure for photovoltaic application, Int. J. Nanomanufacturing 12 (2016) 336–352, https://doi.org/10.1504/IJNM.2016.079233

[14] A. Eftekhari, F. Molaei, H. Arami, Flower-like bundles of ZnO nanosheets as an intermediate between hollow nanosphere and nanoparticles, Mater. Sci. Eng. A 437 (2006) 446–450, https://doi.org/10.1016/j.msea.2006.08.033

[15] G. Shen, D. Chen, C.J. Lee, Hierarchical saw-like ZnO Nanobelt/ZnS nanowire heterostructures induced by polar surfaces, J. Phys. Chem. B 110 (2006) 15689–15693, https://doi.org/10.1021/jp0630119

[16] B.P. Zhang, N.T. Binh, K. Wakatsuki, Y. Segawa, Y. Yamada, N. Usami, M. Kawasaki, H. Koinuma, Formation of highly aligned ZnO tubes on sapphire (0001) substrates, Appl. Phys. Lett. 84 (2004) 4098–4100, https://doi.org/10.1063/1.1753061

[17] S. Zheng, Y. Fu, L. Zheng, Z. Zhu, J. Chen, Z. Niu, D. Yang, PEDOT-engineered Bi2O3 nanosheet arrays for flexible asymmetric supercapacitors with boosted energy density, J. Mater. Chem. A 7 (2019) 5530–5538, https://doi.org/10.1039/C9TA00854C

[18] Q. Yang, X.T. Zhang, M.Y. Zhang, Y. Gao, H. Gao, X.C. Liu, H. Liu, K.W. Wong, W.M. Lau, Rationally designed hierarchical MnO2-shell/ZnO-nanowire/carbon-fabric for high-performance supercapacitor electrodes, J. Power Sources 272 (2014) 654–660, https://doi.org/10.1016/j.jpowsour.2014.09.001

[19] F. Cao, G.X. Pan, X.H. Xia, P.S. Tang, H.F. Chen, Synthesis of hierarchical porous NiO nanotube arrays for supercapacitor application, J. Power Sources 264 (2014) 161–167, https://doi.org/10.1016/j.jpowsour.2014.04.103

[20] K. Sato, H. Katayama-Yoshida, Ferromagnetism in a transition metal atom doped ZnO, Phys. E Low Dimens. Syst. Nanostruct. 10 (2001) 251–255, https://doi.org/10.1016/S1386-9477(01)00093-5

[21] S.M. Abbas, S.T. Hussain, S. Ali, N. Ahmad, N. Ali, S. Abbas, Structure and electrochemical performance of ZnO/CNT composite as anode material for lithium-ion batteries, J. Mater. Sci. 48 (2013) 5429–5436, https://doi.org/10.1007/s10853-013-7336-3

[22] F. Erdemir, E. Tuzcu, S. Bilgin, Ü. Alver, A. Çanakçı, Influence of fluorine doping of zinc oxide on its electrochemical performance in supercapacitors, Mater. Chem. Phys. 259 (2021) 124033, https://doi.org/10.1016/j.matchemphys.2020.124033

[23] D. Bresser, F. Mueller, M. Fiedler, S. Krueger, R. Kloepsch, D. Baither, M. Winter, E. Paillard, S. Passerini, Transition-metal-doped zinc oxide nanoparticles as a new lithium-ion anode material, Chem. Mater. 25 (2013) 4977–4985, https://doi.org/10.1021/cm403443t

[24] I. Neelakanta Reddy, Ch Venkata Reddy, A. Sreedhar, J. Shim, M. Cho, K. Yoo, D. Kim, Structural, optical, and bifunctional applications: Supercapacitor and photoelectrochemical water splitting of Ni-doped ZnO nanostructures, J. Electroanal. Chem. 828 (2018) 124–136, https://doi.org/10.1016/j.jelechem.2018.09.048

[25] Ü. Alver, A. Tanrıverdi, Boron doped ZnO embedded into reduced graphene oxide for electrochemical supercapacitors, Appl. Surf. Sci. 378 (2016) 368–374, https://doi.org/10.1016/j.apsusc.2016.04.015

[26] M. Huang, F. Li, X.L. Zhao, D. Luo, X.Q. You, Y.X. Zhang, G. Li, Hierarchical ZnO@MnO2 core-shell pillar arrays on Ni foam for binder-free supercapacitor electrodes, Electrochim. Acta 152 (2015) 172–177, https://doi.org/10.1016/j.electacta.2014.11.127

[27] M. Law, L.E. Greene, J.C. Johnson, R. Saykally, P. Yang, Nanowire dye-sensitized solar cells, Nat. Mater. 4 (2005) 455–459, https://doi.org/10.1038/nmat1387

[28] C.-C. Lin, H.-P. Chen, S.-Y. Chen, Synthesis and optoelectronic properties of arrayed p-type ZnO nanorods grown on ZnO film/Si wafer in aqueous solutions, Chem. Phys. Lett. 404 (2005) 30–34, https://doi.org/10.1016/j.cplett.2005.01.047

[29] L.E. Greene, B.D. Yuhas, M. Law, D. Zitoun, P. Yang, Solution-grown zinc oxide nanowires, Inorg. Chem. 45 (2006) 7535–7543, https://doi.org/10.1021/ic0601900

[30] Y.W. Heo, D.P. Norton, L.C. Tien, Y. Kwon, B.S. Kang, F. Ren, S.J. Pearton, J.R. LaRoche, ZnO nanowire growth and devices, Mater. Sci. Eng. R Rep. 47 (2004) 1–47, https://doi.org/10.1016/j.mser.2004.09.001

[31] K. Iwata, T. Sakemi, A. Yamada, P. Fons, K. Awai, T. Yamamoto, M. Matsubara, H. Tampo, K. Sakurai, S. Ishizuka, S. Niki, Doping properties of ZnO thin films for photovoltaic devices grown by URT-IP (ion plating) method, Thin Solid Films 451–452 (2004) 219–223, https://doi.org/10.1016/j.tsf.2003.10.095

[32] Y.-B. Hahn, Zinc oxide nanostructures and their applications, Korean J. Chem. Eng. 28 (2011) 1797–1813, https://doi.org/10.1007/s11814-011-0213-3

[33] M.C. Simoes, K.J. Hughes, D.B. Ingham, L. Ma, M. Pourkashanian, Estimation of the thermochemical radii and ionic volumes of complex ions, Inorg. Chem. 56 (2017) 7566–7573, https://doi.org/10.1021/acs.inorgchem.7b01205

[34] R. Swapna, M.C. Santhosh Kumar, Growth and characterization of molybdenum doped ZnO thin films by spray pyrolysis, J. Phys. Chem. Solids 74 (2013) 418–425, https://doi.org/10.1016/j.jpcs.2012.11.003

[35] H.K. Kim, S.H. Huh, J.W. Park, J.W. Jeong, G.H. Lee, The cluster size dependence of thermal stabilities of both molybdenum and tungsten nanoclusters, Chem. Phys. Lett. 354 (2002) 165–172, https://doi.org/10.1016/S0009-2614(02)00146-X

[36] J. Baltrusaitis, B. Mendoza-Sanchez, V. Fernandez, R. Veenstra, N. Dukstiene, A. Roberts, N. Fairley, Generalized molybdenum oxide surface chemical state XPS determination via informed amorphous sample model, Appl. Surf. Sci. 326 (2015) 151–161, https://doi.org/10.1016/j.apsusc.2014.11.077

[37] J.M. Gonçalves, M.I. da Silva, L. Angnes, K. Araki, Vanadium-containing electro and photocatalysts for the oxygen evolution reaction: a review, J. Mater. Chem. A 8 (2020) 2171–2206, https://doi.org/10.1039/C9TA10857B

[38] K. Umar, A. Aris, T. Parveen, J. Jaafar, Z. Abdul Majid, A. Vijaya Bhaskar Reddy, J. Talib, Synthesis, characterization of Mo and Mn doped ZnO and their photocatalytic activity for the decolorization of two different chromophoric dyes, Appl. Catal. A Gen. 505 (2015) 507–514, https://doi.org/10.1016/j.apcata.2015.02.001

[39] T. Peng, D. Zhao, H. Song, C. Yan, Preparation of lanthana-doped titania nanoparticles with anatase mesoporous walls and high photocatalytic activity, J. Mol. Catal. A Chem. 238 (2005) 119–126, https://doi.org/10.1016/j.molcata.2005.04.066

[40] Y. Zhang, M. Muhammed, Critical evaluation of thermodynamics of complex formation of metal ions in aqueous solutions: VI. Hydrolysis and hydroxo-complexes of Zn2+ at 298.15 K, Hydrometallurgy 60 (2001) 215–236, https://doi.org/10.1016/S0304-386X(01)00148-7

[41] M. Yoshikawa, K. Inoue, T. Nakagawa, H. Ishida, N. Hasuike, H. Harima, Characterization of ZnO nanoparticles by resonant Raman scattering and cathodoluminescence spectroscopies, Appl. Phys. Lett. 92 (2008) 113115, https://doi.org/10.1063/1.2901159

[42] M. Navaneethan, J. Archana, M. Arivanandhan, Y. Hayakawa, Functional properties of amine-passivated ZnO nanostructures and dye-sensitized solar cell characteristics, Chem. Eng. J. 213 (2012) 70–77, https://doi.org/10.1016/j.cej.2012.10.001

[43] F. Decremps, J. Pellicer-Porres, A.M. Saitta, J.-C. Chervin, A. Polian, High-pressure Raman spectroscopy study of wurtzite ZnO, Phys. Rev. B 65 (2002) 092101, https://doi.org/10.1103/PhysRevB.65.092101

[44] X. Zhang, X.-F. Qiao, W. Shi, J.-B. Wu, D.-S. Jiang, P.-H. Tan, Phonon and Raman scattering of two-dimensional transition metal dichalcogenides from monolayer,

multilayer to bulk material, Chem. Soc. Rev. 44 (2015) 2757–2785, https://doi.org/10.1039/C4CS00282B
[45] K. Jindal, M. Tomar, R.S. Katiyar, V. Gupta, Raman scattering and photoluminescence investigations of N doped ZnO thin films: local vibrational modes and induced ferromagnetism, J. Appl. Phys. 120 (2016) 135305, https://doi.org/10.1063/1.4964257
[46] P.K. Giri, S. Bhattacharyya, D.K. Singh, R. Kesavamoorthy, B.K. Panigrahi, K.G.M. Nair, Correlation between microstructure and optical properties of ZnO nanoparticles synthesized by ball milling, J. Appl. Phys. 102 (2007) 093515, https://doi.org/10.1063/1.2804012
[47] A.K. Rana, Y. Kumar, N. Saxena, R. Das, S. Sen, P.M. Shirage, Studies on the control of ZnO nanostructures by wet chemical method and plausible mechanism, AIP Adv. 5 (2015) 097118, https://doi.org/10.1063/1.4930598
[48] A.P.A. Oliveira, J.-F. Hochepied, F. Grillon, M.-H. Berger, Controlled precipitation of zinc oxide particles at room temperature, Chem. Mater. 15 (2003) 3202–3207, https://doi.org/10.1021/cm0213725
[49] D. Li, H. Haneda, Morphologies of zinc oxide particles and their effects on photocatalysis, Chemosphere 51 (2003) 129–137, https://doi.org/10.1016/S0045-6535(02)00787-7
[50] S. Komarneni, M. Bruno, E. Mariani, Synthesis of ZnO with and without microwaves, Mater. Res. Bull. 35 (2000) 1843–1847, https://doi.org/10.1016/S0025-5408(00)00385-8
[51] Y. Chang, H.C. Zeng, Controlled synthesis and self-assembly of single-crystalline CuO nanorods and nanoribbons, Cryst. Growth Des. 4 (2004) 397–402, https://doi.org/10.1021/cg034127m
[52] E.W. Shi, C. ZZ, Y. RL, Z. YQ, Crystallography of Nanocrystals Grown In Hydrothermal Environments, Science Press, Beijing, 2004.
[53] D. Andreeva, I. Mitov, T. Tabakova, V. Mitrov, A. Andreev, Influence of iron (II) on the transformation of ferrihydrite into goethite in acid medium, Mater. Chem. Phys. 41 (1995) 146–149, https://doi.org/10.1016/0254-0584(95)01520-5
[54] E. Tronc, P. Belleville, J.P. Jolivet, J. Livage, Transformation of ferric hydroxide into spinel by iron(II) adsorption, Langmuir 8 (1992) 313–319, https://doi.org/10.1021/la00037a057
[55] J.-F. Tang, H.-H. Su, Y.-M. Lu, S.-Y. Chu, Controlled growth of ZnO nanoflowers on nanowall and nanorod networks via a hydrothermal method, CrystEngComm 17 (2014) 592–597, https://doi.org/10.1039/C4CE01940G
[56] Y. Qu, R. Huang, W. Qi, M. Shi, R. Su, Z. He, Controllable synthesis of ZnO nanoflowers with structure-dependent photocatalytic activity, Catal. Today 355 (2020) 397–407, https://doi.org/10.1016/j.cattod.2019.07.056
[57] E.A.A. Júnior, F.X. Nobre, G. da, S. Sousa, L.S. Cavalcante, M.R. de, M.C. Santos, F.L. Souza, J.M.E. de Matos, Synthesis, growth mechanism, optical properties and catalytic activity of ZnO microcrystals obtained via hydrothermal processing, RSC Adv. 7 (2017) 24263–24281, https://doi.org/10.1039/C7RA03277C
[58] J. FAN, T. LI, H. HENG, Hydrothermal growth of ZnO nanoflowers and their photocatalyst application, Bull. Mater. Sci. (2016) 19–26, https://doi.org/10.1007/s12034-015-1145-z
[59] N. Gogurla, A.K. Sinha, S. Santra, S. Manna, S.K. Ray, Multifunctional Au-ZnO plasmonic nanostructures for enhanced UV photodetector and room temperature NO sensing devices, Sci. Rep. 4 (2014) 6483, https://doi.org/10.1038/srep06483
[60] Y.-G. Lin, Y.-K. Hsu, Y.-C. Chen, L.-C. Chen, S.-Y. Chen, K.-H. Chen, Visible-light-driven photocatalytic carbon-doped porous ZnO nanoarchitectures for solar water-splitting, Nanoscale 4 (2012) 6515–6519, https://doi.org/10.1039/C2NR31800H
[61] A. Cots, D. Cibrev, P. Bonete, R. Gómez, Hematite nanorod electrodes modified with molybdenum: photoelectrochemical studies, ChemElectroChem 4 (2017) 585–593, https://doi.org/10.1002/celc.201600644
[62] D. Briggs, Handbook of X-ray photoelectron spectroscopy C. D. Wanger, W. M. Riggs, L. E. Davis, J. F. Moulder and G. E.Muilenberg Perkin-Elmer Corp., Physical Electronics Division, Eden Prairie, Minnesota, USA, 1979. 190 pp. $195, Surf. Interface Anal. 3 (1981) v, https://doi.org/10.1002/sia.740030412
[63] K. Hada, J. Tanabe, S. Omi, M. Nagai, Characterization of cobalt molybdenum nitrides for thiophene HDS by XRD, TEM, and XPS, J. Catal. 207 (2002) 10–22, https://doi.org/10.1006/jcat.2001.3495
[64] A. Ali, M. Ammar, M. Ali, Z. Yahya, M.Y. Javaid, S. ul Hassan, T. Ahmed, Mo-doped ZnO nanoflakes on Ni-foam for asymmetric supercapacitor applications, RSC Adv. 9 (2019) 27432–27438, https://doi.org/10.1039/C9RA05051E
[65] S. Ratha, S.R. Marri, N.A. Lanzillo, S. Moshkalev, S.K. Nayak, J.N. Behera, C.S. Rout, Supercapacitors based on patronite–reduced graphene oxide hybrids: experimental and theoretical insights, J. Mater. Chem. A 3 (2015) 18874–18881, https://doi.org/10.1039/C5TA03221K
[66] C. Sandford, M.A. Edwards, K.J. Klunder, D.P. Hickey, M. Li, K. Barman, M.S. Sigman, H.S. White, S.D. Minteer, A synthetic chemist's guide to electroanalytical tools for studying reaction mechanisms, Chem. Sci. 10 (2019) 6404–6422, https://doi.org/10.1039/C9SC01545K
[67] J. Zhang, H. Feng, Q. Qin, G. Zhang, Y. Cui, Z. Chai, W. Zheng, Interior design of three-dimensional CuO ordered architectures with enhanced performance for supercapacitors, J. Mater. Chem. A 4 (2016) 6357–6367, https://doi.org/10.1039/C6TA00397D
[68] Y. He, L. Xie, S. Ding, Y. Long, X. Zhou, Q. Hu, D. Lin, Core–shell nanostructured Zn–Co–O@CoS arrays for high-performance hybrid supercapacitors, Dalton Trans. 50 (2021) 4923–4931, https://doi.org/10.1039/D1DT00584G
[69] G. Nagaraju, S.C. Sekhar, J.S. Yu, Utilizing waste cable wires for high-performance fiber-based hybrid supercapacitors: an effective approach to electronic-waste management, Adv. Energy Mater. 8 (2018) 1702201, https://doi.org/10.1002/aenm.201702201
[70] M. Yan, Y. Yao, J. Wen, L. Long, M. Kong, G. Zhang, X. Liao, G. Yin, Z. Huang, Construction of a hierarchical NiCo2S4@PPy core–shell heterostructure nanotube array on Ni foam for a high-performance asymmetric supercapacitor, ACS Appl. Mater. Interfaces 8 (2016) 24525–24535, https://doi.org/10.1021/acsami.6b05618
[71] Q. Zhou, J. Xing, Y. Gao, X. Lv, Y. He, Z. Guo, Y. Li, Ordered assembly of NiCo2O4 multiple hierarchical structures for high-performance pseudocapacitors, ACS Appl. Mater. Interfaces 6 (2014) 11394–11402, https://doi.org/10.1021/am501988s
[72] W.-W. Ning, L.-B. Chen, W.-F. Wei, Y.-J. Chen, X.-Y. Zhang, NiCoO2/NiCoP@Ni nanowire arrays: tunable composition and unique structure design for high-performance winding asymmetric hybrid supercapacitors, Rare Met. 39 (2020) 1034–1044, https://doi.org/10.1007/s12598-020-01374-9
[73] S. Goswami, G.R. Dillip, S. Nandy, A.N. Banerjee, A. Pimentel, S.W. Joo, R. Martins, E. Fortunato, Biowaste-derived carbon black applied to polyaniline-based high-performance supercapacitor microelectrodes: sustainable materials for renewable energy applications, Electrochim. Acta 316 (2019) 202–218, https://doi.org/10.1016/j.electacta.2019.05.133
[74] Y.-K. Hsu, Y.-C. Chen, Y.-G. Lin, Characteristics and electrochemical performances of lotus-like CuO/Cu(OH)2 hybrid material electrodes, J. Electroanal. Chem. 673 (2012) 43–47, https://doi.org/10.1016/j.jelechem.2012.03.019
[75] Y. Zhang, Y. Liu, Z. Sun, J. Fu, S. Cheng, P. Cui, J. Zhou, Z. Zhang, X. Pan, W. Han, E. Xie, Versatile electrochemical activation strategy for high-performance supercapacitor in a model of MnO2, J. Mater. Chem. A 7 (2019) 21290–21298, https://doi.org/10.1039/C9TA08278F
[76] K. Ghosh, S.K. Srivastava, Superior supercapacitor performance of Bi2S3 nanorod/reduced graphene oxide composites, Dalton Trans. 49 (2020) 16993–17004, https://doi.org/10.1039/D0DT03594G
[77] T. Lu, L. Pan, H. Li, G. Zhu, T. Lv, X. Liu, Z. Sun, T. Chen, D.H.C. Chua, Microwave-assisted synthesis of graphene–ZnO nanocomposite for electrochemical supercapacitors, J. Alloy. Compd. 509 (2011) 5488–5492, https://doi.org/10.1016/j.jallcom.2011.02.136
[78] Y. Guo, B. Chang, T. Wen, C. Zhao, H. Yin, Y. Zhou, Y. Wang, B. Yang, S. Zhang, One-pot synthesis of graphene/zinc oxide by microwave irradiation with enhanced supercapacitor performance, RSC Adv. 6 (2016) 19394–19403, https://doi.org/10.1039/C5RA24212F
[79] M. Saranya, R. Ramachandran, F. Wang, Graphene-zinc oxide (G-ZnO) nanocomposite for electrochemical supercapacitor applications, J. Sci. Adv. Mater. Devices 1 (2016) 454–460, https://doi.org/10.1016/j.jsamd.2016.10.001
[80] G.R. Dillip, A.N. Banerjee, V.C. Anitha, B. Deva Prasad Raju, S.W. Joo, B.K. Min, Oxygen vacancy-induced structural, optical, and enhanced supercapacitive performance of zinc oxide anchored graphitic carbon nanofiber hybrid electrodes, ACS Appl. Mater. Interfaces 8 (2016) 5025–5039, https://doi.org/10.1021/acsami.5b12322
[81] X. Dong, Y. Cao, J. Wang, M.B. Chan-Park, L. Wang, W. Huang, P. Chen, Hybrid structure of zinc oxide nanorods and three dimensional graphene foam for supercapacitor and electrochemical sensor applications, RSC Adv. 2 (2012) 4364–4369, https://doi.org/10.1039/C2RA01295B
[82] I.Y.Y. Bu, R. Huang, One-pot synthesis of ZnO/reduced graphene oxide nanocomposite for supercapacitor applications, Mater. Sci. Semicond. Process. 31 (2015) 131–138, https://doi.org/10.1016/j.mssp.2014.11.037
[83] H. Mahajan, J. Bae, K. Yun, Facile synthesis of ZnO-Au nanocomposites for high-performance supercapacitors, J. Alloy. Compd. 758 (2018) 131–139, https://doi.org/10.1016/j.jallcom.2018.04.238
[84] S.G. Krishnan, M. Harilal, B. Pal, I.I. Misnon, C. Karuppiah, C.-C. Yang, R. Jose, Improving the symmetry of asymmetric supercapacitors using battery-type positive electrodes and activated carbon negative electrodes by mass and charge balance, J. Electroanal. Chem. 805 (2017) 126–132, https://doi.org/10.1016/j.jelechem.2017.10.029
[85] C. Lamiel, V.H. Nguyen, D.R. Kumar, J.-J. Shim, Microwave-assisted binder-free synthesis of 3D Ni-Co-Mn oxide nanoflakes@Ni foam electrode for supercapacitor applications, Chem. Eng. J. 316 (2017) 1091–1102, https://doi.org/10.1016/j.cej.2017.02.004
[86] C. Pascot, Y. Dandeville, Y. Scudeller, Ph Guillemet, T. Brousse, Calorimetric measurement of the heat generated by a double-layer capacitor cell under cycling, Thermochim. Acta 510 (2010) 53–60, https://doi.org/10.1016/j.tca.2010.06.022
[87] Y. Dandeville, Ph Guillemet, Y. Scudeller, O. Crosnier, L. Athouel, Th Brousse, Measuring time-dependent heat profiles of aqueous electrochemical capacitors under cycling, Thermochim. Acta 526 (2011) 1–8, https://doi.org/10.1016/j.tca.2011.07.027
[88] A.M. Patil, N. Kitiphatpiboon, X. An, X. Hao, S. Li, X. Hao, A. Abudula, G. Guan, Fabrication of a high-energy flexible all-solid-state supercapacitor using pseudocapacitive 2D-Ti3C2Tx-MXene and battery-type reduced graphene oxide/nickel–cobalt bimetal oxide electrode materials, ACS Appl. Mater. Interfaces 12 (2020) 52749–52762, https://doi.org/10.1021/acsami.0c16221
[89] N. Wu, X. Bai, D. Pan, B. Dong, R. Wei, N. Naik, R.R. Patil, Z. Guo, Recent advances of asymmetric supercapacitors, Adv. Mater. Interfaces 8 (2021) 2001710, https://doi.org/10.1002/admi.202001710

View publication stats

International Journal of Biological Macromolecules 209 (2022) 912–922

Contents lists available at ScienceDirect

International Journal of Biological Macromolecules

journal homepage: www.elsevier.com/locate/ijbiomac

An efficient biosynthesis of palladium nanoparticles using Bael gum and evaluation of their catalytic and antibacterial activity

Kondaiah Seku [a,*], G. Bhagavanth Reddy [b], Syed Sulaiman Hussaini [a], Babu Pejjai [c], Mushtaq Hussain [a], D. Madhusudan Reddy [d], Mahmoud A.K. Khazaleh [e], Girija Mangatayaru [b,*]

[a] Department of Engineering, Civil Section (Applied Sciences - Chemistry), University of Technology and Applied Sciences-Shinas, Al-Aqur, Shinas 324, Oman.
[b] Department of Chemistry, Palamuru University, Mahabubnagar, Telangana 509001, India
[c] Department of Science and Humanities, Sri Venkateshwara Engineering College, Karakambadi Road, Tirupati, Andhra Pradesh 517507, India
[d] Department of Microbiology, Palamuru University, Mahbubnagar, Telangana 509001, India
[e] Dept of Civil Engineering, Aqaba University of Technology, Jordan

ARTICLE INFO

Keywords:
Biosynthesis of PdNPs
Bael gum
Carboxymethylated Bael gum
Catalytic properties
And antibacterial activity

ABSTRACT

We report a facile microwave-assisted synthesis of palladium nanoparticles (PdNPs) using Bael gum (BG) and it's carboxymethylated (CMBG) derivative. The prepared nanoparticles (BG@PdNPs and CMBG@PdNPs) were evaluated for antibacterial and catalytic activity in the reduction of organic dye pollutants. The developed synthetic method is simple, low cost and eco-friendly, wherein the process requires no additional reducing or capping agents. The CMBG was prepared via etherification reaction between BG and monochloroacetic acid using Williamson synthesis method. The PdNPs were synthesized using BG and CMBG as stabilizers and reducing agents. The PdNPs were found to be well dispersed spherical, with the crystalline size of the order of 7–21 nm. The results showed that the CMBG@PdNPs were smaller in size (7 ± 2 nm) than those capped with BG@PdNPs (10 ± 2 nm). The catalytic ability of CMBG@PdNPs was examined for the reduction of Methyl Orange (MO), Methyl Red(MR), and Rhodamine-B (RhB) in the presence of $NaBH_4$. The results showed that CMBG@PdNPs exhibited a higher catalytic ability than BG@PdNPs. Moreover, it was found that CMBG@PdNPs served several times as a retrievable and reusable catalyst which is stable even after six cycles of reaction. The CMBG@PdNPs and BG@PdNPs showed excellent antibacterial activity. The results indicate that CMBG@PdNPs have greater potential application as a catalyst in the reduction of organic pollutants and antibacterial activity.

1. Introduction

Nanotechnology and Nanoscience have emerged as a saviour for current generation problems. The applications of nanotechnology have set their roots in all areas of science and technology, stretching from the basic human needs like food and medicine to global issues, i.e., energy, pollution control, and remediation. The need for quality food has led the scientific community, government organizations, and industries to search for new products and protocols based on nanotechnology [1,2]. Nanotechnology has provided a sophisticated and multi-disciplinary approach to drug designing and drug delivery which has revolutionized the whole medical research field [3]. Recently, nanotechnology has played a significant role in the development of transition metal oxides nanocomposites with different dimensions as an electrode for high performance supercapacitor [4,5].

Nowadays, pigments and dyes are found in many industrial effluents discharged by textiles, cosmetics, leather, paper, food, and other chemical processing industries. Dye-contaminated industrial effluents cause adverse effects on the environment as well as human health due to their highly toxic nature. Dye pollutants are highly carcinogenic and chemically more stable [6]. These dyes cannot be easily degraded to nontoxic products and cause adverse effects such as liver and kidney damage, a blood disorder, central nervous system poisoning, and skin irradiation [6]. Catalytic reduction of organic dyes using metal nanoparticles is an interesting subject due to its high efficacy [6]. Engineered nanomaterials have provided a novel approach to the remediation of pollution and its effects. Nanomaterials can effectively remove the pollutants from soil and groundwater [7]. Some other catalysts or adsorbents have been reported for organic pollutants treating polluted water [8]. The nanomaterials have shown great potential in addressing many

* Corresponding authors.
E-mail addresses: Kondaiah.Seku@shct.edu.om (K. Seku), kgirijamangatayaru@gmail.com (G. Mangatayaru).

https://doi.org/10.1016/j.ijbiomac.2022.04.070
Received 26 November 2021; Received in revised form 8 April 2022; Accepted 9 April 2022
Available online 18 April 2022
0141-8130/© 2022 Elsevier B.V. All rights reserved.

of our current generation problems due to their size, structure, specificity, and versatility [9,10]. Therefore, more and more researchers and scientists have started searching for solutions in nanotechnology for problems in their field.

Nanomaterials are generally classified depending on the material as metal-based nanoparticles, carbon-based nanoparticles, organic compound-based nanoparticles, and composite-based nanoparticles. They all display unique properties due to their size, morphology, composition, and agglomeration. Among all, metal nanoparticle-based materials are very special due to their diverse applications ranging from mechanical optical to biomedical [11]. In recent years, nanostructures of gold, silver, and platinum are being widely studied in the biomedical field, leading to their clinical use [8,12,13]. Researchers have shown renewed interest and attention towards the Noble palladium nanoparticles (PdNPs) due to their high chemical and thermal stability [14,15], non-toxicity, high surface area, and its use in several organic reactions as a catalyst like hydrogenation reaction, Suzuki coupling, Heck C—C coupling [16], reduction of toxic organic compounds [17].

PdNPs are being tried as photothermal agents in photothermal therapy [18], photoacoustic agents in photoacoustic imaging for early detection of tumors [19], efficient nanocarriers for genes and drugs [20], and as prodrug activators [21]. The specific surface and pore size distribution of the palladium nanoparticles may influence the catalysis properties [17]. Furthermore, PdNPs have been tested on several cancer cell lines [22] and also as antimicrobial agents on several bacterial strains [23]. The interesting application of PdNPs comes in the form of nanostructured Pd microelectrodes generated by electrodeposition methods as nanoscale biosensors for high-performance diagnostic tools in medicine [24]. In addition to the above applications, PdNPs are also being used for organic synthesis [25], hydrogen storage/sensing [26], fuel cells [27] and catalytic reduction of organic dyes.

The synthesis of PdNPs has been reported by diverse techniques [28], such as thermal decomposition, chemical reduction, and vapour deposition [29]. However, all these synthetic methods have used either expensive and toxic chemicals or required high energy. In recent years, researchers have shown much attention to the green synthesis of PdNPs due to its cost-effectiveness, simplicity, biocompatibility, and non-toxicity [30]. Recently researchers have been reported less toxic and highly biocompatibility palladium metal nanoparticles for biological and catalytic applications [31–33]. Herein, we report a facile biosynthesis of PdNPs in an aqueous medium using BG and CMBG. Gums are natural polymers obtained from marine, plant, and microbial sources. The gum from plant sources comes either from seeds, tree exudates, tubers, and extracts. Gums from different plant sources were being used as food and in traditional medicine [34,35]. The gum obtained from plants contains various bioactive phytochemicals. It is being used in medicine, pharmacology, agriculture, environmental and chemical engineering [36]. Due to their excellent biocompatibility, biodegradability, nontoxicity, and easy accessibility, several gums have been used to prepare medical systems and devices such as wound healing dressings, drug delivery, and artificial tissue engineering scaffolding systems [37]. The green synthesis of metal nanoparticles has improved their application in medicine due to their biocompatible and improved efficacy as compared to physical and chemical methods [38].

Globally, antimicrobial drug resistance has become one of the most significant public health concerns. Microbial infections cause about 3 million deaths annually in developing countries. Most of the deaths due to microbial infections occur in tropical countries despite vast advances in diagnosis and treatment [39]. An estimated $20 billion dollars is the economic cost of multidrug-resistant (MDR) microbes in the U.S. alone [40]. Due to resistance, clinicians are frequently left with no reliable alternative to manage infected patients. As a result, MDR and extensively drug-resistant (XDR) bacteria are a significant public health concern since they are associated with high mortality, morbidity, and treatment costs [41,42]. A promising therapeutic strategy for microbes is nanotechnology by virtue of its high efficacy and therapeutic index [43]. Most bacterial infections can be effectively treated with nanoparticles, especially those involving multi-drug resistant bacteria. Using nanoparticles along with antibiotics provide excellent synergistic effects.

Bael, *Aegle marmelos* (L.) Corrêa is also known as begal-quince, golden apple, and stone apple is one of the medicinal plant species grown in India [44]. It ine of the medicinally important plants mentioned in a renowned ayurvedic medical book called Charaka Samhita [45]. Various parts of the plant are used in ayurvedic and folk medicine as a remedy for different ailments [46]. The fruit and seeds of the plant are used in the treatment of neurological problems, malabsorption, dysentery, edema, dyspepsia, etc. [44]. Beal is also used in food processing and extraction of economically important herbal compounds. Green synthesis of gold nanoplates using BG as a capping agent has been reported [47]. The Bael gum has been found to improve chitosan's film-forming property, and the resulting film showed improved mechanical and electrochemical properties [48]. The PdNPs have been synthesized using various gums derived from plant sources [49,50]. Earlier, our team has reported the synthesis and application of metal nanoparticles capped with natural and modified gums [51–53]. Considering the medical applications and renewed interest of researchers in preparing biogenic nanomaterial, especially from natural gums, motivated us to prepare PdNPs from readily available and low-cost material BG and to study its applications. Moreover, a review of the literature shows no report of the synthesis of PdNPs using bael gum and its applications.

Based on the current study, we report the synthesis of PdNPs using Bael gum (BG) and CMBG. The CMBG was characterized in terms of chemical and physical properties using FTIR, TGA, DSC, XRD, and SEM techniques. BG and CMBG stabilized PdNPs were characterized using FTIR, XRD, DLS, SEM, and TEM techniques. The antimicrobial properties of BG and CMBG stabilized PdNPs were studied. The catalytic efficacy of BG@PdNPs and CMBG@PdNPs was assessed by exploring their ability with Methyl Orange (MO), Methyl Red (MR), Rhodamine-B (RhB) dyes, and antibacterial activity were tested.

2. Materials and methods

2.1. Materials

BG was purchased from the Girijana Cooperative Society of Telangana, India. Sodium tetrachloropalladate and dyes were purchased from Sigma-Aldrich and other chemicals were purchased from Sd fine chem limited, Mumbai, India. All the microbial test strains were procured from the IMTECH Laboratory, Chandigarh, India.

2.2. Carboxymethylation of Bael gum

CMBG was prepared by mixing the collected BG (1g) with 5 mL of distilled water, followed by the addition of 95 mL of ice-cold NaOH solution (55% *w/v*). About 10 mL of monochloroacetic acid (75%, w/v) solution was slowly added over 10 min to the above reaction mixture. The temperature of the reaction mixture was gradually increased up to 65 °C and stirred for 2 h. The pH of the suspension was neutralized with glacial acetic acid. The obtained wet solid mass was washed with methanol and dried in an oven at 50–65 °C [54].

2.3. Synthesis of PdNPs with BG

BG (0.5 g) was dispersed in 50 mL of double distilled water with stirring for 2 h at 60 °C, cooled, and filtered by using Whatman filter paper to get a clear solution. To synthesize BG-capped PdNPs, 5 mL of 1 mM Na_2PdCl_4 and 10 mL of 1% BG solution were taken in a beaker. The reaction mixture was irradiated with Microwave (MWI) at 750 W for 3 min. The resulting reaction mixture showed a grey color indicating the

formation of PdNPs.

2.4. Synthesis of PdNPs with CMBG

CMBG (0.5 g) was dispersed in 50 mL of double distilled water with stirring for 1 h at 60 °C, cooled, and filtered by using Whatman filter paper to get a clear solution. To synthesize CMBG capped PdNPs, 5 mL of 1 mM Na_2PdCl_4 and 10 mL of 1% CMBG solution were taken in a beaker. The reaction mixture was subjected to MWI for 3 min at 750 W. The resulting reaction mixture showed a grey color indicating the formation of PdNPs.

2.5. Characterization techniques

Various physicochemical characterization techniques have been used to determine the formation of CMBG, BG@PdNPs, and CMBG@PdNPs. The morphology of BG and CMBG was examined using SEM (Carl Zeiss SEM with the Oxford EDX attachment, at O·U). DSC and TGA analysis were carried out on STA7200 thermal analysis system, Hitachi was used to perform DSC and TGA studies. The UV-visible spectra were recorded on UV-3200, Shimadzu, Japan. FTIR spectra were carried out using Shimadzu IR Affinity-1. The powder XRD was analyzed by using Rigaku Miniflex. TEM (JEOL2000) was used to measure the size and morphology of the synthesized BG@PdNPs and CMBG@PdNPs and SEM were investigated with the ZEISS EVO instrument. The Zeta potential of the PdNPs was determined using DLS (Malvern instrument Ltd).

2.6. Catalytic reduction of dyes

The synthesized BG@PdNPs and CMBG@PdNPs were tested for catalytic activity for the reduction of MO, MR, and RhB dyes in the presence of $NaBH_4$. About 1.5 mL of 0.5 mM MO solution, 1 mL of 10 mM $NaBH_4$, and 10 mL of double distilled water were stirred for 5 min. 3 mL of the reaction mixture was taken into a cuvette, and 5 mg of PdNPs were added. The catalytic reduction studies were carried out using the UV–Vis Spectrophotometer. A similar approach was used for the catalytic reduction of MR and RhB dyes.

2.7. Antibacterial activity of BG@PdNPs and CMBG@PdNPs

The antibacterial activity of BG@PdNPs and CMBG@PdNPs were tested by using the disc diffusion method. The transferred nutrient agar medium was allowed to solidify in the sterilized Petri dishes. 100 mL of bacterial suspension was transferred into mediated sterilized Petri dishes and incubated at 37 °C for 24 h in an incubator and the formed zone of inhibition was measured.

3. Results and discussion

3.1. Characterization of CMBG

Fig.S1 shows the FTIR spectra of BG and CMBG in the range of 4000–400 cm^{-1}. The FTIR spectra of BG (pure gum) showed a broad absorption peak at 3390 cm^{-1} was attributed to -OH stretching vibrations. The bands observed at 1700, 1510, 1470, 1250, and 1030 cm^{-1} were due to the -C=O functional group, polyphenyl skeletal (aromatic), symmetric stretching of the C-O-C group, stretching vibrations of C—N amide, and C—O stretching vibrations of carboxylic acid respectively. The IR spectrum of CMBG showed a band at 3400–3250 cm^{-1} due to overlapping contributions of free and bonded OH groups of carboxylic acid. The absorptions bands at 1750, 1260, and 700 cm^{-1} were due to -C=O stretching vibrations, C-O-C symmetric stretching vibrations, and C—O wagging, respectively. The absorption bands at 1625, 1450 cm^{-1} were due to COO^- asymmetric stretching vibrations of carboxylate ion and, while the C—O stretch of carboxylic acid appeared at 1050 cm^{-1}. The observed bands of CMBG confirmed the carboxymethylation of BG [47,55]. Fig.S2 shows the X-ray diffraction pattern of BG and CMBG. The XRD of BG did not show any peaks, indicating an amorphous nature of the material. Whereas XRD of CMBG shows the typical characteristic peaks at 2θ equal to 13.10, 14.85, 20.40, 21.50, 26.10, 28.20, 32.00, 36.10, 41.01, and 47.15 degrees, which indicates an increase in the crystallinity of BG on carboxymethylation [56].

The differential thermogravimetric curves of BG and CMBG are shown in Fig. S3. The TGA analysis of mass% versus temperature showed that there are significant regions of mass loss within the thermal curves of these gums. The presence of different components with different structures gums cause them to exhibit different thermal behaviour, which is evident from their TGA curves. For the BG (black line), there are two significant regions of mass loss as observed in the TGA curve of the gum. The region of mass loss of ~20% within the temperature range 20–150 °C due to the moisture traces present in the gum and the second moss loss of 40% between 200 and 400 °C, represents the degradation of the polymer backbone. For the CMBG (redline), there are four significant regions of mass loss as observed in the TGA curve of the CMBG. The region of mass loss of ~20% within the temperature range of 20–100 °C, 20% in the range of 250–350 °C, ~10% in the range of 450–600 °C and of 35% in the range of 600–750 °C. The zone of mass loss at 450–600 °C is due to the degradation of carboxymethyl groups incorporated in the BG. The study showed that CMBG is thermally more stable as compared to that of BG. The yield at 800 °C for the gum (black line) was higher (~17.5%) than that of CMBG (~16%) (red line). These results confirmed the carboxymethylation of BG [51].

The DSC thermograms of BG and CMBG are shown in Fig.S4. DSC thermogram of BG shows a small broad endothermic peak at 45 °C and a broad endothermic peak at 278 °C. The thermal curves of CMBG showed a small broad endothermic peak at 53 °C and a broad endothermic peak at 290 °C. The shifting of endothermic peaks in CMBG was evidence of carboxymethyl group insertion in the BG. Fig.S5 shows the SEM images of BG and CMBG. The BG showed amorphous like images with different shapes. The SEM morphology of CMBG showed crystalline rods and stones-like images, due to the carboxymethylation of BG. All the aforesaid characterizations confirmed that the Bael gum was carboxymethylated.

3.2. Properties of BG@PdNPs and CMBG@PdNPs

The synthesized BG@PdNPs and CMBG@PdNPs were characterized using UV-visible Spectrophotometry, FTIR, powder XRD, DLS, and TEM techniques.

3.2.1. UV-visible spectroscopic studies

The formation of BG@PdNPs and CMBG@PdNPs were studied by using a UV-visible spectrophotometer. The pale yellow color of Pd^{2+} ion changes into black by the addition of BG and CMBG, which indicates the formation of BG@PdNPs and CMBG@PdNPs by reduction of Pd^{2+} to Pd^0. The UV-visible spectra of BG, Na_2PdCl_2 solution, BG @PdNPs, and CMBG@PdNPs were shown in Fig. 1. BG shows a characteristic peak at 260 nm, Pd^{2+} ions showed a peak at 430 nm, whereas the BG@PdNPs and CMBG@PdNPs did not show any specific wavelength maximum in the spectra. Notably, the intensity of Pd(II) precursor absorption peaks will be diminished after its reduction to Pd(0). This confirmed the absence of Pd^{2+} ions in the solution of BG@PdNPs and CMBG@PdNPs and indicated that all the Pd^{2+} ions were reduced to Pd^0. The UV-visible absorption spectra confirmed the formation of BG@PdNPs and CMBG@PdNPs [53].

3.2.2. FTIR spectroscopic studies

Fig. 2 shows the FTIR spectra of BG@PdNPs and CMBG@PdNPs. The spectra of BG@PdNPs showed a strong peak at 3365 $cm^{-1,}$ corresponding to the -OH group. The characteristic bands at 1680, 1280, 1045, and 880 cm^{-1} were due to -C=O, -C-H, C—O, and $-CH_2$ groups. The FTIR

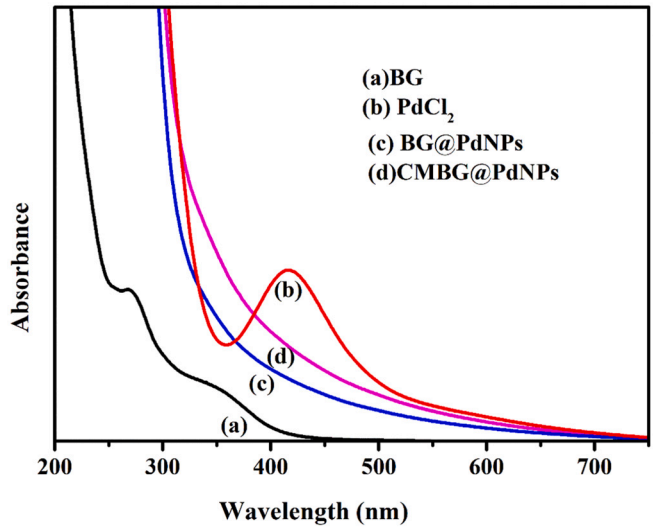

Fig. 1. UV-visible spectra of (a) BG, (b) Pd^{2+} solution, (c) BG@PdNPs and (d) CMBG@PdNPs.

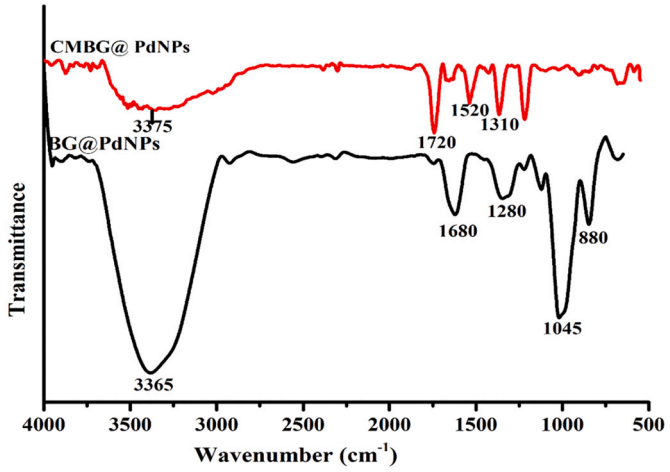

Fig. 2. FTIR Spectra of BG@PdNPs and CMBG@PdNPs.

spectrum of CMBG@PdNPs showed an absorption band at 3375 cm^{-1}, 1720, 1520, 1310, and 1210 cm^{-1} attributed to -OH, -C=O, -C-N, -C-H, and C—O stretching vibrations, respectively. A shift in the -OH and -C=O peaks indicate the capping of PdNPs with carboxyl and hydroxyl groups [53].

3.2.3. Powder - XRD studies

Fig. 3 shows the XRD pattern of BG@PdNPs and CMBG@PdNPs. The X-ray diffractogram of BG@PdNPs showed characteristic peaks at 2θ equal to 38.30, 48.10, 65, and 78.20 degrees and indexed to (111), (200), (220), and (311) planes, respectively. All the peaks indexed were well matched to the face-centered cubic (FCC) lattice. The CMBG@PdNPs showed characteristic peaks at 2θ = 38.65, 48.10, 65.20, and 78.40 degrees and indexed to (111), (200), (220), and (311) planes of FCC structure (JCPDS No. 89–4897), respectively. The XRD spectrum of CMBG@PdNPs showed a high-intensity peak compared to the XRD spectrum of BG@PdNPs, which indicates that the CMBG@PdNPs are highly crystalline in nature when compared with BG@PdNPs. The XRD spectra showed high intensity for the (111) peak, which indicates the preferred growth of PdNPs along the (111) plane [53].

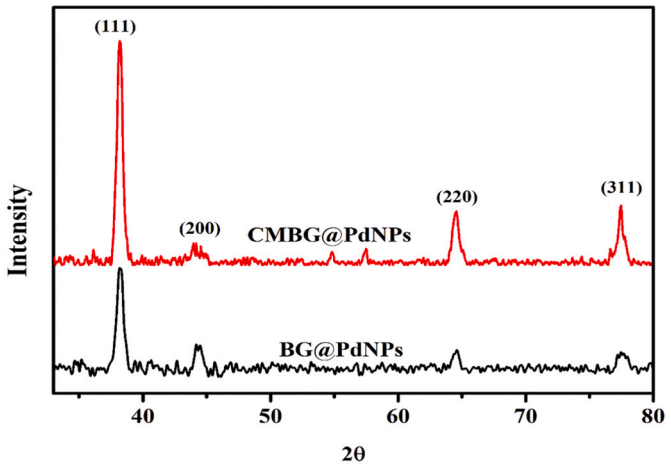

Fig. 3. Powder - XRD pattern of BG@PdNPs and CMBG@PdNPs.

3.2.4. Zeta potential measurements

Stability studies of PdNPs are essential for chemical and biological applications. The stability studies of BG@PdNPs and CMBG@PdNPs were investigated by monitoring with zeta potential. Fig. 4 shows the zeta potential values at −19.5 and 21.5 mV for BG@PdNPs and CMBG@PdNPs, respectively. The zeta potential study indicates that PdNPs are covered with the -ve charged groups like carboxyl and hydroxyl groups. Therefore, the synthesized BG@PdNPs and CMBG@PdNPs are highly stable due to the strong electrostatic repulsions between the PdNPs [53].

3.2.5. Transmission electron microscopic studies

The TEM images of synthesized BG@PdNPs and CMBG@PdNPs are shown in Fig. 5. The Fig. 5a shows that the BG stabilized PdNPs were spherical in shape. The TEM image revealed that the BG effectively protected the PdNPs (BG@PdNPs) from aggregation [51]. The histogram (Fig. 5b) confirmed that the average size dispersal was 10 ± 2 nm. Fig. 5c shows that the CMGK@PdNPs were spherical in shape with a smooth surface. The average particle size distribution histogram is drawn by counting about 100 PdNPs (Fig. 5d). The mean size of the PdNPs was found to be 7 ± 2 nm. The TEM images CMBG@PdNPs showed small-sized nanoparticles.

3.3. Mechanism of BG@PdNPs and CMBG@PdNPs formation

The synthesized BG@PdNPs and CMBG@PdNPs were characterized using several physiochemical characterization techniques. According to FTIR, the BG shows the presence of several functional groups such as hydroxyl, amino, carboxyl, and carbonyl groups. The modified BG contains a -CH_2COOH group along with the other functional groups. Under microwave irradiation, the functional groups of BG bound with the Pd^{2+} ions and reduced them to PdNPs, further preventing their aggregation. Whereas the CMBG of - CH_2COOH groups bound with the Pd^{2+} ions and rapidly reduced them to PdNPs and further prevented them from aggregation. In the FTIR spectra of BG and BG@PdNPs, the shifting of N—H /O-H and C=O peaks 3390–3365, 1680–1700 cm^{-1}, respectively, indicated the formation of BG@PdNPs. In the FTIR spectra of CMBG and CMBG@PdNPs, the shifting of N-H/O-H and C=O peaks 3400–3375, 1750–1720 cm^{-1} respectively indicated the formation of CMBG@PdNPs [53].

As these functional groups are complex in nature, it was confirmed by FTIR wherein it was noticed that hydroxyl, carbonyl, and carboxylic groups had strong affinities for binding with palladium ions in order to form a protective surface layer around the PdNPs that stops aggregation. A possible nanoparticle formation mechanism is presented in Fig. 6.

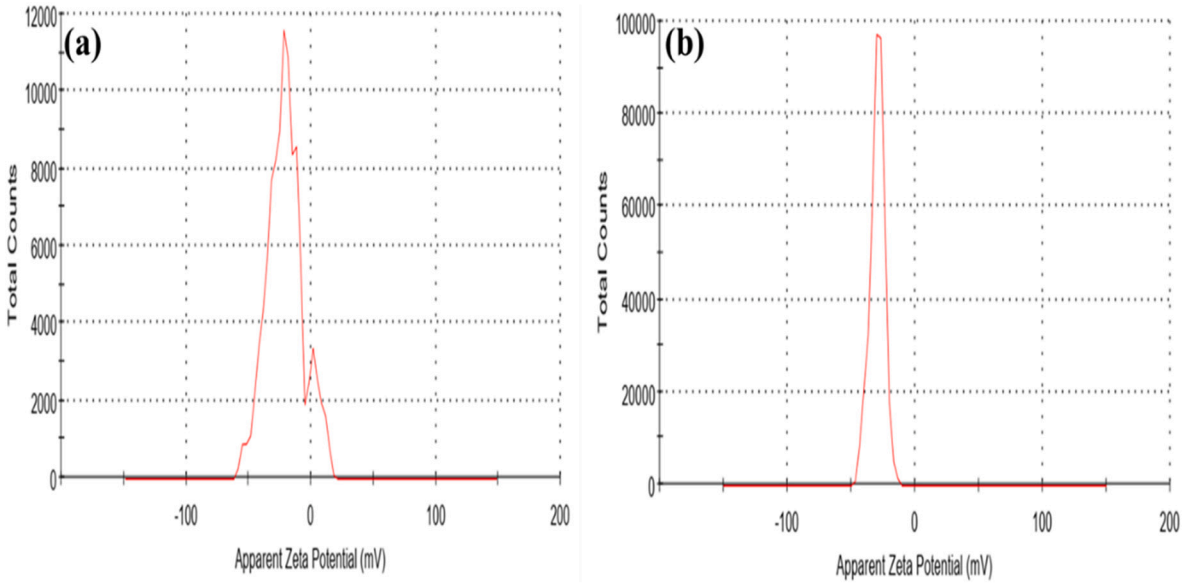

Fig. 4. Zeta potential of BG@PdNPs and CMBG@PdNPs.

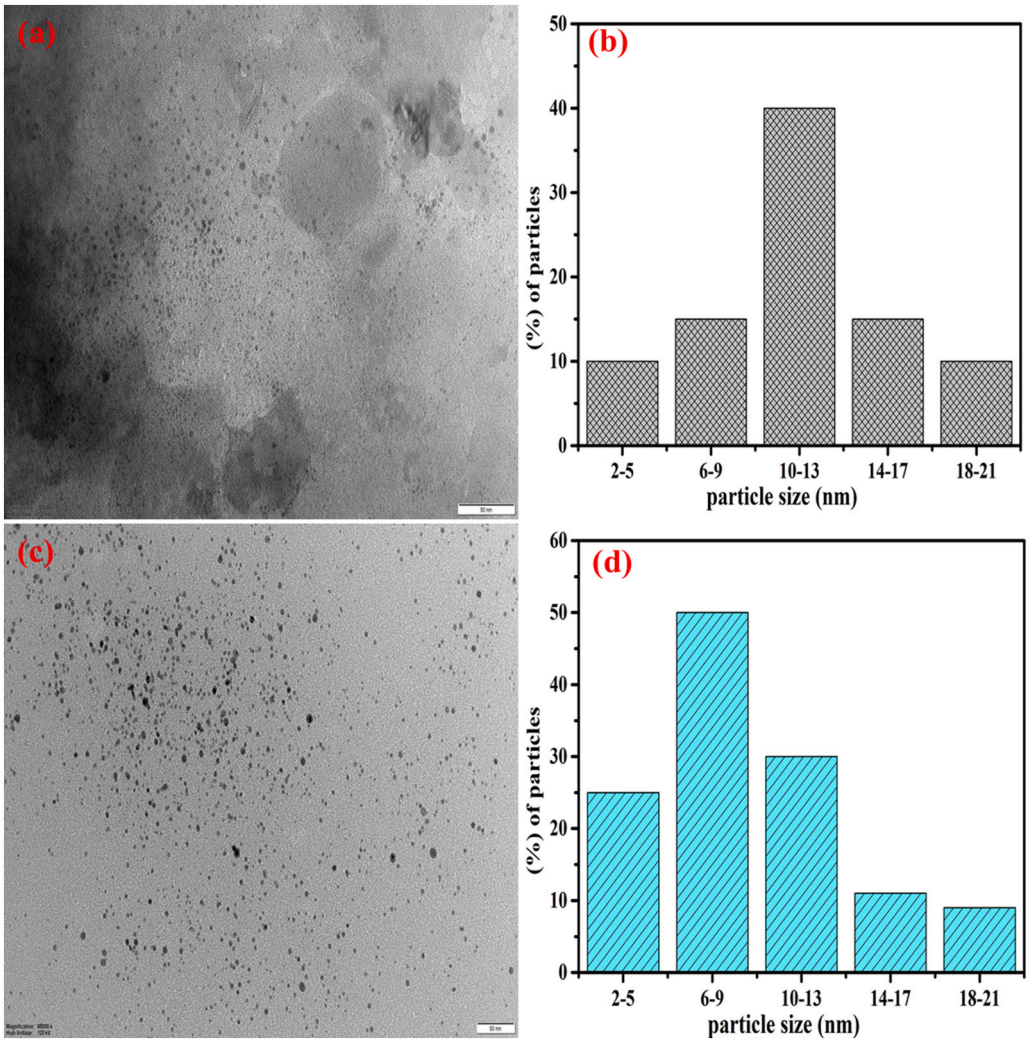

Fig. 5. (a) TEM images of BG@PdNPs; (b) Particle size distribution histogram ofPdNPs; (c) TEM images of CMBG@PdNPs; (d) Particle size distribution histogram of PdNPs.

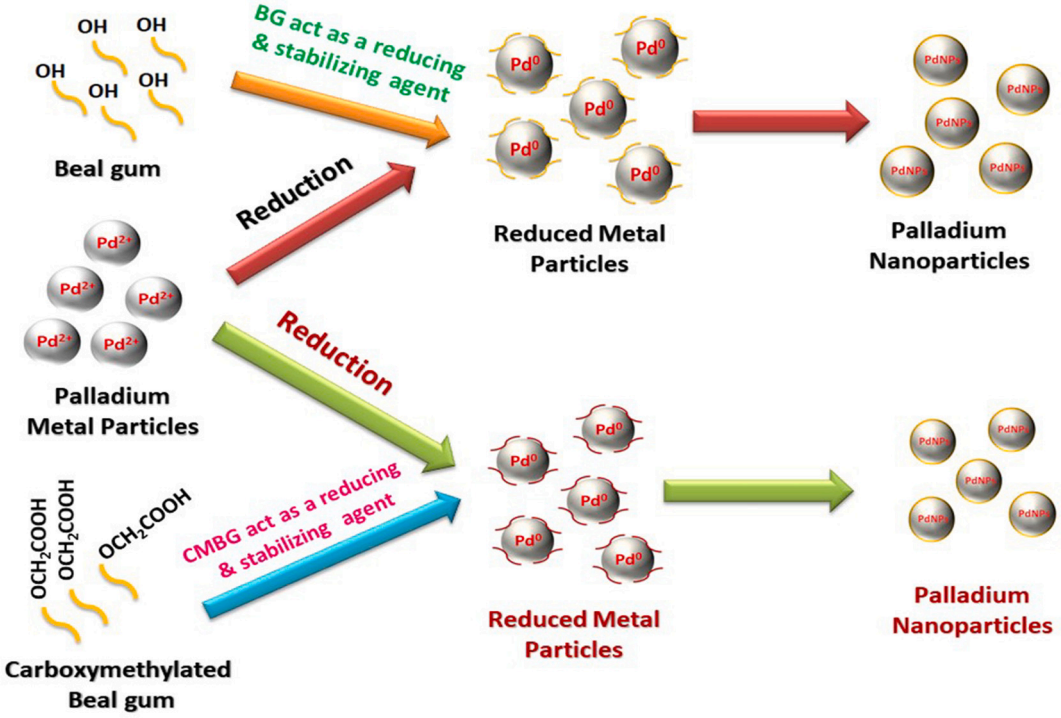

Fig. 6. Mechanism of BG@PdNPs and CMBG@PdNPs formation.

3.4. Catalytic activity of BG@PdNPs and CMBG@PdNPs

3.4.1. MO dye degradation studies

Many chemists have been using $NaBH_4$ as a strong reducing agent for the reduction of the dyes [56,57]. In the present investigation, BG@PdNPs, and CMBG@PdNPs are used as catalysts to remove low concentrations of MO dye by the reduction reaction. Catalytic reduction efficiency of BG @ PdNPs and CMBG @ PdNPs were assessed using MO dye in the presence of $NaBH_4$. Initially, the UV-visible spectra of MO dye were recorded. The UV-visible spectra of MO dye showed two distinct absorption peaks at 340 and 465 nm. MO dye reduction studies were performed by using $NaBH_4$, but there is no noticeable change in the peak intensities even after 30 min (fig. S6). Therefore, it concludes that the MO dye reduction was not complete. However, the addition of a small amount of BG@PdNPs to the mixture prompts the reduction of MO completely within 6 min (Fig. 7a). The catalytic performance of CMBG@PdNPs was also tested by using MO dye in the presence of $NaBH_4$. The reduction of MO was completed within 4 min (Fig. 7b). The rapid decrease in the intensity of two absorption peaks of MO dye with time indicates a complete reduction of MO dye in the presence of CMBG@PdNPs [58,59]. The complete reduction of MO dye takes place in 6 min and 4 min for BG@PdNPs and CMBG@PdNPs, respectively [59]. These results concluded that CMBG@PdNPs have high catalytic activity compared to BG@PdNPs. The efficacy of MO dye was found to be over 94% with BG@PdNPs. The plot of ln (A_t/A_0) versus time (Fig. 7c) yields linear relation ($R^2 = 0.97$), indicating that the pseudo-first-order kinetics and rate constant was found to be 0.964 min^{-1}. However, the efficiency of MO dye was found to be over 96% with the

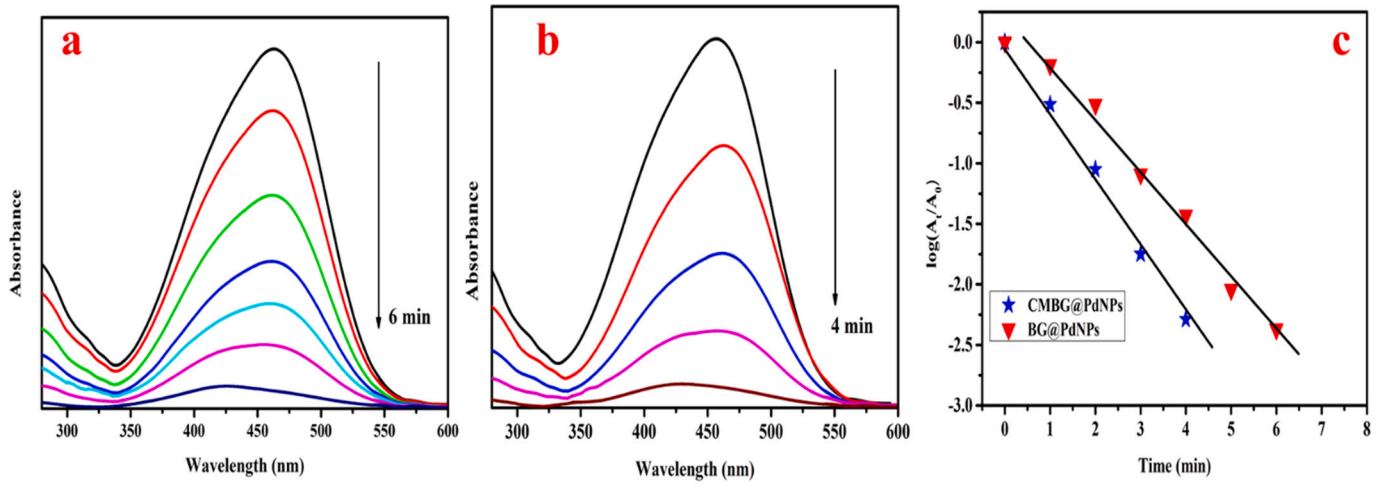

Fig. 7. Catalytic reduction of MO dye: **a)** UV-visible spectra recorded during the reduction of MO dye with $NaBH_4$ in the presence of BG@PdNPs**; b)** UV-visible absorption spectra recorded during the reduction of MO dye with $NaBH_4$ in the presence of CMBG@PdNPs; **c)** plot of ln (A_t/A_0) vs time for the reduction of MO dye with BG@PdNPs and CMBG@PdNPs.

CMBG@PdNPs, and the plot of ln (A_t/A_0) versus time (Fig. 7c) yielded linear relation (R^2 = 0.95), indicating that the pseudo-first-order kinetics and rate constant was found to be 1.192 min^{-1}.

3.4.2. MR dye degradation studies

MR dye is used as an indicator in chemical analysis in the laboratory and also used in textiles for coloring [60]. It causes skin and eye irritation. Prolonged exposure causes to damage the organs (liver). It may cause respiratory tract infection and gastrointestinal digestion problems. Sustainable technologies are essential for the degradation of MR dyes without harming the environment. Catalytic reduction efficacy of BG @ PdNPs and CMBG @ PdNPs were tested using MR dye in the presence of $NaBH_4$. Initially, the UV-visible absorption spectra of MR dye were recorded for reference. The electronic spectra of MR dye showed an absorption maximum at 530 nm ($\pi - \pi^*$). The catalytic reduction of MR dye was evaluated using BG@PdNPs. MR dye reduction studies were initially performed using $NaBH_4$ catalyst, but there is no noticeable change in the peak intensity even after 15 min. It concludes that the MR dye reduction was not completed (Fig.S7). However, 5 mg of BG@PdNPs was added to the reaction mixture, MR reduction was completed within 7 min (Fig. 8a). The catalytic performance of CMBG@PdNPs was also examined by using MR dye in the presence of $NaBH_4$. The reduction of MR dye was completed within 5 min (Fig. 8b). Complete disappearance of maximum absorption wavelength of MR dye (λ_{max} = 530 nm) was observed with time, which indicates a complete reduction of MR dye in the presence of CMBG@PdNPs. The complete reduction of MR dye takes place in 7 min and 5 min for BG@PdNPs and CMBG@PdNPs, respectively. These results concluded that the CMBG@PdNPs have higher catalytic activity than BG@PdNPs [61,62]. The efficacy of MO dye was found to be over 93% with the BG@PdNPs, and the plot of ln(A_t/A_0) versus time (Fig. 8c) yielded linear relation (R^2 = 0.99), indicating that the pseudo-first-order kinetics and rate constant was found to be 0.742 s^{-1} at room temperature [63]. However, the efficiency of MO dye was found to be over 95% with the CMBG@PdNPs, and the plot of ln(A_t/A_0) versus time (Fig. 8c) yield linear relation (R^2 = 0.95), indicating that the pseudo-first-order kinetics and rate constant was found to be 1.092 min^{-1}.

3.4.3. Rhodamine-B dye degradation studies

Rhodamine auramine stain is used to identify mycobacteria directly from clinical samples. RhB is an important dye used in the textile industry. Releasing RhB into the environment is dangerous to aquatic life as, in many cases, it is also mutagenic and carcinogenic for both humans and animals [59]. Catalytic reduction efficiency of BG@PdNPs and CMBG@PdNPs were tested using RhB dye in the presence of $NaBH_4$. Initially, we recorded the UV-visible absorption spectra of RhB dye. The UV-visible spectra of RhB dye aqueous solution showed absorption maximum at 550 nm. RhB dye reduction studies were initially performed using $NaBH_4$ catalyst. Only a slight decrease in the peak intensities was observed after 30 min. It concludes that the RhB dye reduction was not completed (Fig.S8). However, by adding BG@PdNPs to the reaction mixture, RhB dye reduction was completed within 6 min (Fig. 9a). The catalytic performance of CMBG@PdNPs was also assessed by using RhB dye in the presence of $NaBH_4$. The reduction of RhB dye was completed within 4 min (Fig. 9b). The rapid decrease in the intensity of the absorption band of RhB dye with time indicates a complete reduction of RhB dye in the presence of CMBG@PdNPs. The complete reduction of RhB dye takes place in 6 min and 5 min for BG@PdNPs and CMBG@PdNPs, respectively. These results concluded that the CMBG@PdNPs have high catalytic activity compared to BG@PdNPs. The efficacy of RhB dye was found to be over 93% with the BG@PdNPs and the plot of ln(A_0/A_t) versus time (Fig. 9c) yields linear relation (R^2 = 0.99), indicating that the pseudo-first-order kinetics and rate constant was found to be 0.921 min^{-1}. However, the efficiency of RB dye was found to be over 96% with the CMBG@PdNPs and the plot of ln(A_0/A_t) versus time (Fig. 9c) yields linear relation (R^2 = 0.95), indicating that the pseudo-first-order kinetics and rate constant was found to be 1.331 min^{-1}. The catalytic reduction of.

3.4.4. Catalytic mechanism of BG@PdNPs/CMBG@PdNPs

From the aforesaid results, it was found that the reduction of dyes in the presence of $NaBH_4$ was completely negligible. But in the presence of BG@PdNPs/CMBG@PdNPs and $NaBH_4$, a rapid reduction of dyes was observed. From these observations, it is concluded BG@PdNPs and CMBG@PdNPs act as good catalysts for the reduction of MO, MR, and RhB dyes. Based on this, a reasonable mechanism is proposed for the reduction of the dyes (Fig. 10). In the presence of palladium nanoparticles (BG@PdNPs/CMBG@PdNPs), both BH_4^- ions and dye molecules are absorbed together on the surface of PdNPs [53]. Through electrostatic interaction, PdNPs play a key role in the transfer of electrons from BH_4^- (donor) to the analytes (accepter) and all these reactions happen at the surface of PdNPs. As a result of the electron transfer, the dyes will be reduced at the surface of PdNPs [38]. Finally, the formed products are desorbed from the surface of the PdNPs and diffuse out into the bulk of the solution.

Name of dye	Catalyst	Time	Reference
MO	Neem leaves@CuNPs	30 min	[64]

(continued on next page)

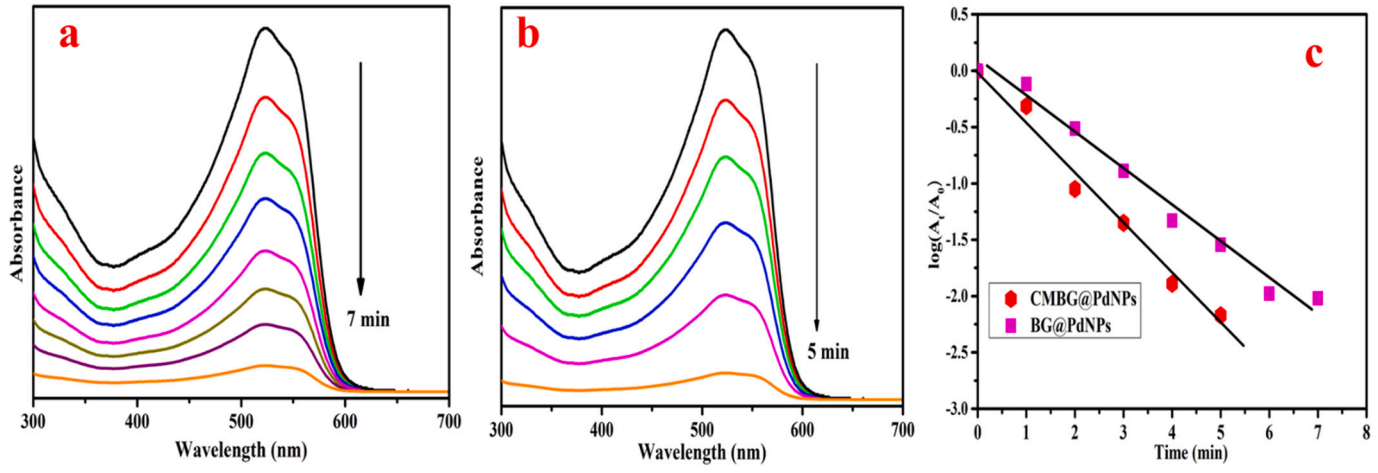

Fig. 8. Catalytic reduction of MR dye: **a)** UV-visible spectra were recorded during the reduction of MR dye with $NaBH_4$ in the presence of BG@PdNPs**; b)** UV-visible absorption spectra were recorded during the reduction of MO dye with $NaBH_4$ in the presence of CMBG@PdNPs; **c)** plot of ln (A_t/A_0) vs time for the reduction of MO dye with BG@PdNPs and CMBG@PdNPs.

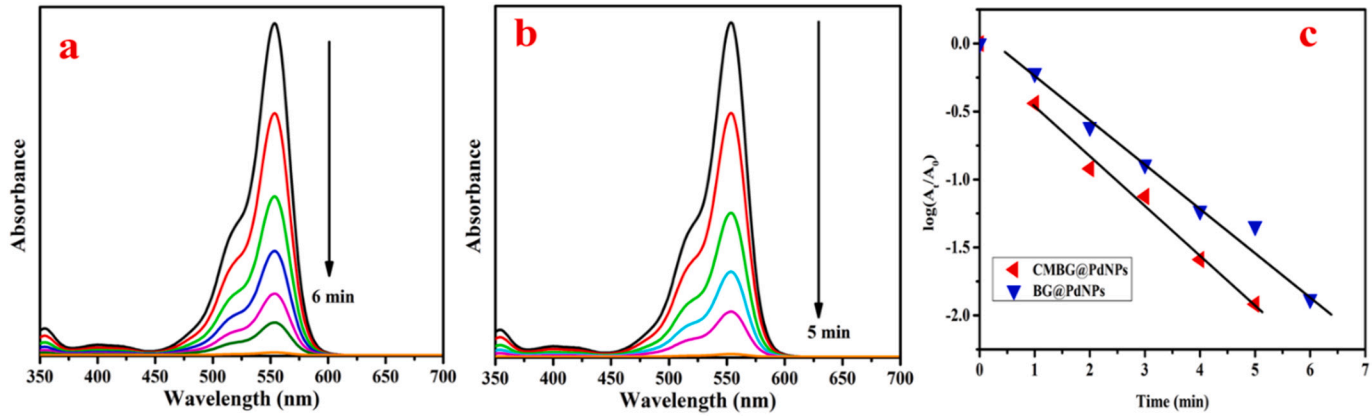

Fig. 9. Catalytic reduction of RhB dye: **a)** UV-visible absorption spectra recorded during the reduction of RhB dye with $NaBH_4$ in the presence of BG@PdNPs; **b)** UV-visible absorption spectra recorded during the reduction of RhB dye with $NaBH_4$ in the presence of CMBG@PdNPs; **c)** plot of ln (A_t/A_0) vs time for the reduction of RhB dye with BG@PdNPs and CMBG@PdNPs.

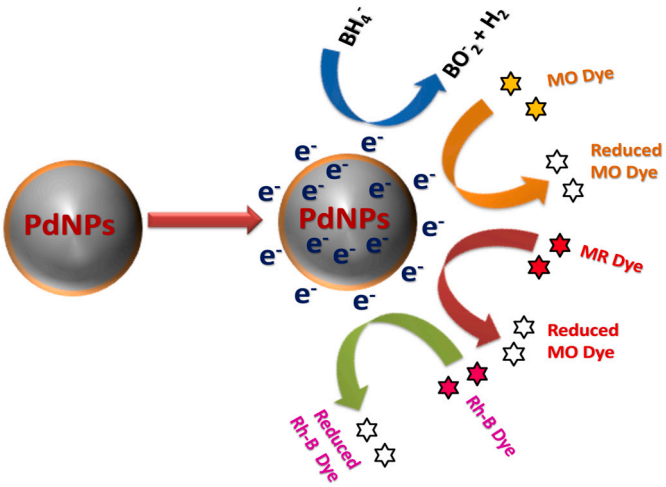

Fig. 10. Schematic representation of plausible mechanism for the reduction of MO, MR, and RhB dyes in the Presence of BG@PdNPs/CMBG@PdNPs and $NaBH_4$.

(*continued*)

Name of dye	Catalyst	Time	Reference
	Dalspinin@AuNPs	10 min	[61]
	green alga@AgNPs	30 min	[62]
	Trigonella foenum-graecum seeds@AgNPs	21 min	[65]
	Pd-NanoCata	6 min	[66]
	AgNPs	30 min	[67]
	CMBG@PdNPs	4 min	Present work
MR	ginger powder@AgNPs	10 min	[68]
	Ag/TP nanocomposites exhibited	10 min	[69]
	Psidium guajava@CuNPs	14 min	[70]
	onion extract@ AgNPs	30 min	[67]
	CMBG@PdNPs	5 min	Present work
RhB	Bael Gum@AgNPs	10 min	[71]
	MC-PDA-Ag	20 min	[72]
	ANL@AuNPs	120 min	[73]
	Colocasia esculentaAgNPs	7 min	[69]
	CMBG@PdNPs	5 min	Present work

3.4.5. Recyclability of CMBG@PdNPs catalysts

The recyclability of a catalyst is an important requirement in any catalytic reaction [74]. The recovery and reuse of CMBG@PdNPs catalysts were examined for several cycles of MO, MR, and RhB reduction processes. The nanoparticles were recovered from the reaction mixture after the end of the reaction. The recovered PdNPs were washed with water and ethanol, dried in a vacuum oven, and used for the next cycle [60]. The result of reusable PdNPs catalysts for the reduction of MO is shown in Fig. S9. The PdNPs exhibited little loss even after six cycles. Similarly, the recycling ability of PdNPs for the reduction reaction of MR and RhB is shown in Figs. S10 and S11, respectively. The PdNPs exhibit very little catalytic activity loss even after six cycles and high stability.

3.5. Antibacterial property of CMBG@PdNPs

Antibacterial activity of CMBG@PdNPs was examined against gram-negative and gram-positive bacteria [75]. The antibacterial activity was determined by the disc diffusion method [44]. The formed zone of inhibitions for CMBG@PdNPs are listed in Table 1. The different concentrations of PdNPs such as 100, 200, and 300 μL were used (Fig. 11). The zone of inhibition for *Pseudomonas aeruginosa* and *Escherichia coli* were 20 ± 0.3 and 21 ± 0.5. Whereas, *Bacillus subtilis* and *Bacillus megaterium* showed the zone of inhibition of 19 ± 0.5 and 18 ± 0.3. The CMBG@PdNPs showed an excellent antibacterial activity towards the *Pseudomonas aeruginosa* and *Escherichia coli* and moderate activity against *Bacillus subtilis* and *Bacillus megaterium*. The antibacterial activity of increases with the increasing concentration of CMBG @PdNPs. These results conclude that the CMBG@PdNPs have good antibacterial activity. These results suggest that CMBG@PdNPs could be used as a good antimicrobial agent in biomedical applications.

4. Conclusions

We established a simple, economically viable, and eco-friendly method for the synthesis of BG@PdNPs and CMBG@PdNPs using BG

Table 1
Antibacterial activity of BG@PdNPs and CMBG@PdNPs at different concentrations.

Microorganisms (bacteria)	Zone of inhibition (mm) at different concentrations			Amoxycillin (standard)
	100 μl	200 μl	300 μl	
Bacillus subtilis	15 ± 0.3	18 ± 0.4	19 ± 0.5	20 ± 0.1
Pseudomonas Aeruginosa	15 ± 0.5	19 ± 0.2	20 ± 0.3	25 ± 0.4
Escherichia coli	16 ± 0.4	18 ± 0.4	21 ± 0.5	23 ± 0.3
Bacillus megaterium	13 ± 0.4	16 ± 0.5	18 ± 0.3	21 ± 0.2

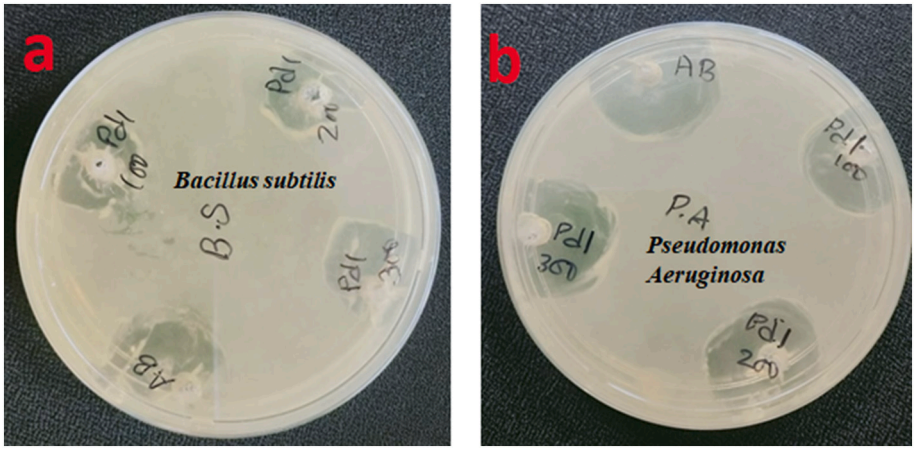

Fig. 11. Antibacterial activity of CMBG@PdNPs.

and CMBG. The powder XRD results showed FCC structure for BG@PdNPs and CMBG@PdNPs and found that CMBG@PdNPs was more crystalline in nature compared to BG@PdNPs. TEM analysis showed an average size of 12 ± 2 nm and 6 ± 2 nm, respectively for BG@PdNPs and CMBG@PdNPs. The BG @ PdNPs and CMBG@PdNPs showed negative zeta potential values of −19.7 mV and −22.4 mV, respectively, indicating that BG @ PdNPs and CMBG@PdNPs are stable. Zeta potential results suggest that CMBG@PdNPs are much more stable than BG@PdNPs. The BG@PdNPs and CMBG@PdNPs showed an excellent catalytic activity towards the reduction of MO, MR, and RhB dyes. The catalytic reduction reaction of these pollutants followed pseudo-first-order reaction kinetics with rate constants 0.964 min^{-1}, 0.742 min^{-1}, and 0.921 min^{-1}, respectively for BG@PdNPs whereas 1.192 min^{-1}, 1.092 min^{-1}, & 1.331 min^{-1} respectively for BG@PdNPs and CMBG@PdNPs. The present investigation concluded that the CMBG@PdNPs have rapid catalytic activity compared to BG@PdNPs. Reproducibility of the catalyst was also investigated, and it was found that CMBG@PdNPs served several times as a retrievable and reusable catalyst and is stable even after six cycles of reaction. The BG@PdNPs and CMBG@PdNPs showed good antimicrobial activity. But CMBG @ PdNPs showed better antibacterial activity than BG @ PdNPs. The present study suggests that CMBG@PdNPs could be used as an effective catalyst for the treatment of wastewater and industrial effluents contaminated by organic pollutants. These results suggest that both BG@PdNPs and CMBG@PdNPs could be used as good antimicrobial agents in biomedical applications.

CRediT authorship contribution statement

Kondaiah Seku: Investigation, Writing – original draft, Funding acquisition. **G. Bhagavanth Reddy:** Conceptualization, Methodology. **Syed Sulaiman Hussaini:** Resources, Project administration. **Babu Pejjai:** Formal analysis, Data curation. **Mushtaq Hussain:** Formal analysis. **D. Madhusudan Reddy:** Data curation. **Mahmoud A.K. Khazaleh:** Data curation. **Girija Mangatayaru:** Data curation, Visualization.

Declaration of competing interest

The authors declare that they do not have any conflict of interest.

Acknowledgement

Dr Kondaiah Seku is thankful to The Ministry of Higher Education, Research and Innovation (MOHERI), Sultanate of Oman, for the financial support from the MOHERI Research Grant (Proposal ID: MOHERI/BFP/RGP/EBR/20/253).

References

[1] N. Dasgupta, S. Ranjan, D. Mundekkad, C. Ramalingam, R. Shanker, A. Kumar, Nanotechnology in agro-food: from field to plate, Food Res. Int. 69 (2015) 381–400, https://doi.org/10.1016/J.FOODRES.2015.01.005.
[2] T. Singh, S. Shukla, P. Kumar, V. Wahla, V.K. Bajpai, I.A. Rather, Application of nanotechnology in food science: perception and overview, Front. Microbiol. 8 (2017) 1501, https://doi.org/10.3389/fmicb.2017.01501.
[3] S. Contera, Nano in medicine, in: Nano Comes to Life, Princeton University Press, 2019, pp. 97–135, https://doi.org/10.2307/j.ctvh1dvwh.8.
[4] G. Fan, Y. Jiang, J. Xin, Z. Zhang, X. Fu, P. Xie, C. Cheng, Y. Liu, Y. Qu, K. Sun, R. Fan, Facile synthesis of Fe@Fe3C/C nanocomposites derived from bulrush for excellent electromagnetic wave-absorbing properties, ACS Sustain. Chem. Eng. 7 (2019) 18765–18774, https://doi.org/10.1021/ACSSUSCHEMENG.9B02913/SUPPL_FILE/SC9B02913_SI_001.PDF.
[5] Y. Ma, X. Xie, W. Yang, Z. Yu, X. Sun, Y. Zhang, X. Yang, H. Kimura, C. Hou, Z. Guo, W. Du, Recent advances in transition metal oxides with different dimensions as electrodes for high-performance supercapacitors, Adv. Compos. Hybrid Mater. 44 (4) (2021) 906–924, https://doi.org/10.1007/S42114-021-00358-2, 2021.
[6] M. Shahid, Z.H. Farooqi, R. Begum, M. Arif, W. Wu, A. Irfan, Hybrid Microgels for Catalytic and Photocatalytic Removal of Nitroarenes and Organic Dyes From Aqueous Medium: A Review 50, 2019, pp. 513–537, https://doi.org/10.1080/10408347.2019.1663148.
[7] A. Galdames, L. Ruiz-Rubio, M. Orueta, M. Sánchez-Arzalluz, J.L. Vilas-Vilela, Zero-valent iron nanoparticles for soil and groundwater remediation, Int. J. Environ. Res. Public Health 17 (2020) 1–23, https://doi.org/10.3390/ijerph17165817.
[8] R. Kumar, A. Umar, R. Kumar, M.S. Chauhan, G. Kumar, S. Chauhan, Engineered science spindle-like co 3 O 4-ZnO nanocomposites scaffold for hydrazine sensing and photocatalytic degradation of rhodamine B dye, Eng. Sci. 16 (2021) 288–300, https://doi.org/10.30919/es8d548.
[9] D. Rohilla, S. Chaudhary, A. Umar, Engineered science An overview of advanced nanomaterials for sensor applications, Eng. Sci. 16 (2021) 47–70, https://doi.org/10.30919/es8d552.
[10] Y. Zhang, Y. Luo, ES food and agroforestry naturally derived nanomaterials for multidisciplinary applications and beyond, ES Food Agrofor. 4 (2021) 1–2, https://doi.org/10.30919/esfaf484.
[11] M.J. Capeness, V. Echavarri-Bravo, L.E. Horsfall, Production of biogenic nanoparticles for the reduction of 4-Nitrophenol and oxidative laccase-like reactions, Front. Microbiol. 10 (2019) 997, https://doi.org/10.3389/fmicb.2019.00997.
[12] M. Arif, Z.H. Farooqi, A. Irfan, R. Begum, Gold nanoparticles and polymer microgels: last five years of their happy and successful marriage, J. Mol. Liq. 336 (2021), 116270, https://doi.org/10.1016/J.MOLLIQ.2021.116270.
[13] Z. Zhai, Q. Wu, J. Li, B. Zhou, J. Shen, Z.H. Farooqi, W. Wu, Enhanced catalysis of gold nanoparticles in microgels upon on site altering the gold–polymer interface interaction, J. Catal. 369 (2019) 462–468, https://doi.org/10.1016/J.JCAT.2018.10.037.
[14] A.B. Sengul, E. Asmatulu, Toxicity of metal and metal oxide nanoparticles: a review, Environ. Chem. Lett. 18 (2020) 1659–1683, https://doi.org/10.1007/s10311-020-01033-6.
[15] J.K. Patra, G. Das, L.F. Fraceto, E.V.R. Campos, M.D.P. Rodriguez-Torres, L. S. Acosta-Torres, L.A. Diaz-Torres, R. Grillo, M.K. Swamy, S. Sharma, S. Habtemariam, H.S. Shin, Nano based drug delivery systems: recent developments and future prospects, J. Nanobiotechnology. 16 (2018) 71, https://doi.org/10.1186/s12951-018-0392-8.
[16] R. Begum, Z.H. Farooqi, J. Xiao, E. Ahmed, A. Sharif, A. Irfan, Crosslinked polymer encapsulated palladium nanoparticles for catalytic reduction and Suzuki reactions in aqueous medium, J. Mol. Liq. 338 (2021), 116780, https://doi.org/10.1016/J.MOLLIQ.2021.116780.

[17] S.J. Lee, Y. Yu, H.J. Jung, S.S. Naik, S. Yeon, M.Y. Choi, Efficient recovery of palladium nanoparticles from industrial wastewater and their catalytic activity toward reduction of 4-nitrophenol, Chemosphere. 262 (2021), 128358, https://doi.org/10.1016/J.CHEMOSPHERE.2020.128358.
[18] D.P. O'Neal, L.R. Hirsch, N.J. Halas, J.D. Payne, J.L. West, Photo-thermal tumor ablation in mice using near infrared-absorbing nanoparticles, Cancer Lett. 209 (2004) 171–176, https://doi.org/10.1016/j.canlet.2004.02.004.
[19] I. Steinberg, D.M. Huland, O. Vermesh, H.E. Frostig, W.S. Tummers, S.S. Gambhir, Photoacoustic clinical imaging, Photoacoustics. 14 (2019) 77–98, https://doi.org/10.1016/j.pacs.2019.05.001.
[20] S. Kang, W. Shin, K. Kang, M.H. Choi, Y.J. Kim, Y.K. Kim, D.H. Min, H. Jang, Revisiting of Pd nanoparticles in Cancer treatment: all-round excellence of porous Pd Nanoplates in gene-Thermo combinational therapy, ACS Appl. Mater. Interfaces 10 (2018) 13819–13828, https://doi.org/10.1021/acsami.8b01000.
[21] J.T. Weiss, J.C. Dawson, K.G. Macleod, W. Rybski, C. Fraser, C. Torres-Sánchez, E. E. Patton, M. Bradley, N.O. Carragher, A. Unciti-Broceta, Extracellular palladium-catalysed dealkylation of 5-fluoro-1-propargyl-uracil as a bioorthogonally activated prodrug approach, Nat. Commun. 5 (2014) 1–9, https://doi.org/10.1038/ncomms4277.
[22] C.P. Adams, K.A. Walker, S.O. Obare, K.M. Docherty, Size-dependent antimicrobial effects of novel palladium nanoparticles, PLoS One 9 (2014), https://doi.org/10.1371/journal.pone.0085981.
[23] G. Fang, W. Li, X. Shen, J.M. Perez-Aguilar, Y. Chong, X. Gao, Z. Chai, C. Chen, C. Ge, R. Zhou, Differential Pd-nanocrystal facets demonstrate distinct antibacterial activity against gram-positive and gram-negative bacteria, Nat. Commun. 9 (2018), https://doi.org/10.1038/s41467-017-02502-3.
[24] L. Soleymani, Z. Fang, E.H. Sargent, S.O. Kelley, Programming the detection limits of biosensors through controlled nanostructuring, Nat. Nanotechnol. 4 (2009) 844–848, https://doi.org/10.1038/nnano.2009.276.
[25] R. Chinchilla, C. Nájera, The Sonogashira reaction: a booming methodology in synthetic organic chemistry, Chem. Rev. 107 (2007) 874–922, https://doi.org/10.1021/cr050992x.
[26] B.D. Adams, A. Chen, The role of palladium in a hydrogen economy, Mater. Today 14 (2011) 282–289, https://doi.org/10.1016/S1369-7021(11)70143-2.
[27] E. Antolini, Palladium in fuel cell catalysis, Energy Environ. Sci. (2009), https://doi.org/10.1039/b820837a.
[28] N.V. Long, D.C. Nguyen, H. Hirata, M. Ohtaki, T. Hayakawa, M. Nogami, Chemical synthesis and characterization of palladium nanoparticles, Adv. Nat. Sci. Nanosci. Nanotechnol. 1 (2010) 35012, https://doi.org/10.1088/2043-6262/1/3/035012.
[29] Z. Han, L. Dong, J. Zhang, T. Cui, S. Chen, G. Ma, X. Guo, L. Wang, Green synthesis of palladium nanoparticles using lentinan for catalytic activity and biological applications, RSC Adv. 9 (2019) 38265–38270, https://doi.org/10.1039/c9ra08051a.
[30] C. Petrarca, E. Clemente, L. Di Giampaolo, R. Mariani-Costantini, K. Leopold, R. Schindl, L.V. Lotti, R. Mangifesta, E. Sabbioni, Q. Niu, G. Bernardini, M. Di Gioacchino, Palladium nanoparticles induce disturbances in cell cycle entry and progression of peripheral blood mononuclear cells: paramount role of ions, J Immunol Res 2014 (2014), https://doi.org/10.1155/2014/295092.
[31] X. Guo, J. Zhang, Y. Cui, S. Chen, H. Sun, Q. Yang, G. Ma, L. Wang, J. Kang, Highly biocompatible jujube polysaccharide-stabilized palladium nanoparticles with excellent catalytic performance, New J. Chem. 43 (2019) 7646–7652, https://doi.org/10.1039/c9nj00950g.
[32] G. Gaikwad, P. Bangde, K. Rane, J. Stenberg, L. Borde, S. Bhagwat, P. Dandekar, R. Jain, Continuous production and separation of new biocompatible palladium nanoparticles using a droplet microreactor, Microfluid. Nanofluid. 25 (2021) 1–15, https://doi.org/10.1007/s10404-020-02410-x.
[33] A. Viswadevarayalu, P.V. Ramana, J. Sumalatha, S.A. Reddy, Biocompatible synthesis of palladium nanoparticles and their impact on fungal species, J. Nanosci. Technol. 2 (2016) 169–172.
[34] G. Sharma, S. Sharma, A. Kumar, A.H. Al-Muhtaseb, M. Naushad, A.A. Ghfar, G. T. Mola, F.J. Stadler, Guar gum and its composites as potential materials for diverse applications: a review, Carbohydr. Polym. 199 (2018) 534–545, https://doi.org/10.1016/j.carbpol.2018.07.053.
[35] R. Mohammadinejad, A. Kumar, M. Ranjbar-Mohammadi, M. Ashrafizadeh, S. S. Han, G. Khang, Z. Roveimiab, Recent advances in natural gum-based biomaterials for tissue engineering and regenerative medicine: a review, Polymers (Basel). 12 (2020) 176, https://doi.org/10.3390/polym12010176.
[36] K.C. Ivanova, E. Bazaka, Natural polymer biomaterials: Advanced applications, in: New Funct. Biomater. Med. Healthc., Woodhead Publishing, New Delhi, India, 2014, pp. 32–70.
[37] H.G. de Oliveira Barud, R.R. da Silva, H. da Silva Barud, A. Tercjak, J. Gutierrez, W. R. Lustri, O.B. de Oliveira, S.J.L. Ribeiro, A multipurpose natural and renewable polymer in medical applications: bacterial cellulose, Carbohydr. Polym. 153 (2016) 406–420, https://doi.org/10.1016/j.carbpol.2016.07.059.
[38] S.A. Kumar, M. Jarvin, S. Sharma, A. Umar, S.S.R. Inbanathan, N.P. Lalla, Facile and green synthesis of MgO nanoparticles for the degradation of Victoria blue dye under UV irradiation and their antibacterial activity, ES Food Agrofor. (2021) 14–19, https://doi.org/10.30919/esfaf519.
[39] WHO/MSD/MER/19.3, Suicide in the world global, Health Estimates 9 (3) (2019) 760–771.
[40] W.R. Miller, J.M. Munita, C.A. Arias, Mechanisms of antibiotic resistance in enterococci 12, 2014, pp. 1221–1236, https://doi.org/10.1586/14787210.2014.956092.
[41] F. Chukwumeze, A. Lenglet, R. Olubiyo, A.M. Lawal, B. Oluyide, G. Oloruntuyi, C. Ariti, D. Gomez, H. Roggeveen, C. Nwankwo, N.A. Augustine, A. Egwuenu, G. Maloba, M. Sherlock, S. Muhammad, H. Wertheim, J. Hopman, K. Clezy, Multi-drug resistance and high mortality associated with community-acquired bloodstream infections in children in conflict-affected Northwest Nigeria, Sci. Rep. 111 (11) (2021) 1–12, https://doi.org/10.1038/s41598-021-00149-1, 2021.
[42] I. Roca, M. Akova, F. Baquero, J. Carlet, M. Cavaleri, S. Coenen, J. Cohen, D. Findlay, I. Gyssens, O.E. Heure, G. Kahlmeter, H. Kruse, R. Laxminarayan, E. Liébana, L. López-Cerero, A. MacGowan, M. Martins, J. Rodríguez-Baño, J. M. Rolain, C. Segovia, B. Sigauque, E. Taconelli, E. Wellington, J. Vila, The global threat of antimicrobial resistance: science for intervention, New Microbes New Infect. 6 (2015) 22–29, https://doi.org/10.1016/J.NMNI.2015.02.007.
[43] S. Hussain, J. Joo, J. Kang, B. Kim, G.B. Braun, Z.G. She, D. Kim, A.P. Mann, T. Mölder, T. Teesalu, S. Carnazza, S. Guglielmino, M.J. Sailor, E. Ruoslahti, Antibiotic-loaded nanoparticles targeted to the site of infection enhance antibacterial efficacy, Nat. Biomed. Eng. 22 (2) (2017) 95–103, https://doi.org/10.1038/s41551-017-0187-5, 2018.
[44] R. Chanda, Phytochemical and pharmacological activity of Aegle marmelos as a potential medicinal plant: an overview, Int. J. Pharm. 6 (2008) 3.
[45] S.K. Roy, R.N. Singh, Bael fruit (Aegle marmelos)-a potential fruit for processing, Econ. Bot. 33 (1979) 203–212, https://doi.org/10.1007/BF02858290.
[46] M.S. Baliga, H.P. Bhat, N. Joseph, F. Fazal, Phytochemistry and medicinal uses of the bael fruit (Aegle marmelos Correa): a concise review, Food Res. Int. 44 (2011) 1768–1775, https://doi.org/10.1016/j.foodres.2011.02.008.
[47] S. Balasubramanian, D. Raghavachari, Green synthesis of triangular au Nanoplates: role of small molecules present in Bael gum, ACS Sustain. Chem. Eng. 5 (2017) 10317–10326, https://doi.org/10.1021/acssuschemeng.7b02346.
[48] K. Halake, H.J. Kim, M. Birajdar, B.S. Kim, H. Bae, C.C. Lee, Y.J. Kim, S. Kim, S. Ahn, S.Y. An, S.H. Jung, J. Lee, Recently developed applications for natural hydrophilic polymers, J. Ind. Eng. Chem. 40 (2016) 16–22, https://doi.org/10.1016/J.JIEC.2016.06.011.
[49] F.J. Osonga, S. Kalra, R.M. Miller, D. Isika, O.A. Sadik, Synthesis, characterization and antifungal activities of eco-friendly palladium nanoparticles, RSC Adv. 10 (2020) 5894–5904, https://doi.org/10.1039/c9ra07800b.
[50] C. Vijilvani, M.R. Bindhu, F.C. Frincy, M.S. AlSalhi, S. Sabitha, K. Saravanakumar, S. Devanesan, M. Umadevi, M.J. Aljaafreh, M. Atif, Antimicrobial and catalytic activities of biosynthesized gold, silver and palladium nanoparticles from Solanum nigurum leaves, J. Photochem. Photobiol. B Biol. 202 (2020), 111713, https://doi.org/10.1016/j.jphotobiol.2019.111713.
[51] K. Seku, B.R. Gangapuram, B. Pejjai, M. Hussain, S.S. Hussaini, N. Golla, K. K. Kadimpati, Eco-friendly synthesis of gold nanoparticles using carboxymethylated gum Cochlospermum gossypium (CMGK) and their catalytic and antibacterial applications, Chem. Pap. 73 (2019) 1695–1704, https://doi.org/10.1007/s11696-019-00722-z.
[52] K. Seku, S.S. Hussaini, B. Pejjai, M.M.S. Al Balushi, R. Dasari, N. Golla, G.B. Reddy, A rapid microwave-assisted synthesis of silver nanoparticles using Ziziphus jujuba mill fruit extract and their catalytic and antimicrobial properties, Chem. Pap. (2020), https://doi.org/10.1007/s11696-020-01386-w.
[53] K. Seku, S. Sulaiman Hussaini, N. Golla, G. Mangatayaru, S.M.V. K, S. D, R. Rapolu, B. Bandi, G. Reddy, Microwave-assisted synthesis of palladium nanoparticles using frankincense resin and evaluation of their catalytic properties, Mater. Lett. 278 (2020), https://doi.org/10.1016/j.matlet.2020.128427.
[54] B.R. Gangapuram, R. Bandi, R. Dadigala, G.M. Kotu, V. Guttena, Facile green synthesis of gold nanoparticles with carboxymethyl gum Karaya, selective and sensitive colorimetric detection of copper (II) ions, J. Clust. Sci. 28 (2017) 2873–2890, https://doi.org/10.1007/s10876-017-1264-3.
[55] S. Balasubramanian, S.R. Bezawada, R. Dhamodharan, Facile aqueous phase synthesis of (200) faceted au-AgCl cubes using Bael gum and its activity toward oxidation and detection of o-PDA, ACS Sustain. Chem. Eng. 4 (2016) 2960–2968, https://doi.org/10.1021/acssuschemeng.5b01279.
[56] Minkal, M. Ahuja, D.C. Bhatt, Carboxymethyl gum katira: synthesis, characterization and evaluation for nanoparticulate drug delivery, RSC Adv. 5 (2015) 82363–82373, https://doi.org/10.1039/c5ra11702j.
[57] M. Cheng, C. Yao, Y. Su, J. Liu, L. Xu, J. Bu, H. Wang, S. Hou, Cyclodextrin modified graphene membrane for highly selective adsorption of organic dyes and copper (II) ions, Eng. Sci. (2021) 1–9, https://doi.org/10.30919/es8d603.
[58] R.B. Rajput, S.N. Jamble, R.B. Kale, Solvothermal synthesis of Anatase TiO2 for the detoxification of methyl Orange dye with improved Photodegradation efficiency, Eng. Sci. 17 (2022) 176–184, https://doi.org/10.30919/es8d534.
[59] R. Jain, M. Mathur, S. Sikarwar, A. Mittal, Removal of the hazardous dye rhodamine B through photocatalytic and adsorption treatments, J. Environ. Manag. 85 (2007) 956–964, https://doi.org/10.1016/j.jenvman.2006.11.002.
[60] B.P. Narasaiah, B.K. Mandal, Remediation of azo-dyes based toxicity by agro-waste cotton boll peels mediated palladium nanoparticles, J. Saudi Chem. Soc. 24 (2020) 267–281, https://doi.org/10.1016/j.jscs.2019.11.003.
[61] C. Umamaheswari, A. Lakshmanan, N.S. Nagarajan, Green synthesis, characterization and catalytic degradation studies of gold nanoparticles against Congo red and methyl orange, J. Photochem. Photobiol. B Biol. 178 (2018) 33–39, https://doi.org/10.1016/J.JPHOTOBIOL.2017.10.017.
[62] D. Borah, N. Das, N. Das, A. Bhattacharjee, P. Sarmah, K. Ghosh, M. Chandel, J. Rout, P. Pandey, N.N. Ghosh, C.R. Bhattacharjee, Alga-mediated facile green synthesis of silver nanoparticles: Photophysical, catalytic and antibacterial activity, Appl. Organomet. Chem. 34 (2020), e5597, https://doi.org/10.1002/AOC.5597.
[63] L. Sun, Q. Shao, Y. Zhang, H. Jiang, S. Ge, S. Lou, J. Lin, J. Zhang, S. Wu, M. Dong, Z. Guo, N self-doped ZnO derived from microwave hydrothermal synthesized zeolitic imidazolate framework-8 toward enhanced photocatalytic degradation of methylene blue, J. Colloid Interface Sci. 565 (2020) 142–155, https://doi.org/10.1016/j.jcis.2019.12.107.

[64] N. Nagar, V. Devra, Activation of peroxodisulfate and peroxomonosulfate by green synthesized copper nanoparticles for methyl orange degradation: a kinetic study, J. Environ. Chem. Eng. 5 (2017) 5793–5800, https://doi.org/10.1016/J.JECE.2017.11.014.
[65] V.K. Vidhu, D. Philip, Catalytic Degradation of Organic Dyes Using Biosynthesized Silver Nanoparticles 56, 2014, pp. 54–62.
[66] V.J. Garole, B.C. Choudhary, S.R. Tetgure, D.J. Garole, A.U. Borse, Palladium nanocatalyst: green synthesis, characterization, and catalytic application, Int. J. Environ. Sci. Technol. 16 (2019) 7885–7892, https://doi.org/10.1007/s13762-018-2173-1.
[67] K. Chand, D. Cao, D. Eldin Fouad, A. Hussain Shah, A. Qadeer Dayo, K. Zhu, M. Nazim Lakhan, G. Mehdi, S. Dong, Green synthesis, characterization and photocatalytic application of silver nanoparticles synthesized by various plant extracts, Arab. J. Chem. 13 (2020) 8248–8261, https://doi.org/10.1016/J.ARABJC.2020.01.009.
[68] M. Ismail, M.I. Khan, S.B. Khan, K. Akhtar, M.A. Khan, A.M. Asiri, Catalytic reduction of picric acid, nitrophenols and organic azo dyes via green synthesized plant supported ag nanoparticles, J. Mol. Liq. 268 (2018) 87–101, https://doi.org/10.1016/J.MOLLIQ.2018.07.030.
[69] M. Ismail, M.I. Khan, M.A. Khan, K. Akhtar, A.M. Asiri, S.B. Khan, Plant-supported silver nanoparticles: efficient, economically viable and easily recoverable catalyst for the reduction of organic pollutants, Appl. Organomet. Chem. 33 (2019), e4971, https://doi.org/10.1002/AOC.4971.
[70] N. Sreeju, A. Rufus, D. Philip, Microwave-assisted rapid synthesis of copper nanoparticles with exceptional stability and their multifaceted applications, J. Mol. Liq. 221 (2016) 1008–1021, https://doi.org/10.1016/j.molliq.2016.06.080.
[71] R. Banu, D. Ramakrishna, G.B. Reddy, G. Veerabhadram, K.G. Mangatayaru, Facile one-pot microwave-assisted green synthesis of silver nanoparticles using Bael gum: potential application as catalyst in the reduction of organic dyes, Mater. Today Proc. 43 (2020) 2265–2273, https://doi.org/10.1016/j.matpr.2020.12.861.
[72] R. Kumar, A. Umar, R. Kumar, M.S. Chauhan, G. Kumar, S. Chauhan, Spindle-like Co3O4-ZnO Nanocomposites Scaffold for Hydrazine Sensing and Photocatalytic Degradation of Rhodamine B Dye. Https://Www.Espublisher.Com/ 16, 2021, pp. 288–300, https://doi.org/10.30919/ES8D548.
[73] D. Baruah, M. Goswami, R.N.S. Yadav, A. Yadav, A.M. Das, Biogenic synthesis of gold nanoparticles and their application in photocatalytic degradation of toxic dyes, J. Photochem. Photobiol. B Biol. 186 (2018) 51–58, https://doi.org/10.1016/j.jphotobiol.2018.07.002.
[74] G. Centi, P. Ciambelli, S. Perathoner, P. Russo, Environmental catalysis: trends and outlook, in: Catal. Today, Elsevier, 2002, pp. 3–15, https://doi.org/10.1016/S0920-5861(02)00037-8.
[75] S.R. Prasad, S.B. Teli, J. Ghosh, N.R. Prasad, V.S. Shaikh, G.M. Nazeruddin, A.G. Al-Sehemi, I. Patel, Y.I. Shaikh, A review on bio-inspired synthesis of silver nanoparticles: their antimicrobial efficacy and toxicity, Eng. Sci. 16 (2021) 90–128, https://doi.org/10.30919/es8d479.

Materials Today: Proceedings xxx (xxxx) xxx

Contents lists available at ScienceDirect

Materials Today: Proceedings

journal homepage: www.elsevier.com/locate/matpr

Synthesis of Cu-doped ZnS nano-powder by chemical co-precipitation process

Padmapriyanka Pegallapati [a], Muniramaiah Reddivari [a], Babu Pejjai [a,b], Thejasree Kummara [a], Tulasi Ramakrishna Reddy Kotte [a,*]

[a] Solar Photovoltaic Laboratory, Department of Physics, Sri Venkateswara University, Tirupati 517502, India
[b] Department of Physics, Sri Venkateswara College of Engineering, Karakambadi Road, Tirupati 517507, India

ARTICLE INFO

Article history:
Available online xxxx

Keywords:
ZnS NPs
Co-precipitation technique
Physical properties

ABSTRACT

Copper doped zinc sulphide nanopowders (ZnS: Cu NPs) were synthesized using chemical co-precipitation technique. The Cu-doping content in the NPs was varied in the range, 0–4 wt%. The undoped and Cu-doped ZnS nanoparticles were prepared at 70 °C and dried at low temperatures. The prepared powders were investigated to understand the structure, surface topography, optical and photoluminescence (PL) properties using appropriate techniques. The X-ray diffraction (XRD) studies of prepared NPs revealed the (1 1 1) plane as the dominant orientation related to the cubic structure of ZnS. Also, XRD spectra exhibited broadening of the crystal planes on increasing Cu-content in the starting solution. The topography studied revealed a change from granular shaped crystals to flower shaped surface morphology upon Cu-doping. From the optical absorption studies, it was noted that increase of Cu-doping in the starting solution, shifted the absorption edge toward the smaller wavelength. The band gap energy of the NPs was evaluated by using Tauc plots, which varied from 3.7 eV to 4.1 eV with increase of Cu-doping. The PL studies indicated a small peak at 440 nm in pure ZnS and large peak at 522 nm that are related to the characteristic bands of ZnS. The properties of ZnS: Cu NPs were analysed for their suitability for mono-grain solar cell application.

Copyright © 2023 Elsevier Ltd. All rights reserved. Selection and peer-review under responsibility of the scientific committee of the International Conference & Exposition on Mechanical, Material and Manufacturing Technology.

1. Introduction

Chalcogenide semiconductors have gained much interest over the last several decades because of excellent physical and chemical properties, which make them ideal for the development of many optoelectronic and photoluminescent devices. ZnS is an important semiconductor of this group that has a large energy gap of 3.68 eV, high optical transmittance and good luminescence emission [1–5]. The research on ZnS nanopowders (NPs) is more attracting because of the quantum confinement effect that shoots up the band gap. Many transition elements like Ag, Cu, Mn and others used in literature as dopants to alter the characteristics ZnS NPs to suite for specific application. Doped ZnS NPs exhibited interesting optical properties, particularly the decay time and emission spectra of doped layers differing from un-doped samples. Among all the transition metal dopants, Cu^{2+} is one of the strongest dopants to interact with the ZnS host lattice. Cu-doped ZnS (ZnS: Cu) powder gives many emissions over a wide spectral range. Further, the literature reports indicated that doping of ZnS with Cu resulted in shifting of the absorption edge to visible region so that Cu-doped ZnS becomes a strong luminescent material.

There are many deposition methods used in the literature to prepare ZnS films. These include hydrothermal synthesis [6], sol–gel process [7], co-precipitation method [8], wet chemical technique [9], microwave-assisted synthesis [10], micro-emulsion method [11] that were used for the preparation of pure and ZnS: Cu NPS with various morphological features. ZnS:Cu NPs were made by Srivastava [12] et al. using zinc acetate, cupric acetate, and sodium sulphide as precursors for Zn, Cu, and S, respectively, at room temperature. They also studied the effect of copper concentration on the photoconductivity characteristics of heat-treated ZnS nanopowders prepared using the chemical co-precipitation technique. Pooja Dwivedi [13] et al. investigated the impact of annealing temperature on the ferromagnetic properties of ZnS: Cu nanoparticles. In their studies, they used zinc acetate,

* Corresponding author.
E-mail address: ktrkreddy@gmail.com (T.R.R. Kotte).

https://doi.org/10.1016/j.matpr.2023.02.419
2214-7853/Copyright © 2023 Elsevier Ltd. All rights reserved. Selection and peer-review under responsibility of the scientific committee of the International Conference & Exposition on Mechanical, Material and Manufacturing Technology.

Please cite this article as: P. Pegallapati, M. Reddivari, B. Pejjai et al., Synthesis of Cu-doped ZnS nano-powder by chemical co-precipitation process, Materials Today: Proceedings, https://doi.org/10.1016/j.matpr.2023.02.419

copper nitrate and sodium sulphide flakes as precursors in chemical co-precipitation method and annealing temperatures varied from 150 °C to 450 °C. Sambasivam [14] et al. used thiophenol as a capping agent and zinc acetate, copper acetate, and sodium sulphide as precursors of Zn, Cu, and S, respectively, to form ZnS:Cu NPs, and reported the ESR and photoluminescence of ZnS NPs. Balavijayalakshmi et al. [15] investigated the physical properties of Cu-doped ZnS NPs at room temperature, prepared by chemical co-precipitation using analytical grade zinc chloride, sodium sulphide, and cupric chloride as Zn, S, and Cu precursors, respectively. Sreenivasulu et al. [16] investigated the luminescence properties of pure and ZnS: Cu nanoparticles synthesised by taking polyvinyl acetate as a capping agent and zinc acetate as Zn-precursor, copper acetate as Cu-precursor, and sodium sulphide as S-precursor.

The literature review on ZnS nanoparticles revealed that in most of the studies either expensive techniques or time-consuming process such as hydrothermal method, sol–gel process, and wet chemical method etc. have been used to synthesize ZnS: Cu nanopowders. However, in the present work, a simple and economic chemical co-precipitation method was used. Further, the literature review also revealed that ZnS: Cu nano-powders have been prepared using co-precipitation method with zinc acetate as a precursor for Zn and sodium sulphide as a precursor for S, whereas either copper chloride or copper acetate was used for Cu-doping as precursor. Some of these studies also used capping agents during the synthesis. However, in the present work, copper sulphate was used as Cu precursor and triethanolamine (TEA) as a complexion agent to synthesize ZnS: Cu nanopowders. Furthermore, in some studies, the ZnS nano-powders have synthesized at room temperature, but further processed (dried) at higher temperatures (>150 °C). However, in the current work, the powders were prepared at 70 °C and dried at 70 °C rather than higher temperatures as mentioned in the literature that could be more economical. In addition, the structural, topographical and optical properties of the ZnS: Cu powders were reported in relation to their Cu-doping content.

2. Experimental details

2.1. Chemicals used

All analytical grade zinc acetate ($Zn(CH_3CO_2)_2$), sodium sulphide (Na_2S) and copper sulphate ($CuSO_4$) were taken as the precursors for Cu, Zn, and S respectively to prepare the starting solutions. Triethanolamine (TEA) was used as the complexion agent with deionized water as solvent.

2.2. Preparation of nanopowders

Zinc acetate was dissolved in double deionized water to prepare 0.01 M Zn-precursor solution. To prepare 0.01 M S-precursor solution, sodium sulphide was dissolved in deionized water. Initially, 1 ml of TEA was added to the Zn-precursor solution and heated to 70 °C for 10 min with constant stirring. S-precursor solution was added to the Zn-precursor solution slowly drop by drop. The color of the reaction bath was changed to white with the formation of prepcipitate. The reaction bath was heated and stirred for 2 h before being cooled to room temperature. Finally, the reaction mixture was centrifuged and thoroughly washed with ethanol and deionized water. The entire reaction mixture was then placed in a vacuum oven and dried for 2 h at 70 °C. To make Cu-doped ZnS nanoparticles, copper sulphate was added to the reaction bath. In relation to Cu-doing, the prepared powders were labelled as CZS Pure (0 wt%), CZS1 (1 wt%), CZS2 (2 wt%), CZS3 (3 wt%), and CZS4 (4 wt%). The preparation of ZnS: Cu (0 – 4 wt%) nanopowders using chemical co-precipitation method is depicted in Fig. 1.

2.3. Characterization of nano powders

The prepared pure and doped ZnS NPs were characterized to investigate the structure and morphology, optical and photoluminescent behavior using appropriate techniques. The structural properties were investigated by using RIGAKU; Miniflex-600 make X-ray diffractometer with Cu Kα radiation (λ = 1.5406 Å). The morphological studies were made with Carl Zeiss EVO MA 15 scanning electron microscopy. The optical absorption behavior was investigated by a UV–Visible double beam spectrophotometer (Make: Cary 5000) using unpolarized light. YVON Florolog-3 (model: FL3-22) was used to evaluate the photoluminescent characteristics of prepared nano powders.

3. Results and discussion

3.1. Structural studies

Fig. 2 shows the X-ray diffraction spectra of Cu-doped ZnS (0–4 wt%) nano powders. The spectra revealed three broad peaks at 28.5°, 47.6°, and 56.3°. The peak broadening indicates that the grown powders were nanocrystalline in nature. The observed peaks were related to the (1 1 1), (2 2 0), and (3 1 1) orientations of ZnS, as noted in ICDD file no: 05-0566. Using these crystal planes, the structure was evaluated to be cubic. Furthermore, the undoped ZnS power had sharper peaks than the doped ones, and the peaks became broader as the Cu-doping content was increased in the powders. This indicates that Cu-doping makes the powder more nano crystalline. The absence of any other peaks showed that the prepared powders were free from impurity phases.

The size of crystallites in pure and Cu-doped ZnS nano powders was calculated using Scherrer's equation, using the (1 1 1) preferred plane, which is given below.

$$D = \frac{0.9\,\lambda}{\beta\cos\theta} \tag{1}$$

In this case, 'λ' stands for the X-ray wavelength used (λ = 1.5406 A°), and 'β' for the full width at half maximum (FWHM) of the (1 1 1) peak with the Bragg angle (θ). The as-prepared crystallite size of the prepared nano powders decreased from 7.73 nm to 3.79 nm with the increase of copper content. This could be due to the variation in ionic radii of Cu^{2+} and Zn^{2+}. The Cu^{+2} (73 pm) has a lower ionic radius than Zn^{+2} (74 pm), so any addition of Cu^{2+} to ZnS results in a decrease in the spacing between Cu^{2+} and Zn^{2+} ions in the ZnS lattice. As the dopant ion acts as a substitutional impurity, a decrease in crystallite size was observed with copper doping in the ZnS:Cu powders. A similar tendency was also reported in the literature in dip-coated ZnS with Cu, Al-doping [17], and sprayed ZnS: Cu thin films [18].

Other structural parameters including dislocation density, micro strain, and specific surface area of pure and Cu-doped ZnS NPs were also calculated in relation to the (1 1 1) plane by using the formulas given below,

$$\text{Dislocation density}, \delta = \frac{1}{D^2} \tag{2}$$

$$\text{Micro strain}, \varepsilon = \frac{\lambda}{D\sin\theta} - \frac{\beta}{4\tan\theta} \tag{3}$$

$$\text{Specific surface area (SSA)}, S = \frac{6 \times 10^3}{\mathrm{D} \times \rho} \tag{4}$$

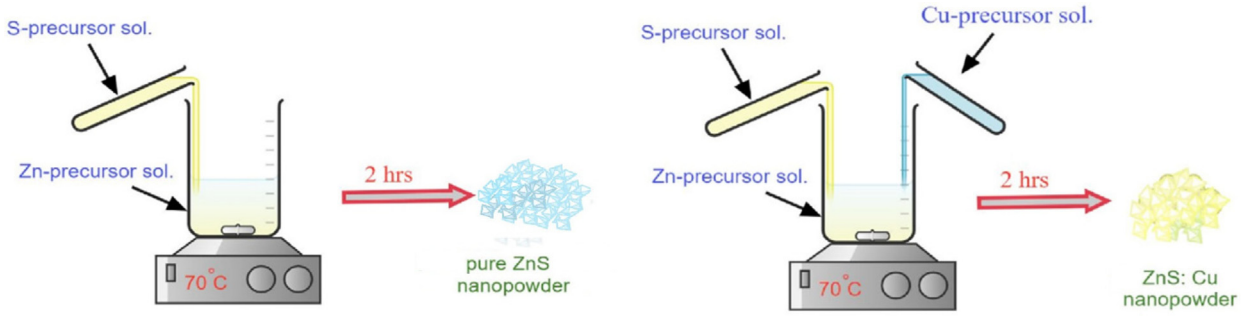

Fig. 1. Synthesis process of ZnS: Cu (0–4 wt%) nano powder.

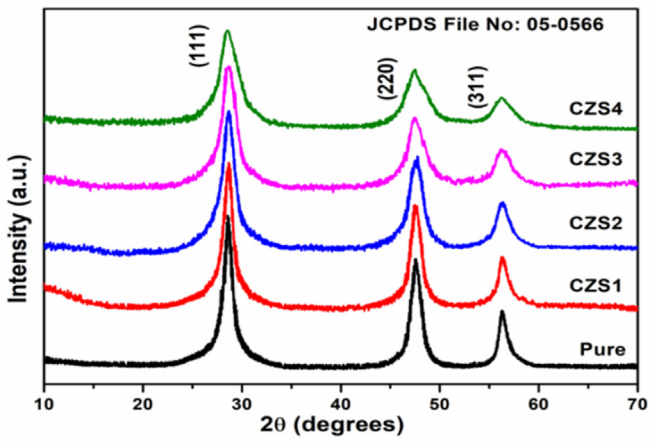

Fig. 2. XRD patterns of pure and Cu-doped ZnS nano powders.

where D = particle size, δ = dislocation density, ε = micro-strain, and ρ = ZnS density (4.09 gm cm^{-3}). The evaluated parameters of D, δ, ε and SSA are plotted in Fig. 3.

3.2. Surface morphology studies

Specific surface area is highly significant in adsorption, heterogeneous catalysis, and surface reactions [19]. The value of dislocation density was observed to be lower for undoped ZnS nano powders, which increased with raise in Cu-content in the powder. The highest value of dislocation density was observed at 4 wt% copper dopant, representing the greatest hardness among all compositions [20]. Similarly, lattice strain and SSA were also increased with Cu-doping in the powders, which indicate degradation in the crystalline quality of the powders. Mallika et al. [21] reported the same results that higher lattice strain caused a reduction in crystallinity and enhanced the peak broadening. Secondly, the high SSA value is a symptom of a high aspect ratio for nanostructured materials, resulting in an increased catalytic activity, which was reported by Sahai et al [22]. The surface morphology of both pure and ZnS: Cu nano powders was examined using a scanning electron microscope (SEM), and the related micrographs are given in Fig. 4. The figure indicates that ZnS: Cu NPs have a spherical shaped particle with a random size distribution for 1 wt% and 2 wt% and changed to flower-like morphology with increase of Cu content to 3 wt%. Further increase of Cu-doping to 4 wt% resulted in cluster formation, resembling a bunch of flowers. Compared to pure ZnS NPs, the particle size was found to be reduced upon Cu-doping. ZnS: Cu NPs with reduced particle size could be useful for light trapping in mono-grain solar cells because of multiple reflections of light rays within the surface layer.

3.3. Optical studies

3.3.1. Optical absorption

The optical characteristics of both as-grown and ZnS: Cu NPs were investigated using UV–Visible absorption spectra. The optical properties were measured from 200 nm to 1200 nm wavelength. Fig. 5 shows the optical absorption spectra of un-doped and ZnS:

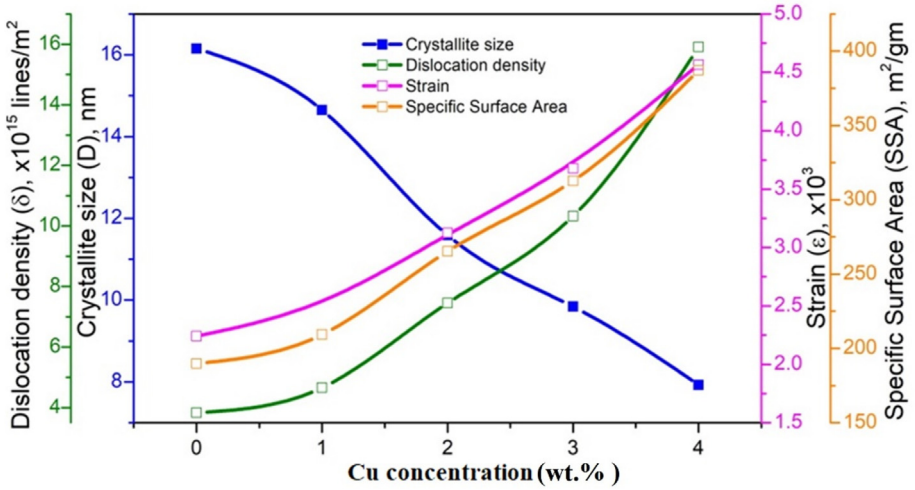

Fig. 3. Variation of Cu concentration versus dislocation density, crystallite size, strain and SSA.

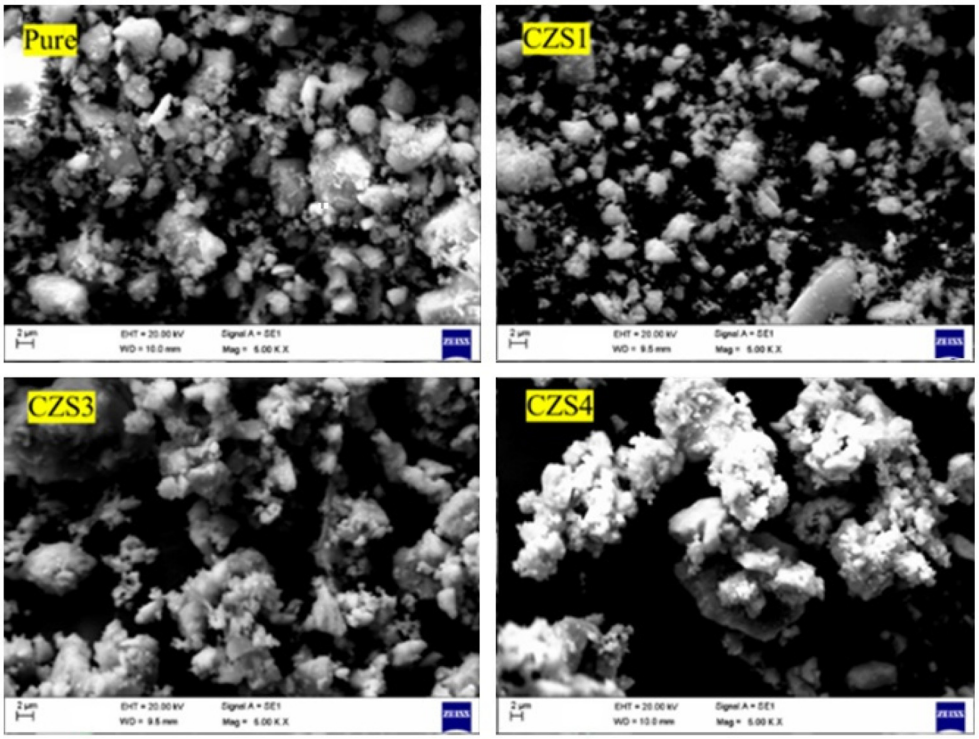

Fig. 4. SEM images of as prepared pure and ZnS: Cu nanoparticles.

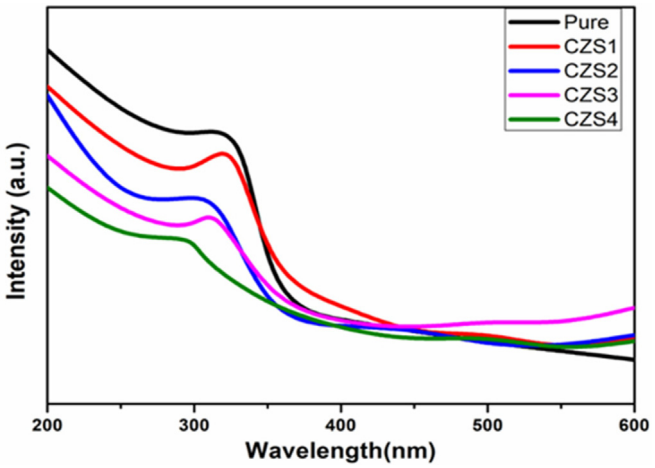

Fig. 5. Absorption spectra of Cu-doped (0–4 wt%) ZnS nanoparticles.

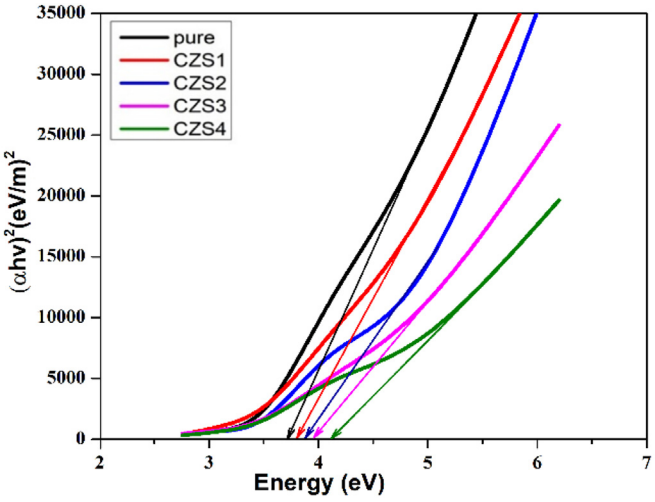

Fig. 6. Tauc plots of pure and Cu-doped ZnS nano powders.

Cu NPs. It can be noted from this figure that the absorbance of undoped and ZnS: Cu NPs decreased with increase of wavelength beyond the absorption maximum. The d-d transitions in Cu^{2+} were responsible for the decrease in absorbance in the lower wavelength region between 350 nm and 550 nm. Fig. 5 also reveals that as Cu-doping content in the powder increases, the absorption edge was shifted to the lower wavelength side, widening the band gap energy.

Using the following relation, the band gap (E_g) of the prepared ZnS: Cu NPs was evaluated,

$$(\alpha h\nu) = A(h\nu - E_g)^{1/2} \quad (5)$$

where A is constant, hv is photon energy, and α is the absorption coefficient. This indicates the presence of direct allowed transition in the prepared nano powders. The extrapolation of $(\alpha hv)^2$ versus hv plots (Fig. 6) onto the X-axis directly gives the energy gap of NPs, which increased from 3.7 eV to 4.1 eV on raising Cu-content in the nano powders. The observed change in energy gap with Cu-doping is similar to the reported results of Wang et al. [23] and Khosravi et al. [24] in literature. Further, the band gap enhancement in NPs of reduced crystallite size with increase of Cu-doping, as noted in XED and SEM analysis is in agreement with the quantum confinement effect.

3.3.2. Photoluminescence

Fig. 7 shows the PL spectra for both pure and Cu-doped ZnS nano powders synthesized at various Cu contents. The PL spectrum of undoped ZnS nano powder revealed the peaks at ~ 440 nm related to blue emission, whereas ZnS: Cu NPs showed peaks at ~ 522 nm, corresponding to green emission because of the

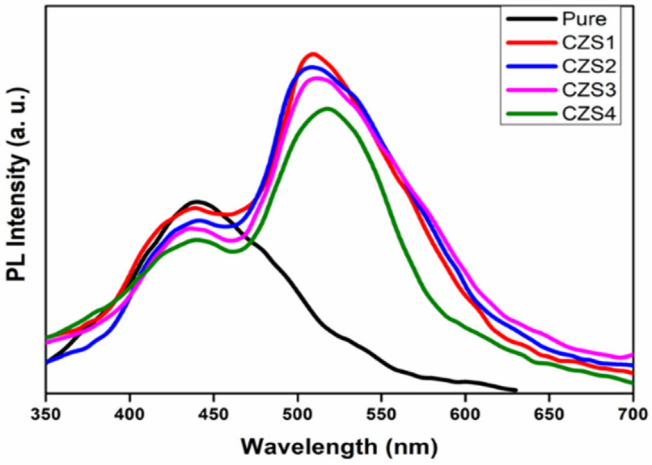

Fig. 7. Variation of PL intensity with wavelength in pure and Cu-doped nano powders.

Cu^{2+} luminescence centres. Doping of ZnS with Cu leads to the creation of defect states in the lattice when Zn^{2+} ions were replaced by Cu^{2+} ions, which resulted in the appearance of peaks at higher wavelength, ~522 nm. When compared to pure ZnS NPs, in the ZnS: Cu powder, the PL peak was moved towards the longer wavelength region, which is in agreement with previously reported results [25–28]. The emission peak began to shift towards the longer wavelength side of the spectrum as Cu-doping content in the powder was increased. When zinc ions in the ZnS lattice were substituted by copper ions upon doing, the formation of luminescence centres corresponding to copper ions triggered the appearance of green emission band in the spectra. This clearly demonstrates that Cu^{2+} ions successfully substituted Zn^{2+} ions in the ZnS lattice.

4. Conclusions

Pure and ZnS: Cu nano powders were prepared by using chemical co-precipitation technique and physical properties were investigated with respect to Cu-doping concentration. All the prepared NPs indicated the (1 1 1) peak as the dominant plane and peak broadening was noticed upon Cu-doping. This resulted in a decrease of crystallite size from 7.73 nm to 3.79 nm. A change in the morphological features was noticed with increase of Cu-doping in ZnS NPs. The energy gap of ZnS nano powders increased upon Cu-doping and the photoluminescence data showed the substitution of Zn^{2+} ions by Cu^{2+} ions in ZnS lattice. Although increase of Cu-doping has decreased the crystallinity, however, it enhanced band gap of the powder. Therefore, such large band gap powders prepared using a Cu-doping of 4 wt% could be useful as a window in mono-grain solar cell development.

Data availability

Data will be made available on request.

Declaration of Competing Interest

The authors declare that they have no known competing financial interests or personal relationships that could have appeared to influence the work reported in this paper.

Acknowledgements

The authors wish to acknowledge the financial support funded by "DEPARTMENT OF SCIENCE & TECHNOLOGY, Ministry of Science & Technology Government of India" (No. DST/INT/RMES/P-11/2016) in association with "Russian Ministry of Education and Sciences (RMES)" Government of Russia.

References

[1] D. Amico, P. Calzolari, A. Ruini, A., New energy with ZnS: novel applications for a standard transparent compound, Sci. Rep. 7 (2017) 16805, https://doi.org/10.1038/s41598-017-17156-w.
[2] D. Amaranatha Reddy, S. Sambasivam, G. Murali, B. Poornaprakash, R.P. Vijayalakshmi, Y. Aparna, B.K. Reddy, J.L. Rao, Effect of mn co-doping on the structural, optical and magnetic properties of ZnS: Cr nanoparticles, J. Alloy 537 (2012) 208–215, https://doi.org/10.1016/j.jallcom.2012.04.115.
[3] C.H. Compd, First-principle study on magnetic properties of Mn/Fe codoped ZnS, J. Mag. Mag. Mater. 324 (2012) 2086–2090, https://doi.org/10.1016/j.jmmm.2012.02.011.
[4] N. Mathiyazhagan, D. Natarajan, Bioremediation on effluents from Magnesite and Bauxite mines using Thiobacillus Spp and Pseudomonas Spp, J. Bioremed. Biodegr. 2 (2011) 115, https://doi.org/10.4172/2155- 6199.1000115.
[5] N. Mathiyazhagan, D. Natarajan, On a Sustainable Future of the Earth's Natural Resources, Springer, Berlin Heidelberg, Berlin, Heidelberg, 2013, pp. 493–508.
[6] T.T. Quynh Hoa, V.L. Van, T.D. Canh, N.N. Long, Preparation of ZnS nanoparticles by hydrothermal method, J. Phys. Conf. Ser. 187 (2008). 10.1088/1742-6596/187/1/012081.
[7] A. Asfaram, M. Ghaedi, S. Agarwal, I. Tyagi, V.K. Gupta, Removal of basic dye Auramine-O by ZnS: Cu nanoparticles loaded on activated carbon: optimization of parameters using response surface methodology with central composite design, RSC Adv. 5 (2015) 18438–18450, https://doi.org/10.1039/C4RA15637D.
[8] M. Kimi, L. Yuliati, M. Shamsuddin, Preparation of high activity Ga and Cu doped ZnS by hydrothermal method for hydrogen production under visible light irradiation, J. Nanomater. 16 (2015) 1–9, https://doi.org/10.1155/2015/195024.
[9] J. Hasanzadeh, A. Taherkhani, M. Ghorbani, Luminescence and structural properties of ZnS: Cu nanocrystals prepared using a wet chemical technique, Chinese J. Phys. 51 (2013) 540–550, https://doi.org/10.6122/CJP.51.540.
[10] M. Narayanan, S. Kumarasamy, M. Ranganathan, S. Kandasamy, G. Kandasamy, K. Gnanavel, Enzyme and metabolites attained in degradation of chemical pesticides Cypermethrin by Bacillus cereus, Mater. Today Proc. 33 (2020) 3640–3645, https://doi.org/10.1016/j.matpr.2020.05.722.
[11] M. Narayanan, N. Devarajan, Z. He, S. Kandasamy, V. Ashokkumar, R. Raja, I.S. Carvalho, Assessment of microbial diversity and enumeration of metal tolerant autochthonous bacteria from tailings of magnesite and bauxite mines, Mate. Today Proc. 33 (2020) 4391–4401, https://doi.org/10.1016/j.matpr.2020.07.652.
[12] R.K. Srivastava, N. Pandey, S.K. Mishra, Effect of Cu concentration on the photoconductivity properties of ZnS nanoparticles synthesized by co-precipitation method, Mater. Sci. Proc. 16 (2013) 1659–1664, https://doi.org/10.1016/j.mssp.2013.06.009.
[13] P. Dwivedi, P. Chauhan, R.K. Rawat, Effect of thermal treatment on synthesized Cu doped ZnS nanoparticles, Mater. Today Proc. (2021) 3138–3143, https://doi.org/10.1016/j.matpr.2021.02.818.
[14] S. Sambasivam, B. Sathyaseelan, D. Raja Reddy, B.K. Reddy, C.K. Jayasankar, ESR and photoluminescence properties of Cu doped ZnS nanoparticles, Spectrochim. Acta Part A: Mol. Biomol. Spectr. 71 (2008) 1503–1506, https://doi.org/10.1016/j.saa.2008.05.009.
[15] J. Balavijayalakshmi, S. Manju, Investigation of structural, optical and morphological properties of copper doped zinc sulphide nanoparticles, Mater. Sci. Semicond. Process 48 (2016) 101–105, https://doi.org/10.1016/j.mssp.2016.03.019.
[16] B. Sreenivasulu B. Rama Sagar S. Venkatramana Reddy B. Sankara Reddy Synthesis and luminescence properties of chemically synthesized ZnS nanomaterials. Ferroelectrics 577 1 2021 91 98 10.1080/00150193.2021.1916353
[17] M. Sathishkumar, M. Saroja, M. Venkatachalam, Influence of (Cu, Al) doping concentration on the structural, optical and antimicrobial activity of ZnS thin films prepared by Sol-Gel dip coating techniques, Optik 182 (2019) 774–785, https://doi.org/10.1016/j.ijleo.2019.02.014.
[18] M.S. Sreejith, D.R. Deepu, C. Sudha Kartha, K. Rajeevkumar, K.P. Vijayakumar, Tuning the properties of sprayed CuZnS films for fabrication of solar cell, Appl Phys Lett 105 (2014). 10.1063/1.4902224.
[19] J.-Y. Park, Y.-J. Lee, K.-W. Jun, J.-O. Baeg, D.J. Yim, Chemical Synthesis and Characterization of Highly Oil Dispersed MgO Nanoparticles, Ind Eng Chem 12 (2006) 882–887.
[20] R. John, R. Rajakumari, Synthesis and Characterization of Rare Earth Ion Doped Nano ZnO, Nano-Micro Lett 4 (2012) 65–72, https://doi.org/10.1007/BF03353694.

[21] Ramachandra Reddy Mallika K. Sowri babu Ch. Sujatha K. Venugopal Reddy Structural and photoluminescence properties of Mg substituted ZnO nanoparticles. Opt Mater 36 2014 879 884 10.1016/j.optmat.2013.12.015
[22] A. Sahai, N. Goswami, Structural and vibrational properties of ZnO nano particles synthesized by the chemical precipitation method, Phys. E 58 (2014) 130–137, https://doi.org/10.1016/j.physe.2013.12.009.
[23] M. Wang, L. Sun, X. Fu, C. Liao, C. Yan, Synthesis and optical properties of ZnS : Cu (II) nanoparticles, Solid State Commun. 115 (2000) 493–496, https://doi.org/10.1016/S0038-1098(00)00218-0.
[24] A.A. Khosravi, M. Kundu, L. Jatwa, S.K. Deshpande, U.A. Bhagwat, M. Sastry, S.K. Kulkarni, Green luminescence from copper doped zinc sulphide quantum particles, Appl. Phys. Lett. 67 (1995) 2702, https://doi.org/10.1063/1.114298.
[25] M. Kuppayee, G.K. Vanathi Nachiyar, V. Ramasamy, Synthesis and characterization of Cu 2+ doped ZnS nanoparticles using TOPO and SHMP as capping agents, Appl. Surf. Sci. 257 (15) (2011) 6779–6786, https://doi.org/10.1016/j.apsusc.2011.02.124.
[26] K. Manzoor, S.R. Vadera, N. Kumar, T.R.N. Kutty, Synthesis and photoluminescent properties of ZnS nanocrystals doped with copper and halogen, Mater. Chem. Phys. 82 (2003) 718–725, https://doi.org/10.1016/S0254-0584(03)00366-3.
[27] W. Zakaria, A.A. Farghali, A. Moneim, N.G. Imam, S.I. El-Dek, Outstanding features of Cu doped ZnS nanoclusters, Nanotech 29 (2018) 21, https://doi.org/10.1088/1361-6528/aab4d1.
[28] G. Murugadoss, Synthesis and photoluminescence properties of zinc sulfide nanoparticles doped with copper using effective surfactants, Particuology 11 (2013) 566–573, https://doi.org/10.1016/j.partic.2012.11.003.

Materials Science in Semiconductor Processing 168 (2023) 107821

Contents lists available at ScienceDirect

Materials Science in Semiconductor Processing

journal homepage: www.elsevier.com/locate/mssp

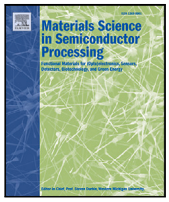

Full length article

Two-stage-processed $AgSbS_2$ films for thin-film solar cells

U. Chalapathi [a,*], Alla Subba Reddy [b], P. Reddy Prasad [c], G. Manjula [d], Sambasivam Sangaraju [e], Rajesh Cheruku [f], Bandar Ali Al-Asbahi [g], Salh Alhammadi [h], C. Parthasaradhi Reddy [i], Krithikaa Mohanarangam [j], B. Purusottam Reddy [a], Si-Hyun Park [a,*]

[a] Department of Electronic Engineering, Yeungnam University, 280 Daehak-ro, Gyeongsan, Gyeongbuk 38541, South Korea
[b] Analytical Development Laboratory, Apicore LLC, New Jersey 08873, USA
[c] Department of Chemistry, Institute of Aeronautical Engineering, Dundigal, Hyderabad, Telangana 500043, India
[d] Department of Physics, Sri Venkateswara College of Engineering, Karakambadi Road, Tirupati, India
[e] National Water & Energy Center, United Arab Emirates University, Al Ain 15551, UAE
[f] Department of Physics, School of Engineering, Dayananda Sagar University, Bengaluru 560068, India
[g] Department of Physics & Astronomy, College of Sciences, King Saud University, P.O. Box 2455, Riyadh 11451, Saudi Arabia
[h] School of Chemical Engineering, Yeungnam University, Gyeongsan-si 38541, South Korea
[i] School of Science and Humanities, Department of Physics, Vel Tech Rangarajan Dr. Sagunthala R&D Institute of Science and Technology, Avadi, Chennai, India
[j] Symbiosis Institute of Technology, Pune Campus, Symbiosis International (Deemed University), Pune, India

ARTICLE INFO

Keywords:
$AgSbS_2$ films
$AgSbS_2$ solar cells
Evaporation
Structural properties
XPS
Optical absorption

ABSTRACT

$AgSbS_2$ has shown promise as an earth-abundant, sustainable light-harvesting material for thin-film solar cells owing to its suitable optoelectronic properties and high stability. Here, we report the fabrication of $AgSbS_2$ thin films using a two-stage process (sequential evaporation of Sb/Ag layers and sulfurization at 300–400 °C for 30 min) and their characterization. X-ray diffractometry revealed the formation of Ag_3SbS_3 and Sb_2S_3 phases, single-phase $AgSbS_2$, and slight decomposition of $AgSbS_2$ and the emergence of monoclinic $AgSbS_2$ at sulfurization temperatures of 300, 350, and 400 °C, respectively. The $AgSbS_2$ films have a cubic crystal structure with a lattice parameter (a) of 0.565 nm. X-ray photoelectron spectroscopy confirmed that the valence states of Ag, Sb, and S were +1, +3, and -2, respectively. Microstructural analysis of the film prepared at 350 °C revealed highly crystalline, large-grains with an average grain size of 5 μm. Optical absorption studied suggested that the $AgSbS_2$ film prepared at 350 °C exhibited a direct bandgap of 1.61 eV. Hall measurements revealed an electrical resistivity of 1.52×10^4 Ωcm, hole mobility of 84.5 $cm^2V^{-1}s^{-1}$, and a carrier concentration of 7.95×10^{12} cm^{-3} for the $AgSbS_2$ film prepared at 350 °C. Finally, $AgSbS_2$ solar cells with glass/Mo/$AgSbS_2$/CdS/indium-tin-oxide/Ag configuration were fabricated (optimal device parameters: efficiency, 1.1%; open-circuit voltage, 519.6 mV; short-circuit current density, 6.63 mA/cm^2; and fill factor, 31.0%). The device processing conditions must be optimized to further improve the efficiency.

1. Introduction

Thin-film photovoltaics is an emerging area of research with considerable potential. The development of inexpensive and effective photovoltaic technology is particularly crucial in this regard. Recently, Cu(In,Ga)Se_2 and CdTe-based photovoltaic technologies have recently achieved optimal levels of development, with their efficiencies exceeding 22% [1]. However, the scarcity and high cost of In and the toxicity of Cd considerably impede the long-term mass production capability of these solar cells. Perovskite solar cells have also gained extensive attention and have achieved efficiencies of over 25% [2] within a span of 10 years. However, the problems associated with their short lifetime and toxicity limit their long-term utility. Ternary compound semiconductors have shown significant potential as alternatives because of their attractive features such as a direct bandgap close to the optimal value (1.45 eV) and high optical absorption coefficient (α). Among them, $AgSbS_2$ has emerged as a promising light-harvesting material because of its non-toxic and earth-abundant elements, as well as its superior stability. $AgSbS_2$ exhibits a direct bandgap of 1.61–1.75 eV [3], high α in the visible region, and p-type electrical conductivity. However, studies on $AgSbS_2$ and its solar cells are quite limited.

Wagner et al. synthesized $AgSbS_2$ films by a pulsed laser deposition in 2004 [4]. Subsequently, Ho and Lee [5] prepared $AgSbS_2$ nanoparticles by heating Ag_2S/Sb-S stacks that were deposited on TiO_2

* Corresponding authors.
E-mail addresses: chalam.uppala@gmail.com (U. Chalapathi), sihyun_park@ynu.ac.kr (S.-H. Park).

https://doi.org/10.1016/j.mssp.2023.107821
Received 14 June 2023; Received in revised form 23 August 2023; Accepted 28 August 2023
1369-8001/© 2023 Elsevier Ltd. All rights reserved.

by successive ionic layer adsorption and reaction. The $TiO_2/AgSbS_2$ electrodes were applied in semiconductor-sensitized solar cells and exhibited an efficiency of 1.28%. Capistrán-Martínez and Nair [6] developed cubic $AgSbS_2$ films and their solar cells via chemical bath deposition (CBD) and heating. They fabricated $AgSbS_2$-based planar heterojunction solar cells with a transparent conducting oxide (TCO)/CdS/$AgSbS_2$/C-Ag configuration, which exhibited a high fill factor (FF) of 0.54, open-circuit voltage (V_{OC}) of 615 mV, short-circuit current density (J_{SC}) of 1.67 mA/cm^2, and efficiency of 0.57%. Daniel et al. [7] prepared cubic $AgSbS_2$ films by annealing thermally evaporated Sb_2S_3/Ag powder and indium-tin-oxide (ITO)/$AgSbS_2$/CdS heterojunctions, which exhibited a photosensitivity of 61%. Zhang et al. [8] fabricated $AgSbS_2$ films via sequential deposition of $AgNO_3$ and $SbCl_3$ solutions onto TiO_2, followed by sulfurization in a H_2S atmosphere. Moreover, they fabricated $AgSbS_2$ semiconductor-sensitized solar cells with fluorine-doped tin oxide (FTO)/TiO_2/$AgSbS_2$/Au structure, which exhibited good photoresponse. Aiswarya et al. [9] prepared monoclinic $AgSbS_2$ by heating CBD-grown Sb_2S_3 and thermally evaporated Ag precursor stacks, and then fabricated solar cells with a glass/FTO/n-CdS/p-$AgSbS_2$/C/Ag configuration. The devices exhibited a maximum conversion efficiency of 1.5%, V_{OC} of 530 mV, J_{SC} of 5.5 mA/cm^2, and FF of 50%. Zhang et al. [3] fabricated $AgSbS_2$ solar cells FTO/TiO_2/$AgSbS_2$/Spiro-OMeTAD/Au configuration using a spin-coating and annealing approach. The solar cells exhibited an optimal efficiency of 2.25%, V_{OC} of 433 mV, J_{SC} of 10.96 mA/cm^2, and FF of 47.50%. Xie et al. [10] reported an improvement in the $AgSbS_2$ solar cell efficiency from 0.27% to 1.30% with selenization of spray-deposited $AgSbS_2$ films. They constructed solar cells in ITO/CdS/$AgSbS_2$/Au configuration, which exhibited a power conversion efficiency (PCE) of 1.30%, V_{OC} of 420 mV, J_{SC} of 8.59 mA/cm^2, and FF of 37.0%. Kai et al. [11] reported the synthesis of $AgSbS_2$ thin films and its solar cells by spray pyrolysis method. The fabricated FTO/compact TiO_2/$AgSbS_2$/spiro-OMeTAD/Au solar cells exhibited a conversion efficiency of 2.09% with a V_{OC} of 440 mV, J_{SC} of 10.49 mA/cm^2, and FF of 45.0%.

Despite these efforts to produce $AgSbS_2$ films and their devices, highly-crystalline and large-grained films have rarely been fabricated. A two-stage process involving metallic precursor deposition followed by sulfurization can permit the growth of highly crystalline and large-grained $AgSbS_2$ films. The two-stage process is relatively advantageous among other deposition methods owing to its scalability and high throughput. CZTS and CTS solar cells fabricated from the two-stage process exhibited the highest conversion efficiencies [12,13]. In the two-stage process, the precursor layer deposition and sulfurization play an important role in the growth of high-quality films. In our previous study, we have used this two-stage process to grow high-quality $CuSbS_2$ films and their solar cells [14]. In the present study, we have used this two-stage process for the growth of $AgSbS_2$ thin films and their solar cells. In the first-stage, the Ag and Sb metallic layers were thermally evaporated followed by sulfurization at different temperatures in the second stage. Highly crystalline single-phase $AgSbS_2$ films were consequently obtained, and the $AgSbS_2$ solar cells constructed in the substrate configuration exhibited a maximum conversion efficiency of 1.1%.

2. Materials and methods

Ag and Sb slugs (4N purity) that were kept in tungsten boats were used as the starting materials to prepare the $AgSbS_2$ films. Prior to the evaporation, soda-lime glass substrates were soaked in chromic acid overnight, washed with detergent soap, and ultrasonically cleaned in acetone, ethanol, and deionized water for 5 min. The cleaned glass substrates were loaded into a vacuum chamber, which was then set to a base pressure of 2×10^{-6} Torr. The thicknesses of Ag and Sb required to form 1 μm thick $AgSbS_2$ were estimated to be 173 and 305 nm, respectively. The thickness Ag was decreased to 160 nm, whereas Sb

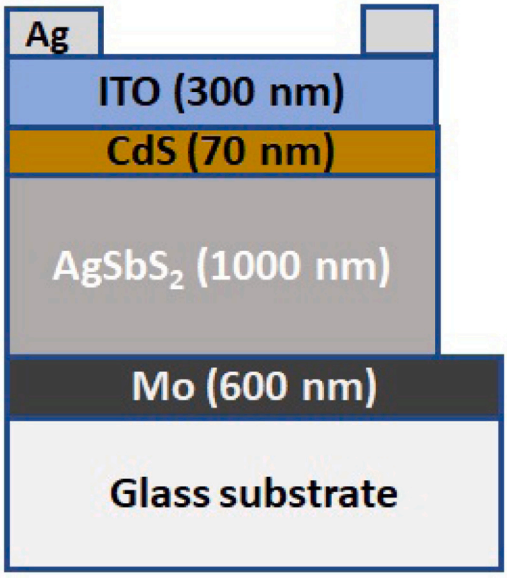

Fig. 1. Schematic of the $AgSbS_2$ thin film solar cell.

was increased to 320 nm by considering the loss of the low melting material Sb during sulfurization. Initially, a 320 nm thick Sb layer was evaporated at 3 Å/s, followed by the evaporation of 160 nm thick Ag at 3 Å/s onto the substrates. The thicknesses of the metallic stacks were measured using a quartz crystal thickness monitor. A substrate rotator was used during the evaporation to uniformly deposit the stacks. No substrate heating was employed during the evaporation. The sequentially evaporated Sb/Ag metallic stacks were subjected to sulfurization in a graphite box placed in a quartz tubular furnace to convert them into $AgSbS_2$ films. Elemental S powder was used as the source of sulfur. N_2 was filled into the quartz tube to atmospheric pressure for obtaining a higher sulfur pressure during the sulfurization to suppress the re-evaporation-induced loss of the elements. The temperature of the furnace was increased at a rate of 10 °C/min up to the desired temperature (300, 350, or 400 °C). The sulfurization was conducted for 30 min, and the temperature was finally decreased to 250 °C at 2 °C/min and then left to decrease naturally.

$AgSbS_2$-based thin-film heterojunction solar cells were fabricated in a substrate configuration with glass/Mo/$AgSbS_2$/CdS/ITO/Ag structure (as shown in Fig. 1) using $AgSbS_2$ layer (1.2 μm thick) deposited at 300–400 °C. A 600 nm thick Mo back contact layer was RF sputtered at a power of 250 W for 90 min. A 70 nm thick CdS layer was coated onto the $AgSbS_2$ absorber via CBD [14]. After the CdS deposition, the $AgSbS_2$/CdS junction was subjected to soft annealing at 100 °C for 4 h on a hot plate to promote stable junction formation. A 300 nm thick ITO window layer was RF sputtered at a power of 150 W for 60 min under an Ar pressure of 7.5×10^{-3} Torr. Finally, the Ag front grid contacts were thermally evaporated to a thickness of 200 nm. Solar cells (0.36 cm^2) were isolated by mechanical scribing for testing.

The crystal structure and phase-purity of the $AgSbS_2$ films sulfurized at different temperatures were evaluated by acquiring grazing incidence X-ray diffraction (GIXRD) patterns using a PANalytical X-ray diffractometer with a Cu K_α (0.15406 nm) source at an incident angle (ω) of 3°. The chemical state of the films was evaluated by X-ray photoelectron spectroscopy (XPS; Thermo Scientific, K-Alpha spectrometer) in the range of 0–1200 eV using an Al K_α source calibrated to the C 1s line. Prior to the XPS measurements, the samples were etched for 60 s to remove surface contamination. The morphologies and thicknesses of the films were accessed by field-emission scanning electron microscopy (FESEM; Hitachi S-4800). The composition of the films was determined by energy-dispersive X-ray spectroscopy (EDS).

The transmittance data of the films was measured by a Cary 5000 UV–Vis-NIR spectrophotometer in the wavelength range 300–2500 nm. The electrical data was measured by a Hall measurement system (ECOPIA: HMS-3000, VER 3.53). The J-V curves of the $AgSbS_2$ solar cells were acquired using a portable solar simulator (PEC-L01), in compliance with the ASTM and IEC standards for AM 1.5 G conditions. Calibration of the simulator was carried out using a silicon solar cell.

3. Results and discussion

3.1. GIXRD analysis

Fig. 2 shows the XRD patterns of the Sb/Ag stacks sulfurized at different temperatures. The standard stick patterns of the Ag_3SbS_3 (JCPDS Card No. 01-087-0709), cubic $AgSbS_2$ (JCPDS Card No. 01-089-3669), and monoclinic $AgSbS_2$ (JCPDS Card No. 019-1137) are also inserted in Fig. 2 to distinguish $AgSbS_2$ peaks. The XRD pattern of the stack sulfurized at 300 °C showed dominant and weak diffraction peaks corresponding to Ag_3SbS_3 (JCPDS card no. 01-087-0709) and Sb_2S_3 (JCPDS card no. 42-1393), respectively (see * and $ symbols in Fig. 2). The formation of the secondary Ag_3SbS_3 and Sb_2S_3 phases indicates the insufficiency of thermal energy at 300 °C for converting the Sb/Ag stacks into $AgSbS_2$. The XRD pattern of the stacks sulfurized at 350 °C showed diffraction peaks matching the standard stick pattern peaks of $AgSbS_2$ (JCPDS card no. 01-089-3669), indicating the complete conversion of the Sb/Ag stacks into secondary-phase-free $AgSbS_2$ within the XRD probe depth. The films exhibited a cubic crystal structure with a lattice parameter of 0.565 nm, which is close to the reported lattice parameter of cubic $AgSbS_2$. The crystallite size of the film, determined using Scherrer's formula [15], was found to be 62 nm. The XRD pattern of the stack sulfurized at 400 °C revealed the emergence of monoclinic $AgSbS_2$ peaks (# symbols in Fig. 2; JCPDS card no. 019-1137) along with cubic $AgSbS_2$. An additional peak corresponding to Ag_3SbS_3 (* symbols in Fig. 2) appeared at 400 °C owing to slight decomposition of the $AgSbS_2$ phase into Ag_3SbS_3 and Sb_2S_3. The disappearance of the Sb_2S_3 peaks could be due to the re-evaporation of the decomposed Sb_2S_3 at 400 °C. Monoclinic $AgSbS_2$ has been reported to be a high-temperature phase, and its presence at this temperature was due to its polymorphic nature. Based on this investigation, the formation of $AgSbS_2$ presumably occurred via a solid-state reaction of Ag/Sb during sulfurization in the following manner: $3Ag + 3Sb + 6S \rightarrow Ag_3SbS_3 + Sb_2S_3 \rightleftharpoons 2AgSbS_2$. The thicknesses of the films sulfurized at 300, 350 and 400 °C were found to be 1.2, 1.2, and 1.1 μm, respectively. We have estimated the X-ray beam sampling depth using the relation $SD = PD \sin\omega$ [16–18], where ω is the grazing incidence, and PD is the penetration depth at which the intensity of the X-ray beam reduces to 1/(e) of its initial value. The X-ray sampling depth at $\omega = 3°$ for $AgSbS_2$ was estimated to be 1050 nm.

3.2. Composition

The elemental compositions of the Sb/Ag stacks sulfurized at three different temperatures are listed in Table 1. The film sulfurized at 300 °C was highly rich in Ag but poor in Sb and S because the low temperature hindered the formation of near-stoichiometric $AgSbS_2$ films. In the stacks that were sulfurized at 350 °C, the atomic percentages of Sb and S increased, whereas that of Ag decreased drastically, with the resulting composition being similar to that of $AgSbS_2$. A further increase in the sulfurization temperature to 400 °C resulted in the formation of a slightly Sb-rich films. Overall, the film sulfurized at 350 °C showed a near-stoichiometric $AgSbS_2$ composition, considering the accuracy limits of the EDS analysis (±2 at.%).

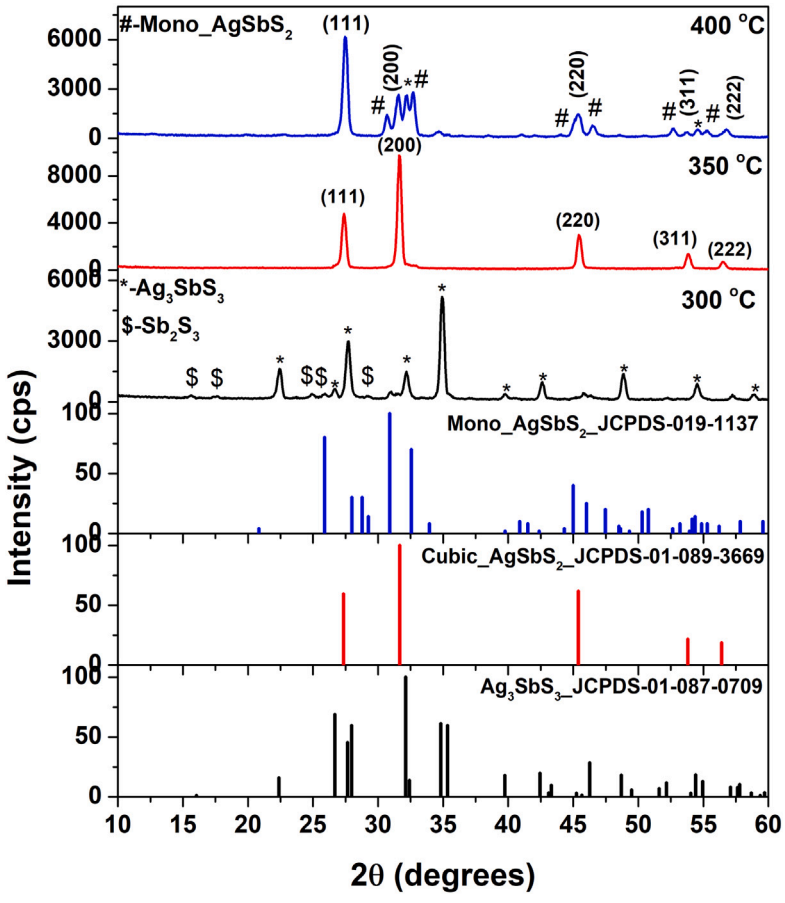

Fig. 2. GIXRD patterns of the $AgSbS_2$ films sulfurized at 300–400 °C.

Table 1
Elemental compositions of $AgSbS_2$ films sulfurized at 300–400 °C.

Sulfurization temperature	Atomic percentage			Ratio	
	Ag	Sb	S	Ag/Sb	S/(Ag+Sb)
300 °C	38.9	18.1	42.9	2.15	0.75
350 °C	24.7	25.4	49.9	0.97	1.0
400 °C	22.7	26.8	50.6	0.84	1.02

3.3. XPS analysis

XPS measurements were performed on the sample prepared at 350 °C to determine the chemical states of the films. The survey scan of the film (Fig. 3a) showed signals due to Ag, Sb, S, and Ar, whereas the high-resolution Ag3d spectrum (Fig. 3b) showed two peaks separated by 6 eV at 373.5 and 367.5 eV, which corresponded to $Ag3d_{5/2}$ and $Ag3d_{3/2}$, respectively. The peak positions and their separation indicate that the oxidation state of Ag was +1 [9,19]. The high-resolution Sb3d spectrum (Fig. 3c) showed two intense peaks that were separated by 9.4 eV at 529.3 and 538.6 eV, which corresponded to $Sb3d_{5/2}$ and $Sb3d_{3/2}$, respectively. These peak positions and their separation suggest that the oxidation state of Sb was +3 [9,19]. Additionally, two minor peaks appeared at 536.6 and 527.2 eV, which were assigned to the Sb^o state that presumably originated from the Ar^+-sputtering-induced reduction, which is commonly appeared in Sb based compounds [9,19,20]. The narrow S2p scan (Fig. 3d) showed two peaks separated by 1.1 eV at 160.9 and 162.0 eV, which were related to $S2p_{3/2}$ and $S2p_{1/2}$, respectively; these results indicate that the oxidation state of S was -2 [9,19]. Therefore, the oxidation states of the elements present in the films could be expressed as $Ag^{+1}Sb^{+3}(S^{-2})_2$.

3.4. Morphology

The surface morphologies and cross-sections of the samples sulfurized at different temperatures were assessed by FESEM (Fig. 4). The FESEM image of the film sulfurized at 300 °C showed two distinct grains with sizes in the range of 1–2 μm. The smaller particles presumably correspond to the Sb_2S_3 phase, whereas the larger ones possibly represent the Ag_3SbS_3 phase observed in the XRD pattern. The cross-sectional FESEM image of this film shows the formation of well adherent film with 1 μm grains extended vertically up to 1.2 μm. The micrograph of the film sulfurized at 350 °C revealed the formation of several 6–8 μm sized grains with a compact morphology and 3–5 μm sized grains in between them. The cross-section of this film shows the formation of columnar grains with increased grain size along the thickness (1.2 μm). The crystallization of the large grains at 350 °C could be due to the complete intermixing of the Ag_3SbS_3 and Sb_2S_3 phases and the formation of single-phase $AgSbS_2$. The surface morphology of the film sulfurized at 400 °C revealed a decrease in the grain size and a few cracks on the film surface, which could have been due to slight re-evaporation of the materials. The cross-sectional image also revealed the formation of large grains extended along the film thickness. Overall, the film formed at 350 °C exhibited a superior grain growth and a morphology appropriate for solar cell applications.

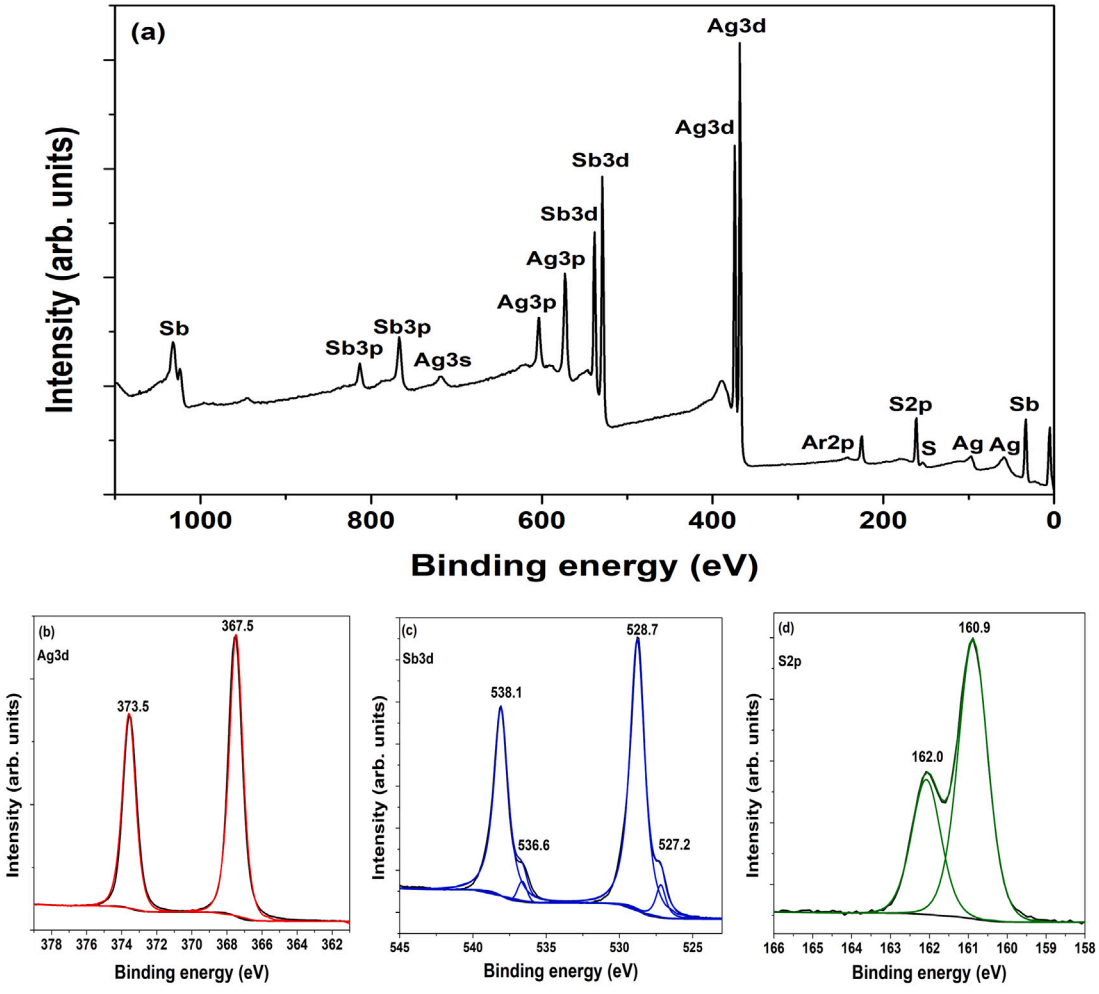

Fig. 3. (a) Survey and narrow-scan XPS profiles of the (b) Cu, (c) Sb, (d) S components of the $AgSbS_2$ film sulfurized at 350 °C.

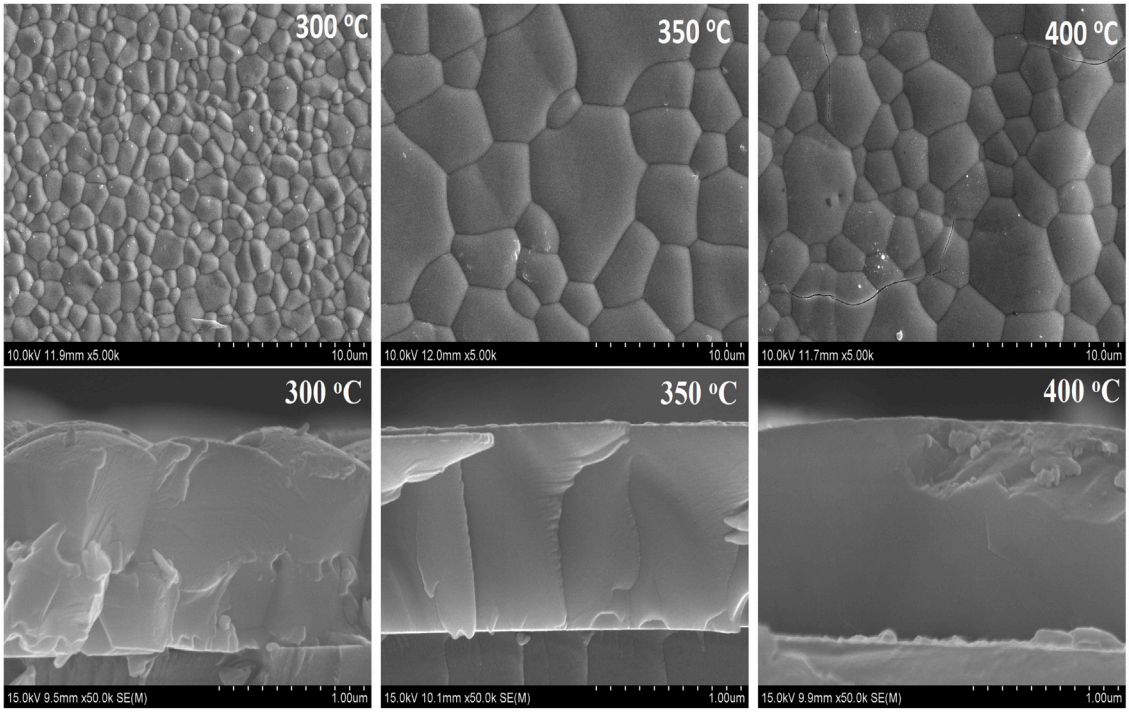

Fig. 4. Surface and cross-sectional FESEM images of the $AgSbS_2$ films sulfurized at 300–400 °C.

3.5. Optical absorption

Spectral transmittance and reflectance curves of the $AgSbS_2$ films sulfurized at different temperatures were acquired (Fig. 5a,b). The film sulfurized at 300 °C exhibited 25% transmittance at higher wavelengths and a continuous decrease in transmittance from 1500 to 750 nm. The reflectance spectrum of this film exhibit interference fringes and an onset of absorption at 750 nm. The transition observed at 750 nm might be due to the dominant Ag_3SbS_3 phase present in the film [21,22]. The film sulfurized at 350 °C showed an enhanced transmittance of over 50% at higher wavelengths and interference fringes owing to the crystallization of the compact, large-grained, and single-phase $AgSbS_2$ films, as indicated by its microstructure. The film exhibited an absorption onset from 845 to 750 nm, which corresponded to the $AgSbS_2$ phase. The reflectance spectrum also exhibit interference fringes and an onset of absorption from 845 nm corresponding to $AgSbS_2$. The film sulfurized at 400 °C showed diminished interference fringes in transmittance and reflectance curves and a continuous decrease in transmittance from 2000 nm owing to the presence of mixed phases monoclinic and cubic $AgSbS_2$ as well as Ag_3SbS_3. The onset of absorption observed at 820 to 720 nm indicates the absorption due to $AgSbS_2$ and Ag_3SbS_3 phases present in the films.

The Tauc plots were constructed for the films sulfurized at 300–400 °C to determine the optical bandgap (Fig. 6). The direct bandgap of the film sulfurized at 300 °C was found to be 1.75 eV, which is close to the reported band gap of Ag_3SbS_3 [21,22]. The direct optical bandgap of the film sulfurized at 350 °C was estimated to be 1.61 eV, which is close to the reported bandgap of $AgSbS_2$ by Zhang et al. [3]. The bandgap of the film sulfurized at 400 °C was found to be 1.71 eV. The increased bandgap of $AgSbS_2$ at 400 °C could be due to the presence of Ag_3SbS_3 secondary phase in the film.

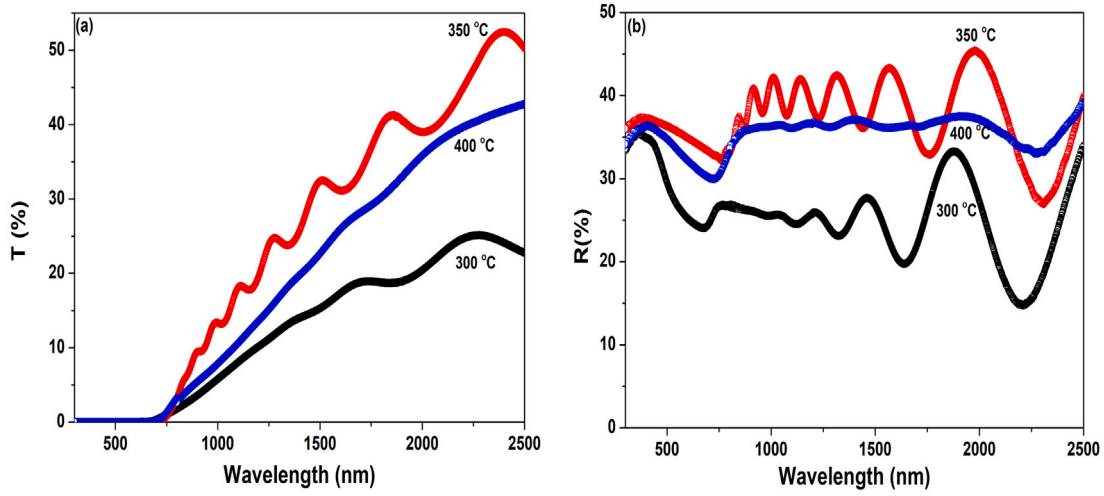

Fig. 5. (a) Spectral transmittance, and (b) reflectance spectra of the $AgSbS_2$ films sulfurized at 300–400 °C.

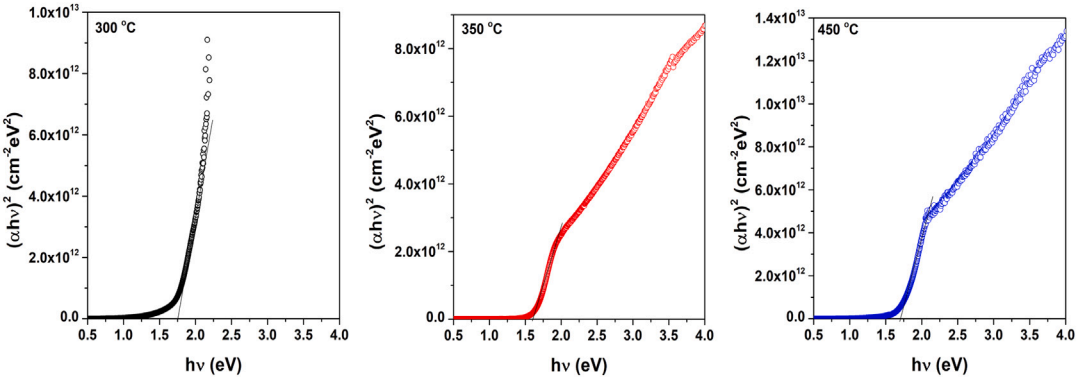

Fig. 6. Tauc plots of the $AgSbS_2$ films sulfurized at 300–400 °C.

3.6. Electrical properties

The electrical properties of the prepared $AgSbS_2$ films are listed in Table 2. The Hall coefficient of the films was determined to be positive owing to their p-type electrical conductivity. The film sulfurized at 300 °C exhibited an electrical resistivity of 4.68×10^3 Ω cm, hole mobility of 22.7 $cm^2\ V^{-1}\ s^{-1}$, and carrier concentration of 5.98×10^{13} cm^{-3}. The increased sulfurization temperature of 350 °C resulted in an increase in the electrical resistivity to 1.52×10^4 Ω cm, hole mobility to 84.5 $cm^2\ V^{-1}\ s^{-1}$, and decrease in the carrier concentration to 7.95×10^{12} cm^{-3} owing to the formation of large-grained and phase-pure $AgSbS_2$ film. The achieved hole mobility of 84.5 $cm^2\ V^{-1}\ s^{-1}$ is lower than the reported hole mobility of $AgSbS_2$ [3]. Further increase in the sulfurization temperature to 400 °C resulted in a slight decrease in electrical resistivity, hole mobility, and an increase in the carrier concentration of the film. The obtained higher carrier concentration for the films sulfurized at 300 and 400 °C than the film sulfurized at 350 °C could be due to the formation of secondary phases.

Table 2
Electrical properties of the $AgSbS_2$ thin films sulfurized at 300–400 °C.

Sulfurization temperature	Electrical properties		
	Resistivity (Ω cm)	Mobility ($cm^2\ V^{-1}\ s^{-1}$)	Carrier concentration (cm^{-3})
300 °C	4.68×10^3	22.2	5.98×10^{13}
350 °C	1.52×10^4	84.5	7.95×10^{12}
400 °C	1.11×10^4	15.1	3.69×10^{13}

3.7. Solar cell performance

$AgSbS_2$ solar cells with Mo/$AgSbS_2$/CdS/ITO/Ag structure were fabricated using the $AgSbS_2$ layers grown at 300–400 °C. The current density/voltage (J-V) characteristics and cell parameters of the $AgSbS_2$ solar cells are shown in Fig. 7(a). The solar cell prepared from the

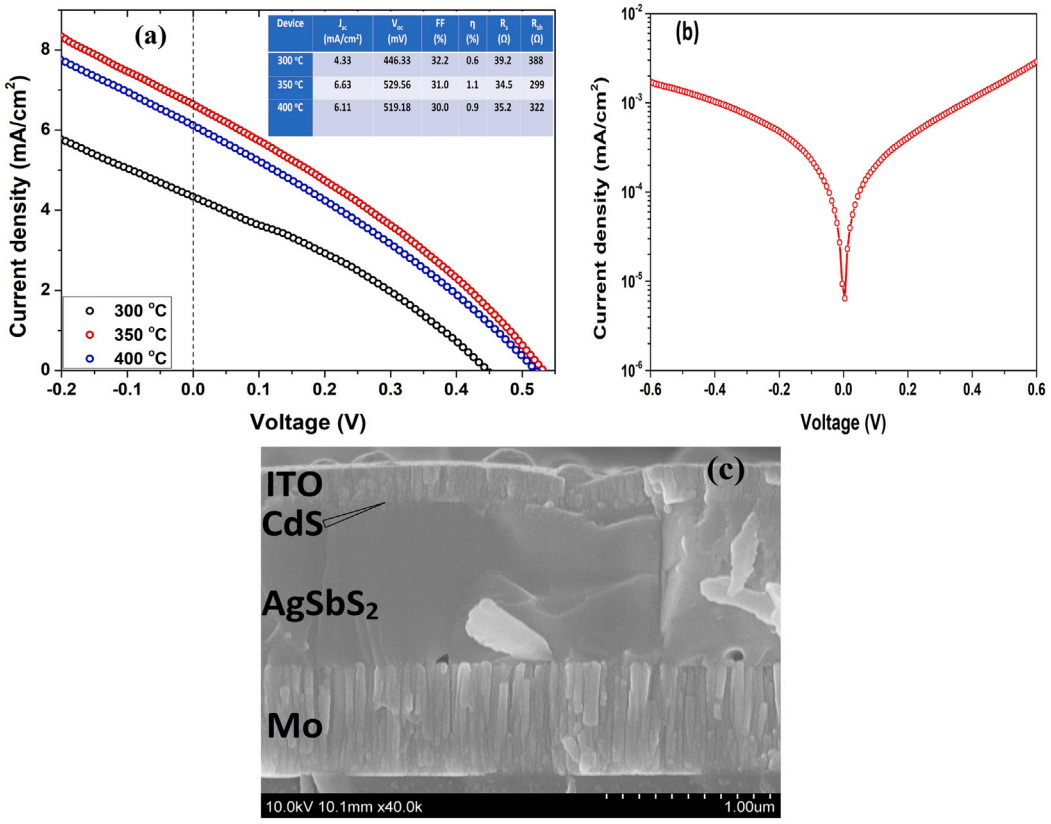

Fig. 7. (a) Light J-V characteristics of the Mo/$AgSbS_2$/CdS/ITO/Ag-structured solar cells fabricated at 300–400 °C, (b) dark J-V characteristics, and (c) cross-sectional FESEM image of the solar cell fabricated at 350 °C.

$AgSbS_2$ layer sulfurized at 300 °C, exhibited a PCE of 0.6%, J_{SC} of 4.33 mA/cm^2, V_{OC} of 446.3 mV, and FF of 32.2%. The solar cell fabricated with the $AgSbS_2$ absorber prepared at 350 °C, exhibited a maximum PCE of 1.1%, J_{SC} of 6.63 mA/cm^2, V_{OC} of 519.6 mV, and FF of 31.0%. The solar cell fabricated with the $AgSbS_2$ layer sulfurized at 400 °C, exhibited a PCE of 0.9%, J_{SC} of 6.11 mA/cm^2, V_{OC} of 519.2 mV, and FF of 30.0%. The lower device performance of the $AgSbS_2$ solar cells fabricated at 300 and 400 °C could be due to the formation of secondary phases in the absorber, whereas the increased efficiency for the solar cells fabricated at 350 °C is attributed to the formation of phase pure films with high crystallinity and large-grains. The dark J-V characteristics of the typical solar cell fabricated at 350 °C are shown in Fig. 7(b) to study the current leakage. The dark J-V curve shows low current density owing to the improved charge transport and reduced recombination loss. The cross-sectional FESEM image of the typical solar cell fabricated at 350 °C is also shown in Fig. 7(c) to see the formation of different layers in the device. The cross-sectional image of the device confirmed the formation of a compact and large-grained absorber sandwiched between the compact Mo and CdS/ITO layers. Notably, the performance of the device reported herein is considerably inferior to the previously reported highest efficiency of 2.2% for $AgSbS_2$ solar cells [3]. However, the V_{OC} of the fabricated device (519.6 mV) is higher than that reported previously. The lower FF value can be attributed to the higher series resistance and lower shunt resistance (Fig. 7a) of the constructed devices. Optimization of the parameters of each layer during the fabrication is anticipated to provide superior results, which is the scope of our future work.

4. Conclusions

$AgSbS_2$ films were prepared by sulfurizing thermally evaporated Sb/Ag metallic precursors at 300–400 °C for 30 min. The films sulfurized at 300 °C contained the Ag_3SbS_3 and Sb_2S_3 phases, whereas those sulfurized at 350 °C contained near-stoichiometric single-phase $AgSbS_2$ with a cubic crystal structure; moreover, the highly crystalline large-grained films exhibited a direct optical bandgap of 1.61 eV and a hole mobility of 84.5 cm^2 V^{-1} s^{-1}. A further increase in the sulfurization temperature to 400 °C led to the emergence of monoclinic $AgSbS_2$, dominant cubic $AgSbS_2$, and an additional Ag_3SbS_3 phase. The solar cells fabricated using the $AgSbS_2$ absorber layer that was prepared by sulfurizing the stacks at 350 °C exhibited a maximum PCE of 1.1%, V_{OC} of 519.6 mV, J_{SC} of 6.63 mA/cm^2, and FF of 31.0%. Further optimization of the processes and clarification of the properties of each layer are imperative for achieving superior device performance.

CRediT authorship contribution statement

U. Chalapathi: Writing – original draft, Software, Investigation, Formal analysis, Data curation, Conceptualization. **Alla Subba Reddy:** Methodology, Investigation. **P. Reddy Prasad:** Methodology, Investigation. **G. Manjula:** Investigation, Methodology. **Sambasivam Sangaraju:** Methodology, Investigation, Formal analysis. **Rajesh Cheruku:** Methodology, Investigation, Formal analysis. **Bandar Ali Al-Asbahi:** Visualization, Validation, Formal analysis. **Salh Alhammadi:** Visualization, Validation, Formal analysis. **C. Parthasaradhi Reddy:** Visualization, Validation. **Krithikaa Mohanarangam:** Visualization, Validation. **B. Purusottam Reddy:** Visualization, Validation, Data curation. **Si-Hyun Park:** Writing – review & editing, Supervision, Resources, Project administration, Funding acquisition.

Declaration of competing interest

The authors declare that they have no known competing financial interests or personal relationships that could have appeared to influence the work reported in this paper.

Data availability

Data will be made available on request

Acknowledgments

This work was supported by the National Research Foundation of Korea (NRF) grant funded by the Korea government (MSIT) (No. 2019R1A2C1089080). Researchers Supporting Project number (RSP2023R348), King Saud University, Riyadh, Saudi Arabia.

References

[1] M. Green, E. Dunlop, J. Hohl-Ebinger, M. Yoshita, N. Kopidakis, K. Bothe, D. Hinken, M. Rauer, X. Hao, Solar cell efficiency tables (version 60), Prog. Photovolt.: Res. Appl. 30 (1) (2022) 687–701.

[2] G.-H. Kim, D.S. Kim, Development of perovskite solar cells with >25% conversion efficiency, Joule 5 (5) (2021) 1033–1035.

[3] L. Zhang, C. Zhu, T. Chen, Solution processed $AgSbS_2$ film for efficient planar heterojunction solar cells, Appl. Phys. Let. 119 (15) (2021) 151906.

[4] T. Wagner, J. Gutwirth, P. Nemec, M. Frumar, M. Vlcek, V. Perina, A. Mackova, V. Hnatovitz, Amorphous chalcogenide $AgSbS_2$ films prepared by pulsed laser deposition, Appl. Phys. A 79 (4) (2004) 1561–1562.

[5] Y.-R. Ho, M.-W. Lee, $AgSbS_2$ semiconductor-sensitized solar cells, Electrochem. Commun. 26 (2013) 48–51.

[6] J. Capistrán-Martínez, P. Nair, Photoconductive thin films of $AgSbS_2$ with cubic crystalline structure in solar cells, Phys. Status Solidi (a) 212 (12) (2015) 2869–2876.

[7] T. Daniel, J. Henry, K. Mohanraj, G. Sivakumar, $AgSbS_2$ and Ag_3SbS_3 absorber materials for photovoltaic applications, Mater. Chem. Phys. 181 (2016) 415–421.

[8] Y. Zhang, J. Tian, K. Jiang, J. Huang, F. Li, P. Wang, H. Fan, Y. Song, $AgSbS_2$ thin film fabricated by in-situ gas-solid reaction and employed in solar cells as a light absorber, Mater. Let. 232 (2018) 82–85.

[9] A. Nadukkandy, S. Devasia, P. Abraham, S. Shaji, D.A. Avellaneda, J.A. Aguilar-Martinez, E.G. Martinez, R.F. Cienfuegos-Pelaes, B. Krishnan, Monoclinic $AgSbS_2$ thin films for photovoltaic applications: Computation, growth and characterization approaches, Mater. Sci. Semicon. Proc. 135 (2021) 106074.

[10] F. Xie, H. Tang, X. Zhao, M. Li, L. Li, J. Cheng, Thin-film solar cells using a selenized silver antimony sulfide absorber prepared by spray pyrolysis deposition, Phys. Status Solidi (RRL)–Rapid Res. Let. 15 (12) (2021) 2000514.

[11] K. Lv, C. Shi, Y. Yang, Q. Wang, X. Sun, W. Chen, The pyrolysis preparation of the compact and full-coverage $AgSbS_2$ thin films and the photovoltaic performance of the corresponding solar cells, J. Mater. Sci. Technol. 98 (2022) 268–271.

[12] W. Wang, M.T. Winkler, O. Gunawan, T. Gokmen, T.K. Todorov, Y. Zhu, D.B. Mitzi, Device characteristics of CZTSSe thin-film solar cells with 12.6% efficiency, Adv. Energy Mater. 4 (7) (2014).

[13] M. Umehara, S. Tajima, Y. Aoki, Y. Takeda, T. Motohiro, $Cu_2Sn_{1-x}Ge_xS_3$ solar cells fabricated with a graded bandgap structure, Appl. Phys. Exp. 9 (7) (2016) 072301.

[14] U. Chalapathi, P.U. Bhaskar, R. Cheruku, S. Sambasivam, S.-H. Park, Evolution of large-grained $CuSbS_2$ thin films by rapid sulfurization of evaporated Cu–Sb precursor stacks for photovoltaics application, Ceramic. Int. (2022).

[15] B. D. Cullity, Elements of X-Ray Diffraction, Addison Wesley, London, 1956, pp. 261–263.

[16] B.E. McCandless, Glancing incidence X-ray diffraction of polycrystalline thin films, MRS Online Proc. Lib. Arch. 865 (2005).

[17] D. Avellaneda, M.T.S. Nair, P.K. Nair, Cu_2SnS_3 and Cu_4SnS_4 thin films via chemical deposition for photovoltaic application, J. Electrochem. Soc. 157 (2010) D346–D352.

[18] U. Chalapathi, B. Poornaprakash, S.-H. Park, Fabrication of Cu_2SnS_3 films by annealing chemically deposited SnS–CuS precursors in a graphite box, J. Mater. Sci., Mater. Electron. 29 (2018) 1451–1462.

[19] A.P. Sreekala, A. Nadukkandy, S. Shaji, D.A. Avellaneda, J.A. Aguilar-Martínez, B. Krishnan, $AgSbS_{2-x}Se_x$ thin films: Structure, composition, morphology and photodetection properties, Mater. Today Commun. 27 (2021) 102362.

[20] V. Vinayakumar, S. Shaji, D. Avellaneda, T.D. Roy, G. Castillo, J. Martinez, B. Krishnan, $CuSbS_2$ thin films by rapid thermal processing of Sb_2S_3-Cu stack layers for photovoltaic application, Sol. Energy Mater. Sol. Cells 164 (2017) 19–27.

[21] A. Tubtimtae, C.-L. Huang, J.-B. Shi, M.-W. Lee, Ag_3SbS_3 thin films formed by annealing hydrothermally synthesized Ag_3SbS_3 nanoparticles, Mater. Let. 177 (2016) 58–60.

[22] C.-L. Chou, N. Suriyawong, B. Aragaw, J.-B. Shi, M.-W. Lee, Ag_3SbS_3 liquid-junction semiconductor-sensitized solar cells, J. Electrochem. Soc. 163 (6) (2016) H445.

J Mater Sci: Mater Electron (2024) 35:844

Effect of KNN substitution on the structural, electrical, and piezo characteristics of lead-free 0.94NBT–0.06$SrTiO_3$ ceramics

Nalamala Srinivasa Rao[1], B. Srikanth[1], T. Anjaneyulu[2], P. Mohan Babu[3], M. Bhaskaraiah[4], K. N. V. Lakshmi[5], and Kuppam Mohan Babu[6,*]

[1] *Department of Chemistry, Government Degree College, Cumbum, AP 523333, India*
[2] *Department of Physics, Narasaraopeta Engineering College, Narasaraopet, AP 522601, India*
[3] *Department of Physics, QIS College of Engineering and Technology, Ongole, AP 523272, India*
[4] *Department of Physics, Rajiv Gandhi University of Knowledge Technologies, RK Valley, Idupulapaya 516330, India*
[5] *Department of Freshman Engineering, Lakireddy BaliReddy College of Engineering, Mylavaram 521230, India*
[6] *Departments of Physics, Sri Venkateswara College of Engineering, Tirupati 517507, India*

Received: 19 December 2023
Accepted: 16 April 2024

© The Author(s), under exclusive licence to Springer Science+Business Media, LLC, part of Springer Nature, 2024

ABSTRACT

The conventional solid-state reaction approach was employed to develop 0.94NBT–0.06$SrTiO_3$ and 0.94NBT–0.06$SrTiO_3$–KNN lead free electro ceramics. Both ceramics coexist in the rhombohedral structural phase (*R*3*c*) and tetragonal structural phase (*P*4*mm*) regions. When $K_{0.5}Na_{0.5}NbO_3$ (KNN) is introduced to 0.94$Na_{0.5}Bi_{0.5}TiO_3$–0.06$SrTiO_3$, the structure grows more symmetric without compromising electrical polarization. The surface morphology of both ceramics is measured by the average grain size, which is reduced somewhat from 3 to 2.6 µm, resulting in the influence of KNN. The composition-induced local structural transition—i.e., the change from order to disorder-occurs when KNN is added to the 0.94NBT–0.06$SrTiO_3$ binary system. Additionally, the depolarization temperature (T_d) increases substantially with the inclusion of KNN. When KNN is present, the coercive field (E_c) dramatically reduces from 32 to 21 kV/cm (~ ΔE = 11 kV/cm), without impairing the remaining remnant polarization (P_r). When compared to 0.94NBT–0.06$SrTiO_3$, the substitution of KNN produces a high strain response of roughly 0.25% (under a mild field of 60 kV/cm). The longitudinal strain value of 140pC/N was determined parallelly. As a result, both of these lead-free ceramics are attractive prospects for next-generation electro ceramic applications.

Address correspondence to E-mail: mohan.kuppam@svcolleges.edu.in

https://doi.org/10.1007/s10854-024-12611-7
Published online: 24 April 2024

1 Introduction

Materials having many window operations are more appealing for today's generation of application. Because of their numerous features, including structural, electrical, and optical ones (*when an f-shell element is present*), ferroelectric materials represent a distinct class [1–4]. Due to a lack of efficiency, performance, and inadequate improvement of those required features, the current generation application still has an open window for the new material system. Ferroelectric systems are better ideal for improving such features by substituting them with alternative cations of appropriate sizes [5–7]. For modern applications such actuators & energy storage, materials having morphotropic phase boundaries (MPB) are more appealing. Due to both structural phases' collective additive qualities, which are the current emphasis at MPB, the desirable attributes are enhanced [8–10]. In light of this, PZT and its derivatives excel for the required commercial need [11–13]. The primary worry is regarding lead (Pb), which is very poisonous and harmful in nature and has significant health concerns, even though Pb-based materials offer outstanding ferro/piezoelectric characteristics for device applications. The European Union's Restriction of Hazardous Substances (ROHs) Directive committee has started to limit hazardous substances including Pb-based electrical and electronic components [14, 15]. There is an open window to replace these lead contained materials to replace the leaf free materials. Sodium bismuth titanate $Na_{0.5}Bi_{0.5}TiO_3$ (NBT) is one attractive contender because to its strong room temperature ferro electricity and good piezoelectric characteristics [16, 17]. MPB solid solutions based on BNT, such as $Na_{0.5}Bi_{0.5}TiO_3$–$BaTiO_3$ (NBT–BT) and $Na_{0.5}Bi_{0.5}TiO_3$–$Bi_{0.5}K_{0.5}TiO_3$ (NBT–BKT), were devised and produced to reduce electrical conductivity while also improving electromechanical responses [18, 19].

Despite significant developments and the demonstration of a few ultrasonic devices with acceptable performance, the overall piezoelectric capabilities of the lead-free substitutes were still inferior to the lead-based system. The issue of how to improve piezoelectric response is not only scientifically fascinating, but also technologically essential for piezoelectric device applications. Kounga and Zhang et al. have reported an extensive electric-field-induced strain response in $Bi_{0.5}Na_{0.5}TiO_3$–$K_{0.5}Na_{0.5}NbO_3$ (BNT–KNN) and $Bi_{0.5}Na_{0.5}TiO_3$–$BaTiO_3$–$K_{0.5}Na_{0.5}NbO_3$ (BNT–BT–KNN) solid solutions with S_{max}/E_{max} values of 300 pm/V and 560 pm/V, respectively [20, 21]. The incorporation of Zr^{4+} to BNT–BKT significantly increased strain up to 0.43% with S_{max}/E_{max} 614 pm/V was obtained [22]. In these very restricted examinations, the elevated strain level was comparable to the conventional PZT technological advances. Zhang et al. ascribed the high strain response to a field-induced antiferroelectric (AFE) to ferroelectric (FE) phase transition, in spite of the domain contribution. However, an AFE–FE shift in phase should always be coupled with a volume change [23, 24]. Jo et al. disproved this notion by concurrently measuring longitudinal and transverse strain. Hussain et al. hypothesized that the high strain was caused by the coexistence of ferroelectric and non-polar phases at ambient temperature. In a nutshell, the fundamental mechanism responsible for the high strain behavior is still discussed.

$SrTiO_3$ (ST) has a perovskite structure with cubic symmetry at room temperature. Previous studies showed that ST replacement of BNT was an effective technique for modifying the dielectric, piezoelectric, and ferroelectric features. At a critical composition of 0.28, Hiruma et al. found an important electric-field produced strain response [25–27]. However, the study focused mainly with room temperature. To encourage practical applications, systematic research of dielectric, ferroelectric, and piezoelectric responses were required. In light of these concerns, a ternary solid solution was devised and manufactured in this paper by adding KNN into the MPB composition 0.94NBT–0.06$SrTiO_3$. The present script focused on enhancing the required properties by introduces KNN into 0.94NBT–0.06$SrTiO_3$. The primary goal was to establish a correlation between the structural and electrical features of these specimens.

2 Experimental procedure

To create the eco-friendly $(1-x)$ 0.94NBT–0.06$SrTiO_3$–x KNN ($x = 0$ & 0.01) ceramics, the usual solid-state approach was used. The raw oxide materials (AR-grade) and carbonate were combined in a stoic proportion based on their weight percentage. These powdered oxides and carbonates were ball milled in ethyl alcohol for 10 h at 300 rpm. These dried powders were calcined at 800 °C for 3 h, milled for 10 h at 300 rpm, and mixed with 4 wt% polyvinyl alcohols for dry powders before being formed into a circular

disc with a radius of (= 10 mm). Finally, these circular discs were sintered in an air medium at 1150 °C for 3 h at a uniaxial heating rate of 5 °C/min. An X-ray diffractometer (CuKα radiation) was used to confirm the structural phase purity of these 0.94NBT–0.06$SrTiO_3$ and 0.94NBT–0.06$SrTiO_3$–xKNN ceramic powders. A field emission scanning electron microscope was employed for examining the surface morphology of these compounds. An impedance analyzer (E4980A; Agilent technologies corporation, Palo Alto, CA) was used to perform temperature-dependent dielectric measurements on the silver coated sintered ceramic discs from 30 to 500 °C with a frequency variation of 10 kHz. In order to evaluate the properties of ferroelectric loops, the samples were thinned down to 0.3 mm and measured with an ion-sputter coater on both sides of printed electrodes. The P–E loop test system (PolyK Technologies, USA) was used to measure the room temperature polarization loops and bipolar strain curves in silicon oil baths. The piezoelectric constant d_{33} was measured using a Berlin court d_{33} meter.

3 Results and discussion

The structural data (X-ray diffraction) of lead-free 0.94NBT–0.06$SrTiO_3$ and 0.94NBT–0.06$SrTiO_3$–KNN ceramics is shown in Fig. 1. These patterns show that both are crystallized into pure perovskite structures without secondary phases coexisting. The morphological structures from 20 to 80° demonstrate that there are no superlattice reflections caused by the oxygen octahedral tilt. Figure 1 shows the enhance portion of the $(111)_{PC}$ pseudocubic representation to confirm the effect/substitution of KNN over the 0.94NBT–0.06$SrTiO_3$. The displacement of the Bragg peak towards the lower angle side of the $(111)_{PC}$ peak indicates diffusion of KNN into 0.94NBT–0.06$SrTiO_3$. These ceramics structural existence is compared with duel phase model, which is found to be in good agreement with the duel phase rhombohedral structural phase ($R3c$) and tetragonal structural phase ($P4mm$) regions. The polarities will be moved parallel to the A-site and B-site cations, as well as the directions of the (111) Bragg peaks, because the rhombohedral structure is non-centrosymmetric and polar in order [28]. As a result, the addition of KNN will cause the long-range polar phase to be interrupted. Rietveld refinement was used to confirm the structural phase contribution/quantitative phase fractions

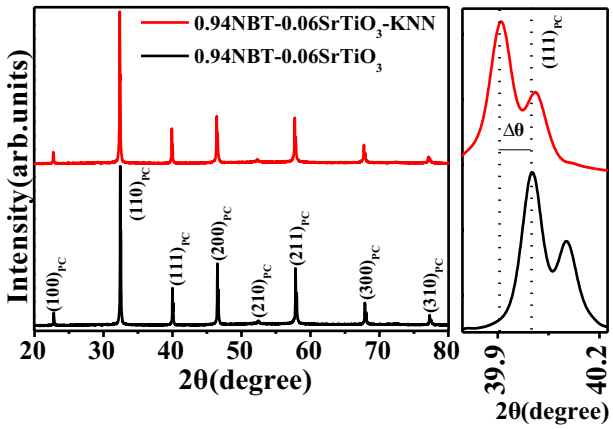

Fig. 1 Room temperature X-ray diffraction patterns of 0.94NBT–0.06$SrTiO_3$ and 0.94NBT–0.06$SrTiO_3$–KNN ceramics. The magnified window of $(111)_{PC}$ Brags reflection shown beside

over the substitution of KNN in 0.94NBT–0.06$SrTiO_3$ structural refinement of the XRD measurement. Several dual phase models, including rhombohedral ($R3c$) and tetragonal ($P4mm$), provide a reasonable match with stable fitting parameters. When compared to the $P4mm$ space group, $R3c$ makes a significant contribution. Table 1 shows the improved parameters for understanding the quality of fit. The refinement graph, as well as the Braggs locations and pseudocubic representations, are illustrated in Fig. 2.

The surface morphology of 0.94NBT–0.06$SrTiO_3$ and 0.94NBT–0.06$SrTiO_3$–KNN is shown in Fig. 3. Both surfaces are pore free according to this surface morphology. Each grain is easily identifiable by its distinctive grain boundaries and homogeneous grain distribution throughout all morphological microstructures. There was no evidence of phase segregation at the grain boundaries. In the presence of KNN, a little fluctuation in grain size throughout the whole surface indicated the compounds even distribution. The line intercept method (*ASTM International*) can be used to assess the grain size distribution of these specimens [29]. The Gaussian distribution function was used to optimize the average grain size, as illustrated in Fig. 2. For 0.94NBT–0.06$SrTiO_3$ and 0.94NBT–0.06$SrTiO_3$–KNN, the average grain size is found to be 3 µm and 2.6 µm, respectively (Fig. 4).

The P–E hysteresis loops for the 0.94NBT–0.06$SrTiO_3$ and 0.94NBT–0.06$SrTiO_3$–KNN ceramics have been evaluated at room temperature under the electric fields of 60–70 kV at frequency

Table 1 The structural refined parameters and lattice constants of 0.94NBT–0.06$SrTiO_3$–KNN ceramics

R3c	0.94NBT–0.06$SrTiO_3$–KNN		
Positions	*x*	*y*	*z*
Na/Bi/Sr/K	0.0000	0.2517	0.0000
Ti/	0.0000	0.2517	0.0000
NaNb	0.3013	0.0296	−0.0614
O	0.1982	0.2521	0.5107
$a=9.4460$ Å, $b=5.4783$ Å, $c=5.6120$ Å, $\alpha=\gamma=90°\beta=125.257°$			
P4mm	0.94NBT–0.06$SrTiO_3$–KNN		
Positions	*x*	*y*	*z*
Na/Bi/Sr/K	0.0010	0.49381	0.2500
Ti/	0.0000	0.2517	0.0000
NaNb	0.2130	0.2870	0.0260
O	−0.0572	0.0020	0.2510
O	0.2130	0.2870	0.0267
$a=3.8844$ Å, $b=3.8844$ Å, $c=3.9449$ Å, $\alpha=\gamma=\beta=90°$			

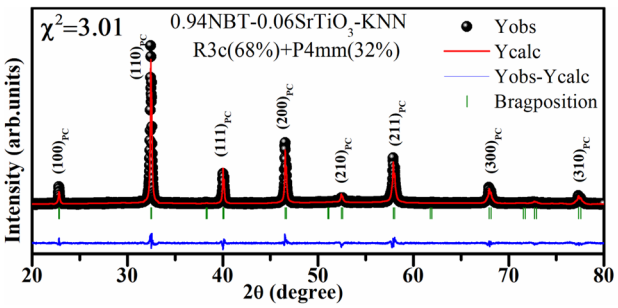

Fig. 2 Rietveld refinement of 0.94NBT–0.06$SrTiO_3$–KNN ceramics

1 Hz. In the presence of electric fields, both compounds display well saturated hysteresis loops with remarkable residual polarization (P_r) and saturation polarization (P_s). The presence of KNN is reduced slightly by the coercive field (E_C), as seen by the impact of substitution of KNN, which leads to domain wall clamping. These loops exhibit ferroelectric activity, and the broad square loops may be approximated using the equation can be found details elsware [30]. The value of R_{sq} for 0.94NBT–0.06$SrTiO_3$ and 0.94NBT–0.06$SrTiO_3$–KNN were found to be 1.98 and 1.81 respectively, which are in good agreement with the ideal square loops. The small reduction of R_{sq} value for 0.94NBT–0.06$SrTiO_3$–KNN is mainly due to the duel phase contribution of i.e., rhombohedral and tetragonal phase. This is found to be the impact of KNN on the structural property of 0.94NBT–0.06$SrTiO_3$.

The temperature-dependent dielectric constant (ε') and loss (tanδ) of 0.94NBT–0.06$SrTiO_3$ and 0.94NBT–0.06$SrTiO_3$–KNN ceramics are shown in Fig. 5 from room temperature to 500 °C at a frequency of 10 kHz. The observed curves were found to be similar to conventional peroskite-based lead-free ceramics. The loss curve clearly identifies the significant phase transition characteristics over the temperature T_d and T_c. The loss curves also follow the 0.94NBT–0.06$SrTiO_3$ and 0.94NBT–0.06$SrTiO_3$–KNN significant trend. When KNN is substituted in 0.94NBT–0.06$SrTiO_3$, the dielectric loss is reduced. The replacement of KNN in 0.94NBT–0.06$SrTiO_3$ reduces the T_d (by 15 °C) as compared to 0.94NBT–0.06$SrTiO_3$–KNN. Because of their diffuse phase transition, both of these ceramics demonstrated typical ferroelectric relaxor behavior. The dielectric constant does not obey the Curie–Weiss formula at this phase transition. The diffusiveness coefficient γ decides whether the material will behave ferroelectrically or not. The calculated γ values are found to be quite comparable, and slight increases for 0.94NBT–0.06$SrTiO_3$–KNN in compared to 0.94NBT–0.06$SrTiO_3$ lead to a more diffusive dielectric response. Figure 5 depicts the acquired results.

Figure 6a shows the d_{33} for 0.94NBT–0.06$SrTiO_3$ and 0.94NBT–0.06$SrTiO_3$–KNN ceramics after

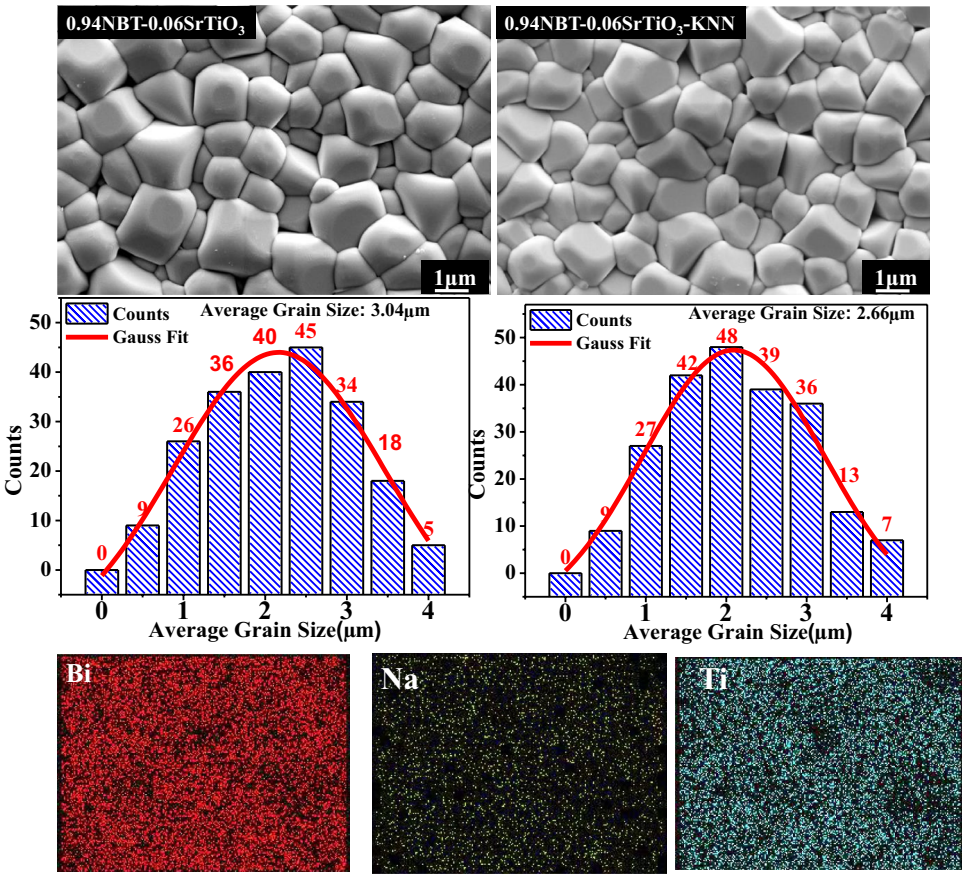

Fig. 3 The surface morphology and average grain size of 0.94NBT–0.06$SrTiO_3$ and 0.94NBT–0.06$SrTiO_3$–KNN ceramics

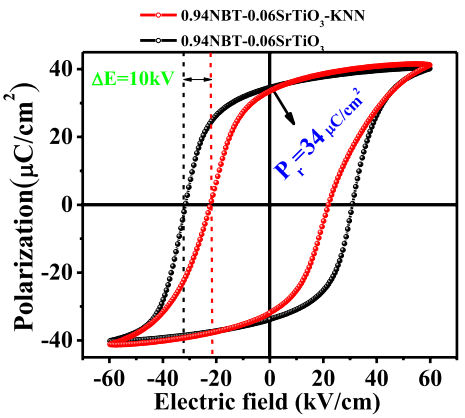

Fig. 4 Electrical polarization curves of 0.94NBT–0.06$SrTiO_3$ and 0.94NBT–0.06$SrTiO_3$–KNN ceramics with respect to the electric fields

25 min of DC poling at 55 kV/cm, d_{33} = 125pC/N for 0.94NBT–0.06$SrTiO_3$ was obtained, which was similar to existing standard reports. The replacement of KNN in 0.94NBT–0.06$SrTiO_3$ improves and achieves d_{33} = 145pC/N at the poling field lesser than 0.94NBT–0.06$SrTiO_3$. The increase in d_{33} could have been attributed to dielectric loss suppression in the presence of KNN [31]. At room temperature, bipolar strain curves of 0.94NBT–0.06$SrTiO_3$ and 0.94NBT–0.06$SrTiO_3$–KNN ceramics can be seen in Fig. 6b. These curves are composed of saturated butterfly shape loops, and the estimated strain value from the graph demonstrates the 0.94NBT–0.06$SrTiO_3$ strong ferroelectric nature. The increase in strain value of 0.94NBT–0.06$SrTiO_3$–KNN demonstrates the influence of KNN substitution in 0.94NBT–0.06$SrTiO_3$. This large shift in 0.94NBT–0.06$SrTiO_3$–KNN is mostly attributable to the secondary phase's contribution. In the presence of KNN, the positive strain (S_{pos}) ΔS increased drastically in 0.94NBT–0.06$SrTiO_3$ [32]. Simultaneously, the negative strain S (S_{neg}) for 0.94NBT–0.06$SrTiO_3$–KNN decreased, owing mostly to the greater dielectric constant.

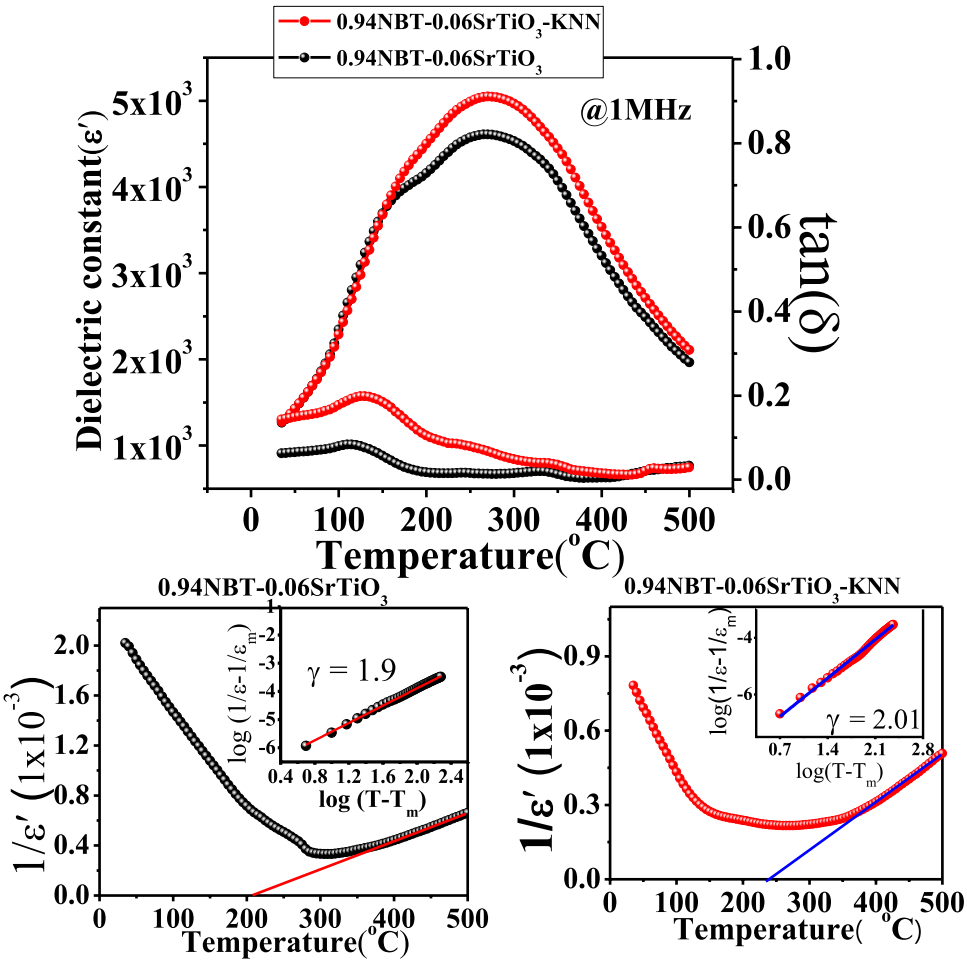

Fig. 5 The dielectric constant and loss with respect to the temperature of 0.94NBT–0.06$SrTiO_3$ and 0.94NBT–0.06$SrTiO_3$–KNN ceramics at 10 kHz. The diffuse constant (γ) of 0.94NBT–0.06$SrTiO_3$ and 0.94NBT–0.06$SrTiO_3$–KNN ceramics shown below the graph

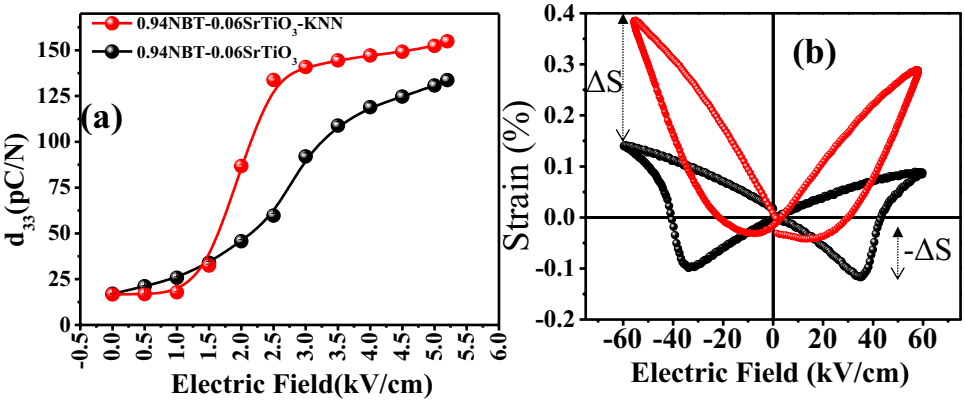

Fig. 6 **a** Piezoelectric coefficient (d_{33}) vs. electric of 0.94NBT–0.06$SrTiO_3$ and 0.94NBT–0.06$SrTiO_3$–KNN ceramics field and **b** Strain (S_{max}) vs Electric field curves of 0.94NBT–0.06$SrTiO_3$ and 0.94NBT–0.06$SrTiO_3$–KNN ceramics

4 Conclusions

In summary, the 0.94NBT–0.06$SrTiO_3$ and 0.94NBT–0.06$SrTiO_3$–KNN specimens were successfully synthesized with high density via the solid-state approach. As seen in Fig. 2, structural features quantitatively bring out additional phase contribution. Ferroelectric experiments showed a considerable increase in ferroelectric character, which was also visible in bipolar strain measurements, which improved by 0.25%. These synthetic chemicals

have been discovered to be beneficial for the present generation of commercial uses in industry.

Acknowledgements

Dr. A Chittibabu, department of physics, C. R. Reddy College of Engineering, is thanked for his assistance with structural refinement.

Author contributions

Nalamala Srinivasa Rao: investigation and methodology, B. Srikanth: data curation and writing draft, T. Anjaneyulu: methodology and data curation, P. Mohan Babu: methodology and data validation, M. Bhaskaraiah: data validation and review and editing the manuscript, K. N. V. Lakshmi: data validation, review and editing the manuscript, Kuppam Mohan Babu: conceptualization, supervision, and review and writing the manuscript.

Data availability

The authors declare that all the data generated or analyzed during this study are included in this manuscript.

Declarations

Conflict of interest The authors declare that they have no conflict of interest.

References

1. K.R. Kandula, S.S.K. Raavi, S. Asthana, Correlation between structural, ferroelectric and luminescence properties through compositional dependence of Nd^{3+} ion in lead free $Na_{0.5}Bi_{0.5}TiO_3$. J. Alloys Compd. **732**, 233–239 (2018)
2. K.R. Kandula, R. Yanamandra, S. Asthana, T. Patri, Observation of electrocaloric effect, thermal energy harvesting and energy storage density capabilities in Eu^{3+} and Nb^{5+} co-substituted lead-free $Na_{0.5}Bi_{0.5}TiO_3$ ceramics. Curr. Appl. Phys. **20**(9), 1066–1072 (2020)
3. K.R. Kandula, K. Banerjee, S.S.K. Raavi, S. Asthana, Enhanced electrocaloric effect and energy storage density of Nd-substituted 0.92NBT-0.08BT lead free ceramic. Phys. Status Solidi A **215**(7), 1700915 (2018)
4. Q. Peng, K.R. Kandula, Z. Xia, C. Zhang, Y. Zhang, Y. Yang, G. Zhang, Electric field induced phase transitions and electrocaloric effect of La^{3+} doped Pb (Zr, Sn, Ti) O_3 ceramics. Ceram. Int. **47**(10), 13939–13947 (2021)
5. K.R. Kandula, S. Asthana, S.S.K. Raavi, Multifunctional Nd^{3+} substituted $Na_{0.5}Bi_{0.5}TiO_3$ as lead-free ceramics with enhanced luminescence, ferroelectric and energy harvesting properties. RSC Adv. **8**(28), 15282–15289 (2018)
6. A. Moure, Review and perspectives of aurivillius structures as a lead-free piezoelectric system. Appl. Sci. **8**(1), 62 (2018)
7. R. Pandey, G. Vats, J. Yun, C.R. Bowen, A.W. Ho-Baillie, J. Seidel, S.I. Seok, Mutual insight on ferroelectrics and hybrid halide perovskites: a platform for future multifunctional energy conversion. Adv. Mater. **31**(43), 1807376 (2019)
8. W.C.W. Cao, L.E.C.L.E. Cross, The ratio of rhombohedral and tetragonal phases on the morphotropic phase boundary in lead zirconate titanate. Jpn. J. Appl. Phys. **31**(5R), 1399 (1992)
9. Z. Hanani, D. Mezzane, M.B. Amjoud, A.G. Razumnaya, S. Fourcade, Y. Gagou, M. Gouné, Phase transitions, energy storage performances and electrocaloric effect of the lead-free $Ba_{0.85}Ca_{0.15}Zr_{0.10}Ti_{0.90}O_3$ ceramic relaxor. J. Mater. Sci.: Mater. Electron. **30**, 6430–6438 (2019)
10. M. Maraj, W. Wei, B. Peng, W. Sun, Dielectric and energy storage properties of $Ba_{(1-x)}Ca_xZr_yTi_{(1-y)}O_3$ (BCZT): a review. Materials **12**(21), 3641 (2019)
11. C.H. Nguyen, S. Pietrzko, R. Buetikofer, The influence of temperature and bonding thickness on the actuation of a cantilever beam by PZT patches. Smart Mater. Struct. **13**(4), 851 (2004)
12. M. Khalili, A.B. Biten, G. Vishwakarma, S. Ahmed, A.T. Papagiannakis, Electro-mechanical characterization of a piezoelectric energy harvester. Appl. Energy **253**, 113585 (2019)
13. K.R. Kandula, T. Patri, S. Asthana, Nd^{3+} and Nb^{5+} co-substitution inducing a large electrocaloric response in $Na_{0.5}Bi_{0.5}TiO_3$ lead-free ceramics. Physica Status Solidi (b) **256**(8), 1900001 (2019)
14. S. Menon, E. George, M. Osterman, M. Pecht, High lead solders (over 85%) solder in the electronics industry: RoHS exemptions and alternatives. J. Mater. Sci.: Mater. Electron. **26**, 4021–4030 (2015)

15. A. Turner, M. Filella, Hazardous metal additives in plastics and their environmental impacts. Environ. Int. **156**, 106622 (2021)
16. E. Aksel, J.L. Jones, Advances in lead-free piezoelectric materials for sensors and actuators. Sensors **10**(3), 1935–1954 (2010)
17. J. Song, J. Wang, Ferroelectric materials for vibrational energy harvesting. Sci. China Technol. Sci. **59**, 1012–1022 (2016)
18. T. Takenaka, H. Nagata, Y. Hiruma, Current developments and prospective of lead-free piezoelectric ceramics. Jpn. J. Appl. Phys. **47**(5S), 3787 (2008)
19. Y. Hiruma, K. Yoshii, H. Nagata, T. Takenaka, Phase transition temperature and electrical properties of $(Bi_{0.5}Na_{0.5})TiO_3$–$(Bi_{0.5}A_{0.5})TiO_3$ (A = Li and K) lead-free ferroelectric ceramics. J. Appl. Phys. **103**(8), 084121 (2008)
20. A.B. Kounga, S.T. Zhang, W. Jo, T. Granzow, J. Rödel, Morphotropic phase boundary in $(1-x)Bi_{0.5}Na_{0.5}TiO_3$–$xK_{0.5}Na_{0.5}NbO_3$ lead-free piezoceramics. Appl. Phys. Lett. (2008). https://doi.org/10.1063/1.2938064
21. S.T. Zhang, A.B. Kounga, E. Aulbach, H. Ehrenberg, J. Rödel, Giant strain in lead-free piezoceramics $Bi_{0.5}Na_{0.5}TiO_3$–$BaTiO_3$–$K_{0.5}Na_{0.5}NbO_3$ system. Appl. Phys. Lett. (2007). https://doi.org/10.1063/1.2783200
22. T. Wang, L. Zhang, J. Liu, A. Zhang, J. Liu, G. Chen, L. Jin, Effects of unique ion B-site modulation on the structure, dielectric and ferroelectric properties of NBT-BT based ceramics. J. Mater. Sci.: Mater. Electron. **34**(4), 270 (2023)
23. M.H. Zhang, L. Fulanović, C. Zhao, J. Koruza, Review on field-induced phase transitions in lead-free $NaNbO_3$-based antiferroelectric perovskite oxides for energy storage. J. Materiomics **9**(1), 1–18 (2023)
24. Y. Liu, J.F. Scott, B. Dkhil, Direct and indirect measurements on electrocaloric effect: recent developments and perspectives. Appl. Phys. Rev. **3**(3), 031102 (2016)
25. W. Krauss, D. Schütz, F.A. Mautner, A. Feteira, K. Reichmann, Piezoelectric properties and phase transition temperatures of the solid solution of $(1-x)(Bi_{0.5}Na_{0.5})TiO_3$–$xSrTiO_3$. J. Eur. Ceram. **30**(8), 1827–1832 (2010)
26. K. Sakata, Y. Masuda, Ferroelectric and antiferroelectric properties of $(Na_{0.5}Bi_{0.5})TiO_3$-$SrTiO_3$ solid solution ceramics. Ferroelectrics **7**(1), 347–349 (1974)
27. Y. Hiruma, Y. Imai, Y. Watanabe, H. Nagata, T. Takenaka, Large electrostrain near the phase transition temperature of $(Bi_{0.5}Na_{0.5})TiO_3$–$SrTiO_3$ ferroelectric ceramics. Appl. Phys. Lett. **92**(26), 262904 (2008)
28. G.O. Jones, P.A. Thomas, Investigation of the structure and phase transitions in the novel A-site substituted distorted perovskite compound $Na_{0.5}Bi_{0.5}TiO_3$. Acta Crystallogr. B **58**(2), 168–178 (2002)
29. J.A. Salem, M.G. Jenkins, Applying ASTM International C1421 to glasses and optical ceramics, in *Proceeding of the 42nd International Conference on Advanced Ceramics and Composites: Ceramic Engineering and Science Proceedings*, vol. 39, issue 2 (2019), pp. 27–39
30. S. Wongsaenmai, S. Ananta, R. Yimnirun, Effects of addition of BT on structural phase formation and electrical properties of relaxor ferroelectric $Pb(In_{0.5}Nb_{0.5})_{(1-x)}Ti_{(x)}O_3$ ceramics. J. Alloys Compd. **474**(1–2), 241–245 (2009)
31. H.J. Seog, A. Ullah, C.W. Ahn, I.W. Kim, S.Y. Lee, J. Park, S.H. Kim, Recent progress in potassium sodium niobate lead-free thin films. J. Korean Phys. Soc. **72**, 1467–1483 (2018)
32. H. Xi, L. Yu, H. Qian, F. Chen, M. Mao, Y. Liu, Y. Lyu, Large strain with low hysteresis in Sn-modified $Bi_{0.5}(Na_{0.75}K_{0.25})_{0.5}TiO_3$ lead-free piezoceramics. J. Mater. Sci. **55**(4), 1388–1398 (2020)

Publisher's Note Springer Nature remains neutral with regard to jurisdictional claims in published maps and institutional affiliations.

Springer Nature or its licensor (e.g. a society or other partner) holds exclusive rights to this article under a publishing agreement with the author(s) or other rightsholder(s); author self-archiving of the accepted manuscript version of this article is solely governed by the terms of such publishing agreement and applicable law.

J Mater Sci: Mater Electron **(2024) 35:454**

Observations on the structural, piezoelectric, and impedance properties of cation-(La and Sn) modified lead zirconium titanate (PLZST) ceramics

Kalpana Tirumalasetti[1], J. Ashok[2], Ravi Gudiguntla[3], N. Ch. Ramesh Babu[4], P. Geetha[5], Virupakshi Prabhakar[6,*], G. Nagaraju[7], A. Chitti Babu[8], and Pandiri Sreedhar[9,*]

[1] *Department of Physics, Andhra Loyola College, Vijayawada, Andhra Pradesh 520 008, India*
[2] *Department of Science and Humanities, SRK Institute of Technology, Enikepadu, Vijayawada, Andhra Pradesh 521108, India*
[3] *Department of Chemistry, Krishna University, Machilipatnam, Andhra Pradesh 521004, India*
[4] *Department of Physics, Rajiv Gandhi University of Knowledge Technologies, Nuzividu, Andhra Pradesh 521202, India*
[5] *Department of Physics, Sri Venkateswara College of Engineering, Tirupati, Andhra Pradesh 517507, India*
[6] *Department of Chemistry, Rajiv Gandhi University of Knowledge Technologies, Ongole, Andhra Pradesh 523225, India*
[7] *Department of Physics, Sri Venkateswara University, Tirupati, Andhra Pradesh 517502, India*
[8] *Department of Physics, Sir. C.R. Reddy College of Engineering, Eluru, Andhra Pradesh 534007, India*
[9] *Department of Chemistry, Geethanjali College of Engineering and Technology, Hyderabad 501305, India*

Received: 19 December 2023
Accepted: 20 February 2024
Published online: 28 February 2024

© The Author(s), under exclusive licence to Springer Science+Business Media, LLC, part of Springer Nature, 2024

ABSTRACT

The structural ambiguity was resolved quantitatively with dual-phase models of *Cc* + *P4mm*. Multiple-phase transition behaviors including Antiferroelectric (AFE) to Ferroelectric transition, transition at depolarization temperature, and AFE to paraelectric state transition were observed among PLZST samples and investigated in detail. The piezoelectric and impedance features of a modified PZT ceramic that has different mole ratios of La and Sn co-substitution are shown here. The principle of Archimedes shows that the synthesized specimens have sufficient density for withstanding high temperatures and higher fields while explaining them. We concentrated on the impedance and piezoelectric coefficients d_{33}, g_{33}, and figure of merit (FOM) of the ideal $PbLaZrSnTiO_3$ (PLZST) composition (50/30/20) in this study. The PLZSTs consist of two phases (*Cc* + *P4mm*), which combine to generate a single phase with a high Sn content and a low La content. These structural correlations coexist with the dual evaluation of impedance and piezoelectric characteristics in order to produce optimum composition. In order to evaluate the impedance features, the property of activation energy for the grains also supports the PLZST (50/30/20) having superior properties among PLZSTs. The optimum composition will meet the current business's commercial needs through multiple windows.

Address correspondence to E-mail: virupakshiprabhakarsku@gmail.com; sreedhar.pandiri@gmail.com

https://doi.org/10.1007/s10854-024-12244-w

1 Introduction

Multifunctional materials or ceramics have attracted a lot attention in the modern era due to their numerous window operations [1–3]. PZT and its analogs are widely used in the communication, medical, and electrical industries due to their low cost and outstanding accuracy. PZT's outstanding characteristics have applications in energy storage devices as well as positive and negative electro-caloric properties [4, 5]. Because of their remarkable properties, multiple organizations [6–9] have looked into the PZT and PLZT systems simultaneously; as a consequence, these materials are opening new avenues to address current generation concerns [10–12]. They showed, for instance that these materials are outstanding for electro-caloric effect cooling because of their significant dipolar entropy shift during the transition from the antiferroelectric to the ferroelectric phase. These ceramic specimens involve crystallite grains of different sizes that are linked together in a variety of arbitrarily ways [9, 13]. These zones of grain amalgamation are referred to as boundaries of grain, and they are greatly impacted by external factors such as heating and cooling, an external electric field, and so on. The interfacial behavior of grain boundaries enables electroceramics [8, 14]. In device application, all ceramic specimens are connected to the system through electrodes. These electrodes can function as a grain-to-grain barrier system with programmable effect settings [15]. Impedance spectroscopy is an invaluable tool to determine the entire profile picture of the grain and grain boundary profile. The results of impedance spectroscopy not only provide values for grain contribution and grain boundary, but also provide a comparable circuit model for modeling [16, 17]. Even if the model has been taken into account, choosing one that works might be hard. A particular model was developed for these PLZST specimens to draw the proper predicted outcomes and provide information for the design of advanced devices. The fault makeup of solid-state specimens plays an important role in these new potential applications. Understanding how desired characteristics interact with imperfections and vacancies on the site was important [18, 19]. The co-substitution of La and Sn in varying ratios affects interior imperfections such as voids at A- and B-sites. Site vacancies and electrons at space charges affect the ferroelectric fatigue or impedance/conductive properties of materials [20–23]. The use of AC impedance analysis for identifying the cause of failure at grain–grain boundaries is an adaptable technique. It must also build its relaxation method by providing distinctive resistance and capacitance values to the grain and grain border effects.

The excellent properties of PZT have drawn a lot of attention in the area of polar-based materials devices. The pure form of PZT has a higher d_{33} value when compared to all polar materials [24]. The increased value of d_{33} in PZT produced by altering the phase boundary additionally indicates an important increase in device effectiveness. Piezo-coefficients have been produced in this instance by averaging many internal ionic crystal polarizations. These piezo-coefficient values are a consequence of stationary charges building up at both ends caused by crystal structural deformation. This domain mobility has discovered applications in power-controlling electric devices [25]. These devices have controls, and their efficiency/performance is evaluated using a figure of merit (FOM).

2 Experimental details

The PZT-based polycrystalline ceramics $(Pb_{0.94}La_{0.06})(Zr_xSn_{0.30}Ti_{0.70-x})O_3$($x$ = 0.54, 0.52, 0.50, and 0.48) have been synthesized using a conventional solid-state reaction. The high-grade raw metal oxide chemical powders of PbO, La_2O_3, TiO_2, ZrO_2, and SnO_2 (99% AR Grade, Chemicals) were used as initial precursors for synthesis. These raw materials were weighed according to their mole ratio and mixed properly. The mixed powders were further mixed properly using ball milling over the time 10 h with 300 rpm for all specimens and then calcined at 840 °C for 3 h. After mixing uniformly, these powders were pressed into circular disks with a uniform thickness of 10 mm diameters by adding 8 wt% of PVA (*Poly vinyl Alcohol*) as binder solution prepared in IPA solution. These circular disks were sintered in alumina crucibles in the presence of PZT powder to play down the lead volatilization and then placed in a box furnace. These circular disks were sintered at 1250 °C for 3 h with a uniaxial rate of heating of 5 °C/min. These ceramics were polished on different emery sheets for a fine thickness of 0.2 mm with a uniform surface. The structural phase purity of polycrystalline ceramics was confirmed by using X-ray diffractometer (XRD, 7000S/L, Shimadzu Corp, Japan) using Cu Kα radiation. The temperature-dependent dielectric and impedance measurements on

the disk with electrodes were performed by using a computer-controlled LCR meter (Tonghui TH2828S, China) within the temperature range from − 5 to 600 °C with a uniform heating rate of 2 °C/min. The specimens were poled electrically at room temperature in a silicon oil bath (DOW CORNING 704) by applying DC electric fields of 0–60 kV/cm for constant time for each equal interval of time. These piezocoefficients were estimated with the help of Piezometer System PM300 (Piezotest Ltd.) operated at a frequency of 100 Hz.

3 Results and discussion

An efficient method for determining the structural distortion of polycrystalline materials is the X-ray diffraction (XRD) technique. Figure 1 shows the XRD patterns of Zr- and Ti-substituted PZT (PLZST) ceramics. Every ceramic was stabilized in a pure perovskite structure, devoid of any secondary phases coexisting with it. Super lattice reflections of monoclinic Cc have been described in literature paired with the room-temperature structure, specifically for PZT [26]. As Zr content increases at the Ti site, the peak combines and appears as a single peak. The existence of dual phase over the substitution of Zr- and Ti-substituted PZT, analyzed phase contribution quantitatively employing a methodical structural refinement procedure. Throughout the series, Rietveld refinement was

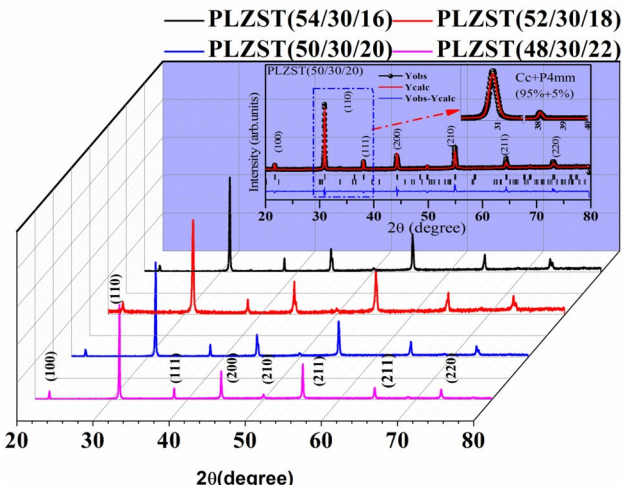

Fig. 1 Powder X-ray diffraction patterns of PLZST (54/30/16), PLZST (52/30/18), and PLZST (50/30/20) and PLZST (48/30/22). Inset shows the Rietveld refined pattern of PLZST(50/30/20), which existing in the *Cc* + *P4mm* duel phase model with reducing tetragonal reflections

performed using full proof software [27]. We choose various dual structural phase models to eform refinement by validating the structural coexistence. In order to determine the coexistence of the structural phase model for PLZST (50/30/20), the clear indication is yielded that fit was extremely good fit with *Cc* + *P4mm*. The quality and goodness of fit for PLZST (50/30/20) are shown in the inset of Fig. 1.The inset shows the evidence of the significant intense Brag reflection of the $(110)_{pc}$ peak's best fit. The refine parameters, atomic positions, and lattice constants are provided in Table 1.

The temperature-dependent dielectric permittivity (ε) and tangent loss (tan δ) of the unpoled samples under a selected frequency of 100 kHz are presented in Fig. 2.The dielectric anomaly indicated by T_m, which is the most significant dielectric constant value and is related to the phase transition from the antiferroelectric to the paraelectric region, was seen in each specimen. For each specimen, the phase transition sequence exhibits a comparable pattern. At the lower temperature side (*before depolarization* T_d), the permittivity decreases with compositional variation and all exhibit broad peaks, suggesting the features of a diffuse phase transition [28, 29]. The dielectric permittivity value is very high for PLZST (50/30/20) compared to other ceramics PLZST (54/30/16), PLZST (52/30/18), and PLZST (48/30/22). A significant improvement in dielectric permittivity indicates that as the Ti^{4+} concentration increases and the Zr^{4+} content decreases simultaneously, the antiferroelectricity gets lower and the ferroelectricity gets higher. At the same time, the temperature corresponding to maximum ε (named as T_m) shifts slightly towards a lower temperature region upon decreasing the ratio of Zr/Ti. All these samples have shown the typical ferroelectric relaxor ferroelectric behavior due to the diffuse phase transition [30].

Figure 3 shows a schematic representation of domains and straightforward distinguished status of grain boundaries, as well as unpoled and poling situations. In terms of quantities, the orientation of domains across a particular axis represents the d_{33} and g_{33} values. Because of the orientation of the [001] plane [31], the maximum values of d_{33} and g_{33} were achieved. These PLZST polycrystalline ceramics' structural phase purity and multi-phase coexistence could have been seen elsewhere [32]. The presence of a dual structural phase [9] within the PLZST (50/30/20) with the co-substitution of La and Sn leads to the superior desirable features of these specimens. After poling the samples at high fields

Table 1 Structural refined parameters of monoclinic Cc and tetragonal P4mm space

Cc	PLZST(50/30/20)		
Positions	*x*	*y*	*z*
Pb/La	0.0000	0.2517	0.0000
Zr/Ti/Sn	0.0000	0.2517	0.0000
O_1	0.3013	0.0296	− 0.0614
O_2	0.1982	0.2521	0.5107
$a=9.5291$ Å, $b=5.4956$ Å, $c=5.5016$ Å, $\alpha=\gamma=90°$, $\beta=125.257°$			
P4mm	PLZST(50/30/20)		
Positions	*x*	*y*	*z*
Pb/La	0.0010	0.49381	0.2500
Zr/Ti/Sn	0.0000	0.2517	0.0000
O_1	0.2130	0.2870	0.0260
O_2	− 0.0572	0.0020	0.2510
O_3	0.2130	0.2870	0.0267
$a=3.8844$ Å, $b=3.8844$ Å, $c=3.9449$ Å, $\alpha=\beta=\gamma=90°$			
$\chi^2=2.51$			

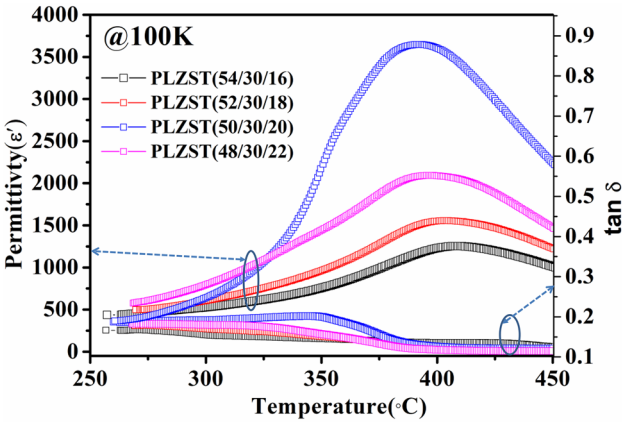

Fig. 2 Temperature dependent of dielectric constant (ε ε′) and loss *tan*(*δ*) of these ceramics at 100 kHz for PLZST (54/30/16), PLZST (52/30/18), PLZST (50/30/20), and PLZST(48/30/22) ceramics, respectively

at room temperature, the piezo-coefficient (d_{33}) and voltage coefficient (g_{33}) were calculated for these PLZST specimens, as shown in Fig. 4a, b. To figure out the systematic domain orientation profile, we estimate the corresponding values of d_{33} and g_{33} of PLZST (50/30/20) after providing the specimen to fields that vary from (0.5–5) kV/cm. The PLZST (50/30/20) d_{33} and g_{33} values develop gradually and achieve saturation at maximum fields. The possibility of electrical, ionic, and orientation polarization in the presence of an electric field is mainly accountable for the enhancement of d_{33} and g_{33} [33]. The FOM is mainly helpful to figure out if materials possess commercial utility dependent on the required features. The parameter FOM will decide the performance of the PLZST in this instance, and calculating the value of FOM employing dielectric loss indicates the PLZST (50/30/20).With the help of FOM, we can estimate the device performance, where piezo material can exist.

The electrical response (*i.e.*, transport characteristics) of polycrystalline samples at different temperatures has been examined with complex impedance spectroscopy [34, 35]. This spectroscopy offers the direction and correlation of the real system and paired electrical circuits with discrete electrical components. Figure 5 displays the Nyquist graphs of PLZST (54/30/16), PLZST (52/30/18), PLZST (50/30/20), and PLZST (48/30/22) at 600 °C. At lower temperatures, the features of a single semicircle apply to the essential conduction mechanism. At the same temperature, the impedance spectrum intercepts alterations towards the origin, indicating that the resistivity property of the material reduces with substitution of La and Sn in PZT. These specimen impedances with compositional variation were reproduced at the same temperature employing a suitable/equivalent circuit built up of bulk resistance

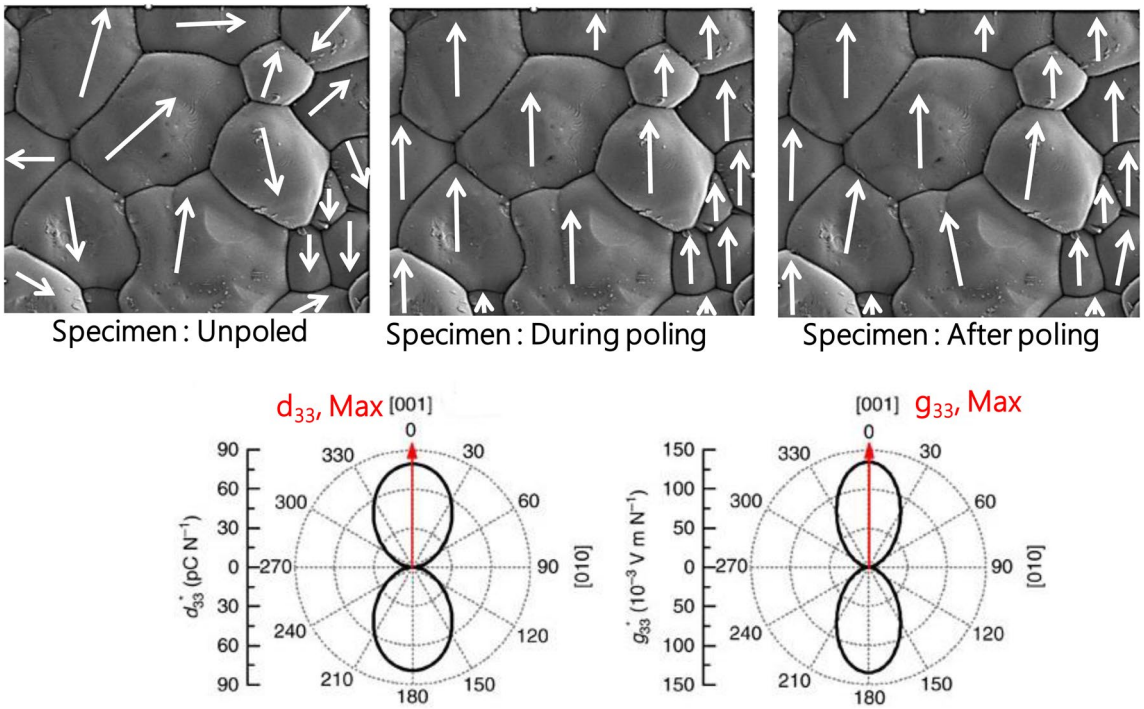

Fig. 3 Schematic representation of domain orientation under unpoled and poled conditions and the axial rotation of domain while, measuring the d_{33} and g_{33} at room temperature

R and CPE (constant phase element) linked in parallel. After fitting, the following equation provides accurate R and CEP data [35].

$$Z = \frac{1}{[T(jw)^P]}, \tag{1}$$

where CPE is represented in capacitance units and is the angular frequency ($\omega = 2\pi f$). The equations for the real (Z′) and imaginary (Z″) impedance components of the similar circuit are provided in the potential reports [35]. The difference in relaxation time is demonstrated by the substitution shifts of La and Sn symmetry (semicircle) size with frequency decreases in quantity. These different time constant values represent non-delay relaxation types. Apart for the PLZST (50/30/20), the peak oscillates from higher to lower frequency, which is the opposite of ideal nature's tendency. In a consequence, the effect of La and Sn substitution on the electrical properties of PLZST is evident across the spectra.

In general, it can be done to create oxygen vacancies while sintering oxide-based perovskites. The normal Ti^{4+} contribution decreases as well oxygen vacancies. The ferroelectric fatigue tolerance is explained by the control of oxygen vacancies in the presence of La^+ ion replacement [34]. Cation substitution impacts behavior and is highly tied to structural defects. The structural shortcomings caused by cation substitution are going to be significant interest. These can be understood through impedance spectroscopy. The plot of the imaginary part of (Z′/Z″) compared to frequency of PLZST(54/30/16), PLZST(52/30/18), PLZST(50/30/20), and PLZST(48/30/22) can be seen in Fig. 6. The aforementioned graphs represent the Debay peaks with the greatest frequency characteristic shifts in the temperature range and just represent the grain contribution. With increasing temperatures, the maximum frequency values of PLZST (54/30/16), PLZST (52/30/18), PLZST (50/30/20), and PLZST (48/30/22) altered towards higher frequencies, reflecting decreases in relaxation time ($\tau = 1/2\pi f_{max}$).

$$\tau = \tau_0 \exp\left(\frac{E_g}{k_{BT}}\right). \tag{2}$$

It is commonly understood that is the relaxation time, ER is the dielectric relaxation activation energy, K_B is the Boltzmann constant, and T is the absolute temperature. The values of E_g in both specimens show

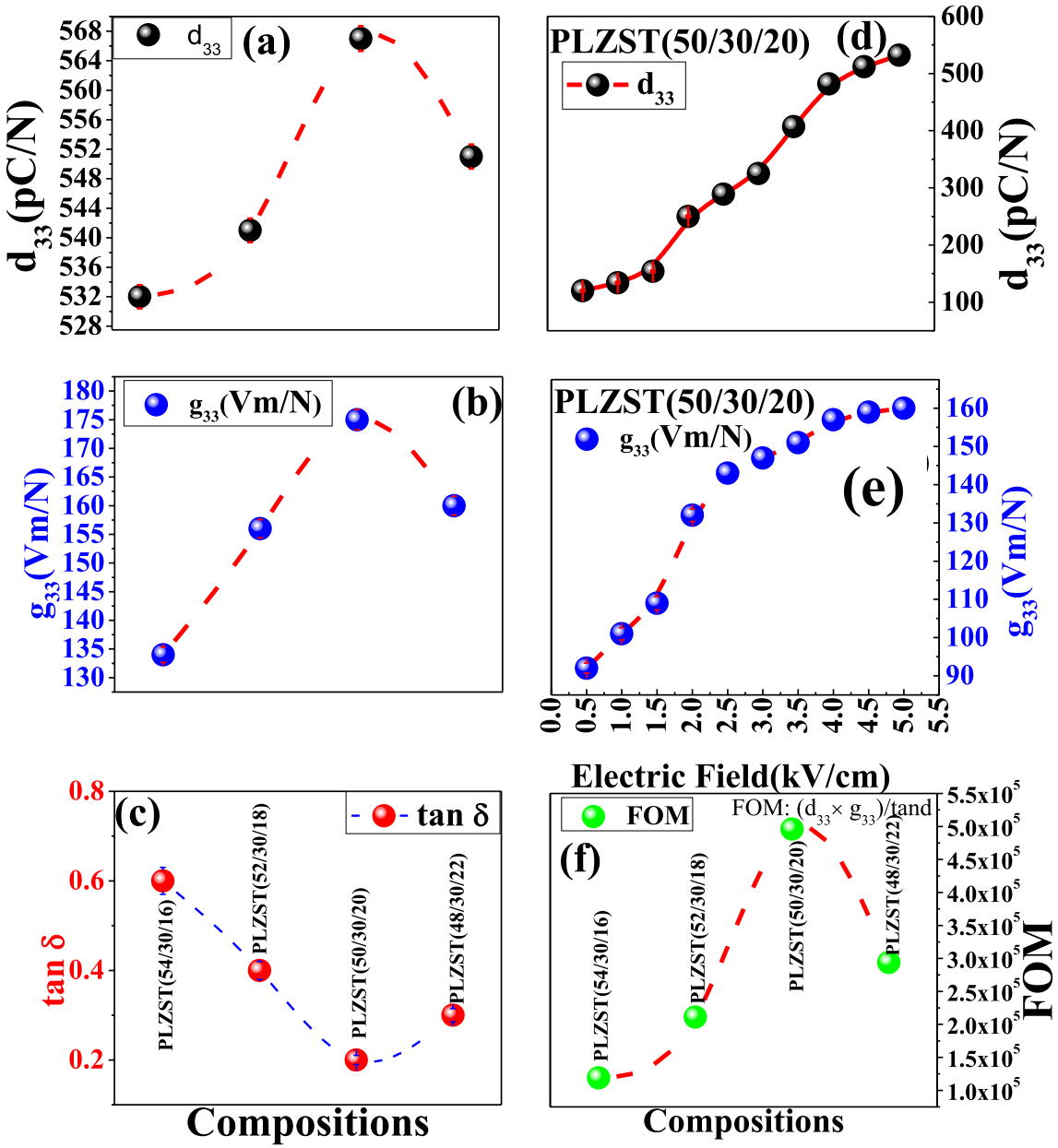

Fig. 4 **a** Room-temperature measurement of Piezo-coefficient (d_{33}) of PLZST(54/30/16), PLZST(52/30/18), PLZST(50/30/20), and PLZST(48/30/22). **b** Piezoelectric voltage coefficient (g_{33}) and dielectric loss (tan δ) @ (**c**), Figure of merit @ (**f**) of PLZST(54/30/16), PLZST(52/30/18), PLZST(50/30/20), and PLZST(48/30/22). The Piezo-coefficient (d_{33}) @ (**d**) and Piezoelectric voltage coefficient (g_{33}) @ (**e**) at different fields for the PLZST (50/30/20)

similar dielectric relaxation. The E_g values here suggest that the existence of oxygen vacancies plays an important role in dielectric relaxation. The activation energy E_g for the smiles is slightly greater than the contribution of the grain boundary. Table 2 shows the values of complete set bulk resistance and capacitance as they sweep the temperature range from 400 to 600 °C. Figure 7 shows the inverse of frequency (relaxation time) versus function of temperature in order to figure out the grain contribution for these specimens. The E_g, value for the PLZST (50/30/20) shows that the structure easily supports the grain or domain orientation for obtaining better d_{33} and g_{33} while achieving lower dielectric loss.

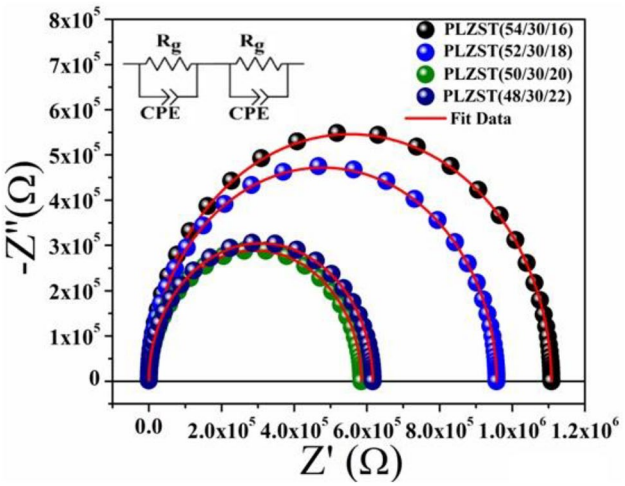

Fig. 5 Experimental and simulated semicircles plot at 600 °C for the PLZST(54/30/16), PLZST(52/30/18), PLZST(50/30/20), and PLZST(48/30/22)

4 Conclusions

A solid-state approach was employed to successfully produce high-density pure phase polycrystalline materials. The structural phase purity of these substances was quantified via structural refinement. From structural phase purity, it was confirmed that PLZST ceramics were successfully synthesized via a solid-state route. The dual phase presence of P4mm and Cc over the co-substitution of $Zr^{4+}$and Ti^{4+} in PLZST (50/30/20) ceramics confirms the contribution of both polarization directions. The piezoelectric and impedance studies suggested that the PLZST (50/30/20) is the most effective composition. The estimated activation energy of these specimens also supports the ideal composition. This perfect chemical is a viable choice for meeting the commercial needs of industries.

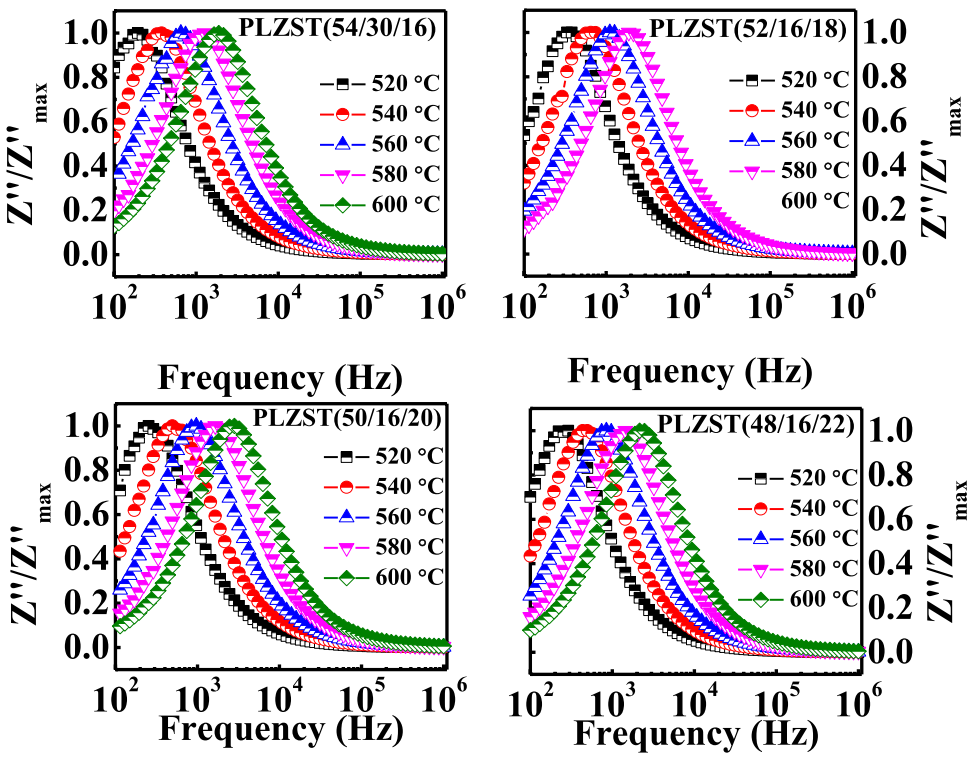

Fig. 6 Frequency dependence of imaginary part of impedance (Z′/Z″) of PLZST(54/30/16), PLZST(52/30/18), PLZST(50/30/20), and PLZST(48/30/22)

Table 2 Bulk resistance R and CPE (constant phase element) of PLZST(54/30/16), PLZST(52/30/18), PLZST(50/30/20), and PLZST(48/30/22)

Temp (°C)	Rg(Ω) PLZST(54/30/16)	CPE(nF)	Rg(Ω) PLZST(52/30/18)	CPE(nF)	Rg(Ω) PLZST(50/30/20)	CPE(nF)	Rg(Ω) PLZST(48/30/22)	CPE(nF)
400	4.38×10^{8}	0.14	7.128×10^{8}	0.1685	3.714×10^{8}	0.2082	3.438×10^{8}	0.2275
420	1.717×10^{8}	0.13	2.374×10^{8}	0.1535	1.41×10^{8}	0.188	1.263×10^{8}	0.2.064
440	1.01×10^{8}	0.124	9.986×10^{7}	0.141	6.159×10^{7}	0.1722	5.53×10^{7}	0.1894
460	5.0049×10^{7}	0.1142	5.142×10^{7}	0.131	3.077×10^{7}	0.1621	2.7×10^{7}	0.1758
480	2.699×10^{7}	0.1078	2.5789×10^{7}	0.1227	1.529×10^{7}	0.1504	1.407×10^{7}	0.164
500	1.453×10^{7}	0.1045	1.39×10^{7}	0.1147	7.682×10^{6}	0.144	7.503×10^{6}	0.1522
520	8.174×10^{6}	0.094	7.588×10^{6}	0.1092	4.046×10^{6}	0.1505	4.29×10^{6}	0.1447
540	4.678×10^{6}	0.09328	4.319×10^{6}	0.1042	2.25×10^{6}	0.154	2.53×10^{6}	0.1373
560	2.73×10^{6}	0.08964	2.549×10^{6}	0.09735	1.3957×10^{6}	0.1407	1.519×10^{6}	0.1296
580	1.6298×10^{6}	0.08555	1.54×10^{6}	0.09307	894,000	0.1155	940,000	0.1243
600	1.107×10^{6}	0.08055	956,800	0.08899	584,800	0.1051	616,000	0.1171

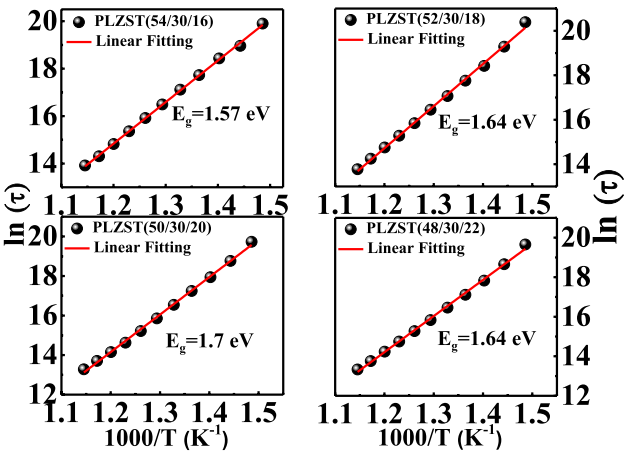

Fig. 7 Inverse frequency (relaxation time) versus temperature of PLZST(54/30/16), PLZST(52/30/18), PLZST(50/30/20), and PLZST(48/30/22)

Acknowledgements

Authors' sincere thanks to Dr. Rajashekar Reddy for his help in refinement and data analysis.

Author contributions

KT: Investigation and methodology, JA: Data curation and writing draft, RG: Methodology and data curation, NCRB, PS: Methodology and data validation, PG: Data validation and review and editing the manuscript, GN, ACB, Data validation, review, and editing the manuscript. VP: Conceptualization, supervision, and review and writing the manuscript.

Funding

The authors have not disclosed any funding.

Data availability

The authors declare that all the data generated or analyzed during this study are included in this manuscript.

Declarations

Conflict of interest The authors declare that they have no conflict of interest.

References

1. K.R. Kandula, S. Asthana, S.S.K. Raavi, Multifunctional Nd^{3+}substituted $Na_{0.5}Bi_{0.5}TiO_3$ as lead-free ceramics with enhanced luminescence, ferroelectric and energy harvesting properties. RSC Adv. **8**, 15282 (2018). https://doi.org/10.1039/C8RA01349G
2. M. Aissa, M. Zannen, H.A. Alzahrani, J. Belhadi, Y. Hadouch, D. Mezzane, A. Lahmar, Multifunctionality of rare earth doped $0.925Na_{0.5}Bi_{0.5}TiO_3$–$0.075K_{0.5}$ $Na_{0.5}NbO_3$

ferroelectric ceramics. J. Alloys Compd. **921**, 166188 (2022). https://doi.org/10.1016/j.jallcom.2022.166188
3. J. Xiao, W. Jiang, D. Han, K. Li, L. Lou, Evolution of crystallographic orientation and microstructure in the triangular adapter of grain continuator of a 3rd-generation single crystal super alloy casting during directional solidification. J. Alloys Compd. **898**, 162782 (2022). https://doi.org/10.1016/j.jallcom.2021.162782
4. M.J. Haun, E. Furman, S.J. Jang, L.E. Cross, Thermodynamic theory of the lead zirconate-titanate solid solution system, part I: phenomenology. Ferroelectrics **99**(1), 13–25 (1989). https://doi.org/10.1080/00150198908221436
5. M. de Oliveira, N.V. Araujo, R.N. Da Silva, T.I. Da Silva, J. Epaarachchi, Use of savitzky–golay filter for performances improvement of SHM systems based on neural networks and distributed PZT sensors. Sensors **18**(1), 152 (2018). https://doi.org/10.3390/s18010152
6. Y. Zhao, X. Hao, Q. Zhang, A giant electrocaloric effect of a $Pb_{0.97}La_{0.02}(Zr_{0.75}Sn_{0.18}Ti_{0.07})O_3$ antiferroelectric thick film at room temperature. J. Mater. Chem. C. **3**, 1694–1699 (2014). https://doi.org/10.1039/C4TC02381A
7. B.A. Tuttle, D.A. Payne, The effects of microstructure on the electrocaloric properties of Pb(Zr, Sn, Ti)O_3 ceramics. Ferroelectrics **37**, 603–606 (1981). https://doi.org/10.1080/00150198108223496
8. Q. Peng, K.R. Kandula, Z. Xia, C. Zhang, Y. Zhang, Y. Yang, G. Zhang, Electric field induced phase transitions and electrocaloric effect of La^{3+} doped Pb (Zr, Sn, Ti)O_3 ceramics. Ceram. Int. **47**(10), 13939–13947 (2021). https://doi.org/10.1016/j.ceramint.2021.01.262
9. K.R. Kandula, T. Shet, M. Nuthalapati, K.L. Rao, A.A. Ansari, A.C. Babu, N.N. Rao, S. Vadnala, R. Bhimireddi, Structural phase modulation in Lanthanum and Tin co-substituted Pb(Zr, Ti)O_3 ceramics and its energy and pyro-energy storage properties. Phys. Status Solidi A **220**, 0421 (2022)
10. A.M. Jalaja, S. Dutta, Ferroelectrics and multiferroics for next generation photovoltaics. Adv. Mater. Lett. **6**(7), 568–584 (2015). https://doi.org/10.5185/amlett.2015.5878
11. J. Rödel, W. Jo, K.T. Seifert, E.M. Anton, T. Granzow, D. Damjanovic, Perspective on the development of lead-free piezoceramics. J. Am. Ceram. Soc. **92**(6), 1153–1177 (2009). https://doi.org/10.1016/S1003-6326(14)63302-1
12. S.J. Buwalda, K.W. Boere, P.J. Dijkstra, J. Feijen, T. Vermonden, W.E. Hennink, Hydrogels in a historical perspective: from simple networks to smart materials. J. Control. Release **190**, 254–273 (2014). https://doi.org/10.1016/j.jconrel.2014.03.052
13. M.D. Ali, F. Majid, A. Aslam, A. Malik, I. Wahid, A.J.C.I. Dahshan, Dielectric and electrical properties of synthesized PBGO/Fe_3O_4 nanocomposite. Ceram. Int. **47**, 26224–26232 (2021). https://doi.org/10.1016/j.ceramint.2021.06.030
14. Y. Li, S. Wu, X. Lv, J. Feng, F. Cheng, Study on the influence of interlayer temperature on microstructure and mechanical properties of submerged arc additively manufactured low-carbon steel and its in-situ toughening mechanism. J. Manuf. Process. **71**, 356–373 (2021). https://doi.org/10.1016/j.jmapro.2021.09.016
15. A.L. Usler, R.A. De Souza, A critical examination of the Mott-Schottky model of grain-boundary space-charge layers in oxide-ion conductors. J. Electrochem. Soc. **168**(5), 056504 (2021). https://doi.org/10.1149/1945-7111/abfb37
16. F.M. Casallas-Caicedo, E. Vera-López, J. Roa-Rojas, Impedance spectroscopy study of electrical response and correlation with structural properties in the $La_2SrFe_2CoO_9$ triple complex perovskite. Phys. B **607**, 412865 (2021). https://doi.org/10.1016/j.physb.2021.412865
17. A. Hassan, Z. Wang, Y.H. Ahn, M. Azam, A.A. Khan, U. Farooq, Y. Cao, Recent defect passivation drifts and role of additive engineering in perovskite photovoltaics. Nano Energy (2022). https://doi.org/10.1016/j.nanoen.2022.107579
18. Y. Zheng, T.J. Slade, L. Hu, X.Y. Tan, Y. Luo, Z. Luo, M.G. Kanatzidis, Defect engineering in thermoelectric materials: what have we learned? Chem. Soc. Rev. **50**, 9022–9054 (2021). https://doi.org/10.1039/D1CS00347J
19. S.S. Dani, A. Tripathy, N.R. Alluri, S. Balasubramaniam, A. Ramadoss, A critical review: impact of electrical poling on longitudinal piezoelectric strain coefficient. Mater. Adv. (2022). https://doi.org/10.1039/D2MA00559J
20. I. Ali, H.A. ElMeleegi, A.A. Moez, Investigation of structural, optical dielectrical and optical conductivity properties of $BaTiO_3$, $Al_{0.01}Ba_{0.99}TiO_3$ and $La_{0.01}Ba_{0.99}TiO_3$ thin films prepared by pulsed laser deposition. Phys. Scr. **94**(12), 125810 (2019). https://doi.org/10.1088/1402-4896/ab1f25/meta
21. A.I. Ali, S. El-Sayed, A. Hassen, Change the ferroelectric properties of $Al_{0.01}Ba_{0.99}TiO_3$ ceramics by $Al_{0.01}Sr_{0.99}TiO_3$ doping. Results. Phys. **14**, 102368 (2019). https://doi.org/10.1016/j.rinp.2019.102368
22. A.I. Ali, A. Hassen, N.C. Khang, Y.S. Kim, Ferroelectric, and piezoelectric properties of $BaTi_{1-x}Al_xO_3$, $0 \leq x \leq 0.015$. AIP Adv. (2015). https://doi.org/10.1063/1.4930859
23. A.I. Ali, C.W. Ahn, Y.S. Kim, Enhancement of piezoelectric and ferroelectric properties of $BaTiO_3$ ceramics by aluminum doping. Ceram. Int. **39**(6), 6623–6629 (2013). https://doi.org/10.1016/j.ceramint.2013.01.099

24. T.F. Schranghamer, M. Sharma, R. Singh, S. Das, Review and comparison of layer transfer methods for two-dimensional materials for emerging applications. Chem. Soc. Rev. **50**, 11032–11054 (2021). https://doi.org/10.1039/D1CS00706H
25. H.P. Kim, H. Wan, C. Luo, Y. Sun, Y. Yamashita, T. Karaki, X. Jiang, A review on alternating current poling for perovskite relaxor-$PbTiO_3$ single crystals. IEEE Trans. Ultrason. Ferroelectric Freq. Control (2022). https://doi.org/10.1109/TUFFC.2022.3181236
26. B. Noheda, J. Gonzalo, L. Cross, R. Guo, S.E. Park, D. Cox, G. Shirane, Tetragonal-to-monoclinic phase transition in a ferroelectric perovskite: the structure of $PbZr_{0.52}Ti_{0.48}O_3$. Phys. Rev. B **61**, 8687–8695 (2000). https://doi.org/10.1103/PhysRevB.61.8687
27. E.A. Pandiscio, Exploring the link between preservice teachers' conception of proof and the use of dynamic geometry software. Sch. Sci. Math. (2002). https://doi.org/10.1111/j.1949-8594.2002.tb18144.x
28. G. Zhang, S. Jiang, Y. Zhang, T. Xie, Pyroelectric properties in three phases coexistence $Pb[(Mn_{0.33}Nb_{0.67})_{0.5}(Mn_{0.33}Sb_{0.67})_{0.5}]0.08(ZrxTi_{1-x})_{0.92}O_3$ lead ceramics. Curr. Appl. Phys. **9**, 1434–1437 (2009). https://doi.org/10.1016/j.cap.2009.03.019
29. X. Ding, L. Xu, Z. Hu, X. Chen, G. Wang, X. Dong, J. Chu, Phase diagram and incommensurate antiferroelectric structure in $(Pb_{1-1.5x}La_x)(Zr_{0.42}Sn_{0.40}Ti_{0.18})O_3$ ceramics discovered by band-to-band optical transitions. Appl. Phys. Lett. **105**, 131909 (2014). https://doi.org/10.1063/1.4897357
30. K.R. Kandula, S.S.K. Raavi, S. Asthana, Correlation between structural, ferroelectric and luminescence properties through compositional dependence of Nd^{3+} ion in lead free $Na_{0.5}Bi_{0.5}TiO_3$. J. Alloys Compd. **732**, 233–239 (2018). https://doi.org/10.1016/j.jallcom.2017.10.186
31. B. Tiwari, T. Babu, R.N.P. Choudhary, AC impedance and modulus spectroscopic studies of $Pb(Zr_{0.35-x}Ce_xTi_{0.65})O_3$(x=0.00,0.05,0.10&0.15) ferroelectric ceramics. Mater. Chem. Phys. **256**, 123655 (2020). https://doi.org/10.1016/j.matchemphys.2020.123655
32. J. Qi, M. Cao, Y. Chen, Z. He, C. Tao, H. Hao, H. Liu, Cerium doped strontium titanate with stable high permittivity and low dielectric loss. J. Alloys Compd. **772**, 1105–1112 (2019). https://doi.org/10.1016/j.jallcom.2018.09.061
33. H. Chen, J. Xing, J. Xi, T. Pu, H. Liu, J. Zhu, Phase, domain, and microstructures in Sr^{2+} substituted low-temperature sintering PZT-based relaxor ferroelectrics. J. Am. Ceram. Soc. **104**(12), 6266–6276 (2021). https://doi.org/10.1111/jace.17989
34. X. Xu, X. Liu, R. Rao, Y. Zhao, H. Du, J. Shi, Electrical properties and conduction mechanisms of K, Ga co-substituted $Na_{0.5}Bi_{0.5}TiO_3$ [NBT] ferroelectrics. Ceram. Int. **46**, 22321–22329 (2020). https://doi.org/10.1016/j.ceramint.2020.05.312
35. I. Rivera, A. Kumar, N. Ortega, R.S. Katiyar, S. Lushnikov, Divide line between relaxor, diffused ferroelectric, ferroelectric and dielectric. Solid State Commun. **149**(3–4), 172–176 (2009). https://doi.org/10.1016/j.ssc.2008.10.026

Publisher's Note Springer Nature remains neutral with regard to jurisdictional claims in published maps and institutional affiliations.

Springer Nature or its licensor (e.g. a society or other partner) holds exclusive rights to this article under a publishing agreement with the author(s) or other rightsholder(s); author self-archiving of the accepted manuscript version of this article is solely governed by the terms of such publishing agreement and applicable law.